EXISTING AND CONCEPTUAL SHIP-GRILLAGE STIFFENER OPTIMIZATION THROUGH MAXIMIZING OVERLOAD CAPACITY UNDER TRANSVERSE LOADS

by

© Jordan M. Norman, B.Eng.

A thesis submitted to the School of Graduate Studies

in partial fulfillment of the requirements for the degree of

Master of Engineering

Faculty of Engineering and Applied Science

Memorial University of Newfoundland

October 2020

St. John's Newfoundland and Labrador Canada

Abstract

The HMCS IROQUOIS naval destroyer was decommissioned in 2015. Six ship hull sections have been sent to Memorial University of Newfoundland for detailed structural analyses. An investigation has been undertaken to determine if significant improvements could be made to the IROQUOIS grillage panels. If significant improvements were possible it was important to determine how the grillage could then be optimized. The study focused on grillage stiffener design. Numerous stiffener designs were tested by varying factors related to their geometric and parametrized dimensions. Both finite element analysis and experimental design techniques were implemented within the study. The statistical significance of the studied factors was analyzed to develop more detailed and specific, experiments. Control runs were tested which consisted of built-T and flat bar stiffened panels, as well as the IROQUOIS grillage panels. An optimized concept grillage was produced which demonstrated an ability to outperform the control runs.

Acknowledgements

I would like to thank my supervisor, Dr. Bruce Quinton, for this opportunity and his continued guidance.

I would like to thank my co-supervisor Dr. Claude Daley for our many inspirational discussions and his infectious enthusiasm for the work.

I would like to thank Dr. Ahmed Elruby for his finite element software tutorials and for his willingness to helping those around him, including myself.

I would like to thank the project partners at DRDC, ABS, and Vard, for this wonderful opportunity and the guidance and direction during my research.

I want to thank my fellow peers, Andrew Greenham, Mahdi Omidali, Lt Matthew Lee Robbins, and Spencer Holloway, for our fruitful discussions and for helping to create an atmosphere where we could freely develop and discuss our evolving ideas.

I would like to thank the academic unit within the Engineering Department at Memorial University of Newfoundland for helping to build an engaging environment where students can reach their full potential.

I would like to thank Mr. Matt Curtis for his constant enthusiasm and drive to ensure that the experimental side of the project was always moving forward.

I would like to thank the Department of Technical Services for their work in helping my research reach its full-scale fruition.

I would like to thank my loving wife, Zara, for putting up with me as I surrounded myself with my research for the last two years, and for pushing me toward my dreams.

I would like to thank Scarlett and Skye for being so understanding while I have been engaged in my studies so deeply.

Lastly, I would like to thank my parents Daphne Norman, Barry Norman, and Cynthia Morgan, for always teaching me that I can do whatever I want in life and for the inspiration you have continually given me.

Table of Contents

List of Tables

List of Figures

List of Symbols, Nomenclature or Abbreviations

Built-T – a stiffener, similar to a formed Tee. However, it is built from two flat bars. Both the web and flange have rectangular cross-sectional shapes.

Exp1 through Exp5 – The five main experiments conducted within this thesis.

First Yield Point – for the purpose of this thesis, has been defined as the point where the material discontinues to behave linearly with respect to a force vs. displacement curve. The definition of first yield point used should not be confused with the general definition of first yield point as it pertains to stress/strain curves. Within the text, first yield point has been used interchangeably with first yield and yield point.

Global Model – A relatively large grillage model consisting of three components: stiffeners, frames, and side-shell plating. Effectively, the Global Model is formed by combining several Local Models and adding transverse frames to connect the stiffener ends. Two versions of the Global Model exist – one found in Exp3 and another found in Exp5. The term becomes most relevant in discussions surrounding Exp5 where the Global Model is compared to a Local Model.

Grillage – for the purpose of this thesis, has been defined as a stiffened-panel side-shell section of a ship. The basic structure consists of a design of three stiffeners attached perpendicular to a side-shell plate. Within the text, grillage has been used interchangeably with stiffened panel and panel.

IBS – An impact, normal to the grillage side-shell, directly between two stiffeners at the middle of their span.

Internal Energy – for the purpose of this thesis, has been used interchangeably with the energy absorption capability of the structure, as well as, simply, energy.

IOS – An impact, normal to the grillage side-shell, directly on a stiffener.

IOSC – An impact, normal to the grillage side-shell, directly on a stiffener at the centre of the stiffener span.

IOSQ – An impact, normal to the grillage side-shell, directly on a stiffener at a quarter-span of the stiffener.

L/10 or L/100 – Length of the stiffener span divided by 10 or 100, respectively.

Local Model – A relatively small grillage model consisting of two components: stiffeners and side-shell plating. The Local Model consists of exactly three stiffeners connected to the side-shell plating. The Local Model was used in Exp4 and Exp5. The term becomes most relevant in discussions surrounding Exp5 where the Global Model is compared to a Local Model.

Optimization – for the purpose of this thesis has been defined as maintaining the grillage weight while maximizing the following properties of the structure: internal energy, first yield point, and overload capacity. Optimization is usually aided by delaying the onset of buckling.

Overload Capacity – for the purpose of this thesis, has been defined as the amount of internal energy a grillage can absorb after the first yield point. Within the text, overload capacity has been used interchangeably with plastic reserve capacity. Regarding

discussions involving internal energy within the elastic regime, sometimes the terms elastic internal energy capacity, elastic capacity, or elastic energy absorption capacity, were used.

S Corrugation or 'S' Corrugation – A corrugation shape which forms a sine wave when viewed from a plan view.

Test1 through Test6 – The six main tests conducted within Exp2 of this thesis.

Traditional Corrugation – A corrugation shape consistent which most corrugated bulkheads. It is similar to S corrugation, except the corrugation consists of straight edges.

Analysis of variance – ANOVA

Boundary Condition – BC

Circular Hollow Section – CHS

Design of Experiments – DOE

Finite Element – FE

Finite Element Analysis – FEA

Finite Element Model/Modelling – FEM

Large Pendulum Apparatus – LPA

Mesh Convergence Analysis – MCA

Polar Class – PC

Response Surface Methodology – RSM

List of Appendices

Chapter 1 Introduction

Traditional stiffeners, such as built-T (a stiffener, similar to a formed Tee, built from two flat bars) and flat bar stiffeners, are largely designed to mitigate structural yielding. For ice-class vessels, a small amount of yielding is acceptable (IACS 2019). However, for non-ice-class vessels, structural yielding is unacceptable (Paik and Thayamballi 2003). Therefore, traditional stiffeners are designed to have high initial stiffness and elastic capacity. As a result, stiffeners oftentimes have a relatively low plastic reserve (the amount of internal energy a structure can absorb after the first yield point, also known as overload capacity). Inadvertently, maximizing a stiffener's elastic capacity could have the effect of diminishing the stiffener's overload capacity.

Under dynamic loading scenarios, most of the structural strength can be lost after yielding occurs. The stiffener is then unable to provide adequate stiffness to the surrounding structure. In many cases, the stiffener would have to be replaced after sustaining even a relatively small amount of plasticity.

A numerical investigation has been undertaken to maximize the stiffener's ability to provide significant plastic capacity in the event of a local collision. The optimized structure has been designed to have equal weight and elastic capacity as compared to industry-standard side-shell stiffeners. Except for Exp1 (one of the five main experiments conducted within this thesis), a frictionless, smooth, rigid indenter has been used to impact the grillages (stiffened-panel side-shell sections of a ship). Further details concerning the rigid indenter can be seen in Section: 3.7 Rigid Indenter Design. The experimental simulations have been set up to be validated against testing results from the large pendulum apparatus

(LPA) to be completed at a later date. The LPA has been developed for experimental ship-ice and ship-ship structural interactions (Gagnon, et al. 2015). The LPA is capable of representing impacts between a test subject, and an indenter. Further details concerning the LPA can be seen in Section: 3.6 Large Pendulum Apparatus. Within the LPA, the concept grillage will be tested and compared to a set of grillages from the HMCS IROQUOIS. The IROQUOIS is a decommissioned Canadian naval destroyer. More information regarding the IROQUOIS can be seen in Section: 1.2 Background.

A concept stiffener design has been achieved and was compared to standard built-T and IROQUOIS grillage stiffeners, under dynamic impact loading conditions. The concept grillage is a variable web-height, flangeless, stiffener that is optimized for impact loading scenarios normal to the side-shell. Three impact scenarios were simulated which consisted of an impact on a stiffener at mid and quarter-span, as well as an impact directly between stiffeners. To deform as much as the standard built-T and flat bar control runs, the concept design was demonstrated to require 19.7 % more impact energy, for indentations as large as 100 mm. Concerning indentations less than 60 mm, the concept design outperformed the IROQUOIS grillages for all load cases studied. Concerning indentations less than 120 mm, the concept design outperformed the IROQUOIS grillages for five out of the six load cases studied.

The conducted work is divided into nine chapters. The introduction chapter defines the background, problem statement, and the motivations for investigating this area of research. Chapter 2 details the literature review. Chapter 3 details the methodology and discusses how experimental simulations were conducted. Chapters 4 through 8 discuss the five major

sets of experimental simulations (one numerical investigation per chapter) along with their results and conclusions. Chapter 9 discusses the overall conclusions and significant insights into the study, as well as future work recommendations.

1.1 Problem Statement

Modern ship design is focused much more on the elastic capacity of ship structures rather than the plastic capacity. Therefore, existing side-shell stiffener arrangements are often optimized to have a high degree of elastic capacity. The conducted work investigates the behaviour of a variety of both conventional and conceptual side-shell grillage stiffeners in an attempt to increase the stiffener's overload capacity without compromising weight or elastic capacity. In elastic design, the structure is optimized for transverse loads by maximizing structural stiffness to lessen deformations. Maximizing structural stiffness also increases the amount of internal energy (energy absorption capability of the structure) required for the structure to yield. However, optimizing a structure for elastic capacity could compromise the plastic reserve capacity of the structure. The conducted work investigates how geometric stiffener alterations relate to significant plastic reserve improvements, without compromising initial stiffness or elastic capacity. All loads were applied transversely and dynamically in impact scenarios.

1.2 Background

The Royal Canadian Navy has recently begun the revitalization process of its fleet of ships. One of the vessels that has been decommissioned from this process was the destroyer known as the HMCS IROQUOIS (see Figure 1.1). After its decommissioning in 2015, from nearly 45 years of service life, six side-shell grillages (see Figure 1.2) were cut from the

vessel's hull and sent to Memorial University of Newfoundland for detailed structural analyses. Each grillage contains three longitudinal Tee stiffeners and is approximately 7 ft by 7 ft in area.

Figure 1.1: HMCS IROQUOIS (Shaw 2013).

Figure 1.2: One of the six HMCS IROQUOIS side-shell grillages.

1.3 Investigation Motivation

Built-T stiffeners are often used in shipbuilding due to their ability to resist mid-span deflection from a central load (bending) due to their cross-sectional properties. In turn, the stiffener has a tremendous amount of initial stiffness and elastic capacity. However, within many dynamic loading scenarios, once yield occurs much of the strength of the stiffener can be lost. Likely due to the inertia of the flange from the dynamic loading, the stiffener web is unable to displace within the direction of the load and buckles locally.

Conversely, the flat bar stiffener (Built-T without a flange) solves the issue of local buckling due to the lack of a flange. However, instead of buckling locally, it trips. Also, without the extra support of the flange at the ends, the stiffener often experiences end-buckling. See Figure 1.3 and Figure 1.4 for visual aids of this phenomenon.

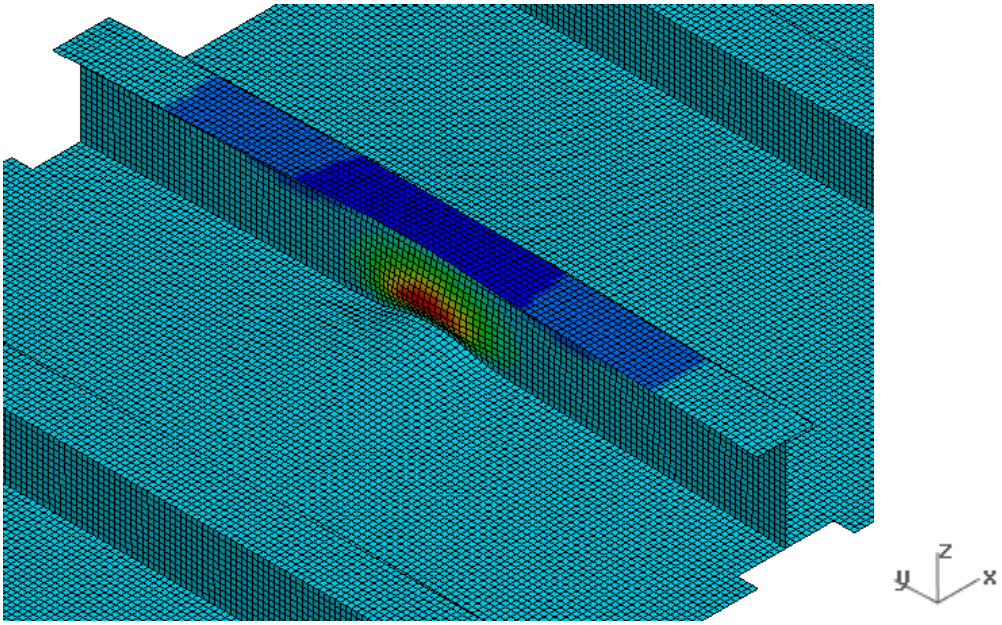

Figure 1.3: Local buckling within a built-T stiffener.

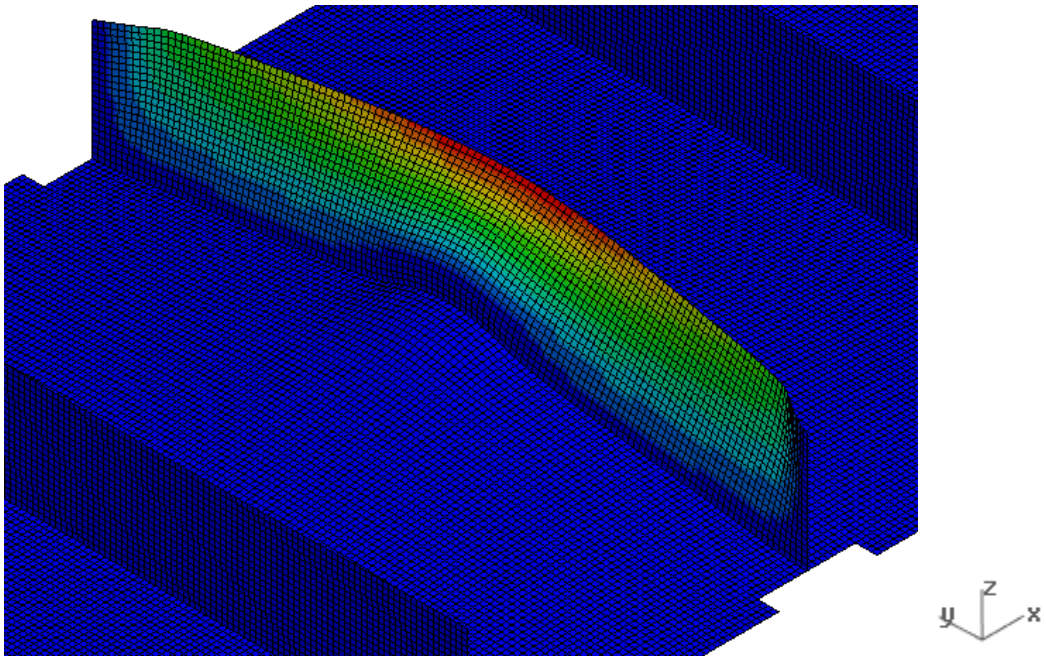

Figure 1.4: Tripping within a flat bar stiffener.

In current shipbuilding, the post-yield behaviour of steel is of little concern since ship designs do not allow for structural yielding (Paik and Thayamballi 2003). More recently, concerning ice-class vessels, the discussion has been opened to explore the post-yield behaviour of materials as most of the structural strength may lay within the region. Therefore, the purpose of this investigation is to identify a more optimal stiffener that maximizes the plastic reserve capacity to make better use of the full range of potential stiffener deformations. An optimized stiffener should be capable of absorbing a significant amount of energy even after large deformations, caused by a dynamic impact loading scenario. The grillage structures from the IROQUOIS were compared to various conventional and conceptual grillage designs. The comparisons were made to better understand how the structure could be improved.

Chapter 2 Literature Review

The following subsections include a review of available, relevant, topics that relate to the conducted work. The major topics for review include impact testing, finite element model (FEM) guidelines, corrugation techniques, overload capacity, buckling modes, and structural optimization (maintaining the grillage weight while maximizing the internal energy, first yield point, and overload capacity). A full-scale version of the finalized concept grillage is intended to be tested in the LPA as a validation for the FEM used throughout the analysis portion of this research. Therefore, it was important to study previous work related to impact scenarios to ensure proper setup and proper result extraction. To simulate the collisions, several indenters have been used in the form of rigid steel indenters as well as various ice shaped indenters. Also, guidelines have been produced, which detail proper FEM techniques involving highly nonlinear impact scenarios. Corrugation has been widely used in the shipbuilding industry in the form of corrugated bulkheads, but not a lot is known about its use in stiffener design. The literature review also details overload capacity, which describes the available capacity of a structural member, generally, within the plastic regime. The three distinct buckling modes related to grillage side-shell stiffeners are local buckling, tripping, and end-buckling. Each buckling mode is distinct from one another and often require different mitigation techniques. Lastly, the literature review discusses optimization – a technique that has been employed in many fields as a tool to ensure that processes are highly efficient. Moreover, optimization has been explored specifically related to various types of steel structures.

2.1 Impact Load Testing

An example of previous research involving the LPA involves an impact panel known as the NRC Impact Panel (Gagnon 2008). The NRC Impact Panel was used as the test subject, which was impacted by an ice cone. In his doctoral dissertation, (Quinton 2015) conveniently detailed the ice formation process utilized in modern ice-ship impact interactions. The goal of the experiment involving the NRC Impact Panel was to verify that the impact panel was capable of providing accurate data, which in turn validated the capabilities of the LPA. The study showed that the impact panel was fit for purpose within the constraints of the testing environment (Sopper, et al. 2015). More details concerning the Impact Module can be seen in (Gagnon 2008).

The LPA has been designed to facilitate other full-scale impacts, like the one proposed in this research. Instead of an ice indenter, a steel indenter can be used to perform high-energy impact scenarios. Using a rigid steel indenter aids in the study of the grillage side of the pendulum by introducing a more controlled environment. The rigid indenter side of the pendulum does not deform plastically and deforms elastically only negligibly.

2.1.1 Sliding Loads

Though sliding loads (or moving loads) were not investigated explicitly within this research, recent studies have found it non-conservative to omit their contribution to certain structural impact scenarios. Therefore, the conclusions of such studies were considered for future work.

Sliding loads refer to impacts which do not occur normal to the test subject. (Quinton 2008) demonstrated that moving loads, on ship structures, can significantly decrease the structural capacity of a ship structure. It is often not conservative to ignore sliding load effects. As predicted by (Quinton 2008), …" the normal direction structural reaction of a steel plate subject to a moving object that incites a plastic plate response is considerably weaker than that exerted on a stationary object applying the same normal direction load." Extensive research has shown that plastic buckling is induced at a much lower load for sliding loads compared to stationary loads (Quinton 2015). Through the use of a frictionless/rigid indenter, the tests showed that structural capacity losses were a real consequence (Quinton, et al. 2017). Therefore, moving loads cannot be ignored whenever there is a possibility of plasticity. The two structural members that are often least conservatively predicted by moving loads are the hull plating and frames. Extensive research has shown that the induction of plastic buckling can be induced at a much lower load magnitude for sliding loads compared to stationary loads (Quinton 2015).

In research involving IACS design ice loads, a sliding load scenario was applied to Polar Class 1-7 (PC1-7) vessels to determine the effect compared to ice-strengthened vessels (Quinton 2019). Both built-Ts and flat bar framed grillages were examined. It was found that there was no appreciable difference between sliding and stationary design loads for built-T frames with PC1-4. However, there was a noticeable difference for PC5-7 vessels – the more extreme result for the moving load case. For flat bar PC1-7, the sliding load case was more significant than the stationary case. The residual deflections were more than twice as much compared to the built-Ts (Quinton 2019). This investigation has shown that

built-Ts offer higher strength than flat bar frames concerning the prevention of plastic deformation, under similar loading scenarios.

2.2 Finite Element Model Guidelines

In recent years, an extensive amount of research has been done in the area of FEM generation concerning ship collisions. Many of these include finite element (FE) validation models (Kim and Daley 2018). Two scholarly papers have been thoroughly examined throughout the following subsections regarding FEM creation of ship collisions (Quinton, et al. 2016; Ringsberg, et al. 2018).

The stationary impact benchmark study was referenced for all modelling of geometric and parametrization space of the concept grillage (Ringsberg, et al. 2018). The benchmark study involved collision simulations organized by the MARSTRUCT Virtual Institute. Fifteen research groups participating in the study. The main point of the study was to determine acceptable practices for creating reasonable FEMs for ship-collision purposes. A case study was analyzed, which was analogous to a ship-ship (bulbous bow impacting side-shell) collision. The following information was used to control the experimental process to allow for cross-comparison of experimental data:

- The geometry of the FEM
- Parametrized geometric dimensions
- True stress-strain data from tensile strength testing of the side-shell material
- Boundary conditions (BCs) of the rigid frame
- The contact point between the indenter and double hull
- Rigid indenter material properties

- Experimental conditions such as termination time, load rate, and the displacement-controlled conditions

Each of the fifteen experimenters followed the above process and submitted a detailed report of their findings. The results were based on three outputs: the reaction force-indenter displacement curve, the internal energy-indenter displacement curve, and a list of the corresponding displacements at particular structural member failures. A reinforced frame was used to constrain the test grillage and simulate clamped BCs. The indenter was slowly (as not to induce plasticity) pushed against the grillage ten times to relax the residual stresses caused by welding the grillage to the support frames. In physical tests, the indenter experienced a displacement rate of 4 mm/s. However, within the FE space, a higher impact rate was used. The dynamic effects in the nodal forces were checked to ensure the mass/inertia did not affect the results. A nonlinear elastic-plastic constitutive material model, with isotropic hardening, was used. However, since the physical tests were carried out at relatively low speeds, strain-rate hardening was ignored. All mesh elements used were four-node shell elements with five through-thickness integration points. Contact was used to simulate the collision between the grillage and indenter. Within LS-DYNA, "automatic surface-to-surface" was used for contact between the indenter and grillage, while "automatic single surface' was implemented for all contact between other components.

The results from all simulators showed low scatter and a general agreement between results – despite model differences in element size, BCs, material model and material data used. Also, it was shown that no statistical difference was observed between the results in the

two FE software used for computation – ABAQUS and LS-DYNA. The graphical results of internal energy vs. displacement and force vs. displacement showed no trend between the two methods. Based on the low scatter and relative agreeance of the data, it was shown that the results of the benchmark study could serve as a guideline for FEMs involving ship collisions.

In addition to stationary testing, sliding load guidelines were also consulted for a complete, thorough, review. A recent paper provides guidelines for finite element analysis (FEA) of sliding loads on hull structures, causing plastic deformation (Quinton, et al. 2016). It was assumed that no tearing or puncture occurred.

There are two basic forms of FEA code: implicit and explicit. While it is important to note that both codes are not mutually exclusive, they are, however, better suited for different situations. Ship impacts occur in a relatively short period. The need to view the FE behaviour on a short time-step to adequately capture the structural behaviour renders the implicit method inefficient. Therefore, explicit FE codes were primarily used. To conserve computational power for FE testing, linear elements were used wherever possible.

Any region of the model that was expected to experience geometric and material nonlinearities was modelled using at least five through-thickness integration points to capture to model's behaviour adequately. Also, shell elements were primarily used due to the structural member aspect ratios of beams and plates. Beam elements near the impact area were not recommended as they do not model localized changes in cross-section shape, which can occur when considering large deformations. Once the element type was selected and a mesh was applied to the geometry, a detailed mesh convergence analysis (MCA) was

conducted. A new MCA should be employed whenever the stress gradient of a model changes. Particular attention should be given to areas near an impact (as these areas can experience significant geometric nonlinearities), as well as areas consisting of geometric discontinuities. The LS-DYNA default Belytschko-Tsay shell element, including warping stiffness considerations, was found to be sufficient at describing FEMs involving ship impacts (Quinton 2015). Element quality checks should always be performed, both before and after loading, to ensure the minimum quantity of elements in the model pass warpage, skew, Jacobian, and aspect ratio checks. Hourglassing, shear locking, and volumetric locking should each be considered where appropriate, depending on whether reduced or fully integrated elements are employed.

It has been shown that a bi-linear elastic-plastic model was capable of representing the nonlinear behaviour of steel hulls (Quinton, et al. 2016). However, when possible, a multi-linear elastic-plastic material model should be used (Quinton 2015). In either case, particular attention should be placed on kinematic and isotropic hardening as either could dominate in sliding load scenarios. The Cowper-Symonds strain-rate hardening model may be consulted for strain-rate dependent plasticity when the appropriate constants are known. As fracture was outside of the scope of (Quinton, et al. 2016), there were no recommended practices for representing fracture strain.

Recent laboratory experiments have proven that moving load capacities for ship grillage members were found to be inversely proportional to the stiffness of the BCs (Quinton 2015). Therefore, simply applying clamped or fixed BCs would not necessarily represent the model accurately. It is necessary to move the extents of the model far enough away

from the impact that no plasticity occurs at the BCs, to ensure that the FEM results are not dependant on the BCs.

FEA software packages, such as LS-DYNA, often contain many solution controls that affect the solution process. A potentially significant solution control to monitor would be the precision level used to solve the model. Generally, simulations involving more than 200,000 time-steps should implement a double-precision solver to mitigate the accumulation of round-off error. Otherwise, a single-precision solver can be used.

2.3 Corrugation

Corrugated structures are commonly used in ship construction in the form of corrugated bulkheads. Corrugated bulkheads are useful because they eliminate the need for stiffening, lessen corrosion rates, and make for easier maintenance (Sang-Hoon and Dae-Eun 2018). Perhaps most importantly, they lower the mass of the structure which is vital for structural optimization. The most critical design variable for corrugated bulkheads is the depth of the waveform (Sang-Hoon and Dae-Eun 2018). Though corrugation is a common technique in bulkhead design, it is not generally used for stiffeners. However, corrugated stiffeners on a grillage may lessen the overall weight by eliminating the need for stiffener flanges. Unfortunately, detailed calculations to optimize the various geometric properties of corrugated ship plates only exist for bulkheads, not stiffeners. Since the loading conditions for bulkheads are not the same as for plate stiffeners, bulkhead corrugation practices are not necessarily helpful.

2.4 Plastic Reserve (Overload Capacity) of Stiffeners

Generally, overload capacity refers to a structure's capacity under a load higher than what is allowed by a set of rules (Kõrgesaar, et al. 2018). Current Polar Rules allow for only a marginal amount of plasticity in ship structures (IACS 2019). Considerations for structural plastic reserve capacity is being neglected due to a lack of understanding as to which geometric parameters are responsible for its increase, and because rules and regulations currently do not allow significant structural plasticity. However, it has been shown that a stiffener's overload capacity can be altered based on geometric alterations such as changes to the cross-sectional parameters such as web height, web thickness, flange width, and flange thickness. Also, bulb flat, as well as flat-bar, stiffeners have been shown to have significant plastic reserve compared to Built-Ts (Kujala 1994).

Another study on overload response provides insight related to transversely stiffened grillage panels under varying sized patch loads (Kõrgesaar, et al. 2018). The objective of the study was to initiate the understanding of limit states, using an ice-strengthened ship, concerning buckling and fracture of ice. Two geometric options were explored as part of the analysis: grillage frames and isolated frames. Furthermore, both model configurations studied two frame types: flat bar and L-frames.

The FEA within (Kõrgesaar, et al. 2018) demonstrated several key results related to overload capacity. The study found that there was a relationship between the patch load length and the deformation mode. Also, within the elastic regime, the frames carry a large portion of the load. However, once the structure yields more of the load is absorbed in membrane plate stretching. L-frames, compared to flat bars, tended to lessen overload

capacity due to local failure within the frame. Furthermore, it was discovered that the frames were much more susceptible to significant plastic strain compared to the shell. Therefore, the frames were more likely to fracture than the shell plating.

The study shown in (Kõrgesaar, et al. 2018) conceded that much work was left to be done within the immediate research field. The article suggested that other frame designs should be tested to compare to the results found from flat bars and L-frames. Also, typical geometry was missing from the models such as brackets, lightening holes, and other reinforcements. Lastly, it was noted that the ice load was represented by a uniform pressure patch. In reality, the interaction between ice and ship structures is a much more complex phenomenon. The interaction should be considered for a more realistic scenario.

Much of the structural strength may be found within its plastic reserve capacity. Therefore, the plastic response was monitored within all experimental simulations in an attempt to understand the factors that contribute to its maximization.

2.5 Buckling Modes

There are three general buckling modes of concern to stiffeners: local buckling, tripping, and end-buckling. Local buckling occurs within the stiffener web at the impact site where the web of the stiffener buckles. Tripping occurs, again, when the stiffener buckles near the impact site. However, when a stiffener trips, the buckling occurs at the top-edge of the stiffener, parallel to the side-shell. Also, tripping is not always localized. DNVGL defines tripping as a sideways buckling of a stiffener top (DNV-GL 2015). Tripping can occur in both the web and the flange of a stiffener. Lastly, end-buckling occurs near the ends of the

stiffener. Generally, if the stiffener ends are soft, the buckling is less pronounced. End-buckling can occur in both the web and the flange of a stiffener.

Buckling can be graphically represented in the form of force vs. displacement plots (Daley, et al. 2017). Areas of the curves where the slope becomes nonlinear are indicative of buckling within the structure, which is consistent with a loss in energy (Daley, et al. 2017).

2.6 Structural Optimization

Stiffened panels are commonly used in the marine industry. To lower the weight of these structures while maintaining stiffness and strength, optimization techniques can be employed. One of the first steps to any optimization application is to define a suitable investigation method (Ringsberg, et al. 2012). During the concept grillage design phase, it is essential to be able to identify at what point the structure is quantifiably optimized. Two tools that can be used to identify optimization are FEA and design of experiments (DOE). DOE can be used to formulate a concise set of experimental runs and analyze the results, while FEA is used to extract results from the FEMs. Once the data has been analyzed, a thorough benchmarking process must be applied through a series of full-scale LPA tests. DOE has been proven to be a fundamental tool in optimization and has been used to develop a regression equation involving the plastic response of ship structures due to ice loading (Abraham 2008). Once the various factors are chosen which may affect grillage optimization, DOE can be implemented (either through to use of a factorial analysis or response surface methodology (RSM)) to determine the statistical significance of the studied factors.

Generally, yield strength and buckling strength are among the top choices for the design criteria for stiffened panels (Zhongwei and Mayuresh 2017). However, the yield criterion does not consider any plastic reserve strength that the material may have. That is to say, the yield criterion is too conservative. The highest load a structure can withstand can be observed in its ultimate strength (Kim and Daley 2018).

Chapter 3 Methodology

An optimal grillage was designed to be tested in an LPA in an attempt to discover a more efficient, optimized, grillage design. Five sets of experimental simulations were conducted utilizing FEA and oftentimes DOE (Exp1, Exp3, and Exp4). Each experiment was analyzed to determine significant insights and areas of improvement for subsequent experiments or future work. All experiments conducted utilized stiffened side-shell panels. The experiments focused heavily on the stiffener design more so than the side-shell design. All stiffener designs were compared against controls in the form of built-T and flat bar stiffeners. All experimental simulations were conducted dynamically in impact scenarios.

3.1 Experiment Matrix

Within Exp1, an experimental design was conducted on flangeless corrugated stiffeners. Corrugation was tested due to its ability, in bulkhead design, to eliminate the need for additional stiffening and lessen the overall weight of the structure (Sang-Hoon and Dae-Eun 2018). Three corrugation parameters were varied through the implementation of an experimental design to determine if a corrugated stiffener could improve the grillage performance. The plastic reserve capacity was not yet analyzed. A goal of Exp1 was to create a controlled experimental setup without complicating the FEMs. It is often useful in FEA to first start simple before complicating the design. With a complicated design, it is sometimes difficult to precisely conclude the cause of effects within the results.

Exp2 was completed in the form of a more general exploratory experiment. Exp2 was performed as an investigation to determine how altering the shape of the stiffener would

result in a more optimal design. The tested stiffeners included flat bar, bulb, corrugation, Circular Hollow Section (CHS), web-bracket stiffeners, and variable web height stiffeners. In some cases, many alterations to the geometry were considered, such as web height, web thickness, flange width, and flange thickness. It was useful to test many common stiffener designs, in a controlled way, to determine which stiffeners performed more optimally, and why.

The circular radius, variable web height, stiffener from Exp2 was further studied in Exp3. Exp3 utilized a relatively large FEM referred to as the Global Model (a relatively large grillage model, formed by combining several Local Models, consisting of three components: stiffeners, frames, and side-shell plating). Effectively, the Global Model included an array of Local Models (a relatively small grillage model consisting of exactly three stiffeners connected to the side-shell plating) with frames at the ends of the central stiffeners. The experimental simulations were completed to determine how altering the stiffener dimensions affected the optimality of the structure. A rigorous experimental design was built using DOE to accommodate a manageable number of experimental runs, while still being capable of determining statistical results. The web height and thickness, and flange width and thickness were varied throughout the experimental designs.

Exp4 continued with the circular radius variable web height stiffener design. However, unlike Exp3, Exp4 utilized the Local Model. With the flange omitted, the web height and thickness were varied within the experimental design. As was the case with Exp3, a rigorous experimental design was built using DOE to analyze the statistical significance of

the studied design factors. Exp4 yielded an optimal design based on the dynamic load cases and geometry studied.

Once the Concept Grillage was defined, it was compared to the IROQUOIS grillages in Exp5. Since the IROQUOIS grillage stiffener masses were slightly lower than the control run masses, the experimental design from Exp4 was consulted to determine an updated set of optimal factor levels based on the new stiffener weight.

3.2 Optimization Definition

Optimization has been defined as maintaining the weight of the grillage while improving the energy absorption capabilities of the structure. Also, the first yield point (the point where the material discontinues to behave linearly with respect to a force vs. displacement curve) of the optimized structure must be maintained or increased. Lastly, the overload capacity of the structure must be maximized, without interfering with the former constraints. It is important to note that the term optimization was used merely to describe the process of maximizing/maintaining the responses of the conducted work.

Structures that were being tested for optimization were compared to a combination of control runs in the form of built-T, flat bar, and IROQUOIS stiffened panels, depending on the experiment. In general, optimization was achieved by delaying the onset of buckling as much as possible.

The energy absorption capabilities, as they pertain to optimization, were obtained from two methods of calculating the internal energy of the stiffened panel, which were shown to be identical. The first method included integrating the BC force, or contact force, by the

maximum displacement of the model. The second method involved gathering the internal energy data directly from LS-DYNA. Within the text, energy absorption has been used interchangeably with either internal energy or, simply, energy.

The first yield point, as it pertains to optimization, was determined from noting the first point at which the BC force, or contact force, vs. displacement plots became nonlinear. It was defined as the point where the force-displacement behaviour stopped behaving linearly. The description of the first yield point used for optimization should not be confused with the first yield point as it pertains to the material stress/strain curves. Within the text, first yield point has been used interchangeably with first yield or yield point.

The overload capacity, as it pertains to optimization, was defined as the amount of internal energy the grillages were able to absorb, after the first yield point. Within the text, overload capacity has also been used interchangeably with plastic reserve capacity. Regarding discussions involving internal energy within the elastic regime, sometimes the terms elastic internal energy capacity, elastic capacity, or elastic energy absorption capacity, were used.

It should be noted that the built-T control stiffener was not optimized. It should also be noted that the flat bar control stiffener was optimized as part of Exp4 since the factor levels included the flat bar shape.

3.3 Control Stiffeners

Two stiffeners were used for control FEMs throughout the experiments: a built-T and a flat bar. The built-T is a stiffener, based on the simplified panel stiffeners (see Section: 7.2.1 Local Model), used for testing within the LPA. The flat bar is a stiffener designed to have

the same weight and web slenderness ratio as the built-T control run. The slenderness ratio was calculated by dividing the web height by the web thickness. Note that the slenderness ratio of the flange was ignored since the flat bar was flangeless. Both control stiffeners were meant to be comparable to one another for FEM comparisons within the experiments.

See Table 3.1 for the scantlings of the built-T and flat bar control stiffeners. As can be seen in the table, to create the flat bar from the built-T, effectively, the weight of the flange was redistributed into the stiffener web. Therefore, compared to the built-T, the flat bar web was taller as well as thicker to equate the weights of the control stiffeners. Throughout the experiments, the number of stiffeners and the extents of the FEM change, but the scantlings of the control stiffeners remain constant. See Figure 3.1 and Figure 3.2 for the visuals of the control stiffeners.

Table 3.1: Scantlings for the control stiffeners.

Control Stiffener	Span	Web Thickness	Web Height	Flange Thickness	Flange Width	Weight	Slenderness Ratio
	mm	mm	mm	mm	mm	kg	mm/mm
Built-T	1360	7.9	170	8	102	23.1	21.4
Flat bar	1360	10.0	215	-	-	23.0	21.5

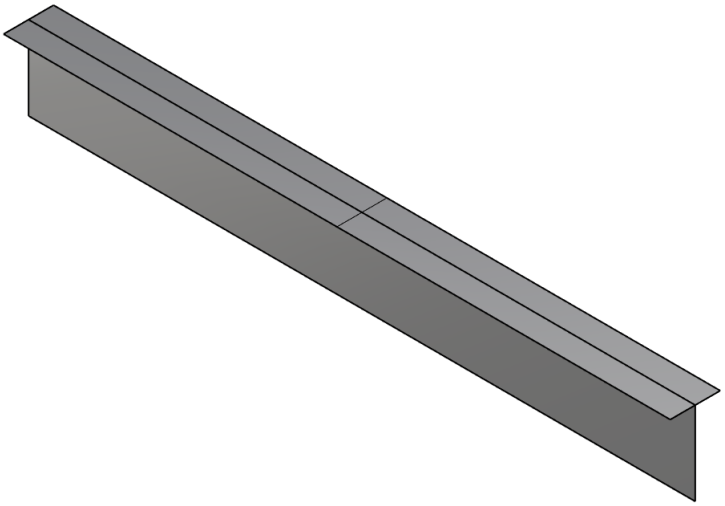

Figure 3.1: Built-T control stiffener.

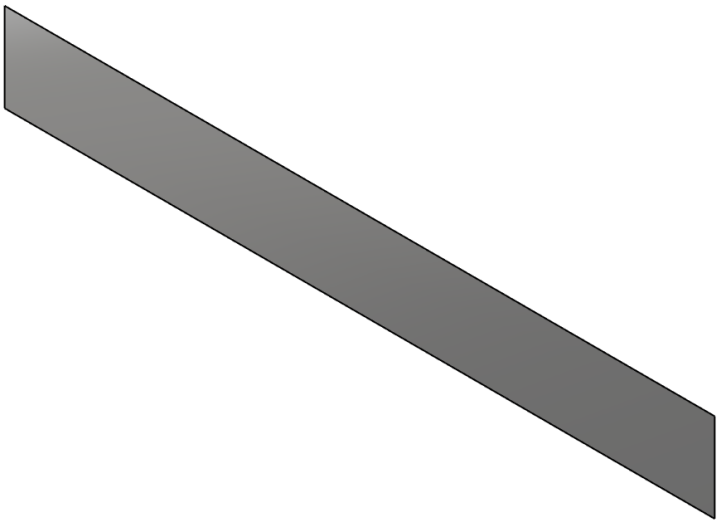

Figure 3.2: Flat bar control stiffener.

Scantlings related to the various FEMs throughout Exp2, Exp3, and Exp4, can be found in Appendix C2, Appendix D2, and Appendix E2, respectively. Since the scantlings of the models within Exp1 and Exp5 did not change significantly between runs, they can simply be found within the text in Sections: 4.1 Model Parts and 8.2 Model Parts, respectively.

3.4 Finite Element Analysis

FEA was the main tool used throughout the conducted work, which was utilized by each of the five sets of experimental simulations (Exp1 through Exp5). The FEMs within this thesis were constructed based on guidelines and a benchmark study within Section: 2.2 Finite Element Model Guidelines, which outline best practices for modelling nonlinear ship structural accidental loading conditions.

3.4.1 Numerical Model Inputs

For conciseness, the FEM inputs have been outlined within the following subsections. Note that many of the FEMs within the conducted work consisted of similar model inputs and controls.

With the exception of Exp1, all experimental simulations were completed utilizing an explicit time-integration FEA solver. The time-step, which is calculated based on the speed of sound through the material, will always be within range to capture nonlinear and unstable structural behaviour (Quinton, et al. 2016). The conducted work deals primarily with impact scenarios.

An implicit solver was used for Exp1 which involved a static loading scenario with an elastic material model. The FEMs within Exp1 were solved in one time-step. Unlike explicit solvers, time-step size can be user-defined for implicit solvers. Therefore, implicit solvers are well suited for FEMs which can be solved in large time-steps (such as static and quasi-static analyses).

3.4.1.1 Boundary Conditions

With the exception of Exp2, the BCs used for all FEMs were fixed-fixed at the extents of the models (see Figure 4.4). These fully restricted conditions mimic the experimental setup with the robust LPA grillage carriage. Within Exp2, symmetrical BCs were used, in addition to fixed-fixed BCs, to reduce model size.

3.4.1.2 Loading Conditions

For Exp2 through Exp5, the load was applied dynamically using the rigid indenter dome (see Section: 3.7 Rigid Indenter Design), in the normal direction (see Figure 3.4). For Exp2 through Exp4, rigid body motion of the dome was used to apply the load. Firstly, the Dome was located 5 mm from the test subject as to ensure the parametrized thickness of the side-shell did not interfere with the solid dome. Then, the dome was displaced according to the load curve shown in Figure 3.3. The velocity of the load corresponds to 3.67 m/s. The dome was translated from a displacement of 0 mm to 220 mm. At time 0.06 s, the dome retracted at a velocity of -3.67 m/s, until the termination time was reached. The velocity was chosen based on the testable impact velocity range of the LPA. The Dome was only permitted to translate in the z-axis (see Section: 3.9 Coordinate System), all other translations and rotations were constrained.

For Exp1, a pressure was applied directly to the side-shell to simulate an applied load. For Exp5, the dome was given an initial velocity to simulate an impact scenario. For additional information concerning the load conditions related to Exp1 and Exp5, see Section: 4.2.2: Loading Conditions and 8.3.1: Loading Conditions, respectively.

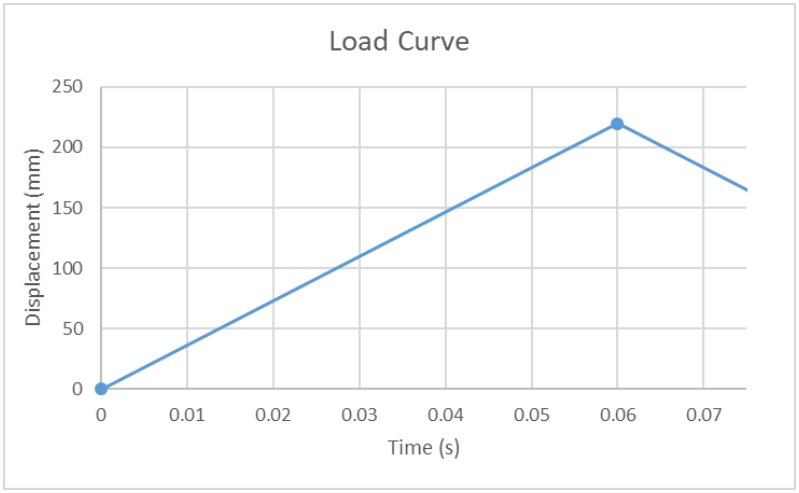

Figure 3.3: Exp2, Load Curve.

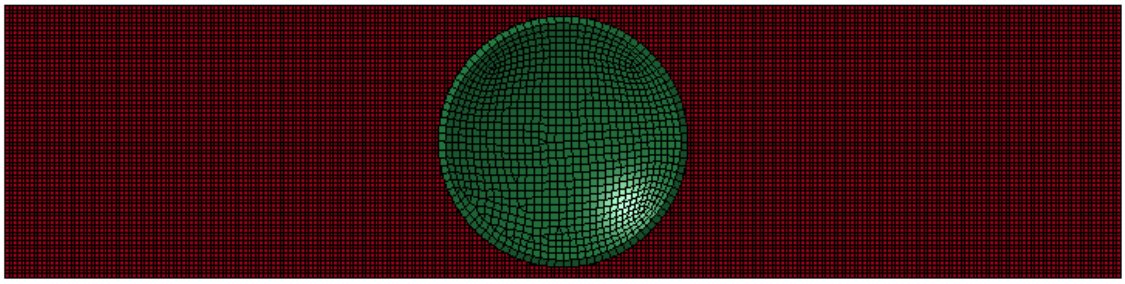

Figure 3.4: Exp2, Dome position relative to Grillage.

3.4.1.3 Contact

For Exp2 through Exp5, frictionless, automatic surface-to-surface penalty-based contact was used between the grillage side-shell and the dome. Within automatic surface-to-surface contact, a slave and master are arbitrarily defined. Since automatic surface-to-surface contact is a two-way contact algorithm, the distinction of slave and master does not affect the FEM. The dome was defined as the slave while the side-shell was defined as the master. However, surface-to-surface ensures that contact is detected between the slave through the master, as well as the master through the slave. Automatic surface-to-surface contact is

often used in dynamic impacts where it is not guaranteed which direction the contact will occur, due to the dynamics of the collision.

Significant cases of tripping and local buckling sometimes resulted in unintended penetration between the stiffener web and side-shell. This issue could have been solved by defining contact between the stiffener web and side-shell. However, since the issue only occurred in FEMs with significant cases of tripping and local buckling, the affected FEMs were automatically determined to be suboptimal regardless. It should be noted that this issue did not occur for the optimal design, the built-T and flat bar control, or the IROQUOIS FEMs.

3.4.1.4 Model Controls

The only two significant controls that were altered from LS-DYNA's default setup was the termination time and the time-step. The FEMs were set to terminate once the load was removed, and all residual stresses had sufficiently dissipated.

Exp1 was solved in one time-step since it was a static elastic, analysis. Exp2 through Exp5 were analyzed using an explicit solver which automatically generates a stable time-step.

3.4.1.5 Material Models

For Exp2 through Exp5, a bi-linear plastic kinematic material model was used to represent all deformable materials within the FEMs. For Exp1, a linear elastic material model was chosen. General steel properties were chosen simply to analyze the trends between the FEMs for statistical comparisons. For the rigid indenter dome material properties, see

Section: 3.7 Rigid Indenter Design. No failure criteria were implemented as only trends between the runs were being analyzed.

3.4.1.6 Element Types

Belytschko-Tsay shell elements were used exclusively for deformable elements throughout experimentation. The shell elements were given five through-thickness integration points to better capture any material or geometric nonlinearities. LS-DYNA's recommended shear factor of 5/6 was applied. All FEMs were meshed primarily with quadrilateral elements. Some triangular elements were sometimes required to preserve element quality wherever significant curvature existed in the geometry.

The default constant stress solid elements were used to create the rigid indenter dome for impact testing.

3.4.1.7 Mesh Convergence

An MCA was completed for each experiment to ensure that the results were independent of further refinements in the FE mesh. All controls and parameters within the FEMs remained constant except for the change in average element size. The data was plotted to determine the largest average element size which could accurately represent the model. The largest element size was preferable due to the decrease in the required computational power.

3.4.1.8 Result Extraction

Data was output in the form of d3plots and ASCII plots, which produced various elemental and nodal structural responses. Results from the d3plots were extracted from von Mises

stress vs. displacement plots, while results from the ASCII plots were extracted from BC force and contact force vs. displacement plots. Internal energy vs. displacement plots were also consulted which were compared to integrated force vs. displacement plots to ensure that the plots were equal, and that no energy was being lost to other forms.

The von Mises stress of the highest stressed element in the model, at the end of the simulation, was plotted against the maximum displacement in the model. The goal was to produce low von Mises stress values throughout the prescribed displacement. A low von Mises stress is consistent with the model being able to deflect without failure occurring, which was a product of an optimized grillage. Care should be taken when considering the von Mises stress values since a bi-linear material model was implemented with no failure strain identified. For data collection purposes, only the trends between the von Mises data of FEMs were considered. It should be noted that the von Mises data was collected once the load was relaxed, and once the amplitude of dynamic vibrations within the von Mises stress data had dissipated considerably. In should be noted that, stress can be seen to build up in the side-shell, without propagating into the stiffener web, in several of the FEMs throughout the conducted work (for example, see Figure 4.8 and Figure 4.10). In thesis instances, the relative strength of the stiffener is much higher than the side-shell. Therefore, the side-shell will yield before the stiffener, resulting in large side-shell deformations and large stress values.

The force vs. displacement data was plotted in two forms: BC force vs. displacement and contact force vs. displacement. For clarity, the BC force refers to the force at the BCs. Each data point of the BC force vs. displacement plots corresponds to the total reaction force at

the BCs of the whole model versus the maximum displacement in the model. It was confirmed that the total BC force matched the total contact force within each FEM. In later experiments, contact force was used exclusively since it experienced fewer dynamic effects that produced cleaner data.

Since internal energy is the integral of force and displacement (see Equation [1]), the goal was to produce high force values throughout the prescribed displacement. Since the force vs. displacement values did not often have a constant slope, the function must be integrated to find its actual value. Internal energy was monitored since a relatively steep decline in the slope of a force vs. displacement curve can suggest that buckling has occurred, which was consistent with a loss in energy (Daley, et al. 2017). For Exp4 and Exp5, energy vs. displacement plots were analyzed by integrating the area under the force vs. displacement curves.

The general form of the equation describing the relationship between energy, force, and displacement involves integrating the force with respect to the displacement (see Equation [1]). Since the integral of force and displacement is equal to energy, the goal was to determine which stiffener configuration provided the lowest amount of displacement per unit force. A low displacement per unit force would produce the largest slope and would, therefore, produce the highest energy absorption per unit force. Since, within the elastic regime, the force vs. displacement plot produced a constant slope, the equation did not have to be integrated, instead, Equation [2] could be used.

$$E = \int F(x)\, dx \qquad [1]$$

$$E = \frac{1}{2}Fx \quad [2]$$

Where: E = Energy (J)

F = Force (N)

x = Displacement (m)

3.4.2 Benchmarking

The FEMs were built based on considerations for best practices, as were outlined in 2.2 Finite Element Model Guidelines. The FE method implemented within the guidelines and benchmark study was heavily incorporated for the FEM creation phase. Therefore, the conducted numerical investigation within this thesis is benchmarked based on the methodology of previously published benchmarked FEMs.

Since the built-T and flat bar control FEMs were based on FEMs from the literature, there are limitations to the benchmarking efforts. Especially concerning the conceptual stiffener designs, it is assumed that these models which could not be benchmarked will yield accurate results since the models have all been created with highly similar FEA methodology. It is assumed that the relative differences between the FEMs will not invalidate the results.

It should be noted that the built-T control stiffener utilized within Exp1 through Exp4 was designed to be a replica of the simplified panel stiffeners. A simplified panel (see Section: (see Section: 7.2.1 Local Model) has been tested within the LPA as part of a proof of concept test for the research project. The resultant panel deformations from the actual test were within an acceptable range as compared to the FEM deformations seen within this

thesis. However, the results of this actual test were insufficient to fully benchmark the conducted work. When possible, a more rigorous actual test of the optimal design will be completed within the LPA, as detailed in Section: 9.2.1.1 Validation Study Outline. The subsequent documented results of this test will be used to validate the optimal design detailed within this thesis.

3.5 Design of Experiments

DOE was the secondary main tool used throughout the conducted work. Three of the five conducted experiments utilized DOE (Exp1, Exp3, and Exp4). DOE is a technique used to correlate the relationship between experimental factors and responses by analyzing the variation of the studied factors. A factor is an experimental variable that is manipulated to determine its relationship with a response (Mason, et al. 2003). All factors studied in this thesis were continuous numerical. Analysis of variance (ANOVA) was the main tool implemented through the use of DOE. ANOVA compares differences in means of data sets by analyzing the variance within the data.

DOE was used mainly to develop a robust, minimalistic, set of experimental runs that were capable of extracting the statistical significance of the studied factors. A run is a single set of factor-levels used to collect experimental results on a response (Mason, et al. 2003). A level refers to a factor value (Mason, et al. 2003). Factors can either contain a minimum and maximum level, or a range of levels. Concerning this research, runs were produced in the form of FEMs with all FEA controls and inputs remaining constant, except for the studied factors.

Each experimental design contained multiple runs to gather a sufficient amount of information regarding the statistical significance of each factor studied. An experimental design, or design, is a complete set of experimental runs used to determine statistical results (Mason, et al. 2003).

RSM was used to accurately make predictions regarding the whole design space – not just the maxima and minima. The design space, also known as the experimental region or the factor space, refers to all of the possible factor-level combinations which can be explored through experimentation (Mason, et al. 2003). RSM is necessary for optimizing factor levels (Montgomery 2017). An optimal design was implemented to minimalize the number of runs necessary to produce a robust design. Optimal designs are experimental designs that are often used to efficiently analyze a wide variety of designs as they are capable of analyzing irregular and nonstandard designs (Montgomery 2017).

3.5.1 DOE Result Analysis

Analyzing results from an experimental design follows a fairly linear methodology to ensure that the results from the design can be relied upon. First, the fit summary of the data must be analyzed. A fit summary determines whether the results fit a linear, two-factor-interaction, or quadratic curve. Two-factor-interactions refer to joint factor effects where the effect of one factor depends on the effect of another (Mason, et al. 2003). The effects within the model represent the average response between two factor-level combinations (Mason, et al. 2003). Whichever fit summary curve fits the design more closely should often be used.

The ANOVA must then be assessed. Any p-values greater than 0.05 (based on a 95% confidence interval) must be rejected from the model. Next, the predicted R^2 value must be compared to the adjusted R^2 value of the model. The adjusted R^2 value changes based on the number of predictors in the model. The difference between the predicted R^2 and adjusted R^2 value should not be greater than 0.2 (Stat-Ease, Inc. 2018). Also, the signal to noise ratio must be checked to ensure it is greater than 4 (Stat-Ease, Inc. 2018). The signal to noise ratio is a summary statistic that compares information related to the mean and variance (Montgomery 2017).

There are three requirements for ANOVA, the data must: fit a normal distribution, have approximately equal variance, and be independent of the run order (randomization). Run replications were not necessary since there is no (or a negligible amount of) variance between finite element results with the same inputs. Replication refers to a repeat of a run within an experimental design (Mason, et al. 2003). Moreover, for similar reasoning, randomization of the run order was not necessary since there can be no bias between experimental results conducted using a computer simulation. If the data is determined to be unable to fit a normal distribution or have equal variance, a transformation must be applied to the factor levels and the DOE result analysis must be completed again, beginning with the fit summary.

Once the data is determined to fit a normal distribution and have equal variance, a confirmation run must be completed to ensure that the design is capable of predicting accurate results within the design space. A confirmation run is completed using a set of factor levels not used within the runs of the design. The responses of the confirmation run

are analyzed to determine if they fall within the predicted responses, based on a confidence interval. A successful confirmation run indicates that the design space can be navigated to determine an optimal set of factor levels, whereas a failed confirmation run indicates that the design is incapable of predicting accurate results within the design space.

3.5.2 Weight as a Response

As seen in Section: 3.2: Optimization Definition, optimality has been defined to include the maintaining of weight for the optimal design. Initially, it was planned that each FEM test run would be the same weight – however, there was an issue with this. A mixture experimental design would be required to ensure that each FEM total weight was equal for every experimental run, by manipulating the studied experimental factors. Within mixture designs, the factors are dependent upon one another. Ultimately, this cross-factor dependency results in a more complicated design requiring additional runs to ensure that the design power is sufficiently high (Montgomery 2017).

To reduce the number of runs, and in turn reduce the required computational time, weight was treated as an experimental response for experiments including DOE. Treating weight as a response allowed for stiffeners of varying weights to be tested. Once results were obtained, the weight could then be constrained to match the control runs for direct comparisons. For clarity, weight remained constant for all runs within Exp2 and Exp5 since experimental designs were not implemented.

3.6 Large Pendulum Apparatus

An apparatus has been designed and manufactured which can be used to study damage to structural specimens mounted within the device (Gagnon, et al. 2015). The device consists of two pendulums that can house various structures. Regarding Figure 3.5, the leftmost pendulum houses either an ice cone indenter or a rigid indenter mounted in front of three load cells. These indenters can be used to impact various structures, located on the rightmost pendulum, for scientific studies. The rightmost pendulum houses a carriage that can contain ship grillages such as simplified panels, IROQUOIS panels, and concept grillage panels. The associated impact energies can be calculated based on the known kinematic energies associated with the corresponding pendulum impact velocities (see Equation [14]). For example, if both pendulums were set at a drop angle of 55° (from horizontal) the impact energy and relative velocity would be approximately 31 kJ and 5.32 m/s, respectively (Gagnon, et al. 2015). Each of the two pendulums of the structure consists of four parallel arms which make up one pendulum each. Bearings were attached to the upper extents of the arms to ensure a negligible-friction swing. Based on the design of the pendulum, the pendulum specimens do not rotate in any degree of freedom as the pendulum swings. The horizontal translation helps ensure that impact interactions between each pendulum of the apparatus occur parallel to one another. The apparatus consists of a toothed braking system that prevents multiple hits per swing. Mass can be added or taken away from either side of the LPA to alter the total mass (energy) of the system.

Figure 3.5 contains a profile view of the LPA. As can be seen, the leftmost side has been modified to accommodate a rigid indenter (see Section: 3.7 Rigid Indenter Design). More information regarding the LPA can be seen in (Gagnon, et al. 2015).

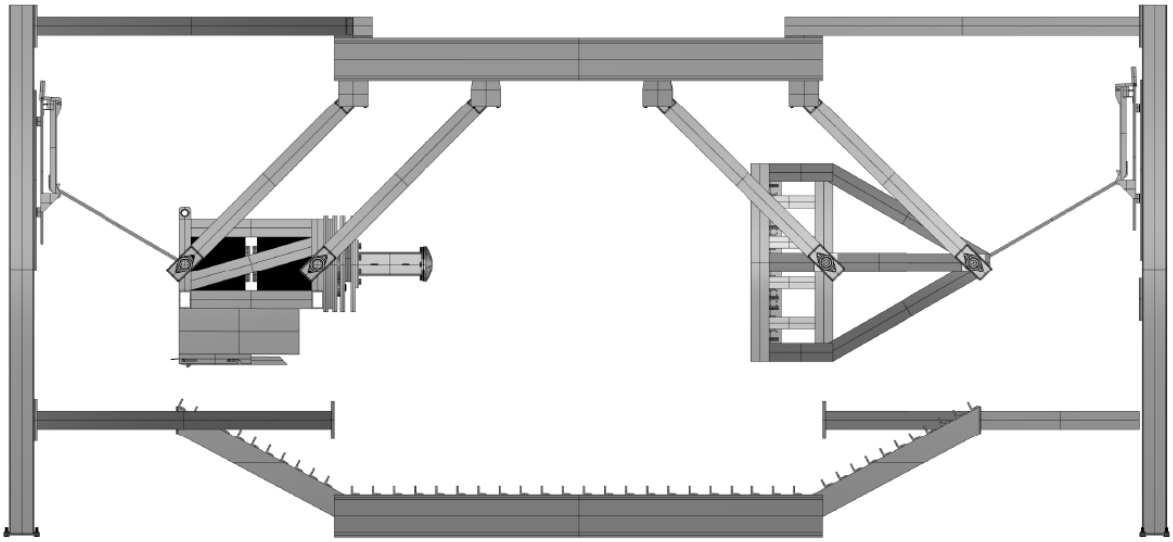

Figure 3.5: Large pendulum apparatus, including rigid indenter – left, and grillage panel within the carriage – right. A modified version of the design is found in (Gagnon, et al. 2015).

3.7 Rigid Indenter Design

The rigid indenter was designed for impact testing in the LPA. All modelling of the parts, assemblies, and fabrication drawings was completed in SOLIDWORKS.

To ensure rigidity of the structure, all of the steel, excluding the shaft, was fabricated from HS-100 steel with a yield stress of 690 MPA. The shaft was cut from a pre-existing square hollow section. A cross-beam was added to the inside, which further strengthened the structure.

Since the impact interaction within the LPA occurs perpendicular to the indenter, there were two types of indenter failure modes of concern: compressional failure, and elastic column buckling. Since the length of the shaft was small compared to the shortest cross-section dimension, elastic column buckling was not a concern. Due to compression, the maximum von Mises stress in the shaft occurred from simple compression and was a function of the applied force divided by the shaft cross-sectional area. Therefore, to ensure no plasticity in the shaft, it was critical to ensure that the ratio of the maximum applied load to the cross-sectional area did not exceed 235 MPa.

As can be seen in Figure 3.8, the dome was located at the end of the indenter. For FEM purposes, since the whole structure was assumed to be rigid, the only part required to be modelled was the dome. The dome was modelled as a rigid material with the following steel material properties:

- Young's modulus = 2.07e11 Pa
- Poisson's ratio = 0.3
- Density = 2.742e6 kg/m^3

The density entered into LS-DYNA reflected the appropriate mass of the dome combined with the rest of the rigid indenter and assembly on the leftmost pendulum arm (see Figure 3.5), a total of approximately 3141 kg. The density was calculated based on the known volume of the dome, as well as the known masses.

The modelled dome had an effective radius of 254 mm, a width of 304.8 mm, and a height of 50.8 mm (see Figure 3.6). Once imported into LS-PrePost, the dome was meshed with one layer of solid elements.

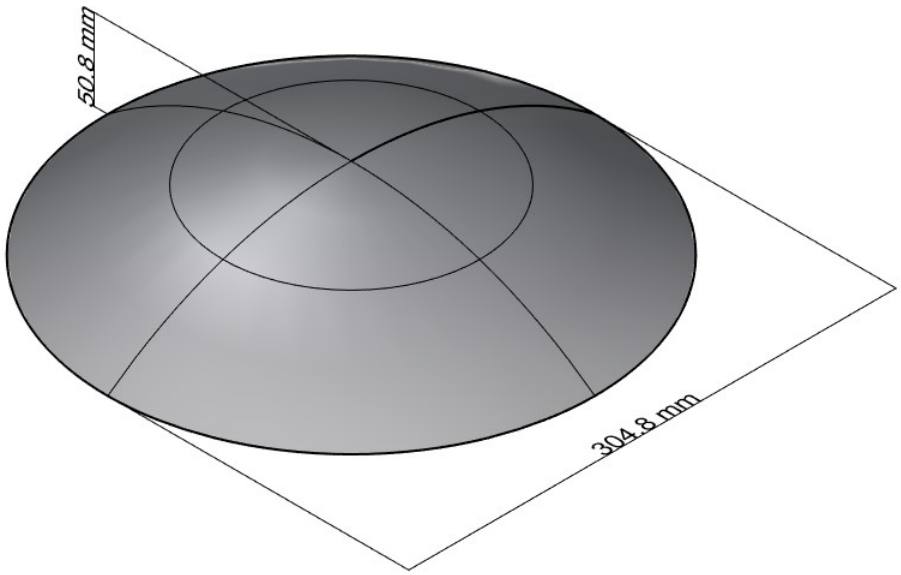

Figure 3.6: Rigid Indenter Dome.

The thickness of the solid element mesh was arbitrarily set it 15 mm (see Figure 3.7). Since the Dome was rigid, the thickness of the elements did not affect the results. The dome was meshed primarily with brick elements. The Dome was used for all test runs in Exp2 and subsequent testing.

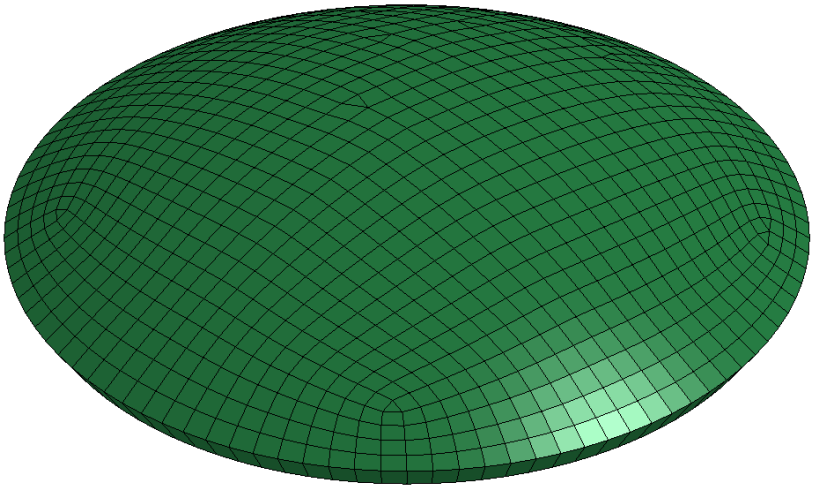

Figure 3.7: Rigid Indenter Dome Meshed in LS-PrePost.

3.7.1 Rigid Indenter Parts

The rigid indenter was formed from multiple parts. See Figure 3.8 for an isometric view of the fully assembled rigid indenter. Figure 3.9 shows the labels for all parts discussed within the following subsections. Figure 3.10 is included to show that the cross-beam sits within the CHS beam. See Appendix A for more information regarding the rigid indenter fabrication drawings.

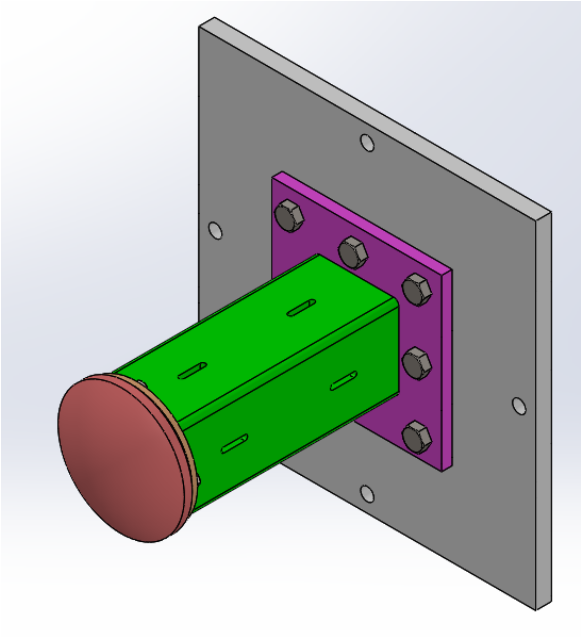

Figure 3.8: Rigid Indenter Full Assembly, Isometric View.

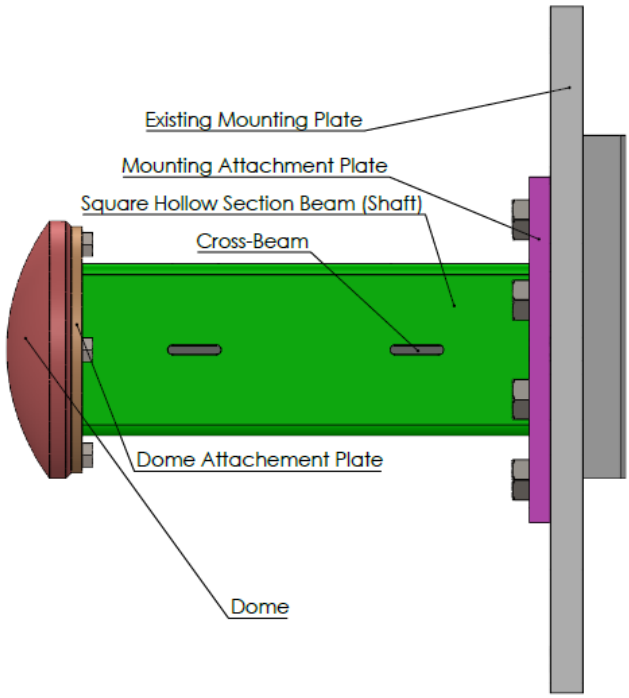

Figure 3.9: Rigid Indenter Full Assembly with Descriptions.

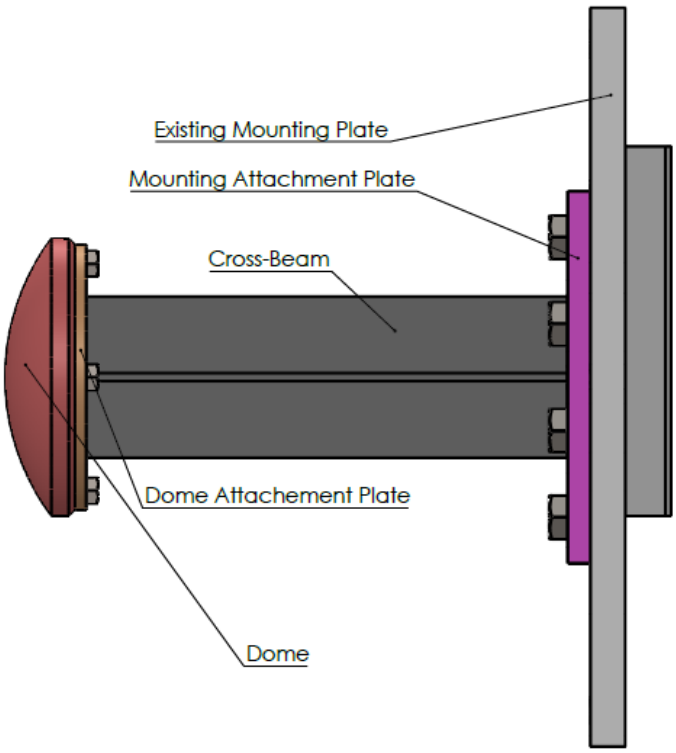

Figure 3.10: Rigid Indenter Full Assembly with Descriptions, excluding Square Hollow Section Beam.

3.7.1.1 Existing Mounting Plate

An existing mounting plate, used for the ice cone holder, was modified by tapping eight holes for indenter mounting. The resultant plate could then be used in both ice cone and rigid indenter impact testing.

3.7.1.2 Mounting Attachment Plate

The mounting attachment plate served as a welding surface for the cross-beam. The mounting attachment plate was then bolted to the existing mounting plate. Fine thread bolts were utilized to ensure sufficient thread engagement in the threaded hole.

3.7.1.3 Square Hollow Section Beam

A square hollow section beam was modified to be used as the shaft of the indenter. The shaft's length was adjusted to ensure the overall length of the indenter, in its constructed configuration, matched the overall length of a 30° ice cone. Weld slots were cut on each of the four faces for cross-beam welding.

3.7.1.4 Dome Attachment Plate

The dome attachment plate served as the mounting surface for the detachable dome (indenter head). A male plug was used to hold the dome while it was bolted in place using four bolts. Fine thread bolts were utilized to ensure sufficient thread engagement in the threaded hole. The dome attachment plate was welded to the other end of the cross-beam. It was essential to ensure that the diameter of the dome attachment plate was less than or equal to the dome diameter, so no interference could occur between the dome attachment plate and the grillage during testing.

3.7.1.5 Dome

The spherical dome served as the indenter head. It was the contact point for experimentation. The spherical shape was chosen to induce both membrane stress and through-thickness shear within the test grillages. The dome had a 1 inch lip for ease of handling since it was a detachable component that required some amount of manual handling. A female plug was cut out which matched the male plug on the dome attachment plate.

3.7.1.6 Cross-Beam

The cross-beam was fitted and welded inside the square hollow section beam for additional compressional support. One end was welded to the mounting attachment plate while the other end was welded to the dome attachment plate. Additional weld material was applied through the square hollow section beam weld slots.

3.8 Software

Rhino (Robert McNeel & Associates) was used for all modelling used for FE purposes. Once the geometric dimensions were assigned in Rhino, the model was imported into HyperMesh (ALTAIR) for meshing. HyperMesh is a convenient software package that specializes in providing a quick and efficient mesh that is often free from element quality issues. However, element quality was still examined later in the process, when the mesh was in its post-analysis, deformed state. The meshed geometry was then imported into LS-PrePost (Livermore Software Technology Corp.) for model preprocessing. LS-PrePost was used for all preprocessing and post-processing of all FEMs. Preprocessing of the models includes applying loads, BCs, parameters, and any controls necessary to analyze the models. LS-DYNA (Livermore Software Technology Corp.) was then used to process the model and acquire results for the model. Once results were obtained, LS-PrePost was used to observe the results. SOLIDWORKS (Dassault Systèmes) was used for creating the fabrication drawings for the rigid indenter and was occasionally used for generating geometric dimensioning diagrams. Design Expert (Stat-Ease, Inc.) was used for all DOEs within all applicable experiments.

3.9 Coordinate System

All software utilized share the same coordinate system orientation shown in Figure 3.11.

The axes were defined based on a typical stiffener local coordinate system:

- X, refers to the perpendicular direction
- Y, refers to the axial or longitudinal direction
- Z, refers to the normal to the side-shell (transverse) direction

The origin was located mid-plate with respect to the x and y-axes and was located where the stiffener meets the side-shell with respect to the z-axis.

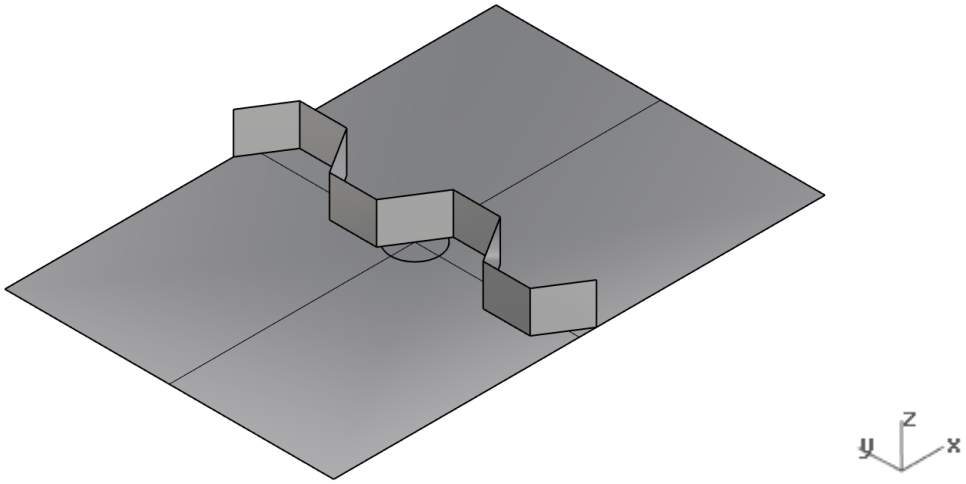

Figure 3.11: Typical stiffener-side-shell configuration with axes noting the coordinate system.

Chapter 4 Exp1 – Corrugation

Within Exp1, an experimental design was conducted utilizing corrugated stiffener webs. Corrugation was tested due to its ability, in bulkhead design, to eliminate the need for additional stiffening and lessen the overall weight of the structure (Sang-Hoon and Dae-Eun 2018). In bulkhead design, the additional stiffening refers to bulkhead stiffeners. In the context of a side-shell stiffener, the concept of eliminating the need for stiffening was extrapolated to determine if the flange could be eliminated. Three corrugation parameters were varied through the implementation of an experimental design to determine if a corrugated stiffener could aid in optimizing the grillage.

Two different corrugation shapes were experimented with within this thesis – traditional (a corrugation shape consistent which most corrugated bulkheads) and 'S' shaped corrugation (a corrugation shape which forms a sine wave when viewed from a plan view, see Figure 4.1 and Figure 4.2, respectively). However, all runs within this experimental simulation (i.e. Exp1) utilize traditional corrugation. The traditional corrugation type consisted of straight edges, whereas the 'S' type was formed from sinusoidal waveforms. More information regarding the 'S' type can be seen within Exp2. Waveform depth is the most significant parameter for corrugation (Sang-Hoon and Dae-Eun 2018). Therefore, the waveform depth was varied along with the two other parameters which define the shape of traditional corrugation.

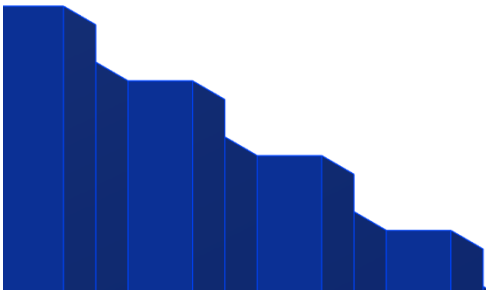

Figure 4.1: Traditional corrugation type.

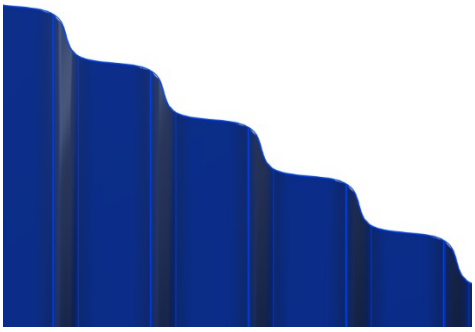

Figure 4.2: 'S' corrugation type.

4.1 Model Parts

The FEM consisted of a grillage model (see Figure 4.3) which was created in Rhino. For simplicity, all model parts (side-shell, stiffener flanges, and stiffener webs) were given parametrized thicknesses of 7.9375 mm. The remaining constants related to the FEMs were:

- Side-shell width, x-direction = 2032 mm.
- Side-shell length, y-direction = 1360 mm.
- Web height, z-direction = 170 mm.
- The material properties and FEM controls.

Keeping constants between test subjects allowed for the direct comparison of responses by mitigating bias.

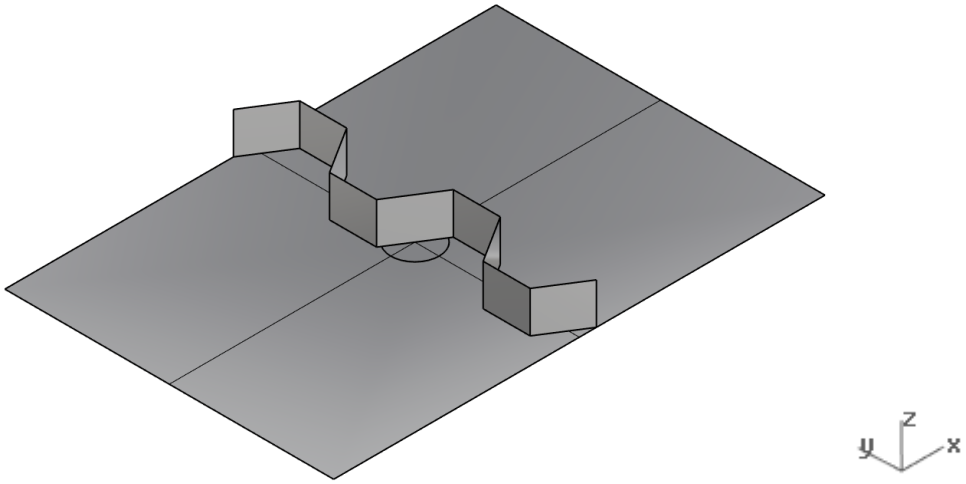

Figure 4.3: Exp1 Grillage.

4.2 LS-PrePost and LS-DYNA

See the below subsections for information related to the construction of the FEMs within LS-DYNA.

4.2.1 Boundary Conditions

The BCs used in the model were fixed-fixed around the perimeter of the model, and at the stiffener ends, shown in Figure 4.4.

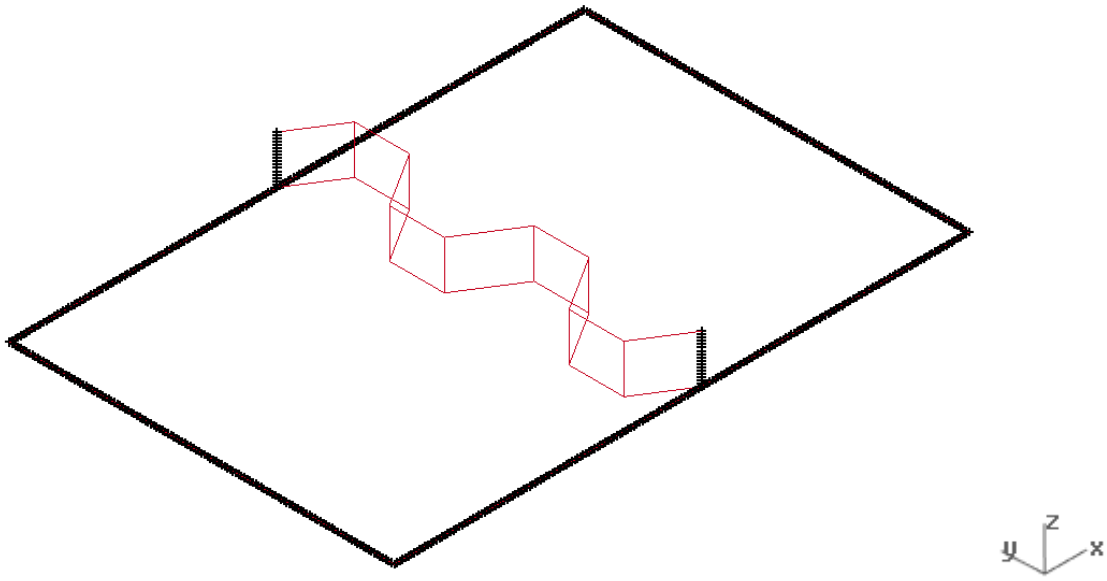

Figure 4.4: Exp1, BCs for Run1. Each BC node was annotated with a black “x”.

4.2.2 Loading Conditions

For subsequent numerical experiments (Exp2 through Exp5) a rigid indenter was used to apply the load to the side-shell of the grillage. However, Exp1 instead utilized a parametrized applied pressure. The rigid indenter was not yet implemented in an attempt to simplify the model.

A pressure of 700 kPa was applied to a circular load patch (see Figure 4.5), in the direction normal to the side-shell, in a single step. Since the analysis performed was static and explored only the elastic regime of the material, the magnitude of the force was inconsequential (as long as yield did not occur).

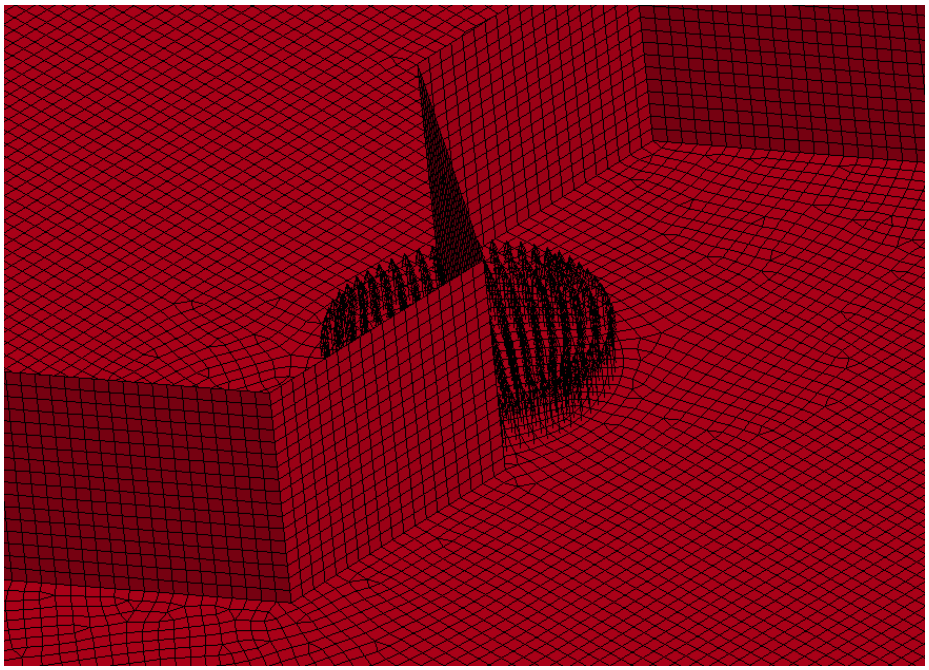

Figure 4.5: Exp1, Uniformly distributed load patch.

The load patch was located directly in the middle of the side-shell, and directly in the middle of the slant length corrugation parameter, x_3. The load patch area was 0.0314 m^3. Converting the pressure-area into a force gives an applied load of 22 kN.

4.2.3 Termination Time

The models were set to terminate at 1 s.

4.2.4 Data Output

Data was output in the form displacement readings from d3plots which were taken at the centremost element of the plate – at the impact site.

4.2.5 Material Properties

The grillages were modelled using an elastic material model with the following steel material properties:

- Young's modulus = 2.07e11 Pa
- Poisson's ratio = 0.3
- Density = 7833 kg/m^3

The main concern at this stage was proving whether or not corrugated stiffeners could maintain high elastic energy absorption as compared to the built-T and flat bar control stiffeners. An elastic material model was implemented with no consideration for post-yield behaviour since the optimal grillage must at least perform as well as the control runs to be considered optimal.

4.2.6 Mesh Convergence Study

Several runs were prepared based on the geometry of Run8. Run 8 was chosen for the convergence study since it had the smallest corrugation parameters of all the runs. Based on Figure 4.6 and Table 4.1, four runs were prepared with varying average element sizes. Since the load was applied in the form of a pressure, the corresponding displacement was used for the analysis and then plotted against the number of elements in the model. The mesh is considered converged when the results are independent of further refinements in the FE mesh. As can be seen from Figure 4.6 and Table 4.1, the mesh was effectively converged with an average element size of 10 mm. Therefore, all experimental runs were prepared with an average element size of 10 mm. It should be noted that no geometry had a thickness greater than 10 mm.

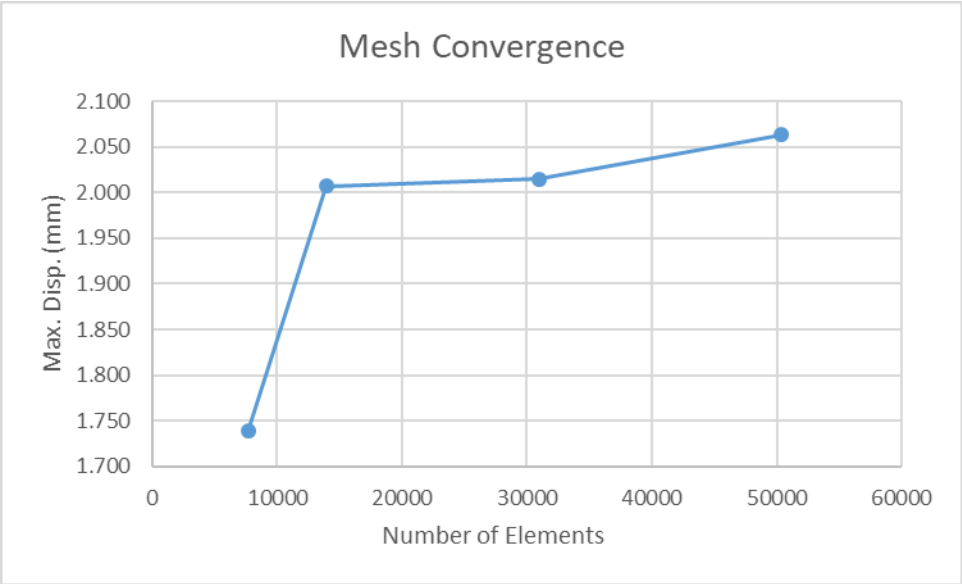

Figure 4.6: Exp1, Mesh convergence plot of Max. Disp. vs. the number of elements.

Table 4.1: Exp1, Mesh Convergence Data.

# of elements -	Max. Displacement mm	Avg. Element Size mm
7698	1.739	20
13928	2.007	15
30981	2.015	10
50330	2.063	8

4.2.7 LS-DYNA Cards

Several cards were invoked within LS-DYNA to achieve the desired effects intended for the simulation:

CONTROL_TERMINATION

The simulation was set to terminate using ENDTIM = 1.

CONTROL_IMPLICIT_GENERAL

The simulation was solved, implicitly, in one step using IMFLAG = 1 and DT0 = 1.

DEFINE_CURVE

To simulate a linear load curve, three points were used: (0, 0), (1.0, 1.0), and (1.1, 1.0). A scale factor was applied to achieve the desired load using SFO = 7e-5.

MAT_ELASTIC

An elastic material model was built using the following material properties: RO = 7833, E = 2.07e11, and PR = 0.3.

SECTION_SHELL

The shear factor was changed from 1 to 5/6 using SHRF = 0.8333. Also, five through-thickness integration points were used by invoking NIP = 5.

4.3 Experimental Design, Factors, and Responses

An optimal, RSM, experimental design was implemented to determine if there existed a set of corrugation parameters which would result in a more optimal stiffener design, compared to the built-T and flat bar control runs. The experimental design consisted of 13 runs. Three factors define the shape of traditional corrugation (see Figure 4.7). A wide range of factor levels was tested to ensure that the design space was adequately explored:

1. Waveform depth, x_1, 20 – 200 mm
2. Waveform breadth, x_2, 20 – 200 mm
3. Slant length, x_3, 10 – 200 mm

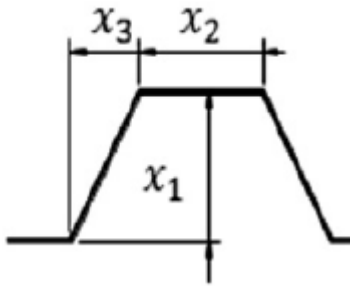

Figure 4.7: Corrugation parameters (Sang-Hoon and Dae-Eun 2018).

For analysis purposes, two responses were of concern – the weight of the grillage panels and the maximum displacement from the origin of the models. The weight of the grillages was monitored to determine the relationship between weight and displacement. The weight response was measured as a percent-difference compared to the built-T control run. It was a goal to minimize the weight difference compared to the Built-T as it was ideal to produce a lightweight grillage. Displacement was monitored as it directly relates to the internal energy required to deform the grillages under the applied load (see Equation [1]).

Design Expert was used to produce a series of runs. See Table 4.2.

Table 4.2: Exp1 Run Order in Design Expert.

	Factor 1	Factor 2	Factor 3
Run	A: Depth of Waveform	B: Breadth of Waveform	C: Angle of Waveform
Units	mm	mm	deg
1	194.286	194.286	57.6
2	92.3286	92.3286	45.6
3	23.4857	115.857	54
4	189.929	92.3286	56.7
5	194.286	194.286	45
6	20	194.286	65
7	20	20	45
8	20	20	65
9	194.286	85.3571	45
10	115.857	22.6143	54
11	86.2286	194.286	45
12	115.857	115.857	64.5673
13	194.286	20	65

4.4 Results

Due to the large quantity of FEM runs, FEM visuals have only been shown for three runs: the built-T control run, the flat bar control run, and Run8. Run8 was chosen since it was used for the MCA. The built-T control run visuals related to the von Mises stress and maximum displacement data can be seen in Figure 4.8 and Figure 4.9, respectively.

Since the models remained visual undeformed, the von Mises stress and displacement visual figures within this Section also serve as visuals of the undeformed geometry.

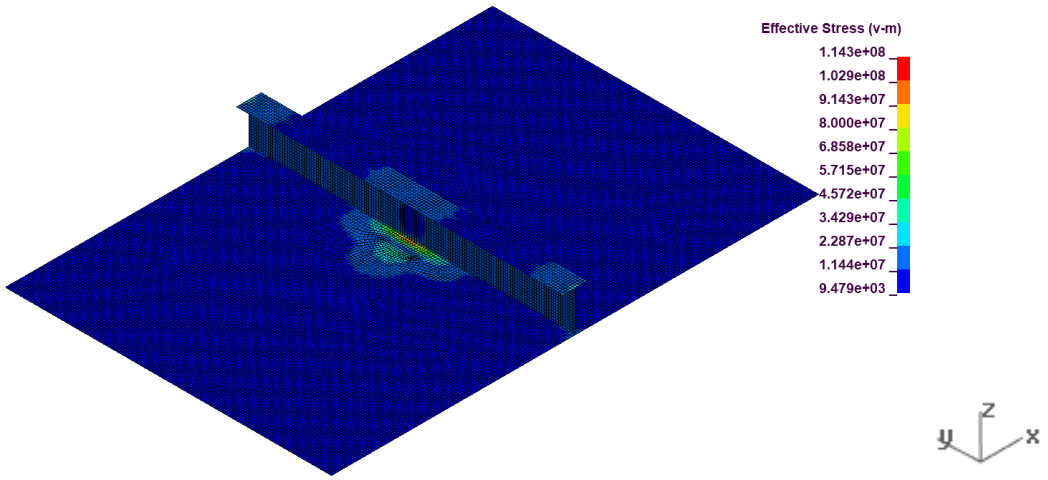

Figure 4.8: Exp1, Control – Built-T von Mise Stress.

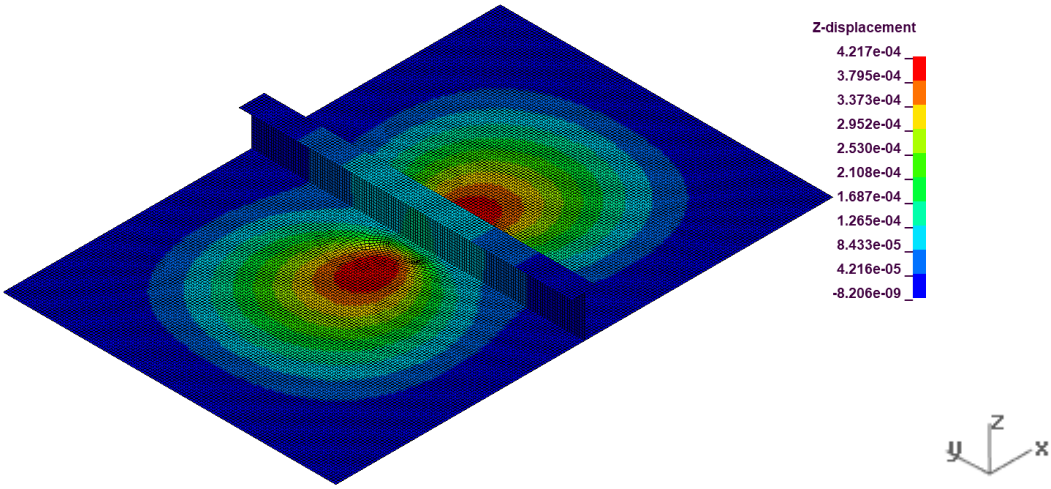

Figure 4.9: Exp1, Control – Built-T Maximum Displacement.

The flat bar control run visuals related to the von Mises stress and maximum displacement data can be seen in Figure 4.10 and Figure 4.11, respectively.

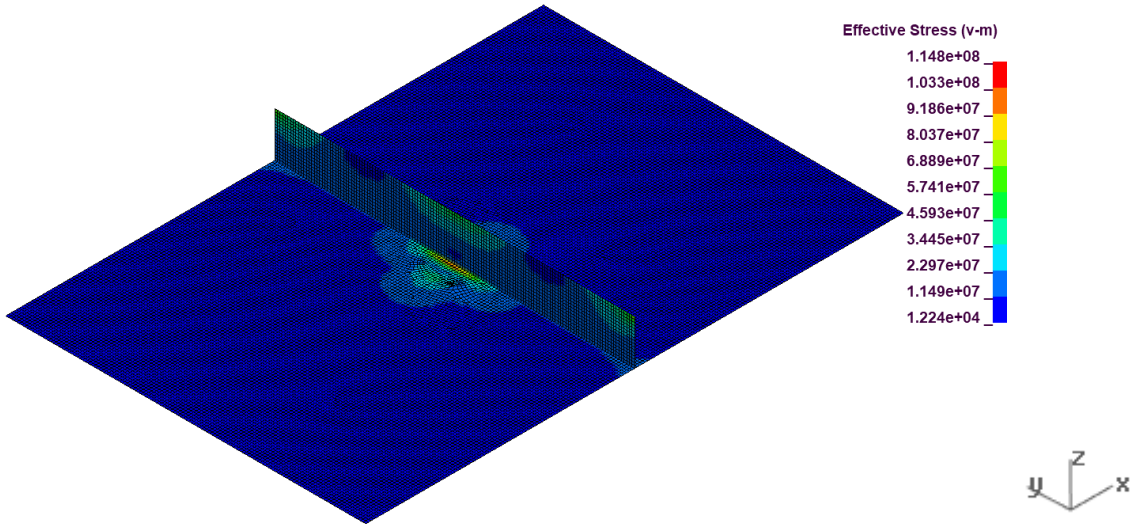

Figure 4.10: Exp1, Control – Flat bar von Mise Stress.

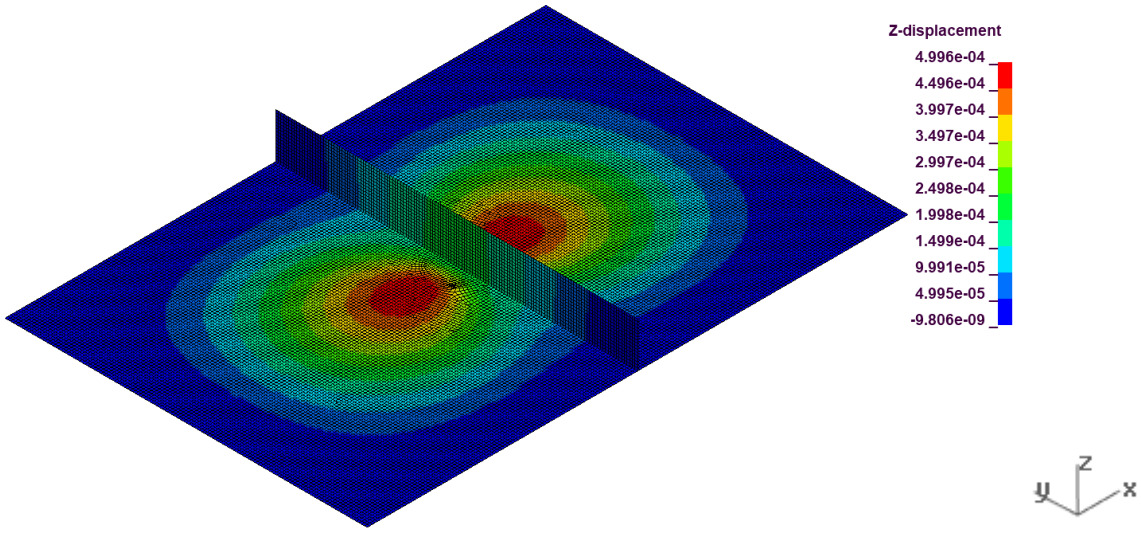

Figure 4.11: Exp1, Control – Flat bar Maximum Displacement.

The Run8 visuals related to the von Mises stress and maximum displacement data can be seen in Figure 4.12 and Figure 4.13, respectively.

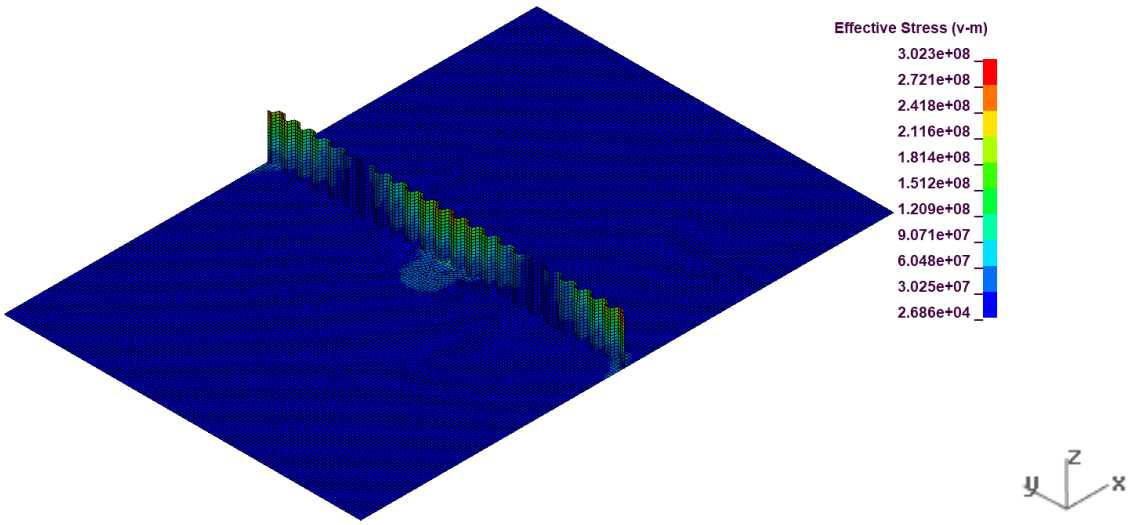

Figure 4.12: Exp1 von Mise Stress.

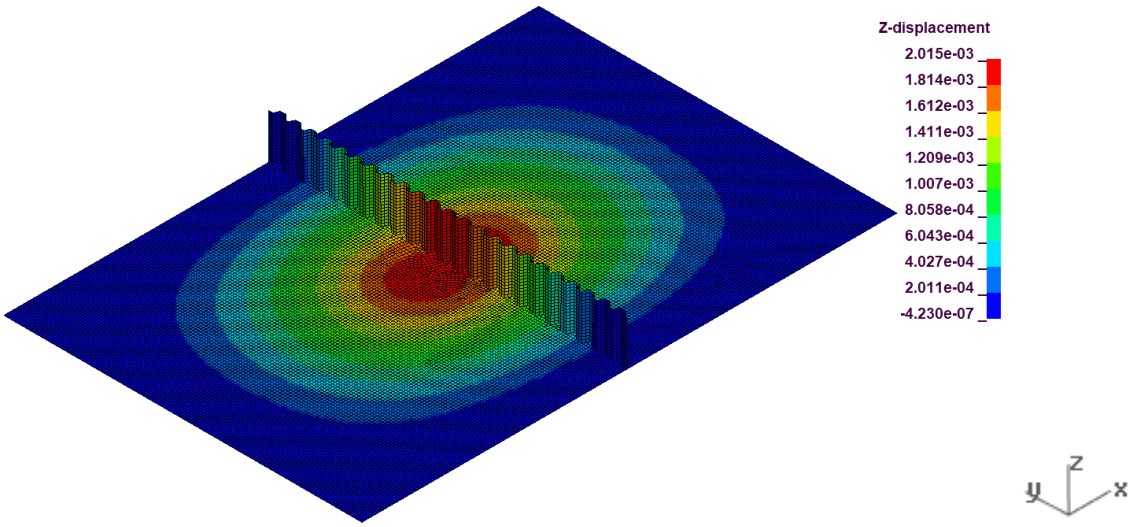

Figure 4.13: Exp1 Maximum Displacement.

See Appendix B1 for visuals for all run geometry, von Mises stress results, and maximum displacement results. As can be seen in Table 4.3, all of the corrugated stiffeners provided a higher level of displacement compared to the built-T and flat bar stiffeners.

Table 4.3: Exp1, Displacement Results.

Run Number -	Disp. Max. mm
1	8.90
2	6.80
3	1.45
4	9.53
5	5.46
6	1.40
7	1.50
8	1.89
9	7.35
10	9.72
11	5.66
12	9.06
13	10.70
Built-T	0.42
Flat Bar	0.50

Note that the maximum displacement values recorded in Table 4.3 were collected for the node at the origin of each of the models. Conversely, the maximum displacement values shown in Figure 4.9, Figure 4.11, Figure 4.13, and Appendix B1 refer to the maximum displacement within the whole model. Due to the corrugation shape, oftentimes, the maximum displaced node was not at the centre of the model, even though the load was applied to the centre of the model.

4.4.1 Experimental Design Model Checking

Both responses passed model checks related to the quality of the experimental design data. An inverse transformation was applied to the weight response data set to ensure the data fit a normal distribution and had equal variance. See Appendix B2 for the raw data from Design Expert related to the model checking.

4.4.2 Confirmation Run

The confirmation run was selected based on the criteria shown in Table 4.4. The table shows the criteria by which the optimal design for assessed. Both weight and displacement were set to be maximized.

Note: Regarding Table 4.4, the weight response has been shown in its transformed, inverse, scale. Therefore, it would appear that the response was being maximized when it was being minimized.

Table 4.5 shows five possible solution factor levels consistent with optimization predicted by the experimental design. Generally, the lower the solution number, the more optimal the design factor levels should be. Therefore, solution 1 was chosen for the confirmation run.

Table 4.4: Exp1, Experimental Design Confirmation Run Constraints.

Name	Goal	Lower Limit	Upper Limit	Importance
A: Depth of Waveform (mm)	is in range	20	194.286	1
B: Breadth of Waveform (mm)	is in range	20	194.286	1
C: Angle of Waveform (deg)	is in range	45	65	1
Weight (%)	maximize	0.00692	0.0158	5
Disp. (mm)	minimize	0	1.4	5

Table 4.5: Exp1, Experimental Design Solutions.

Number	Depth of Waveform (mm)	Breadth of Waveform (mm)	Angle of Waveform (deg)	Weight (%)	Disp. (mm)
1	**20.000**	**194.285**	**45.002**	**75.588**	**0.286**
2	20.000	194.286	45.201	75.413	0.293
3	20.000	194.285	45.279	75.344	0.295
4	20.000	194.285	45.566	75.093	0.304
5	20.000	194.285	45.750	74.932	0.310

Using the corrugation parameters outlined in Table 4.5 a confirmation test was built and run to determine whether the model was capable of predicting accurate results (see Figure 4.14 and Figure 4.15).

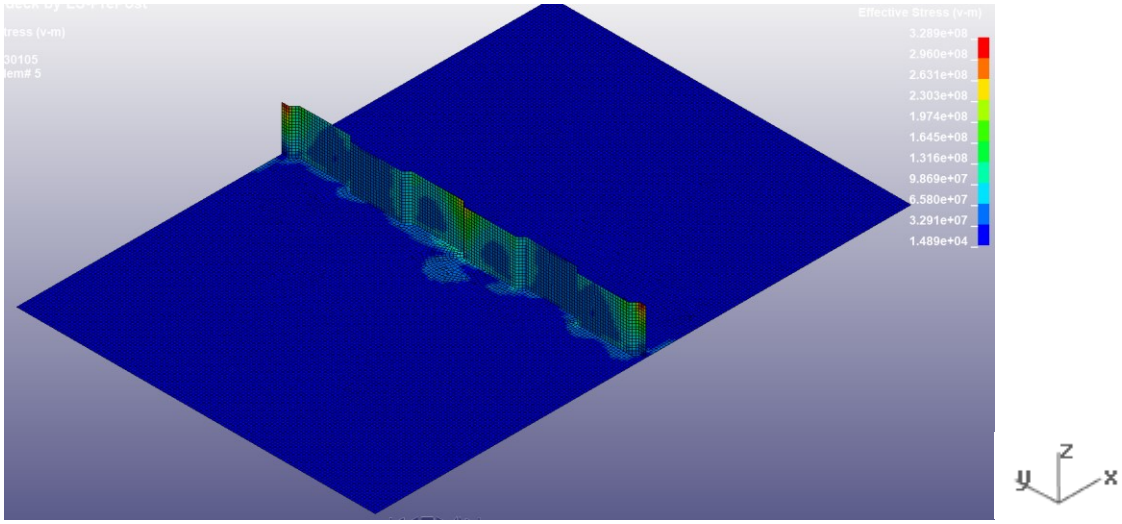

Figure 4.14: Exp1, Confirmation Run - von Mises stress.

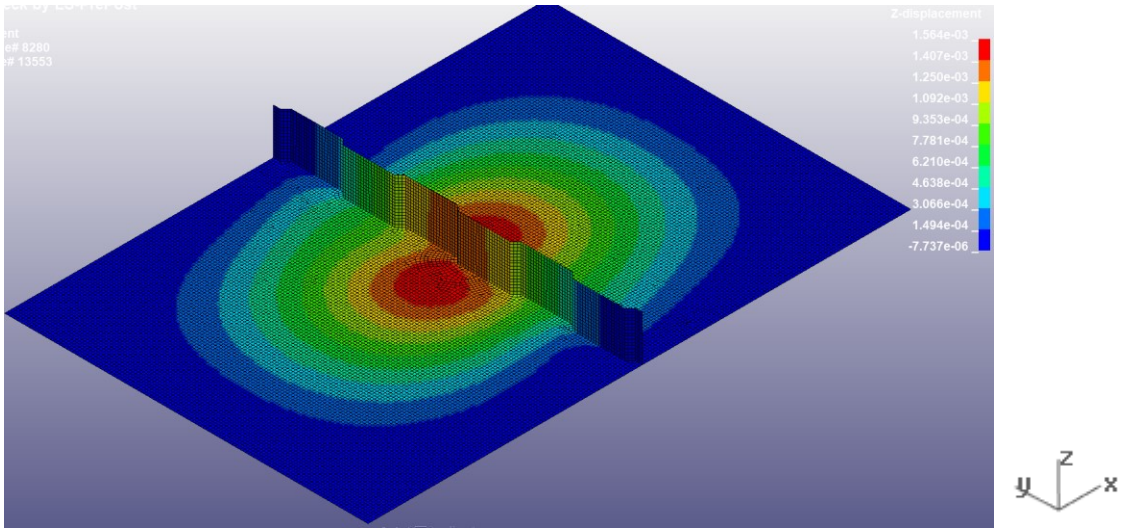

Figure 4.15: Exp1, Confirmation Run – z displacement.

The weight and the measured maximum out-of-plane displacement of the plate were 64.4 kg and 1.564 mm, respectively.

Table 4.6 shows the results of the confirmation run. The predicted mean column refers to the average predicted value of the corresponding response based on the experimental design results. The 95% PI low and high columns refer to the 95% confidence interval that the measured response, within FEA, will fall within the predicted value range. The data mean column refers to the measured response. Therefore, if the data mean value falls within the 95% PI low and high values, it can be said that the experimental design is capable of predicting accurate results within the design space. Based on the data mean values in the table, the model predicted the weight and displacement accurately.

Table 4.6: Exp1, Experimental Design Confirmation Run Results.

Two-sided Confidence = 95%

Response	Predicted Mean	Predicted Median	Std Dev	95% PI low	Data Mean	95% PI high
Weight (%)	76.17	75.5899	6.70115	61.6508	64.43	97.67
Disp. (mm)	0.286	0.286185	0.552828	-1.57463	1.564	2.147

Based on the optimal design corrugation parameters suggested in Table 4.5, it was interesting to note that the parameters approach the shape of a flat bar. The optimal design suggested that a flat bar produced the optimal stiffener compared to the corrugation levels tested. It seems that even with a small amount of corrugation, the initial displacement values were much higher than the flat-webbed-stiffener.

No elements failed element quality checks. See Appendix B3 for more information related to the element quality checks of the Confirmation Run. In Exp2, additional tests were conducted on corrugated stiffeners (on both traditional and 'S' shaped corrugation) as well as on several other stiffener shapes.

4.5 Discussion and Conclusions

An experimental design was completed utilizing various traditional corrugated stiffener designs. Three experimental factors were manipulated within the experiment, each related to the shape of the corrugation: waveform depth, waveform breadth, and slant length. An optimal, RSM, experimental design was used to determine an optimal set of corrugation parameters within the factor levels tested. 13 experimental runs were prepared, along with two control runs in the form of a built-T and a flat bar stiffener.

Once the experiment was completed, a confirmation run confirmed that the design was capable of predicting accurate results. The experiment revealed that the optimal shape for corrugation converged on a flat bar profile web shape. It appeared that any introduction of corrugation made the stiffener too soft and dramatically decreased its ability to absorb energy within the elastic region. For optimality, a stiffener must be about to perform as well as, or better than, the control runs within the elastic regime. An additional experiment was prepared, in the form of Exp2, which both built off of the conclusions found within Exp1, and also more broadly explored different stiffener types.

Chapter 5 Exp2 – Exploratory

Exp2 was conducted to examine the effect that geometric alterations would have on energy absorption as well as the relationship between elemental stresses and displacement. In particular, post-yielding behaviour was considered. Even though the corrugated stiffener failed to produce an optimized structure, perhaps its post-yield behaviour would be substantially better. Also, many other geometric structural modifications were tested in the form of common and uncommon stiffener designs.

Unlike Exp1, this Chapter (i.e. Exp2) did not follow a strict experimental design. Instead, a more explorative experimental method was followed. Here, it was not of interest to find the most optimal stiffener conditions. Instead, the goal was to identify some ideas which show promise for future rigorous experimental testing.

The stiffener web and flange thicknesses, web heights, and flange widths were manipulated on a case-by-case basis to ensure the stiffener weight and web slenderness ratios remained constant. In cases where no flange was present, the thickness and height of the web had to be increased to ensure the FEM's weight was being preserved, while simultaneously preserving the web slenderness ratio.

Exp2 was broken down into six tests (the six main tests conducted within Exp2 of this thesis, Test1 – Test6). Each test consisted of between four to seven runs. To make the overall analysis more manageable, each test was first analyzed separately. Later, all tests were analyzed together.

5.1 Model Parts

The FEM consisted of two basic model parts, each was created in Rhino: the grillage (see Figure 5.1) and the rigid indenter. Refer to Section: 3.7 Rigid Indenter Design, for information regarding the Rigid Intender model. For simplicity, the side-shell was given a parameterized thickness of 7.9375 mm. The remaining constants related to the FEMs were:

- Side-shell width, x-direction = 330.2 mm.
- Side-shell and stiffener length, y-direction = 1360 mm.
- The weight of each stiffener.
- The slenderness ratio of each web as well as each flange. In the cases of CHS stiffeners, this rule did not apply since slenderness ratios between straight cross-sections are not comparable to those of circular cross-sections.
- The material properties and FEM controls.

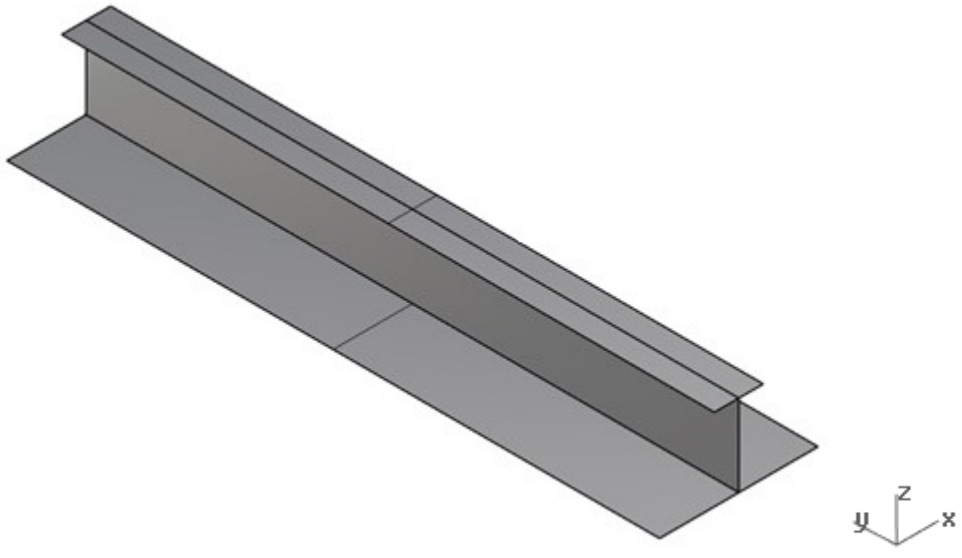

Figure 5.1: Exp2 Grillage.

5.2 LS-PrePost and LS-DYNA

See the below subsections for information related to the construction of the FEMs within LS-DYNA.

5.2.1 Boundary Conditions

The BCs at the edges of the model perpendicular to the stiffener consisted of fixed-fixed BCs, shown in Figure 5.2. The four nodes at the side-shell vertices were also fixed-fixed.

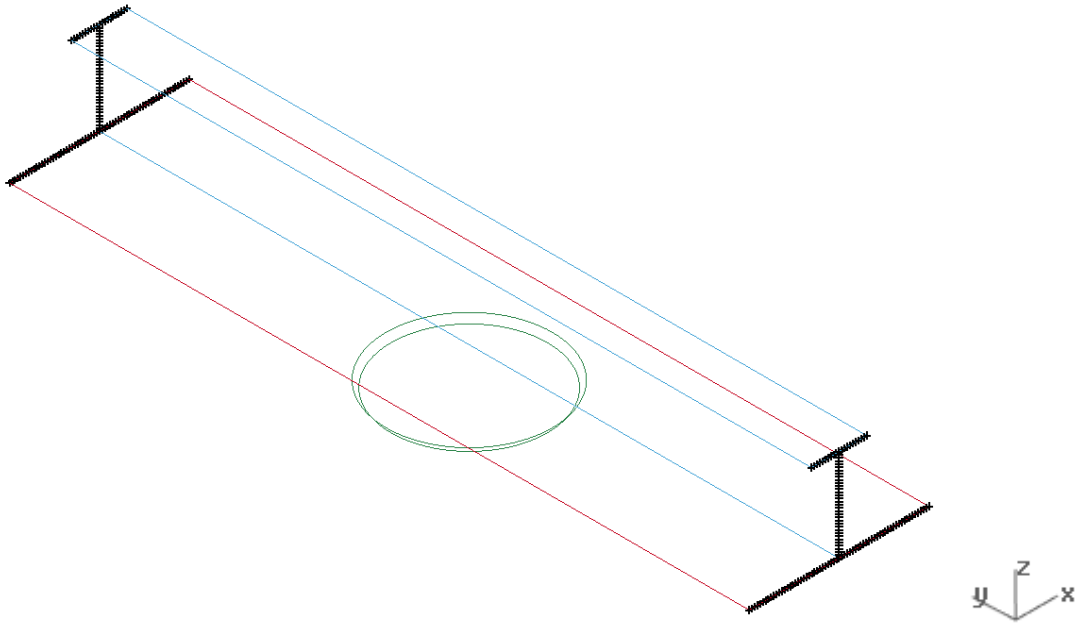

Figure 5.2: Exp2, Boundary Conditions of the built-T. Each fixed-fixed BC node was annotated with a black “x”.

Whereas the BCs at the edges of the model parallel to the stiffener consisted of symmetrical BCs, shown in Figure 5.3. Translations in the x-axis, as well as rotations about the y and z-axes, were fixed. Other degrees of freedom were left free. The symmetrical BCs allowed for a smaller side-shell with less overall calculations and a shorter run time of the analyses. Using symmetrical BCs in the manner also reflected the load, as well as the stiffener.

However, the associated bias was blocked out since the bias was mimicked within every run.

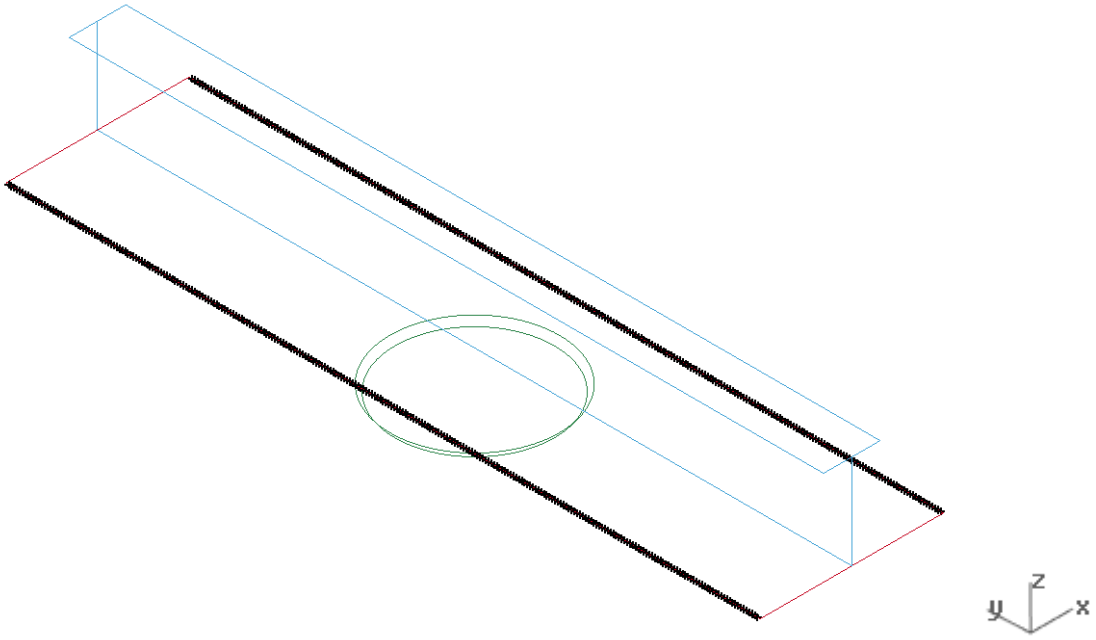

Figure 5.3: Exp2, Boundary Conditions of the built-T. Each symmetrical BC node was annotated with a black “x”.

It should be noted that a side-shell width of 330.2 mm (13 inches) was chosen to be large enough so that the indenter would never interfere with the BCs, as the rigid indenter’s width was 12 inches. The side-shell width was also minimized to conserve computation time.

5.2.2 Loading Conditions

The load was applied as per Section: 3.4.1.2 Loading Conditions.

5.2.3 Termination Time

The models were set to terminate at 0.075 s.

5.2.4 Contact

Contact was applied as per Section: 3.4.1.3 Contact.

5.2.5 Data Output

Data was output in the form of d3plots and ASCII plots at a frequency of 1000 Hz. The force data consisted of the BC forces.

5.2.6 Material Properties

The grillages were modelled using a bi-linear, plastic kinematic, material model with the following steel material properties:

- Young's modulus = 2e11 Pa
- Poisson's ratio = 0.3
- Density = 7850 kg/m^3
- Yield strength = 420.6 MPa
- E_{tan} = 308 MPa

5.2.7 Mesh Convergence Study

Several runs were prepared based on the geometry of the Circular Curve model from Test6. Based on Figure 5.4, five runs were prepared with varying average element sizes. Since the indenter was impacting the plate with a prescribed displacement, the corresponding contact force was used for the analysis and then plotted against time. As can be seen in the plot, there were no appreciable changes to the force vs. time plots for the different mesh sizes. Therefore, all experimental runs were prepared with an average element size of 20 mm. It should be noted that no geometry had a thickness greater than 20 mm.

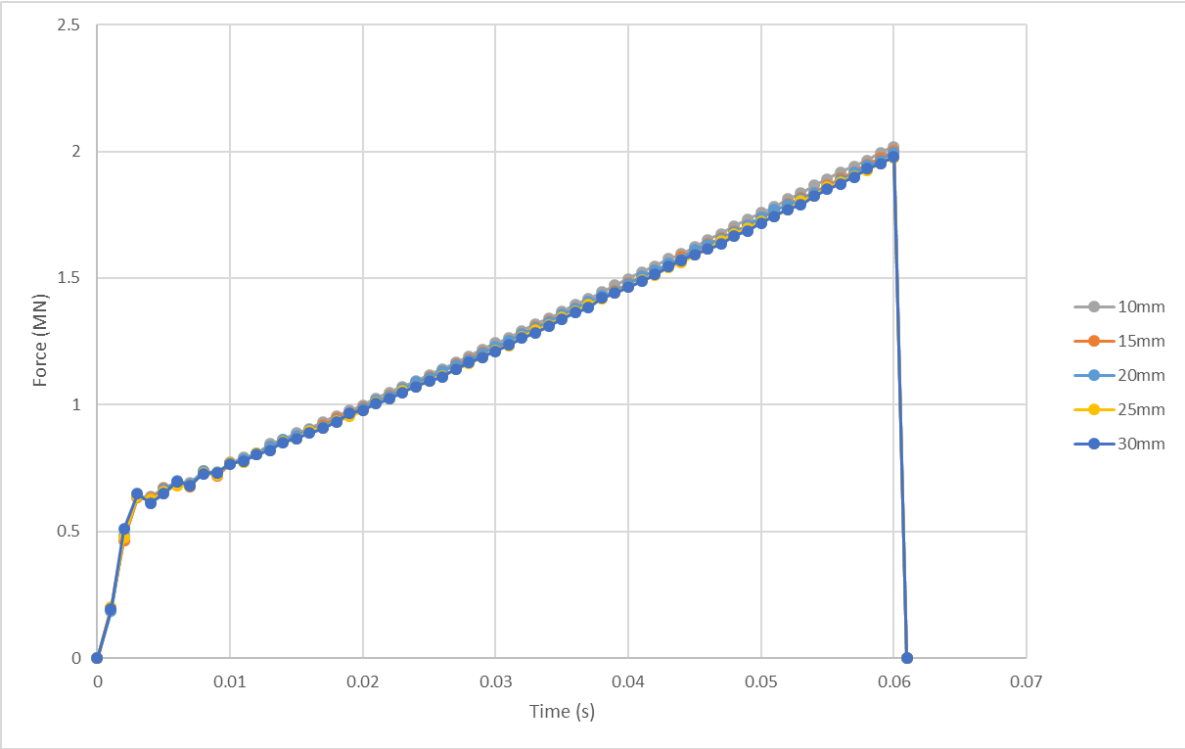

Figure 5.4: Exp2, Mesh convergence plot of force vs. time.

5.2.8 LS-DYNA Cards

Several cards were invoked within LS-DYNA to achieve the desired effects intended for the simulation:

BOUNDARY_PRESCRIBED_MOTION_RIGID

Rigid body motion of the indenter was achieved using the following fields: DOF = 3 and VAD = 2.

CONTACT_AUTOMATIC_SURFACE_TO_SURFACE

Contact was defined between the indenter and side-shell. To collect contact forces both SPR and MPR were set to 1.

CONTROL_TERMINATION

The simulation was set to terminate using ENDTIM = 0.075.

DATABASE_ASCII_option

Nine ASCII options were turned on for high fidelity result extraction: BNDOUT, ELOUT, GLSTAT, MATSUM, NODOUT, RBDOUT, RCFORC, SLEOUT, SPCFORC. Each was given a DT of 0.001.

DATABASE_BINARY_D3PLOT

For visualizing the simulation, DT = 0.001 was used.

DATABASE_BINARY_INTFOR

The internal forces were collected using DT = 0.001.

DATABASE_HISTORY_NODE_ID

The appropriate node was selected for ASCII NODOUT.

DEFINE_CURVE

To simulate a linear load curve, four points were used: (0, 0), (0.06, 0.22), (0.12, 0), and (0.13, 0).

MAT_PLASTIC_KINEMATIC

A, bi-linear, plastic kinematic material model was built using the following material properties: RO = 7850, E = 2e11, PR = 0.3, SIGY = 4.206e8, ETAN = 3.08e8, SRC = 3200, and SRP = 5.

MAT_RIGID

The properties used were: RO = 2.742e6, E = 2e11, and PR = 0.3. Also, CMO, CON1 and CON2 were invoked to properly restrict the rigid body from x and y translations, as well as x, y, and z rotations using 1, 4, and 7, respectively.

SECTION_SHELL

The shear factor was changed from 1 to 5/6 using SHRF = 0.8333. Also, five through-thickness integration points were used by invoking NIP = 5.

5.2.9 Strain-Rate Hardening

Cowper-Symonds strain-rate hardening was implemented for the material model within Exp2. According to Equation [3], high tensile steel Cowper-Symonds parameters were used; 3200 and 5 (Paik and Thayamballi 2003) for C and p, respectively. It should be noted that strain-rate hardening accounts for the high von Mises stress values seen within the results of this Chapter.

$$\gamma = 1 + \left(\frac{\dot{\varepsilon}}{C}\right)^{\frac{1}{p}} \qquad [3]$$

Where: γ = Dynamic scale factor

$\dot{\varepsilon}$ = Strain-rate (1/s)

C = Cowper-Symonds parameter (1/s)

p = Cowper-Symonds parameter

5.3 Results

Due to the large quantity of FEM runs, FEM visuals have only been shown for select runs within each Test. The built-T control run visuals related to the undeformed geometry and the maximum von Mises stress data can be seen in Figure 5.5 and Figure 5.6.

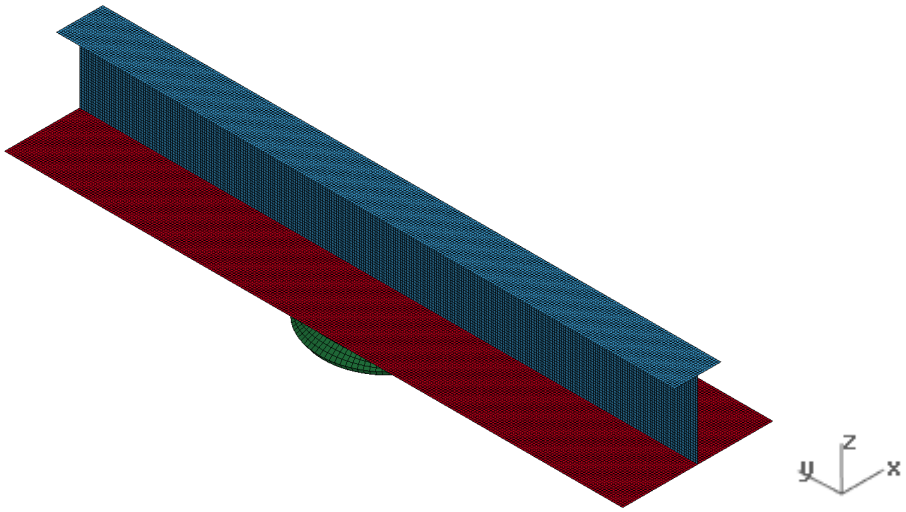

Figure 5.5: Exp2, Control – Built-T, Geometry:

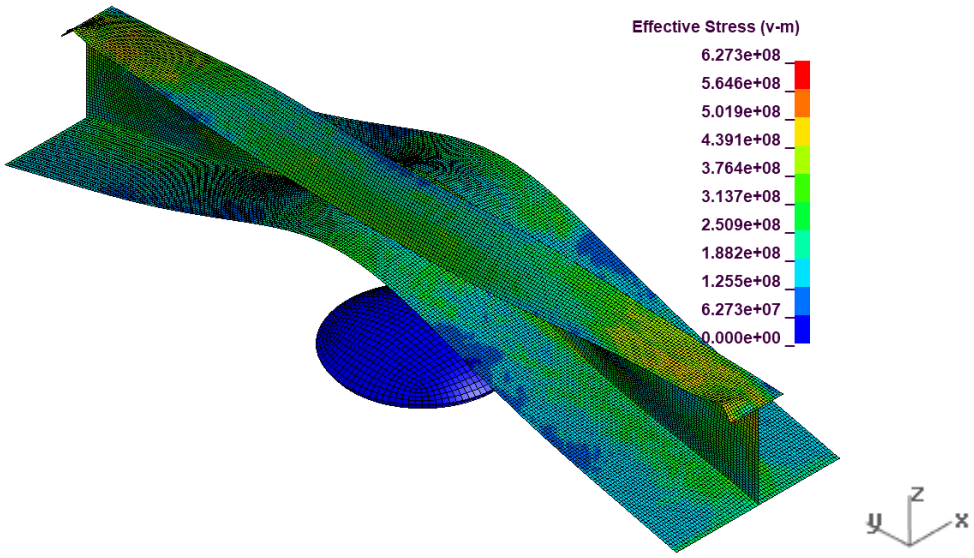

Figure 5.6: Exp2, Control – Built-T, von Mise Stress.

The flat bar control run visuals related to the undeformed geometry and the maximum von Mises stress data can be seen in Figure 5.7 and Figure 5.8.

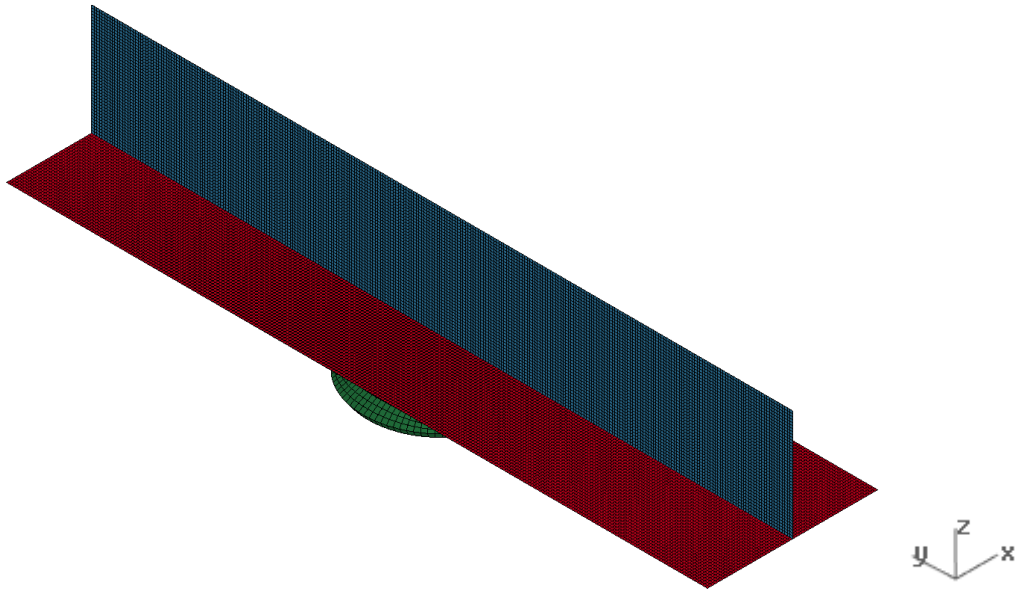

Figure 5.7: Exp2, Control – Flat Bar, Geometry.

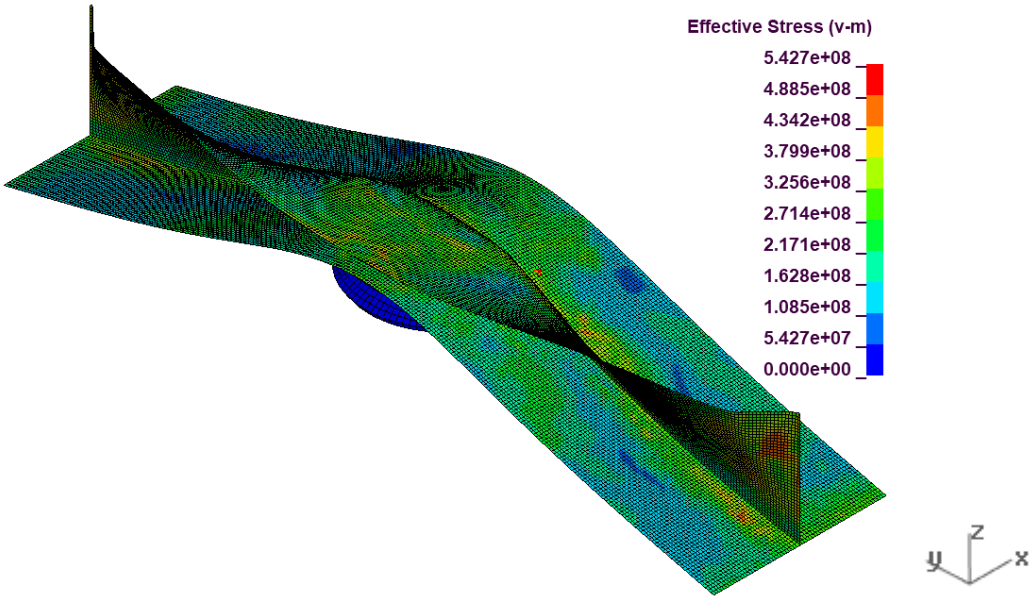

Figure 5.8: Exp2, Control – Flat Bar, von Mise Stress.

See Appendix C1 for visuals for all run geometry and von Mises stress results.

See Appendix C2 for information regarding the scantlings of the experimental runs found in Exp2. The following definitions relate to the column headings located in Appendix C2:

Deflection (Web Height) – Only used in Test5 and Test6 regarding deflection diagrams. The deflection of a beam from deflection diagram calculations. Converted to centre span web height.

Impact Force – Only used in Test5 and Test6 regarding deflection diagrams. The theoretical impact force that would deflect a fixed-fixed, uniform cross-section, beam a required amount. Not to be confused with impact forces within the results of this Chapter.

Depth, x_1, Breadth, x_2, Slant, x_3 – The depth, breadth, and slant each respectively corresponds to corrugation parameters related to traditional corrugation. Refer to Figure 4.7 for more detail.

Angle – The angle refers to the traditional corrugation angle between the slant and the depth of corrugation. See Equation [4] and Figure 4.7 for more detail.

$$\tan^{-1}\frac{x_1}{x_3} \quad [4]$$

Longitudinal Length – The longitudinal length refers to the linear length of the web that was connected to the stiffener. In straight webbed scenarios, such as with the flat bar and built-T cases, the length was constant at 1.36 m (the length of the side-shell). However, in cases involving corrugation, the effective length was larger than 1.36 m due to the weaving pattern of corrugation.

5.3.1 Test1 – Traditional Corrugation

To expand on the analysis of Exp1, traditional corrugated stiffeners were further examined well into the plastic regime. Since it was shown in Exp1 that as the corrugation was minimized the energy absorption of the grillage increased, four traditional corrugation runs (Trad. Corr. 1 through 4) were compiled with smaller corrugation than tested in Exp1. Each run consisted of a flangeless corrugated flat bar. For runs 1 through 4, the runs were built with corrugation parameters (x_1, x_2, and x_3) each equal to 10 mm, 8 mm, 6 mm, and 4 mm, respectively.

The Trad. Corr. 1 run visuals related to the undeformed geometry and the maximum von Mises stress data can be seen in Figure 5.9 and Figure 5.10, respectively. Trad. Corr. 1 was chosen for visual clarity since its corrugation parameters were the largest of the Test1 runs.

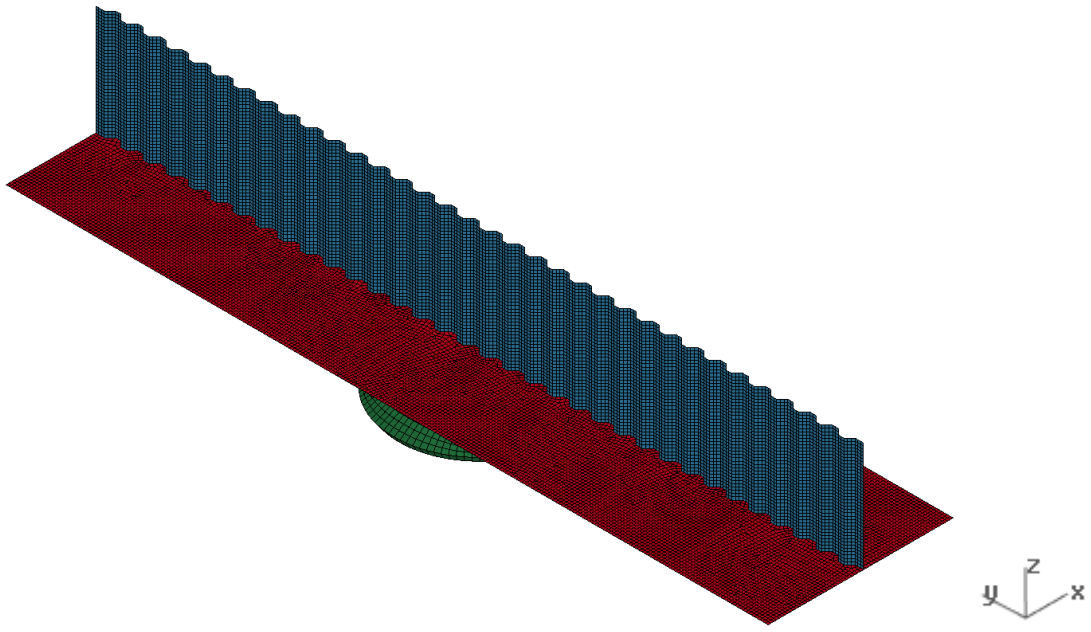

Figure 5.9: Exp2, Trad. Corr. 1 Geometry.

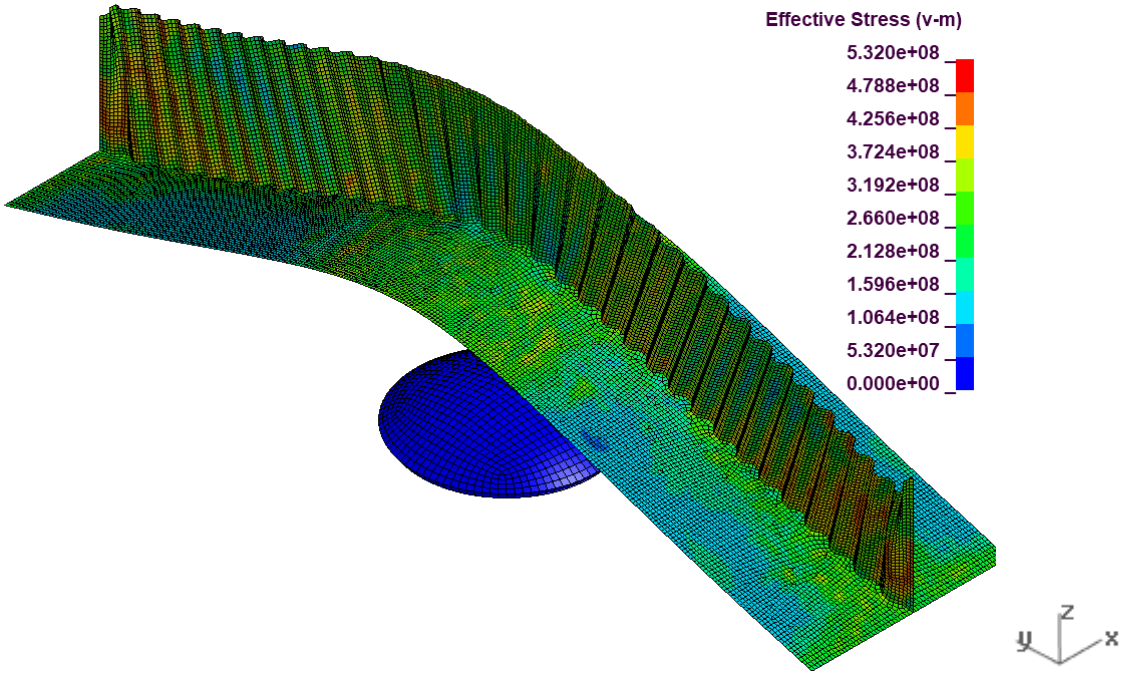

Figure 5.10: Exp2, Trad. Corr. 1 von Mise Stress.

Significant end-buckling was observed on the web of the stiffener of each run. However, there was no significant web tripping or local buckling at the indentation site. It seems that, due to the shape of the corrugation, the stiffener was able to "spread" apart at the top of the stiffener which stopped tripping and local buckling from being able to occur (or at least sufficiently delay the onset of buckling). However, corrugation was not able to eliminate end-buckling.

Regarding Figure 5.11, for the four corrugation runs, within the overload region, there was a near-linear increase in stress as the models responded to the rigid body motion of the indenter. The models reached a maximum von Mises stress, of approximately 950 MPa, at the end of the indentation. The control runs produced a different shape compared to the corrugation runs. The built-T reached a maximum stress quickly in the analysis, which then

gradually decayed. Whereas the corrugated runs sloped positively to a maximum stress state. Also, the built-T's maximum stress state was ~1200 MPa, about 350 MPa higher than that of the corrugated runs. Therefore, it was likely that the built-T would have yielded before the corrugated stiffeners. The flat bar reached an overall lower maximum stress than any of the other runs, with a value of approximately 900 MPa. Also, the flat bar experienced a steep decrease in stress at a displacement of 125 mm. No other run experienced such a decrease. It should be noted that the relatively high von Mises data present was due to the strain-rate hardening implemented within the material model (see Section: 5.2.9 Strain-Rate Hardening).

Regarding Figure 5.12, for the corrugated runs, within the overload region, there was a near-linear increase in force as the model responded to the rigid body motion of the indenter. However, though the overall internal energy capacity of the built-T and flat bar runs was higher than the corrugated runs, the control runs experienced a steep decrease in force at 125 mm (exactly where the flat bar was observed to have a decrease in stress). The decrease phenomenon was consistent with, and therefore likely due to, the local buckling and tripping. Moreover, a series of dynamic slope declines were visible at the beginning of each test which was consistent with end-buckling. All things considered, even though the control runs buckled, their ability to absorb energy even in their buckled state still equalled that of the corrugated runs. Additionally, the elastic energy absorption of the control runs was much greater than the corrugated runs.

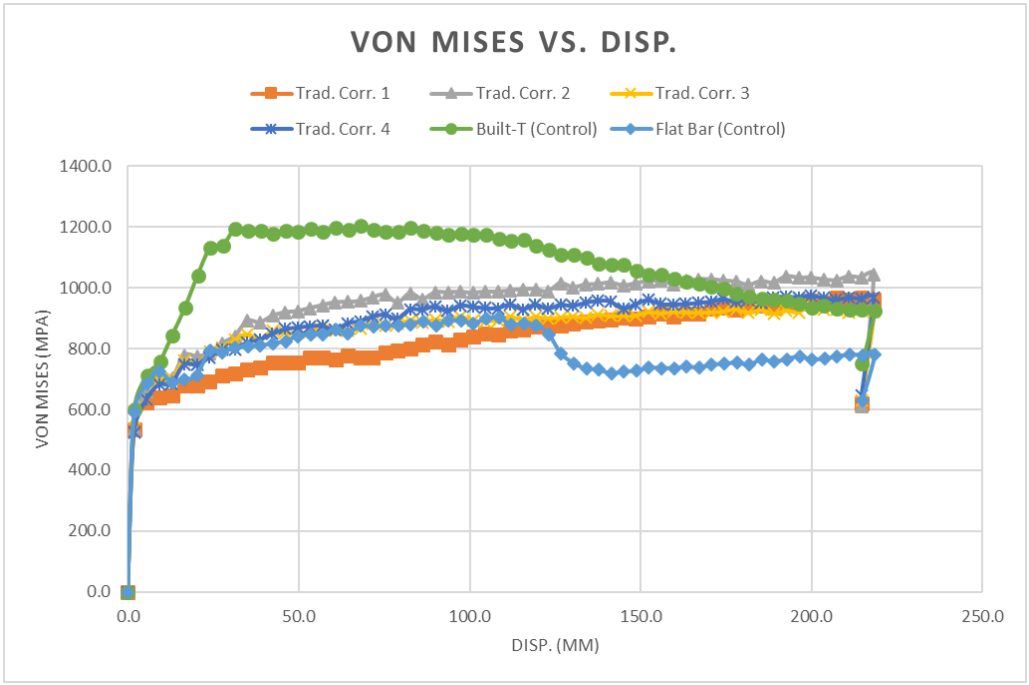

Figure 5.11: Exp2, von Mises vs. Disp. plot for Test1 runs and control runs.

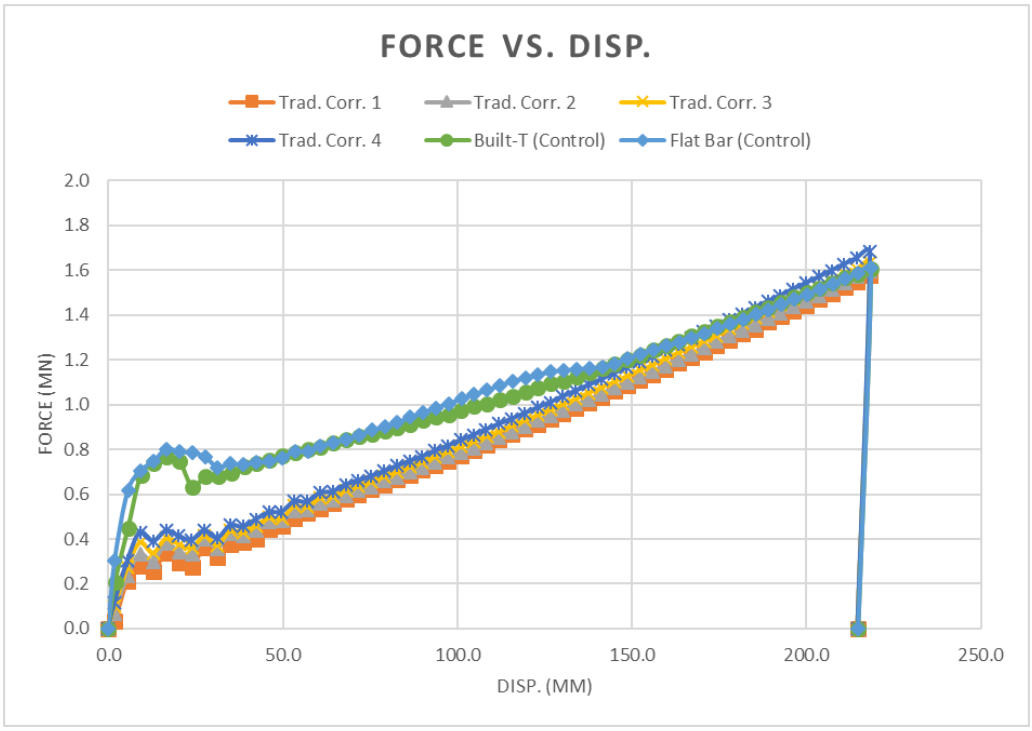

Figure 5.12: Exp2, Force vs. Disp. plot for Test1 runs and control runs.

5.3.2 Test2 – 'S' Corrugation

Within Test2, the second type of corrugation was examined in the form of 'S' corrugation. The 'S' shape was similar in appearance to the traditional shape except it followed a sinusoidal shape with fewer possible areas for stress to concentrate. See Figure 4.1 and Figure 4.2 for more details.

For S. Corr. 1 through 7, the runs were built with constant corrugation parameters: wavelength = 40 mm, and an amplitude of 5 mm. See Figure 5.13. The corrugation parameters were kept constant to better compare the behaviour of each 'S' model with one another.

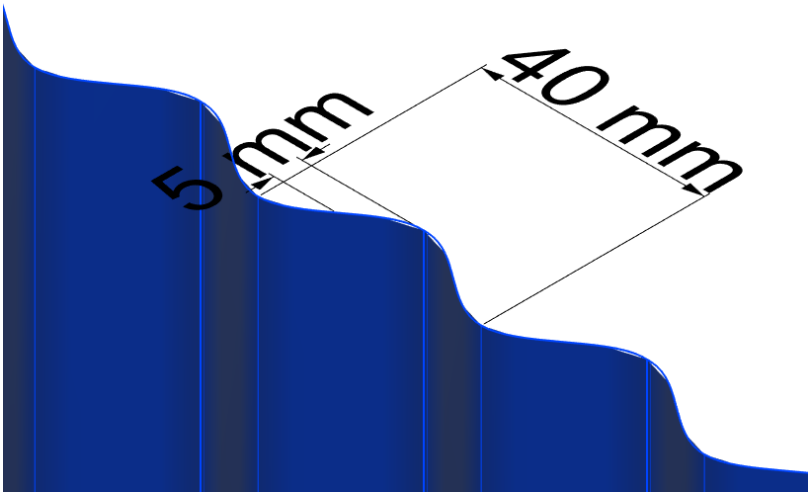

Figure 5.13: S Corr. relevant dimensions.

Below is a brief description of each model:

- S Corr. 1 was a flat bar with corrugation (similar to runs Trad. Corr. 1-4).
- S Corr. 2 was a built-T with corrugation.
- S Corr. 3 was a built-T with a corrugated web and an un-corrugated flange.

- S Corr. 4 was an L stiffener with corrugation.
- S Corr. 5 was a built-T with a corrugated web and an un-corrugated split-flange.
- S Corr. 6 was a built-T with an un-corrugated web and a corrugated flange.
- S Corr. 7 was a flat bar with diagonal corrugation.

The S. Corr. 4 run visuals related to the undeformed geometry and the maximum von Mises stress data can be seen in Figure 5.14 and Figure 5.15, respectively. S. Corr. 4 was chosen since it best-represented geometries tested within Test2.

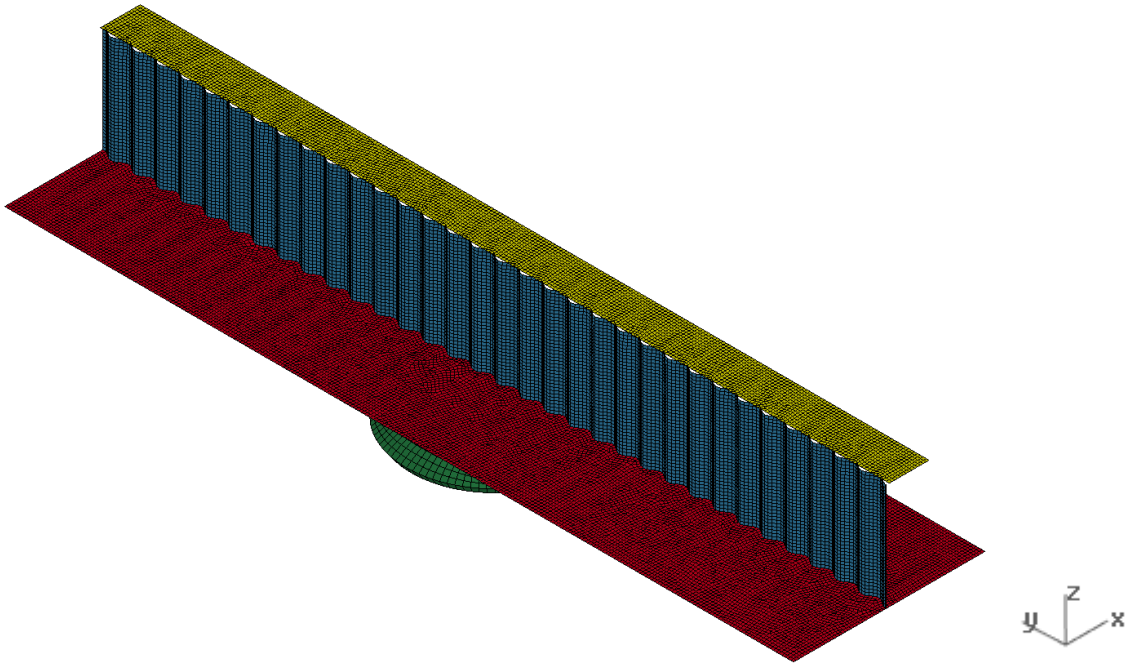

Figure 5.14: Exp2, S Corr. 4 Geometry.

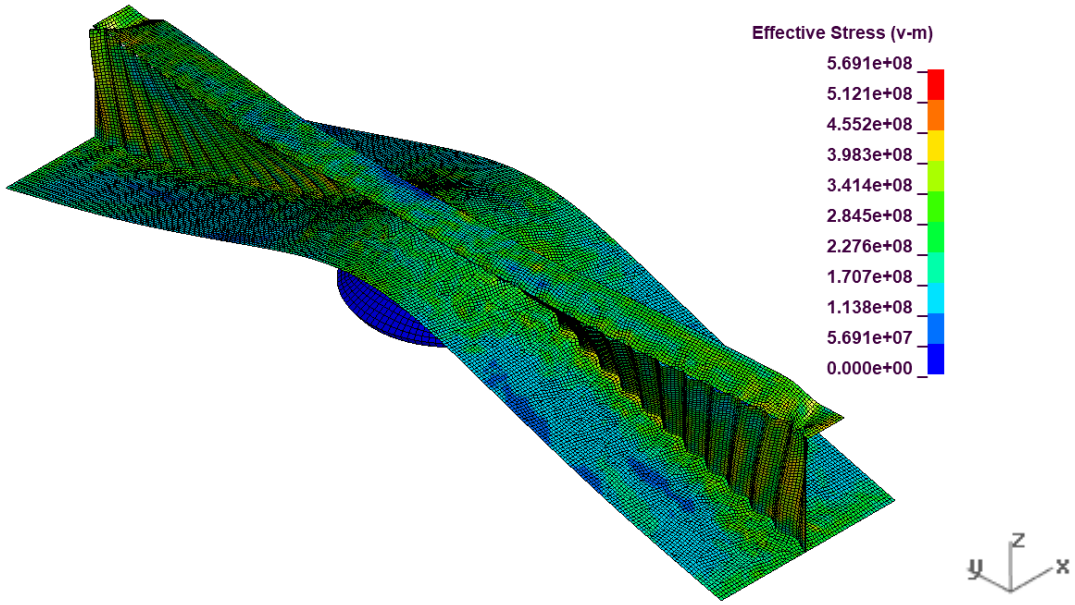

Figure 5.15: Exp2, S Corr. 4 von Mise Stress.

Significant local buckling or tripping was present in each model, except for Run1. Each model also suffered from a large amount of end-buckling, except for S. Corr. 1. Therefore, visually, it seems that Run1 had less of an issue with buckling than the other models.

Regarding Figure 5.16, for the seven S Corr. runs, within the overload region, there was a near-linear increase in stress as the models responded to the rigid body motion of the indenter. The models reached a maximum von Mises stress, of approximately 720 – 1000 MPa, at the end of the indentation. Also, the built-T's maximum stress state was about 200 MPa higher than that of the highest stress S Corr. Case. The flat bar reached an overall maximum stress within the range of the S Corr. Runs., with a value of approximately 900 MPa. Also, the flat bar experienced a steep decrease in stress at a displacement of 125 mm. The only other run to experience such a decrease was Run4, which had an L cross-sectional stiffener arrangement. It was interesting to note that while some of the other runs were also

built-T's, they did not experience steep decreases in stress like the built-T and S Corr. 4 runs.

Regarding Figure 5.17, for all runs, within the overload region, there was a near-linear increase in force as the model responded to the rigid body motion of the indenter. However, several runs experienced sharp decreases in force which was indicative of buckling. Both Run1 and 2 (which experienced the least amount of local buckling and tripping) also had the lowest elastic energy absorption capacity of all the runs. Moreover, a series of dynamic slope declines were visible at the beginning of each test which was consistent with end-buckling. All things considered, even though the control runs buckled, their ability to absorb energy even in their buckled state still equalled that of the corrugated runs. Additionally, the elastic energy absorption of the control runs was much greater than the corrugated runs.

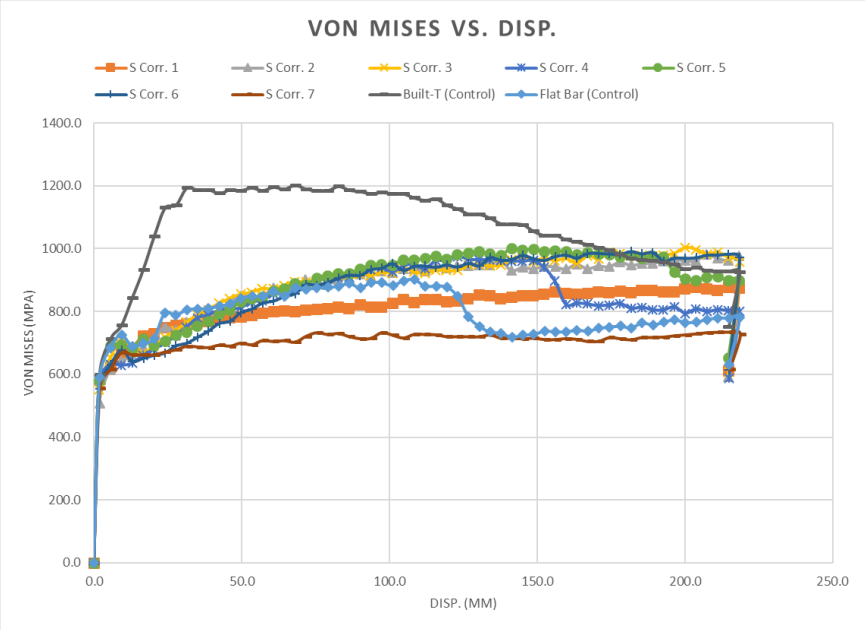

Figure 5.16: Exp2, von Mises vs. Disp. plot for Test2 runs and control runs.

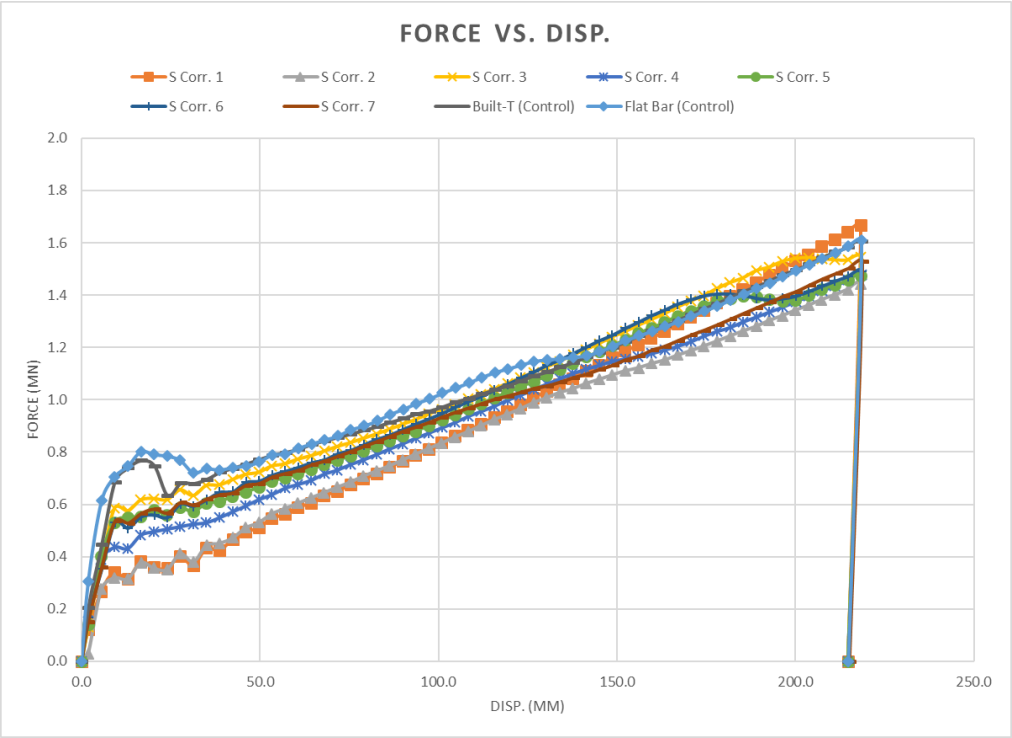

Figure 5.17: Exp2, Force vs. Disp. plot for Test2 runs and control runs.

5.3.3 Test3 – Bulb, Circular Hollow Section, and Non-Uniform Flange Built-T's

After testing varying configurations of corrugated stiffeners without any success several other stiffener variations were tested which did not contain any corrugation. A bulb stiffener was designed according to the dimensions shown in Figure 5.19. A standard bulb design was chosen, then altered slightly to match the appropriate web slenderness ratio and overall weight. Due to their distinct cross-sectional shape, bulb stiffeners were difficult to model properly using shell elements. The alternative would be to use solid elements. However, to ensure accurate bending calculations relative to the adjacent elements, at least five solid elements must use used through its thickness. Therefore, meshing the bulb with solid elements would require much more computational power than with shells. Instead,

the bulb stiffener was meshed using shell elements by approximating the cross-sectional shape of the bulb. The dimensions of the bulb stiffener can be found in Figure 5.19.

Concerning Figure 5.18, the two rectangles within the middle image represent the same area as the more complicated respective shapes of the leftmost image. The rightmost image was meshed with shell elements with thicknesses equal to the thickness of the middle image.

Two CHS stiffeners were created to be tested. The first CHS had a thickness equal to that of the control runs, with an appropriate radius to ensure the weight was correct. The second CHS was a mixture of a built-T and a CHS. The slenderness ratio was not held since slenderness ratios between straight cross-sections were not comparable to those of circular cross-sections. Due to the added web cross-sectional material due to the added CHS, the slenderness ratios were adjusted proportionally to the difference in the cross-sectional area.

Additionally, two non-uniform flanged built-T test runs were designed. For built-Ts, during a dynamic impact normal to the side-shell, the center of the web span tends to become compressed between the side-shell and the stiffener flange. This compression often leads to premature local buckling of the stiffener web (see Section: 1.3 Investigation Motivation). Therefore, both non-uniform flanged runs were created with a wide flange at the stiffener ends to decrease end-buckling. The wide flange tapered off to a narrow flange toward the centre of the span.

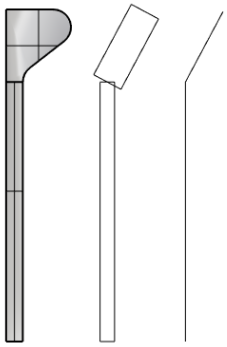

Figure 5.18: Creation of Bulb geometry.

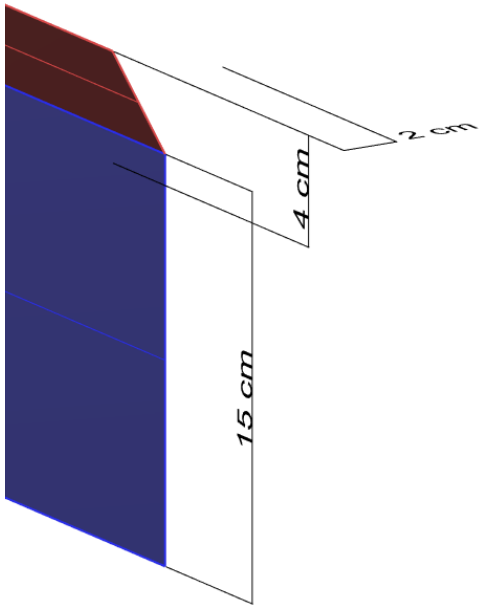

Figure 5.19: Bulb relevant dimensions.

Below is a brief description of each model.

- Bulb was a bulb stiffener.
- CHS (Constant Thickness) was a CHS with a thickness equal to that of the built-T control run.
- CHS with Flange was a CHS combined with a built-T.

- Non-Uniform Flange 1 was a built-T with a non-uniform cross-sectional area along its span.
- Non-Uniform Flange 2 was a built-T with a non-uniform cross-sectional area along its span.

The Bulb run visuals related to the undeformed geometry and the maximum von Mises stress data can be seen in Figure 5.20 and Figure 5.21, respectively.

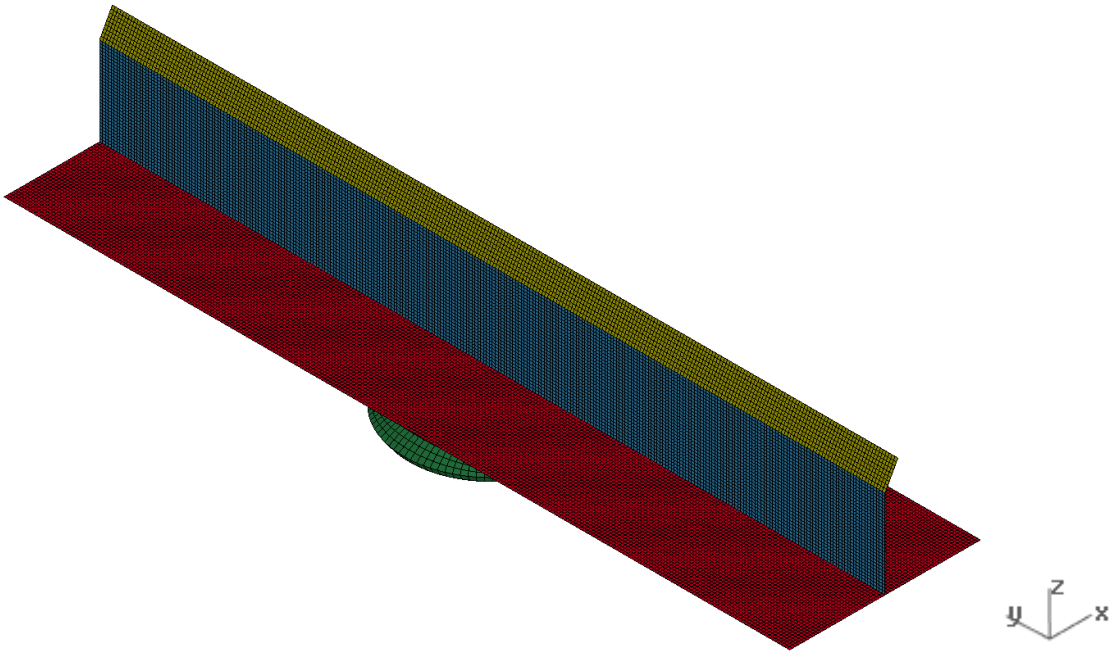

Figure 5.20: Exp2, Bulb Geometry.

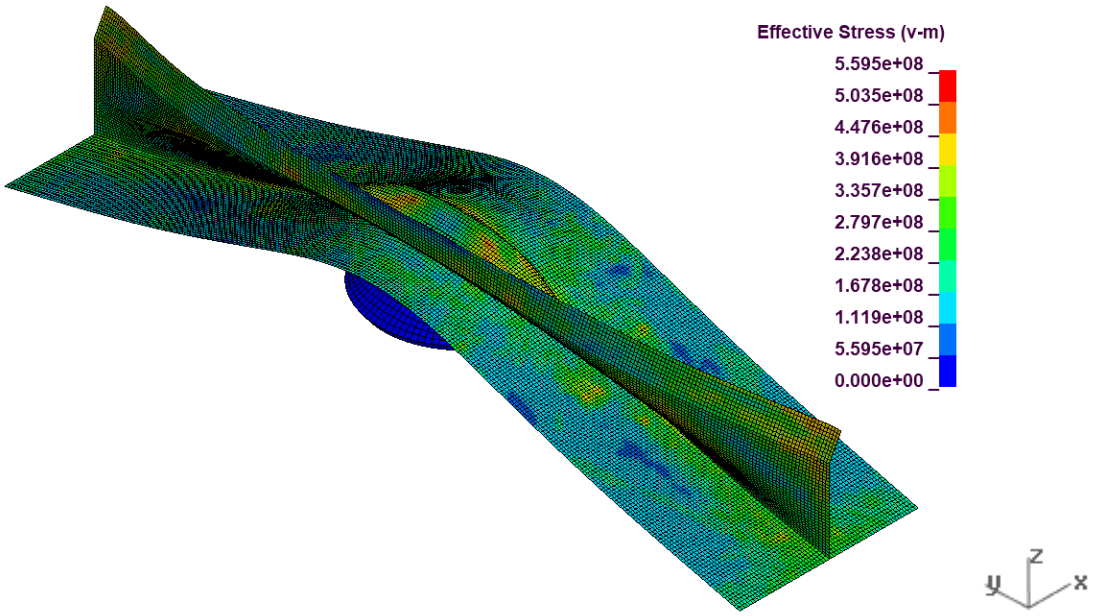

Figure 5.21: Exp2, Bulb von Mise Stress.

The CHS with Flange run visuals related to the undeformed geometry and the maximum von Mises stress data can be seen in Figure 5.22 and Figure 5.23, respectively.

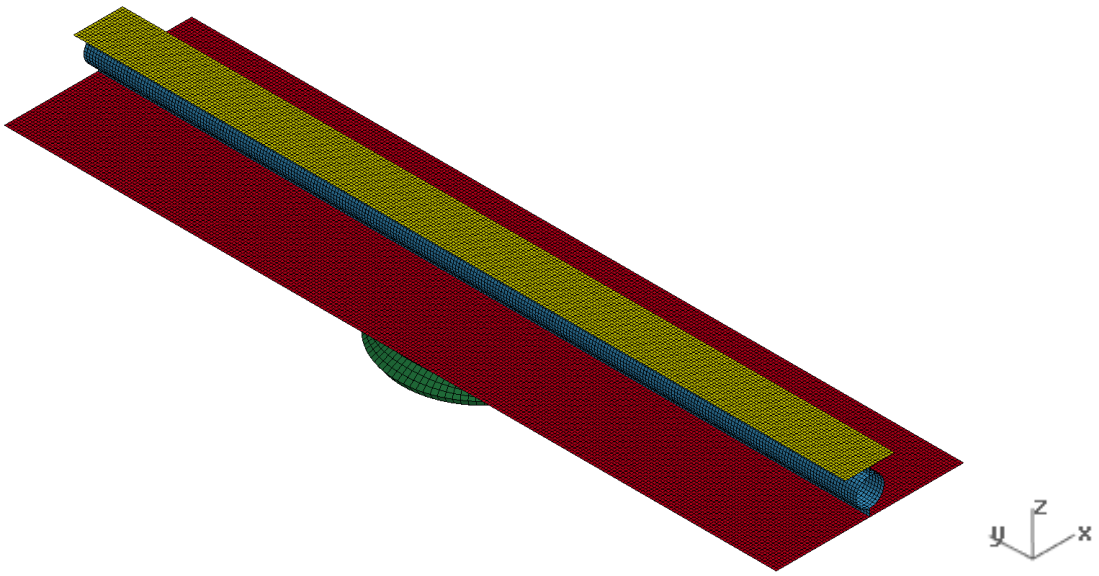

Figure 5.22: Exp2, CHS with Flange Geometry.

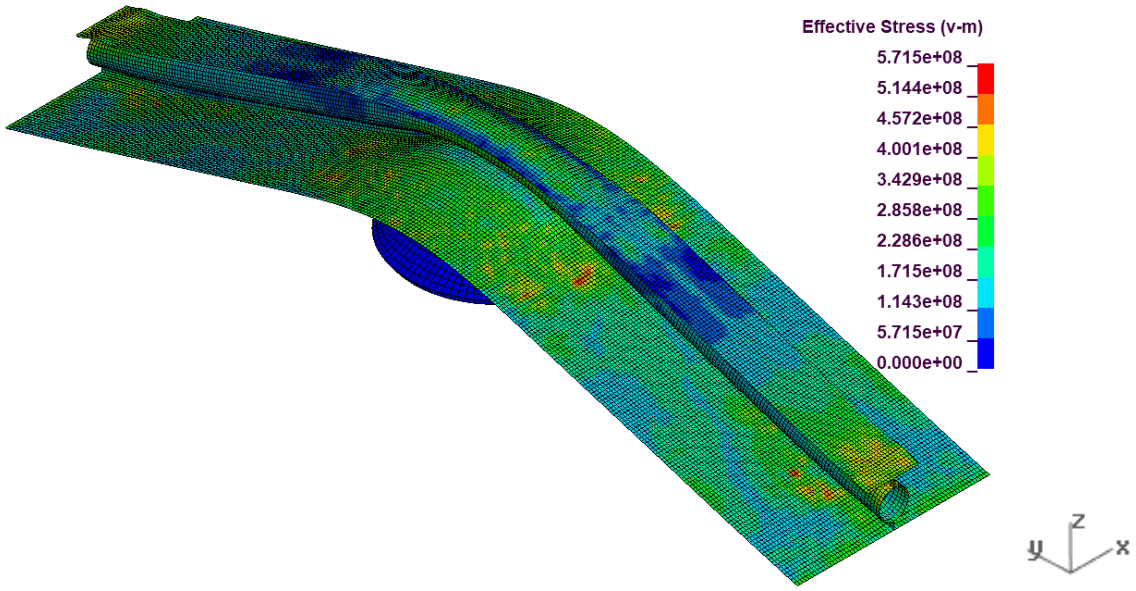

Figure 5.23: Exp2, CHS with Flange von Mise Stress.

The Non-Uniform Flange 1 run visuals related to the undeformed geometry and the maximum von Mises stress data can be seen in Figure 5.24 and Figure 5.25, respectively.

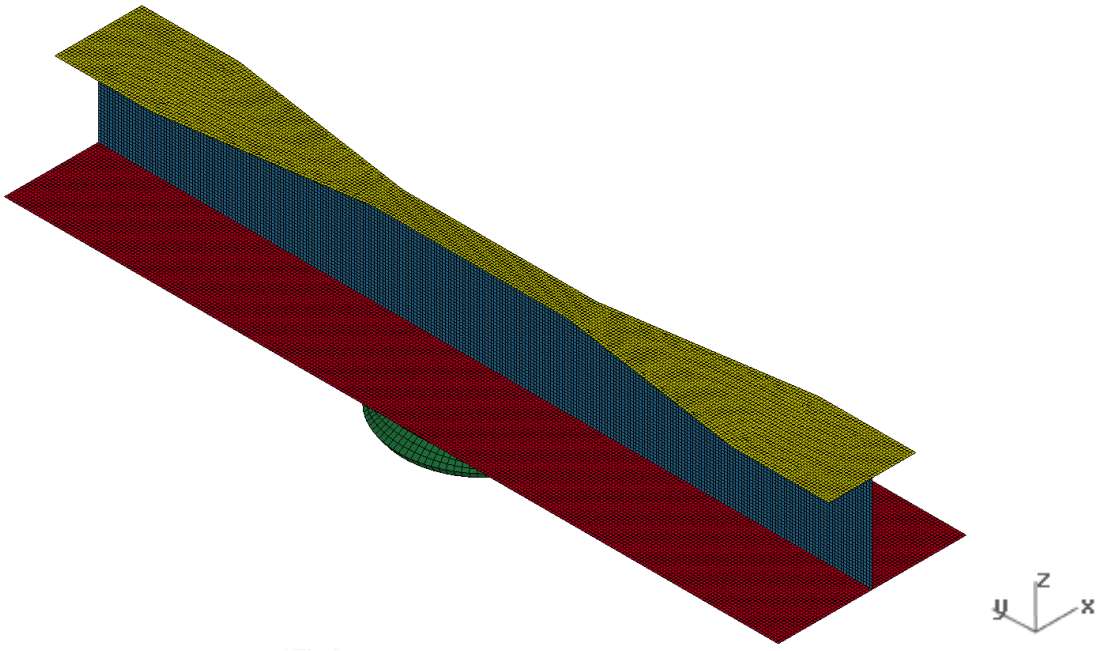

Figure 5.24: Exp2, Non-Uniform Flange 1 Geometry.

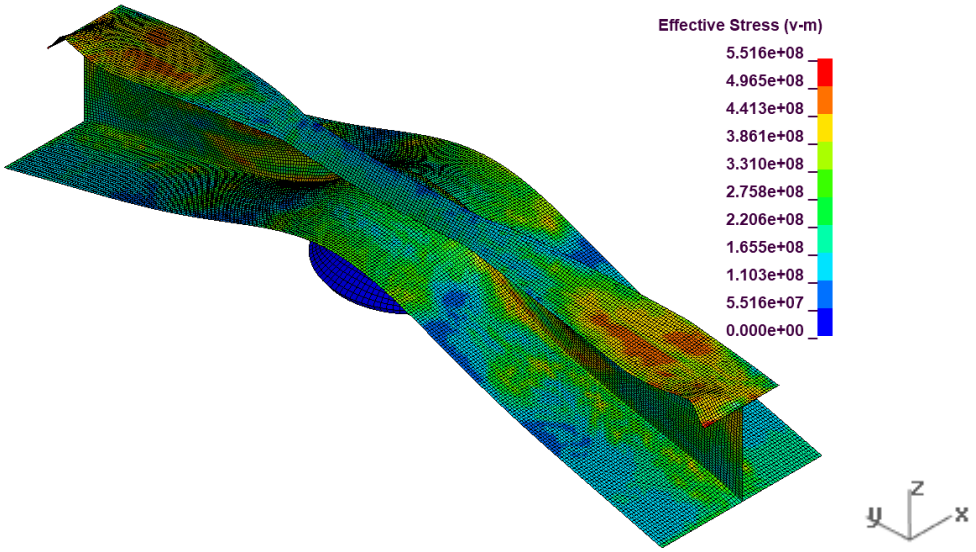

Figure 5.25: Exp2, Non-Uniform Flange 1 von Mise Stress.

Significant local buckling or tripping was present in each model. The Bulb did not experience significant end-buckling, nor did the CHS models. Both Non-Uniform Flange models did experience severe end-buckling, even though the widened flange was intended to combat the end-buckling.

Regarding Figure 5.26, the two Non-Uniform Flange runs, and the built-T run performed similarly. Throughout the impact, the built-T had an approximate 50 MPa higher stress than the other two runs. However, toward the end of the impact run Non-Uniform Flange 1 ended with the highest stress at near 980 MPa. The most notable case was the Bulb which experienced a stress decrease of about 180 MPa at a displacement of 40 mm. The two CHS runs experienced the most steady-state behaviour with a gradual increase in stress throughout the test, with a stress range of 650 MPa to 750 MPa.

Regarding Figure 5.27, the two CHS runs experienced the most unique behaviour with steep, steady-state slopes. While all other runs ended with a force of about 1.6 MN, the two CHS runs ended with a much higher force, of just over 1.8 MN. The force increase was proportional to an increase in energy absorption. However, both CHS runs had the lowest elastic energy absorption capabilities of all other runs. The elastic energy absorption must be at least equal to the control runs to be considered for further optimal concept grillage testing. All runs, except for the CHS runs, performed similarly despite their dramatic differences in geometry. It should be noted that the buckling was not apparent on the force vs. displacement plot (Figure 5.27). It was likely that buckling started initially at the beginning of the impact, which explained why initial energy absorption was relatively low. In totality, there was no clear advantage of either of the test runs compared to the control runs.

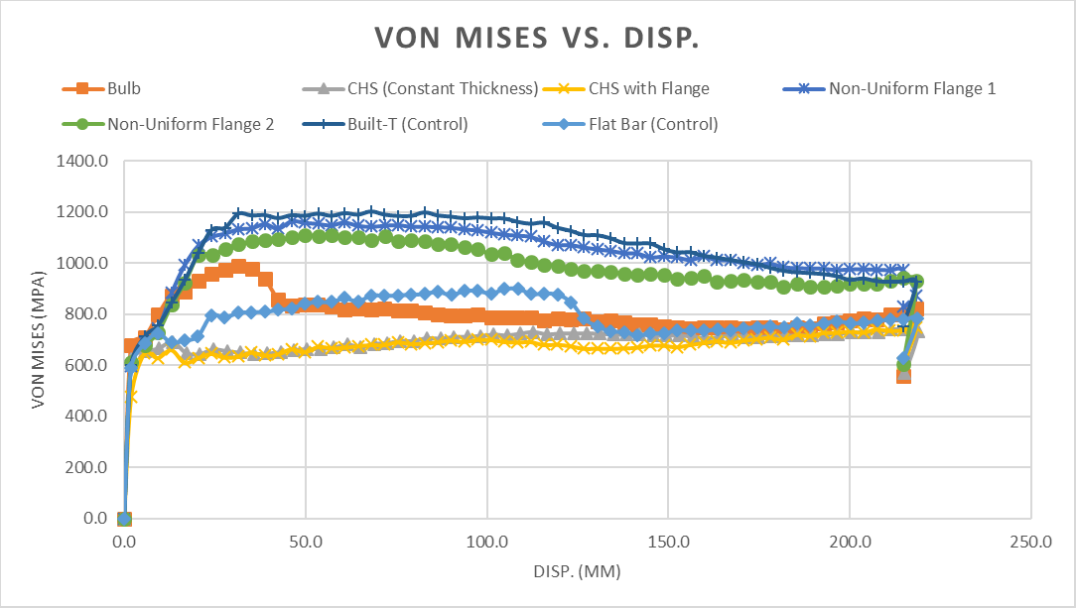

Figure 5.26: Exp2, von Mises vs. Disp. plot for Test3 runs and control runs.

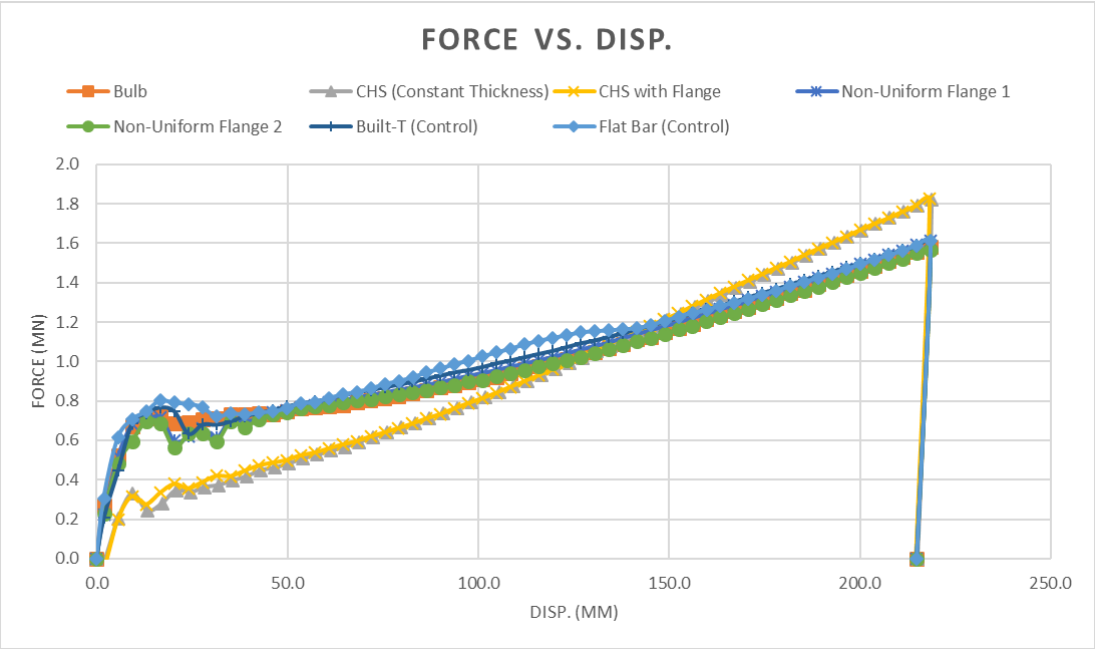

Figure 5.27: Exp2, Force vs. Disp. plot for Test3 runs and control runs.

5.3.4 Test4 – Flat bars with Brackets

In the shipbuilding industry, a common solution to stiffener buckling is to add brackets to the stiffener ends, as well as to the web of the stiffener. Tests were completed with five models which were very similar to the built-T control model, except the flange was removed and its material was repurposed into brackets to analyze how adding brackets would change the experimental responses. Therefore, the web height and thickness, and flange thickness, remained the same as the built-T (except for Run5 which had a portion of its web ends converted into brackets). Note that the width of the web brackets changed between runs, as well as the size and shape of the end brackets.

Below is a brief description of each model.

- Flat Bar with Brackets 1, seven rectangular web brackets centred at the middle of the span, as well as two end brackets at each end.
- Flat Bar with Brackets 2, nine rectangular web brackets centred at the middle of the span, as well as a triangular end bracket at each end.
- Flat Bar with Brackets 3, seven rectangular web brackets centred at the middle of the span, as well as two square hollow section end brackets at each end.
- Flat Bar with Brackets 4, seven rectangular web brackets centred at the middle of the span, as well as a triangular end bracket at each end.
- Flat Bar with Brackets 5, seven rectangular web brackets centred at the middle of the span, as well as two end brackets at each end. Also, some of the material at the web ends were moved to end brackets.

The Flat Bar with Brackets 1 run visuals related to the undeformed geometry and the maximum von Mises stress data can be seen in Figure 5.28 and Figure 5.29, respectively. Flat Bar with Brackets 1 was chosen since it best-represented geometries tested within Test4.

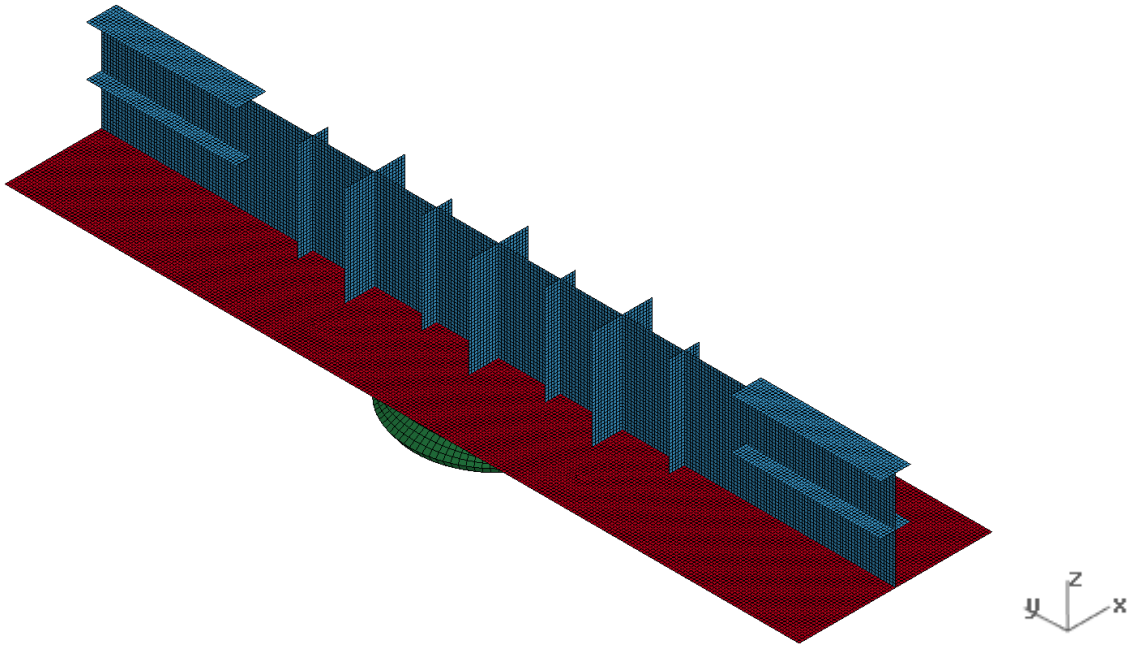

Figure 5.28: Exp2, Flat Bar with Brackets 1 Geometry.

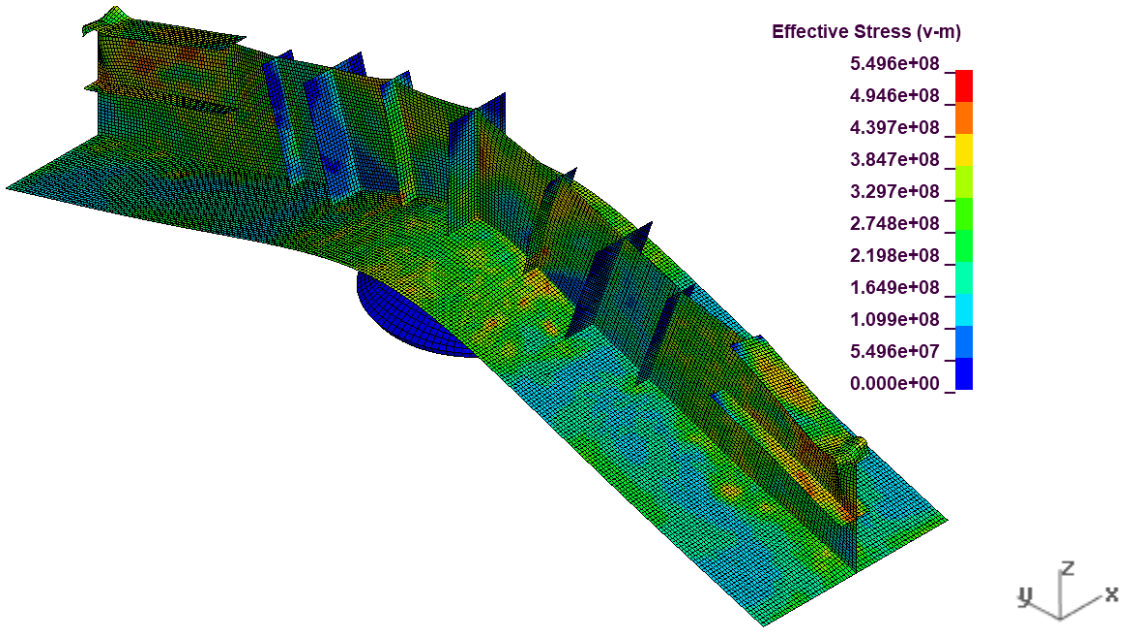

Figure 5.29: Exp2, Flat Bar with Brackets 1 von Mise Stress.

The brackets seemed to solve the buckling issues in several of the models. The only model to exhibit buckling at the mid-span (tripping in this case), was Run3. It was also the only model with the width of its mid-span brackets shortened. However, in many cases, the end brackets did very little to cease buckling at the ends. The only model to show little to no end-buckling was Run5, which shared the same geometry as Run1, except it had a reduced web height at the ends and an extra end bracket.

Regarding Figure 5.30, all Flat Bar with Bracket runs (except for Run5) performed similarly to one another. Run1 had the highest stress at the end of the run with a von Mises stress of ~1175 MPa. Run2 had the highest stress near the beginning of the run with a stress ~100 MPa higher than the other runs. Run5 followed a unique stress vs. displacement path compared to the other four runs. Run5's stress vs. displacement curve closely resembled the flat bar run instead and showed the overall lowest stress out of the other runs in this test.

Regarding Figure 5.31, though Run5 showed significant promise concerning its stress vs. displacement curve, its energy absorption was rather low in its force vs. displacement curve. All runs ended at approximately the same force, just over 1.6 MN. However, the elastic force of each curve varied wildly. The control runs had the highest elastic force values, followed by Run3, 1, 4, 2, and 5 (in order).

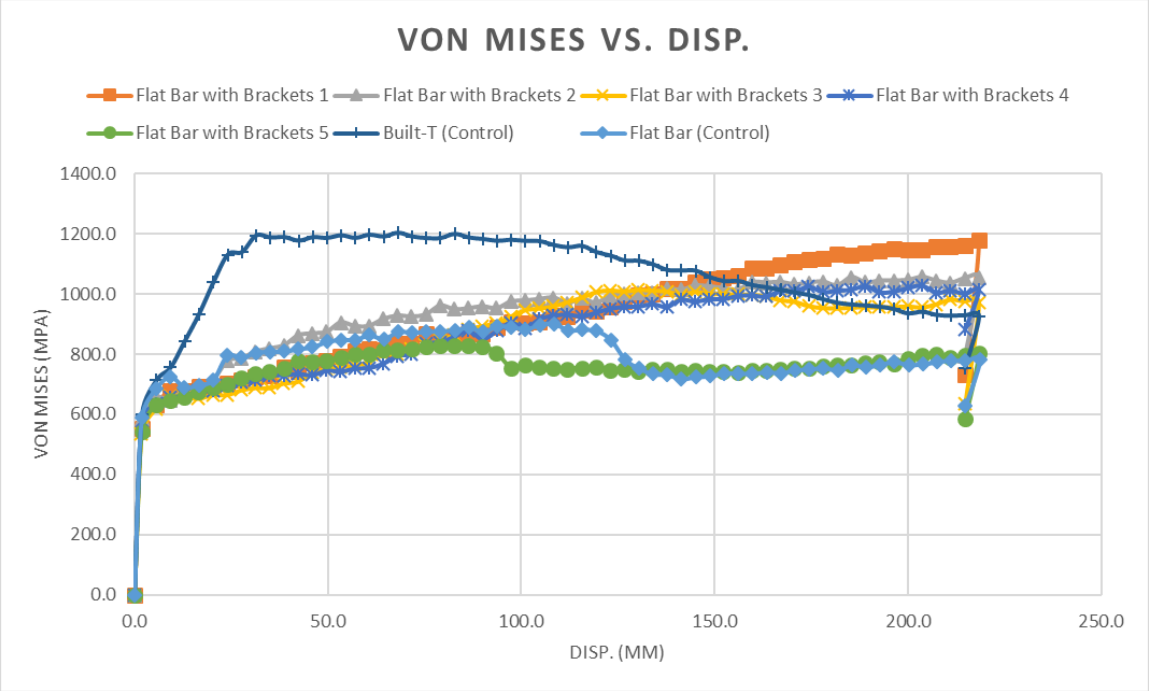

Figure 5.30: Exp2, von Mises vs. Disp. plot for Test4 runs and control runs.

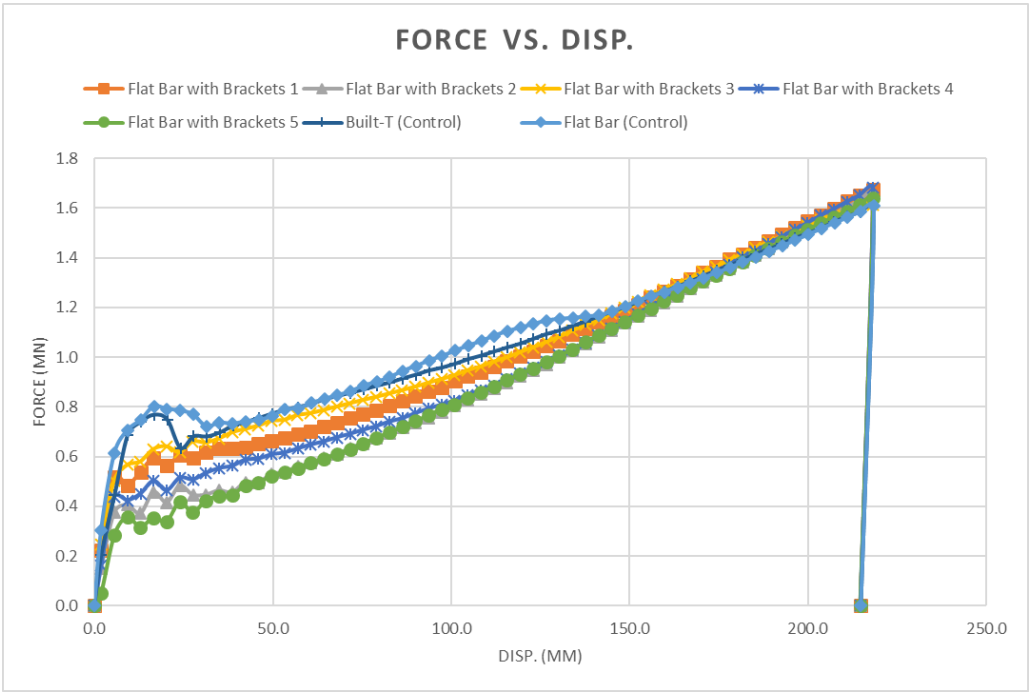

Figure 5.31: Exp2, Force vs. Disp. plot for Test4 runs and control runs.

Despite its lack of energy absorption ability, the only model to show little to no end-buckling was Run5, which was the only model with a non-uniform web height throughout its span. Also, non-uniform flange width has been tested with several models, but non-uniform web height has not been looked into thoroughly. Therefore, varying the web height of the stiffener was examined further in Test5 and Test6.

5.3.5 Test5 – Web Height Flat Bars

Within Test5, the goal was to produce a set of test runs with stiffener web profiles represented by deflection curves. The deflection curves were generated based on the built-T control runs since it had a uniform cross-section. The resultant deflection diagram shapes were converting into stiffener web profiles.

When a fixed-fixed beam is centrally loaded with what is effectively a point load, it assumes a shape which can be predicted by a deflection diagram. In reality, a point load must be represented by a distributed load since the load must act over some area. Therefore, an appropriate load case was identified in the form of Figure 5.32 which best approximates the impact present within the FEMs. In the case of the rigid indenter impacting the grillage, upon analyzing the residual indentations in the test runs, it was noted that the diameter of the impact zone, “c”, was approximately 327 mm. Note that concerning the FEMs, “d” will be equal to L/2.

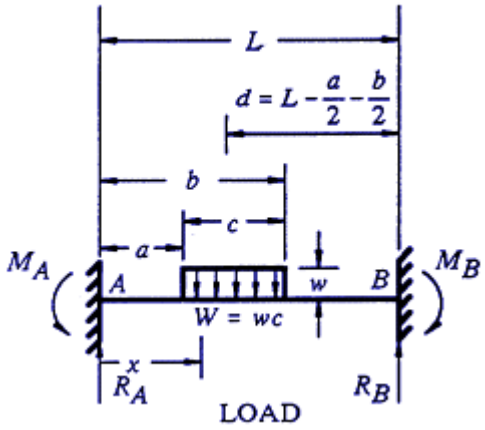

Figure 5.32: Fixed-fixed partial uniformly distributed load (Boeing Design Manual, Rev G. 1994).

The deflections calculated from the distributed load-deflection diagram calculations (see Appendix C3) were treated as if they were the central-span stiffener web heights. Calculations for the reaction forces and moments were completed according to Equations [5] through [8] (Boeing Design Manual, Rev G. 1994):

$$R_A = \frac{wc}{4L^2}\left(12d^2 - \frac{8d^3}{L} + \frac{2bc^2}{L} - \frac{c^3}{L} - c^2\right) \quad [5]$$

$$R_B = wc - R_A \quad [6]$$

$$M_A = -\frac{wc}{24L}\left(\frac{24d^3}{L} - \frac{6bc^2}{L} + \frac{3c^3}{L} + 4c^2 - 24d^2\right) \quad [7]$$

$$M_B = \frac{wc}{24L}\left(\frac{24d^3}{L} - \frac{6bc^2}{L} + \frac{3c^3}{L} + 2c^2 - 24d^2 + 24dL\right) \quad [8]$$

Referring to Table 5.1, it is important to note that the impact force column does not reflect actual applied loads on the grillage. Instead, the impact force simply refers to the required load necessary to deflect a uniform cross-section beam to the corresponding deflection. The

test runs were then constructed with profiles matching the shape of the deflection curves with central-span web heights equal to the deflections seen in the table.

Table 5.1: Calculated web heights along with their corresponding applied force.

	Deflection (Web Height) mm	Impact Force MN
DeflectCurve1	11.97	1.6
DeflectCurve2	52.59303734	7.03
DeflectCurve3	93.21610886	12.46
DeflectCurve4	133.8391804	17.89
DeflectCurve5	174.4622519	23.32
DeflectCurve6	215.0853234	28.75

Based on the input forces and resultant deflections shown in Table 5.1, Figure 5.33 shows the deflection plotted against the span of the stiffener, where "X" refers to the axial distance along the span. The curves on the plot represent stiffener web profiles.

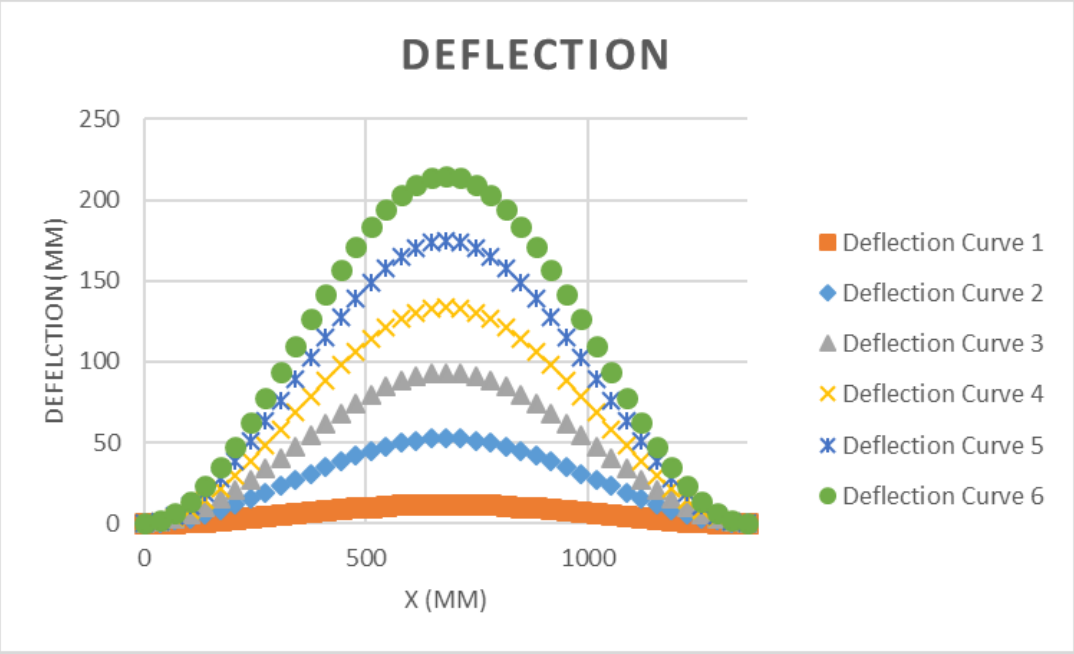

Figure 5.33: Deflection Curves to be used for stiffener height.

To ensure the web contained an equal amount of material in each run, the stiffener end-span height was appropriately adjusted to maintain the shape of the profile. Note that Run1 had such a slight web height difference at the centre of its span compared to its ends (12 mm), that it was effectively a flat bar.

The Deflection Curve 4 run visuals related to the undeformed geometry and the maximum von Mises stress data can be seen in Figure 5.34 and Figure 5.35, respectively. Deflection Curve 4 was chosen since it performed most optimally of the runs within Test5.

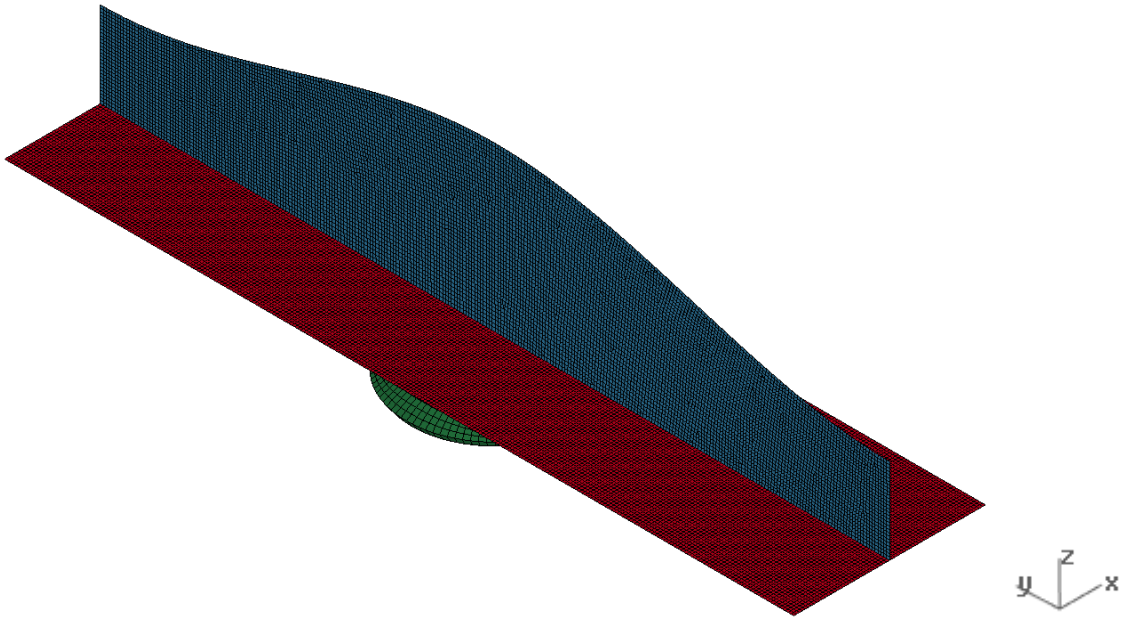

Figure 5.34: Exp2, Deflection Curve 4 Geometry.

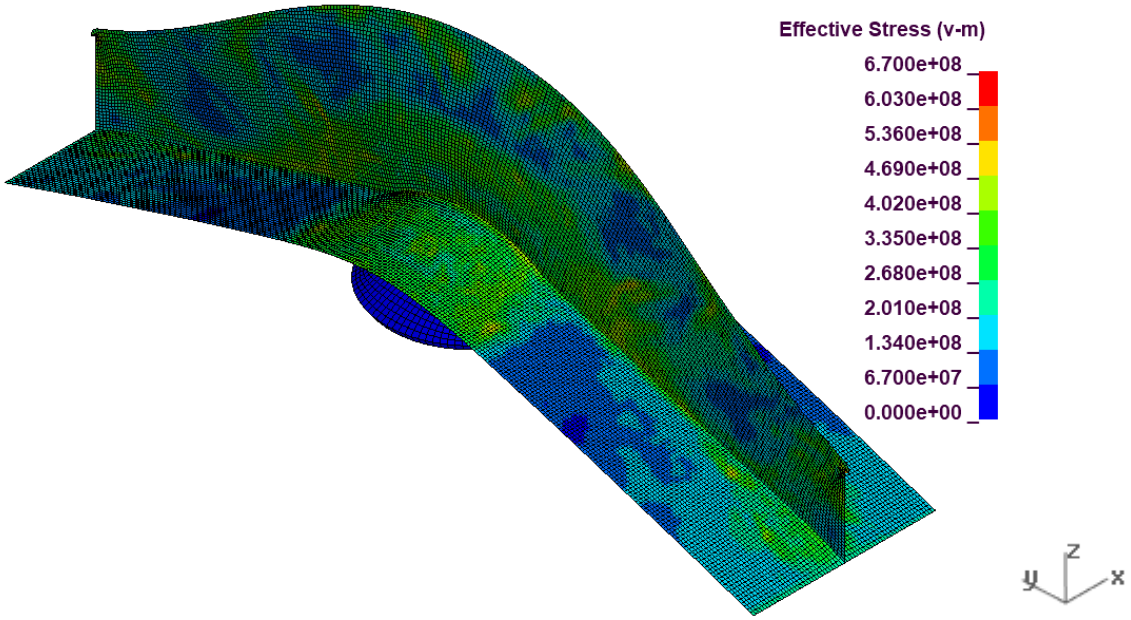

Figure 5.35: Exp2, Deflection Curve 4 von Mise Stress.

Regarding Figure 5.36, the maximum von Mises stress of the flat bar was the lowest of all runs (900 MPa). As usual, the built-T had the highest maximum von Mises stress at 1200 MPa. Several models showed large decreases in stress over small changes in displacement. The flat bar, Run1, Run2, and Run 6 demonstrated a large stress-drop at ~120 mm. The highest stress reported by any of the non-control runs was 1150 MPa by Run4.

Regarding Figure 5.37, each of the runs demonstrated an elastic capacity similar to both of the control runs, marking Test5 as the first simulation thus far to be able to do so. After first yield, a significant pattern began to emerge from Runs1-6. As the central span web height increased and the end web height decreased, trends can be seen in the overload capacity and the buckling point. By manipulating the web height, it was possible to both maximize the overload capacity and control at what displacement buckling occurred.

Regarding Figure 5.37, Run4 demonstrated the highest amount of overload capacity and showed no significant evidence of energy loss due to buckling throughout the whole displacement. However, one main concern with designing stiffeners based on deflection curves is that the produced stiffeners were likely only optimized for impacts that occurred at the centre of the span, based on the distinct profile shape. To be thorough, the next test explored the behaviour of inverse deflection curves, as well as circular web height curves. Circular web height curves may be better optimized for an impact anywhere along the stiffener since they have a smaller change in web height per unit distance along the length of the stiffener span.

From observing Figure 5.37, buckling can be seen in the form of losses in force per displacement. By comparing Figure 5.37 to Figure 5.38, the losses in force can be seen through the extent of tripping in the stiffener webs. As can be seen, Deflection Curve 4 buckled very little even after 220 mm of displacement from the indenter. See Appendix C1 for enlarged images of those shown in Figure 5.38.

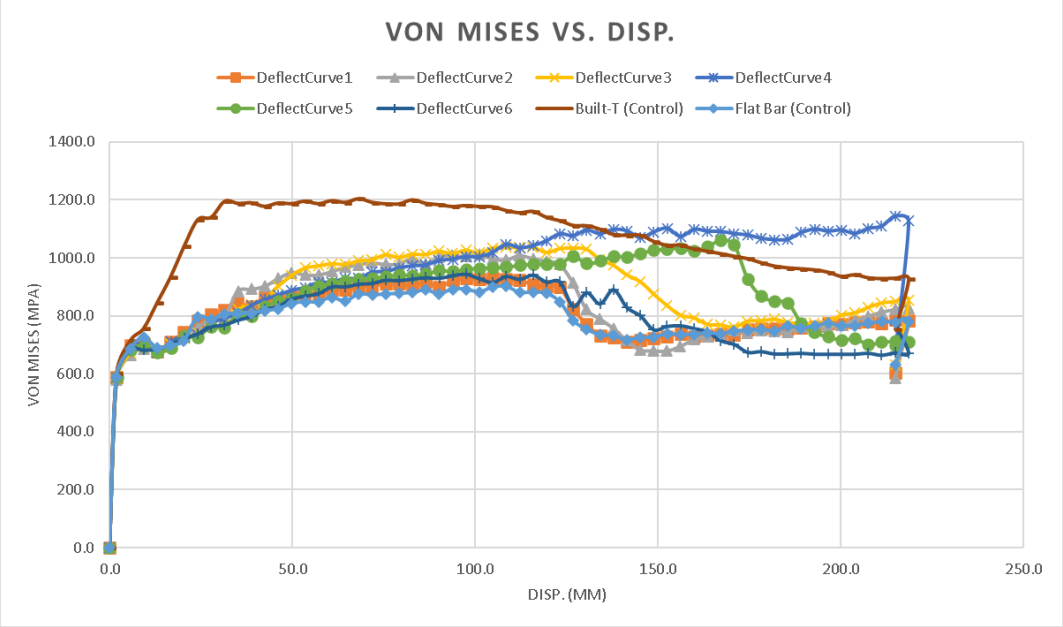

Figure 5.36: Exp2, von Mises vs. Disp. plot for Test5 runs and control runs.

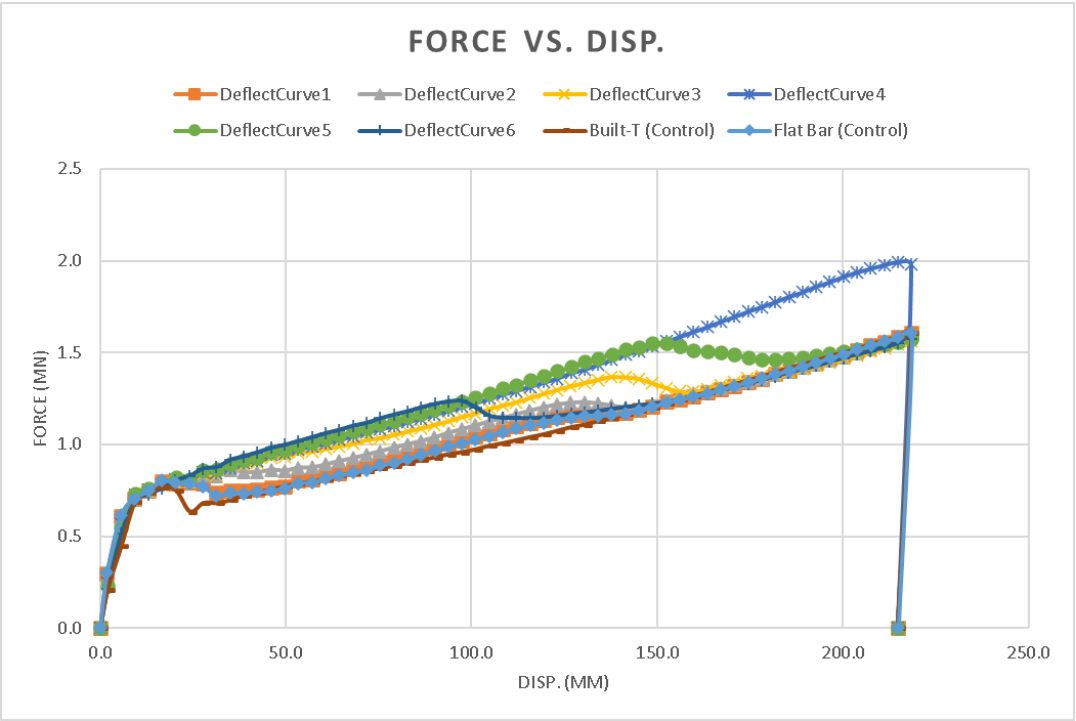

Figure 5.37: Exp2, Force vs. Disp. plot for Test5 runs and control runs.

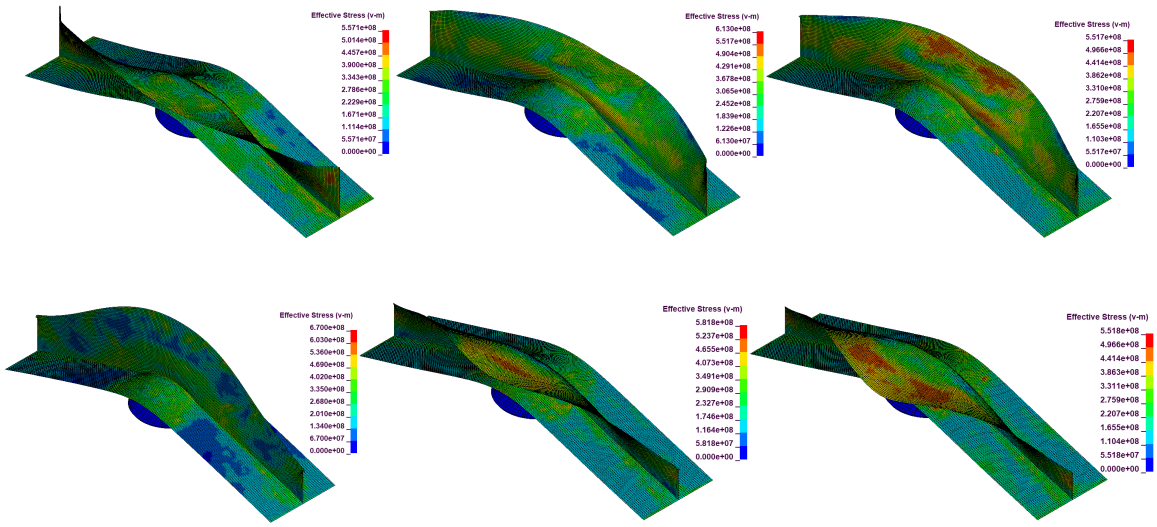

Figure 5.38: Tripping comparisons between Deflection Curve runs. Top row – Deflection Curves 1, 2 and 3. Bottom row – Deflection Curves 4, 5, and 6.

5.3.6 Test6 – Web Height Flat Bars (cont.)

A sixth a final test was completed for Exp2, the exploratory experiment. A model was tested which resembled a similar stiffener design to what was shown in Test5 with a more general circular profile shape instead of the profile shape of a fixed-fixed beam deflection diagram. The radius of curvature was based on the best performing deflection curve model. Another model was created with the same circular shape, except inverted. These tests were completed to be a more general solution to impact scenarios since the shape of deflection curves distinctly applies to mid-span stiffener impacts.

Additionally, three other models were tested which consisted of inverse deflection curves (the inverse web height of what was tested in Test5). Therefore, Inv. Deflection Curves 1, 2, and 3 had increased end stiffener height and reduced mid-span stiffener height. The shape was defined based on the same calculations shown in Figure 5.32, Figure 5.33, Table 5.1, Appendix C3, and Equations [5] through [8].

Below is a brief description of each model:

- Circular Curve was a flat bar with a varied web height, according to a circular radius.
- Inv. Circular Curve was a flat bar with a varied web height, according to a circular radius.
- Inv. Deflection Curve 1, 2 and 3, were flat bars with a varied web height, according to the shape of a deflection diagram.

The Circular Curve run visuals related to the undeformed geometry and the maximum von Mises stress data can be seen in Figure 5.39 and Figure 5.40, respectively.

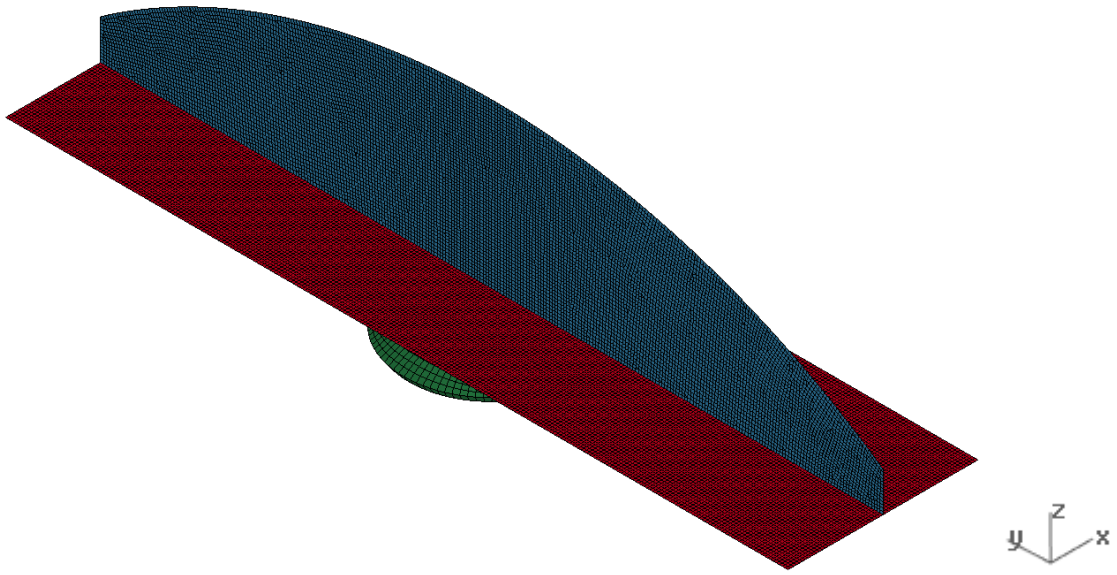

Figure 5.39: Exp2, Circular Curve Geometry.

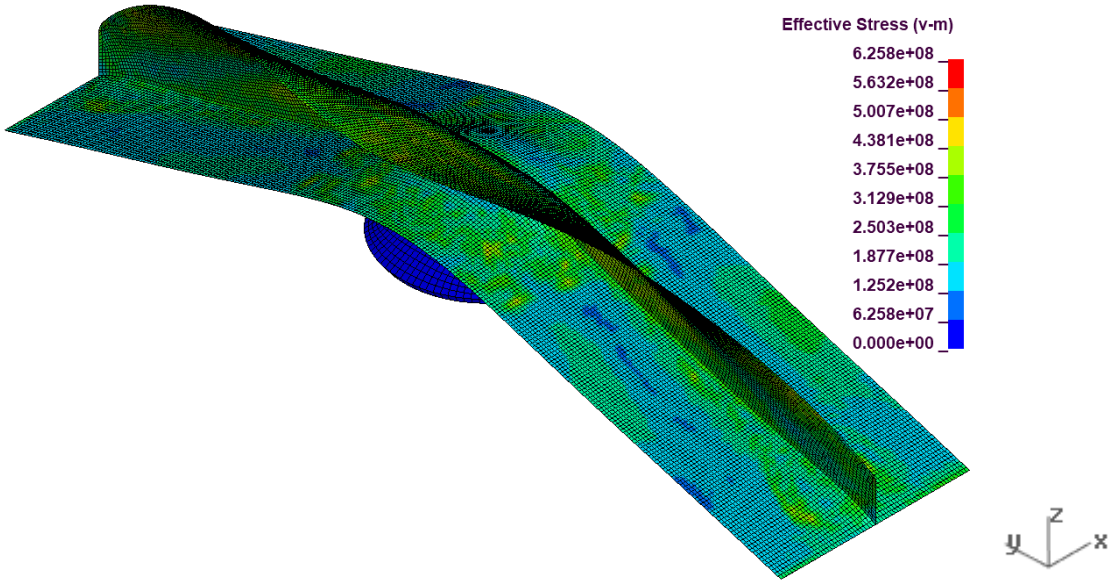

Figure 5.40: Exp2, Circular Curve von Mise Stress.

The Inv. Deflection Curve 3 run visuals related to the undeformed geometry and the maximum von Mises stress data can be seen in Figure 5.41 and Figure 5.42, respectively.

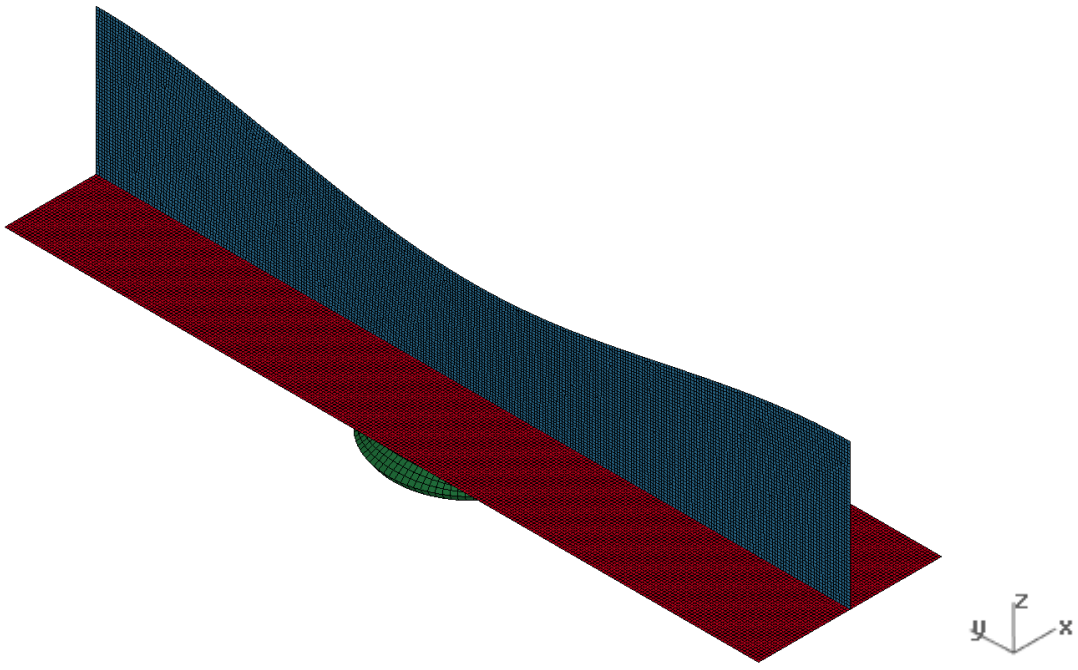

Figure 5.41: Exp2, Inv. Deflection Curve 3 Geometry.

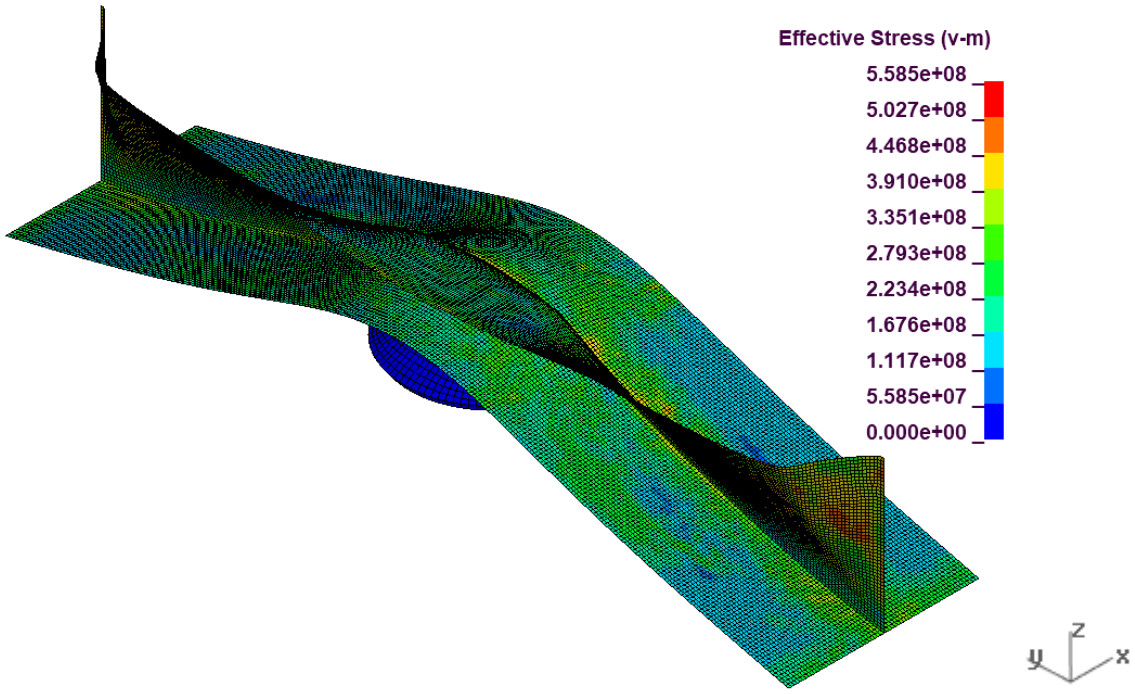

Figure 5.42: Exp2, Inv. Deflection Curve 3 von Mise Stress.

Before looking at all Test6 data as a whole, three key cases were analyzed separately. Initially, the circular curve and inverse circular curve data were compared. Secondly, the deflection curve runs were compared to their inverse counterparts. Finally, all Test6 data were analyzed as a whole.

Regarding Figure 5.43, the inverse circular curve run demonstrated the lowest maximum stress with a maximum von Mises stress of ~850 MPa. Both the circular curve and the flat bar runs performed similarly with maximum von Mises stress of ~950 MPa and ~900 MPa, respectively.

Regarding Figure 5.44, the regular circular curve was outperformed by the control runs and the inverse curve run, concerning their elastic energy absorption capacity. However, the circular curve run demonstrated significantly more overload capacity, especially as the

displacement increased. Overall, the inverse circular curve run was outperformed by the other runs concerning overload capacity.

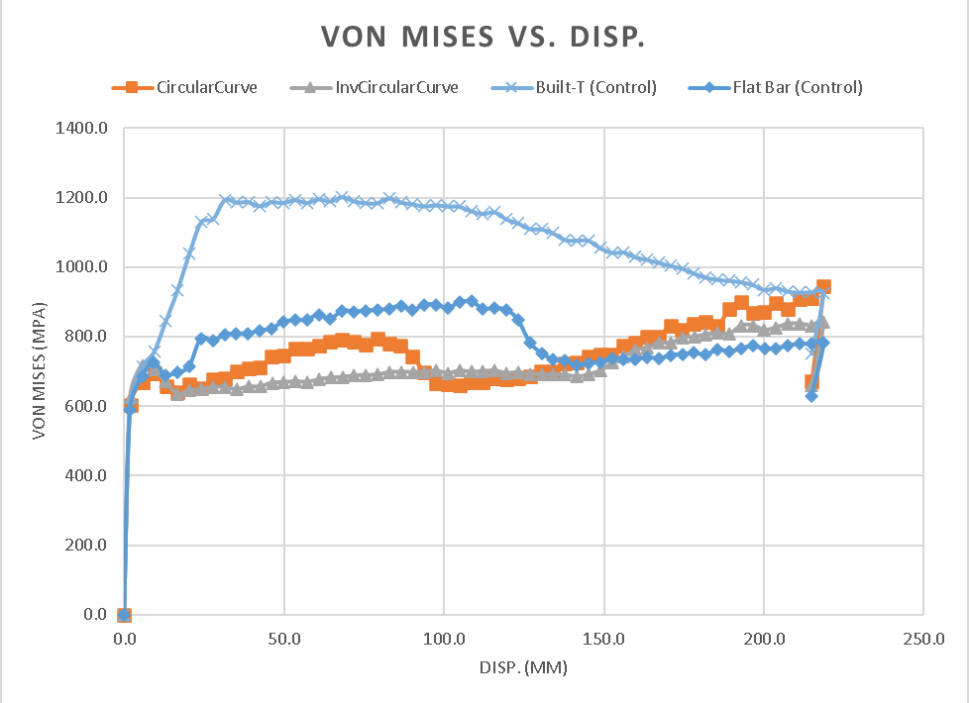

Figure 5.43: Exp2, von Mises vs. Disp. plot for Circular Curve comparisons and control runs.

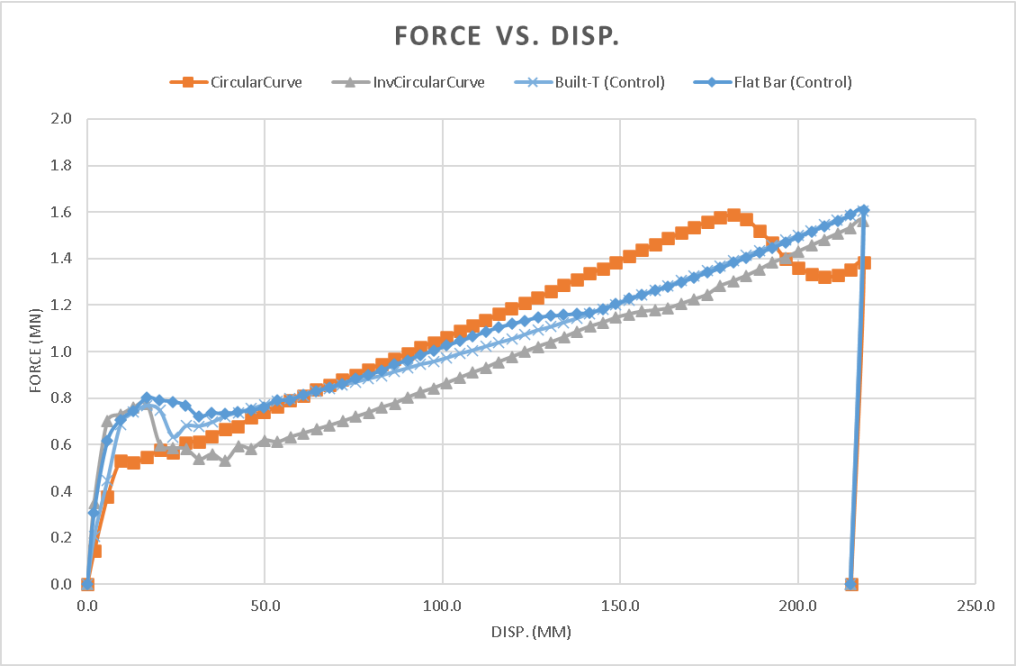

Figure 5.44: Exp2, Force vs. Disp. plot for Circular Curve comparisons and control runs.

Regarding Figure 5.45, most runs performed similarly. Of the non-control runs, the Defection Curve 3 run reached the highest maximum stress with a value of ~1050 MPa, then experienced a decrease to ~800 MPa, at a displacement of ~150 mm.

Regarding Figure 5.46, all experimental curves performed similarly concerning first yield and elastic capacity. The Defection Curve 3 run demonstrated the highest overload capacity. Each inverse curve was outperformed by their non-inverse counterparts. Finally, all runs were analyzed together for a more global analysis.

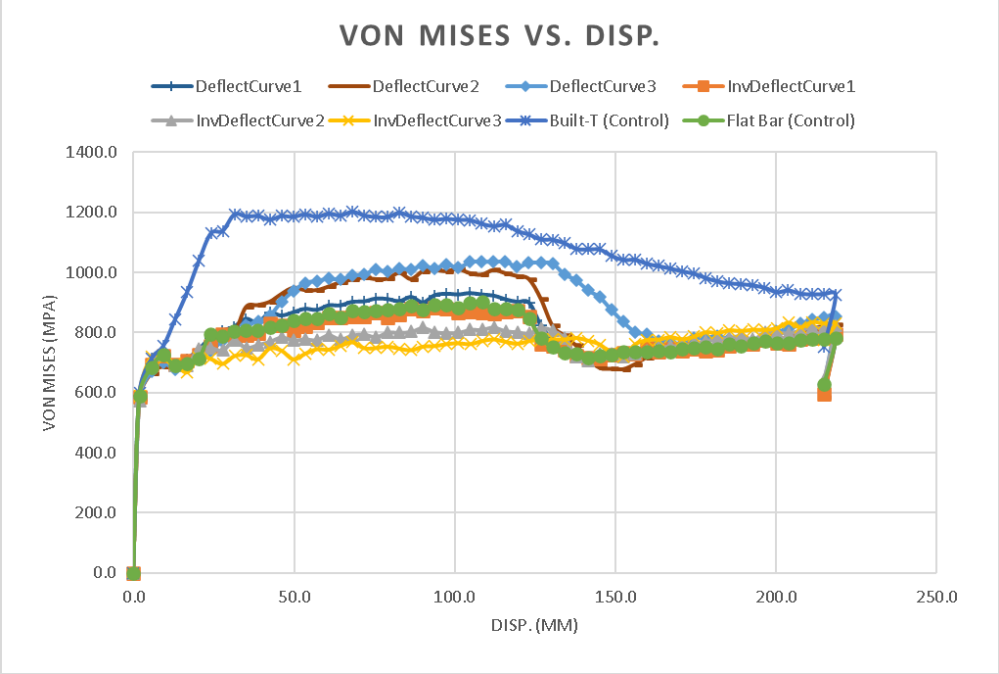

Figure 5.45: Exp2, von Mises vs. Disp. plot for Defection Curve comparisons and control runs.

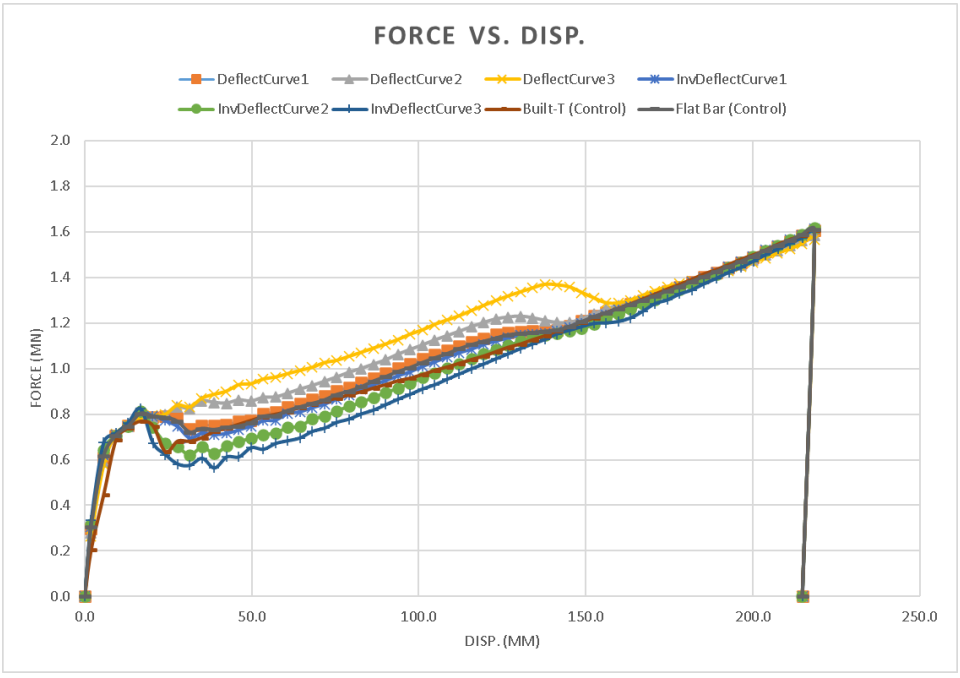

Figure 5.46: Exp2, Force vs. Disp. plot for Defection Curve comparisons and control runs.

Regarding Figure 5.47, all experimental runs showed a similar maximum von Mises stresses between 650 MPa and 900 MPa. Each of the control runs reached higher maximum stresses than any other runs.

Regarding Figure 5.48, one run showed more overall energy absorption capacity than any of the other runs, even the control runs – the circular curve run. With that being said, the circular curve run did experience significant buckling at ~180 mm. However, the buckling occurred quite far into the plastic region. The stiffener would likely ultimately fail before reaching this point with a more accurate material model. Both matching the elastic internal energy and increasing the overload capacity were shown to be possible.

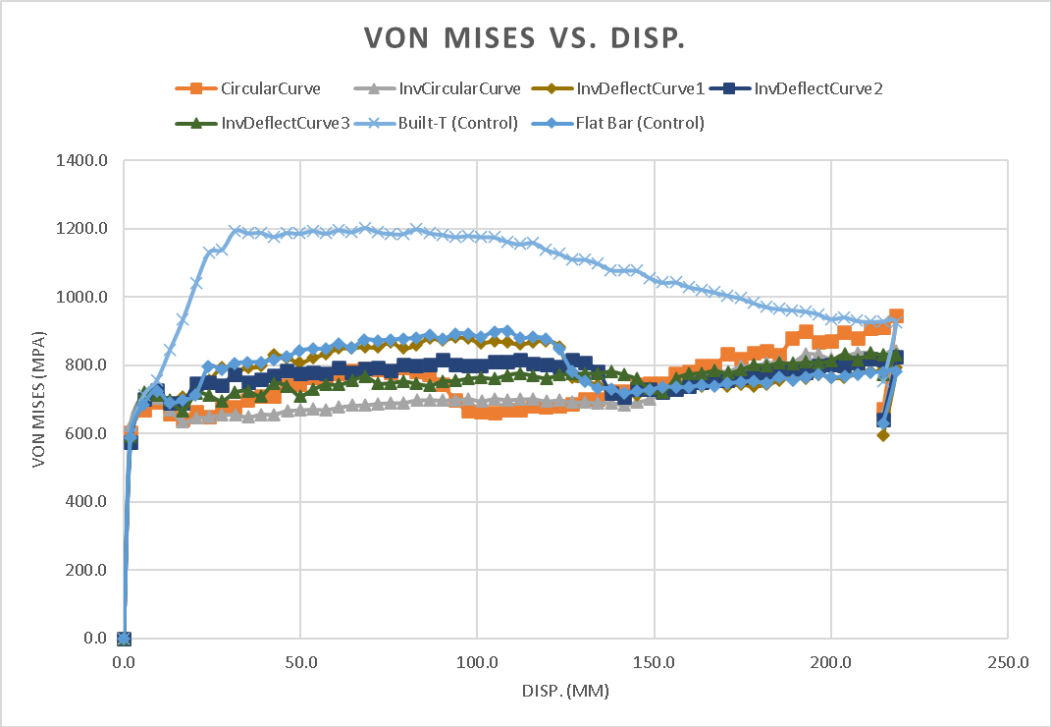

Figure 5.47: Exp2, von Mises vs. Disp. plot for all Test6 runs and control runs.

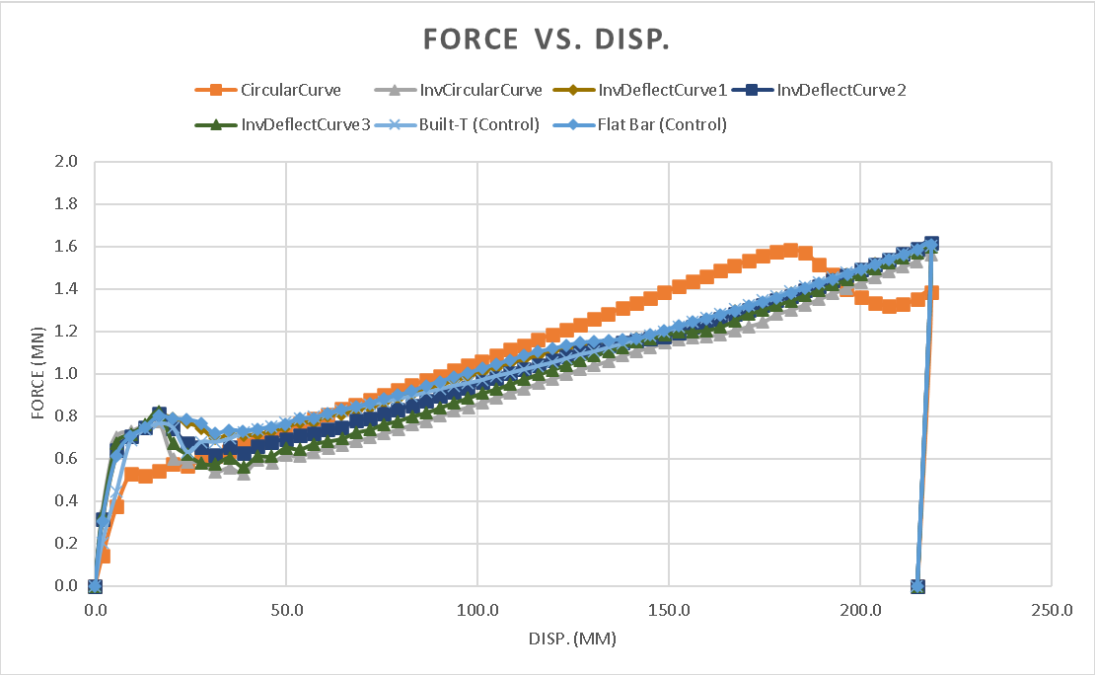

Figure 5.48: Exp2, Force vs. Disp. plot for all Test6 runs and control runs.

See Appendices C4 and C5 for a view of all von Mises vs. displacement plots and force vs. displacement plots from Exp2, respectively.

The Circular Curve model from Test6 was used for element quality checks since it was shown to be the most optimally performing model from Exp2. Two elements (0.113 % of the elements in the model) failed the maximum skew quality check. The maximum skew in the model was 48.8. See Appendix C6 for more information related to the element quality checks of Test6.

5.4 Deflection Curves and Optimality

Stiffeners were tested with profile shapes adapted to match beam fixed-fixed deflection curves (see Figure 5.49). Interestingly, these runs were capable of matching the control runs concerning first yield and were also shown to dramatically increase the overload

capacity (see Figure 5.37). However, they were abandoned for further testing due to one major flaw. The curves were designed assuming an impact, normal to the side-shell, directly in the middle of the stiffener span. If a different impact location were chosen, the resultant deflection curve shape would be translated along the stiffener span. Since, in collision scenarios, it is often difficult to predict where impacts will occur, the deflection curve was abandoned. However, there may conceivably be scenarios where accidental impacts are guaranteed to occur at particular points along the stiffener span. In such situations, designing stiffener web profiles based on beam deflection curves may be beneficial, and should be tested further.

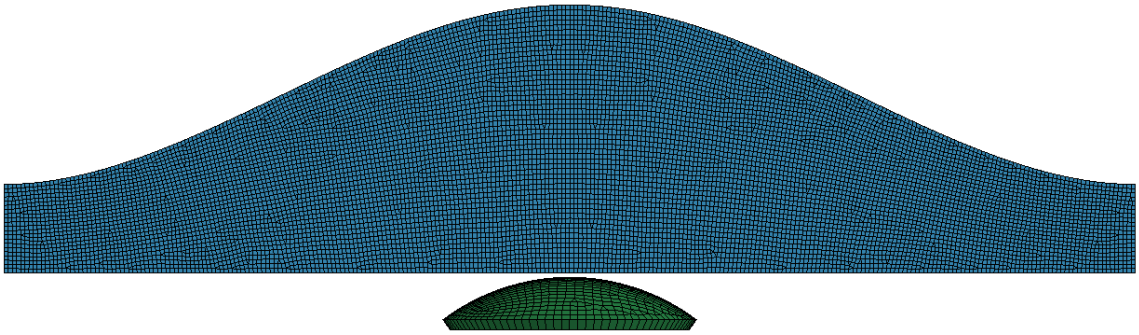

Figure 5.49: Profile view of Deflection Curve 6 within Exp2, before impact.

5.5 Axial Tension/Compression under Normal Loads

Under a load from an impact, normal to the side-shell, the middle of the stiffener span behaves differently compared to at its ends.

Figure 5.50 shows a profile view of a stiffener being impacted at the centre of its span, normal to the side-shell. With fixed-fixed ends, the stiffener experiences both axial tension and compression along its span. In terms of axial forces, at the centre of the span, the

stiffener elements were primarily in tension, whereas near the ends of the span some elements are being compressed. Therefore, to optimize the structure, it was likely that a non-uniform cross-sectional structure (as was tested within Figure 5.50) may be necessary to mitigate the varying buckling modes along the stiffener span.

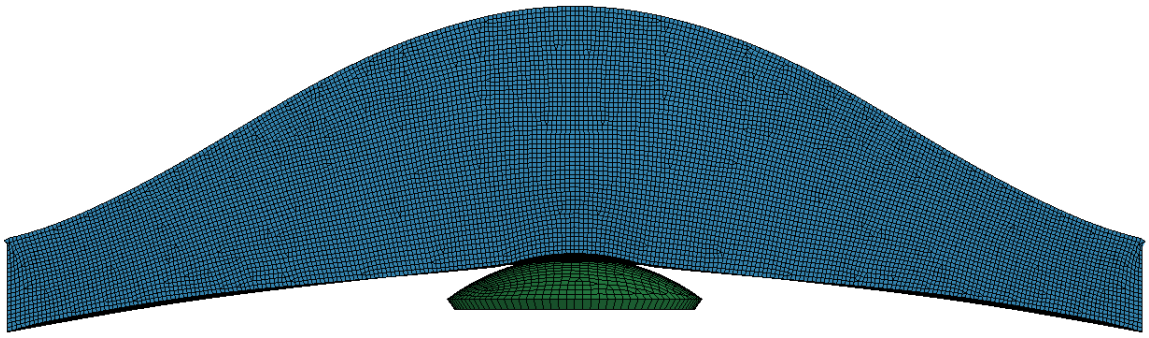

Figure 5.50: Profile view of Deflection Curve 6 within Exp2, during impact.

5.6 Discussion and Conclusions

Exp2 was conducted with a general exploratory approach consisting of several key stiffener shapes. The goal of Exp2 was to broadly discover which stiffener types had optimality potential – and later focus on these particular designs or closely.

Regarding the control runs, the built-T locally buckled excessively but did not buckle at the ends or trip. The flat bar tripped and buckled at the ends excessively but did not buckle locally. Each control model had unique buckling issues concerning overload capacity.

Test1 was completed with a focus on traditional corrugation which concluded that optimality was achieved as the corrugation parameters approached a flat bar – within the levels of the factors tested. Therefore, there might have existed a more optimal design between a flat bar and the smallest corrugation tested. After completing the test, it was

discovered that even though the control runs buckled, their ability to provide energy absorption even in their buckled state still equalled that of the corrugated runs. Additionally, the elastic energy absorption of the control runs was much greater than the corrugated runs.

Test2 was performed with a different type of corrugation – 'S' corrugation. Similar to traditional corrugation, 'S' corrugation assumes the shape of a sinusoidal function. 'S' corrugation contains fewer areas for stress to concentrate due to its smoother shape. Similar to traditional corrugation, even though the control runs buckled, their ability to provide energy absorption even in their buckled state still equalled that of the corrugated runs.

In Test3, three different stiffener shapes were tested: bulb flats, CHSs, and non-uniform flanged built-T's. Regarding the force vs. displacement plots, the two CHS runs experienced the most unique behaviour with steep, steady-state slopes. However, both CHS runs had the lowest elastic energy absorption capacity of all other runs. All runs, except for the CHS runs, performed similarly despite their dramatic differences in geometry. There was no clear advantage of either of the test runs compared to the control runs.

Within Test4, the effect of adding brackets to flat bars was observed. The data was then compared to that of the control runs to statistically analyze the benefits of using brackets. Though one of the runs showed significant promise concerning its stress vs. displacement curve, its force was rather low in its force vs. displacement curve. All runs ended at approximately the same force, just over 1.6 MN. However, the initial force of each curve varied wildly. The control runs had the highest elastic force values, followed by Run3, 1, 4, 2, and 5 (in that order). All runs ended at approximately the same force, demonstrating

no significant benefit to the plastic reserve capacity of the structure. Also, the initial force of each curve varied wildly. Despite its lack of energy absorption capabilities, the only model to show little to no end-buckling was a stiffener with a varying web height. Therefore, varying the web height of the stiffener was examined further in Test5 and Test6.

Test5 examined the effect of creating stiffeners with profiles matching the shape of general beam deflection curves. Each of the runs demonstrated an elastic capacity similar to both of the control runs, marking Test5 as the first simulation thus far to be able to do so. Run4 demonstrated the highest amount of overload capacity and showed no significant evidence of energy loss due to buckling throughout the whole displacement.

To be thorough, Test6 explored the behaviour of inverse deflection curves, as well as circular web height curves. Circular web height curves may be better optimized for an impact anywhere along the stiffener since they have a smaller change in web height per unit distance along the length of the stiffener span. One run showed more overall energy absorption capacity than any of the other runs, even the control runs – the circular curve run. Both matching the elastic internal energy and increasing the overload capacity were shown to be possible.

Within Test5 and Test6, deflection curves were used to create the profile shape of the stiffener webs. However, they were designed assuming an impact, normal to the side-shell, directly in the middle of the stiffener span. If a different impact location were chosen, the resultant deflection curve shape would be translated along the stiffener span. Since, in collision scenarios, it is often difficult to predict where impacts will occur, the deflection curve was abandoned. However, there may be scenarios where accidental impacts are

guaranteed to occur at particular points along the stiffener span. In such situations, designing stiffener web profiles based on beam deflection curves may be beneficial, and should be tested further.

The experiment also demonstrated that the stiffener experiences both axial tension as well as axial compression along its span, from the induced bending moment caused by the impact. The corresponding buckling modes were different depending on the location along the span. Therefore, a non-uniform cross-sectional stiffener may be needed to mitigate both buckling modes simultaneously. Exp3 was then conducted which focused on developing a robust experimental design to accurately identify if and how elastic energy absorption can be maximized in the stiffener and panel, as well as how overload capacity can be better optimized.

Chapter 6 Exp3 – Variable Web Height with Global Model

Based on what can be learned from Exp1 and Exp2, this Chapter (i.e. Exp3) explores in more detail the variable web height stiffener. Significant geometric parameters which define the stiffener shape were systematically altered, through the use of an experimental design, based on previous test results to better inform where stiffener material could be redistributed. Also, flanges have been added to the stiffener ends to aid in the prevention of end-buckling. A robust experimental design was implemented to analyze the behaviour of the models. The levels were also strategically chosen so that the average weight of the experimental runs would be near the weight of the control runs.

Several corrections and alterations were made to the experiment from lessons learned through previous unsuccessful experimental simulations. It was determined that both the contact forces and BC forces gave similar results. The only notable difference was that the contact force showed much fewer dynamics compared to the BC forces. Therefore, contact forces were used for producing the force vs. displacement plots. An effort was made to sample data from the force vs. displacement plots more evenly to make better use of the available produced data. For Exp3, two samples were collected near the yield point, and two were collected within the plastic region. Also, as can be seen in all previous force vs. displacement plots in Exp2, the material typically yielded early into the analysis. To increase the fidelity of the yield responses, data were sampled at ten times the rate compared to Exp2. Additionally, the experimental design levels were enlarged to increase the chance that the design space captured the optimality of the responses. Lastly, the geometric model was enlarged (Global Model) to replace fixed-fixed stiffener ends with frames.

6.1 Load Cases

So far, all experimental simulations have tested stiffeners loaded at the centre of the stiffener span (IOSC) to induce maximum bending conditions. Two remaining conditions have not yet been explored: impact between two stiffeners at the centre of the stiffener span (IBS), and impacting on stiffener at a quarter-span (IOSQ) (see Figure 6.1).

The optimal stiffener must be optimized for both maximum bending and maximum shear load conditions, which were the worst-case loading scenarios for highly local impacts normal to the side-shell. For a stiffener with fixed-fixed end conditions (similar to what was tested in Exp2 and 3), a mid-span impact induces a maximum bending moment at the point of contact as well as at the ends of the stiffener. Also, the entire span of the stiffener experiences a maximum internal shear. For a simply supported beam, a mid-span impact induces a maximum bending at the impact site. Also, similar to a fixed-fixed beam, the entire span of the beam experiences a maximum internal shear (Hibbeler 2011). Therefore, as the stiffener-ends become more capable of resisting a moment, the induced bending moment becomes higher at the ends. With that being said, both loading conditions were tested including an impact normal to the side-shell at the centre of the stiffener span, as well as an impact near the end of the stiffener span. Additionally, a third load case was tested which included an impact directly between two stiffeners, in the middle of their spans. This third impact may cause the stiffener to trip more easily.

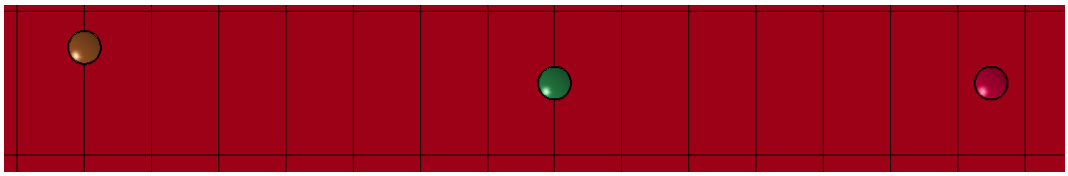

Figure 6.1: Three load cases examined. Left - Impact on stiffener near the end of the span, Middle - Impact on stiffener at the centre of the span, Right - Impact between stiffeners.

According to Figure 6.1, the leftmost dome demonstrates an IOSQ. This load scenario induces the highest level of shear between the stiffener end and the perpendicular connected frame. The centre dome demonstrated an impact that has been heavily explored throughout this thesis – IOSC. This load scenario induces the highest amount of deformation in the stiffener perpendicular to the side-shell. The rightmost dome demonstrates an IBS, at the centre of their span. This load scenario induces the highest amount of tripping potential of the stiffeners. Three of these load cases make up the worst-case failure scenarios for stiffeners, under the studied conditions.

- Load Case 1 – IOSQ (intender translated longitudinally by 320.95 mm, or one-quarter of a stiffener span)
- Load Case 2 – IOSC
- Load Case 3 – IBS

6.1.1 Load Case Convergence Study

Since three loading cases were being studied per run, to reduce computation run time, it was desirable to create a model that included each load case simultaneously. A convergence study was completed to ensure that the results of each load case were independent of the

other load case impacts. To begin, each load case was tested separately in the same model (built-T control) to determine the individual results for each load case, for comparison.

With the known results of each load case isolated in three separate models, the three load cases could be implemented into the same model to determine if the results were independent of each other. It was concluded that at least fourteen feet (seven stiffeners) must separate the impact interactions to ensure that the results of each load case were independent of the other load cases.

As can be seen from Figure 6.2, Figure 6.3, and Figure 6.4, the data agreed well on each plot which demonstrates that the model containing all load cases could be used to determine results from the simulations.

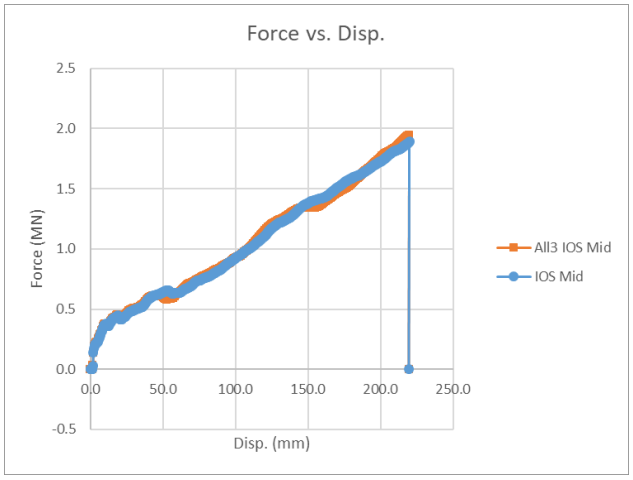

Figure 6.2: Force vs. displacement curve for impact on stiffener, at the centre of the span. Circle - Model containing only one load case, Square – Model containing each load case simultaneously.

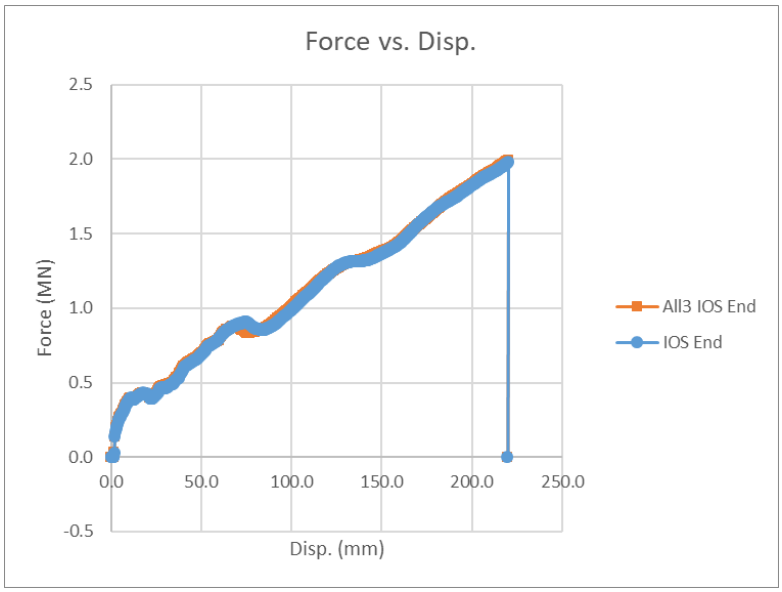

Figure 6.3: Force vs. displacement curve for impact on stiffener, at a quarter-span. Circle - Model containing only one load case, Square – Model containing each load case simultaneously.

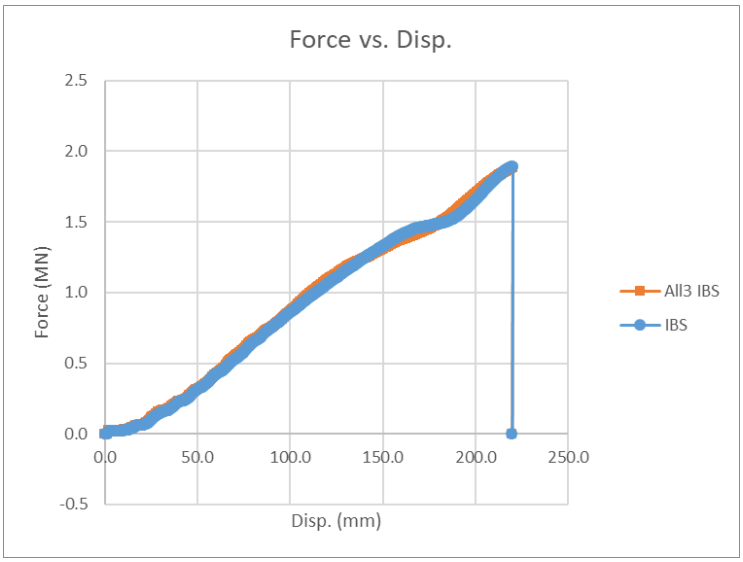

Figure 6.4: Force vs. displacement curve for impact between stiffeners. Circle - Model containing only one load case, Square – Model containing each load case simultaneously.

6.2 Model Parts

Refer to Section: 3.7 Rigid Indenter Design, for information regarding the Rigid Intender model.

6.2.1 Global Model

The grillage geometry (see Figure 6.5) was significantly altered for Exp3. The basic components of the model such as stiffener configuration, stiffener spacing, and plate thickness, remained the same. However, at the stiffener ends the model was extended and frames were added.

For simplicity, the side-shell and frames were given a parametrized thickness of 7.9375 mm. The remaining constants related to the FEMs were:

- Stiffener spacing = 609.6 mm.
- Stiffener length = 1283.8 mm.
- Side-shell width, x-direction = 16053 mm.
- Side-shell length, y-direction = 3851 mm.
- Frame length = 16053 mm.
- The material properties and FEM controls.

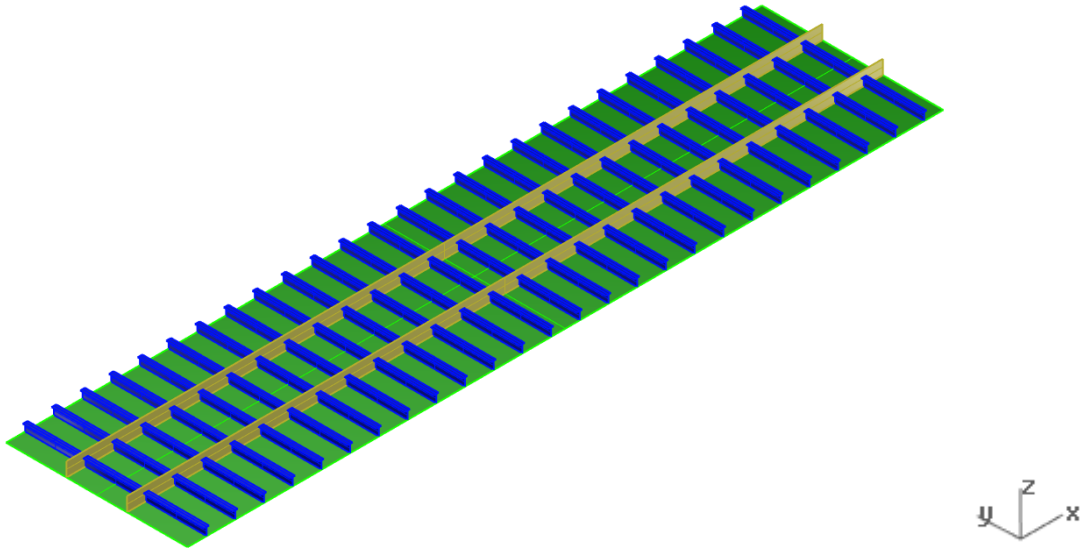

Figure 6.5: Exp3 Grillage.

6.3 LS-PrePost and LS-DYNA

See the below subsections for information related to the construction of the FEMs within LS-DYNA.

6.3.1 Boundary Conditions

The BCs used in the model consisted of fixed-fixed BCs at the edges of the model perpendicular to the stiffener, shown in Figure 6.6.

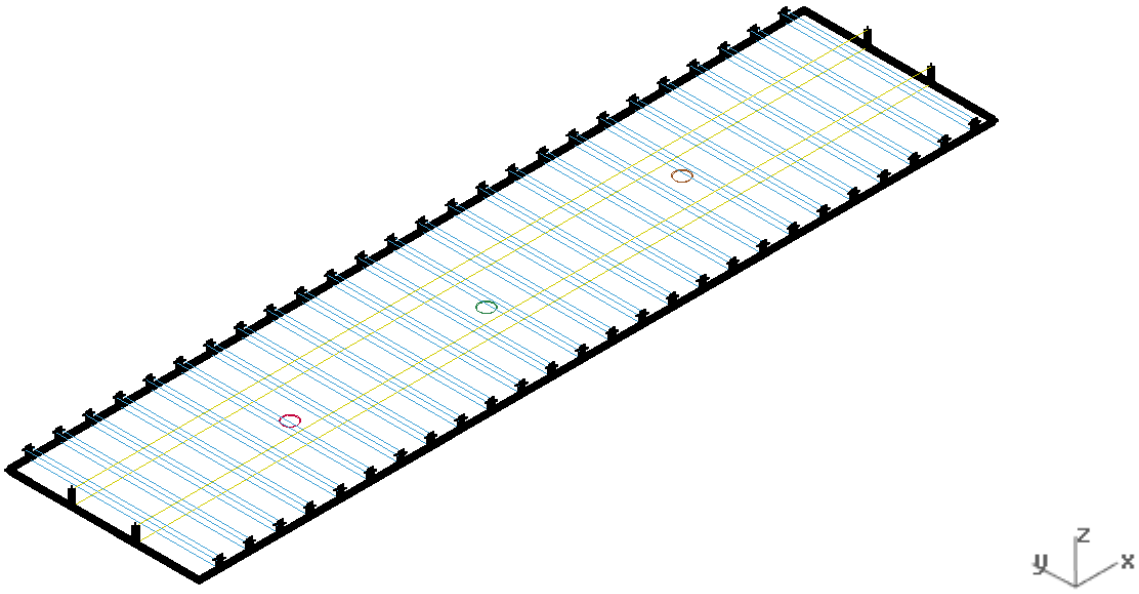

Figure 6.6: Exp3, Boundary Conditions of the built-T. Each BC node was annotated with a black “x”.

6.3.2 Loading Conditions

The load was applied as per Section: 3.4.1.2 Loading Conditions. See Section: 6.1 Load Cases, for more information regarding the three load cases which were tested.

6.3.3 Termination Time

The models were set to terminate at 0.075 s.

6.3.4 Contact

Contact was applied as per Section: 3.4.1.3 Contact.

6.3.5 Data Output

Data was output in the form of d3plots and ASCII plots at a frequency of 10,000 Hz. The frequency was changed from 1000 Hz to 10,000 Hz to increase the fidelity of the results,

particularly near the yield point. The force data consisted of the contact forces at the impact sites.

6.3.6 Material Properties

The grillages were modelled using a bi-linear, plastic kinematic, material model with the following steel material properties:

- Young's modulus = 2.07e11 Pa
- Poisson's ratio = 0.3
- Density = 7850 kg/m^3
- Yield strength = 350 MPa
- E_{tan} = 1 GPa

6.3.7 Mesh Convergence Study

Several runs were prepared based on the geometry of Run27. Based on Figure 6.7, Figure 6.8, and Figure 6.9, each figure contains three runs that were prepared with varying average element sizes. Since the indenter was impacting the plate with a prescribed displacement, the corresponding contact force was used for the analysis and then plotted against time. As can be seen in the plots, there were no observable changes to the force vs. time plots for the different mesh sizes.

It is possible that buckling could greatly affect the convergence of the mesh (see Figure 7.5 for confirmation of this possibility). Though there was no buckling present within the plots, other runs within the experimental design may contain buckling. Therefore, all experimental runs were prepared with an average element size of 12 mm regardless to help

promote accurate data near the region of any buckling. It should be noted that no geometry had a thickness greater than 12 mm.

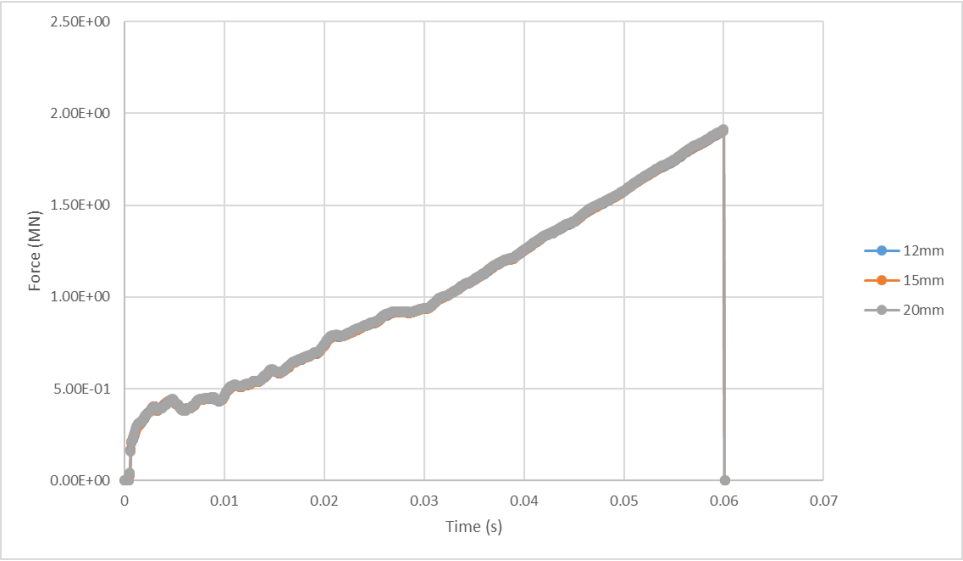

Figure 6.7: Exp3, Mesh convergence plot of force vs. time, Load Case 1.

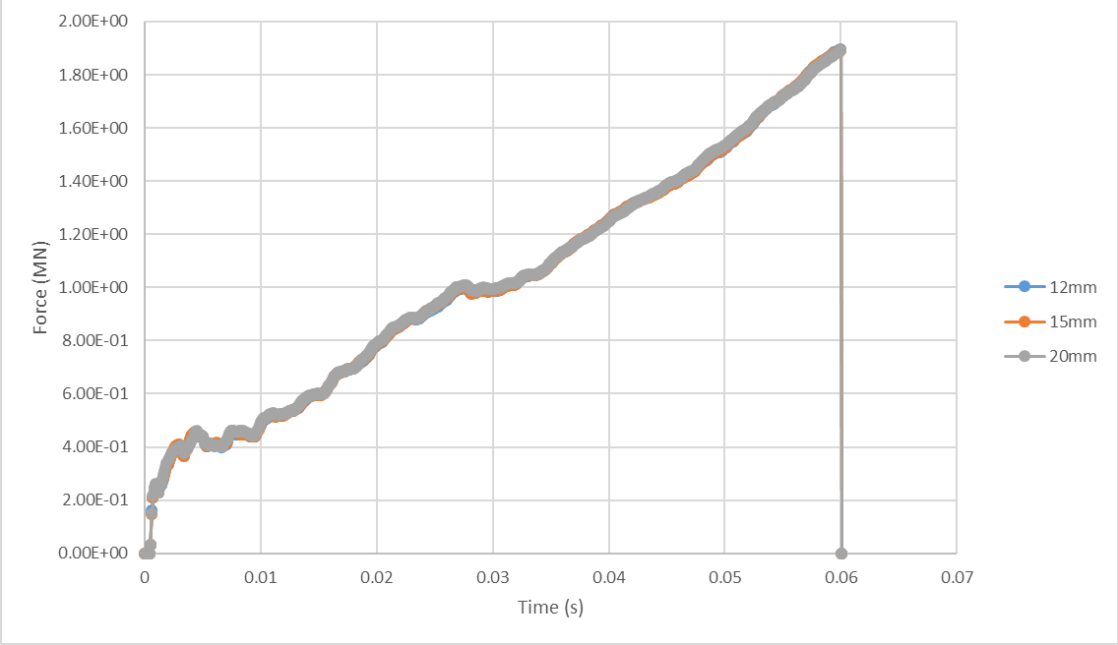

Figure 6.8: Exp3, Mesh convergence plot of force vs. time, Load Case 2.

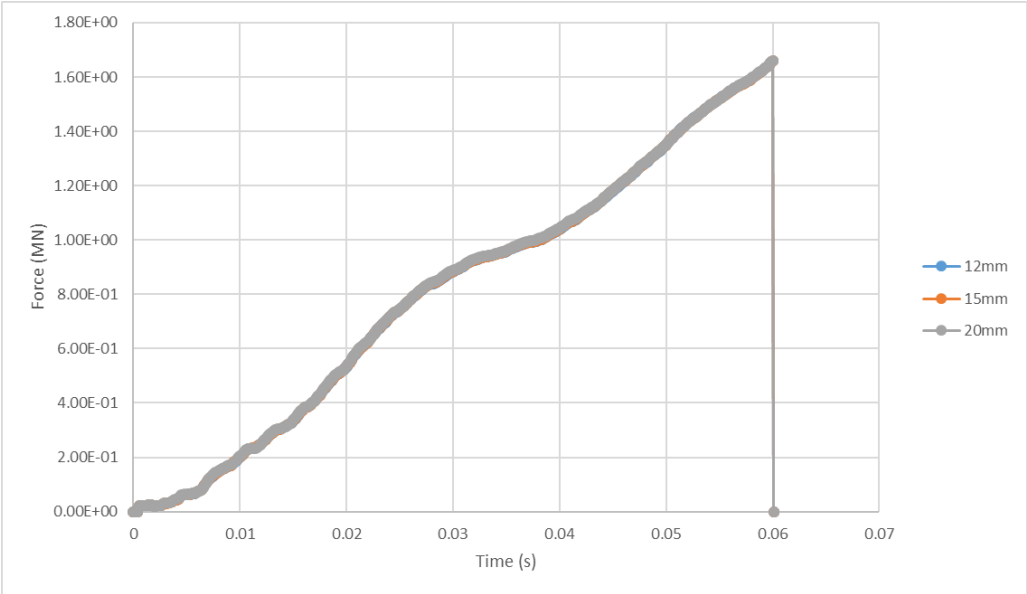

Figure 6.9: Exp3, Mesh convergence plot of force vs. time, Load Case 3.

6.3.8 LS-DYNA Cards

Several cards were invoked within LS-DYNA to achieve the desired effects intended for the simulation:

BOUNDARY_PRESCRIBED_MOTION_RIGID

Rigid body motion of the indenter was achieved using the following fields: DOF = 3 and VAD = 2.

CONTACT_AUTOMATIC_SURFACE_TO_SURFACE

Contact was defined between the indenter and side-shell. To collect contact forces both SPR and MPR were set to 1.

CONTROL_TERMINATION

The simulation was set to terminate using ENDTIM = 0.061.

DATABASE_ASCII_option

Nine ASCII options were turned on for high fidelity result extraction: BNDOUT, ELOUT, GLSTAT, MATSUM, NODOUT, RBDOUT, RCFORC, SLEOUT, SPCFORC. Each was given a DT of 0.0001.

DATABASE_BINARY_D3PLOT

For visualizing the simulation, DT = 0.01 was used.

DATABASE_BINARY_INTFOR

The internal forces were collected using DT = 0.01.

DATABASE_HISTORY_NODE_ID

The appropriate node was selected for ASCII NODOUT.

DEFINE_CURVE

To simulate a linear load curve, four points were used: (0, 0), (0.06, 0.22), (0.12, 0), and (0.13, 0).

MAT_PLASTIC_KINEMATIC

A, bi-linear, plastic kinematic material model was built using the following material properties: RO = 7850, E = 2.07e11, PR = 0.3, SIGY = 3.5e8, and ETAN = 1e9.

MAT_RIGID

The properties used were: RO = 2.742e6, E = 2.07e11, and PR = 0.3. Also, CMO, CON1 and CON2 were invoked to properly restrict the rigid body from x and y translations, as well as x, y, and z rotations using 1, 4, and 7, respectively.

SECTION_SHELL

The shear factor was changed from 1 to 5/6 using SHRF = 0.8333. Also, five through-thickness integration points were used by invoking NIP = 5.

6.4 Experimental Design, Factors, and Responses

An optimal, RSM, experimental design was implemented to determine the optimal design within the given levels of factors studied. The chosen six factors combined to form 31 experimental runs, as well as two control runs (built-T and flat bar).

Exp3 consisted of six experimental factors that were chosen to be systematically varied throughout the experimental runs. See Figure 6.10 for more information regarding factor definitions. A wide range of factor levels was tested to ensure that the design space was adequately explored.

A. Stiffener End Web Height, H_w, 12 – 120 mm
    - The height of the stiffener at its end from the side-shell it the top of the stiffener
B. Mid-Span Stiffener Height, H_{w2}, 12 – 240 mm
    - The height of the stiffener at the centre of its span from the stiffener end web height to the top of the stiffener
C. Web Thickness, T_w, 8 – 12 mm

D. Flange Length, L_f, 0 – 641.9 mm

- The linear length of the flange

E. Flange Width, W_f, 24 – 120 mm

F. Flange Thickness, T_f, 8 – 12 mm

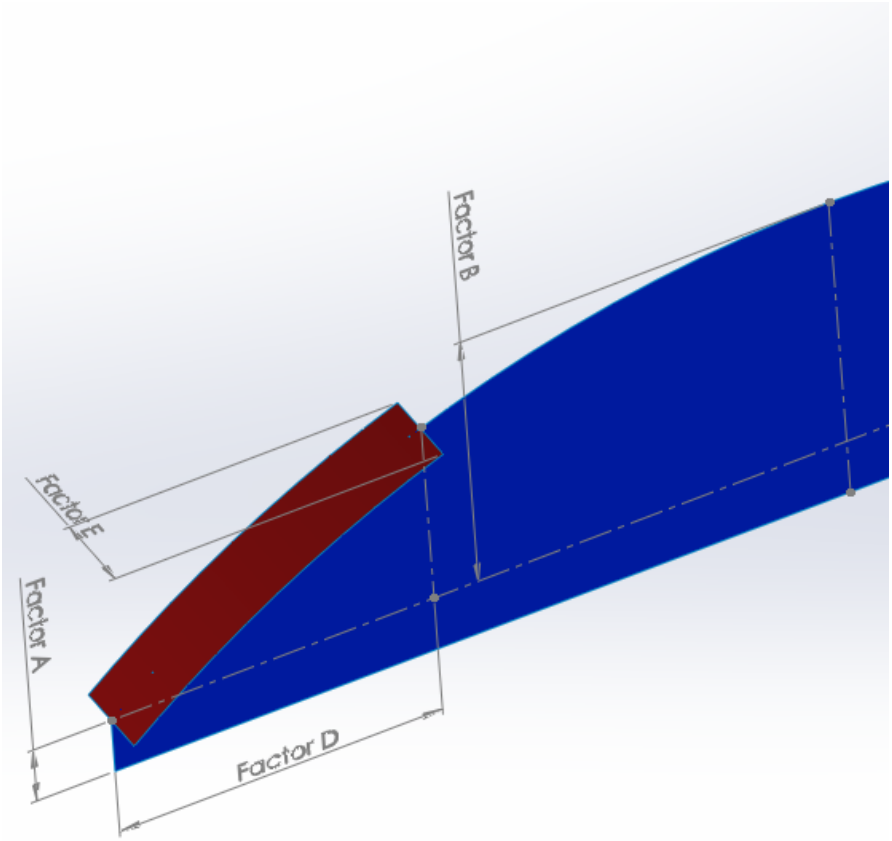

Figure 6.10: Exp3, Factor definitions.

For analysis purposes, four responses were of concern – the force associated with the following displacements: first yield, L/100 (length of the stiffener span divided by 100), and L/10 (length of the stiffener span divided by 10), and at 200 mm. The first yield point was chosen to gather information regarding the first yield point. 200 mm was chosen to

measure the force well into the overload region. L/100 and L/10 were chosen to further sample a wide range of data within the force vs. displacement plots.

Each of the four displacements was converted into forces via visually inspecting the force vs. displacement plots. It was determined that on average first yield occurred at ~17 mm, L/100 occurred at 12.838 mm, and L/10 occurred at 128.38 mm. See the below-listed responses for more clarity:

- Weight (weight of each stiffener configuration)
- L/100 – Span length divided by 100. Corresponding force at a displacement of 12.838 mm
- First Yield – Corresponding force at a displacement of 10 mm (average displacement when the slope became nonlinear)
- L/10 – Span length divided by 10. Corresponding force at a displacement of 128.38 mm
- Maximum – Corresponding force at a displacement of 200 mm

Weight was treated as a response and targeted to be equal to the control runs. L/100, First Yield, L/10, and Maximum were collected for each of the three load cases for a total of 13 responses. Data points were read directly from the plots corresponding to the particular response of concern.

Design Expert was used to produce a series of runs. See Table 6.1.

Table 6.1: Exp3 Run Order in Design Expert.

	Factor 1	Factor 2	Factor 3	Factor 4	Factor 5	Factor 6
Run	A: Hw	B: Hw2	C: Tw	D: Lf	E: Wf	F: Tf
Units	mm	mm	mm	mm	mm	mm
1	12	105.48	11	191.094	30.24	12
2	120	12	8.6	641.9	24	12
3	14.16	88.38	12	266.389	120	9.4
4	12	170.46	8	641.9	120	8
5	35.22	49.62	9.64	0	74.4	8
6	12	240	12	0	24	8
7	66	12	12	320.95	74.4	8
8	120	78.12	8.36	6.419	78.24	10.8
9	66.54	240	11.3518	430.073	91.2	8
10	93	240	8	0	120	8.2
11	19.02	49.62	8	320.95	24	9.3
12	120	12	12	0	120	8
13	120	240	12	324.159	38.4	12
14	12	12	12	641.9	24	8
15	67.08	148.8	8	481.425	86.4	12
16	55.74	195.54	10.36	641.9	24	10.2
17	108.66	92.94	12	641.9	77.76	9.6
18	12	240	9.2	269.598	82.56	10.38
19	12	12	9.6	641.9	84.96	10.94
20	120	240	10.1	0	62.4	9.98
21	120	240	8	641.9	45.12	8
22	73.02	12	12	38.514	31.68	10.1993
23	89.22	12	8.26	458.959	115.2	8.5
24	74.4138	240	8	0	24	12
25	62.7343	143.1	11.5373	464.733	76.4189	12
26	120	240	9.5	641.9	120	10.5976
27	119.46	124.86	10.3	234.294	24	8.12
28	12	12	8	0	120	12
29	12	240	12	641.9	120	12
30	96.78	12	11	353.045	120	12
31	67.62	198.96	11.2278	0	111.84	11.58

6.5 Results

Due to the large quantity of FEM runs, FEM visuals have only been shown for three runs: the built-T control run, the flat bar control run, and Run27. Run27 was chosen since it was

used for the MCA. The built-T control run visuals related to the undeformed geometry and the von Mises data for the three load cases can be seen in Figure 6.11, Figure 6.12, Figure 6.13, and Figure 6.14.

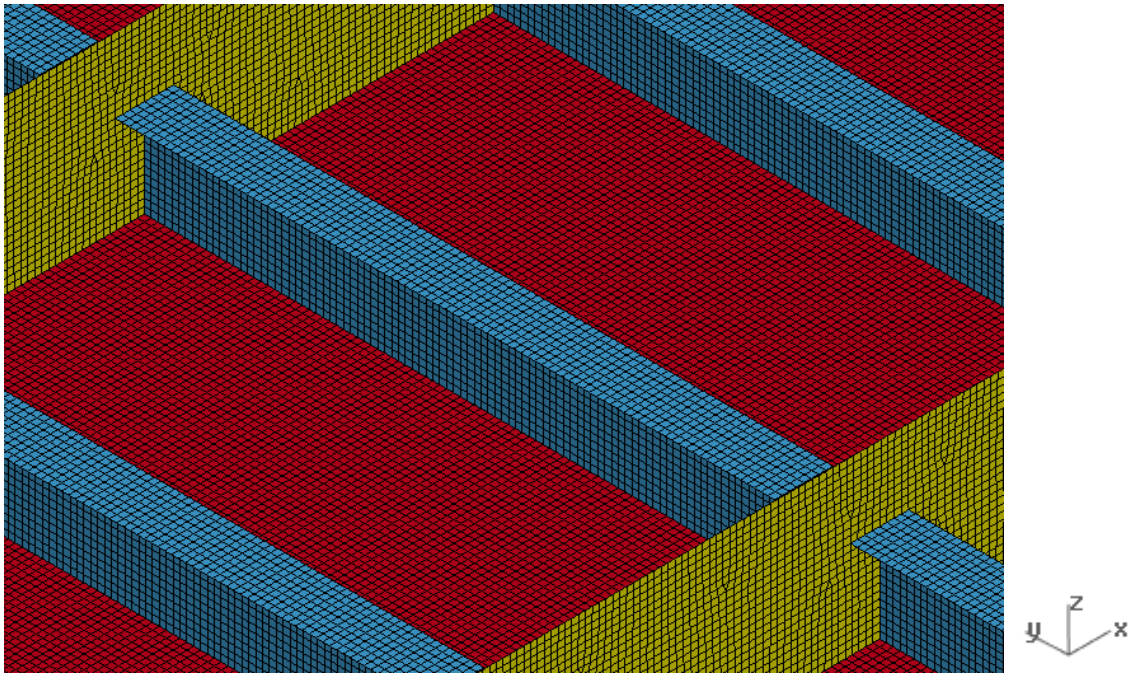

Figure 6.11: Exp3, Control – Built-T Geometry.

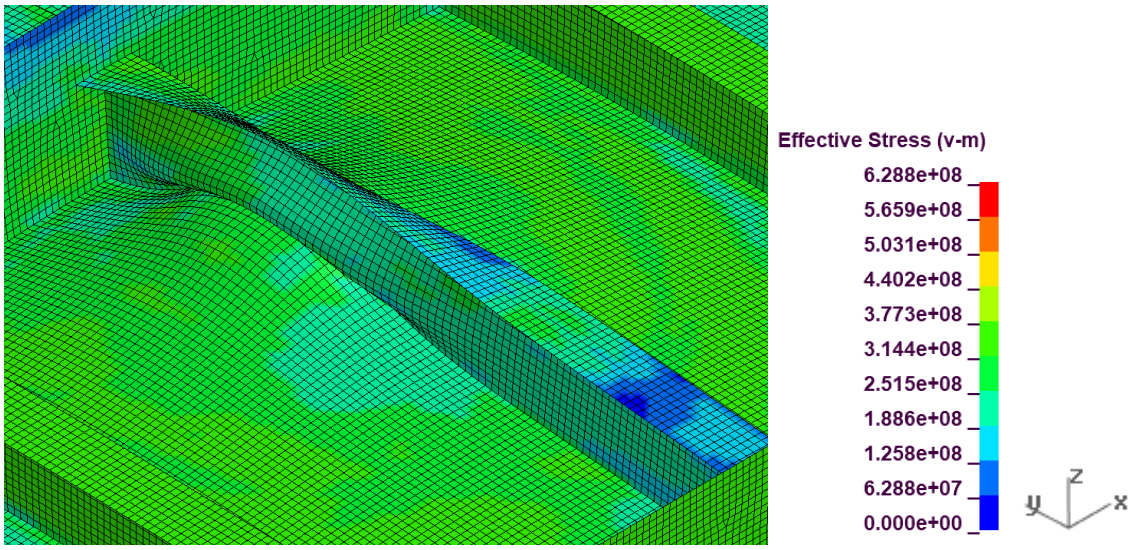

Figure 6.12: Exp3, Control – Built-T von Mise Stress, Load Case 1.

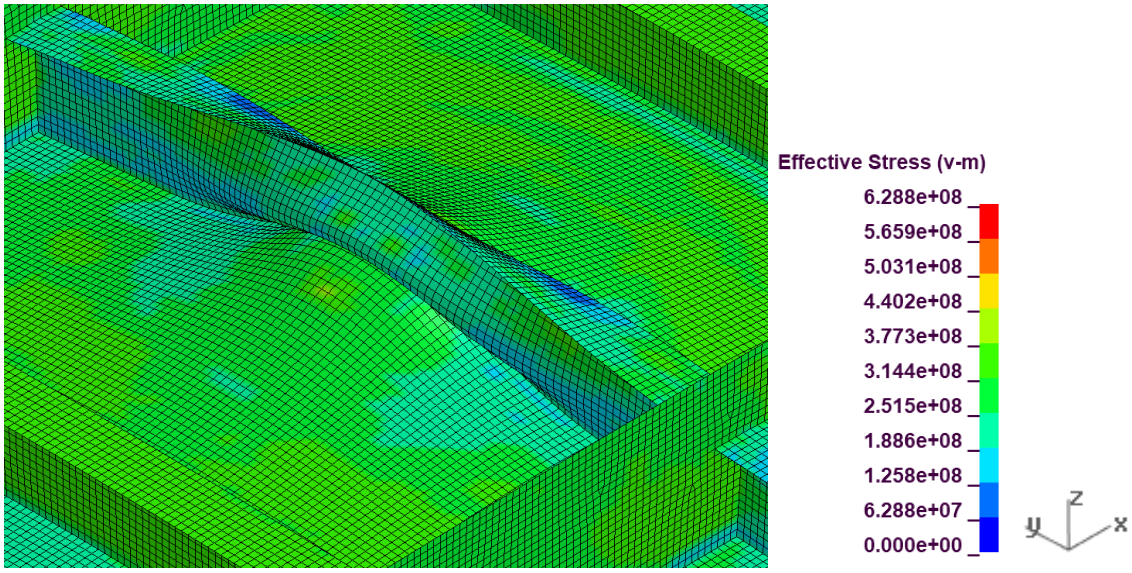

Figure 6.13: Exp3, Control – Built-T von Mise Stress, Load Case 2.

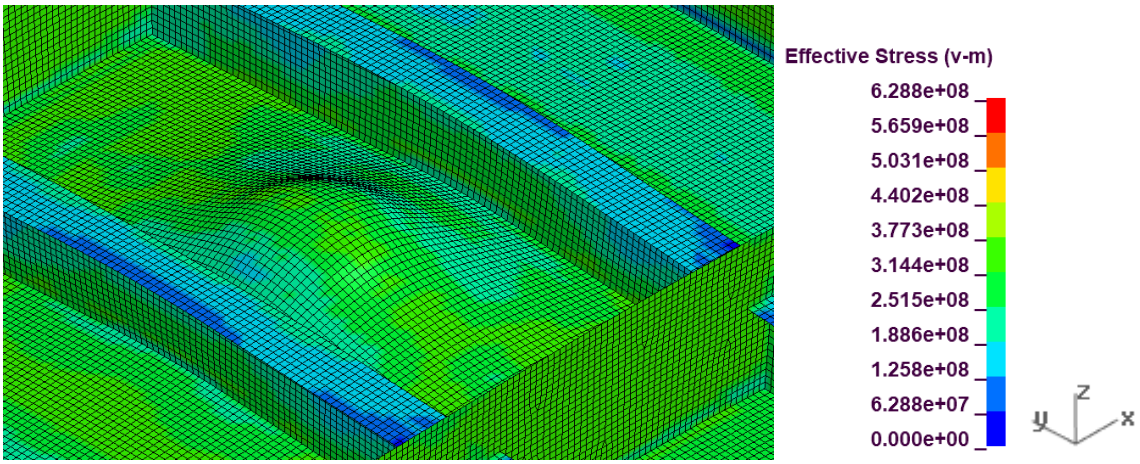

Figure 6.14: Exp3, Control – Built-T von Mise Stress, Load Case 3.

The flat bar control run visuals related to the undeformed geometry and the von Mises data for the three load cases can be seen in Figure 6.15, Figure 6.16, Figure 6.17, and Figure 6.18.

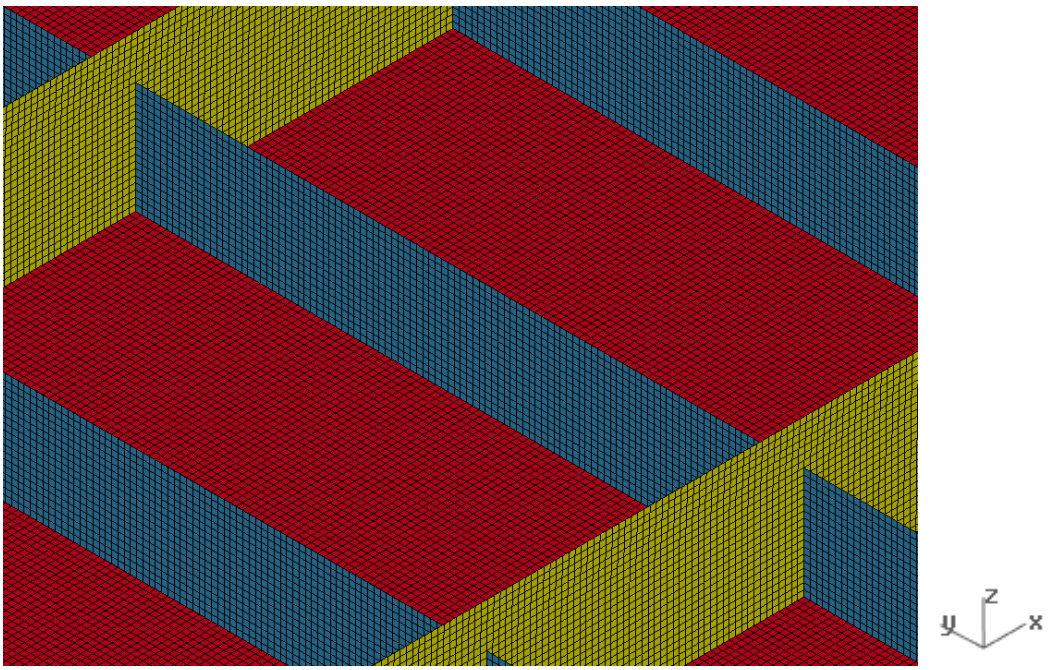

Figure 6.15: Exp3, Control – Flat Bar Geometry.

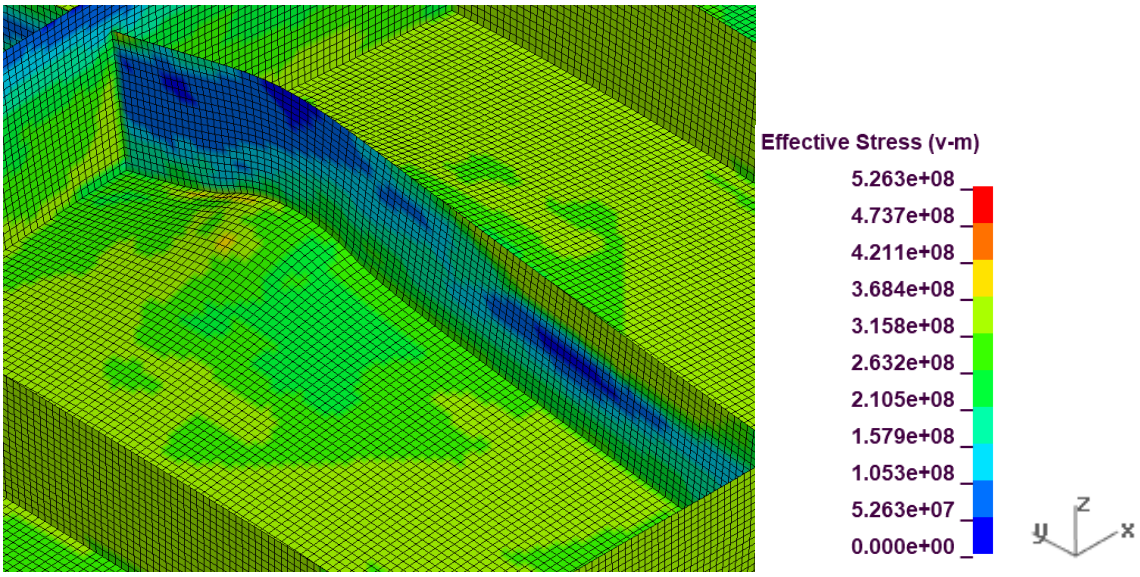

Figure 6.16: Exp3, Control – Flat Bar von Mise Stress, Load Case 1.

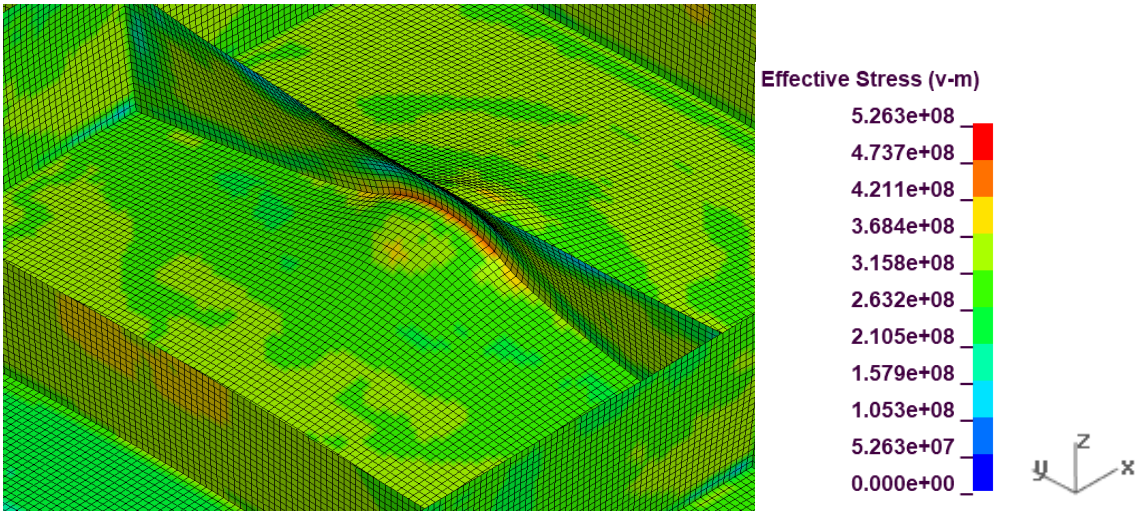

Figure 6.17: Exp3, Control – Flat Bar von Mise Stress, Load Case 2.

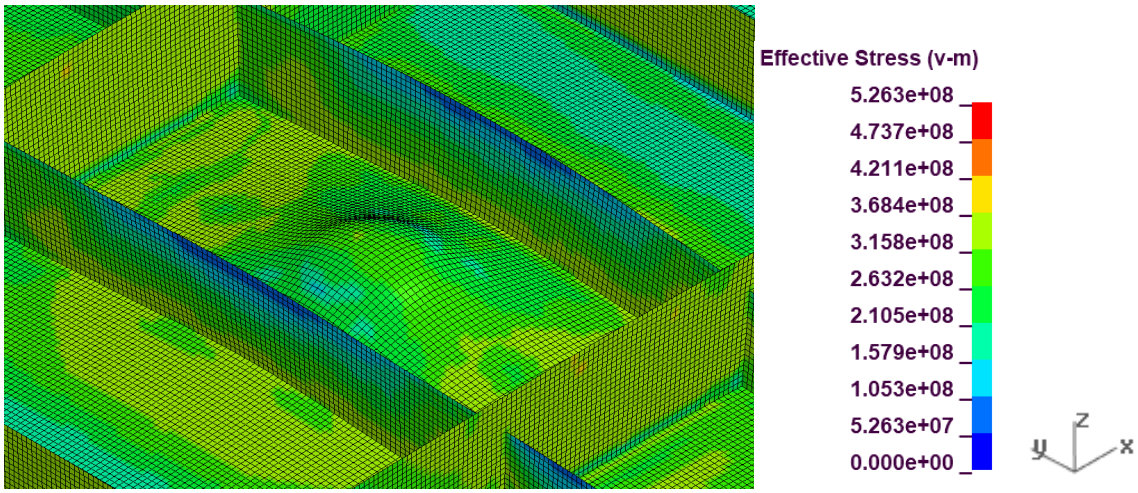

Figure 6.18: Exp3, Control – Flat Bar von Mise Stress, Load Case 3.

The Run27 visuals related to the undeformed geometry and the von Mises data for the three load cases can be seen in Figure 6.19, Figure 6.20, Figure 6.21, and Figure 6.22.

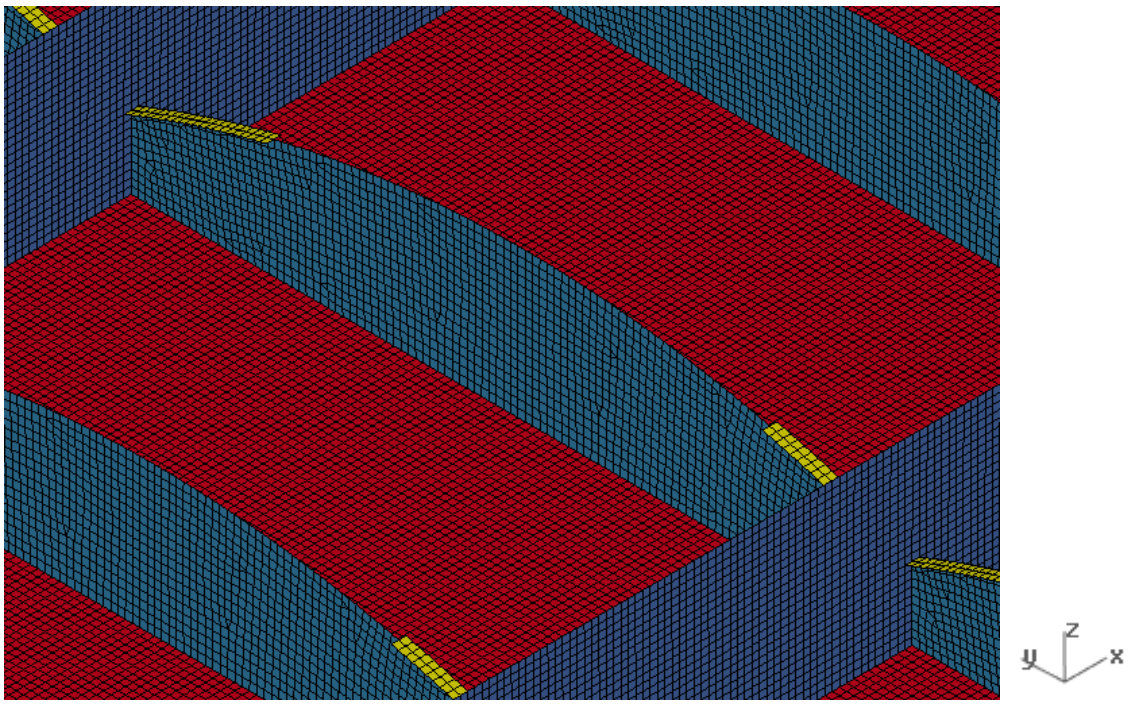

Figure 6.19: Exp3, Run27 Geometry.

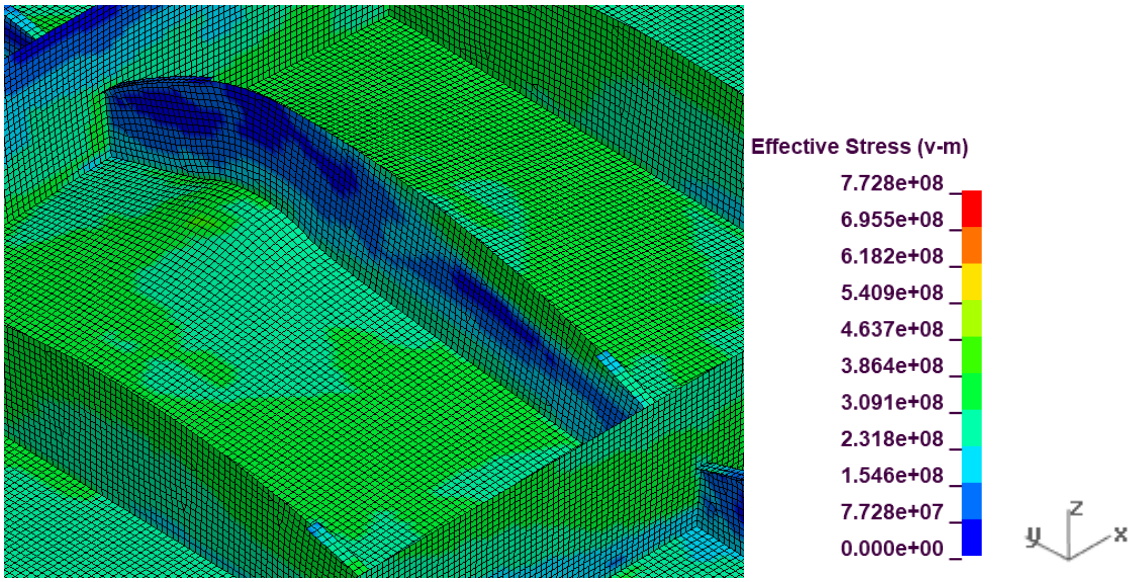

Figure 6.20: Exp3, Run27 von Mise Stress, Load Case 1.

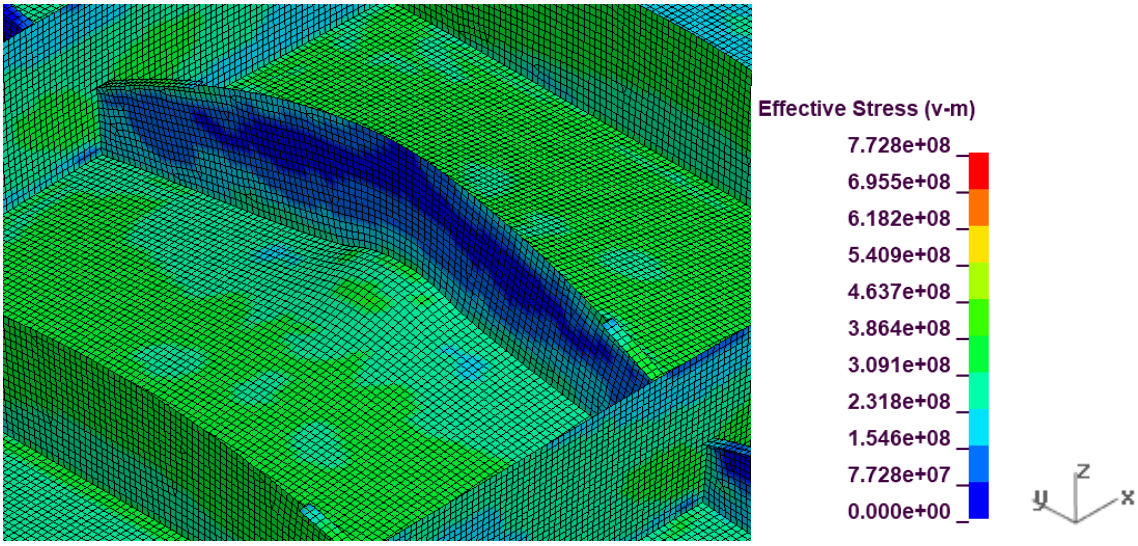

Figure 6.21: Exp3, Run27 von Mise Stress, Load Case 2.

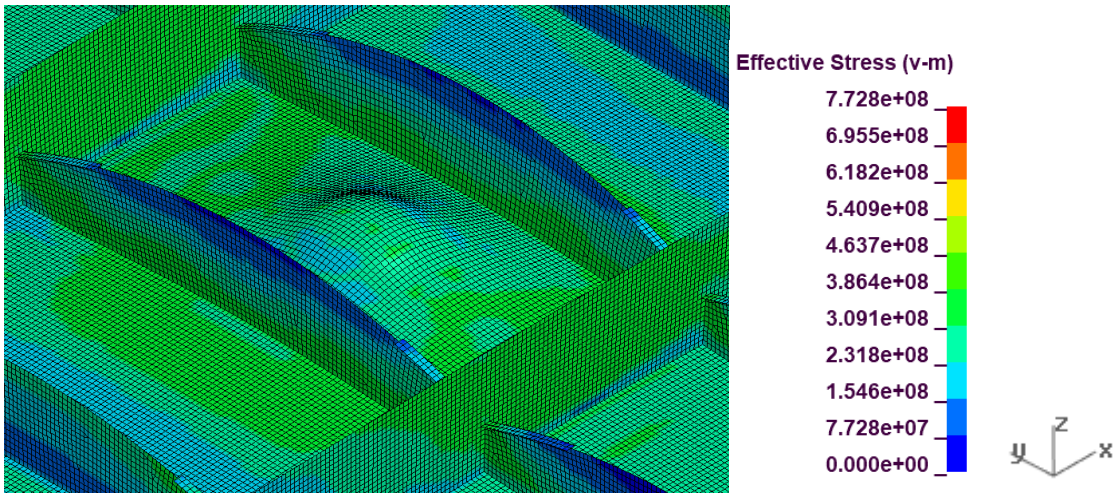

Figure 6.22: Exp3, Run27 von Mise Stress, Load Case 3.

See Appendix D1 for visuals for run geometry and von Mises stress results. Within Appendix D1, due to the large quantity of experimental results within Exp3, visuals have only been shown for the undeformed geometry and maximum von Mises stress state for Load Case 2 (impact on a stiffener in the middle of its span). However, for the control runs, visuals for the undeformed geometry and maximum von Mises stress state for all three load cases were shown.

See Appendix D2 for information regarding the scantlings and responses of the experimental runs found in Exp3. See Appendix D3 for more information regarding the von Mises vs. displacement plots for Load Case 2. See Appendices D4, D5, and D6 for more information regarding the force vs. displacement plots.

6.5.1 Experimental Design Model Checking

Each of the thirteen responses passed model checks related to the quality of the experimental design data. Square root transformations were applied to both the IOSC

(L/100) and IOSC (First Yield) responses. Transformations were applied to ensure the data fit a normal distribution and had equal variance. See Appendix D7 for the raw data from Design Expert related to the model checking.

6.5.2 Confirmation Runs

The confirmation run was obtained using a set of response constraints consistent with optimizing the design. Weight was set to a target weight of 21.75 kg based on the weight of the control runs, while all other responses were maximized. See Table 6.2 for more information.

Table 6.2: Exp3, Experimental Design Confirmation Run Constraints.

Name	Goal	Lower Limit	Upper Limit	Importance
A: Hw (mm)	is in range	12	120	3
B: Hw2 (mm)	is in range	12	240	3
C: Tw (mm)	is in range	8	12	3
D: Lf (mm)	is in range	0	641.9	3
E: Wf (mm)	is in range	24	120	3
F: Tf (mm)	is in range	8	12	3
Weight (kg)	is target = 21.75	1.61859	22	1
IOS Mid L/100 12.84mm (MN)	maximize	0.179554	0.812	3
IOS Mid First Yield 17mm (MN)	maximize	0.190541	0.860041	3
IOS Mid L/10 128.4 mm (MN)	maximize	0.316271	1.43984	3
IOS Mid Max 200 mm (MN)	maximize	1.03026	1.93571	3
IOS End L/100 12.84 mm (MN)	maximize	0.0368904	0.612124	3
IOS End First Yield 17 mm (MN)	maximize	0.0464747	0.68386	3
IOS End L/10 128.4 mm (MN)	maximize	0.462822	1.38283	3
IOS End Max 200 mm (MN)	maximize	1.14732	1.9418	3
IBS L/100 12.84 mm (MN)	maximize	0.0283344	0.0351864	3
IBS First Yield 17 mm (MN)	maximize	0.0404181	0.0645899	3
IBS L/10 128.4 mm (MN)	maximize	0.398941	1.22793	3
IBS Max 200 mm (MN)	maximize	1.07021	1.84004	3

Table 6.3 shows five possible solution factor levels consistent with optimization predicted by the experimental design. Solution 1 was chosen for the confirmation run. A confirmation test was then built and run to determine whether the model was capable of predicting accurate results, and if so, to determine the optimum concept grillage within the factors and levels tested.

Table 6.3: Exp3, Experimental Design Solutions.

Number	Hw (mm)	Hw2 (mm)	Tw (mm)	Lf (mm)	Wf (mm)	Tf (mm)
1	**117.899**	**113.733**	**10.398**	**641.899**	**24.000**	**8.000**
2	119.054	93.740	11.042	641.899	24.001	8.177
3	119.475	153.710	9.047	640.385	24.000	8.000
4	115.730	82.902	11.771	634.309	24.000	8.000
5	119.960	91.346	10.965	641.898	24.000	8.594

Based on Table 6.2 and Table 6.3, the optimal design suggested that both the flange width, W_f (factor E), and the flange thickness, T_f (factor F), should be at their minimum levels.

In order words, the suggested optimal design could be consistent with the removal of the flange entirely. Therefore, two confirmation runs were built based on the suggested conditions shown in Table 6.3 – one with a flange and one without. The results of each were then compared for similarity. However, since removing the flange would result in a lighter structure, they would not be directly comparable unless additional weight was added to the web to compensate. Therefore, Confirmation Run 2 was built with equal weight compared to Confirmation Run 1, but with its thickness increased from 11.125 mm to 12.2 mm. The stiffener end web height, H_w (Factor A), and the mid-span stiffener height, H_{w2} (Factor B), remained constant to preserve the shape of the profile of the stiffener.

6.5.2.1 Confirmation Run 1 (With Flange)

The responses of the confirmation run can be seen in the Data Mean column of Table 6.4. Based on the 95 % confidence interval, the model accurately predicted the results of every response examined. Therefore, the model can be used to predict accurate results.

Table 6.4: Exp3, Experimental Design Confirmation Run 1 Results.

Two-sided Confidence = 95%

Response	Predicted Mean	Predicted Median	Std Dev	95% PI low	Data Mean	95% PI high
Weight (kg)	21.735	21.735	0.23092	21.1284	22.28	22.3415
IOS Mid L/100 12.84mm (MN)	0.340599	0.338472	0.0537466	0.227858	0.374	0.4709
IOS Mid First Yield 17mm (MN)	0.427986	0.427012	0.0408106	0.333268	0.439	0.532358
IOS Mid L/10 128.4 mm (MN)	1.1413	1.1413	0.0544293	1.00938	1.103	1.27323
IOS Mid Max 200 mm (MN)	1.65775	1.65775	0.120794	1.3905	1.705	1.92499
IOS End L/100 12.84 mm (MN)	0.421939	0.421939	0.0232911	0.365185	0.396	0.478693
IOS End First Yield 17 mm (MN)	0.45922	0.45922	0.0245974	0.399283	0.448	0.519157
IOS End L/10 128.4 mm (MN)	1.17342	1.17342	0.0408102	1.07232	1.099	1.27452
IOS End Max 200 mm (MN)	1.73851	1.73851	0.0921405	1.53466	1.744	1.94237
IBS L/100 12.84 mm (MN)	0.0326854	0.0326854	0.00117299	0.0301798	0.034	0.035191
IBS First Yield 17 mm (MN)	0.060941	0.060941	0.000567382	0.0591666	0.06	0.0627153
IBS L/10 128.4 mm (MN)	1.01343	1.01343	0.0704382	0.857592	0.962	1.16927
IBS Max 200 mm (MN)	1.55828	1.55828	0.0409149	1.46257	1.506	1.654

See Figure 6.23, Figure 6.24, Figure 6.25, and Figure 6.26, for more information regarding the geometry and von Mises stress data at the end of the analysis.

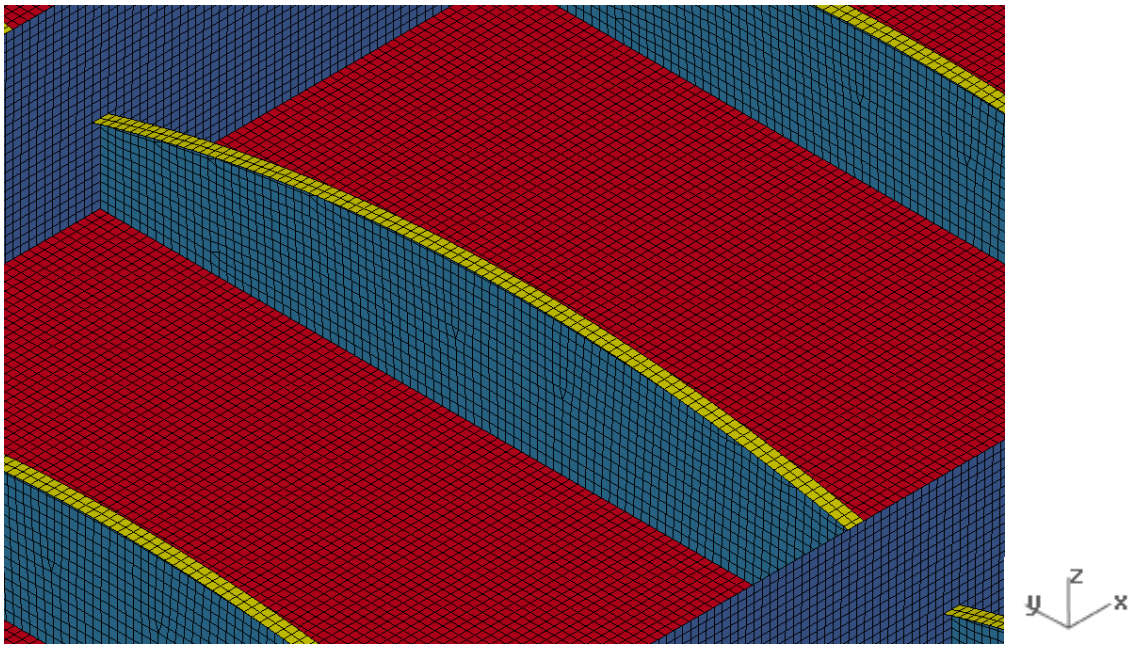

Figure 6.23: Exp3, Confirmation Run 1 Geometry.

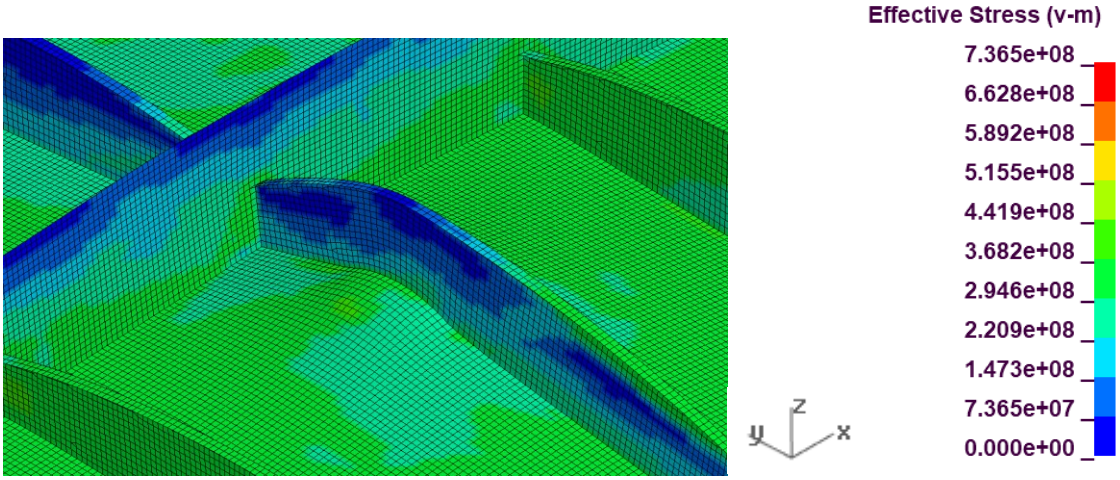

Figure 6.24: Exp3, Confirmation Run 1 - von Mises stress, Load Case 1.

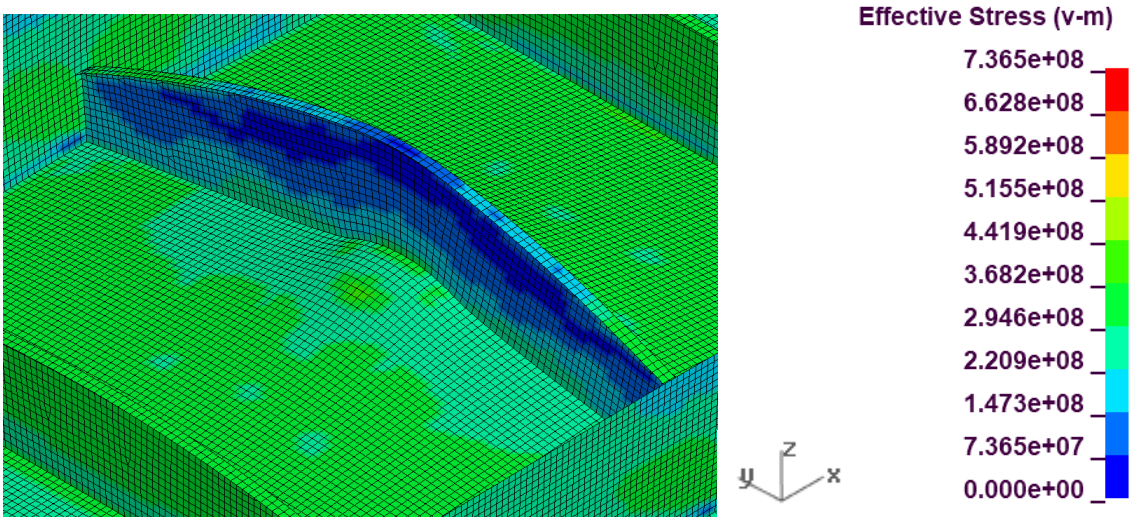

Figure 6.25: Exp3, Confirmation Run 1 - von Mises stress, Load Case 2.

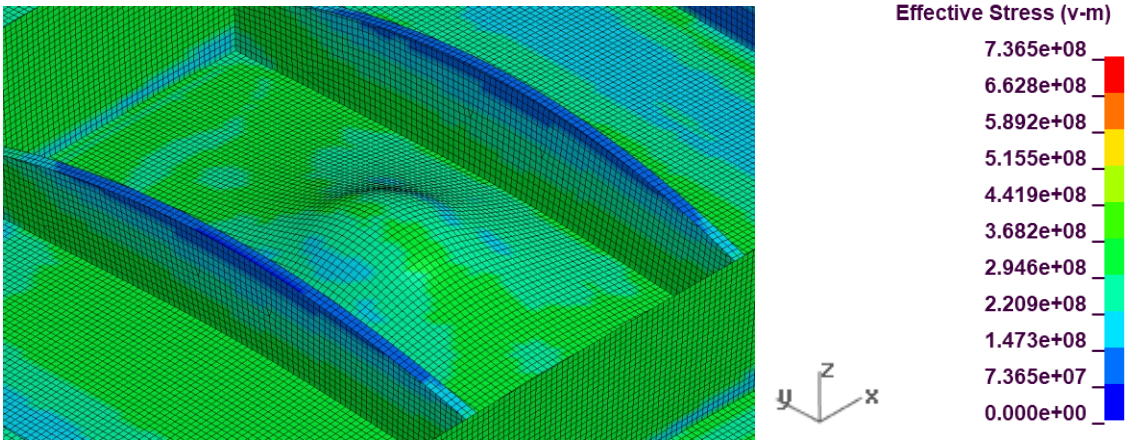

Figure 6.26: Exp3, Confirmation Run 1 - von Mises stress, Load Case 3.

As can be seen in Figure 6.27, Figure 6.28, and Figure 6.29, the optimized confirmation run performed adequately within the elastic region of the plots. However, the confirmation run did not outperform the control runs within the post-yield region of the plots. The underperformance was likely due to the narrow levels for the stiffener end web height, H_w (Factor A) (see Table 6.2 and Table 6.3 for more details). When a factor is suggested to be

maximized, it is a good indicator that a more optimal level lay outside of the chosen level range (design space).

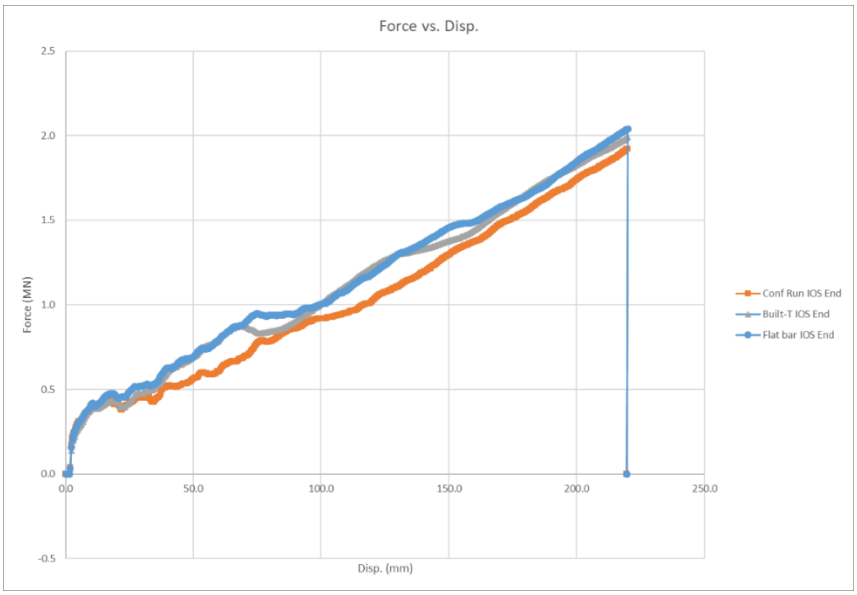

Figure 6.27: Exp3, Force vs. Disp. plot for Confirmation Run 1 and control runs, Load Case 1.

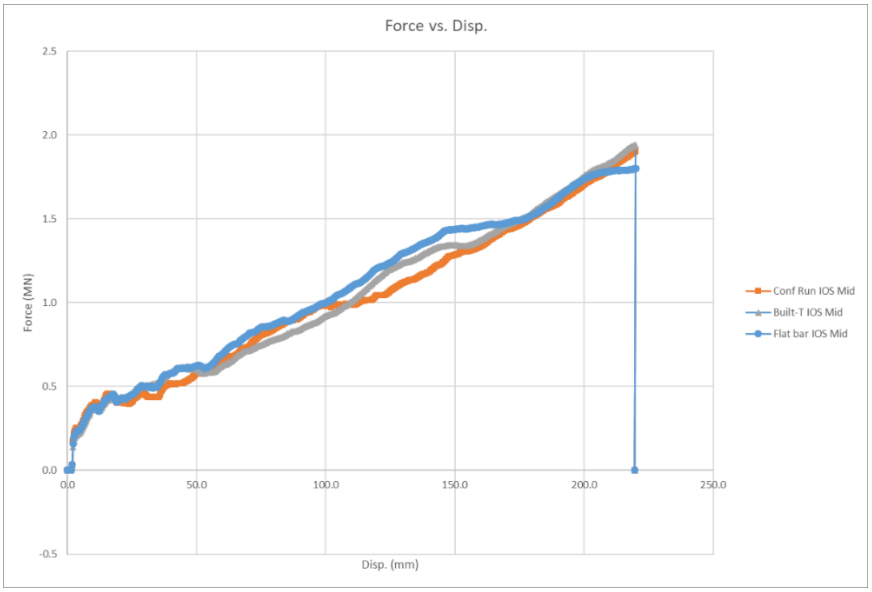

Figure 6.28: Exp3, Force vs. Disp. plot for Confirmation Run 1 and control runs, Load Case 2.

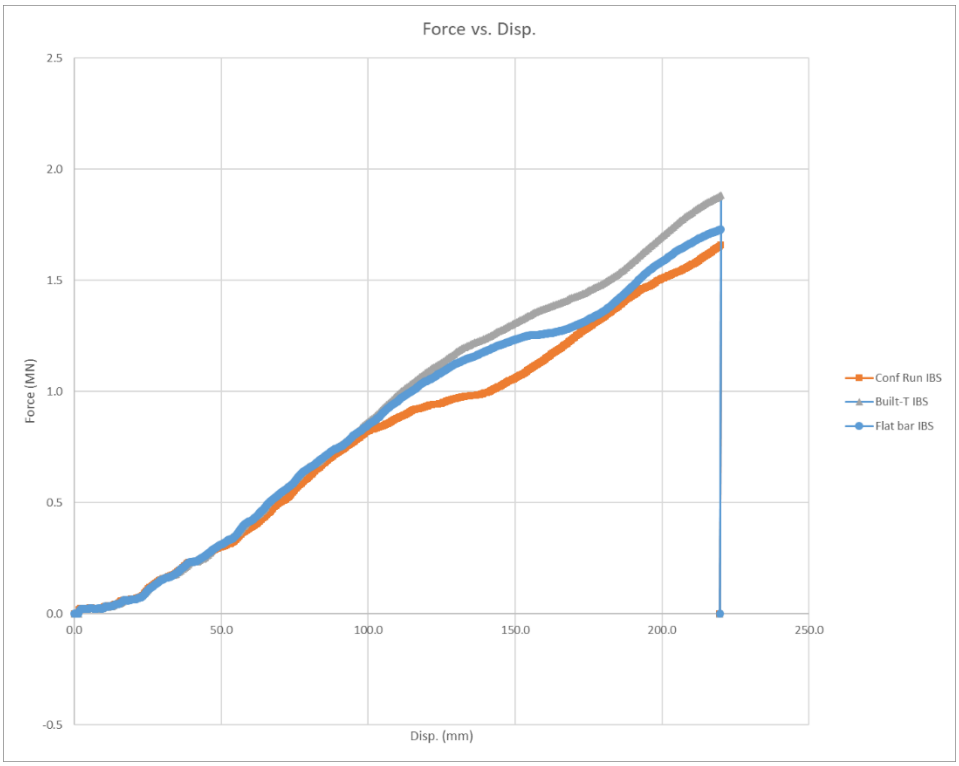

Figure 6.29: Exp3, Force vs. Disp. plot for Confirmation Run 1 and control runs, Load Case 3.

No elements failed element quality checks. See Appendix D8 for more information related to the element quality checks of Confirmation Run 1.

6.5.2.2 Confirmation Run 2 (Without Flange)

An identical copy of Confirmation Run 1 was built and analyzed without a flange. To compensate for the consequent reduction in weight, additional thickness was added to the stiffener web, preserving the shape of the web profile.

The comparison of both confirmation runs shown in Figure 6.34, Figure 6.35, and Figure 6.36, demonstrate the results of force vs. displacement with and without the flange. It was evident that the flange added no significant advantage over the flangeless option. Moreover,

running an experimental design with a flange requires 6 experimental factors, resulting in a minimum of 31 experimental runs. By comparison, running a flangeless design requires only 3 factors, resulting in a minimum of 13 experimental runs. Therefore, since the flange has been shown to add no significant value to the response, coupled with the fact that a flange requires many more experimental runs, further experimentation was completed without the flange.

See Figure 6.30, Figure 6.31, Figure 6.32, and Figure 6.33, for more information regarding the geometry and von Mises stress data at the end of the analysis.

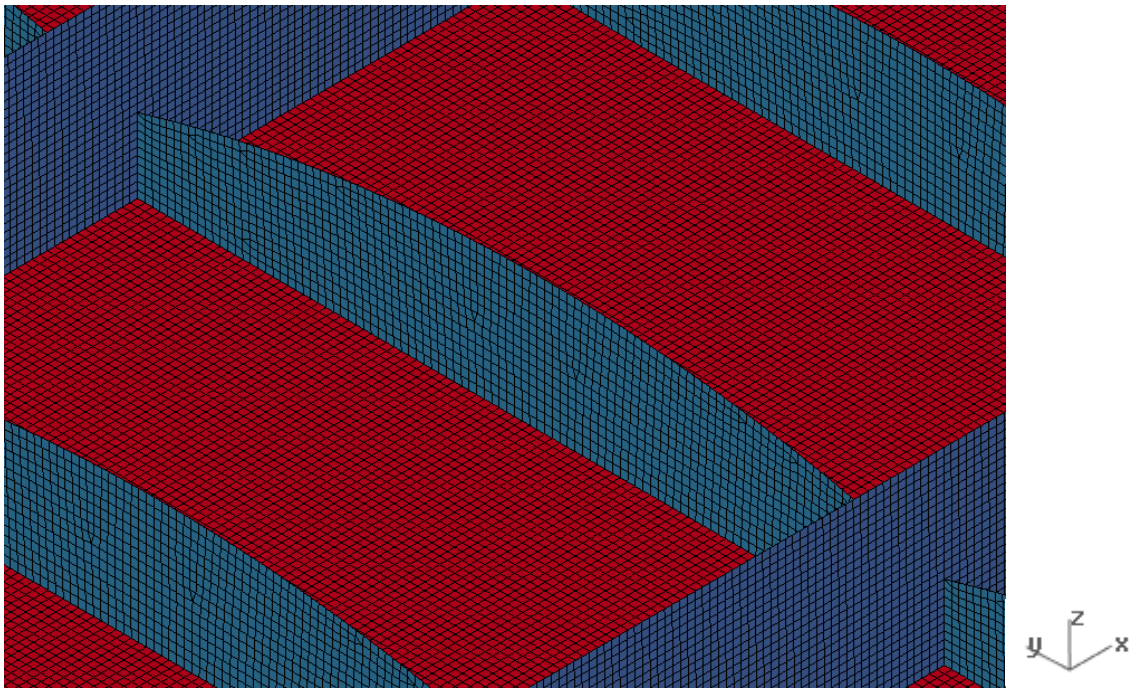

Figure 6.30: Exp3, Confirmation Run 2 Geometry.

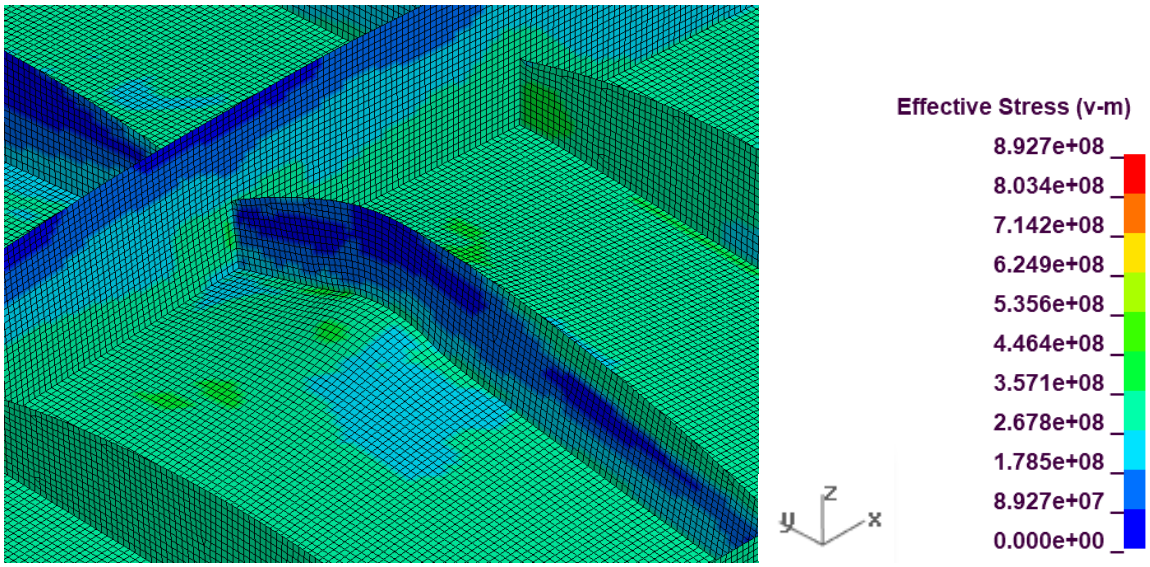

Figure 6.31: Exp3, Confirmation Run 2 - von Mises stress, Load Case 1.

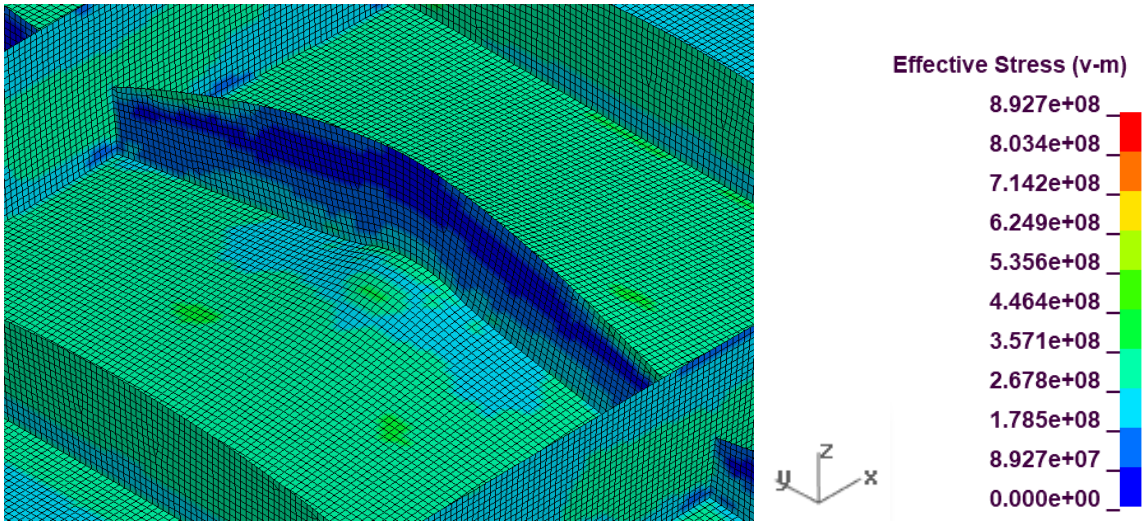

Figure 6.32: Exp3, Confirmation Run 2 - von Mises stress, Load Case 2.

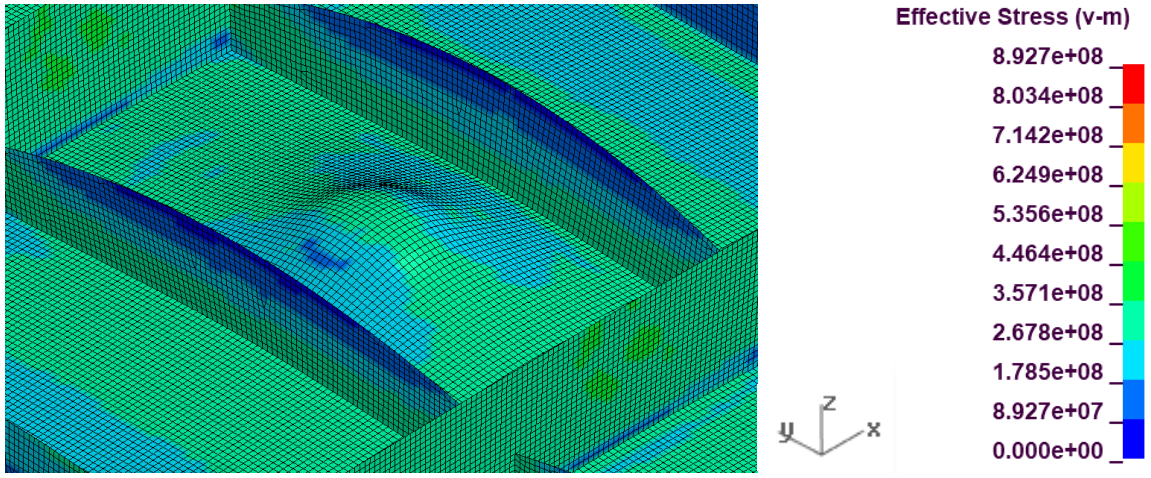

Figure 6.33: Exp3, Confirmation Run 2 - von Mises stress, Load Case 3.

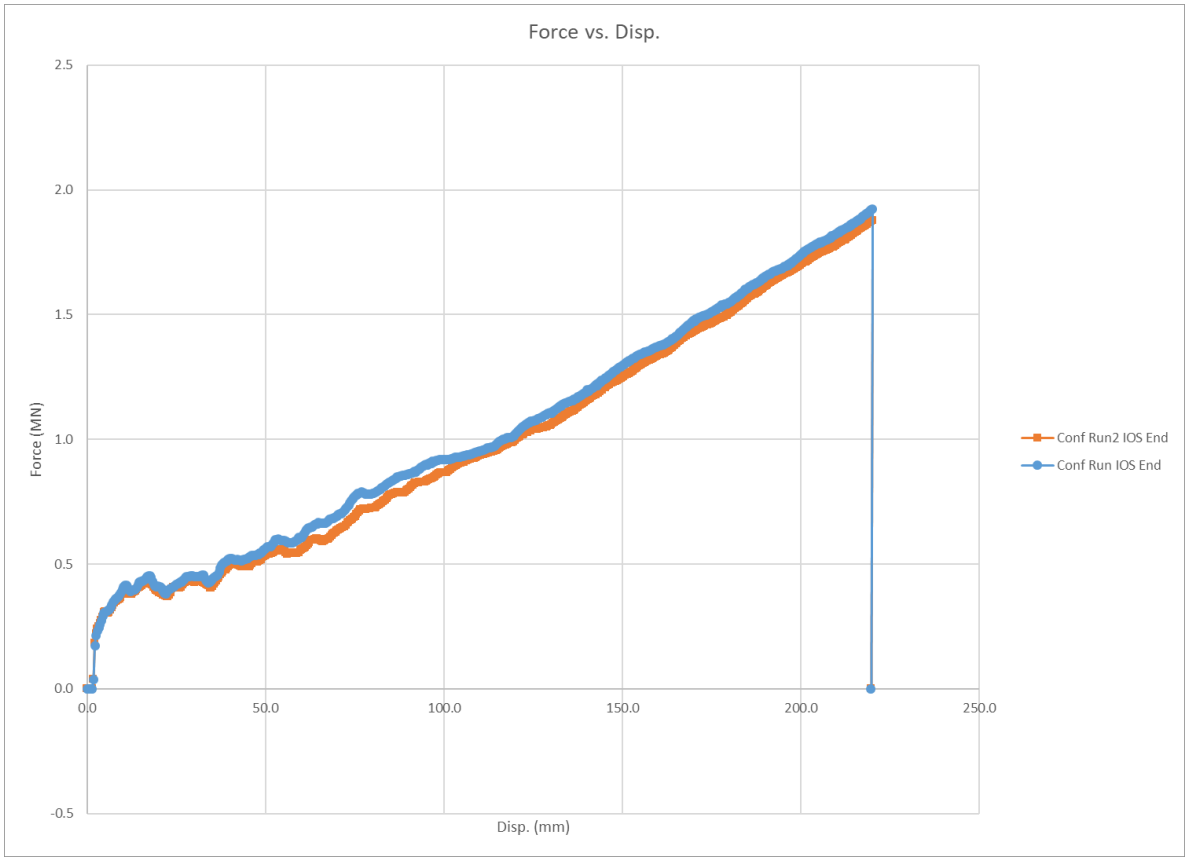

Figure 6.34: Exp3, Force vs. Disp. plot for Confirmation Run 1 and 2, Load Case 1.

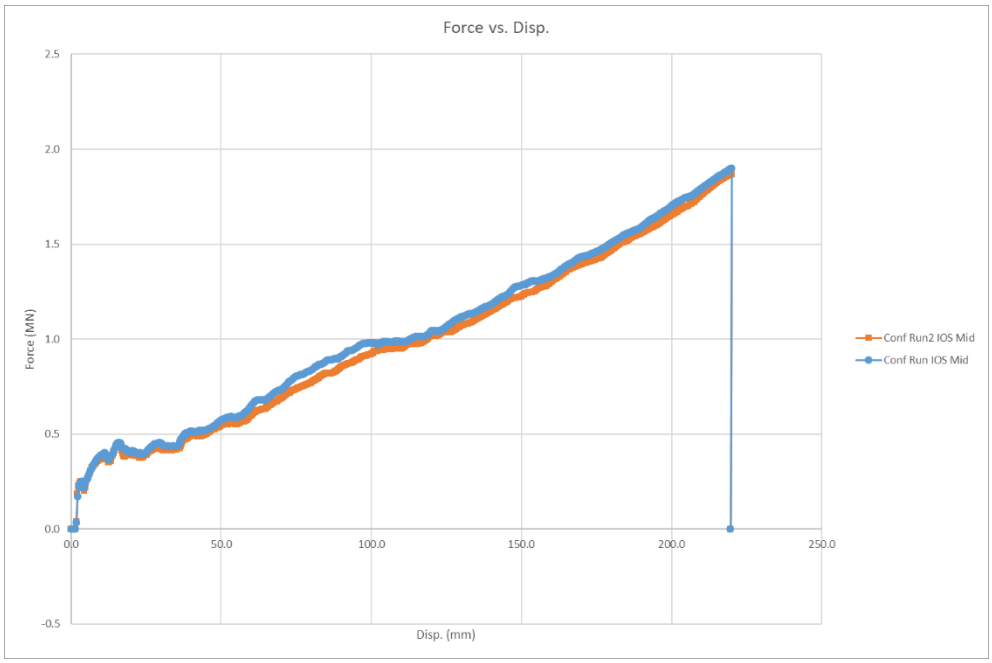

Figure 6.35: Exp3, Force vs. Disp. plot for Confirmation Run 1 and 2, Load Case 2.

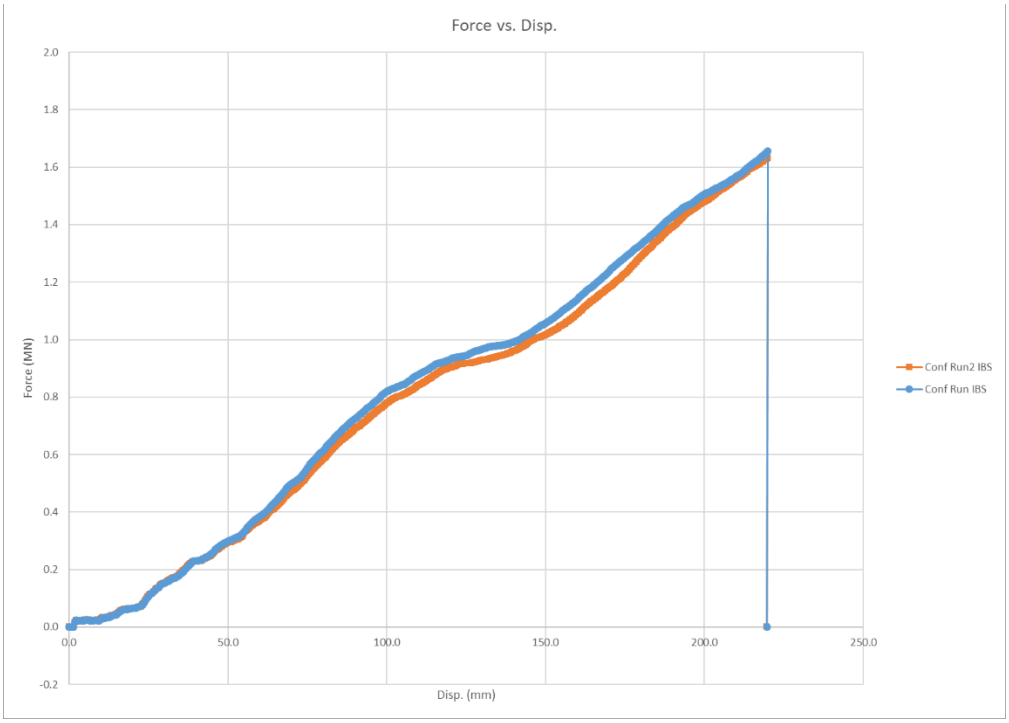

Figure 6.36: Exp3, Force vs. Disp. plot for Confirmation Run 1 and 2, Load Case 3.

No elements failed element quality checks. See Appendix D8 for more information related to the element quality checks of the Confirmation Run 2.

6.6 Relationship between Flange and Stress vs. Strain Curve

It has been demonstrated in Exp3 that, under particular conditions, the flange would not be necessary for a side-shell stiffener. Under yield failure criteria, the built-T shape provides low displacement values per unit force. However, the stiffener's overload capacity was quite low, as it buckled almost immediately post-yield.

As can be observed in Figure 6.37, the yield portion of the curve (before the inflection point) was quite small. Assuming a failure strain of 0.25, the plastic (post-yield) potion of the graph was much larger. This diagram puts into perspective just how small the range of strains is where using a flange is beneficial. Moreover, it has been demonstrated in Exp3 that a variable web height stiffener can perform just as well as a flanged stiffener, within the yield regime, under similar conditions.

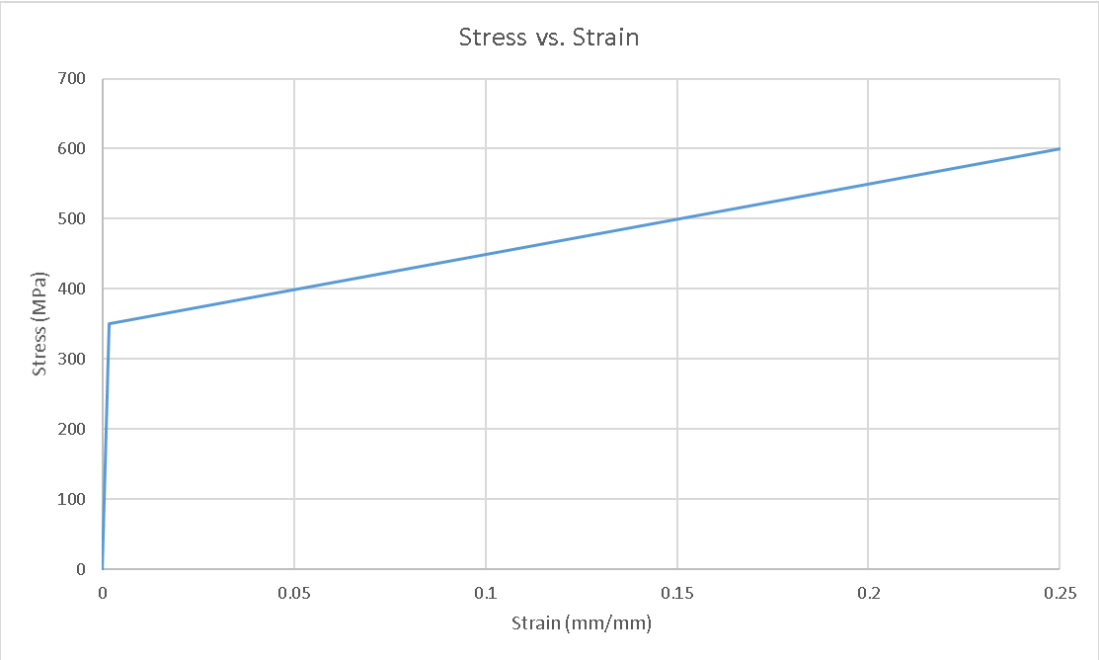

Figure 6.37: Exp3, General stress vs. strain curve.

6.7 Discussion and Conclusions

Exp3 was conducted as a more in-depth study into one of the stiffener designs found in Exp2 – the variable web height stiffener, with end-flanges. An experimental design was implemented which studied six experimental factors defining the shape of the stiffener. Three factors defined the shape of the web, while the remaining three defined the shape of the flange. An optimal, RSM, experimental design was implemented with 31 runs included.

Several changes were implemented from lessons learned from unsuccessful experimentation. Most significantly, the size of the model was enlarged to incorporate frame structures at the stiffener ends to simulate more realistic stiffener end conditions. A total of three load cases were tested: an IOSQ, an IOSC, and an IBS.

Since three loading cases were being studied per run, to reduce computation run time, it was desirable to create a model that included each load case simultaneously. A convergence study was completed to ensure that the results of each load case were independent of the other load case impacts. To begin, each load case was tested separately in the same model (built-T control) to determine the actual individual results for each load case. Then, all three load cases were analyzed within the same model, by varying the number of stiffeners between load cases until the data matched the individual results. It was concluded that at least fourteen feet (seven stiffeners) must separate the impact interactions to ensure that the results of each load case were independent of the other load cases.

Concerning both the built-T and flat bar control runs, depending on the load case scenario the buckling modes were quite different and/or more pronounced. The built-T stiffener experienced excessive local buckling leading to tripping within both IOS (impact, normal to the grillage side-shell, directly on a stiffener) load cases. However, for the IBS load case, the built-T demonstrated little to no buckling. Comparing both IOS load cases for the flat bar, an IOSQ did not cause any buckling of the stiffener, whereas an IOSC caused significant tripping. Similar to the built-T IBS, the flat bar stiffener did not experience significant plasticity.

Once the data was collected from LS-DYNA, it was plotted in the form of force vs. displacement curves. For analysis purposes, four responses were of concern – the forces which corresponded to the displacements at first yield, L/100, and L/10, and 200 mm. Each of the four responses was collected for the three load cases resulting in 12 responses, plus the weight response.

Two confirmation runs were completed to determine optimal factor levels to be compared to the control runs. The first confirmation run used a flanged stiffener, whereas the second confirmation run used a flangeless stiffener. To equate the weights of the confirmation runs, a thicker web was used for the flangeless stiffener.

For the first confirmation run, based on the 95 % confidence interval, the model accurately predicted the results of every response examined. The model performed adequately within the elastic region of the plots. However, the confirmation run did not outperform the control runs within the post-yield region of the plots. The underperformance was likely due to the fact that the levels of the stiffener end web height, H_w (Factor A) should be widened to capture optimality.

The results for both confirmation runs were compared to determine the significance of the flange. Based on the results, it was evident that the flange added no significant advantage over the flangeless option. Moreover, running an experimental design with a flange requires 6 experimental factors, resulting in a minimum of 31 experimental runs. By comparison, running a flangeless design requires only 3 factors, resulting in a minimum of 13 experimental runs to navigate the design space. Therefore, the flange was eliminated from further testing. Under yield failure criteria, the built-T provides low displacement values per unit force. However, the stiffener's overload capacity was quite low, as it buckled almost immediately post-yield.

Chapter 7 Exp4 – Concept Grillage

Exp4 explores in more detail the variable web height stiffener. Exp3 utilized the Global Model, whereas this experiment (i.e. Exp4) utilized the Local Model. Using the Local Model allowed the FEA to mimic the test conditions of the LPA. Exp3 concluded that a stiffener flange did not appear to be statistically significant in optimizing the stiffener. By removing the flange, a simpler experimental design was possible with half the number of factors – three instead of six. Therefore, only 13 runs were required to navigate the design space, as opposed to 31. The goal of this experimental simulation was to optimize the grillage for the LPA.

Moreover, Exp4 changed the responses that were collected. In Exp3, responses were collected in the form of forces associated with various levels of indentation (displacement). For Exp4, instead, the energy was calculated based on the force vs. displacement curves, at various locations. However, for determining first yield, the force was still used. More information can be found in Section: 7.5 Results.

7.1 Load Cases

As the model was to be set up in the LPA, Load Case 1 was not possible to be tested. Both Load Cases 2 and 3 were possible to be tested since they were both examples of mid-stiffener-span impacts. Load Case 2 was chosen as, compared to Load Case 3, it had the highest likelihood of causing stiffener buckling.

7.2 Model Parts

Refer to Section: 3.7 Rigid Indenter Design, for information regarding the Rigid Intender model.

7.2.1 Local Model

The grillage (see Figure 7.1) used in Exp4 was similar to that used in Exp1, except additional stiffeners were added to resemble the simplified panels, as well as the IROQUOIS panels. The Local Model was used to mimic what can be placed in the LPA (see Section: 9.2.1.1 Validation Study Outline). The middle stiffener was centred on the side-shell allowing the rigid indenter to impact directly on the middle stiffener, at the centre of its span.

For simplicity, the side-shell was given a parametrized thickness of 7.9375 mm. The remaining constants related to the FEMs were:

- Stiffener spacing = 609.6 mm.
- Stiffener length = 1283.8 mm.
- Side-shell width, x-direction = 2032 mm.
- Side-shell length, y-direction = 1283.8 mm.
- The material properties and FEM controls.

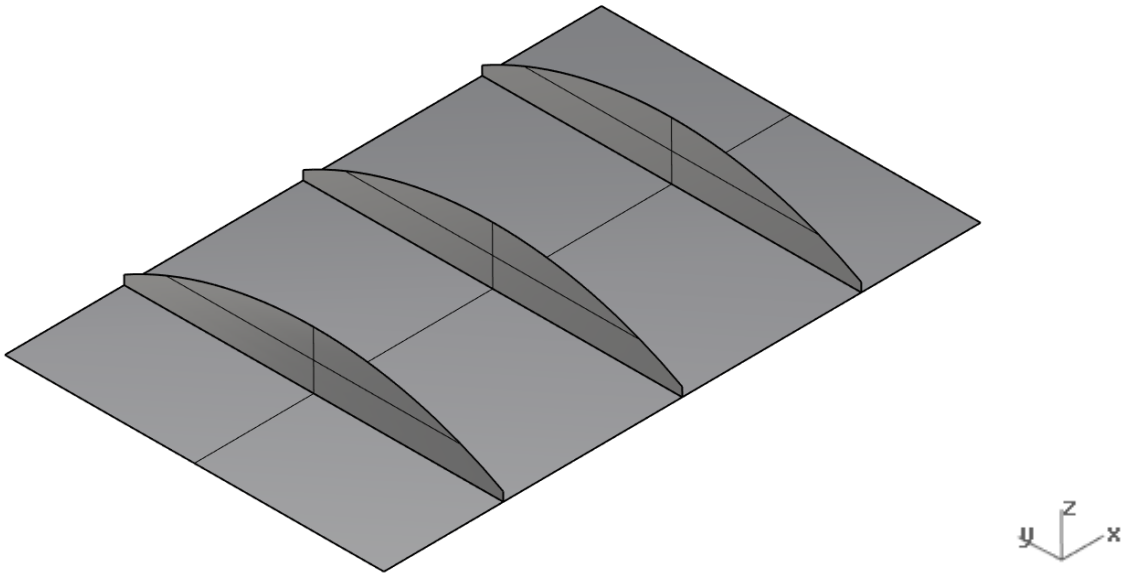

Figure 7.1: Exp4 Grillage.

See Figure 7.2, Figure 7.3, and Figure 7.4, for pictures regarding one of the two simplified panels. The simplified panel shown in the figures was a four-stiffener variant used for testing impacts between stiffeners. It should be noted that the simplified panel used within the simulations was a three-stiffener variant used for impacts directly on a stiffener.

Figure 7.2: Simplified panel with mounting brackets.

Figure 7.3: Simplified panel stiffener with rigid mounting brackets.

Figure 7.4: Simplified panel – impact between stiffeners variation.

7.3 LS-PrePost and LS-DYNA

See the below subsections for information related to the construction of the FEMs within LS-DYNA.

7.3.1 Boundary Conditions

The BCs used in the model consisted of fixed-fixed BCs and were applied in the same manner as seen in Figure 4.4.

7.3.2 Loading Conditions

The load was applied as per Section: 3.4.1.2 Loading Conditions.

7.3.3 Termination Time

The models were set to terminate at 0.075 s.

7.3.4 Contact

Contact was applied as per Section: 3.4.1.3 Contact.

7.3.5 Data Output

Data was output in the form of d3plots and ASCII plots at a frequency of 10,000 Hz. The force data consisted of the contact forces at the impact sites.

7.3.6 Material Properties

The grillages were modelled using material properties as seen in 6.3.6 Material Properties.

Note: For Exp4, the material properties were to be updated based on uniaxial tensile strength testing. However, the tests were not yet completed and could not be implemented.

7.3.7 Mesh Convergence Study

Several runs were prepared based on the geometry of Run6. Based on Figure 7.5, each figure contained three runs that were prepared with varying average element sizes. Since the indenter was impacting the plate with a prescribed displacement, the corresponding contact force was used for the analysis and then plotted against time. As can be seen in the plots, there were little observable changes to the force vs. time plots for the different mesh sizes.

However, this study demonstrated that buckling could cause a variance between curves. Since accurately quantifying buckling behaviour was considered important for determining an optimal grillage, and since Exp4 was anticipated to yield an optimal concept grillage design, a minimum element size was used for every part in the models, equal to their associated thickness. With that being said, none of the experimental runs included a mesh size coarser than 25.4 mm.

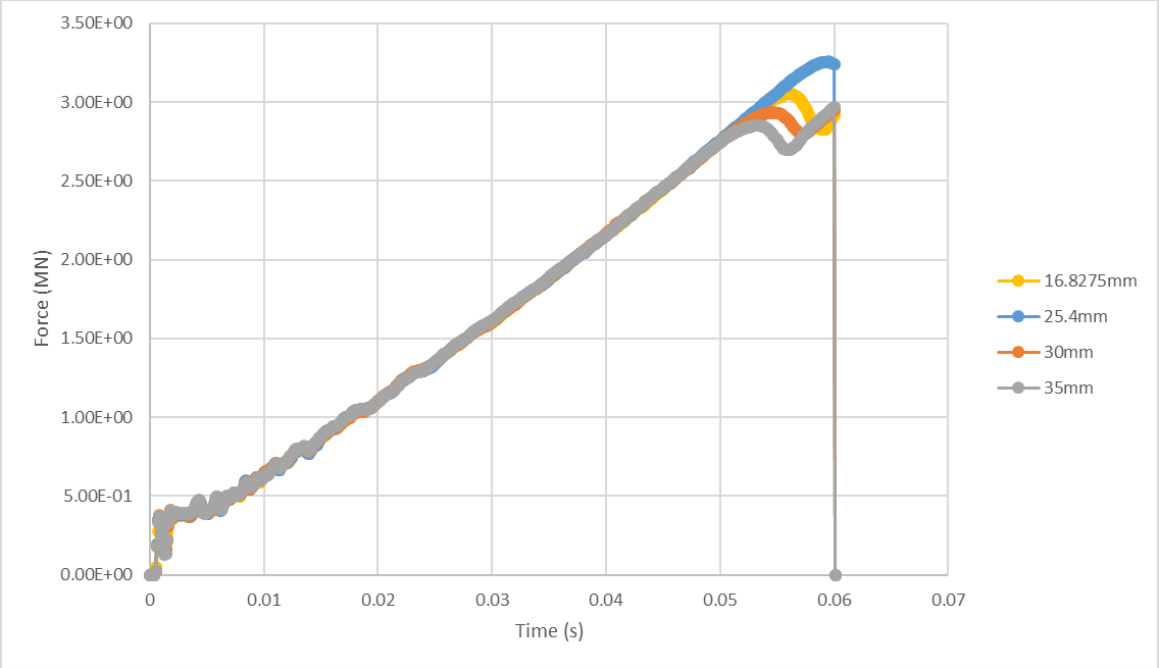

Figure 7.5: Exp4, Mesh convergence plot of force vs. time.

7.3.8 LS-DYNA Cards

Several cards were invoked within LS-DYNA to achieve the desired effects intended for the simulation:

BOUNDARY_PRESCRIBED_MOTION_RIGID

Rigid body motion of the indenter was achieved using the following fields: DOF = 3 and VAD = 2.

CONTACT_AUTOMATIC_SURFACE_TO_SURFACE

Contact was defined between the indenter and side-shell. To collect contact forces both SPR and MPR were set to 1.

CONTROL_TERMINATION

The simulation was set to terminate using ENDTIM = 0.061.

DATABASE_ASCII_option

Nine ASCII options were turned on for high fidelity result extraction: BNDOUT, ELOUT, GLSTAT, MATSUM, NODOUT, RBDOUT, RCFORC, SLEOUT, SPCFORC. Each was given a DT of 0.0001.

DATABASE_BINARY_D3PLOT

For visualizing the simulation, DT = 0.01 was used.

DATABASE_BINARY_INTFOR

The internal forces were collected using DT = 0.01.

DATABASE_HISTORY_NODE_ID

The appropriate node was selected for ASCII NODOUT.

DEFINE_CURVE

To simulate a linear load curve, four points were used: (0, 0), (0.06, 0.22), (0.12, 0), and (0.13, 0).

MAT_PLASTIC_KINEMATIC

A, bi-linear, plastic kinematic material model was built using the following material properties: RO = 7850, E = 2.07e11, PR = 0.3, SIGY = 3.5e8, and ETAN = 1e9.

MAT_RIGID

The properties used were: RO = 2.742e6, E = 2.07e11, and PR = 0.3. Also, CMO, CON1 and CON2 were invoked to properly restrict the rigid body from x and y translations, as well as x, y, and z rotations using 1, 4, and 7, respectively.

SECTION_SHELL

The shear factor was changed from 1 to 5/6 using SHRF = 0.8333. Also, five through-thickness integration points were used by invoking NIP = 5.

7.4 Experimental Design, Factors, and Responses

An optimal, RSM, experimental design was implemented to determine the optimal design within the given levels of factors studied. The chosen three factors combined to form 26 experimental runs, as well as one control, built-T, run.

Exp4 consisted of three experimental factors that were chosen to be systematically varied throughout the experimental runs. A wide range of factor levels was tested to ensure that the design space was adequately explored. See Figure 6.10 for more information regarding factor definitions (ignoring factors related to the flange).

A. Stiffener End Web Height, H_w, 25.4 – 300 mm
    - The height of the stiffener at its end from the side-shell it the top of the stiffener
B. Mid-Span Stiffener Height, H_{w2}, 0 – 300 mm
    - The height of the stiffener at the centre of its span from the stiffener end web height to the top of the stiffener
C. Web Thickness, T_w, 6.35 – 25.4 mm (1/4 – 1 inch)

Note: The minimum level of the mid-span stiffener height, H_{w2} (Factor B), was 0. With a value of 0, the corresponding structure was a flat bar. Therefore, a flat bar control run was not included since a flat bar was already being tested within the factor levels. A built-T control run was still included.

Note: Though the suggested number of runs for a three-factor optimal design was 13, instead, 26 runs were used to ensure the design power was at least 80 % for each effect within the design. The design power quantifies the probability that the design will be capable of revealing the active effects within the model. (Anderson and Whitcomb 2014) recommends ensuring a design power of 80-95%.

Unlike Exp3, three of the responses were acquired in the form of energies associated with the force vs. displacement curves. For example, from a displacement of 50-100 mm, the curve was integrated to determine the energy associated with the curve between those limits. For analysis purposes, five responses were of concern – weight, first yield, and the energy associated with the following displacement ranges: 0-50 mm, 50-100 mm, and 100-

150 mm. Similar to Exp3, weight was treated as a response and targeted to be equal to the control run.

See the below-listed responses for more clarity:

1. Weight (weight of each stiffener configuration)
2. First Yield – The force at which the force vs. displacement curve first becomes nonlinear, read directly from each plot.
3. Energy from 0-50 mm – Corresponding energy at a displacement range of 0-50 mm of indentation.
4. Energy from 50-100 mm – Corresponding energy at a displacement range of 50-100 mm of indentation.
5. Energy from 100-150 mm – Corresponding energy at a displacement range of 100-150 mm of indentation.

Design Expert was used to produce a series of runs. See Table 7.1.

Table 7.1: Exp4 Run Order in Design Expert.

	Factor 1	Factor 2	Factor 3
Run	A: Hw	B: Hw2	C: Tw
Units	mm	mm	mm
1	300	300	13.3985
2	25.4	300	6.35
3	176.43	165	6.731
4	25.4	0	6.35
5	128.375	300	25.4
6	30.892	165	16.8275
7	300	111	25.4
8	300	0	6.35
9	176.43	6	16.8275
10	25.4	0	25.4
11	206.636	180	17.1912
12	117.391	133.5	25.4
13	300	298.677	25.4
14	205.263	300	6.35
15	25.4	300	18.7325
16	161.327	0	15.8915
17	170.938	147.816	14.8272
18	300	0	25.4
19	300	154.5	12.827
20	142.22	144	15.0177
21	25.4	117	6.35
22	25.4	193.5	25.4
23	300	183.492	6.35
24	166.819	0	6.35
25	160.298	153.209	16.2776
26	25.4	0	16.0655

7.5 Results

Due to the large quantity of FEM runs, FEM visuals have only been shown for two runs: the built-T control run and Run6. Run6 was chosen since it was used for the MCA. The built-T control run visuals related to the undeformed geometry and the maximum von Mises stress data can be seen in Figure 7.6 and Figure 7.7, respectively.

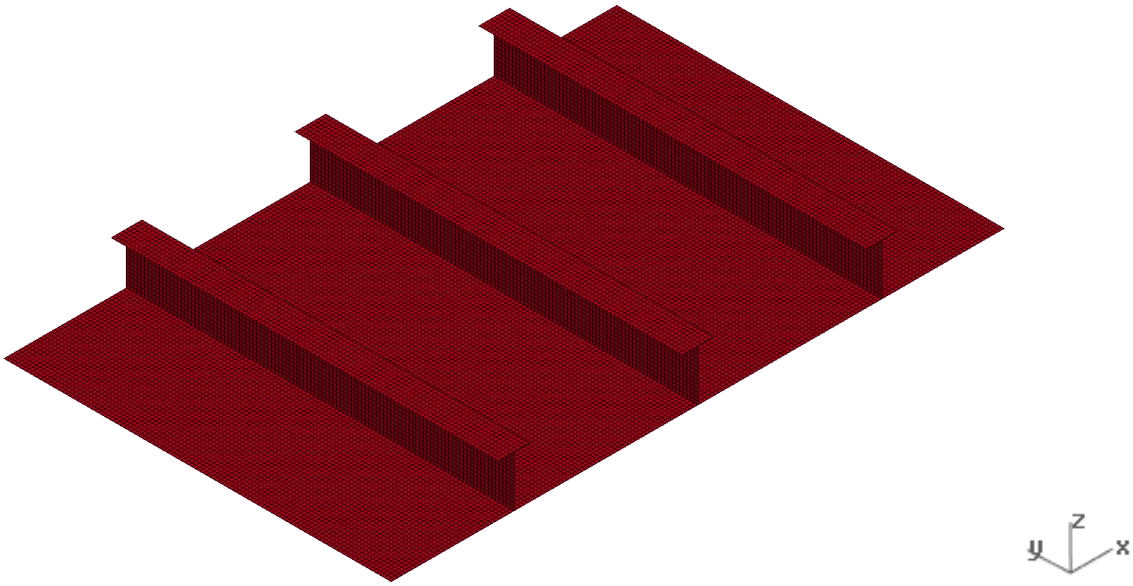

Figure 7.6: Exp4, Control – Built-T Geometry.

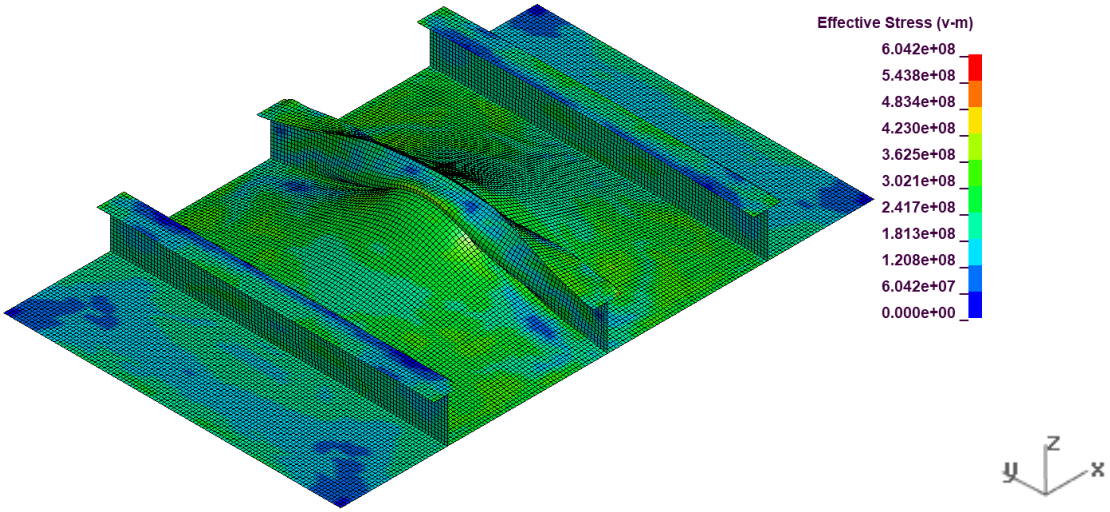

Figure 7.7: Exp4, Control – Built-T von Mise Stress.

The Run6 visuals related to the undeformed geometry and the maximum von Mises stress data can be seen in Figure 7.8 and Figure 7.9, respectively.

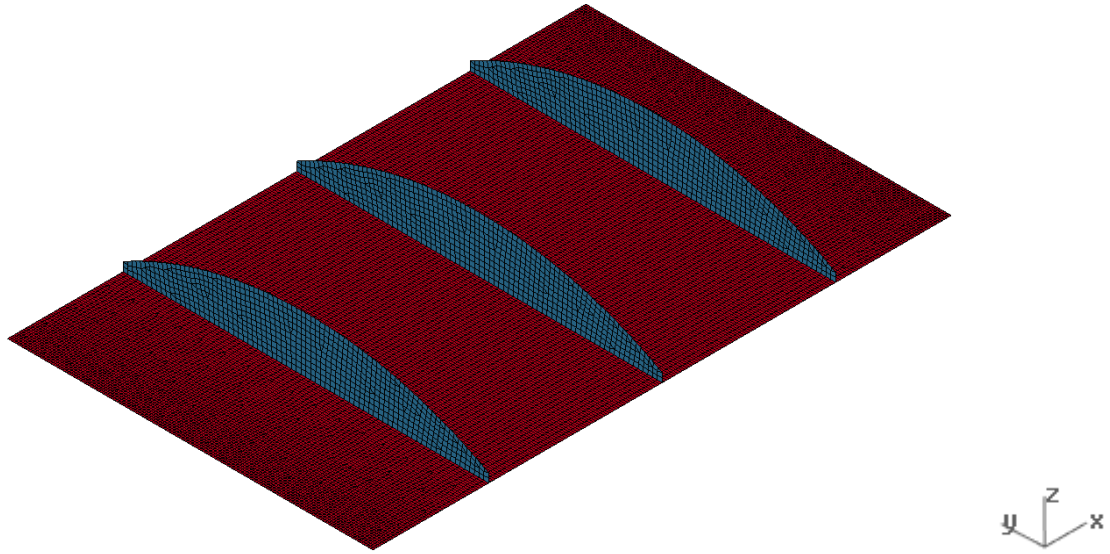

Figure 7.8: Exp4, Run6 Geometry.

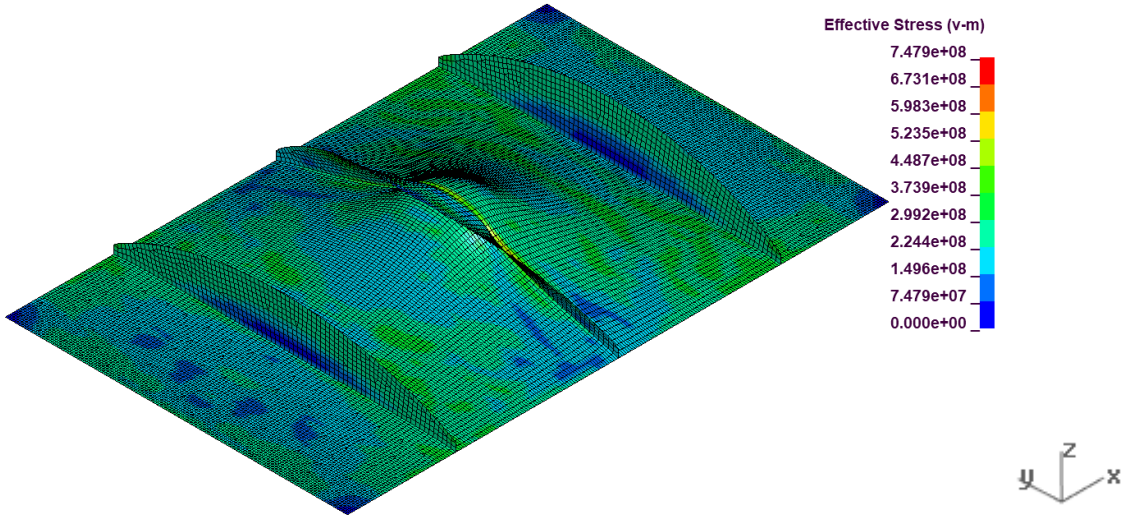

Figure 7.9: Exp4, Run6 von Mise Stress.

Once the data was collected from LS-DYNA, it was plotted in the form of force vs. displacement similar to what was done in Exp2 and Exp3. Although, within Exp4, Energy vs. displacement plots were also analyzed.

See Appendix E1 for visuals for all run geometry and von Mises stress results. See Appendix E2 for information regarding the scantlings and responses of the experimental runs found in Exp4. See Appendices E3, E4, and E5 for more information regarding the von Mises vs. displacement, force vs. displacement and energy vs. displacement plots, respectively.

7.5.1 Experimental Design Model Checking

Each of the five responses passed model checks related to the quality of the experimental design data. A square root transformation was applied to the First Yield response. Natural logarithmic transformations were applied to the Energy at 0-50 mm and 100-150 mm responses. An inverse square root transformation was applied to the Energy at 50-100 mm response. Transformations were applied to ensure the data fit a normal distribution and had equal variance. See Appendix E6 for the raw data from Design Expert related to the model checking.

7.5.2 Confirmation Runs

Several confirmation runs were obtained using a set of response constraints consistent with optimizing the design. Weight was set to a target weight of 21.75 kg based on the weight of the control run, while all other responses were maximized. See Table 7.2 for more information.

Note: Regarding Table 7.2, several responses have been shown in their transformed, inverse, scale. Therefore, it would appear that the Energy 50-100 mm response was being minimized when it was being maximized.

Table 7.2: Exp4, Experimental Design Confirmation Run Constraints.

Name	Goal	Lower Limit	Upper Limit	Importance
A: Hw (mm)	is in range	25.4	300	3
B: Hw2 (mm)	is in range	0	300	3
C: Tw (mm)	is in range	6.35	25.4	3
Weight (kg)	is target = 21.75	1.62544	23	1
First Yield (MN)	maximize	0.194422	1.84662	3
Energy 0-50mm (MNmm)	maximize	1.49525	4.78974	5
Energy 50-100mm (MNmm)	minimize	0.079731	0.204341	5
Energy 100-150mm (MNmm)	maximize	3.90833	5.04805	5

Three sets of solution factor levels consistent with optimization, based on the results of the experimental design, can be seen in Table 7.3. Confirmation test runs were then built and analyzed to determine whether the model was capable of predicting accurate results, and if so, to determine the optimum concept grillage within the factors and levels tested.

Table 7.3: Exp4, Experimental Design Solutions.

Conf. Run	Hw (mm)	Hw2 (mm)	Tw (mm)
1	**83.02**	**111.65**	**13.69**
2	132.20	133.21	9.93
3	134.09	153.70	9.13

7.5.2.1 Confirmation Run 1

The responses of the confirmation run can be seen in the Data Mean column of Table 7.4. Based on the 95 % confidence interval, the model accurately predicted the results of every response examined. Therefore, the model can be used to predict accurate results.

Table 7.4: Exp4, Experimental Design Confirmation Run 1 Results.

Two-sided Confidence = 95%

Response	Predicted Mean	Predicted Median	Std Dev	95% PI low	Data Mean	95% PI high
Weight (kg)	21.7113	21.7113	0.119541	21.4477	21.7731	21.9749
First Yield (MN)	0.382767	0.380676	0.0565083	0.265234	0.354	0.516918
Energy 0-50mm (MNmm)	24.2132	24.0024	3.19507	17.7675	23.2834	32.4252
Energy 50-100mm (MNmm)	54.5589	54.0465	6.1194	42.5085	53.2454	71.0088
Energy 100-150mm (MNmm)	84.9239	84.6285	7.08374	70.01	86.1518	102.299

See Figure 7.10 and Figure 7.11, for more information regarding the geometry and von Mises stress data at the end of the analysis.

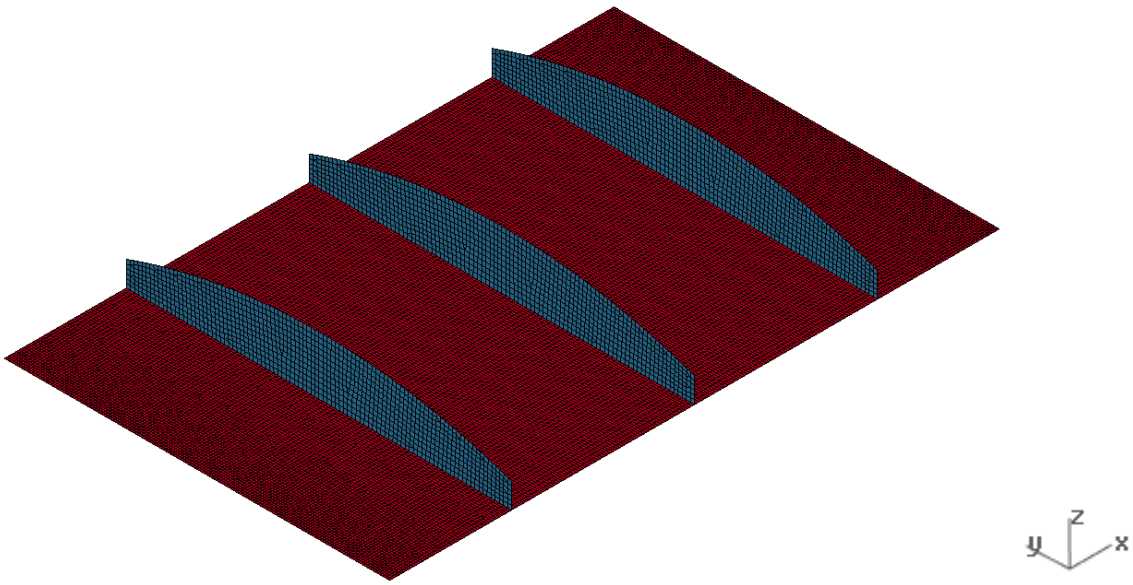

Figure 7.10: Exp4 Confirmation Run 1 Geometry.

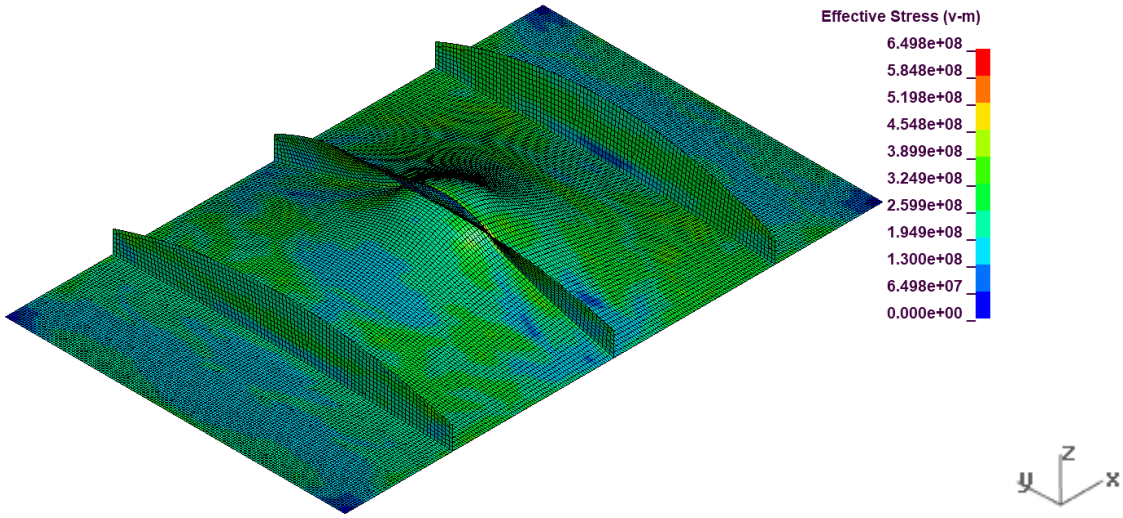

Figure 7.11: Exp4, Confirmation Run 1 - von Mises stress.

Two elements (0.00667 % of the elements in the model) failed the minimum jacobian quality check. The minimum jacobian in the model was 0.51. See Appendix E7 for more information related to the element quality checks of Confirmation Run 1.

7.5.2.2 Confirmation Run 2

The responses of the confirmation run can be seen in the Data Mean column of Table 7.5. Based on the 95 % confidence interval, the model accurately predicted the results of every response examined. Therefore, the model can be used to predict accurate results.

Table 7.5: Exp4, Experimental Design Confirmation Run 2 Results.

Two-sided Confidence = 95%

Response	Predicted Mean	Predicted Median	Std Dev	95% PI low	Data Mean	95% PI high
Weight (kg)	22.002	22.002	0.119541	21.7373	22.2218	22.2666
First Yield (MN)	0.456733	0.454642	0.0617408	0.325617	0.464	0.60515
Energy 0-50mm (MNmm)	26.1285	25.901	3.4478	19.1533	28.0942	35.026
Energy 50-100mm (MNmm)	53.1575	52.6709	5.88621	41.5152	59.1181	69.0108
Energy 100-150mm (MNmm)	82.8857	82.5973	6.91373	68.2855	82.846	99.9087

See Figure 7.12 and Figure 7.13, for more information regarding the geometry and von Mises stress data at the end of the analysis.

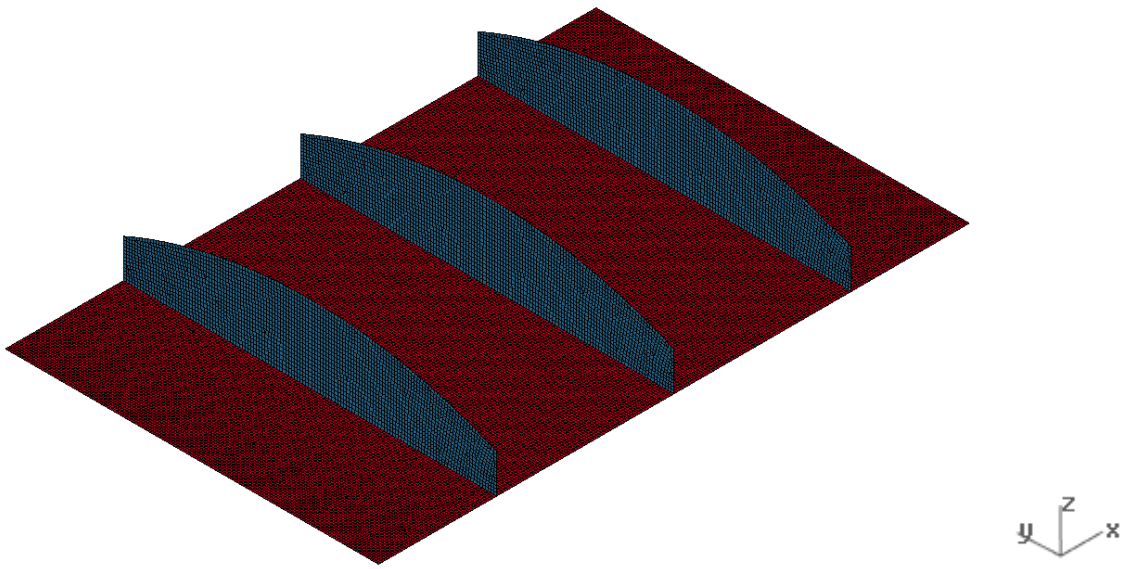

Figure 7.12: Exp4 Confirmation Run 2 Geometry.

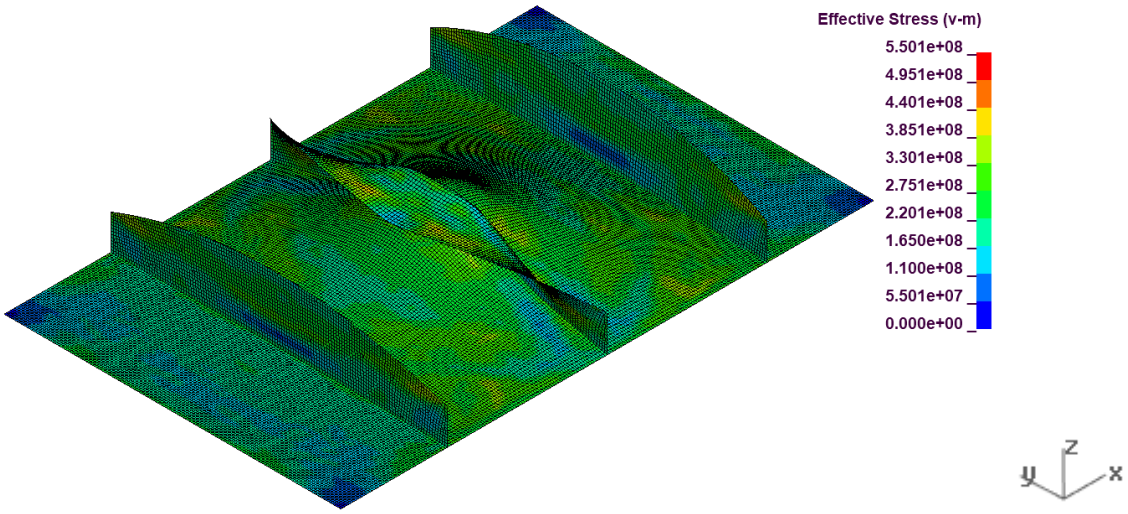

Figure 7.13: Exp4, Confirmation Run 2 - von Mises stress.

One element (0.00238 % of the elements in the model) failed the minimum jacobian quality check. The minimum jacobian in the model was 0.297. See Appendix E7 for more information related to the element quality checks of Confirmation Run 2.

7.5.2.3 Confirmation Run 3

The responses of the confirmation run can be seen in the Data Mean column of Table 7.6. Based on the 95 % confidence interval, the model accurately predicted the results of every response examined. Therefore, the model can be used to predict accurate results.

Table 7.6: Exp4, Experimental Design Confirmation Run 3 Results.

Two-sided Confidence = 95%

Response	Predicted Mean	Predicted Median	Std Dev	95% PI low	Data Mean	95% PI high
Weight (kg)	21.7434	21.7434	0.119541	21.4778	21.8628	22.009
First Yield (MN)	0.45207	0.449979	0.0614241	0.321171	0.492	0.600454
Energy 0-50mm (MNmm)	25.7534	25.5292	3.3983	18.8489	28.4357	34.5769
Energy 50-100mm (MNmm)	51.7161	51.2553	5.64947	40.476	55.0891	66.9924
Energy 100-150mm (MNmm)	81.3222	81.0392	6.78331	66.9316	73.9296	98.1204

See Figure 7.14 and Figure 7.15, for more information regarding the geometry and von Mises stress data at the end of the analysis.

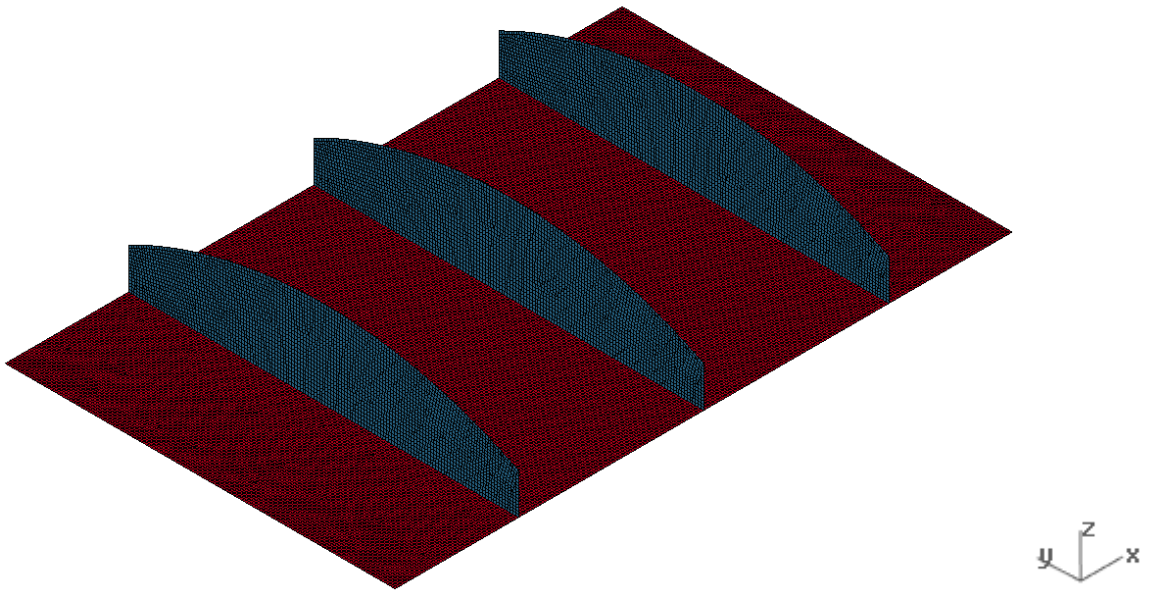

Figure 7.14: Exp4 Confirmation Run 3 Geometry.

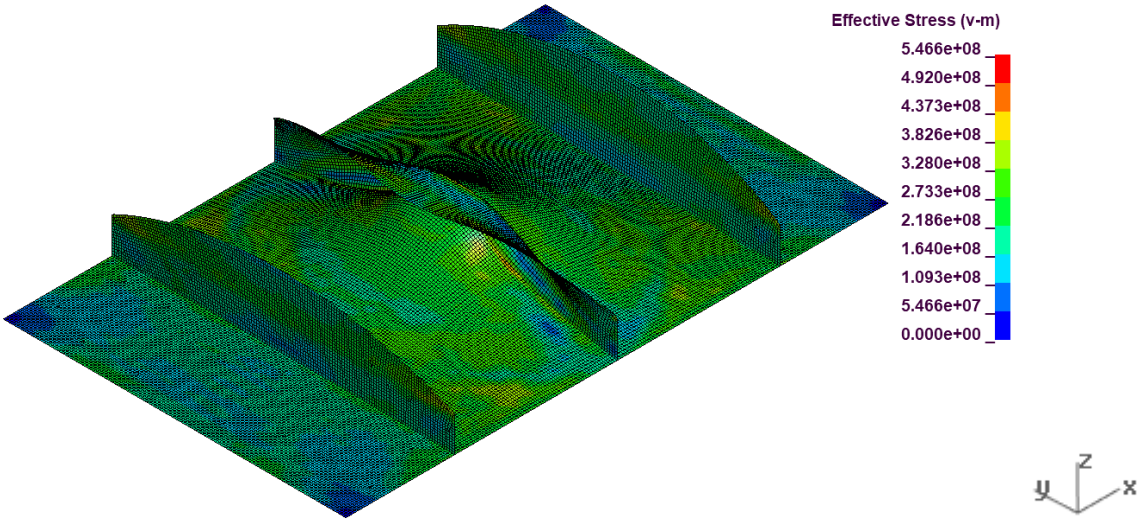

Figure 7.15: Exp4, Confirmation Run 3 - von Mises stress.

Two elements (0.00425 % of the elements in the model) failed the minimum jacobian quality check. The minimum jacobian in the model was 0.3. See Appendix E7 for more information related to the element quality checks of Confirmation Run 3.

7.5.2.4 Summary

As can be seen in Figure 7.16, Confirmation Run 1 demonstrated the lowest first yield point. As having a yield point at or higher than the built-T was a requirement for optimality, Confirmation Run 1 was not considered further. Confirmation Run 2, however, matched the first yield point of the built-T and also outperformed the built-T's overload capacity. Confirmation Run 3 also matched the first yield point and outperformed concerning overload capacity. However, the overload capacity was highest for Confirmation Run 2. Therefore, Confirmation Run 2 was chosen to be the optimal design for the concept grillage.

Disclaimer: The Optimal Design was determined to be more optimal than the control runs but was not intended to be considered the most optimal configuration possible. However, it has been demonstrated to be the most optimal design based on the factors studied within Exp4. A more optimal design likely exists outside of what was studied within this thesis.

As can be seen in Figure 7.17, the delayed buckling of the optimal design gives it its extra energy absorption. The optimal design buckled at ~120 mm, whereas the built-T buckled immediately after its yield point (~20 mm). Figure 7.18 shows the energy vs. displacement plot. As can be seen, the Optimal Design plot remained above the built-T plot throughout the entire displacement.

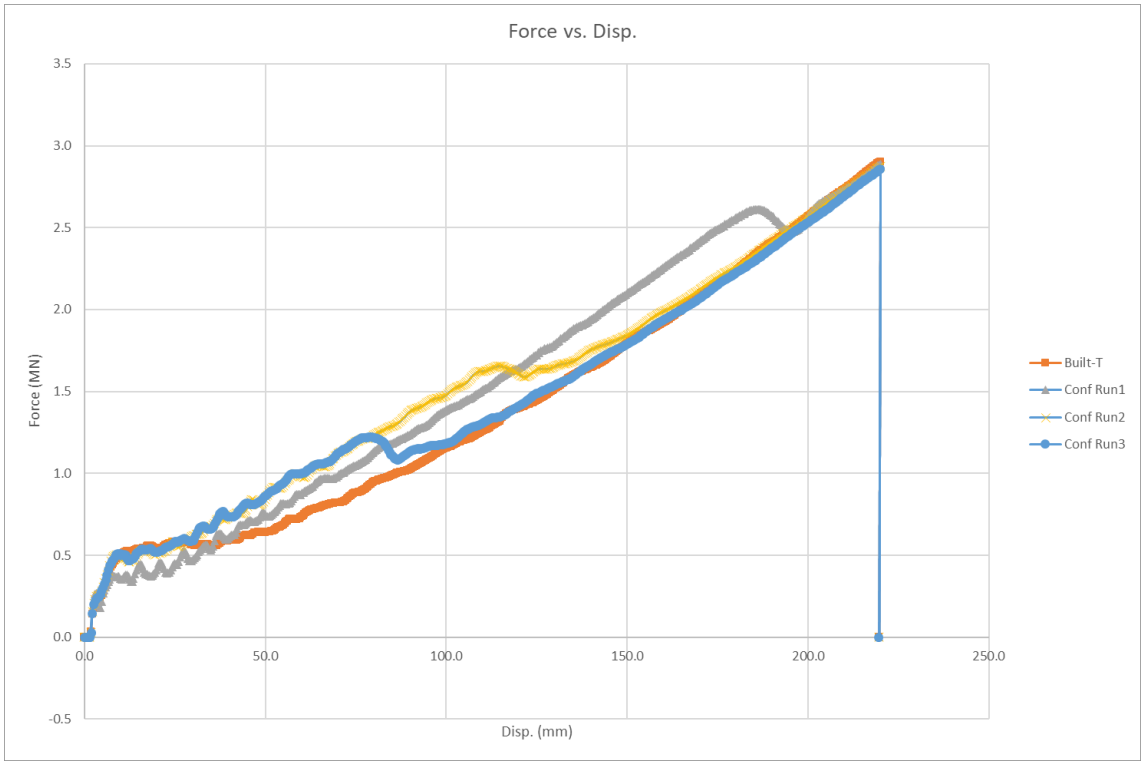

Figure 7.16: Exp4, Force vs. Disp. plot for the Confirmation Runs and control run.

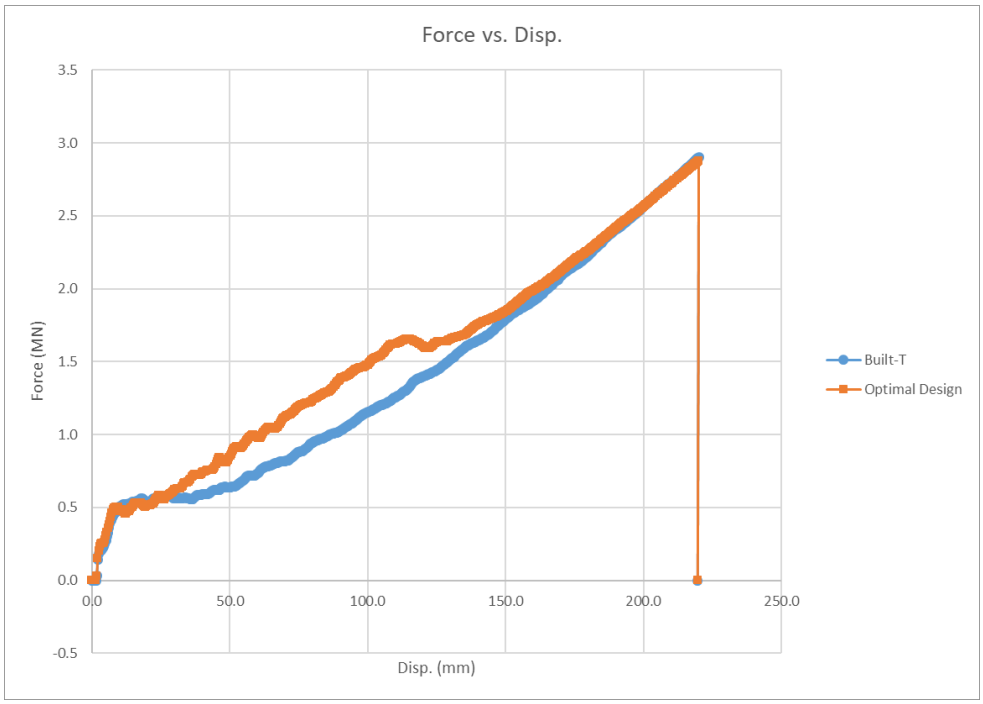

Figure 7.17: Exp4, Force vs. Disp. plot for the Optimal Design and control run.

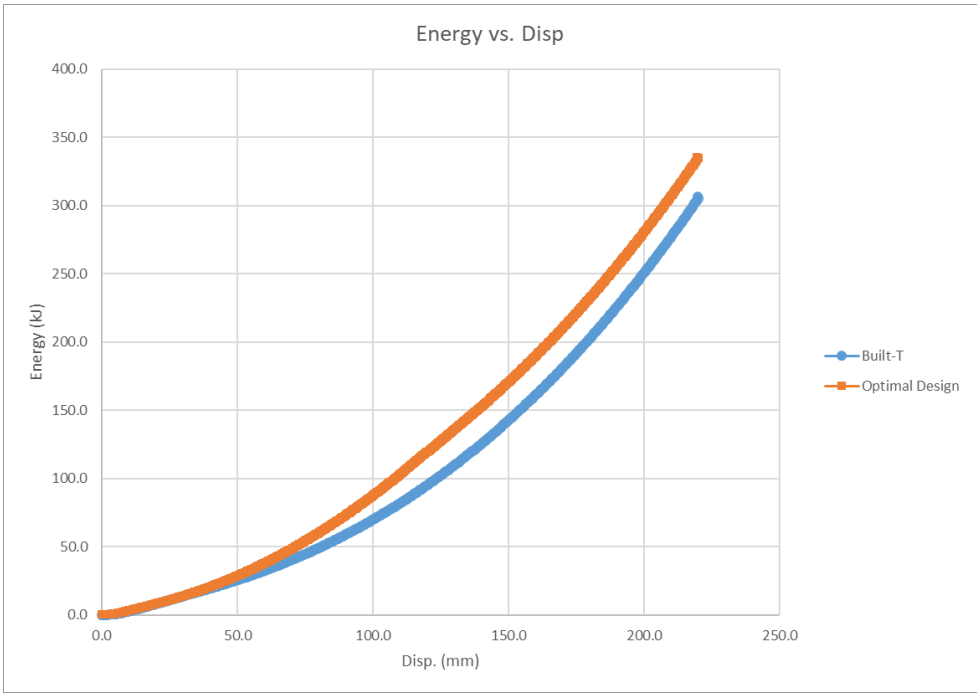

Figure 7.18: Exp4, Energy vs. Disp. plot for the Optimal Design and control run.

Regarding Figure 7.17 and Table 7.7, both curves were integrated over a range of 0-150 mm to quantify the increase in energy of the optimal design. The optimal design outperformed the built-T concerning energy absorption by 9.1 % over a range of 0-50 mm, 19.7 % over a range of 0-100 mm, and 16.1 % over a range of 0-150 mm.

Table 7.7: Energy percent difference between built-T and optimal design.

	Energy		
	MNmm 0-50mm	MNmm 0-100mm	MNmm 0-150mm
Built-T	25.5	70.0	142.7
Optimal	28.1	87.2	170.1
% Diff.	**9.1**	**19.7**	**16.1**

See Figure 7.19 for a visual comparison of the built-T control run and optimal design. After 110 mm of indentation (see Figure 7.17), it can be seen that the built-T suffered local buckling as well as tripping. The concept grillage did not suffer any form of buckling.

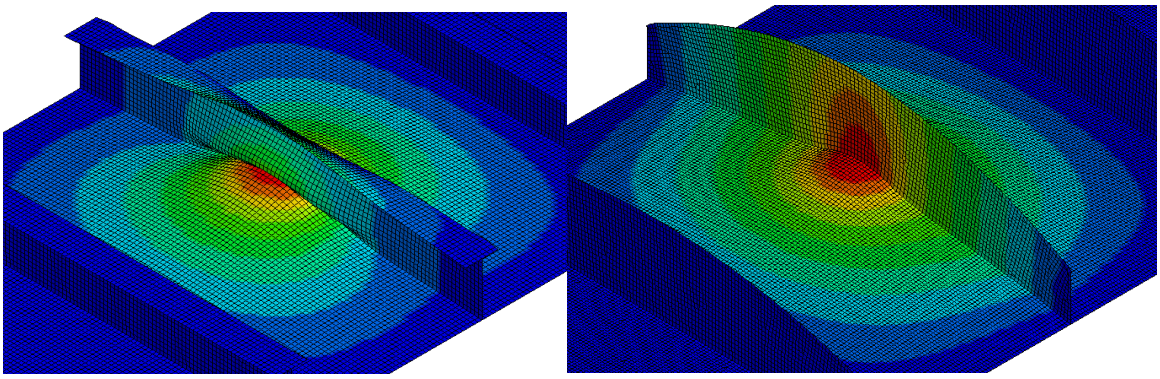

Figure 7.19: Built-T compared to optimal design, post-impact of 110 mm.

7.6 Relationship between Web Height and Stiffener End Conditions

One of the biggest differences between the setups of Exp3 and Exp4 was the size of the models. Exp3 had frames at the stiffener ends, whereas Exp4 had fixed-fixed stiffener ends. Frames would provide much softer stiffener end conditions compared to the fixed-fixed end conditions. The suggested optimal design for Exp3, which had relatively soft stiffener end conditions, had a much lower web height compared to the optimal design suggested for Exp4, which had perfectly stiff end conditions. Therefore, with softer end conditions, the optimal design approached a uniform height web, flat bar, stiffener. However, when stiffer end conditions were implemented, a stiffener with significant variable-height web could be beneficial. It should be noted that even though altering the stiffener span length was not included within any of the experimental factors, it is likely to also affect the relationship between web height and stiffener end conditions (see Section: 9.2 Future Work).

7.7 Discussion and Conclusions

Exp4 was based on both, the conclusions of Exp3 as well as the testable conditions within the LPA. The flangeless design of the stiffener allowed for an experimental design with three factors that defined the shape of the web. An optimal, RSM, experimental design was implemented with 26 runs included. A Local Model was used for FEA purposes, which can be inserted into the LPA. Moreover, Exp4 changed the way responses were collected. In Exp3, responses were collected in the form of forces associated with various levels of indentation (displacement). For Exp4, instead, the energy was calculated directly, based on the force vs. displacement curves. The first yield point was still represented by a force.

Since a minimum level of 0 was chosen for the mid-span stiffener height, H_{w2} (Factor B), a flat bar was a possible outcome for the optimal design. Therefore, the flat bar was omitted from the control runs.

As the model was to be set up in the LPA, Load Case 1 was not possible to be tested. Load Case 2 was chosen as, compared to Load Case 3, it had the highest likelihood of causing stiffener buckling (though, Exp5 later explored all three load cases).

Concerning the built-T control run, as usual, it experienced significant local buckling immediately following first yield leading to eventual tripping of the stiffener. Also, the built-T experienced end-buckling in the flange.

Once the data was collected from LS-DYNA, it was plotted in the form of force vs. displacement and energy vs. displacement curves. Three of the responses were acquired in the form of energies associated with the force vs. displacement curves – the energy between 0-50 mm, 50-100 mm, and 100-150 mm. The other two responses were first yield point and weight.

Three confirmation runs were prepared with slightly varied factor levels, each consistent with optimizing the grillage. Based on the 95 % confidence interval, all three confirmation runs accurately predicted the results of every response examined. Therefore, the model can be used to predict accurate results. Comparing the three confirmation runs, Confirmation Run 1 performed least optimally concerning first yield. Since having a yield point at or higher than the built-T was a requirement for optimality, Confirmation Run 1 was not considered further. Confirmation Run 2, however, matched the first yield point of the built-

T and also outperformed the built-T's overload capacity. Confirmation Run 3 also matched the first yield point and outperformed concerning overload capacity. However, the overload capacity was highest for Confirmation Run 2. Therefore, Confirmation Run 2 was chosen to be the optimal design for the concept grillage.

Based on Exp4 and previous analyses, the delayed buckling of the optimal design contributed to its extra energy absorption. The optimal design buckled at ~120 mm, whereas the built-T buckled immediately after its yield point (~20 mm). Also, the Confirmation Run 2 (Optimal Design) energy vs. displacement plot remained above the built-T plot throughout the entire displacement. The optimal design outperformed the built-T concerning energy absorption by 9.1 % over a range of 0-50 mm, 19.7 % over a range of 0-100 mm, and 16.1 % over a range of 0-150 mm.

The suggested optimal design for Exp3, which had relatively soft stiffener end conditions, had a much lower web height compared to the optimal design suggested for Exp4, which had perfectly stiff end conditions. Therefore, when the end conditions were softer, the optimal design approached a uniform height web, flat bar, stiffener. However, with stiffer end conditions, a stiffener with a significant variable-height web could be beneficial.

Chapter 8 Exp5 –Concept Grillage vs. IROQUOIS Grillage

Once an optimal design was achieved, it was of interest to compare the design to the IROQUOIS grillages under testable, comparable, conditions. This experimental simulation (i.e. Exp5) was included as a more appreciable way of understanding the concept grillage's behaviour in a more realistic collision scenario. Instead of using a prescribed displacement, an impact was simulated.

A rigorous experimental design was avoided within this experiment in favour of a simpler, comprehensible, analysis. The goal was not to quantify statistical significance between the factors but to determine if the optimal grillage performed optimally compared to the IROQUOIS side-shell grillages, under various loading conditions. Throughout the investigation, all experimental parameters were kept constant except for model size, stiffener type, and load case. Twelve unique runs were created based on the three factors tested.

Two models were tested: The Local Model and the Global Model. The Local Model consisted of a grillage configuration including three stiffeners connected of a side-shell, similar to what was used in Exp4. The Global Model consisted of a grillage configuration including, effectively, nine Local Models connected, separated by frames. The important difference to note between the Local and Global Models was that the Local Model had infinitely stiff stiffener ends, whereas the Global Model consisted of frames at the stiffener ends, which represented softer stiffener end conditions.

Two stiffener types were tested – the IROQUOIS formed tee stiffeners and the concept grillage stiffeners. The IROQUOIS stiffeners were formed, meaning the cross-sectional shape included curvature where the web and flange connect (see Figure 8.1). Information regarding the three load cases can be seen in Section: 6.1 Load Cases. The results were obtained in the form of contact force vs. displacement plots, as well as internal energy vs. displacement plots.

8.1 Effective Flange

Due to complications in modelling the formed cross-section of the IROQUOIS stiffeners, an effective flange thickness was used to approximate the shape of the flange cross-section. Modelling curvature within a cross-section using shell elements is not possible. Solid elements can be used to approximate the shape, but many elements would be required which would drive the computational time to unrealistic levels. An alternate approach would be to calculate an "effective" flange thickness which averages the varied flange thickness, shown in Figure 8.1. The resultant shape of the flange cross-section would be a rectangle, which can easily be represented by shell elements. The new stiffener cross-section would have a negligible difference in the cross-sectional area and the second moment of area compared to the original shape, making it comparable to the IROQUOIS stiffeners.

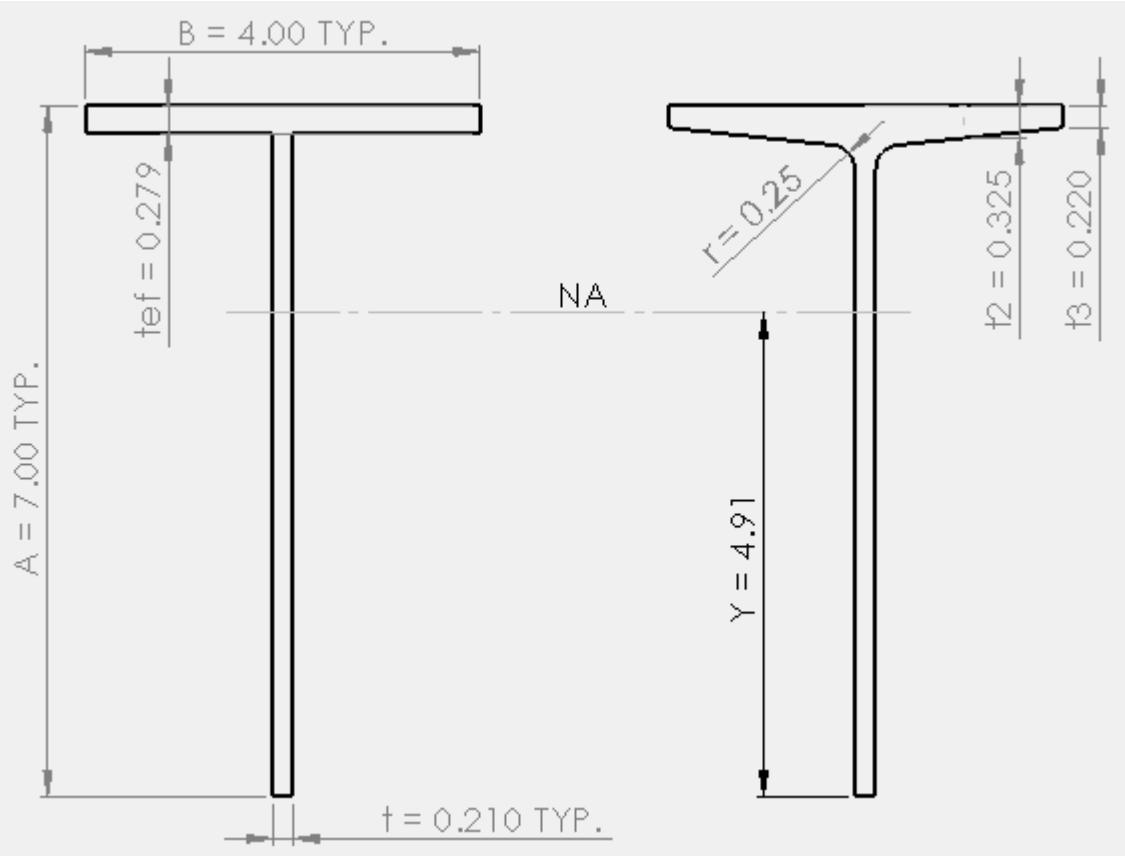

Figure 8.1: Cross-section of the IROQUOIS stiffener with an equivalenced effective flange (left) and a formed flange (right) – units in inches.

Two effective thicknesses were calculated based on a set of equations seen in Equations [9] and [10] to develop an equivalenced effective flange thickness, based on the IROQUOIS formed stiffener. The first effective flange thickness, t_{ef1}, was associated with equating the cross-sectional area. The second effective flange thickness, t_{ef2}, was associated with equating the second moment of area. A mean average effective thickness was then found, t_{ef}, to use within the FEMs.

Calculating "t_{ef1}" involved several known values, the: cross-sectional area of the stiffener, web thickness, web height, and flange width. The general form of the equation for

calculating the area of a rectangle was implemented in the form of Equation [9]. Solving Equation [9] for "t_{ef1}" yielded 0.277 inches.

$$AREA = (A - t_{ef1}) * t + B * t_{ef1} \quad [9]$$

Where: AREA = Cross-sectional stiffener area (2.52 inches^2)

A = Stiffener depth (inch)

t_{ef1} = Effective flange thickness associated with equating the cross-sectional area (0.277 inches)

t = Stiffener web thickness (inch)

B = Stiffener flange breadth (inch)

Calculating "t_{ef2}" involved several known values, the: cross-sectional second moment of area of the stiffener, cross-sectional area of the stiffener, web thickness, web height, and flange width. The general form of the equation for calculating the second moment of area of a rectangular cross-section, including the parallel axis theorem, was implemented in the form of Equation [10]. Solving Equation [10] for "t_{ef2}" yielded 0.281 inches.

$$I = \left[\frac{t(A-t_{ef2})^3}{12} + t(A - t_{ef2})\left(\frac{A-t_{ef2}}{2} - Y\right)^2\right] + \left[\frac{Bt_{ef2}{}^3}{12} + (Bt_{ef2})\left(A - \frac{t_{ef2}}{2} - Y\right)^2\right] \quad [10]$$

Where: I = Cross-sectional stiffener second moment of area (12.98 inches^4)

t_{ef2} = Effective flange thickness associated with equating the cross-sectional second moment of area (0.281 inches)

Y = Distance from datum to the neutral axis, with datum at the bottom end of the stiffener (4.911 inches)

Using Equation [11], the mean of both effective flange thicknesses was found to be 0.279 inches. The mean value was used for the subsequent FEMs within this Chapter.

$$t_{ef} = \frac{t_{ef1}+t_{ef2}}{2} \quad [11]$$

Where: t_{ef} = Mean Effective flange thickness used within the IROQUOIS FEMs.

8.2 Model Parts

Refer to Section: 3.7 Rigid Indenter Design, for information regarding the Rigid Intender model. Refer to Section: 7.2 Model Parts, for information regarding the Local Model.

Along with the Local Model, a version of the Global Model used in Exp3 was implemented (see Figure 8.2). However, since only one load case was being tested per run, the model was made the be slightly smaller, but still considerably larger than the Local Model. The grillage model used in Exp5 contained the same geometric components as the model from Exp3.

For simplicity, the side-shell was given a parametrized thickness of 7.9375 mm. The remaining constant geometric dimensions of the grillage were:

- Stiffener spacing = 609.6 mm.
- Stiffener length = 1283.8 mm.
- Side-shell width, x-direction = 5690 mm.
- Side-shell length, y-direction = 3851 mm.

- Frame length = 5690 mm.

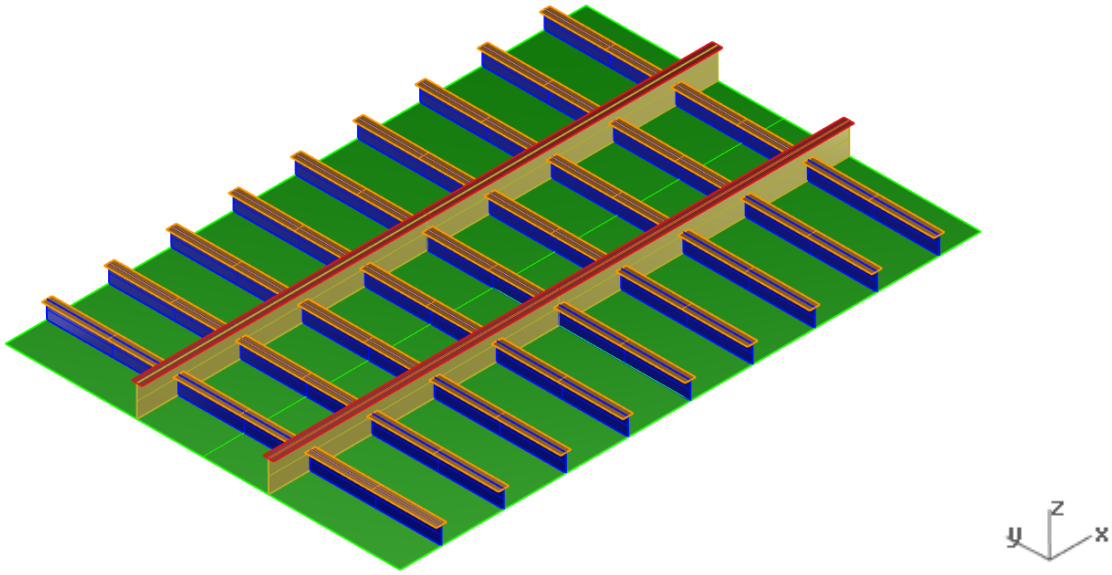

Figure 8.2: Exp5 Global Model Grillage, with IROQUOIS-equivalent stiffeners.

8.3 LS-PrePost and LS-DYNA

The FEMs within this Chapter were created based on models within Exp3 and Exp4. For the Local Model, refer to Section: 7.3 LS-PrePost and LS-DYNA, for information regarding the BCs, model controls, and the MCA. For the Global Model, refer to Section: 6.3 LS-PrePost and LS-DYNA, for information regarding the BCs, model controls, and the MCA. A minimum element size was used for every part in the models, equal to their associated thickness. The only exception where Exp5 diverged from previous experimental conditions was concerning loading conditions.

The grillages were modelled using material properties as seen in 6.3.6 Material Properties.

8.3.1 Loading Conditions

Exp5 was completed using a unique load condition, compared to previous experiments. Exp5 simulated an impact scenario. Instead of a prescribed displacement, the indenter was given an initial impact velocity of 5.295 m/s, consistent with a pendulum arm angle of 50º (shown in Table 8.1). To achieve an initial velocity of the indenter, the VZ field within the INITIAL_VELOCITY_GENERATION card was invoked within LS-DYNA. Also, the mass of the indenter was altered to reflect a total leftmost pendulum arm mass of 4500 kg, as opposed to the usual 3141 kg.

Since the LPA consisted of two pendulum arms, an effective velocity was calculated to determine a velocity that would equate the energy of a fixed-fixed panel with one swinging indenter (simulation) to the full-scale pendulum with a swinging indenter and panel. See Section: 8.4 The Effective Velocity of Pendulum.

8.3.2 LS-DYNA Cards

Several cards were invoked within LS-DYNA to achieve the desired effects intended for the simulation:

CONTACT_AUTOMATIC_SURFACE_TO_SURFACE

Contact was defined between the indenter and side-shell. To collect contact forces both SPR and MPR were set to 1.

CONTROL_TERMINATION

The simulation was set to terminate using ENDTIM = 0.1.

DATABASE_ASCII_option

Nine ASCII options were turned on for high fidelity result extraction: BNDOUT, ELOUT, GLSTAT, MATSUM, NODOUT, RBDOUT, RCFORC, SLEOUT, SPCFORC. Each was given a DT of 0.0001.

DATABASE_BINARY_D3PLOT

For visualizing the simulation, DT = 0.01 was used.

DATABASE_BINARY_INTFOR

The internal forces were collected using DT = 0.01.

DATABASE_HISTORY_NODE_ID

The appropriate node was selected for ASCII NODOUT.

INITIAL_VELOCITY_GENERATION

Instead of rigid body motion, an initial velocity was applied by invoking VZ = 5.295. See Table 8.1 for reference.

MAT_PLASTIC_KINEMATIC

A, bi-linear, plastic kinematic material model was built using the following material properties: RO = 7850, E = 2.07e11, PR = 0.3, SIGY = 3.5e8, and ETAN = 1e9.

MAT_RIGID

The properties used were: RO = 3.928e6, E = 2.07e11, and PR = 0.3. Also, CMO, CON1 and CON2 were invoked to properly restrict the rigid body from x and y translations, as well as x, y, and z rotations using 1, 4, and 7, respectively.

SECTION_SHELL

The shear factor was changed from 1 to 5/6 using SHRF = 0.8333. Also, five through-thickness integration points were used by invoking NIP = 5.

8.4 The Effective Velocity of Pendulum

The LPA consists of two pendulums (one carrying the indenter and the other carrying the grillage). Though both pendulums swing simultaneously on the LPA, all simulated models were created with an indenter impacting a fixed-fixed panel. Therefore, to equate the simulation model to the LPA, a fixed-fixed panel solution was demonstrated and compared to a FEM of the actual LPA. Refer to Figure 3.5 to better visualize the discussions present within this Section.

8.4.1 Fixed-Fixed Panel Solution

The fixed-fixed panel solution involves a stationary grillage being impacted by the rigid indenter. The stationary grillage has an arm angle of 0°. Whereas the rigid indenter carriage has an arm angle adjusted appropriately to deliver the same impact energy onto the grillage as if both sides were moving.

The impact velocity can be calculated according to Equations [12] and [13] (Gagnon, et al. 2015), based on the pendulum arm angle. Then, according to Equations [14] to [18], the effective velocity (equivalent impact speed) can be calculated based on the true pendulum speed. Within Table 8.1, the corresponding equivalent impact speed and true pendulum speed can be seen for a variety of arm angles.

Table 8.1: Initial impact velocity as well as equivalent impact velocity.

Gravitational Constant	9.81	m/s^2
Pendulum Arm Length	2	m
Pendulum Mass	3141	kg

Pendulum Angle [DEG]	Pendulum Speed [m/s]	Kinetic Energy (1 carriage) [Nm]	Total Kinetic Energy (2 Carriages) [Nm]	Equivalent Impact Speed (1 moving Carriage) [m/s]
5	0.386	235	469	0.546
10	0.772	936	1872	1.092
15	1.156	2100	4200	1.635
20	1.538	3717	7433	2.176
25	1.917	5774	11548	2.712
30	2.293	8256	16513	3.243
35	2.664	11145	22290	3.767
40	3.030	14418	28836	4.285
45	3.390	18050	36100	4.794
50	3.744	22014	44027	5.295
55	4.091	26279	52558	5.785
60	4.429	30813	61626	6.264

$$v_{1,2} = \sqrt{2gL(1 - \cos\theta_{1,2})} \quad [12]$$

$$E_{1,2} = \frac{1}{2} m_{1,2} v^2{}_{1,2} \quad [13]$$

Where: v_1 = Velocity of the indenter-side pendulum arm

v_2 = Velocity of the grillage-side pendulum arm

g = Acceleration due to gravity (constant)

L = Length of either pendulum arm (constant)

θ_1 = Arm angle of the indenter-side pendulum arm

θ_2 = Arm angle of the grillage-side pendulum arm

E_1 = Kinematic energy of the indenter-side pendulum arm

E_2 = Kinematic energy of the grillage-side pendulum arm

m_1 = Mass of the indenter-side pendulum arm

m_2 = Mass of the grillage-side pendulum arm

$$E_{fs} = \frac{1}{2}m_1 v_1^2 + \frac{1}{2}m_2 v_2^2 \quad [14]$$

$$m_1 = m_2 \quad [15]$$

$$v_1 = v_2 \quad [16]$$

$$E_{fs} = E_s \quad [17]$$

$$v_{eff}^2 = \frac{2E_s}{m_1} \quad [18]$$

Where: E_{fs} = Kinematic energy of the actual model

E_s = Kinematic energy of the simulation model

v_{eff} = Effective velocity of the grillage-side pendulum arm for a fixed-fixed panel simulation

8.4.2 Pendulum Mimic Solution

The Pendulum mimic solutions mimic the LPA by allowing both the rigid indenter carriage and grillage carriage to swing within the FEM.

The solution involving changing the simulation model setup would simulate the actual experiment as is. However, several changes would have to be made to the FEM itself:

- Mass must be added to the grillage-side to simulate the whole carriage assembly.
- BCs on the grillage must be changed to allow translations and rotations consistent with the pendulum arm degrees of freedom.
- The grillage-side must be given an initial velocity (see Table 8.1), equal to the indenter side.

8.4.3 Solution Comparisons

Both solutions were compared in FE space as a proof of concept to ensure that the fixed-fixed panel approach matched the pendulum mimic approach. Both models included identical controls and geometry. The models differed only in their approach to simulating the impact. An arm angle of 50° was used for each solution.

Concerning Table 8.1, for the fixed-fixed panel solution, the indenter-side velocity was set to 5.295 m/s and the grillage velocity was set to 0 m/s (0° arm angle). For the pendulum mimic solution, both the input indenter velocity and panel velocity were set to 3.744 m/s.

As can be seen in Figure 8.3, both approaches yielded negligible differences in results. Therefore, an effective equivalent velocity was calculated using Equations [14] through [18], and the fixed-fixed panel approach was used for Exp5.

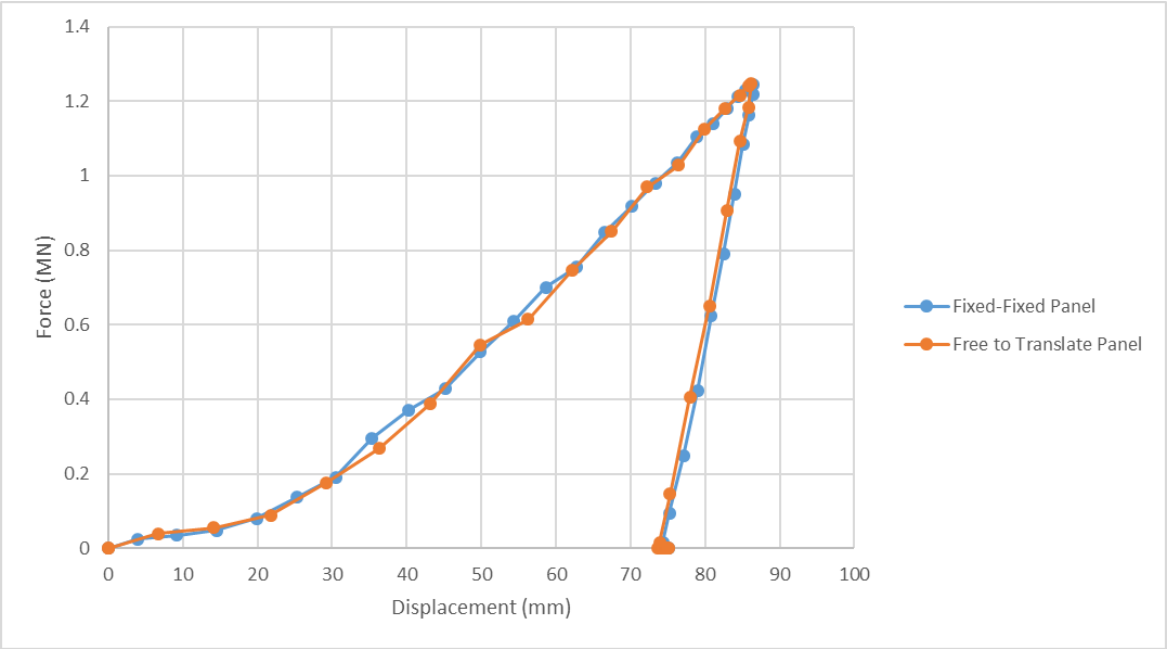

Figure 8.3: Comparison of fixed-fixed model vs. free to translate model.

It was interesting to note that the velocities required to equal the fixed-fixed panel simulation to the actual model differ by a factor of $\sqrt{2}$, based on the squared velocity terms in Equation [14]. Therefore, it can be said that to equate the energy between the fixed-fixed panel model and an LPA model, the velocity of the former pendulum arm should be $\sqrt{2}$ times the velocity of latter pendulum arms. See Equation [19] for more clarity.

$$v_{fs}\sqrt{2} = v_s \qquad [19]$$

8.5 Results

Twelve runs were analyzed through a combination of the three studied factors:

1. IROQUOIS, Local Model, Load Case 1
2. IROQUOIS, Local Model, Load Case 2
3. IROQUOIS, Local Model, Load Case 3

4. IROQUOIS, Global Model, Load Case 1
5. IROQUOIS, Global Model, Load Case 2
6. IROQUOIS, Global Model, Load Case 3
7. Concept Grillage, Local Model, Load Case 1
8. Concept Grillage, Local Model, Load Case 2
9. Concept Grillage, Local Model, Load Case 3
10. Concept Grillage, Global Model, Load Case 1
11. Concept Grillage, Global Model, Load Case 2
12. Concept Grillage, Global Model, Load Case 3

Due to the large quantity of FEM runs, FEM visuals have only been shown for two runs: Run1 and Run11. Run1 and Run11 were chosen since, between the two models, they demonstrated both stiffener types, both model sizes, and two of the three load cases. The Run1 visuals related to the undeformed geometry and the maximum von Mises stress data can be seen in Figure 8.4 and Figure 8.5, respectively.

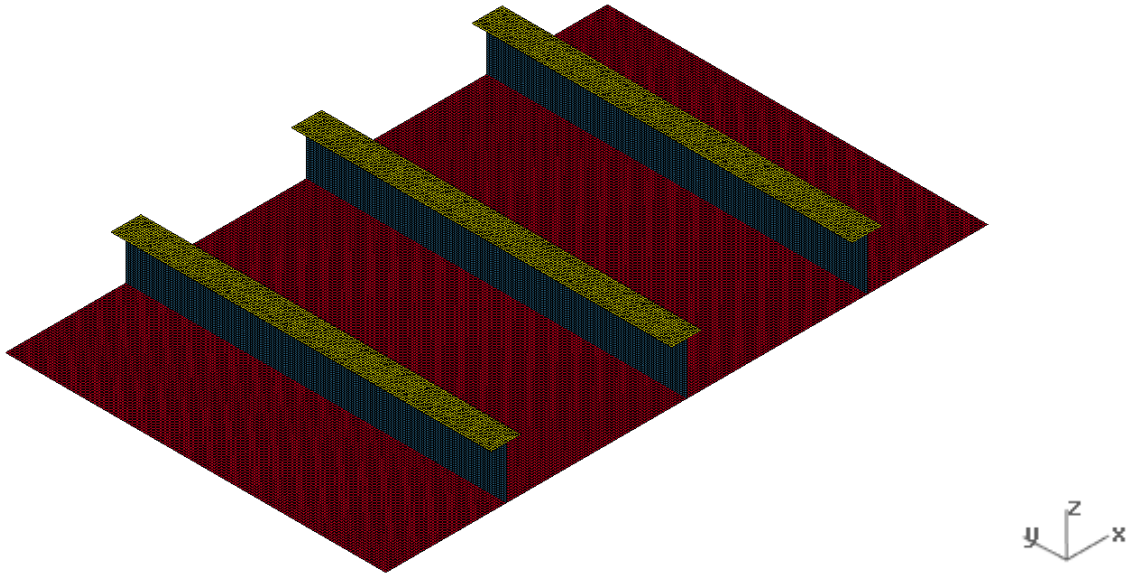

Figure 8.4: Exp5, Run1 Geometry.

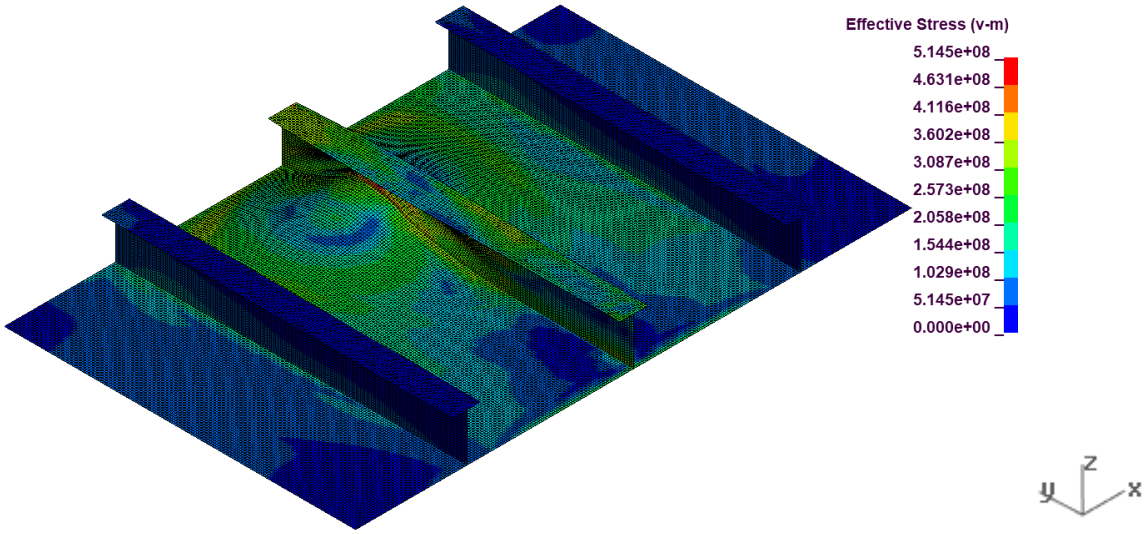

Figure 8.5: Exp5, Run1 von Mise Stress.

The Run11 visuals related to the undeformed geometry and the maximum von Mises stress data can be seen in Figure 8.6 and Figure 8.7, respectively.

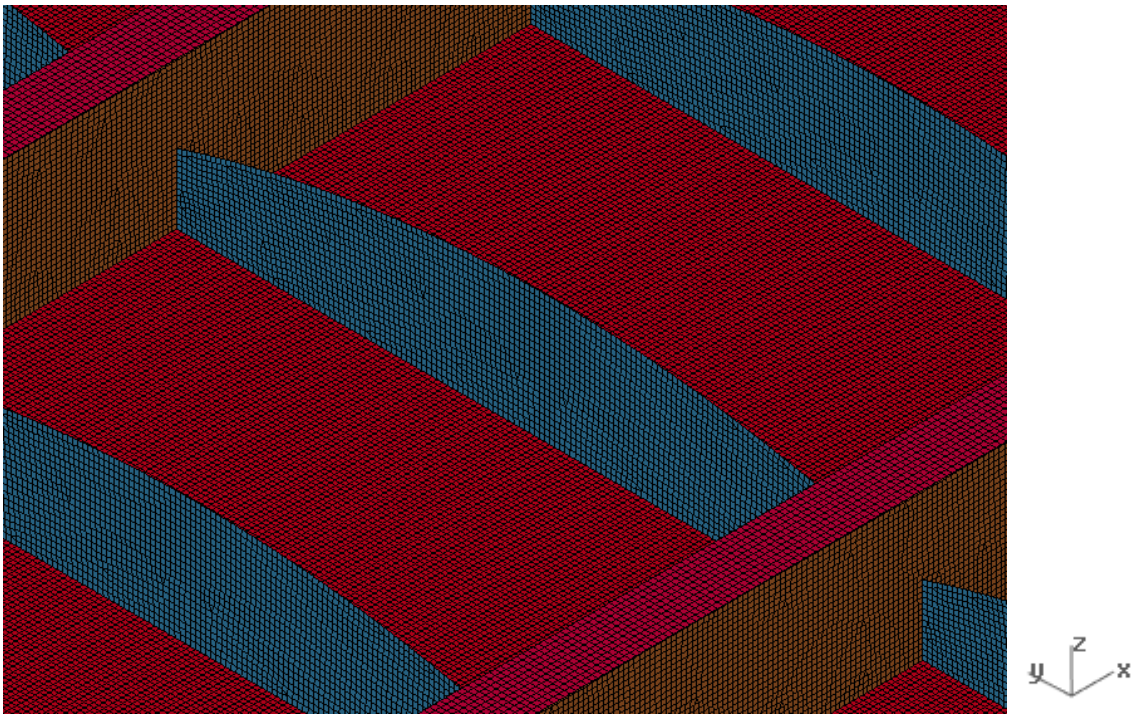

Figure 8.6: Exp5, Run11 Geometry.

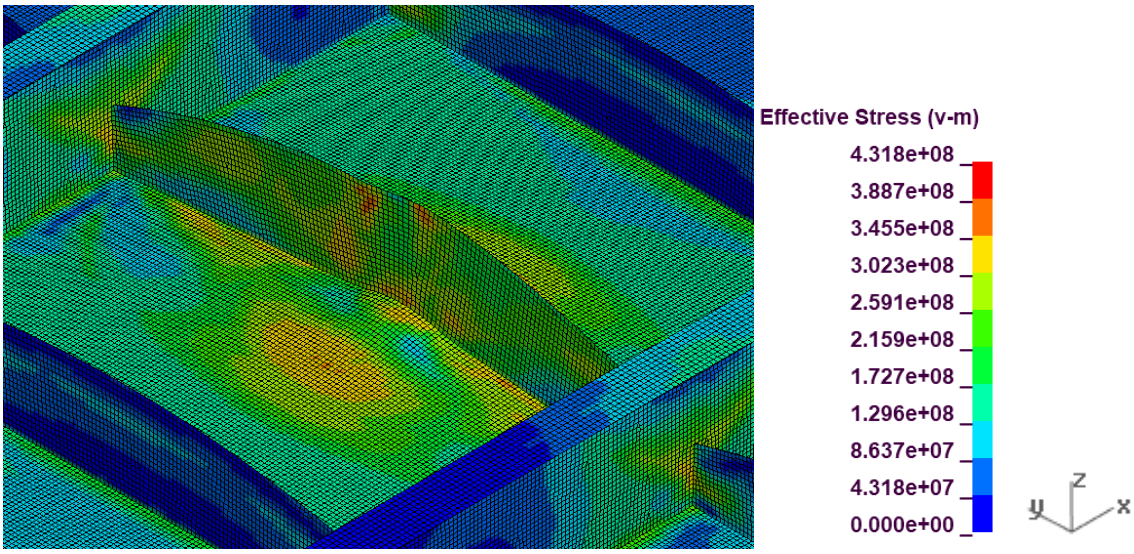

Figure 8.7: Exp5, Run11 von Mise Stress.

See Appendix F1 for visuals for all run geometry and von Mises stress results. The IROQUOIS runs were compared with their corresponding concept grillage runs. In other words, six comparisons were considered concerning the aforementioned twelve runs:

1. Runs 1 and 7
2. Runs 2 and 8
3. Runs 3 and 9
4. Runs 4 and 10
5. Runs 5 and 11
6. Runs 6 and 12

It should be noted that the Concept Grillage tested throughout Exp5 was not a replica of the Concept Grillage determined from Exp4. Since the IROQUOIS stiffeners were significantly lighter than the usual control runs, the experimental design from Exp4 was reassessed to develop an optimal design for the lighter weight. By lowering the weight to match the weight of the IROQUOIS stiffeners, the optimal design parameters changed. See Table 8.2 for the scantlings used for the Optimal Design within this Chapter.

Table 8.2: Exp5, Experimental Design Solution.

A Hw mm	B Hw2 mm	C Tw mm
120.00	100.00	8.80

Once the data was collected from LS-DYNA, it was plotted in the form of force vs. displacement and energy vs. displacement plots. The results of the comparison of the

IROQUOIS and concept stiffeners, for the Local Models loaded according to load case 1, can be seen in Figure 8.8 and Figure 8.9. It can be seen that the concept grillage performed significantly better than the IROQUOIS grillage. The optimized concept design had significantly higher internal energy throughout the entire displacement of the indenter.

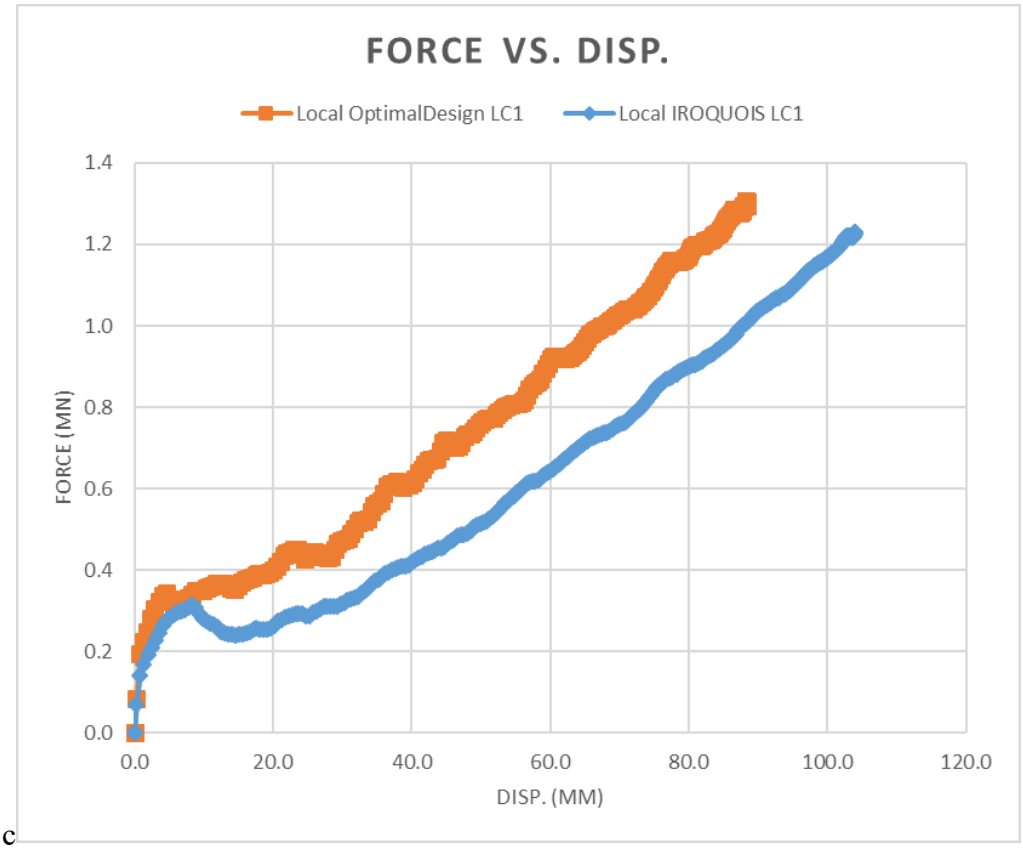

c

Figure 8.8: Exp5, Optimal vs. IROQUOIS, Force vs. Disp. plot for Runs 1 and 7.

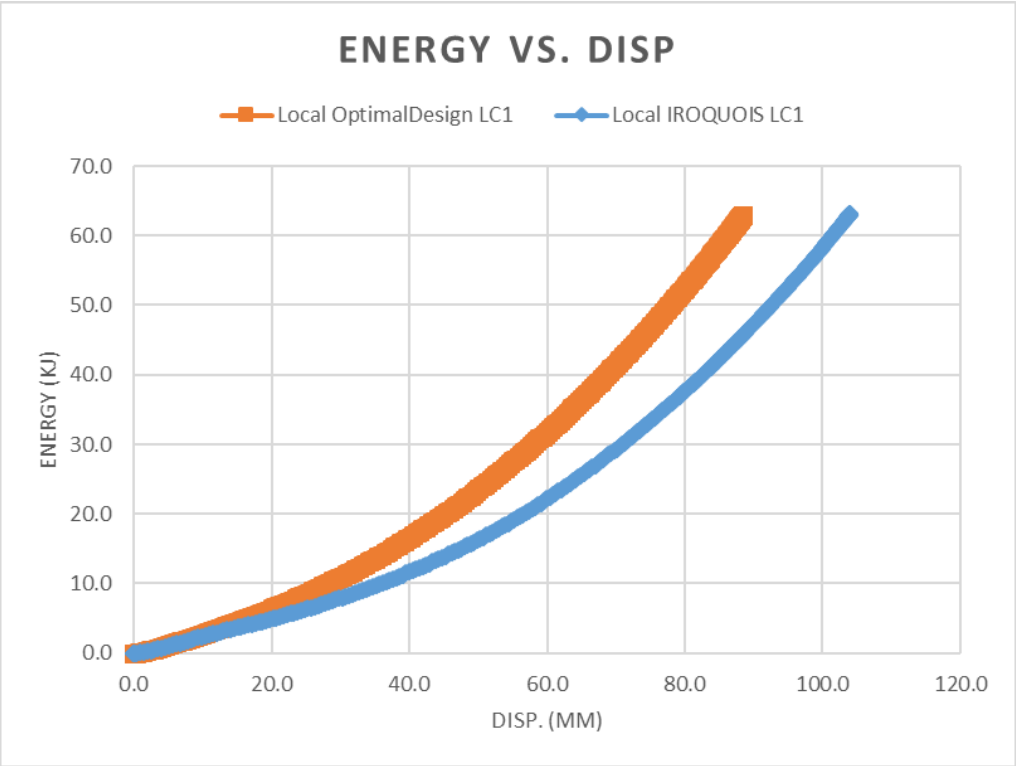

Figure 8.9: Exp5, Optimal vs. IROQUOIS, Energy vs. Disp. plot for Runs 1 and 7.

The results of the comparison of the IROQUOIS and concept stiffeners, for the Local Models loaded according to load case 2, can be seen in Figure 8.10 and Figure 8.11. It can be seen that the concept grillage performed significantly better than the IROQUOIS grillage. The optimized concept design had significantly higher internal energy throughout the entire displacement of the indenter.

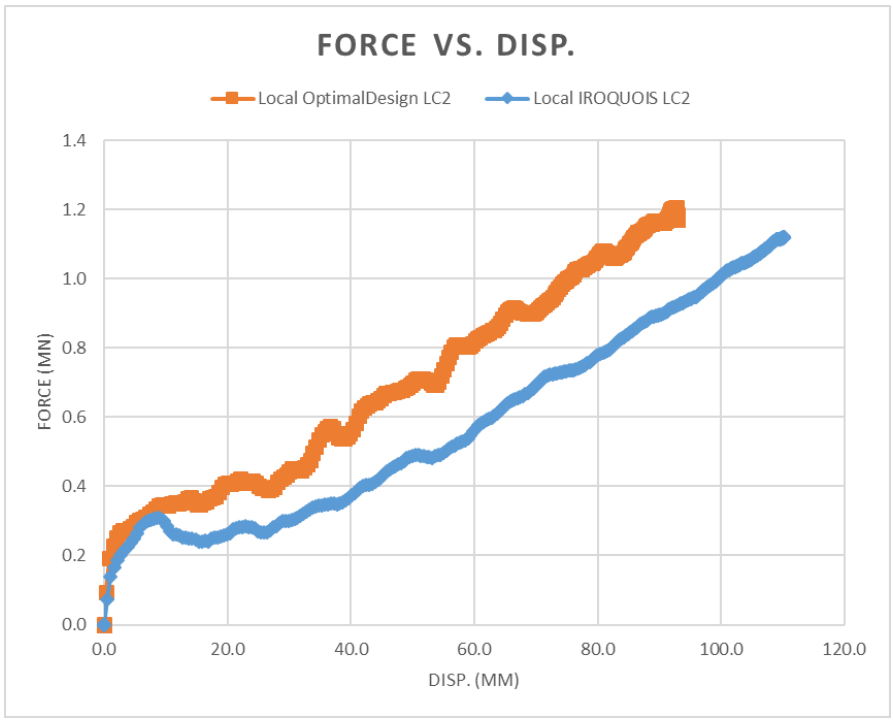

Figure 8.10: Exp5, Optimal vs. IROQUOIS, Force vs. Disp. plot for Runs 2 and 8.

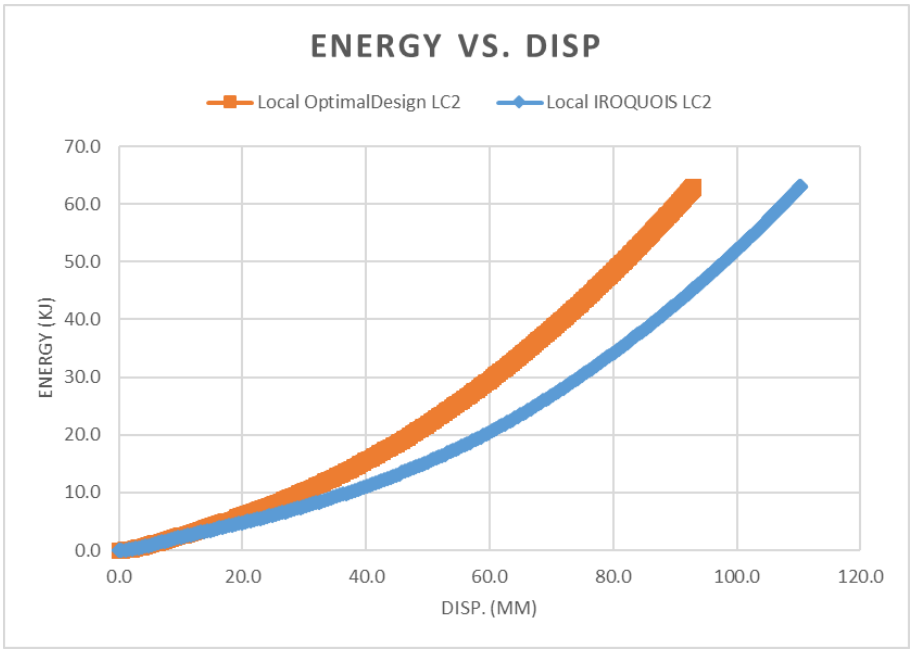

Figure 8.11: Exp5, Optimal vs. IROQUOIS, Energy vs. Disp. plot for Runs 2 and 8.

The results of the comparison of the IROQUOIS and concept stiffeners, for the Local Models loaded according to load case 3, can be seen in Figure 8.12 and Figure 8.13. It can be seen that the concept grillage performed similarly to the IROQUOIS grillage throughout the entire displacement of the indenter.

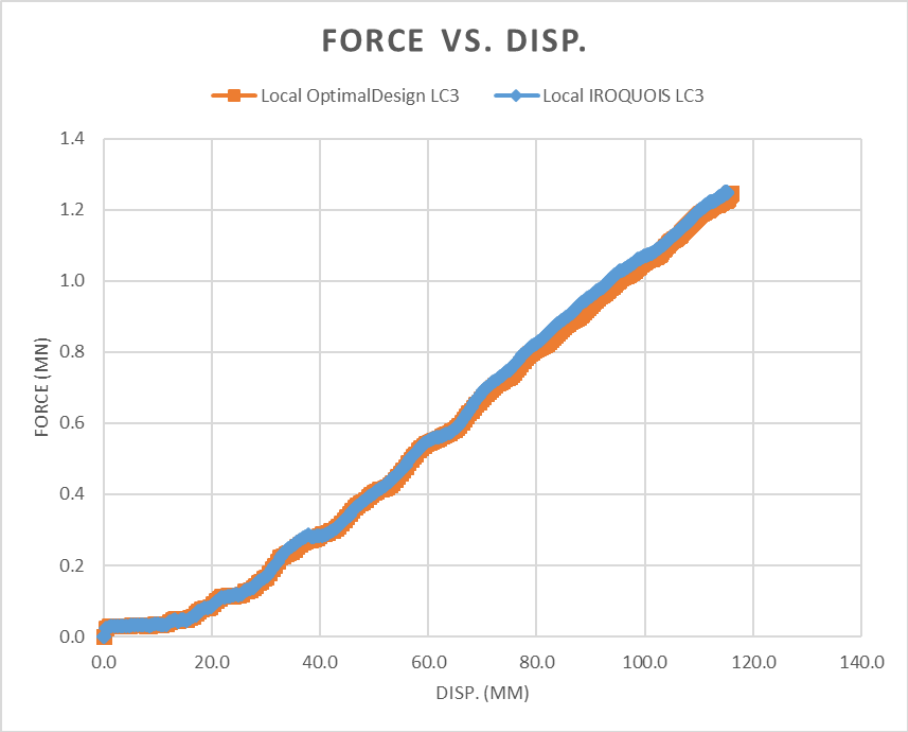

Figure 8.12: Exp5, Optimal vs. IROQUOIS, Force vs. Disp. plot for Runs 3 and 9.

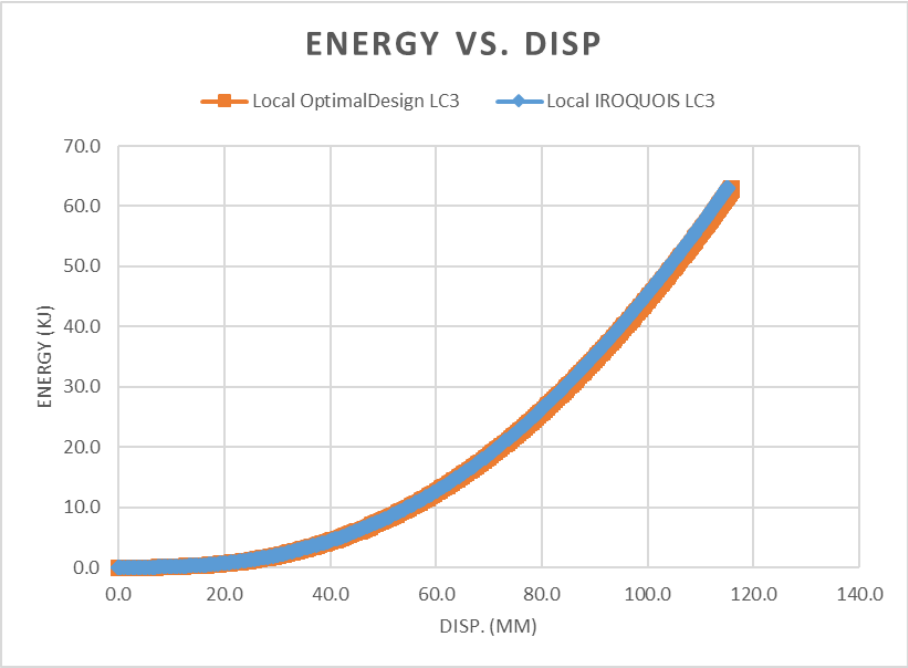

Figure 8.13: Exp5, Optimal vs. IROQUOIS, Energy vs. Disp. plot for Runs 3 and 9.

The results of the comparison of the IROQUOIS and concept stiffeners, for the Global Models loaded according to load case 1, can be seen in Figure 8.14 and Figure 8.15. It can be seen that the concept grillage performed significantly better than the IROQUOIS grillage. The optimized concept design had a significantly higher internal energy up to and including a displacement of ~95 mm, as can be seen in the force vs. displacement plot. However, from observing the energy vs. displacement plot, the total internal energy remained higher for the concept grillage throughout the entire displacement of the indenter.

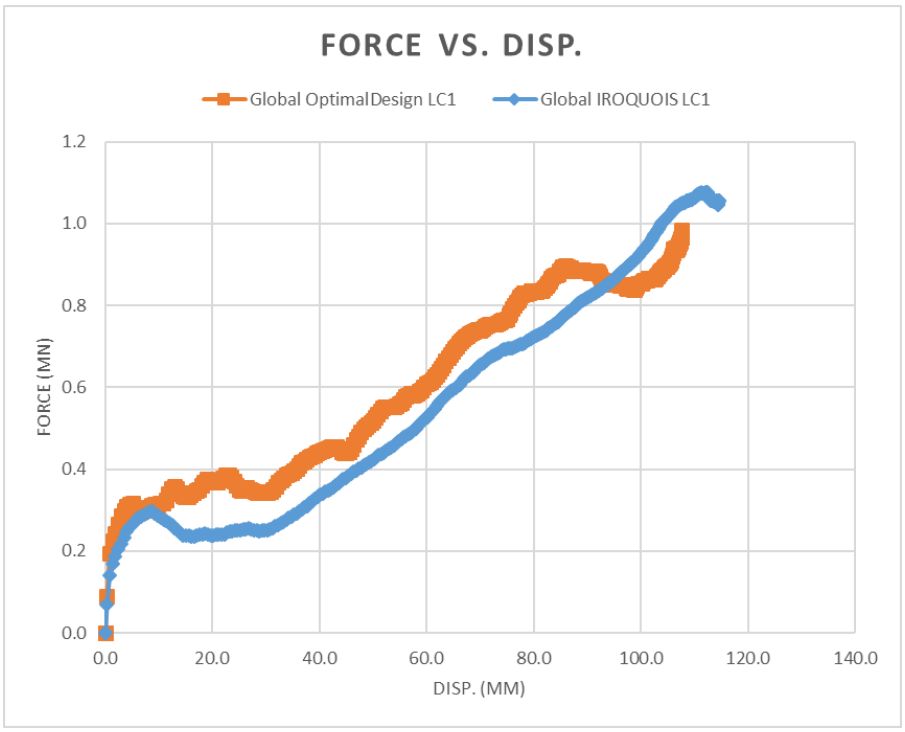

Figure 8.14: Exp5, Optimal vs. IROQUOIS, Force vs. Disp. plot for Runs 4 and 10.

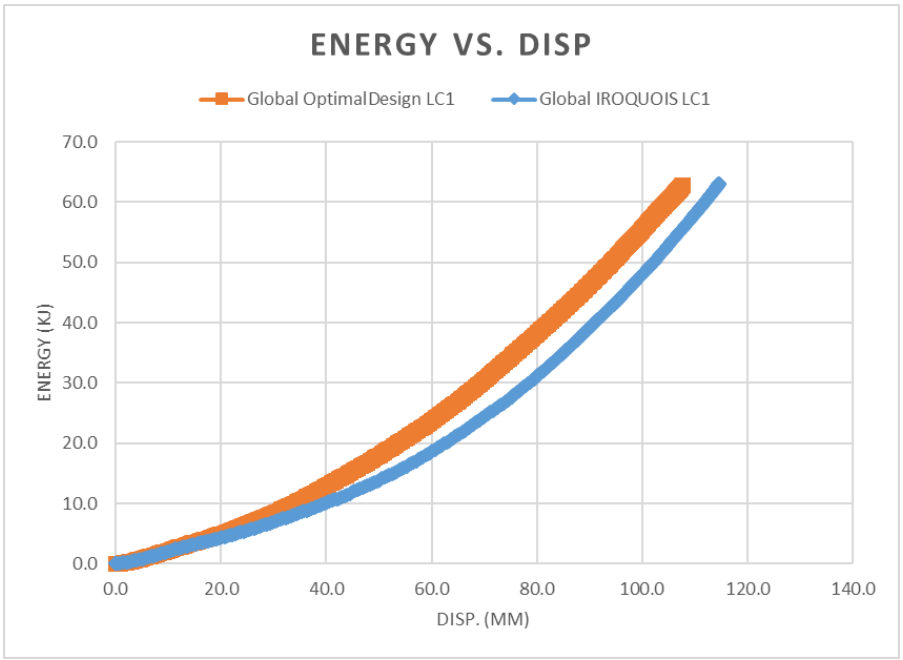

Figure 8.15: Exp5, Optimal vs. IROQUOIS, Energy vs. Disp. plot for Runs 4 and 10.

The results of the comparison of the IROQUOIS and concept stiffeners, for the Global Models loaded according to load case 2, can be seen in Figure 8.16 and Figure 8.17. It can be seen that the concept grillage performed significantly better than the IROQUOIS grillage. The optimized concept design had significantly higher internal energy throughout the entire displacement of the indenter.

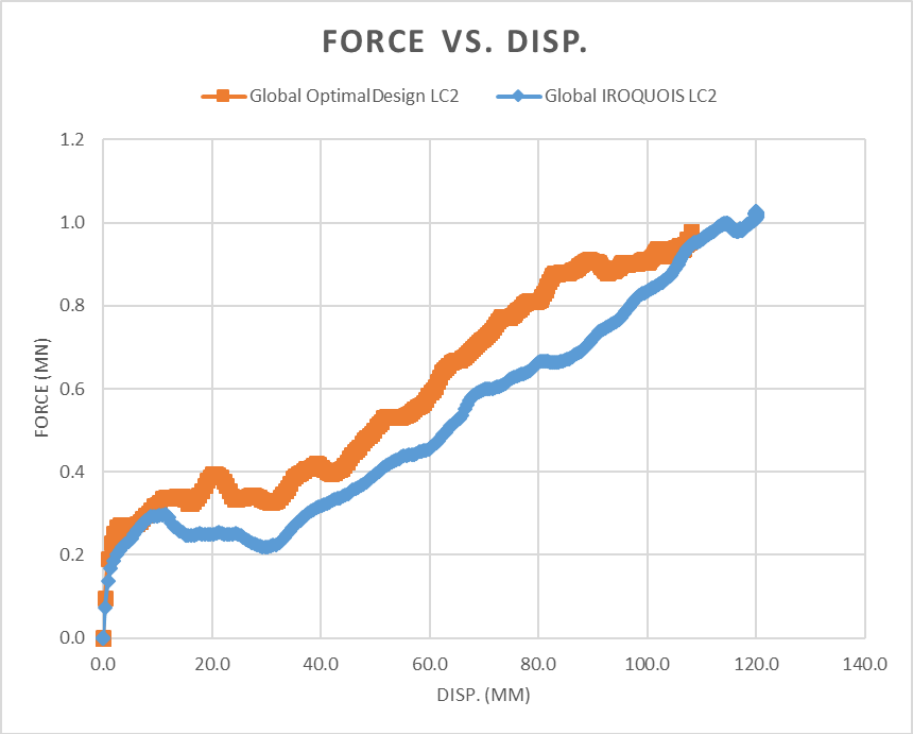

Figure 8.16: Exp5, Optimal vs. IROQUOIS, Force vs. Disp. plot for Runs 5 and 11.

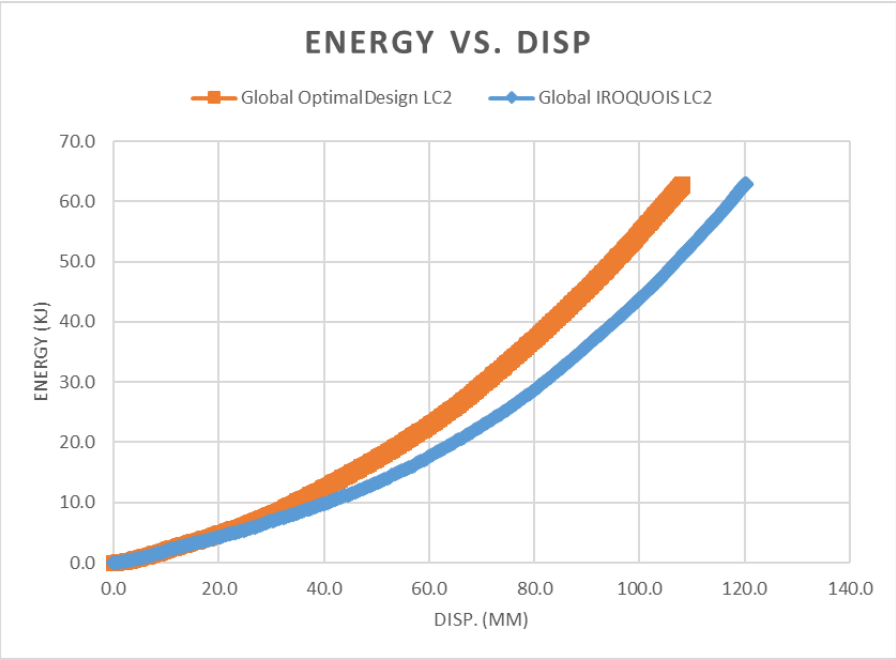

Figure 8.17: Exp5, Optimal vs. IROQUOIS, Energy vs. Disp. plot for Runs 5 and 11.

The results of the comparison of the IROQUOIS and concept stiffeners, for the Global Models loaded according to load case 3, can be seen in Figure 8.18 and Figure 8.19. It can be seen that the behaviour of the concept grillage remained equal to that of the IROQUOIS up until a displacement of ~60 mm, after which the IROQUOIS grillage performs better.

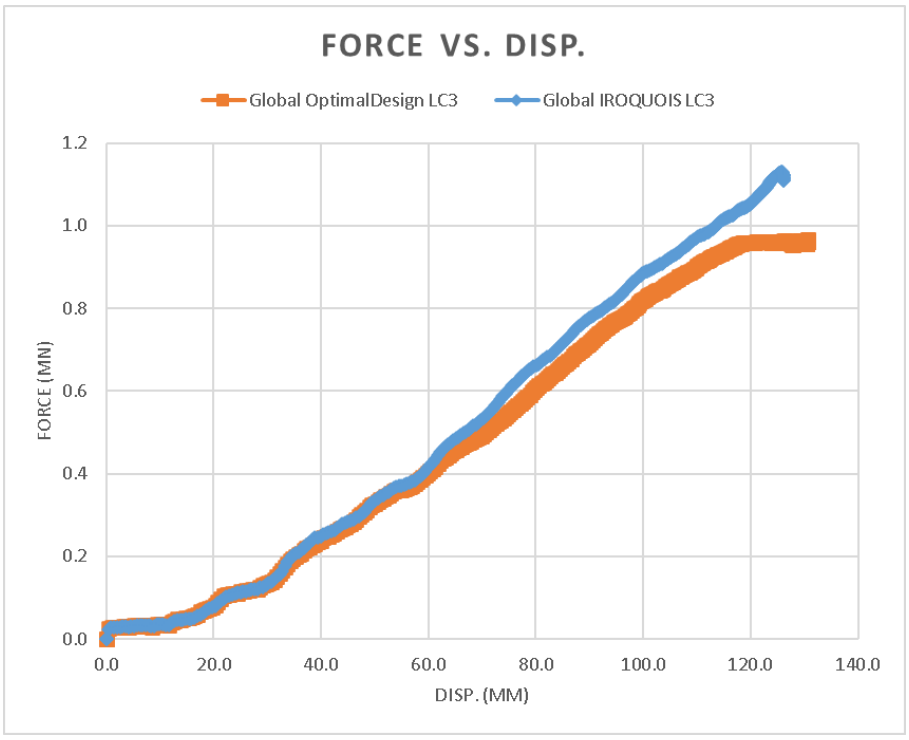

Figure 8.18: Exp5, Optimal vs. IROQUOIS, Force vs. Disp. plot for Runs 6 and 12.

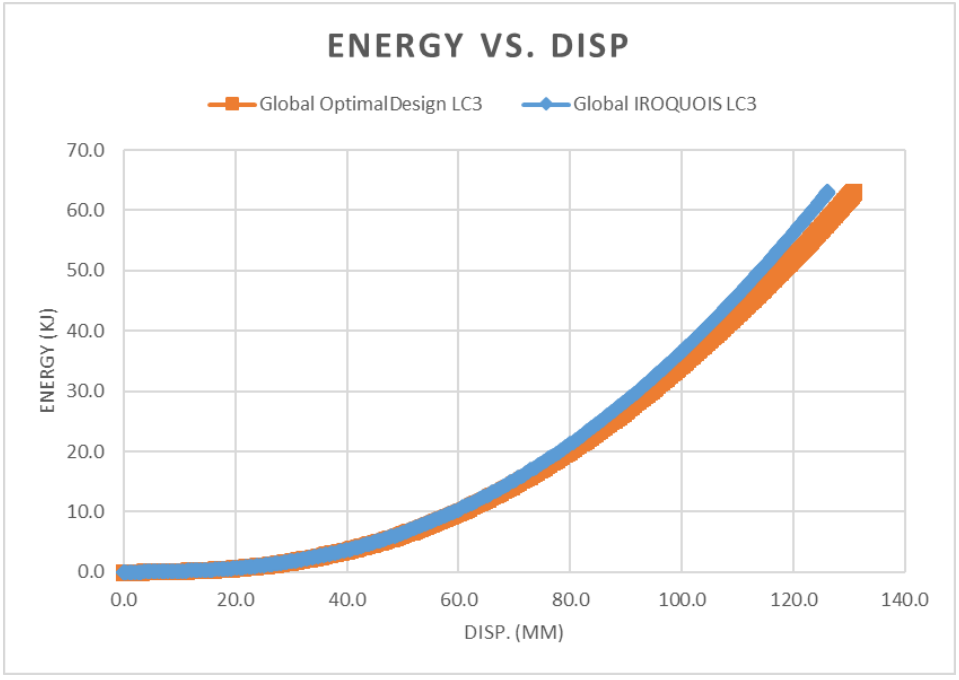

Figure 8.19: Exp5, Optimal vs. IROQUOIS, Energy vs. Disp. plot for Runs 6 and 12.

The concept grillage outperformed the IROQUOIS grillage in all test runs for displacements between 0 and ~60 mm. After a displacement of ~60 mm the Global Model of the concept grillage, under load case 3 conditions, begins to underperform. All other models outperform the IROQUOIS grillage up until a displacement of ~95 mm. After a displacement of ~95 mm the Global Model of the concept grillage, under load case 1 conditions, begins to underperform – through the overall internal energy remains higher for the concept grillage. Overall, for moderate indentations (0 – 60 mm) the concept grillage adds a significant amount of internal energy to the stiffened panel combination, compared to the IROQUOIS grillage, with no drawback.

It can be said that the concept grillage model outperformed the IROQUOIS model in all cases, within the Local Model. Note that the optimal grillage parameters used to create the concept grillage model in this experiment were developed in Exp4 based on a Local Model, not a Global Model. Comparing the Local and Global Models, it can be seen that the concept grillage performed optimally when the end conditions were stiffer, as was the case with the Local Models.

Note: As a form of analytical benchmarking, in Table 8.1 note that the total kinetic energy for two carriages, associated with a 50° impact, is approximately 63 kJ. As can be seen in each of the energy vs. displacement plots (Figure 8.9, Figure 8.11, Figure 8.13, Figure 8.15, Figure 8.17, and Figure 8.19), the maximum internal energy reached within each of the plots was approximately 63 kJ, as expected.

8.6 Discussion and Conclusions

An optimal design concept grillage was developed from simulations completed within Exp4. Further testing was completed within Exp5 to both compare the IROQUOIS grillages to the concept grillage and compare the Local Model to a larger Global Model. A more realistic impact scenario was examined. Instead of using a prescribed rigid body motion of the indenter, an initial velocity was applied to the indenter to simulate a high-energy impact. Twelve unique runs were developed based on three factors: stiffener type, model size, and load case. Since modelling cross-sectional curvature using shell elements is difficult, an effective flange thickness was calculated based on the formed tee. An effective flange thickness allowed for both the cross-sectional area and second moment of area to be approximately the same as for the formed tee.

The optimal stiffener design from Exp4 was slightly modified to be comparable to the lighter-weight IROQUOIS grillages. The verified experimental design from Exp4 was consulted to develop an optimal set of factor levels to produce a stiffener that weighed the same as the IROQUOIS stiffeners. The important difference to note between the Local and Global Models was that the Local Model had infinitely stiff stiffener ends, whereas the Global Model consisted of frames at the stiffener ends, which represented softer stiffener end conditions. The IROQUOIS and optimal stiffened panels were compared, under controlled conditions, to examine the difference in responses. The internal energy was plotted for each stiffener type for three load conditions: IOSQ, IOSC, and IBS.

Since Exp5 was the first experiment to simulate an impact within the LPA, the simulation had to be tested to ensure it was predicting valid results. The LPA includes two masses,

one on each pendulum arm, that swing together and meets in the middle. In other words, the apparatus assumes symmetry about both pendulum arms, concerning mass and associated impact energy. Since the FEM included one swinging pendulum arm impacting a fixed-fixed grillage, the total impact energy had to be equated.

Up to a displacement of ~60 mm, the concept grillage outperformed the IROQUOIS grillage within all load cases, with both the Local and Global Models. Between ~60 and ~95 mm of displacement, one IROQUOIS model outperforms the concept grillage under load case 3 conditions, within the Global Model. All other concept grillage models outperform the IROQUOIS models. Between ~95 mm and the end of indentation, one IROQUOIS model outperformed the concept grillage under load case 1 conditions, within the Global Model. All other concept grillage models outperform the IROQUOIS models.

Therefore, the concept grillage model outperformed the IROQUOIS model in all cases, within the Local Models. Also, all concept grillage models outperformed the IROQUOIS models for moderate amounts of indentation (0 – ~60 mm).

Comparing the Local and Global Models, it can be seen that the concept grillage performed optimally when the end conditions were stiffer, as was the case with the Local Models.

Chapter 9 Final Conclusions and Recommendations

Five sets of numerical experiments (Exp1 through Exp5) were conducted based on altering stiffener geometry to produce a stiffened panel configuration that was optimized to maximize internal energy absorption. Exp1 was completed utilizing various traditional corrugated stiffener designs. The experiment revealed that the optimal shape for corrugation converged on a flat profile shape – a flat bar stiffener. Any introduction of corrugation made the stiffener too soft and dramatically decreased its ability to absorb energy within the elastic region.

Exp2 was completed using an exploratory experimental approach. Several different stiffener types were tested under controlled conditions to determine the variability between the different stiffener types and to determine which were better stiffeners, and why. It was shown that stiffener web profiles constructed from beam deflection curves could be best optimized compared to all runs tested within Exp2. Since, in collision scenarios, it is often difficult to predict where impacts will occur, the deflection curve was abandoned. However, there may be scenarios where accidental impacts are guaranteed to occur at particular points along the stiffener span. The experiment also demonstrated that the stiffener experiences both axial tension and compression depending on the location along the span. Therefore, it was possible that optimizing the stiffener could mean different changes at the stiffener ends compared to the middle of the stiffener span.

Exp3 was completed based on the circular curve, non-uniform web height flat bar, run from Exp2. The circular curve run showed the most promise and was investigated further using a robust experimental design. Based on the results of both runs, it was determined that,

under the tested conditions, a stiffener flange was not statistically significant to the performance of the stiffener and was omitted from future testing.

Exp4 was completed, using a flangeless stiffener, to determine an optimal, concept grillage, design. The FEM was adapted to be compatible with the LPA by implementing the Local Model. The optimal design outperformed the built-T concerning energy absorption by 9.1 % over a range of 0-50 mm, 19.7 % over a range of 0-100 mm, and 16.1 % over a range of 0-150 mm. Based on the suggested optimal design for Exp3 and Exp4, it can be said that as the stiffener end conditions get stiffer, the variable web height stiffener becomes more optimal.

Lastly, Exp5 was completed to compare the optimal design to the IROQUOIS panels, using a Local and Global Model, as well as three load cases. A rigid indenter impact scenario was used for tests. An appropriate FEM was developed to use as a valid comparison to the future full-scale tests. Up to a displacement of ~60 mm, the concept grillage outperformed the IROQUOIS grillage within all load cases, with both the Local and Global Models. Between ~60 and ~95 mm of displacement, one IROQUOIS model outperforms the concept grillage under load case 3 conditions, within the Global Model. All other concept grillage models outperform the IROQUOIS models. Between ~95 mm and the end of indentation, one IROQUOIS model outperforms the concept grillage under load case 1 conditions, within the Global Model. All other concept grillage models outperform the IROQUOIS models. The concept grillage model outperformed the IROQUOIS model in all cases, within the Local Models. Also, all concept grillage models outperformed the IROQUOIS models for moderate amounts of indentation (0 – ~60 mm). Comparing the Local and Global Models,

it can be seen that the concept grillage performed optimally when the end conditions were stiffer, as was the case in the Local Models.

9.1 Summary of Significant Insights

Several notable insights were made regarding all completed analyses and subsequent results. Firstly, corrugated stiffeners, using any variation of tested corrugation parameters, did not provide adequate internal energy absorption within the elastic regime to be considered for further testing.

In nearly all experimental simulations, built-T stiffeners were shown to significantly buckle and lose their ability to absorb internal energy. Within the elastic regime, built-T's are an ideal shape for stiffeners. However, their overload capacity was low compared to other stiffener designs, such as the concept grillage.

Within Exp2, stiffeners were tested with profile shapes adapted to match beam fixed-fixed deflection curves. Interestingly, these runs were shown to perform significantly better than the control runs. However, they were abandoned for further testing due to one major flaw. The deflection curves used to create the profile shape were created assuming an impact, normal to the side-shell, directly in the middle of the stiffener span. If a different impact location were chosen, the resultant deflection curve shape would be translated along the stiffener span. Since, in collision scenarios, it is often difficult to predict where impacts will occur, the deflection curve was abandoned. However, there may be scenarios where accidental impacts are guaranteed to occur at particular points along the stiffener span. In

such situations, designing stiffener web profiles based on beam deflection curves may be beneficial, and should be tested further.

Under a load from a mid-span impact, normal to the side-shell, the stiffener experiences both axial tension as well as axial compression along with different locations of its span. At the centre of the span, the stiffener elements were in tension, whereas near the ends some elements were being compressed. Therefore, perhaps optimizing the stiffener could mean different changes to the ends compared to the middle of the stiffener span.

Based on both of the confirmation runs from Exp3, it was shown that a flange was not statistically significant to improving the first yield point of the structure, nor the energy absorption capabilities of the structure. Furthermore, under yield failure criteria, the built-T shape provides low displacement values per unit force. However, the stiffener's overload capacity was quite low, as it buckled almost immediately after yielding. Moreover, it has been demonstrated that a variable web height stiffener could perform just as well as a flanged stiffener, within the yield regime, under similar conditions.

Exp4 proved that under the conditions tested, it was possible to optimize a grillage using a variable web height stiffener. The optimal design outperformed the built-T concerning energy absorption by 9.1 % over a range of 0-50 mm, 19.7 % over a range of 0-100 mm, and 16.1 % over a range of 0-150 mm.

Experiments have shown that there is a relationship between stiffener web height and relative stiffener end stiffness. The suggested optimal design for Exp3, which had relatively soft stiffener end conditions, had a much lower optimal web height compared to the optimal

design suggested for Exp4, which had perfectly stiff end conditions. Therefore, with softer end conditions, the optimal design approached a uniform height web, flat bar, stiffener. However, when stiffer end conditions were implemented, a stiffener with significant variable-height web could be beneficial.

It was shown that an LPA impact could be simulated using FEA. The FEM can be created with one fixed-fixed pendulum arm and another free-to-rotate pendulum arm. An equivalent velocity, based on Equation [19], must be applied to the moving pendulum arm to equate the energy of the actual model to the FEM.

Up to a displacement of ~60 mm, the concept grillage outperformed the IROQUOIS grillage within all load cases, with both the Local and Global Models. Between ~60 and ~95 mm of displacement, one IROQUOIS model outperforms the concept grillage under load case 3 conditions, within the Global Model. All other concept grillage models outperform the IROQUOIS models. Between ~95 mm and the end of indentation, one IROQUOIS model outperforms the concept grillage under load case 1 conditions, within the Global Model. All other concept grillage models outperform the IROQUOIS models. The concept grillage model outperformed the IROQUOIS model in all cases, within the Local Models. Also, all concept grillage models outperformed the IROQUOIS models for moderate amounts of indentation (0 – ~60 mm).

9.2 Future Work

Future work consists of alterations to the FEM to better match the future full-scale experiment, as well as ideas and lessons-learned which were not implemented into the experiments.

All simulations were implemented using a rigid indenter. However, it may be beneficial to compare results to a model with a deformable indenter since some energy was consumed through the elastic deformation of the indenter. Additionally, in a simulation, impacting the indenter directly on a stiffener can be guaranteed. Whereas, in a full-scale test the impact could occur off-centre, slightly between stiffeners. The resultant impact could cause additional tripping. Therefore, it could prove insightful to simulate a slightly off-centre impact.

Subsequent impacts were not tested with any of the simulations. It is possible that multi-hit analyses could interact with the behaviour of the models and have an effect on optimality. For example, an IOS impact could be tested followed by an IBS impact.

Additionally, all stiffener/side-shell grillage combinations tested consisted of 90º, plate-to-plate configurations. More unique designs could be tested consisting of sandwich panels and varying the angle that the stiffener makes to the side-shell.

Throughout all experiments, the force at the BCs, or the contact force, was compared to the maximum displacement of the grillage. Since the goal was to find a stiffener-side-shell combination which was optimal, the force data between the stiffener and side-shell was never analyzed separately. To get a better idea of how the force was absorbed throughout

the stiffener compared to the side-shell, the BC force at the stiffener ends can be separated from the plate ends for a comparison.

Concerning the experimental design factors and levels, in the interest of conserving time gathering experimental simulation results, several potentially significant experimental factors were omitted. Several factors, as well as many others, could influence the behaviour of the stiffened panel, such as plate thickness, stiffener span, and stiffener spacing.

There may be scenarios where accidental impacts are guaranteed to occur at particular points along the stiffener span. In such situations, designing stiffener web profiles based on beam deflection curves may be beneficial, and should be tested further. It would also be recommended to test impacts on a quarter-span stiffener, as well as impacts between stiffeners. The results can then be compared to the optimal design. During accidental loading, it may also be appropriate to test sliding loads.

Castellated beams are created when a beam's web is cut longitudinally to later reassemble the two pieces with an effective 50 % increased web height. The newly formed beam will consequently contain lightening holes. Castellated beams were not explicitly studied. However, there is at least one key point that castellated beams share with the conducted work. The resultant stiffener profile shape should be easily cut with little material wastage. One way to ensure minimal wastage would be to mimic the longitudinal cut method of castellated beams. Future work regarding this research could focus more on the ability for shipyards to form the proposed optimal design. The current optimal design would require much material wastage due to the circular curvature along the top edge of the web's profile.

Since the conducted work considered dynamic load cases only, it could prove insightful to compare the optimal design to a quasi-static analysis. For dynamic impacts, there are added inertial effects associated with compression between the stiffener flange and side-shell. Therefore, dynamic impacts may be responsible for the local buckling seen in many of the built-T FEMs.

The conducted work only considered loads normal to the side-shell. Perhaps axial forces associated with hogging and sagging moments could alter the optimal design. Therefore, axial forces could be added to the stiffener in combination with the rigid indenter impacts to determine the axial force effects.

A relationship between stiffener web height and relative stiffener end stiffness has been established. However, the relationship was not quantified. Additional testing could be done, utilizing DOE, to form a regression equation to better understand the relationship. Systematically fixing/freeing the various degrees of freedom at the BCs could affect the optimal web height at the centre of the stiffener span.

The limitations of the conducted work should be noted and can be seen in the form of some of the future work suggestions within this Section. Most notably, the study did not investigate the effect that axial loading would have on the optimal design. Due to the reduced cross-sectional area at the ends of the stiffener, it is thought that axial loading would cause a significant loss of structural capacity to the optimal design. Additionally, the conducted work did not study the effect of quasi-static loading conditions. Under quasi-static loads, the stiffener flange could prove to be much more significant to the structure

due to the reduced inertial effects of the flange. Both axial loading and quasi-static load applications should be tested to further this work.

9.2.1 COVID-19 Impact Statement

Fortunately, COVID-19 did not make a significant impact on the experiments found in the conducted work. All experiments discussed within were completed in the form of numerical simulations completed on a computer – sometimes remotely when necessary. COVID-19 did not affect the original methodology, nor did it affect the results of the conducted work. However, COVID-19 did affect the intended full-scale validation of the proposed optimal concept grillage design.

It was originally intended that a full-scale validation experiment would be conducted within the LPA, towards the end of the study. Within this work, this validation experiment would have appeared in the form of Exp6, immediately succeeding Exp5. It should be noted that the validation study will still be completed, when possible, to validate this research. The validation study will be subsequently published.

9.2.1.1 Validation Study Outline

There are two possible geometric options for full-scale testing of the optimal design. Both are identical in concept but are different in weight and, therefore, in scantlings. For comparisons directly comparable to the simplified panels, a full-scale geometric model of the optimal design should be built according to the dimensions shown for “Conf. Run2” within Table 7.3. For comparisons directly comparable to the IROQUOIS panels, a full-scale geometric model of the optimal design should be built according to the dimensions within Table 8.2.

A pre-built full-scale rigid indenter, as described within Section: 3.7 Rigid Indenter Design, will be used as the indenter. The LPA discussed within Section: 3.6 Large Pendulum Apparatus, will be used to house the experiment. Regarding Figure 3.5, the rigid indenter will be mounted to the left side of the pendulum, and the concept grillage will be mounted to the right side of the pendulum, within the grillage-housing carriage. Five tests will be completed using the same grillage. The first test will be completed using a 10° pendulum arm angle. Subsequent tests will be completed at increasing intervals of 10°. A total of five tests will be completed – one at each arm angle of 10°, 20°, 30°, 40°, and 50°. After each test, results will be verified before continued testing.

It should be noted that any grade of steel can be used for validation. Since the material will remain constant between the five tests, its effect will be blocked out. More importantly, an accurate material model will be built within LS-DYNA in the form of a multi-linear model. The appropriate card to invoke within LS-DYNA to form the multilinear model is MAT_PIECEWISE_LINEAR_PLASTICITY (this model should be used in place of the MAT_PLASTIC_KINEMATIC card which was used for Exp2 through Exp5). To determine appropriate stress-strain material model curvature, uniaxial strength testing should first be completed on samples of the steel to be used to create the concept grillage for testing. The LS-DYNA material model should mimic the behaviour from the uniaxial strength testing. The following fields within the MAT_PIECEWISE_LINEAR_PLASTICITY card will be populated with the appropriate data from the tensile testing: RO, E, PR, EPS1-EPS8, and ES1-ES8.

It should be noted that the loading conditions should be taken from Section: 8.3.1 Loading Conditions, within Exp5. In other words, the rigid indenter should be assigned an appropriate initial velocity corresponding to the appropriate arm angle for each test (the equivalent Impact Speed column of Table 8.1 should be consulted). The appropriate card to invoke to achieve this effect is INITIAL_VELOCITY_GENERATION. Within INITIAL_VELOCITY_GENERATION the VZ field should be changed for each test based on the desired arm angle. Within the FEA, the Fixed-Fixed Panel Solution will be applied shown in Section: 8.4.1 Fixed-Fixed Panel Solution. The BCs and all other controls (suggested termination time, contact, integration points, and data output) should all be applied according to Section: 7.3 LS-PrePost and LS-DYNA, while the LS-DYNA cards should be applied according to 8.3.2 LS-DYNA Cards.

Results will be extracted in two forms: force and displacement. The LPA is equipped with three load cells that measure the full-scale impact force of the collision. The full-scale displacement will be accurately measured using a FARO arm. To validate the model, the full-scale impact force and mid-point displacement can be compared to the FEA contact force and mid-point displacement. The FEA results will be in the form of force vs. displacement curves similar to what was shown in Section: Results, within Exp5.

Bibliography

Abraham, Jacob. 2008. "Plastic Response of Ship Structure Subject of Ice Loading (Master's thesis)." St. John's, Newfoundland.

ALTAIR. n.d. "HyperMesh v14.0 [Computer Software]."

Anderson, Mark J., and Patrick J. Whitcomb. 2014. "Employing Power to 'Right-Size' Design of Experiments." *ITEA* 40-44. https://cdnm.statease.com/pubs/employing-power-and-precision-to-right-size-DOE.pdf.

1994. *Boeing Design Manual, Rev G.*

Daley, Claude G., Katherine H. Daley, John Dolny, and Bruce W.T. Quinton. 2017. "Overload response of flatbar frames to ice loads." *SHIPS AND OFFSHORE STRUCTURES* S68-S81.

Dassault Systèmes. n.d. "SOLIDWORKS Education Edition SP4.0 [Computer Software]."

DNV-GL. 2015. "Buckling DNVGL-CG-0128." *Class Guideline.* October. https://rules.dnvgl.com/docs/pdf/DNVGL/CG/2015-10/DNVGL-CG-0128.pdf.

Gagnon, Robert. 2008. "A new impact panel to study bergy bit / ship collisions." *Proceedings of 19th IAHR International Symposium on Ice.* Vancouver, British Columbia, Canada. 783-790.

Gagnon, Robert, Claude Daley, and D. Bruce Colbourne. 2015. "A large double-pendulum device to study load, pressure distribution and structure damage during

ice impact tests in the lab." *POAC15.* Trondheim, Norway: Port and Ocean Engineering under Arctic Conditions.

Hibbeler, Russell C. 2011. *Mechanics of Materials: Eighth Edition.* Upper Saddle River, NJ: Pearson Prentice Hall.

IACS. 2019. "Requirements concerning: POLAR CLASS." *International Association of Classification Societies.* December 4. http://www.iacs.org.uk/download/1803.

Kim, Hyunmin, and Claude Daley. 2018. "Evaluation of large structural grillages subjected to ice loads in experimental and numerical analysis." *Marine Structures* 467-502.

Kõrgesaar, Mihkel, Pentti Kujala, and Jani Romanoff. 2018. "Load carrying capacity of ice-strengthened frames under idealized ice load and boundary conditions." *Marine Structures* 18-30.

Kujala, P. 1994. "On the statistics of ice loads on ship hull in the baltic (Doctoral dissertation)." *Mechanical Engineering Series No. 116.*

Livermore Software Technology Corp. n.d. "LS-DYNA R11.1.0 [Computer Software]."

—. n.d. "LS-PrePost V4.5.24 [Computer Software]."

Mason, Robert L., Richard F. Gunst, and James L. Hess. 2003. *Statistical Design and Analysis of Experiments With Applications to Engineering and Science.* Second. Hoboken, New Jersey: John Wiley and Sons Publication.

Montgomery, Douglas C. 2017. *Design and Analysis of Experiments: Ninth Edition.* Hoboken, NJ: John Wiley & Sons, Inc.

Paik, Jeom Kee, and Anil Kumar Thayamballi. 2003. *Ultimate limit state design of steel plated structures.* West Sussex, England: John Wiley & Sons, Ltd.

Quinton, Bruce W.T. 2015. "Experimental and Numerical Investigation of Moving Loads on Hull Structures (Doctoral dissertation)." (Memorial University of Newfoundland).

Quinton, Bruce W.T. 2019. "Lateral (sliding) motion of design ice loads on IACS polar classed structures." *Ships and Offshore Structures* 281-291. doi:10.1080/17445302.2019.1580844.

Quinton, Bruce W.T. 2008. "Progressive Damage to a Ship's Structure due to Ice Loading (Master's thesis)." (Memorial University of Newfoundland).

Quinton, Bruce W.T., Claude Daley, D. Bruce Colbourne, and Robert Gagnon. 2017. "Experimental investigation of accidental sliding loads on the response of hull plating." *Proceedings of the 6th International Conference On Marine Structures (Marstruct 2017).* Dubrovnik, Croatia. 513-522.

Quinton, Bruce W.T., Claude Daley, Robert Gagnon, and D. Bruce Colbourne. 2016. "Guidelines for the nonlinear finite element analysis of hull response to moving loads on ships and offshore structures." *Ships and Offshore Structures.*

Ringsberg, Jonas W., Hüseyin Sağlam, Md. Asaduzzaman Sarder, and Anders Ulfvarson. 2012. "Lightweight design of offshore platform marine structures optimisation of

weight to strength utilisation of corrugated shell plating." *Ships and Offshore Structures* 38-53.

Ringsberg, Jonas W., Jörgen Amdahl, Bai Qiao Chen, Sang-Rai Cho, Sören Ehlers, Zhiqiang Hu, Jan M. Kubiczek, et al. 2018. "MARSTRUCT benchmark study on nonlinear FE simulation of an experiment of an indenter impact with a ship side-shell structure." *Marine Structures* (ELSEVIER) 59: 142–157.

Robert McNeel & Associates. n.d. "Rhinoceros 5.0 Educatinal Lab License [Computer Software]."

Sang-Hoon, Shin, and Ko Dae-Eun. 2018. "A study on minimum weight design of vertical corrugated bulkheads for chemical tankers." *International Journal of Naval Architecture and Ocean Engineering* 10: 180-187.

Shaw, Doug. 2013. *HMCS Iroquois DDG280.* April 27th. http://www.shipspotting.com/gallery/photo.php?lid=1791504.

Sopper, Regina, Robert Gagnon, Claude Daley, and D. Bruce Colbourne. 2015. "Measurements of spatial and temporal variations in ice impact pressures." *International Conference on Port and Ocean Engineering.* Trondheim, Norway: Port and Ocean Engineering under Arctic Conditions.

Stat-Ease, Inc. 2018. "Design Expert 11.1.0.1 64-bit [Computer software]."

Zhongwei, L., and P. Mayuresh. 2017. "Structural Optimization of Elasto-Plastic Beam-Columns under Uniaxial Compression." *SNAME Maritime Convention.* Houston, Texas. https://www.researchgate.net/publication/320840493.

Appendices

Appendix A – Rigid Indenter Fabrication Drawings

4 3 2 1

B B

Threaded Through Hole
1 1/4" NF. TYP.

* Existing Plate Modification. Ten Threaded Holes.

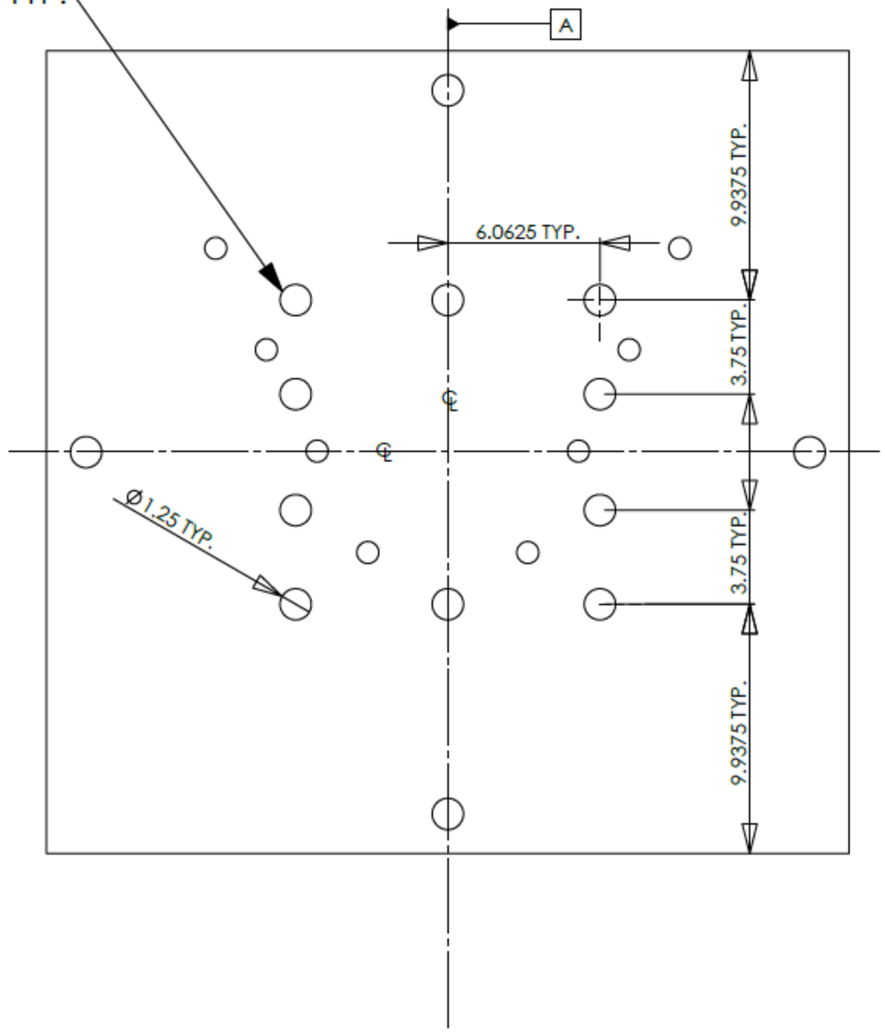

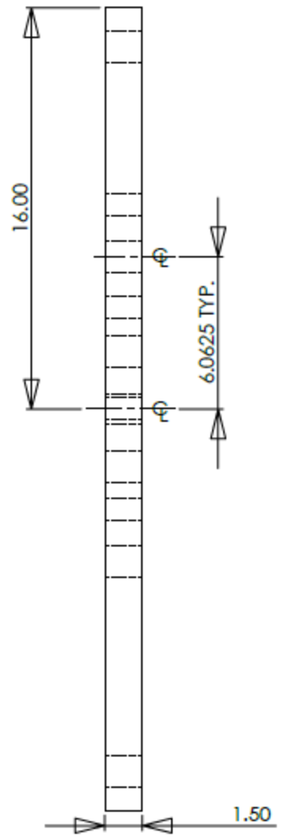

VIEW A-A

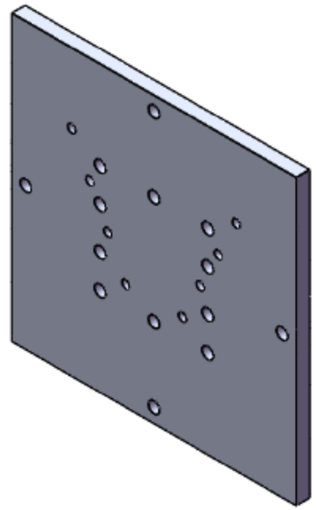

Scale 1:10

A A

	NAME	DATE
DRAWN	JN	06/25/19
CHECKED		
COMMENTS:		

UNLESS OTHERWISE SPECIFIED:
DIMENSIONS ARE IN INCHES
TOLERANCES:
FRACTIONAL ±
MATERIAL
DO NOT SCALE DRAWING

TITLE:
Ice Plate Modification

SIZE	DWG. NO.	REV
B	1.	3

SCALE: 1:5 SHEET 1 OF

4 3 2 1

*No threads

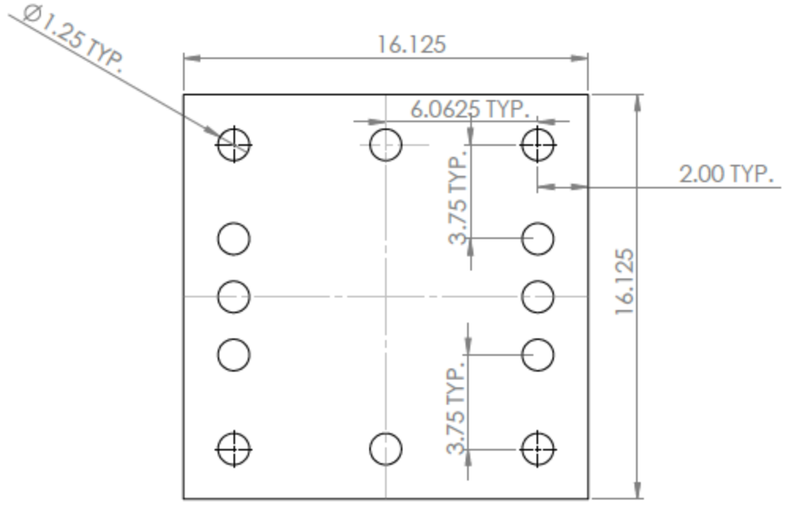

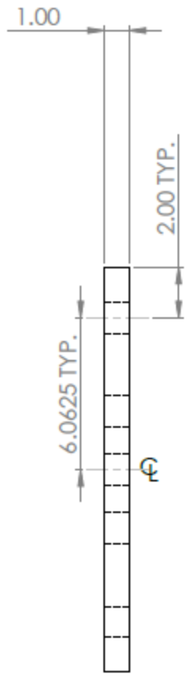

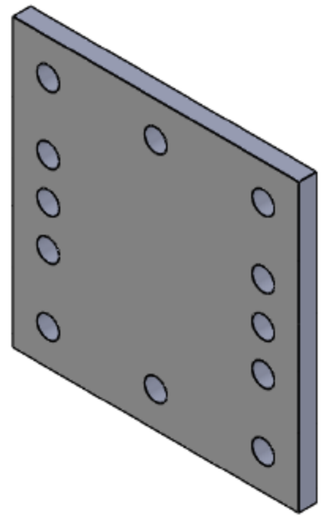

	NAME	DATE
DRAWN	JN	06/20/19
CHECKED		
COMMENTS:		

UNLESS OTHERWISE SPECIFIED:
DIMENSIONS ARE IN INCHES
TOLERANCES:
FRACTIONAL ±
MATERIAL
DO NOT SCALE DRAWING

TITLE:
Ice Plate Attachment Plate

SIZE	DWG. NO.	REV
B	2.	3

SCALE: 1:5 SHEET 1 OF

*Existing beam behind Tech. Services.

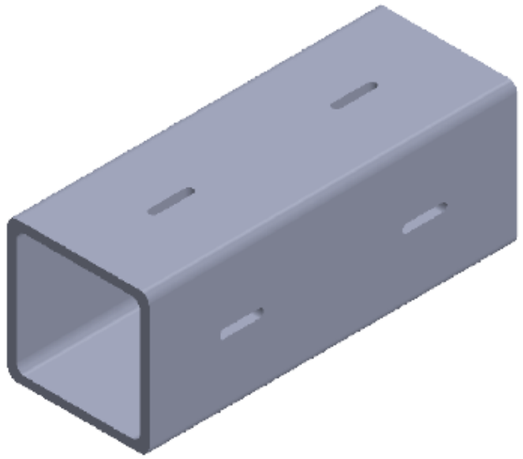

All Four Sides

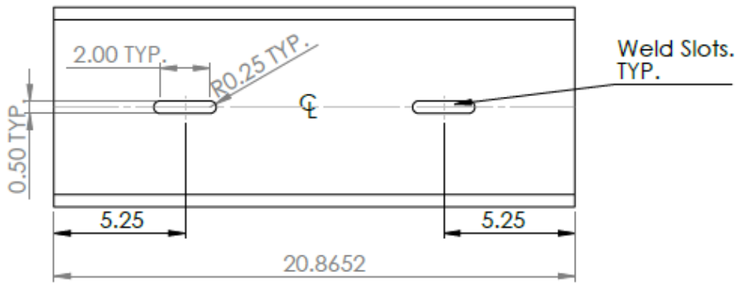

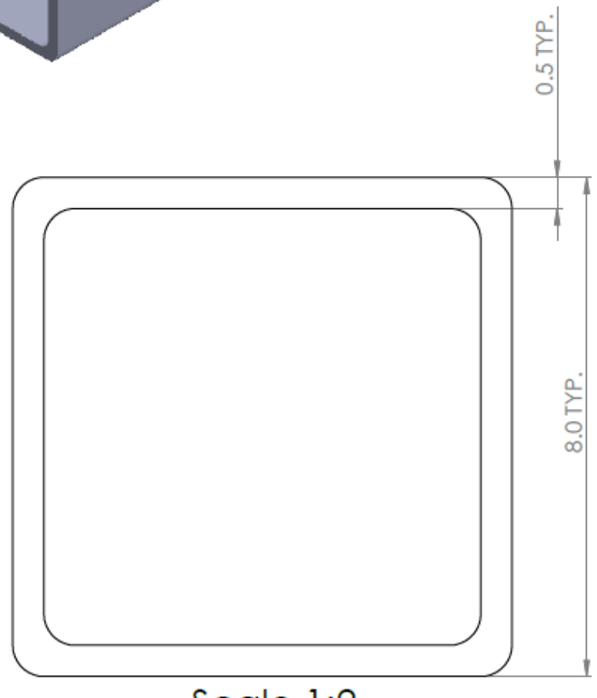

Scale 1:2

Dimensions shown for measuring purposes only.

		NAME	DATE
	DRAWN	JN	06/25/19
UNLESS OTHERWISE SPECIFIED:	CHECKED		
DIMENSIONS ARE IN INCHES TOLERANCES: FRACTIONAL ±	COMMENTS:		
MATERIAL			
DO NOT SCALE DRAWING			

TITLE: Existing Square H.S.S.

SIZE	DWG. NO.	REV
B	3.	4
SCALE: 1:5		SHEET 1 OF

*Holes Not Threaded. Holes Through All.

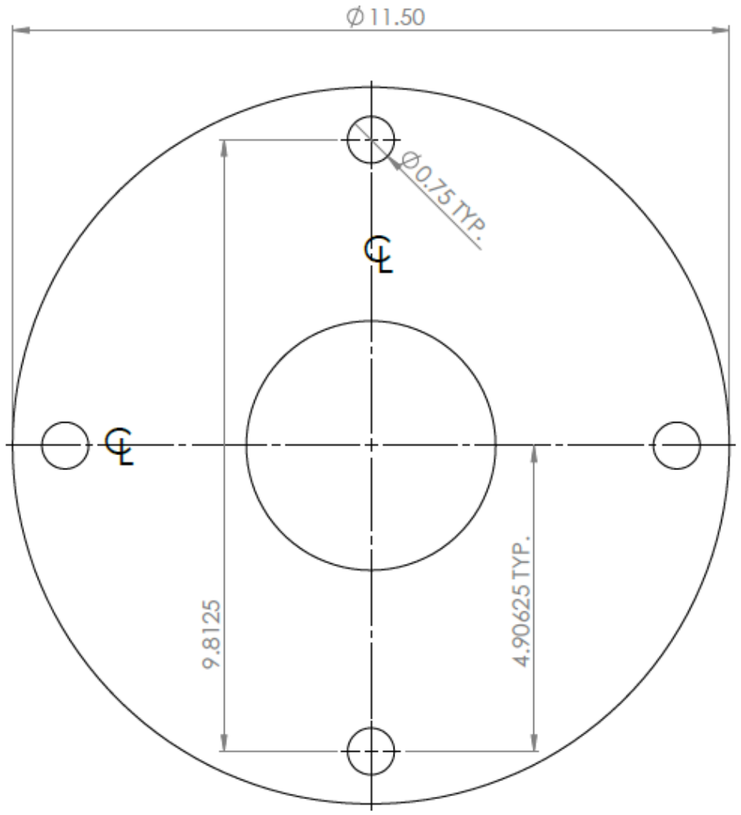

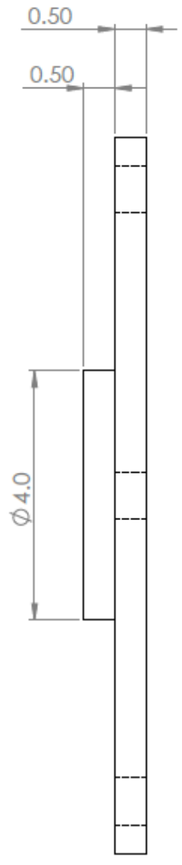

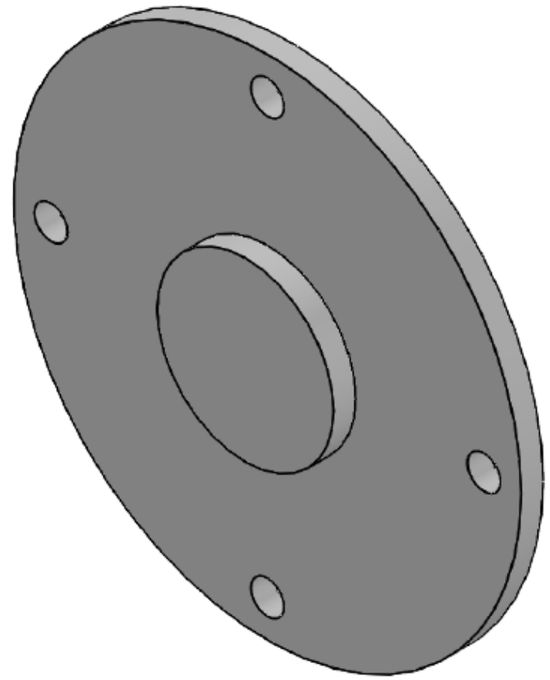

		NAME	DATE
	DRAWN	JN	06/20/19
UNLESS OTHERWISE SPECIFIED:	CHECKED		
DIMENSIONS ARE IN INCHES TOLERANCES: FRACTIONAL ±	COMMENTS:		
MATERIAL			
DO NOT SCALE DRAWING			

TITLE: Dome Attachment Plate

SIZE	DWG. NO.	REV
B	4.	3

SCALE: 1:2 SHEET 1 OF

*Made from Solid Steel Plate

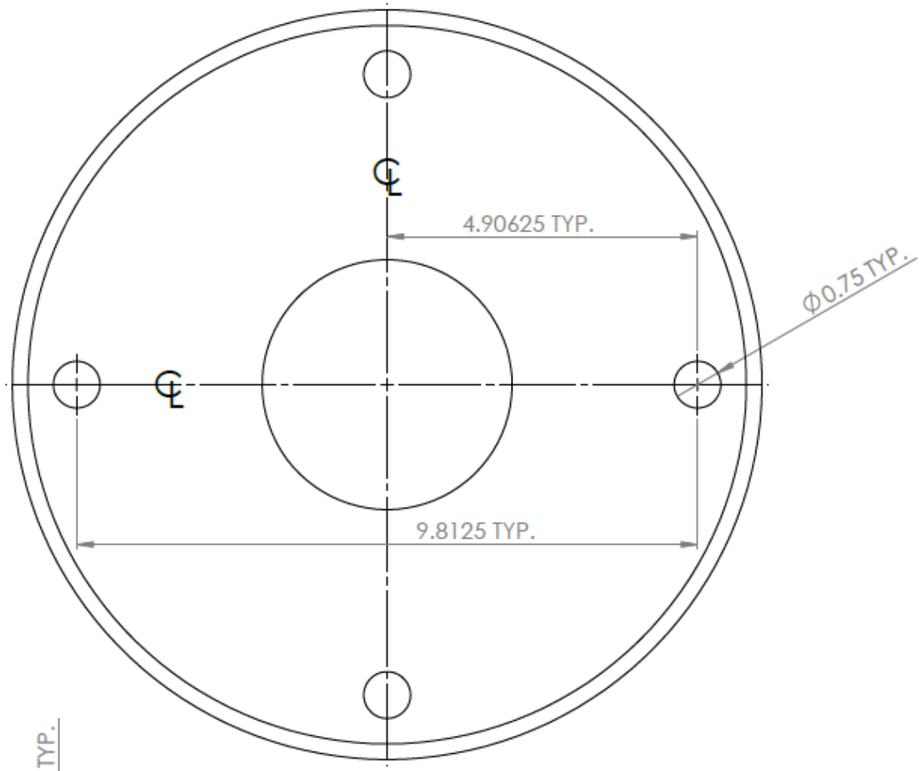

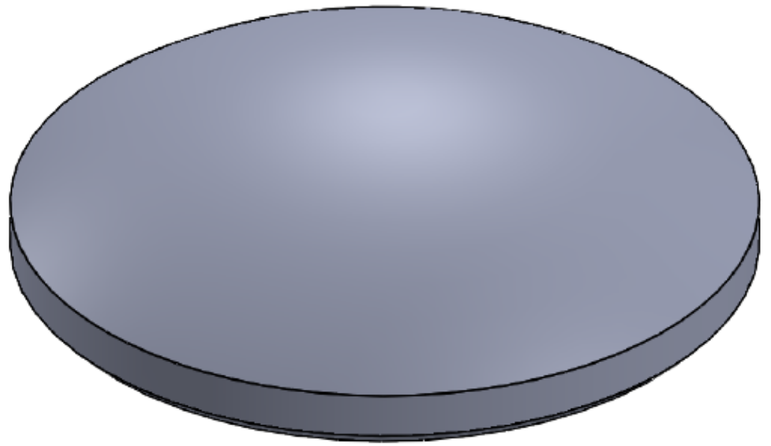

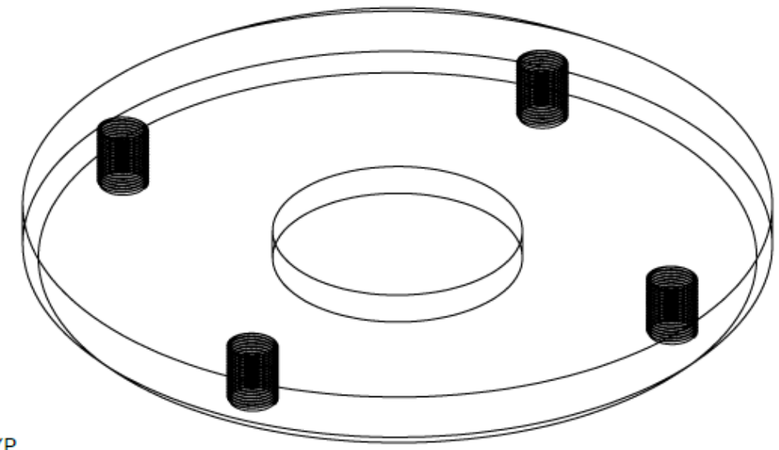

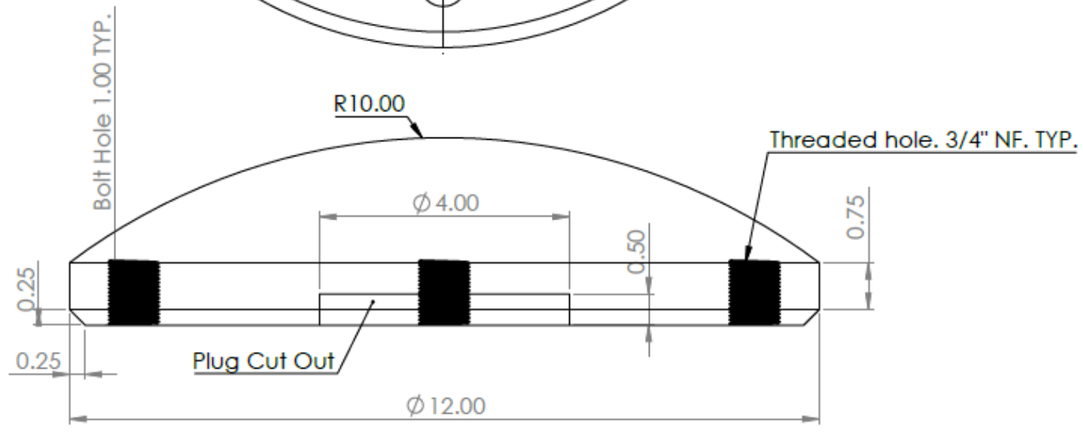

		NAME	DATE
	DRAWN	JN	06/25/19
UNLESS OTHERWISE SPECIFIED:	CHECKED		
DIMENSIONS ARE IN INCHES TOLERANCES: FRACTIONAL ±	COMMENTS:		
MATERIAL			
DO NOT SCALE DRAWING			

TITLE: Dome

SIZE	DWG. NO.	REV
B	5.	3

SCALE: 1:2 SHEET 1 OF

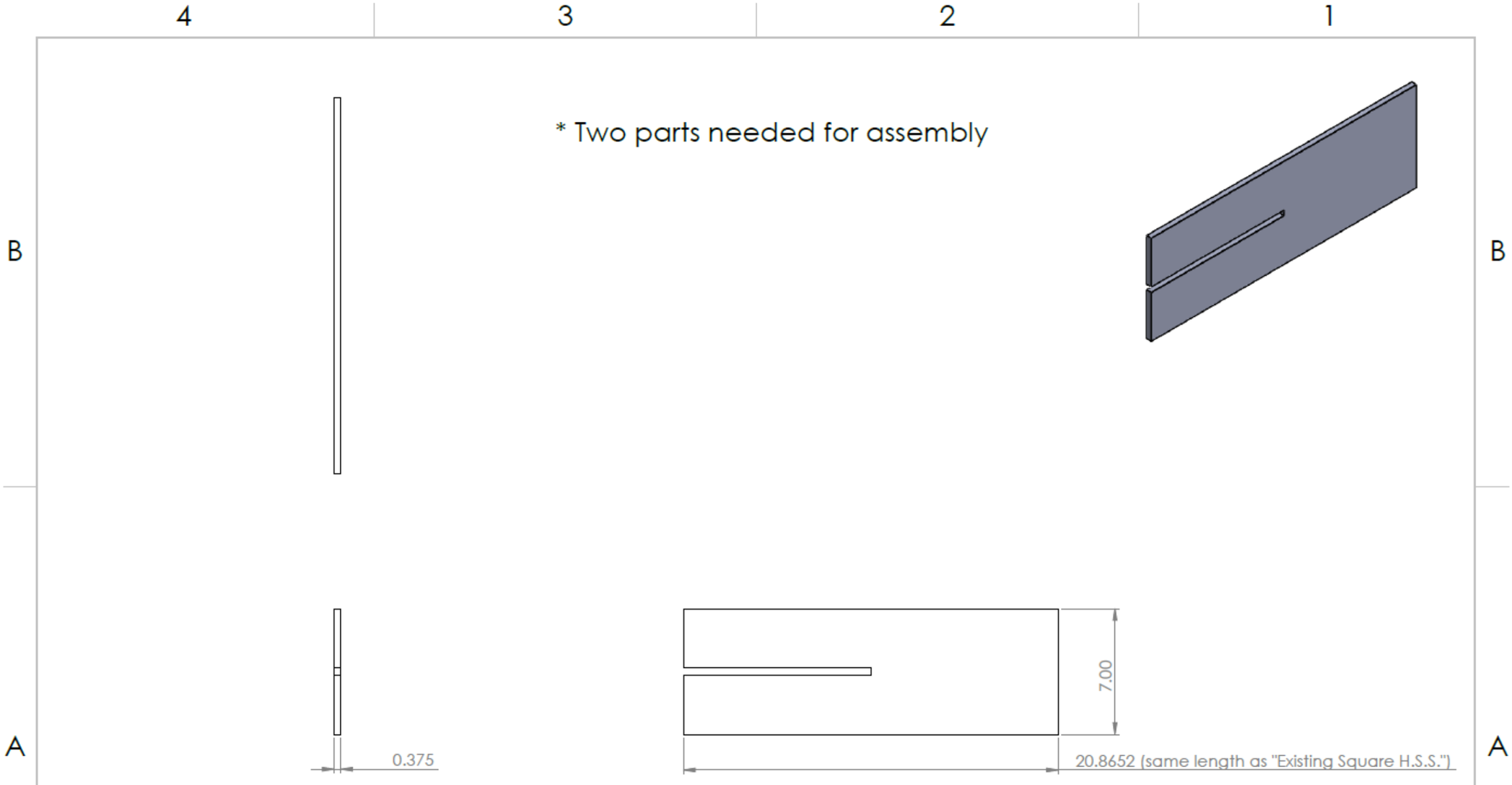
4
3
2
1
B
A
* Two parts needed for assembly
0.375
7.00
20.8652 (same length as "Existing Square H.S.S.")
NAME
DATE
DRAWN
JN
06/25/19
UNLESS OTHERWISE SPECIFIED:
CHECKED
DIMENSIONS ARE IN INCHES
TOLERANCES:
FRACTIONAL ±
COMMENTS:
MATERIAL
DO NOT SCALE DRAWING
TITLE:
X-Beam
SIZE
B
DWG. NO.
6.
REV
2
SCALE: 1:5
SHEET 1 OF

ITEM NO.	PART INFO	DESCRIPTION	QTY.
1	X-Beam	DWG 6	2

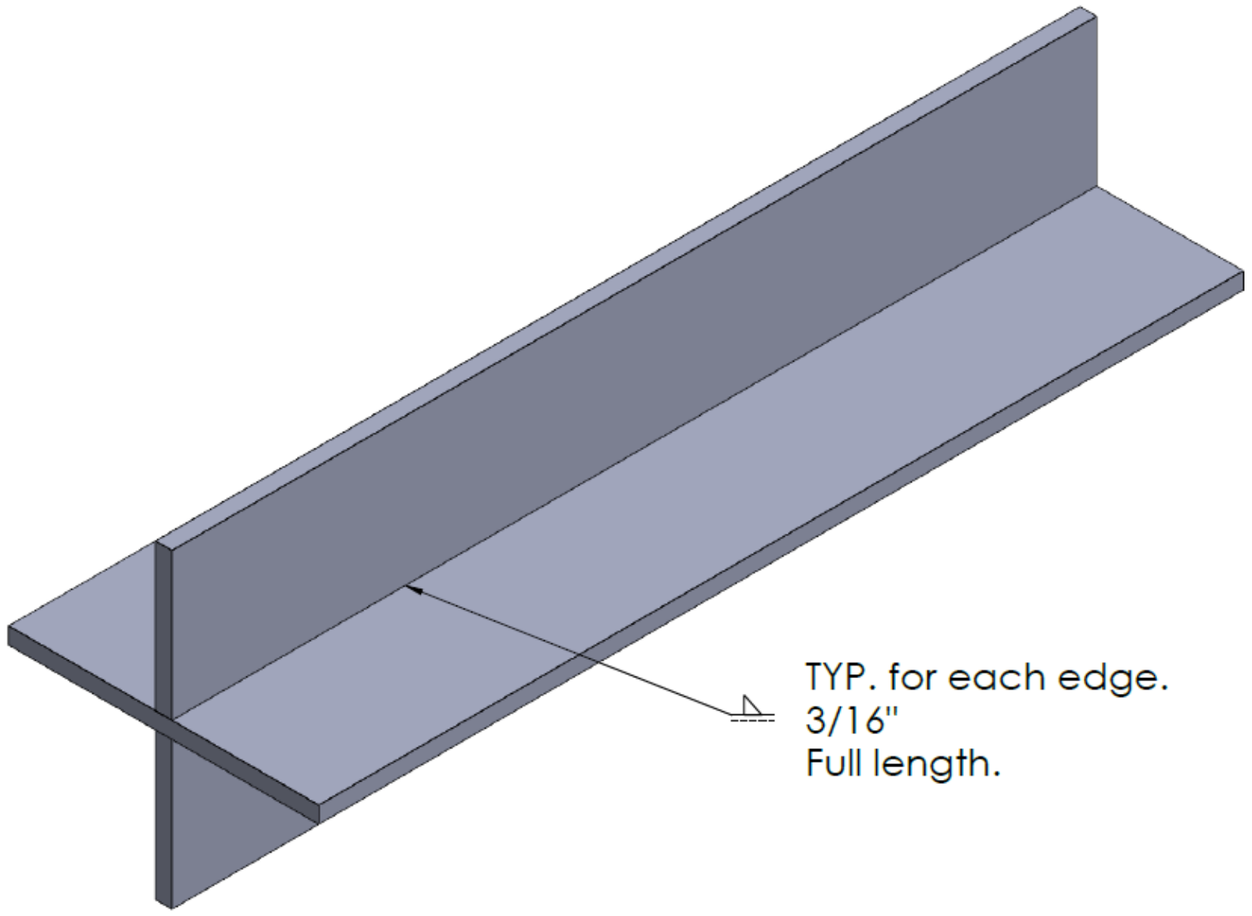

		NAME	DATE
	DRAWN	JN	06/25/19
UNLESS OTHERWISE SPECIFIED:	CHECKED		
DIMENSIONS ARE IN INCHES TOLERANCES: FRACTIONAL ±	COMMENTS:		
MATERIAL			
DO NOT SCALE DRAWING			

TITLE: Weld Details 1 (X-Beam Assembly)

SIZE	DWG. NO.	REV
B	7.	2
	SCALE: 1:2	SHEET 1 OF

ITEM NO.	PART INFO	DESCRIPTION	QTY.
1	Ice Plate Attachment Plate	DWG 2	1
2	XBeam Assembly	DWG 7	1

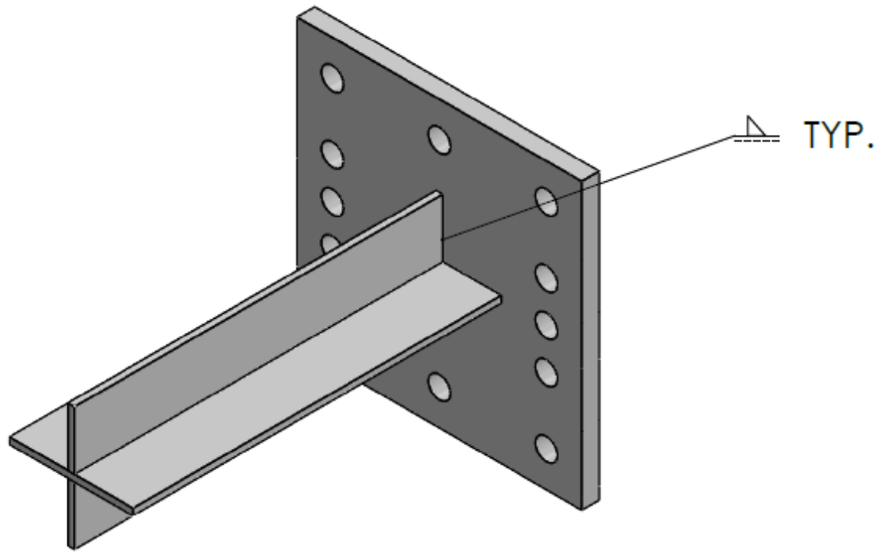

		NAME	DATE
	DRAWN	JN	06/25/19
UNLESS OTHERWISE SPECIFIED:	CHECKED		
DIMENSIONS ARE IN INCHES TOLERANCES: FRACTIONAL±	COMMENTS:		
MATERIAL			
DO NOT SCALE DRAWING			

TITLE: Weld Details 2

SIZE	DWG. NO.	REV
B	8.	1

SCALE: 1:5 SHEET 1 OF

ITEM NO.	PART INFO	DESCRIPTION	QTY.
1	Ice Plate Attachment Plate	DWG 2	1
2	Square Hollow Beam	DWG 3	1
3	XBeam Assembly	DWG 7	1

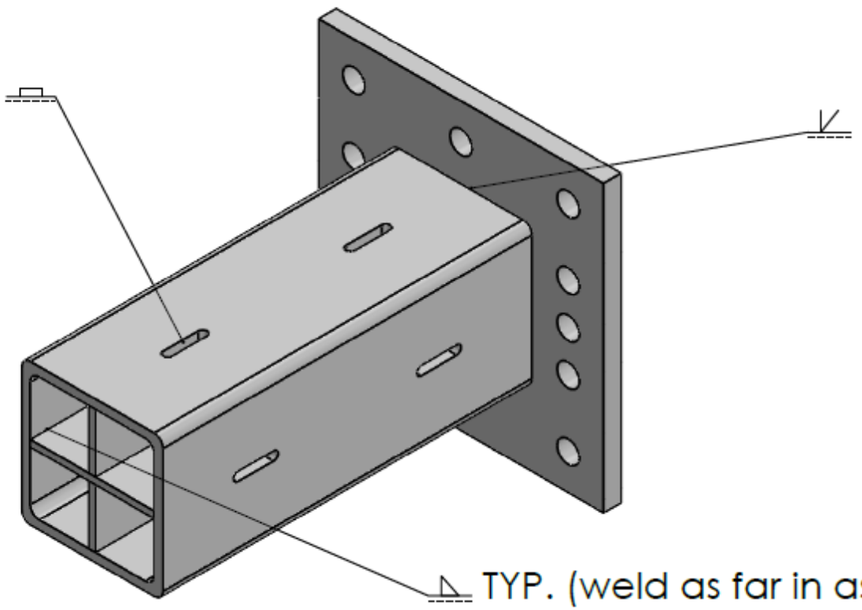

		NAME	DATE
	DRAWN	JN	06/25/19
UNLESS OTHERWISE SPECIFIED:	CHECKED		
DIMENSIONS ARE IN INCHES TOLERANCES: FRACTIONAL±	COMMENTS:		
MATERIAL			
DO NOT SCALE DRAWING			

TITLE: Weld Details 3

SIZE	DWG. NO.	REV
B	9.	1

SCALE: 1:5 SHEET 1 OF

ITEM NO.	PART INFO	DESCRIPTION	QTY.
1	Dome Attachment Plate	DWG 4	1
2	Weld Details 3	DWG 9	1

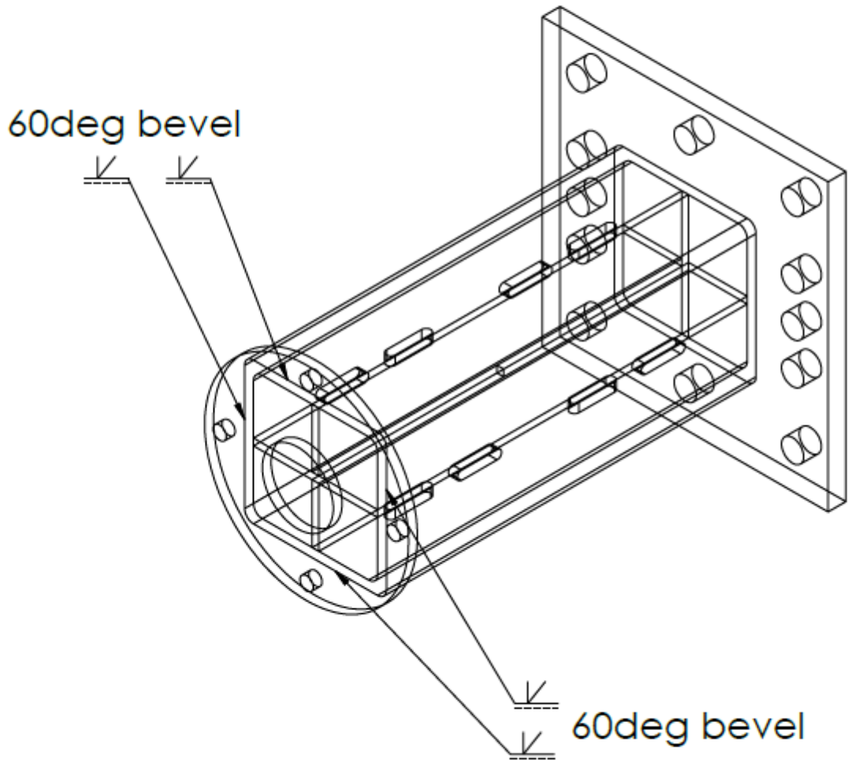

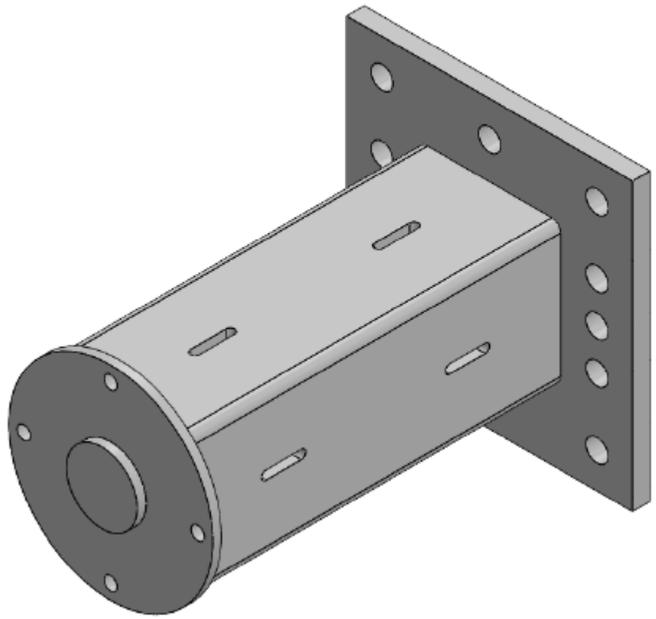

		NAME	DATE
	DRAWN	JN	06/25/19
UNLESS OTHERWISE SPECIFIED:	CHECKED		
DIMENSIONS ARE IN INCHES TOLERANCES: FRACTIONAL±	COMMENTS:		
MATERIAL			
DO NOT SCALE DRAWING			

TITLE: Weld Details 4

SIZE	DWG. NO.	REV
B	10.	1

SCALE: 1:5 SHEET 1 OF

ITEM NO.	PART INFO	DESCRIPTION	QTY.
1	Ice Plate	DWG 1	1
2	Dome	DWG 5	1
3	Dome Attachment Plate	DWG 4	1
4	Ice Plate Attachment Plate	DWG 2	1
5	1.25"x12TPI Bolt	2.375" long (1.5" threaded)	10
6	Square Hollow Beam	DWG 3	1
7	0.75"x16TPI Bolt	1 3/8" long (1" threaded)	4
8	XBeam Assembly	DWG 7	1

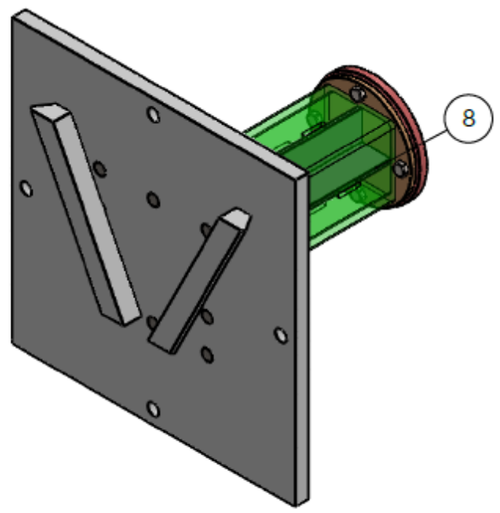

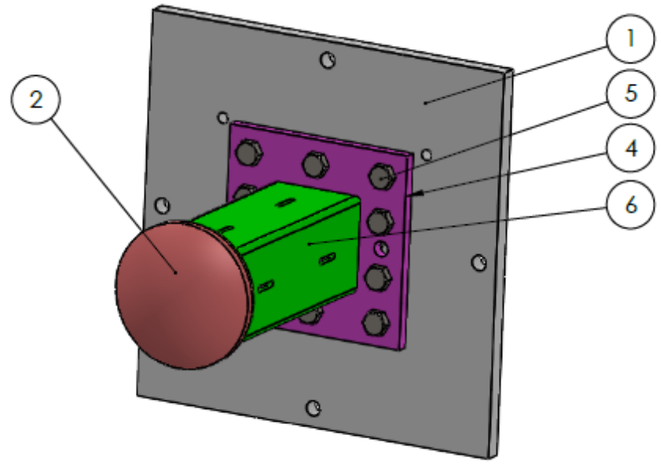

		NAME	DATE
	DRAWN	JN	06/25/19
UNLESS OTHERWISE SPECIFIED:	CHECKED		
DIMENSIONS ARE IN INCHES TOLERANCES: FRACTIONAL±	COMMENTS:		
MATERIAL			
DO NOT SCALE DRAWING			

TITLE: Full Assembly

SIZE	DWG. NO.	REV
B	11.	3

SCALE: 1:10 SHEET 1 OF

Appendix B – Exp1 Appendices

Appendix B1 – Geometry, von Mises Stress, and Maximum Displacement Visuals

Note: Since the models remained visual undeformed, the von Mises stress and displacement visuals also serve as visuals regarding the undeformed geometry.

Control – Built-T, von Mise Stress:

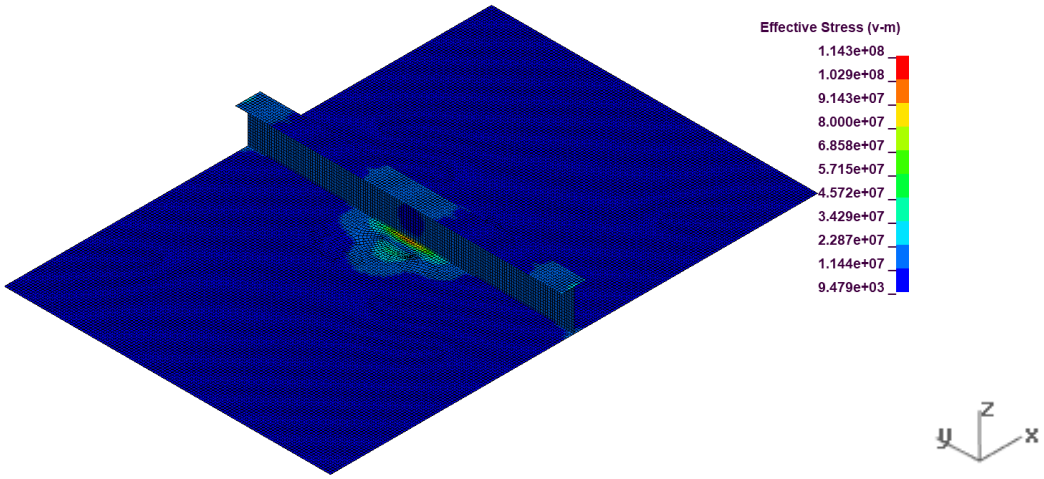

Control – Built-T, Maximum Displacement:

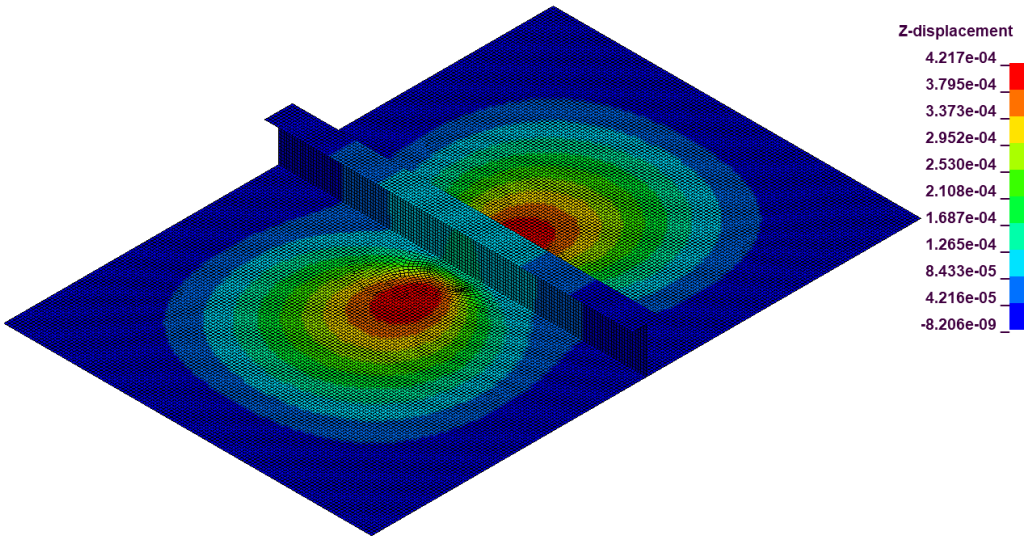

Control – Flat bar, von Mise Stress:

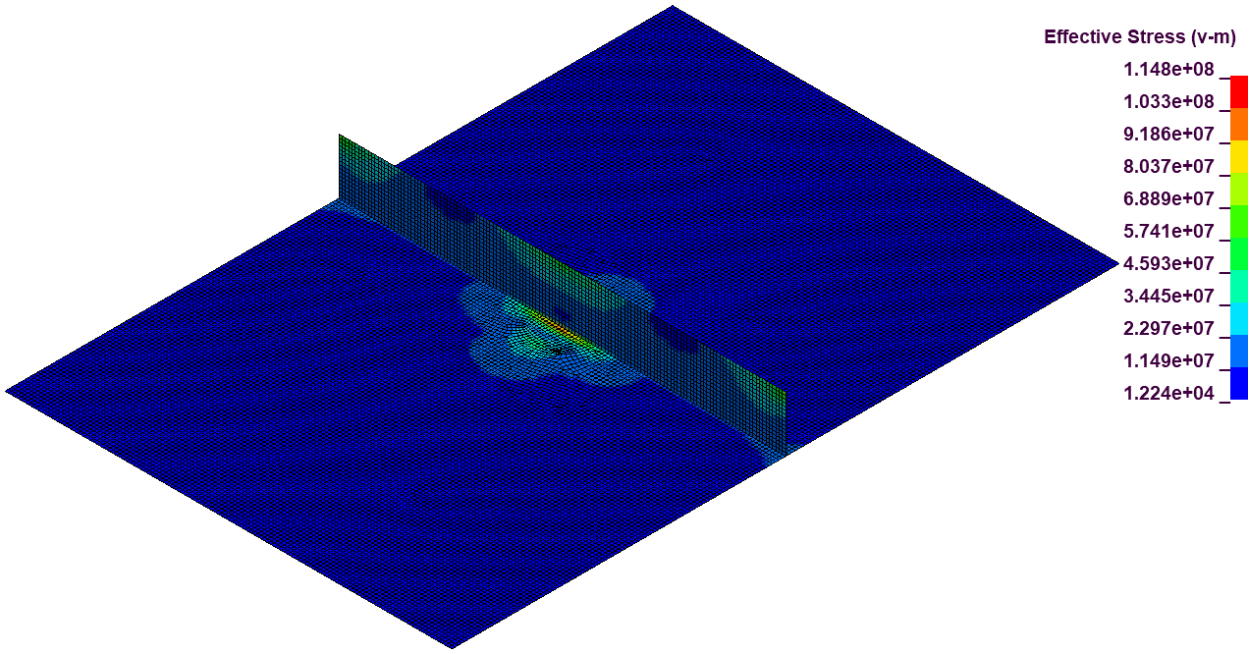

Control – Flat bar, Maximum Displacement:

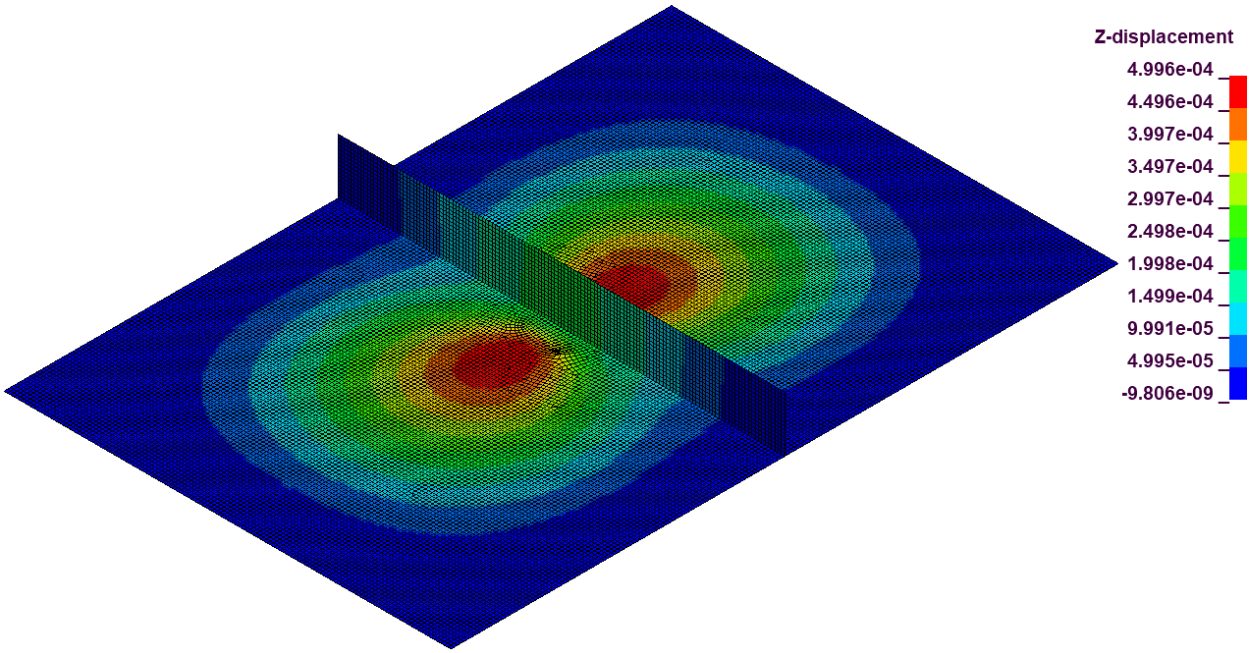

Run1, von Mise Stress:

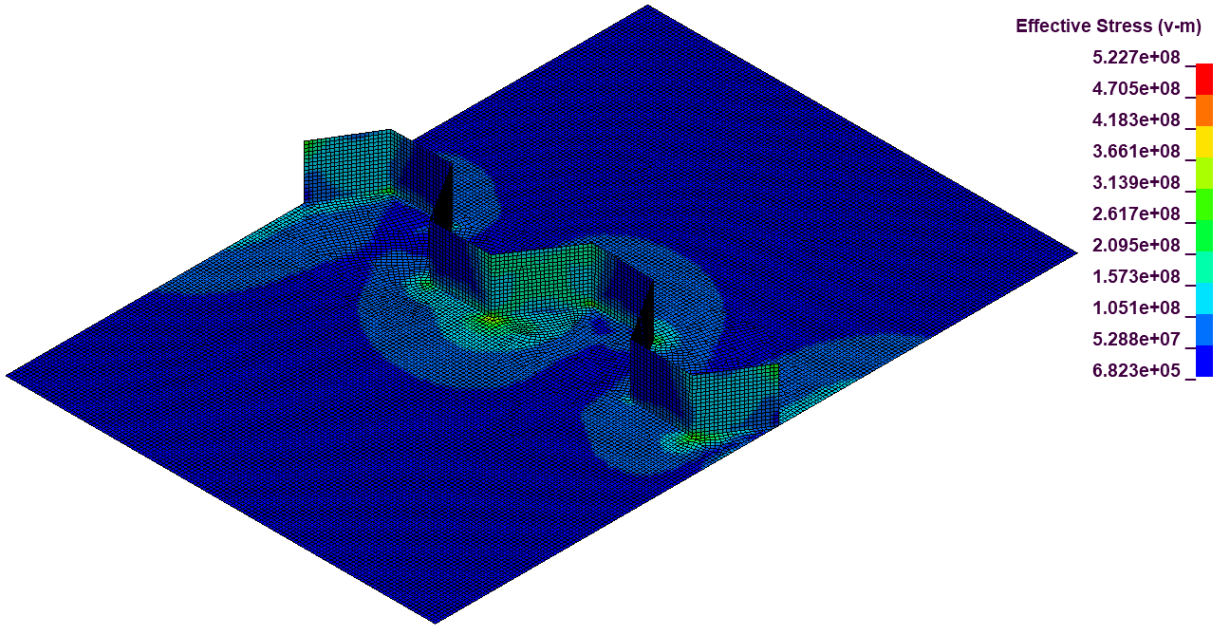

Run1, Maximum Displacement:

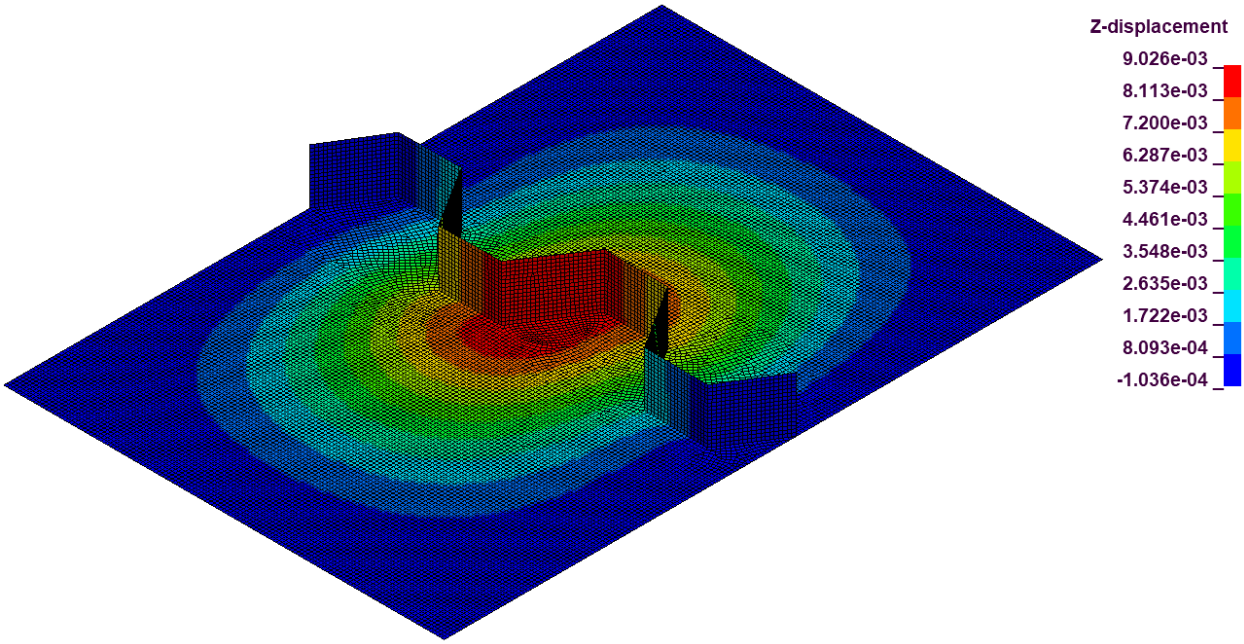

Run2, von Mise Stress:

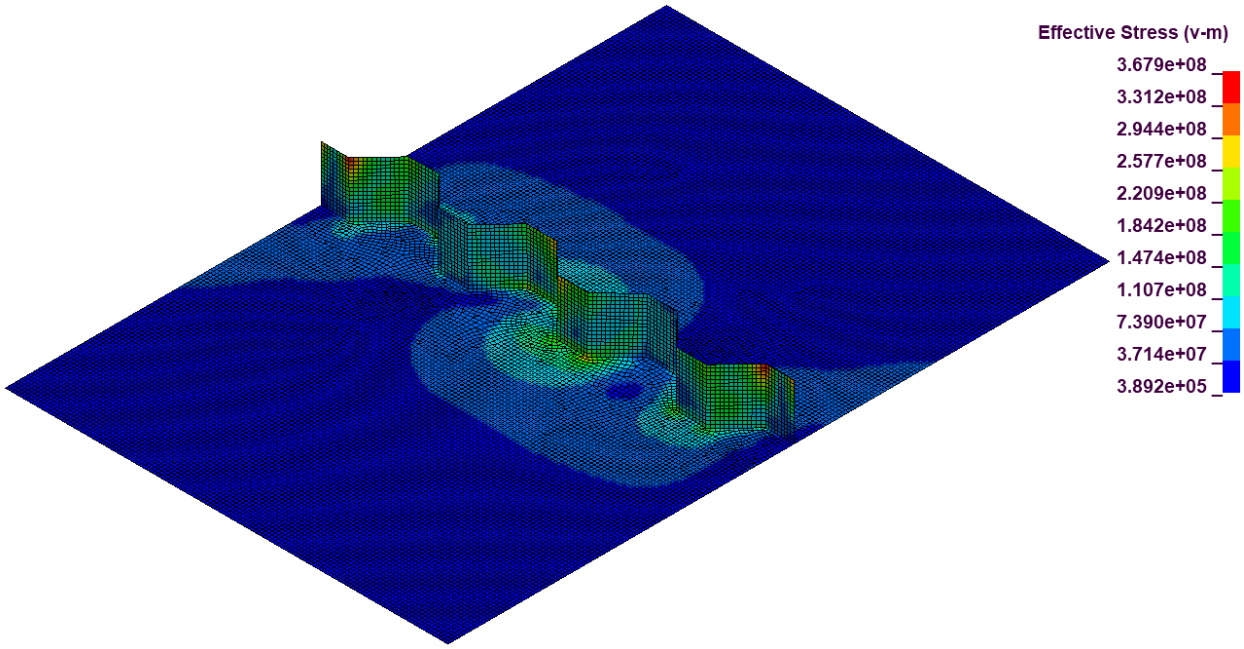

Run2, Maximum Displacement:

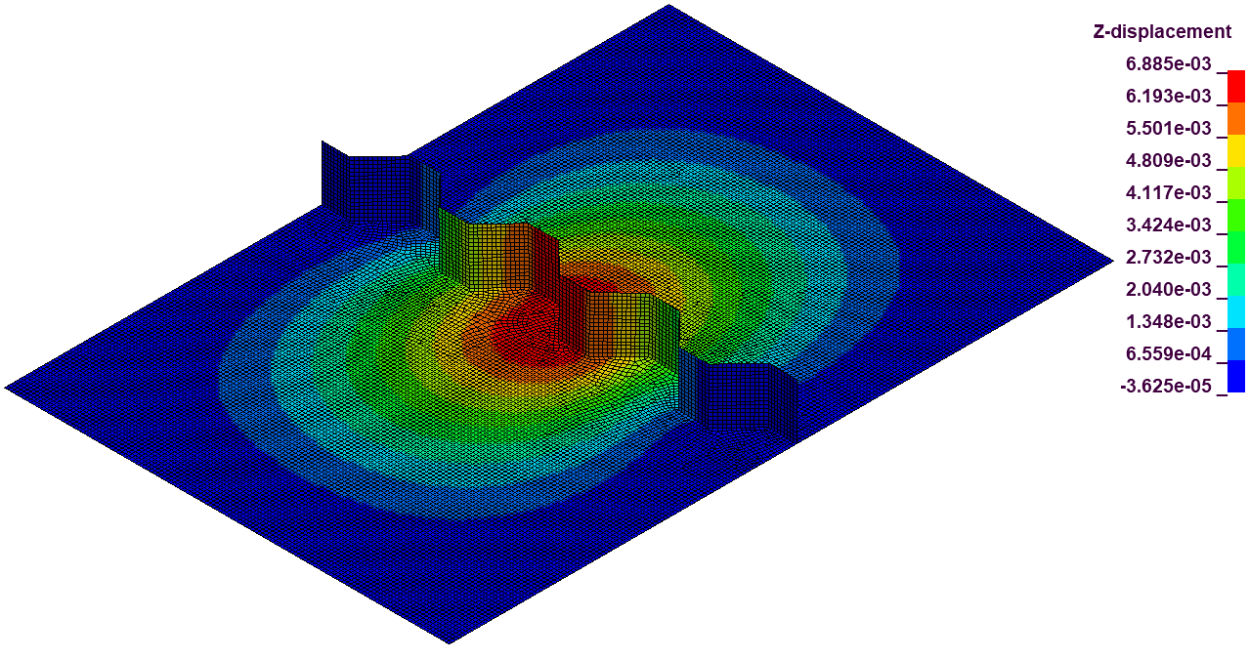

Run3, von Mise Stress:

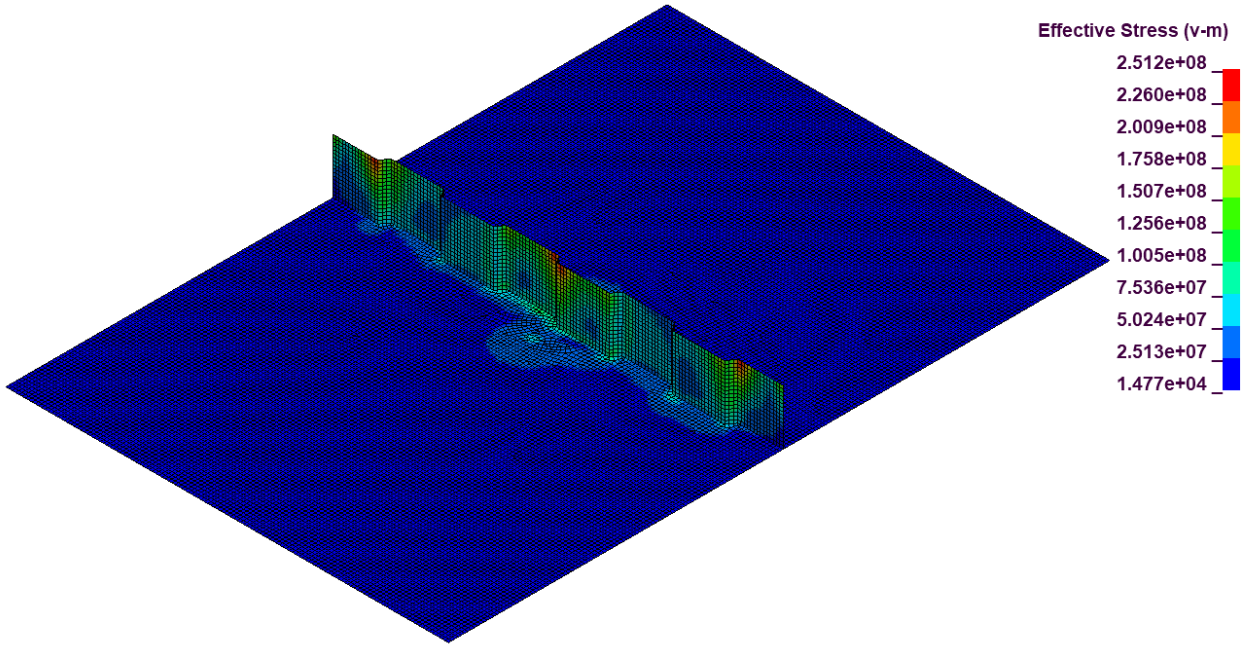

Run3, Maximum Displacement:

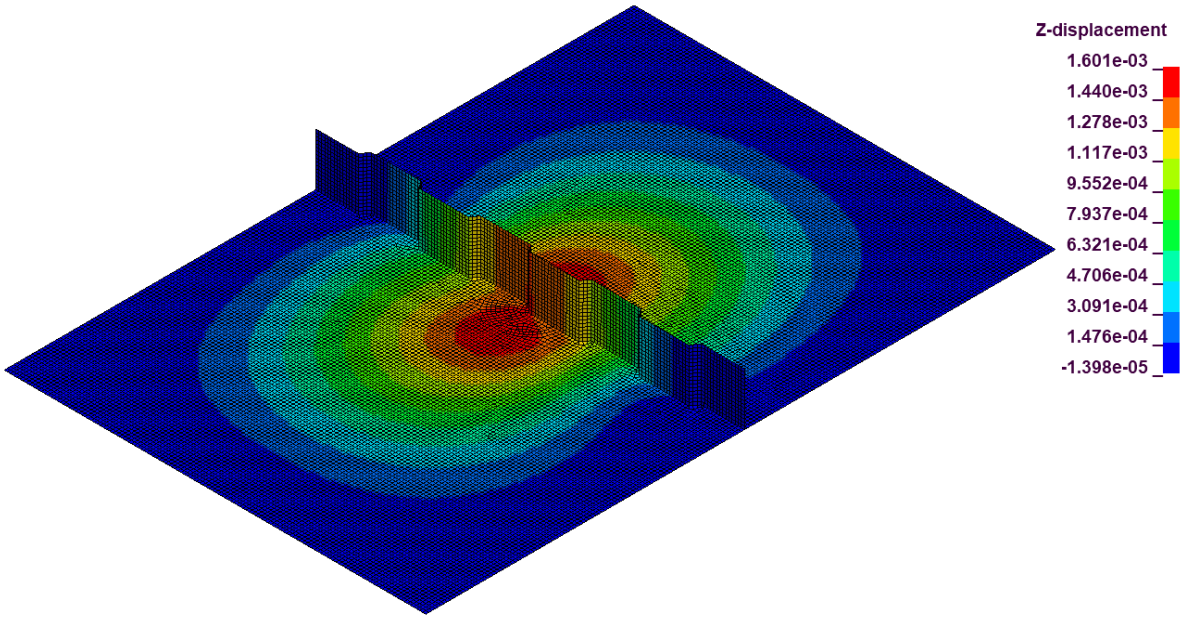

Run4, von Mise Stress:

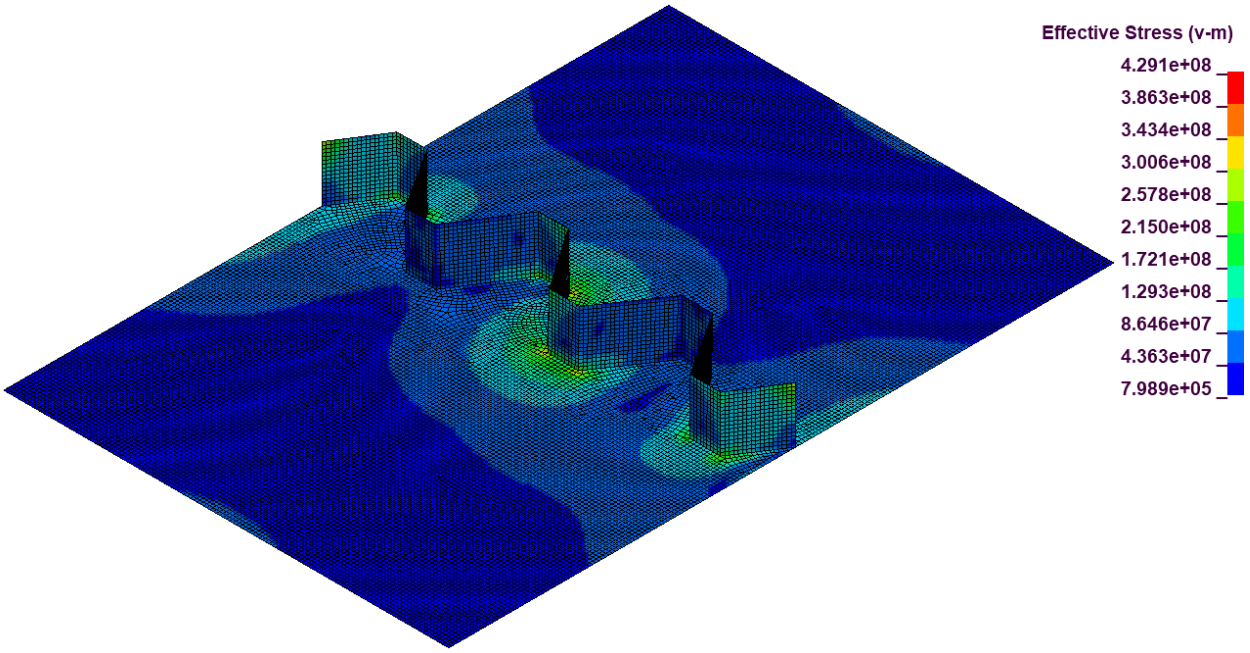

Run4, Maximum Displacement:

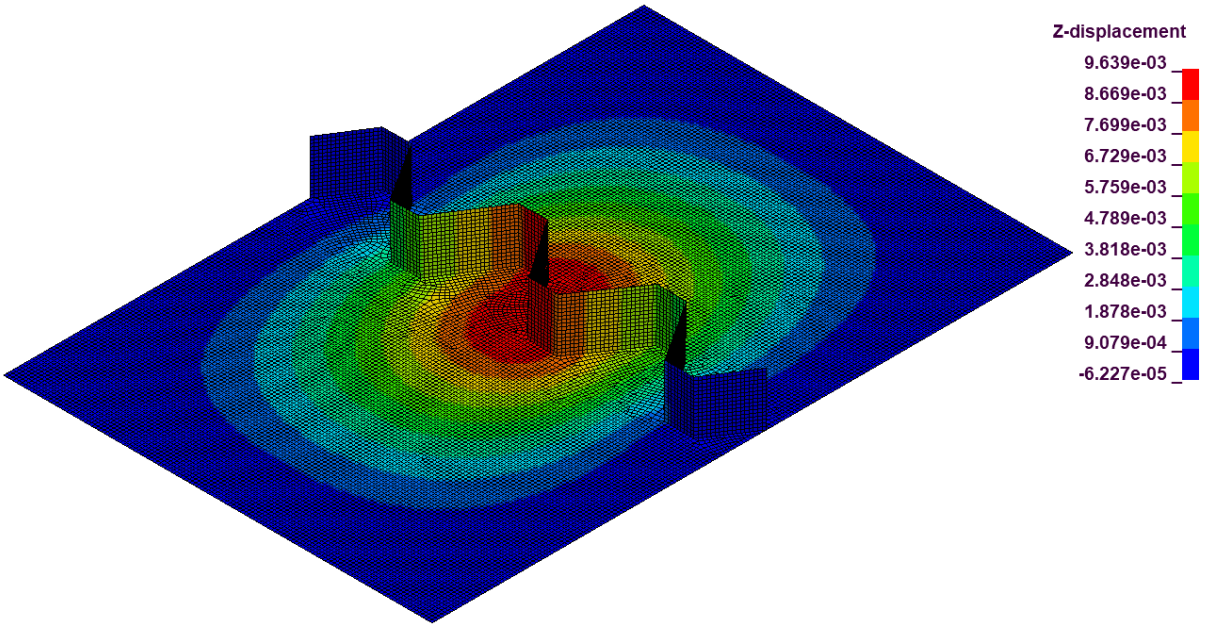

Run5, von Mise Stress:

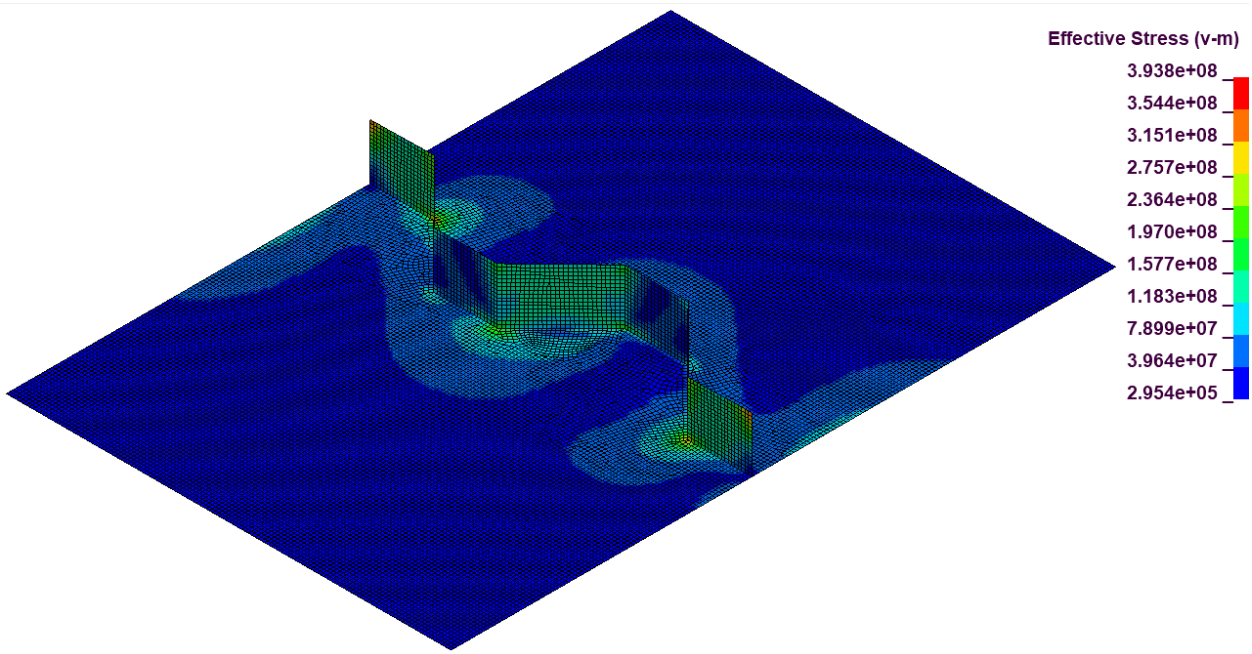

Run5, Maximum Displacement:

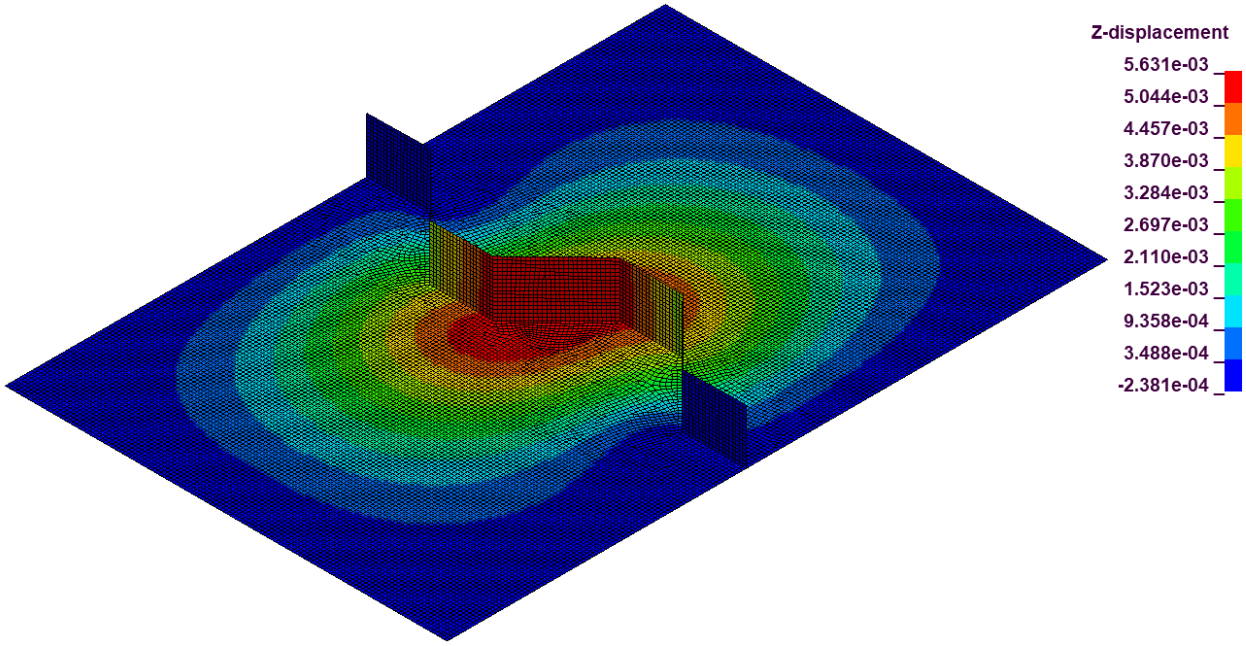

Run6, von Mise Stress:

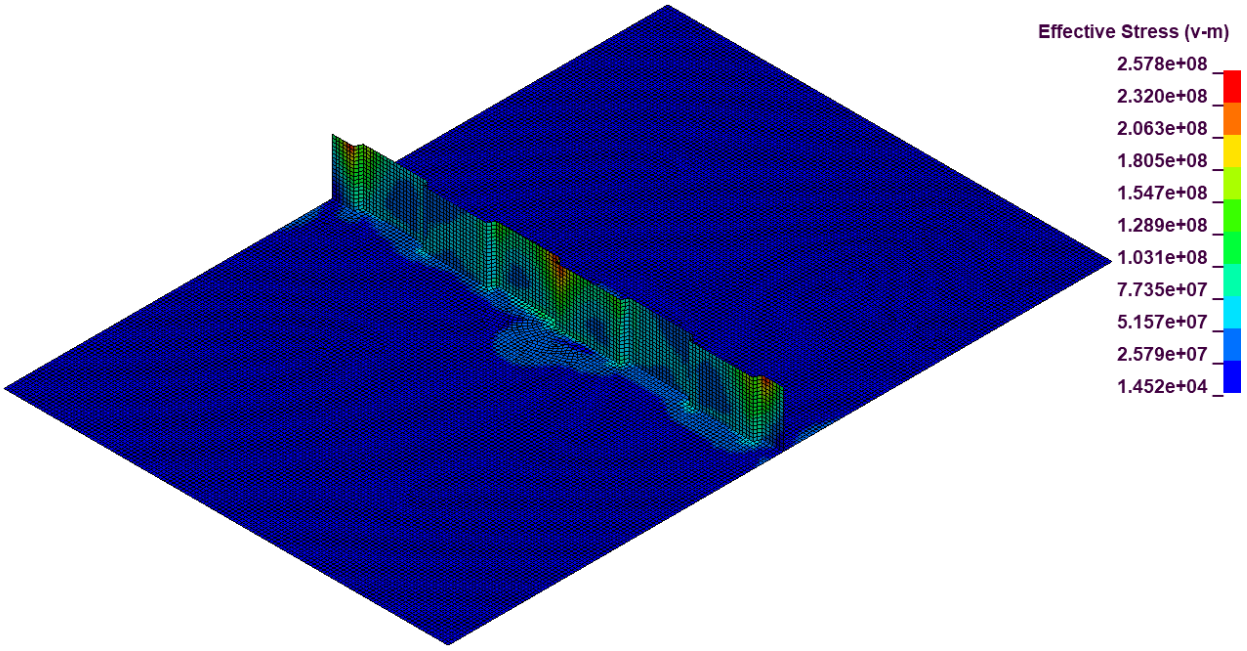

Run6, Maximum Displacement:

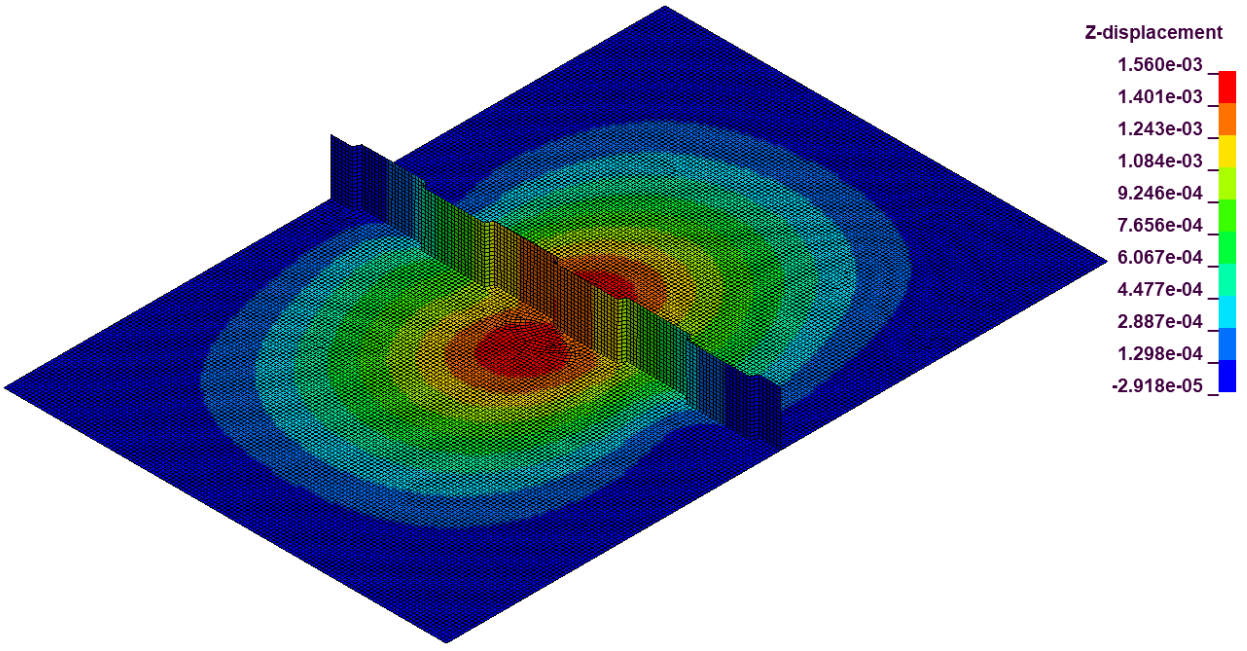

Run7, von Mise Stress:

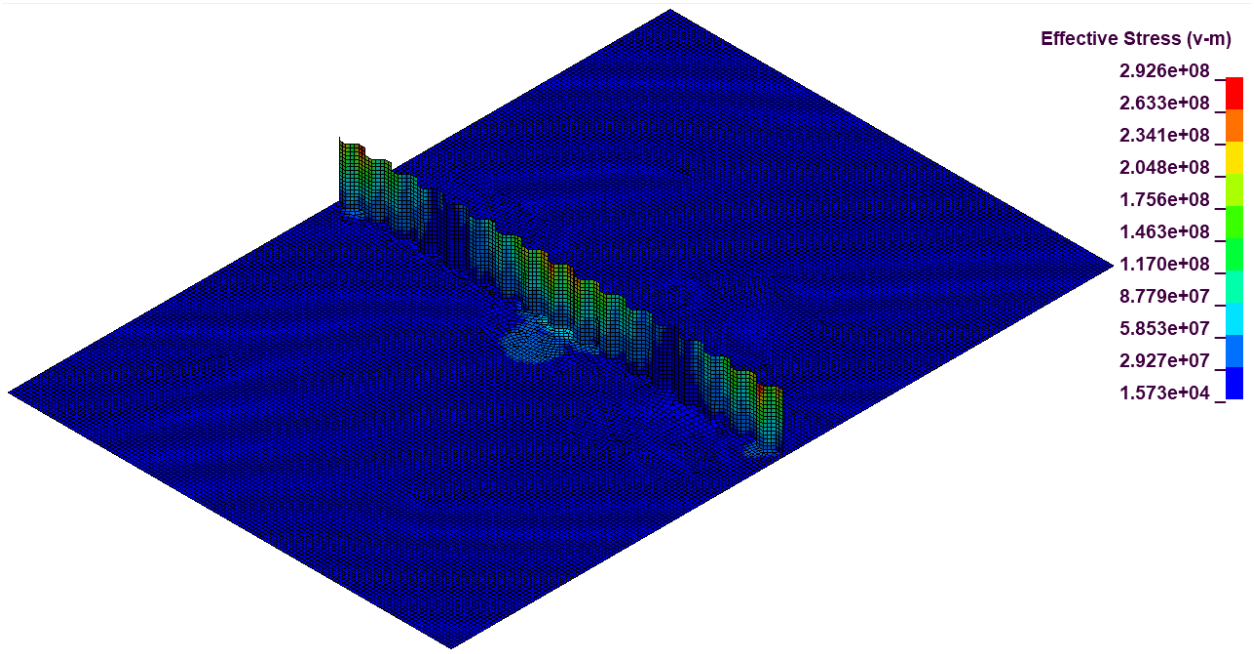

Run7, Maximum Displacement:

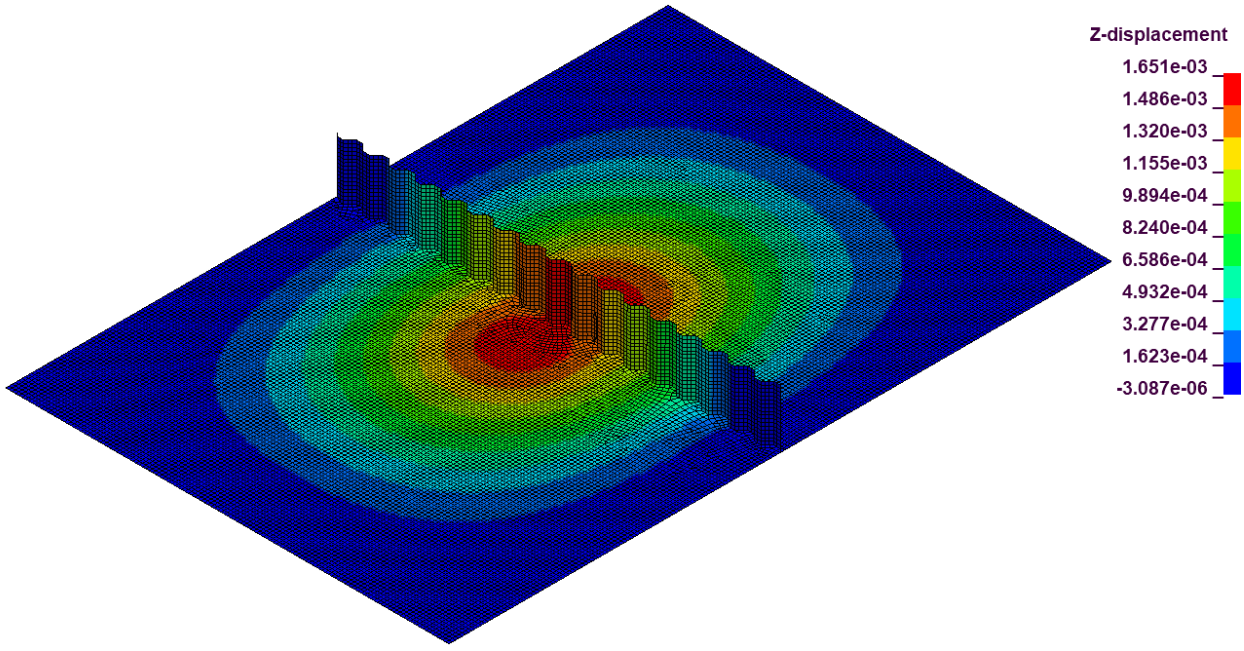

Run8, von Mise Stress:

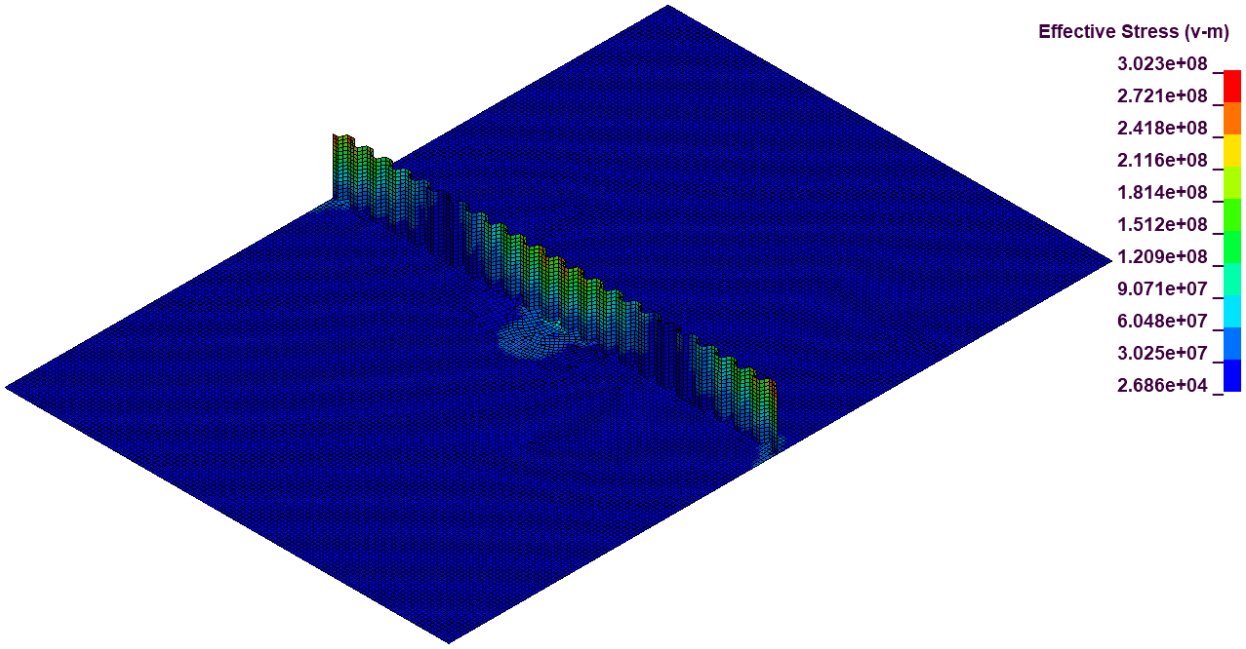

Run8, Maximum Displacement:

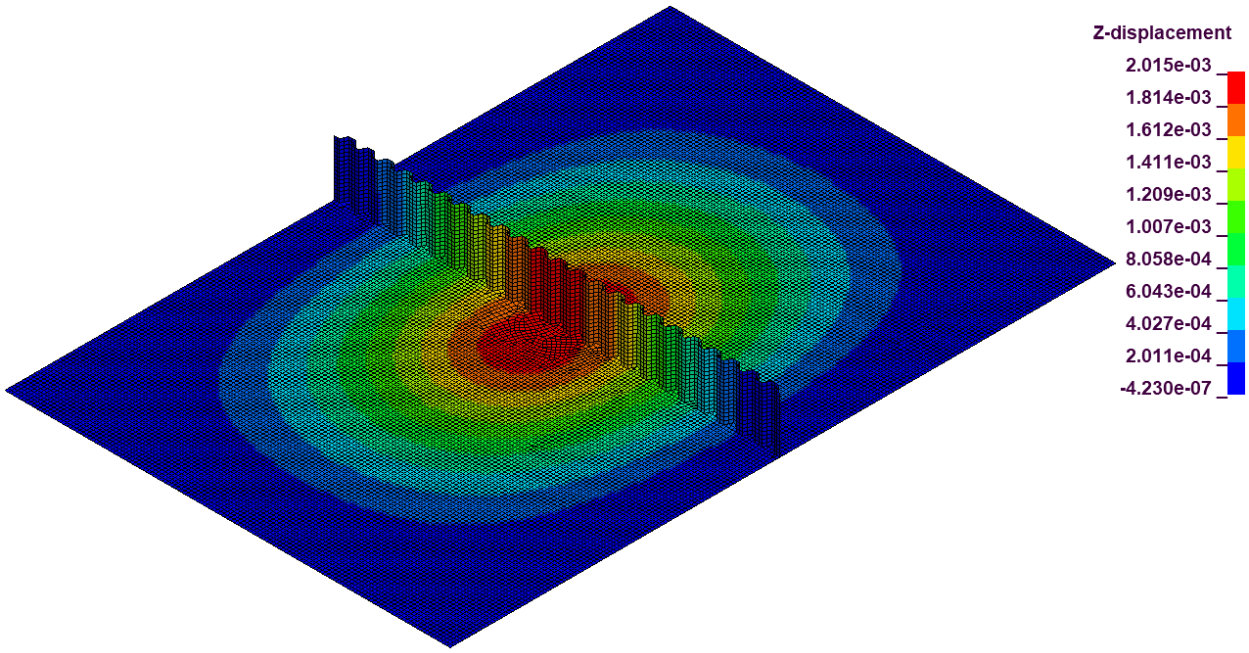

Run9, von Mise Stress:

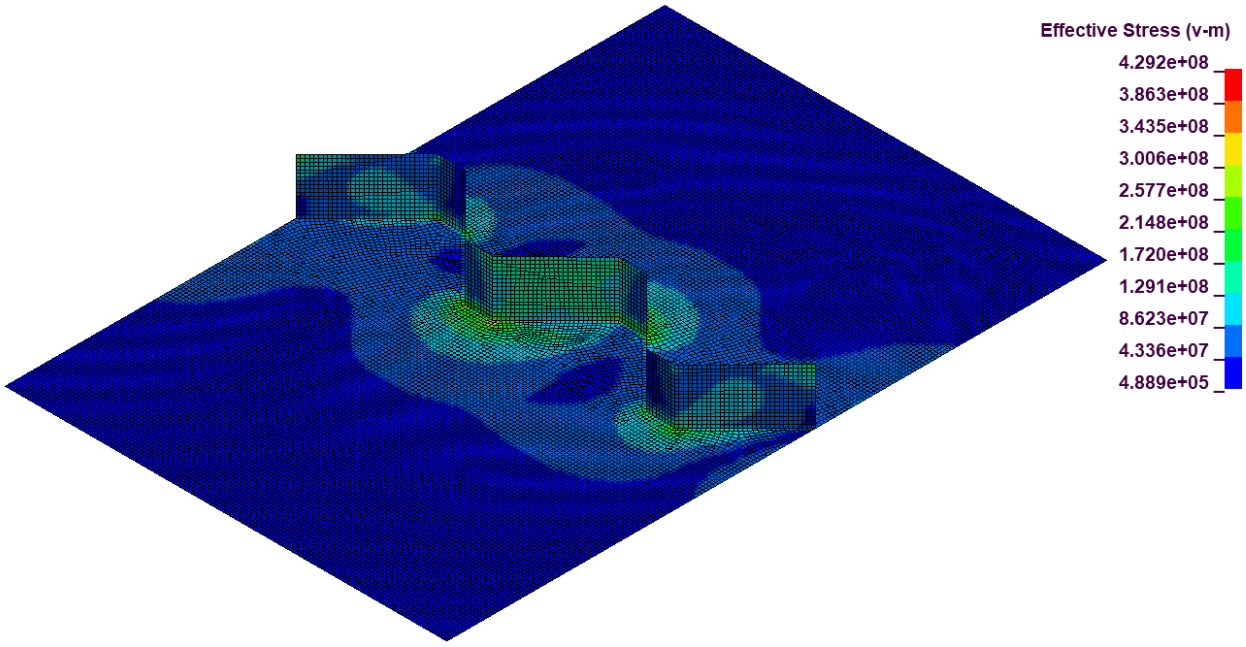

Run9, Maximum Displacement:

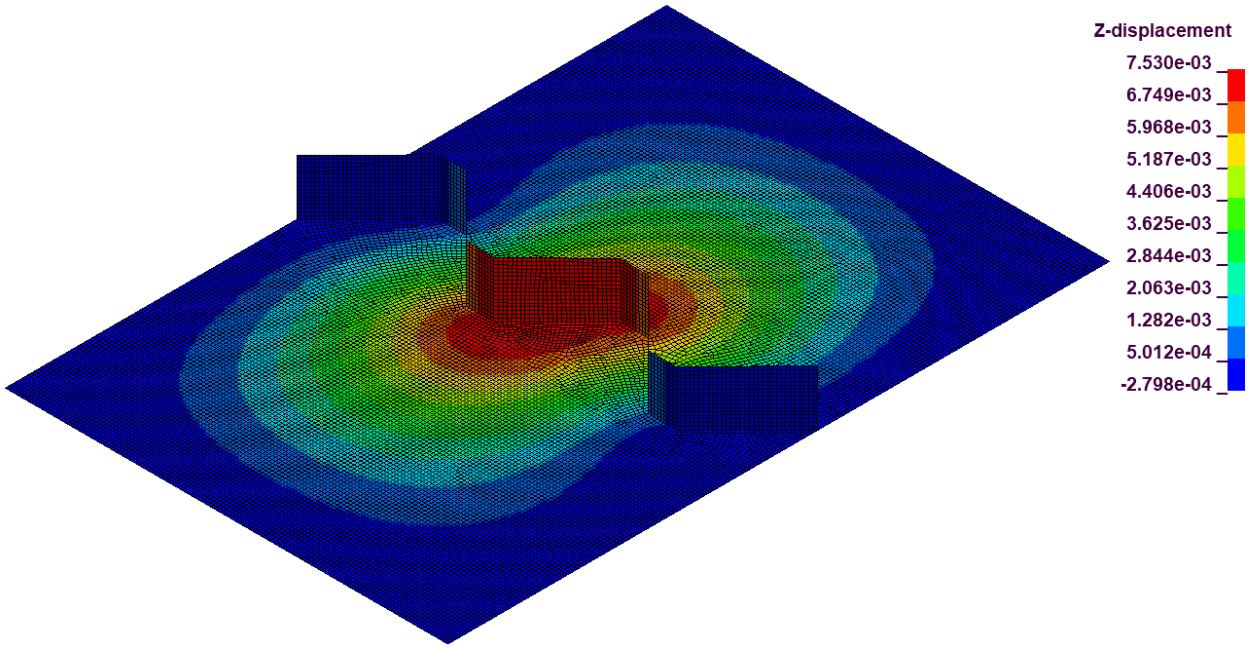

Run10, von Mise Stress:

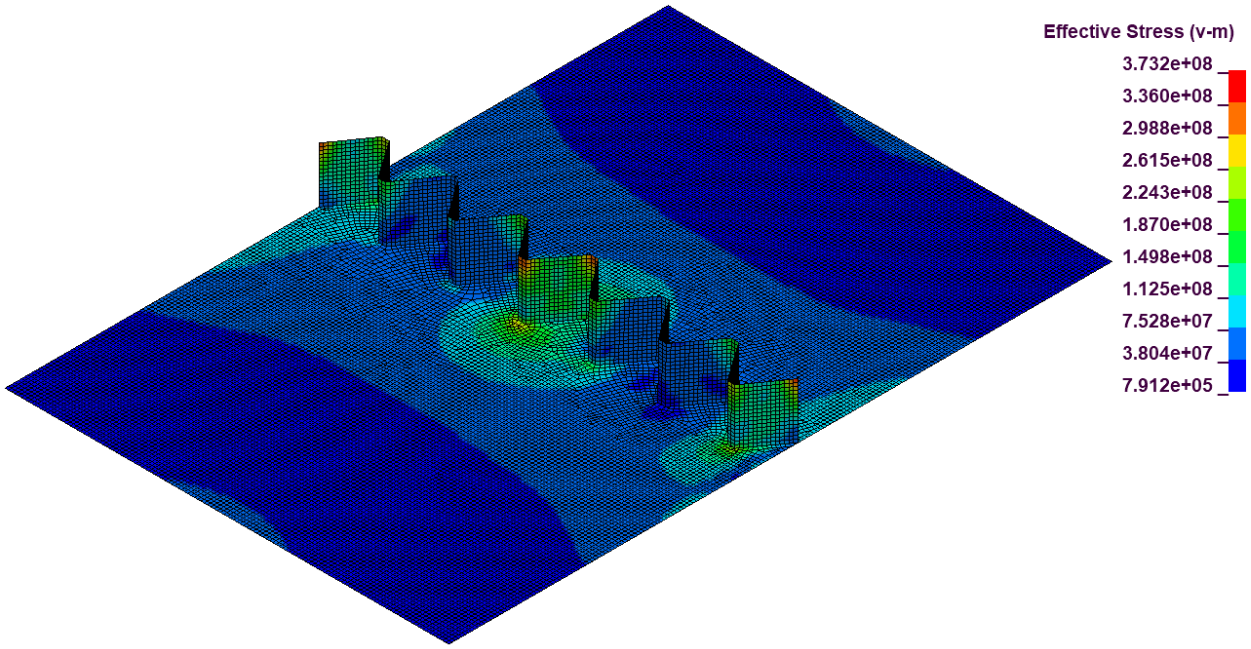

Run10, Maximum Displacement:

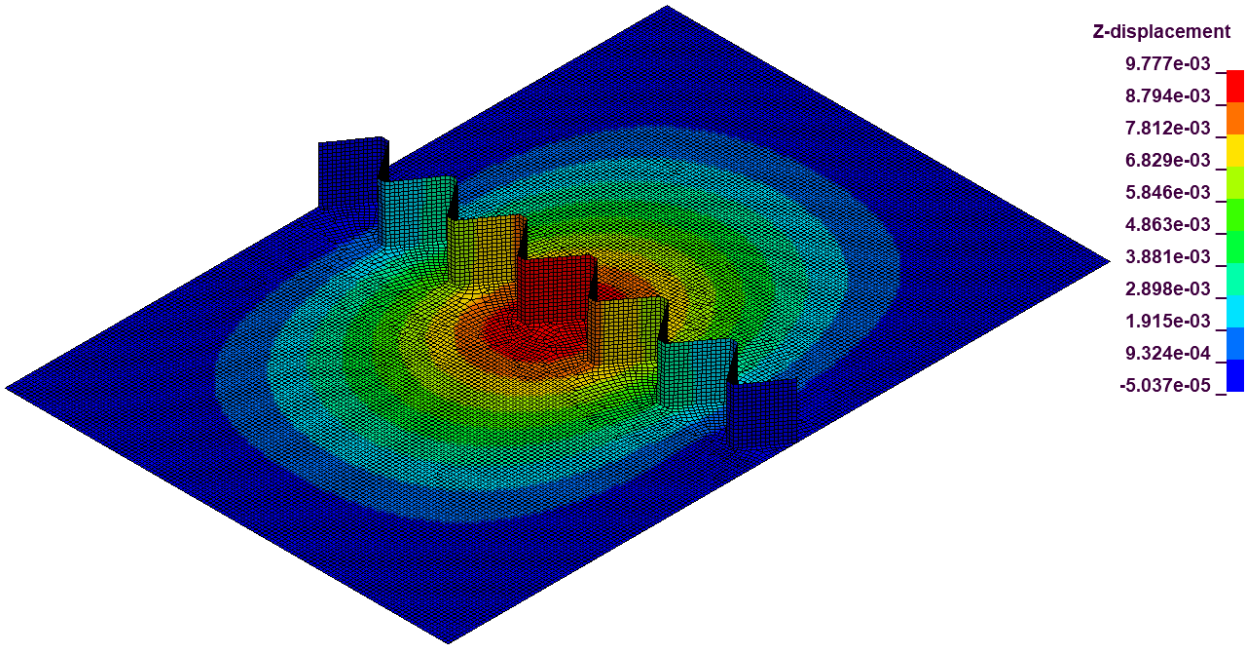

Run11, von Mise Stress:

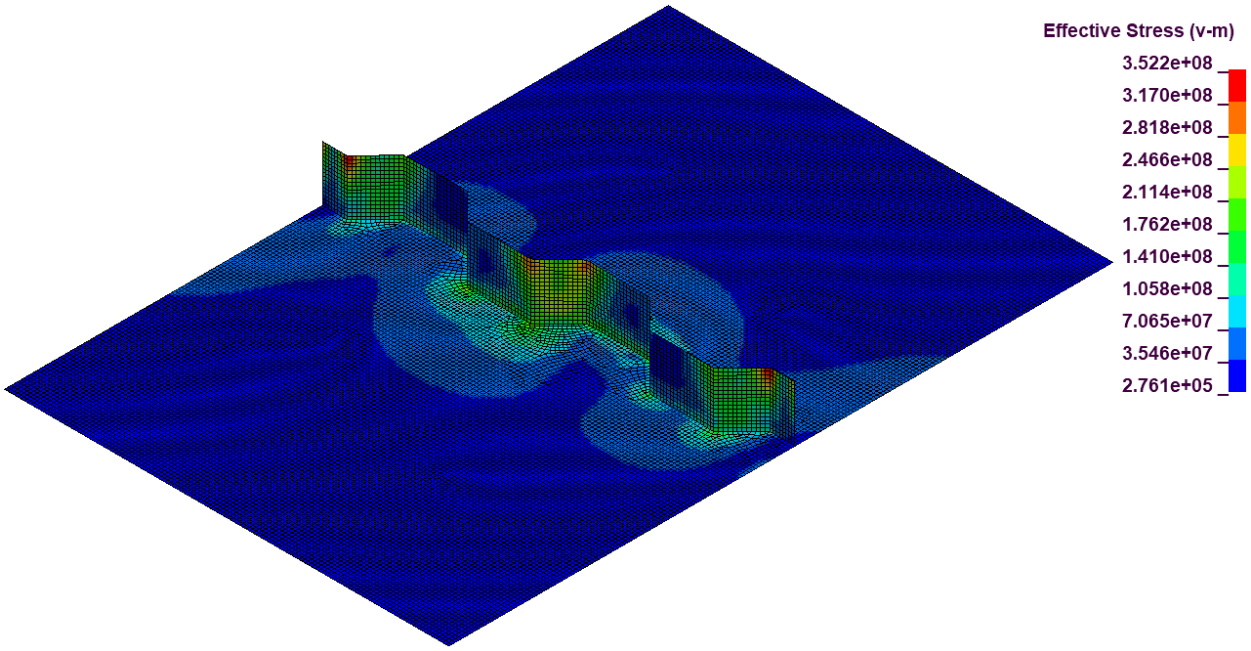

Run11, Maximum Displacement:

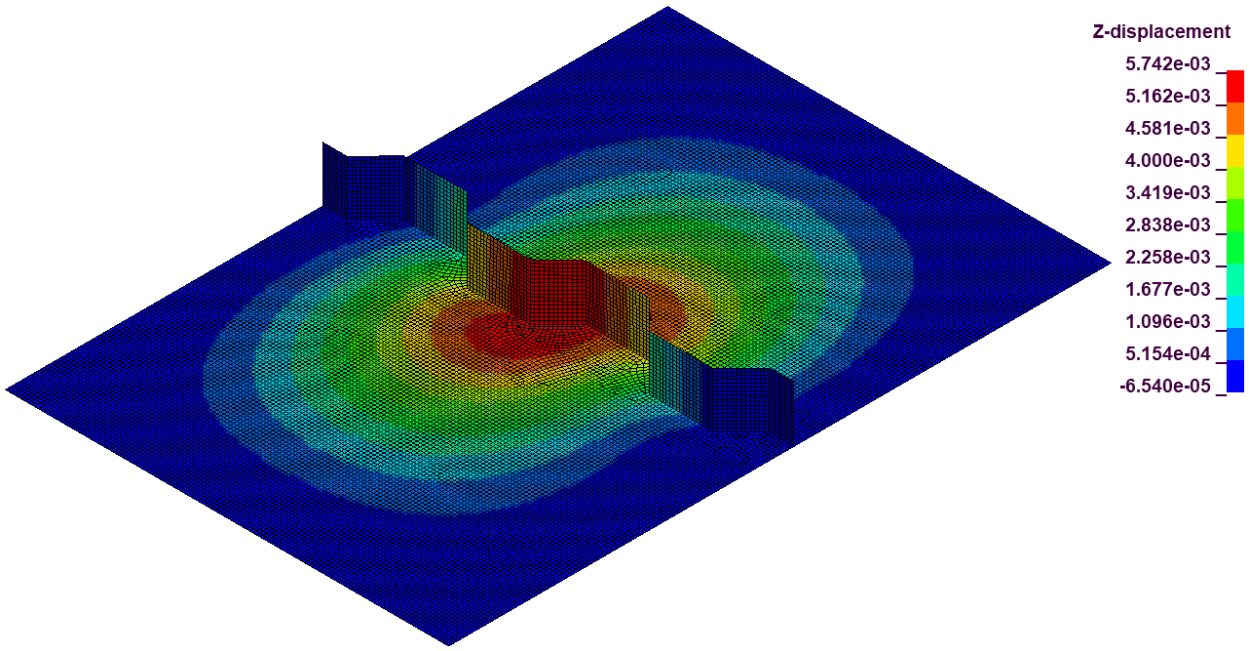

Run12, von Mise Stress:

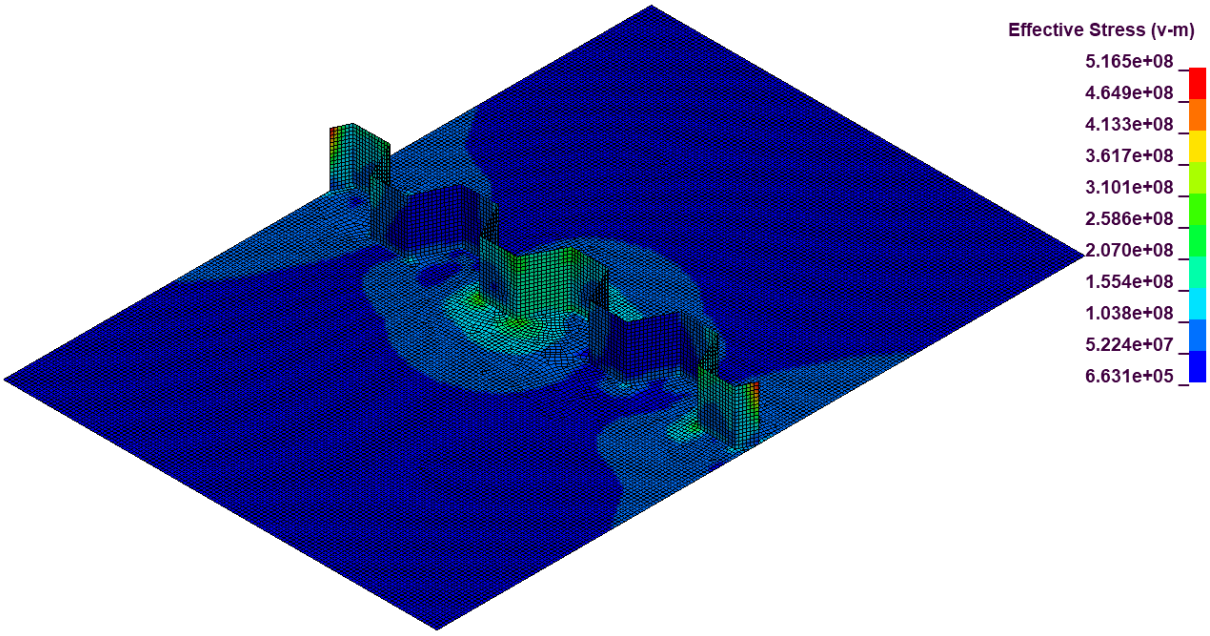

Run12, Maximum Displacement:

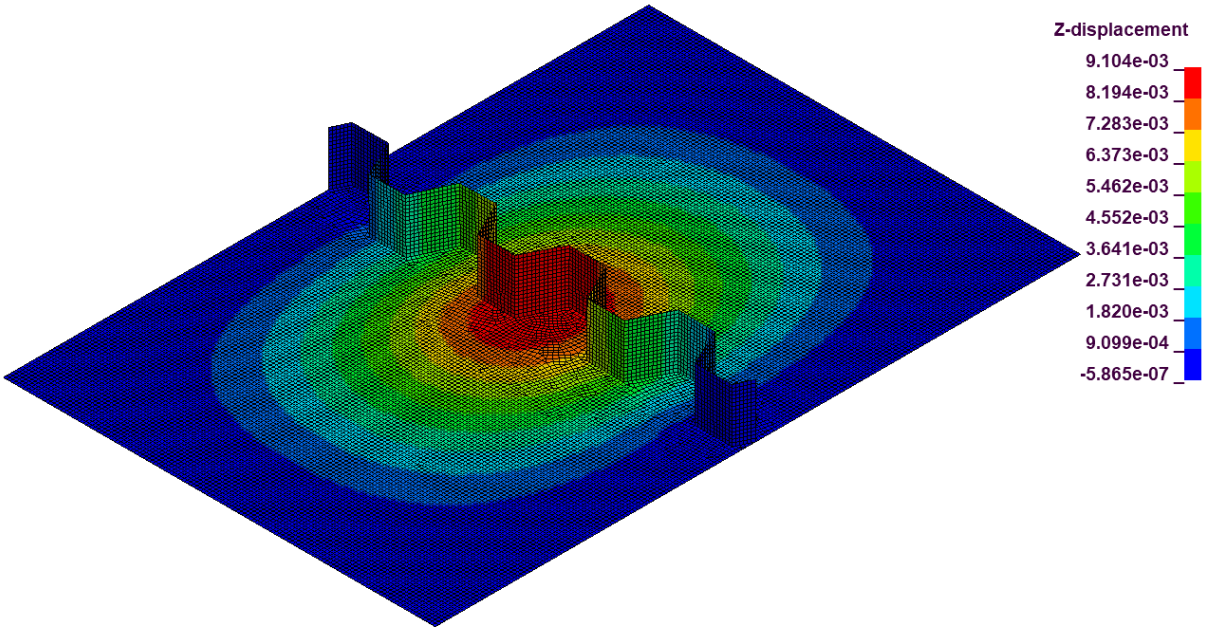

Run13, von Mise Stress:

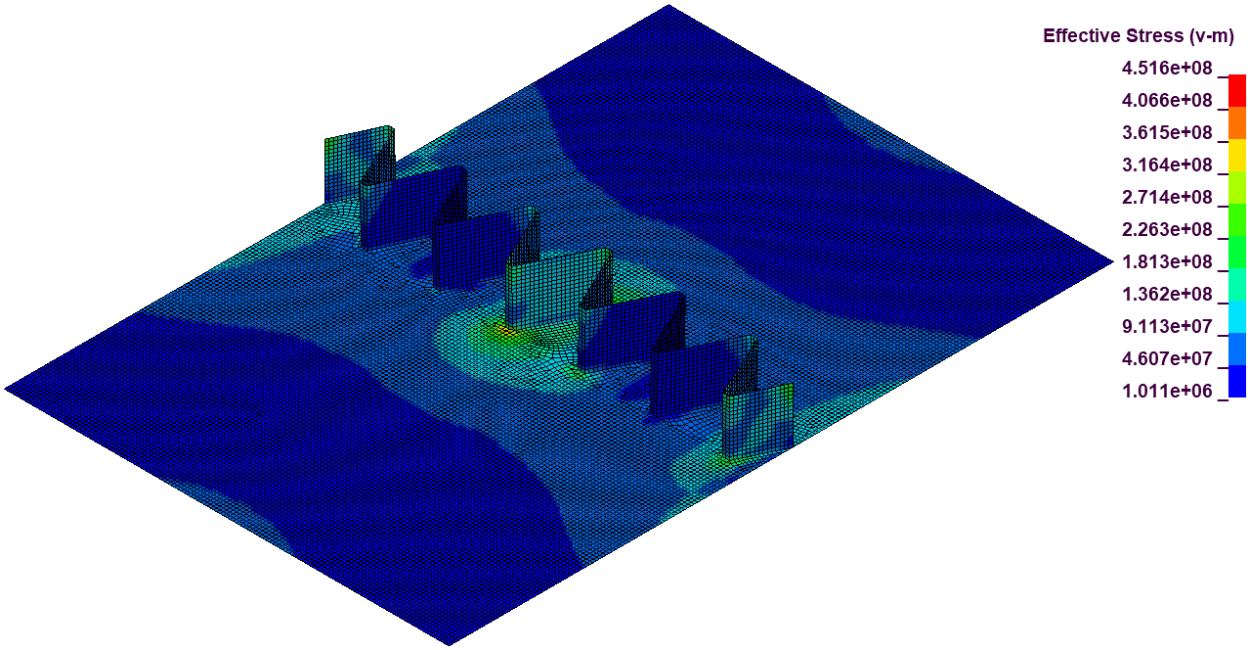

Run13, Maximum Displacement:

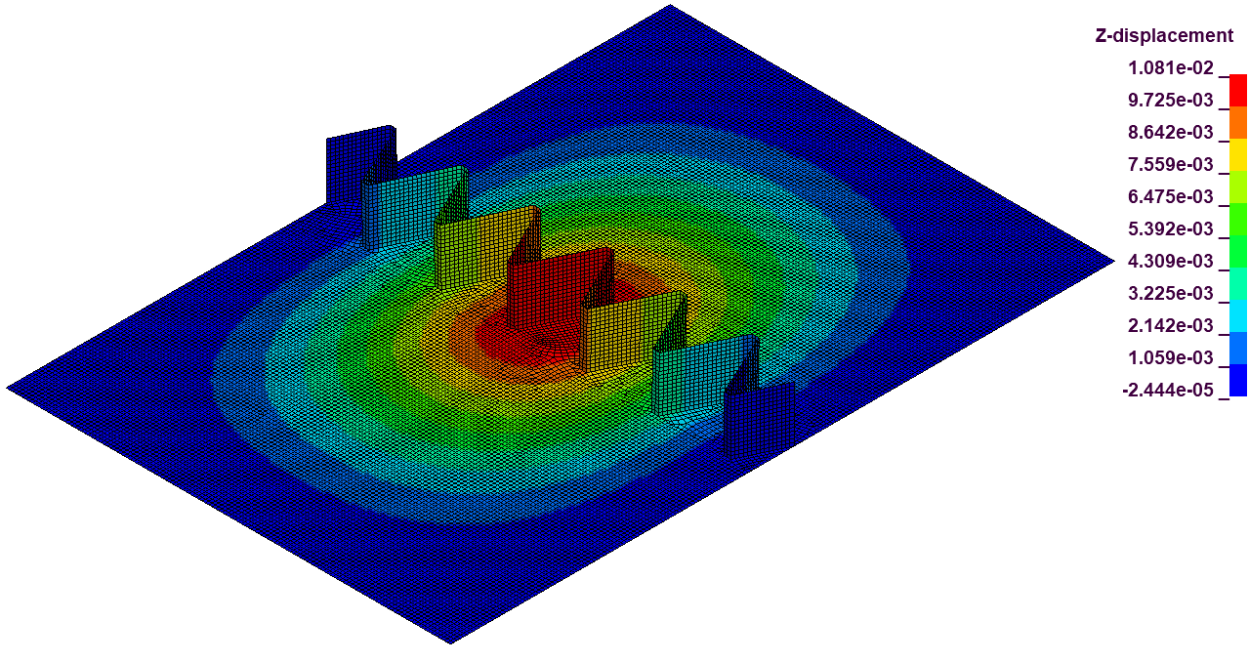

Appendix B2 – Design Expert Output

Response 1 – Weight:

Source	Sequential p-value	Lack of Fit p-value	Adjusted R^2	Predicted R^2	
Linear	**0.0002**		**0.8443**	**0.7148**	**Suggested**
2FI	0.0570		0.9276	0.7694	
Quadratic	0.7683		0.8961	-0.0224	
Cubic					Aliased

Source	Sum of Squares	df	Mean Square	F-value	p-value	
Model	0.0001	2	0.0000	25.26	0.0001	significant
A-Depth of Waveform	0.0000	1	0.0000	29.82	0.0003	
C-Angle of Waveform	0.0000	1	0.0000	15.50	0.0028	
Residual	0.0000	10	1.354E-06			
Cor Total	0.0001	12				

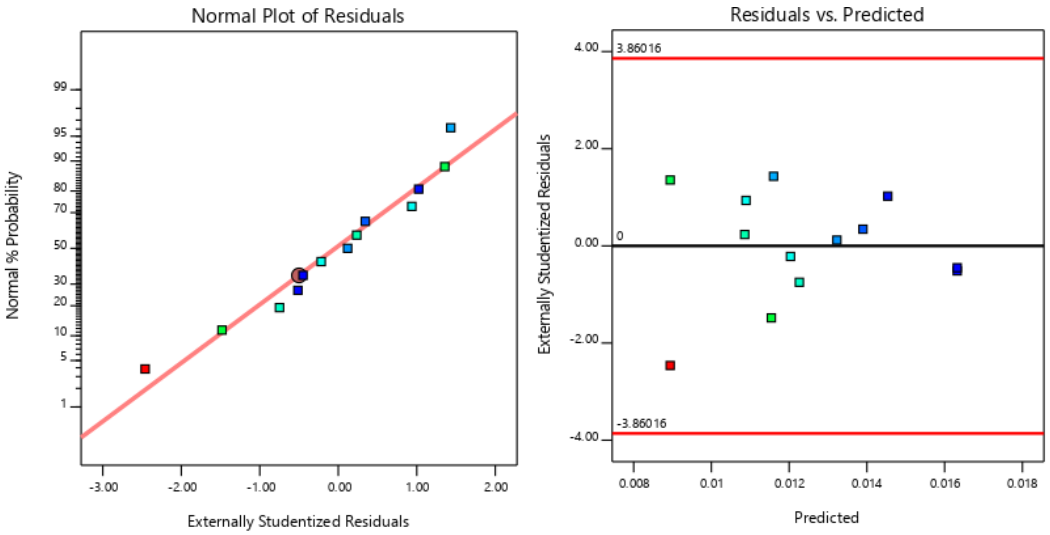

Response 2 – Displacement:

Source	Sequential p-value	Lack of Fit p-value	Adjusted R^2	Predicted R^2	
Linear	0.0041		0.6742	0.5155	
2FI	0.5292		0.6532	-0.1432	
Quadratic	**0.0046**		**0.9865**	**0.8483**	**Suggested**
Cubic					Aliased

Source	Sum of Squares	df	Mean Square	F-value	p-value	
Model	145.74	5	29.15	95.38	< 0.0001	significant
A-Depth of Waveform	115.08	1	115.08	376.55	< 0.0001	
B-Breadth of Waveform	2.74	1	2.74	8.97	0.0201	
C-Angle of Waveform	9.03	1	9.03	29.56	0.0010	
AC	2.65	1	2.65	8.68	0.0215	
A^2	26.11	1	26.11	85.45	< 0.0001	
Residual	2.14	7	0.3056			
Cor Total	147.88	12				

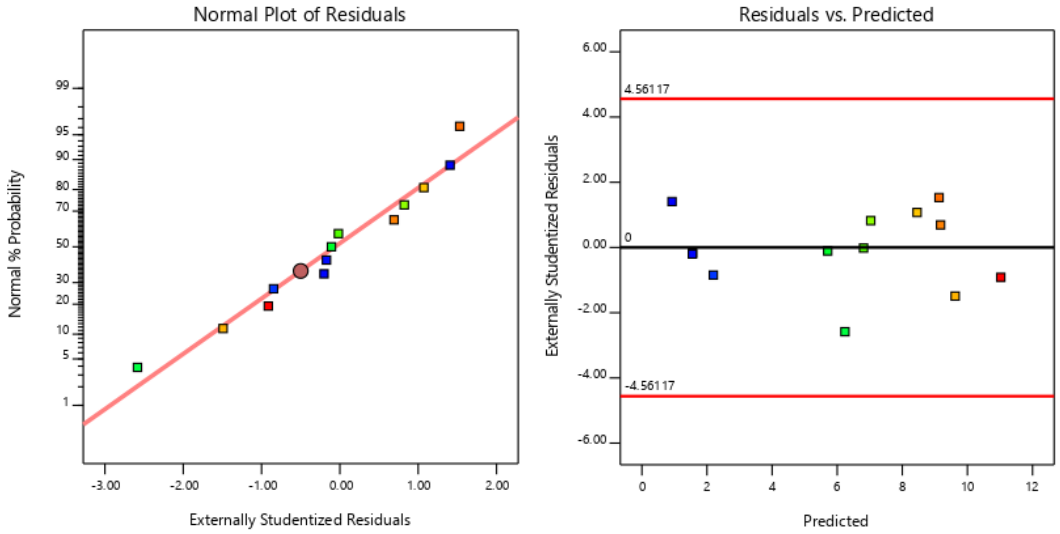

Appendix B3 – Element Quality Checks

Quality Name	Min. val	Max. val	Allowable	#Violated(%)
Aspect Ratio	1	2.17	10	0(0%)
Warpage	0	0.141	10	0(0%)
Min Quad Angle	44	90	45	1(0.0033%)
Max Quad Angle	90	144	135	5(0.0165%)
Min Tria Angle	40	58.9	30	0(0%)
Max Tria Angle	61.7	94.8	120	0(0%)
Skew	0	35.3	45	0(0%)
Jacobian	0.617	1	0.6	0(0%)

#QUADS(%):30119(99.5%), #TRIAS(%):160(0.528%), #TOTAL OF FAILED(%):0(0%)

Appendix C – Exp2 Appendices

Appendix C1 – Geometry and von Mises Stress Visuals

Control – Built-T, Geometry:

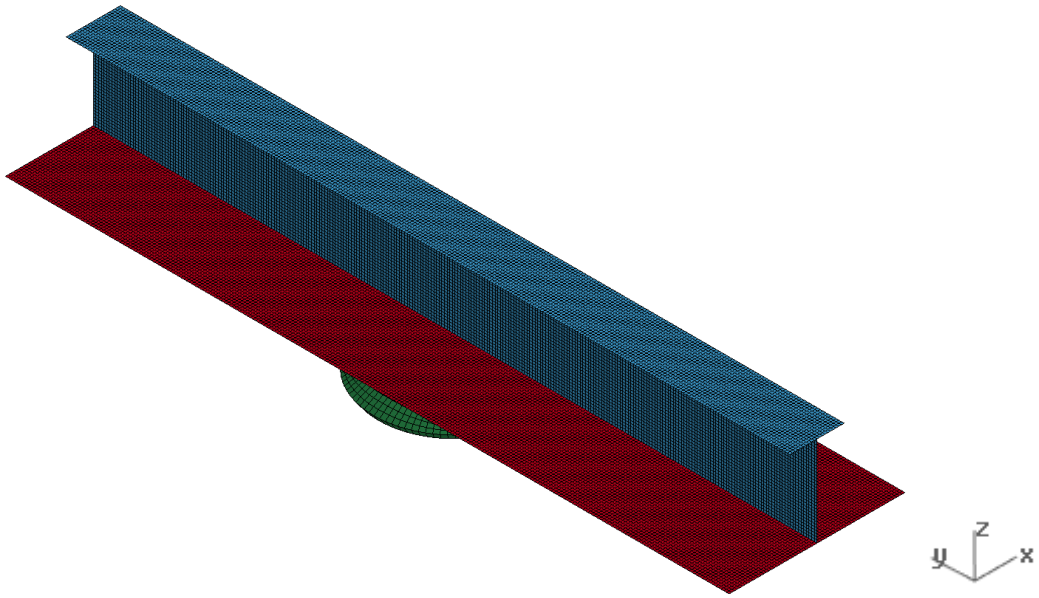

Control – Built-T, von Mise Stress:

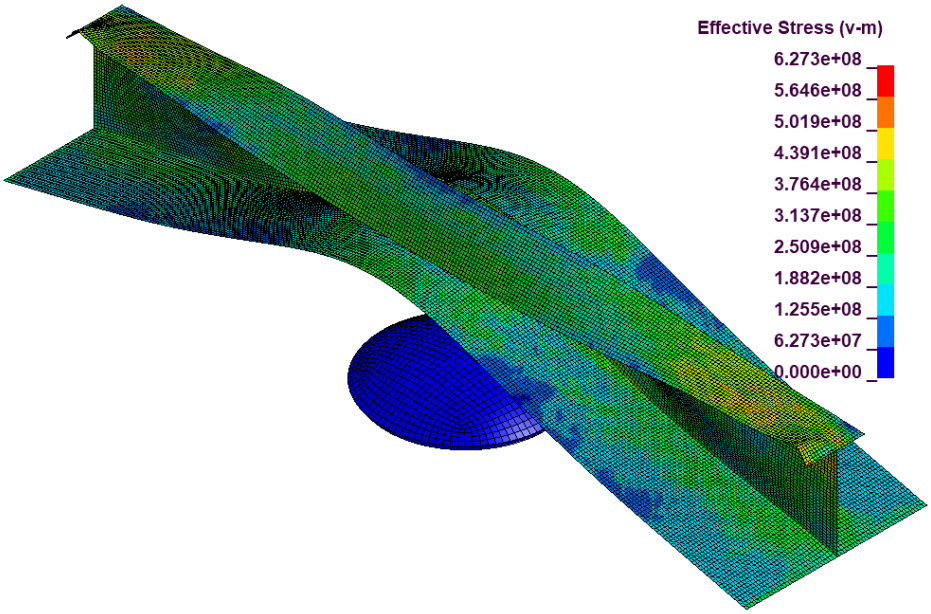

Control – Flat Bar, Geometry:

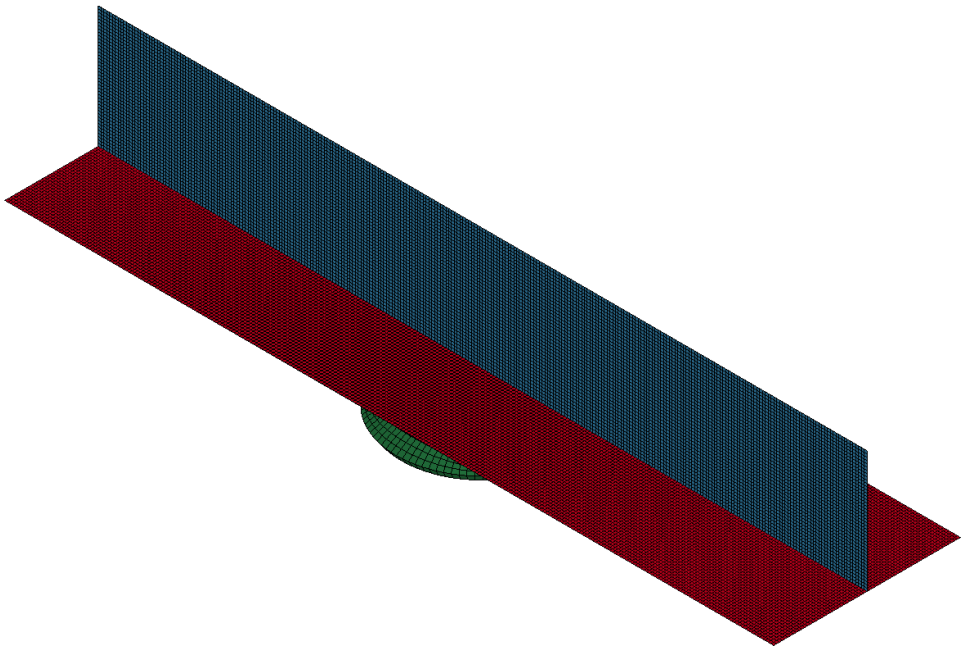

Control – Flat Bar, von Mise Stress:

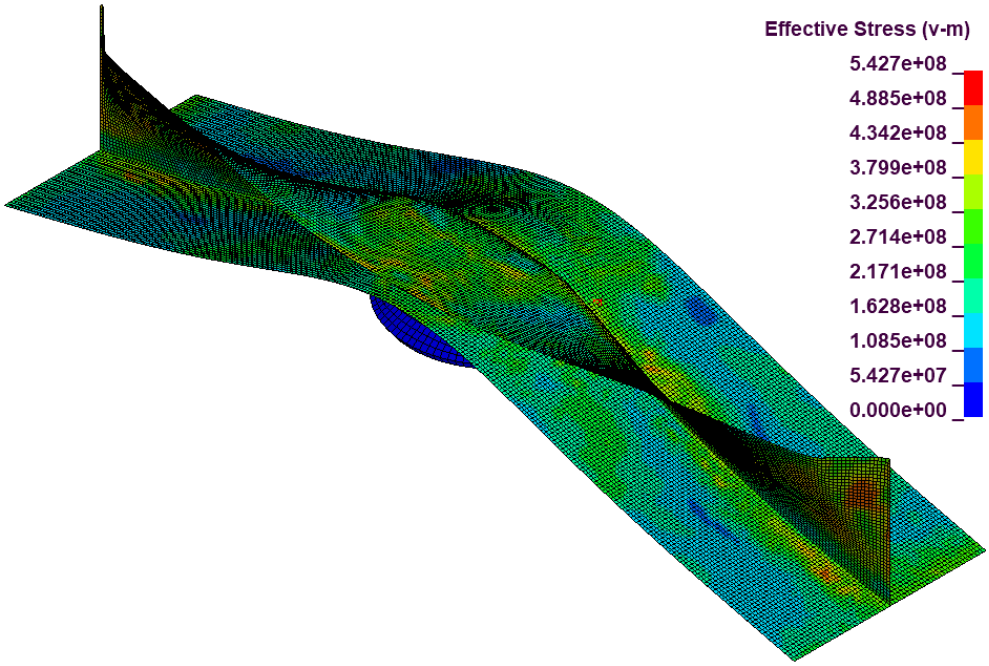

Trad. Corr. 1, Geometry:

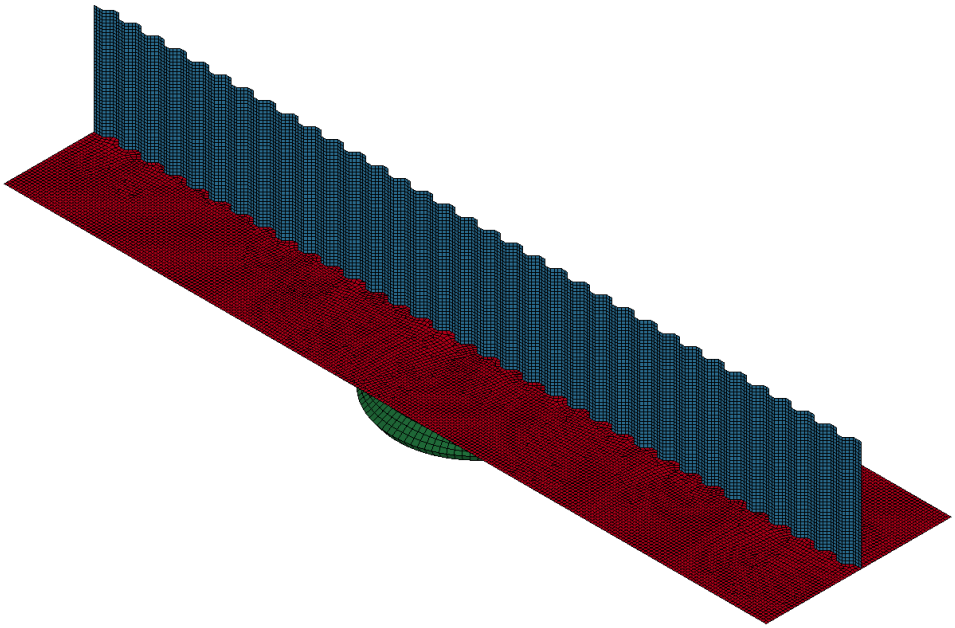

Trad. Corr. 1, von Mise Stress:

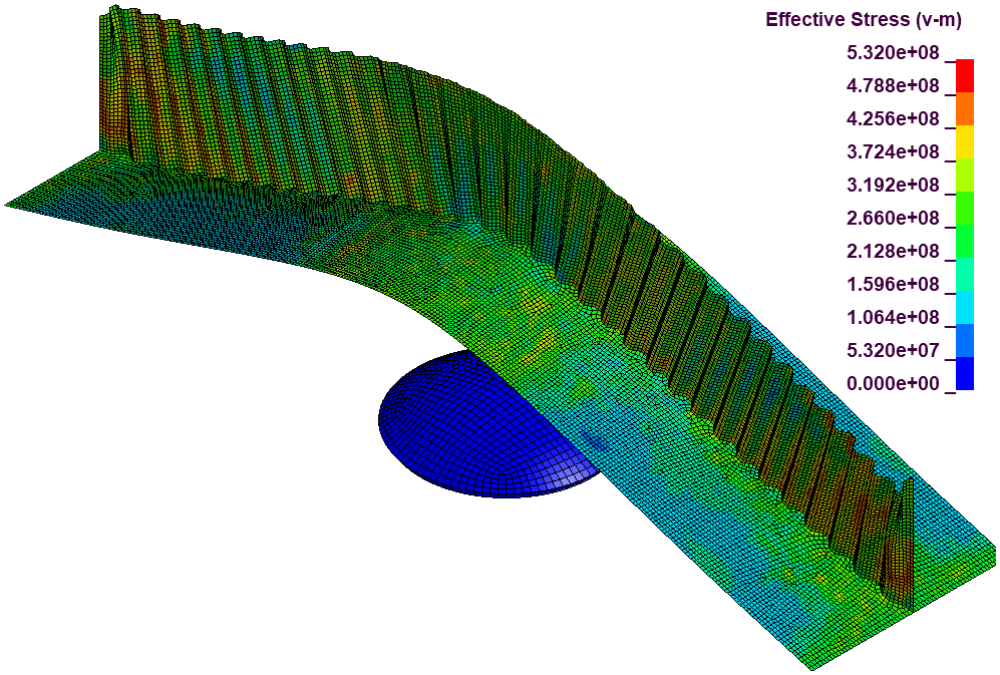

Trad. Corr. 2, Geometry:

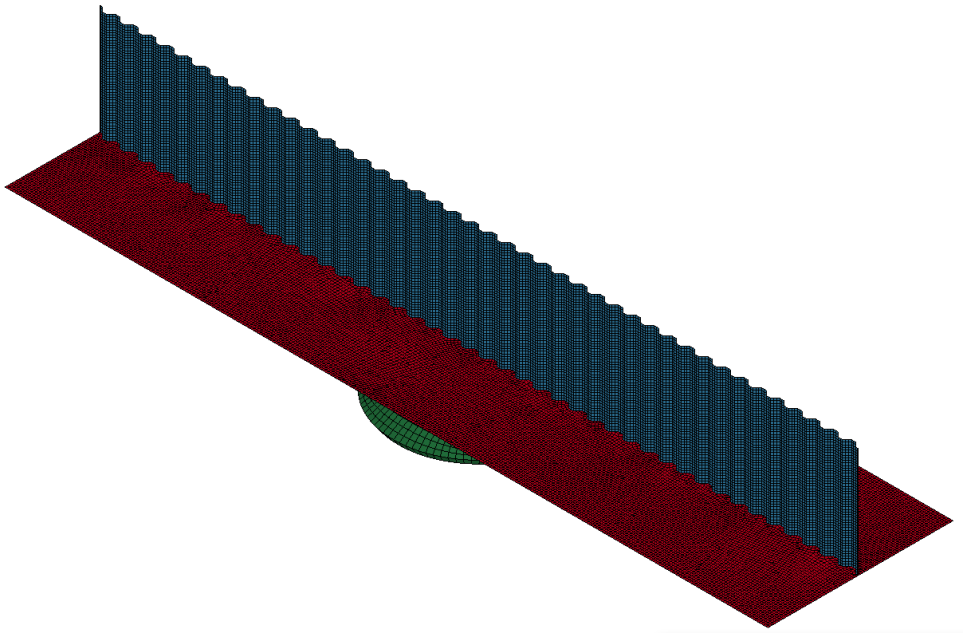

Trad. Corr. 2, von Mise Stress:

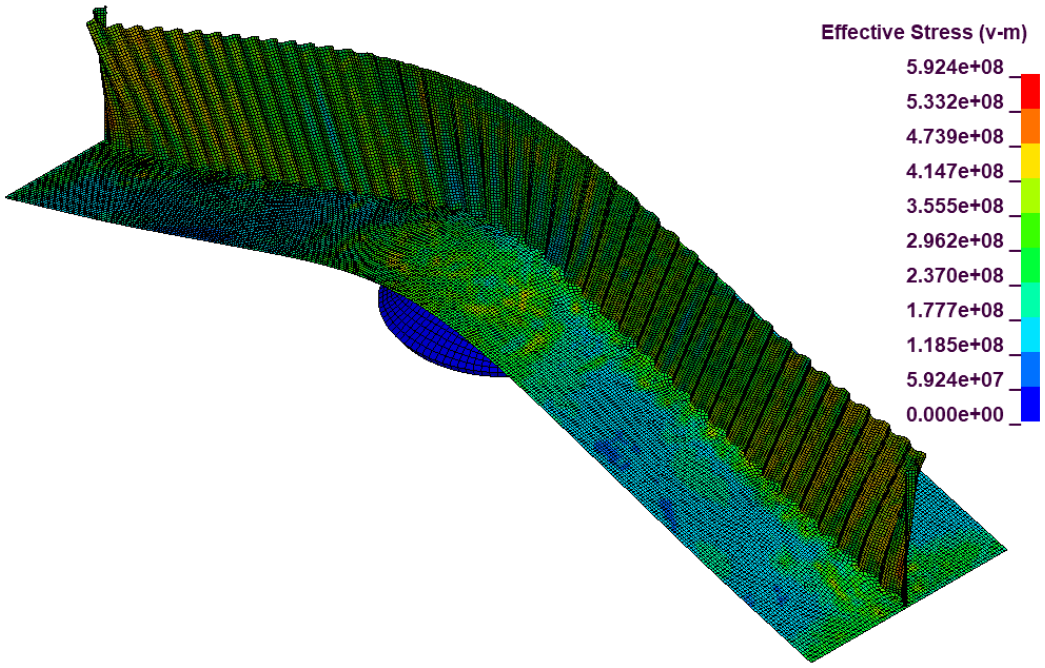

Trad. Corr. 3, Geometry:

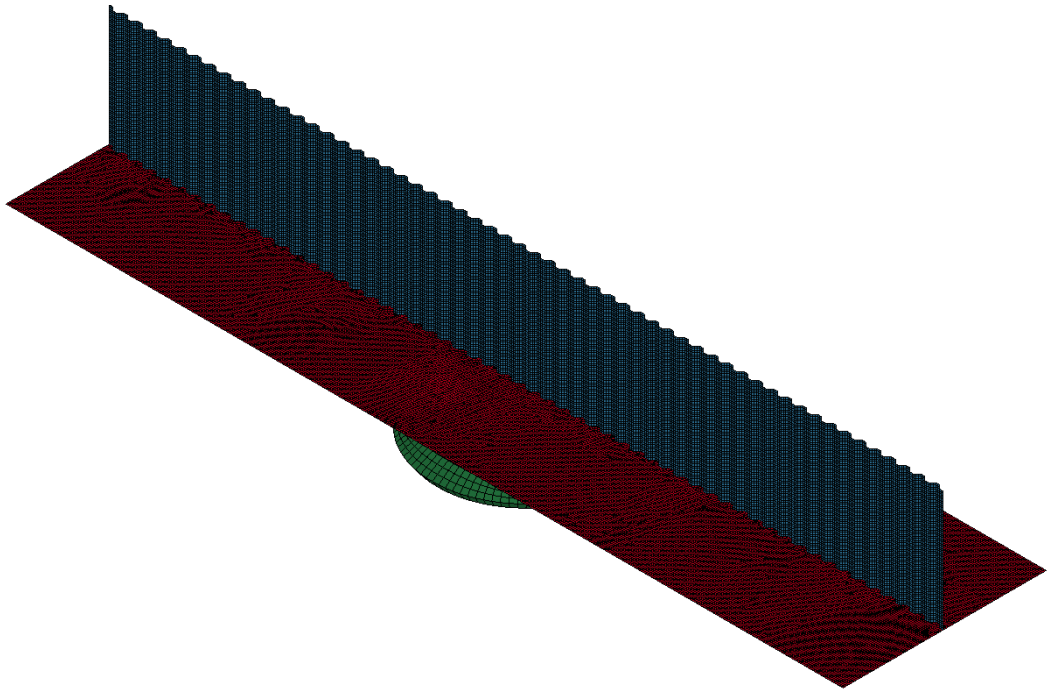

Trad. Corr. 3, von Mise Stress:

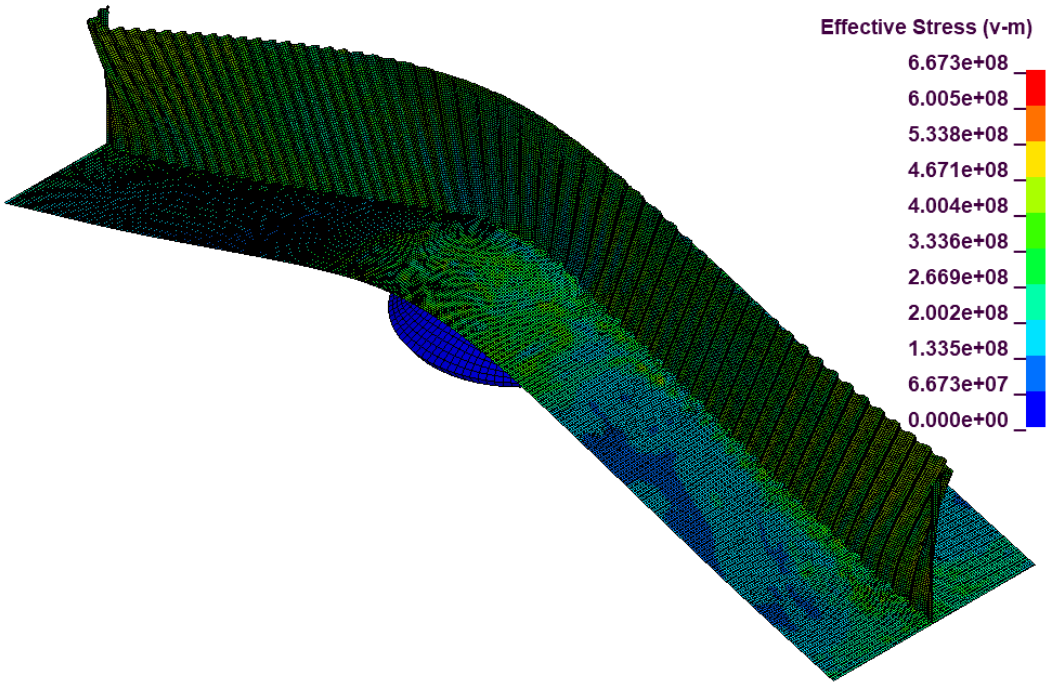

Trad. Corr. 4, Geometry:

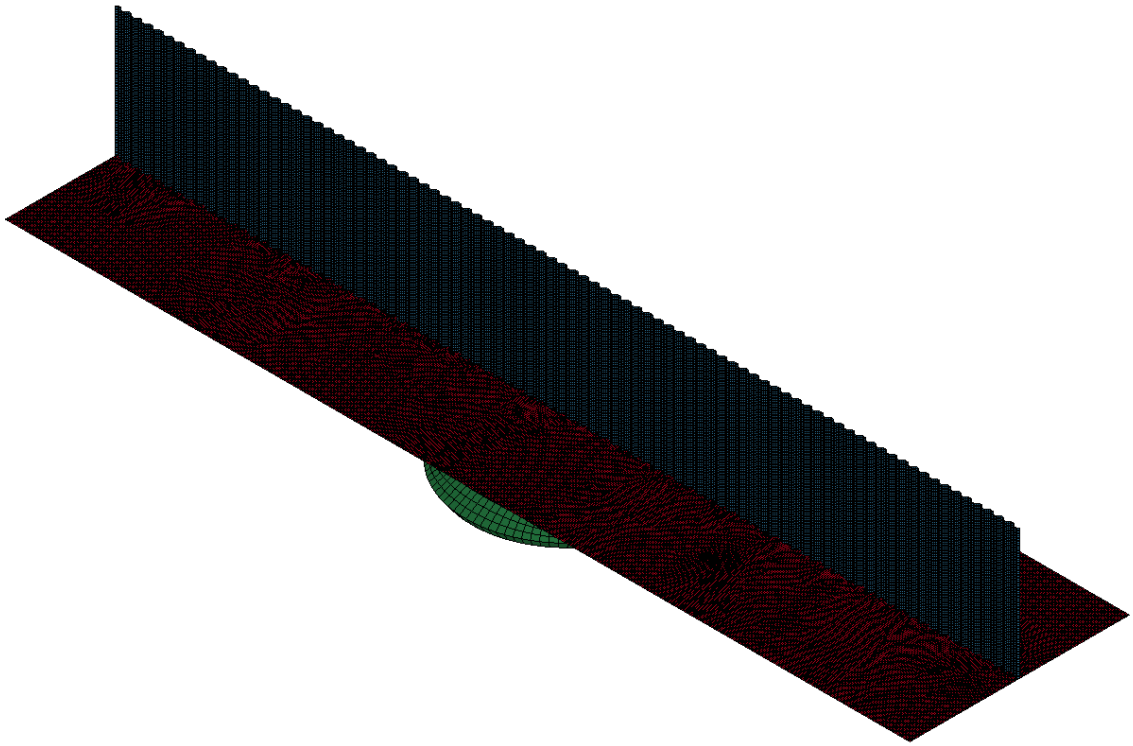

Trad. Corr. 4, von Mise Stress:

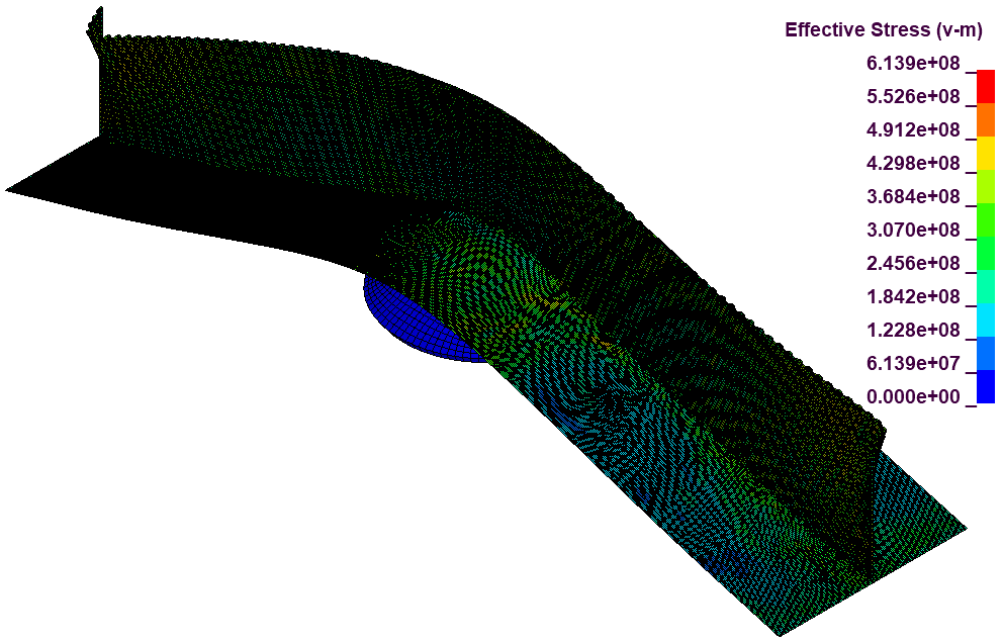

S Corr. 1, Geometry:

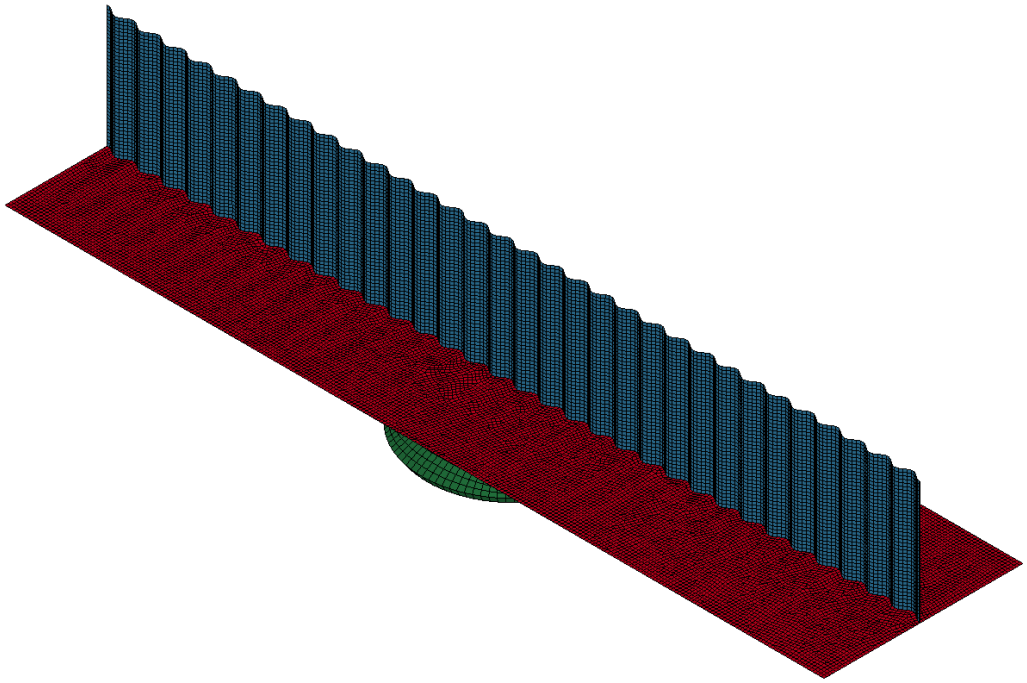

S Corr. 1, von Mise Stress:

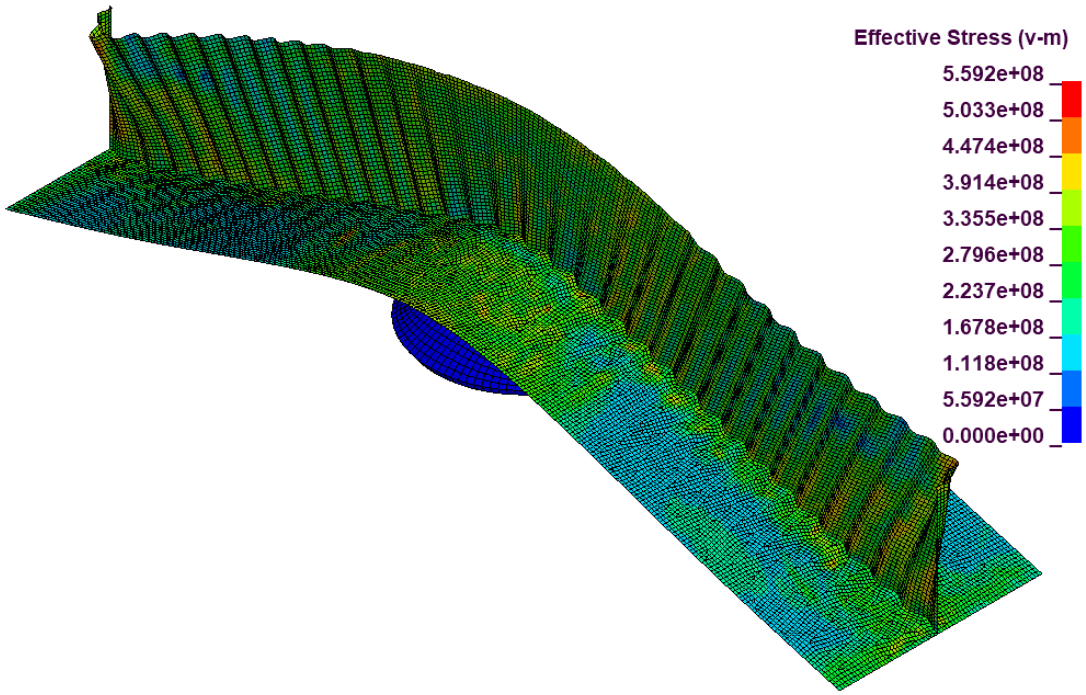

S Corr. 2, Geometry:

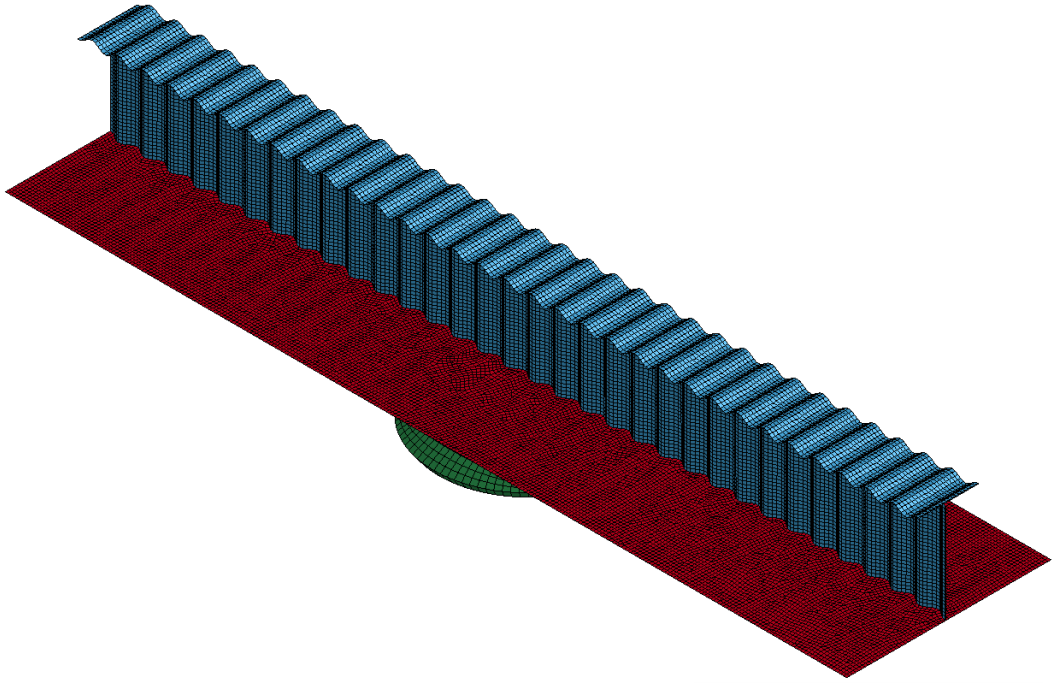

S Corr. 2, von Mise Stress:

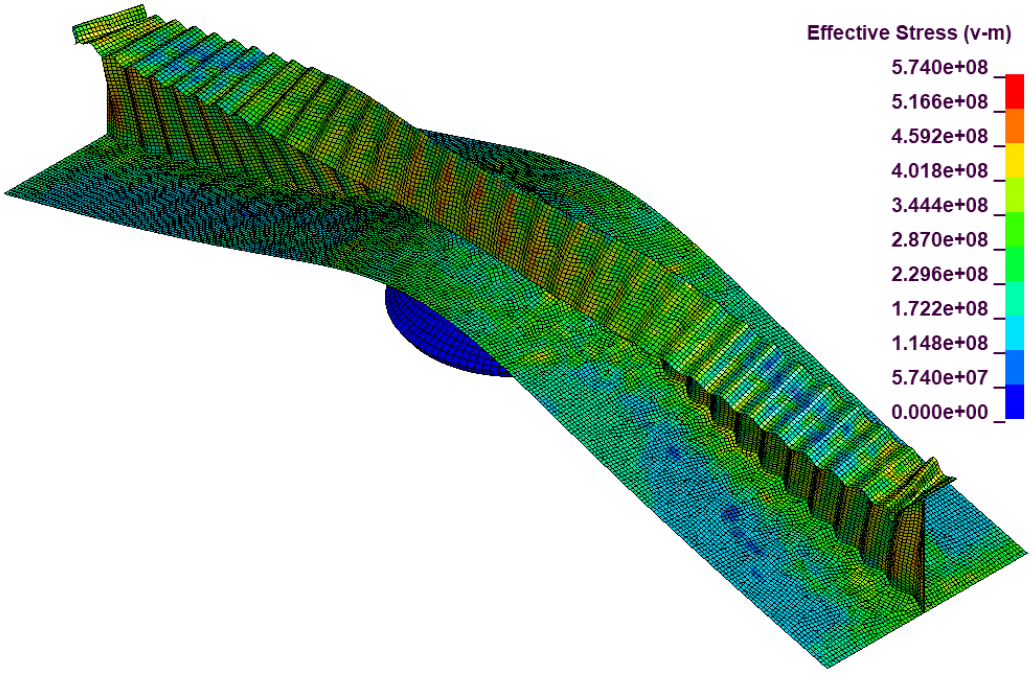

S Corr. 3, Geometry:

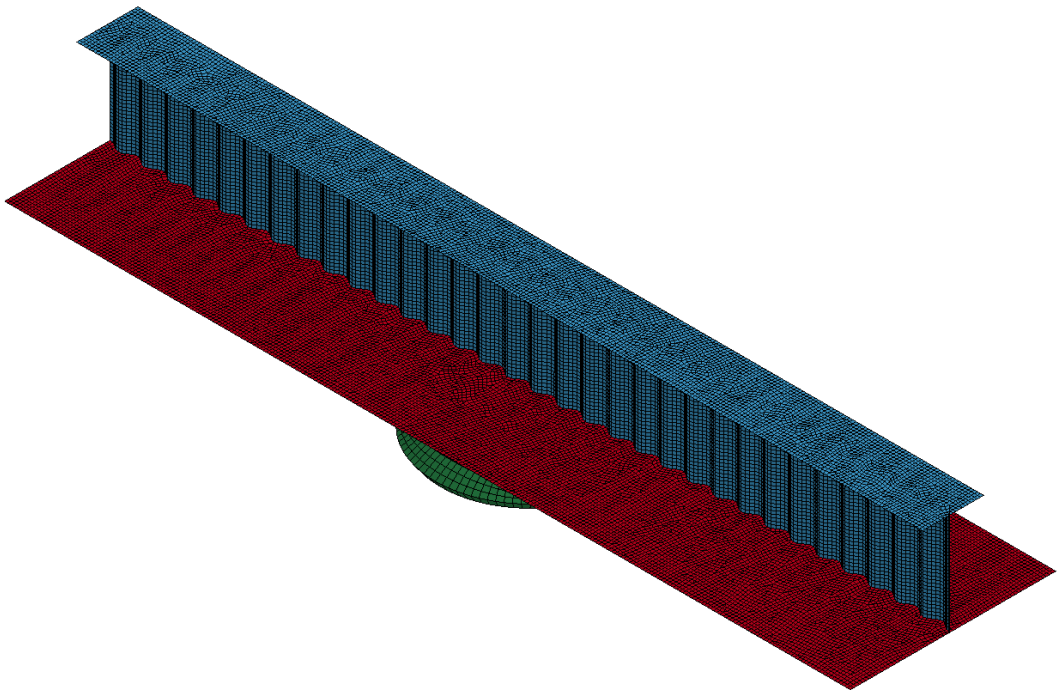

S Corr. 3, von Mise Stress:

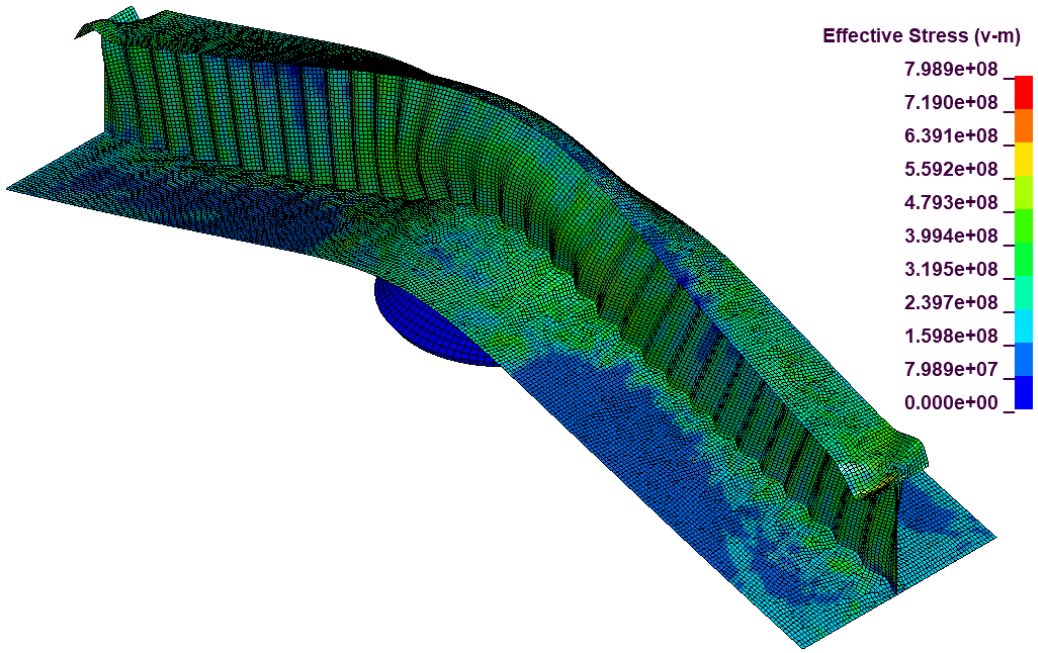

S Corr. 4, Geometry:

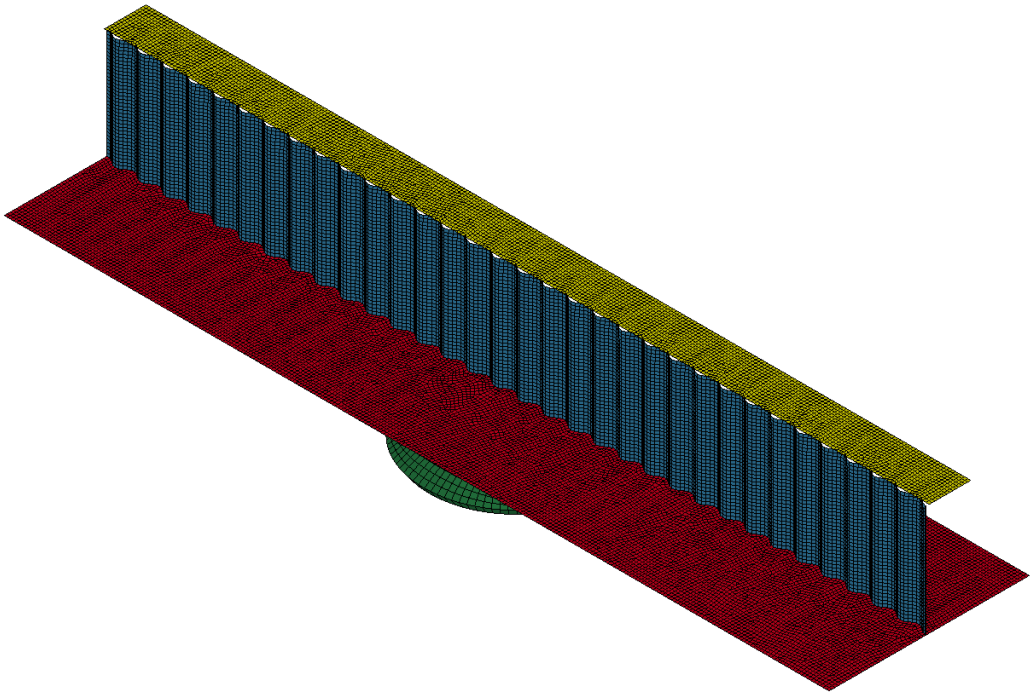

S Corr. 4, von Mise Stress:

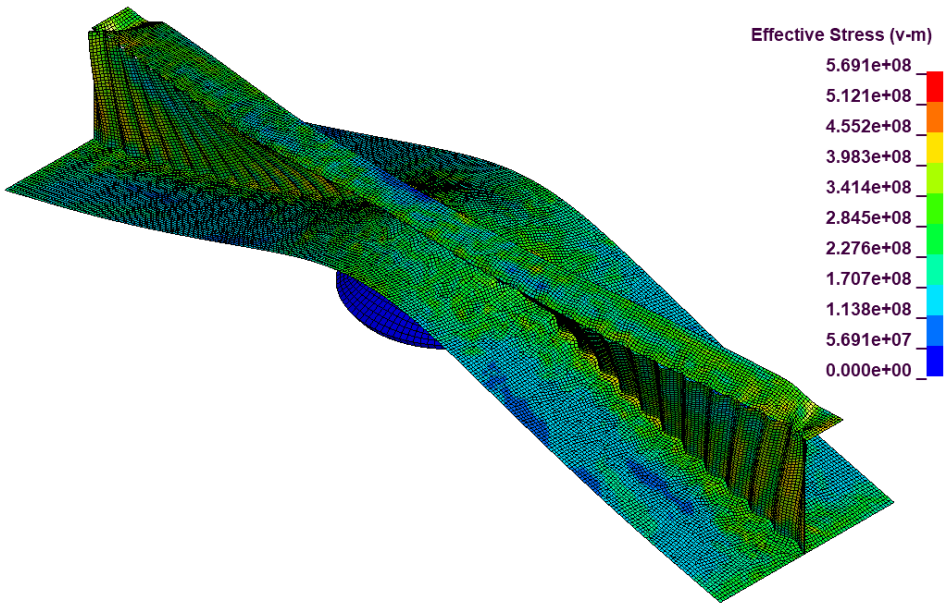

S Corr. 5, Geometry:

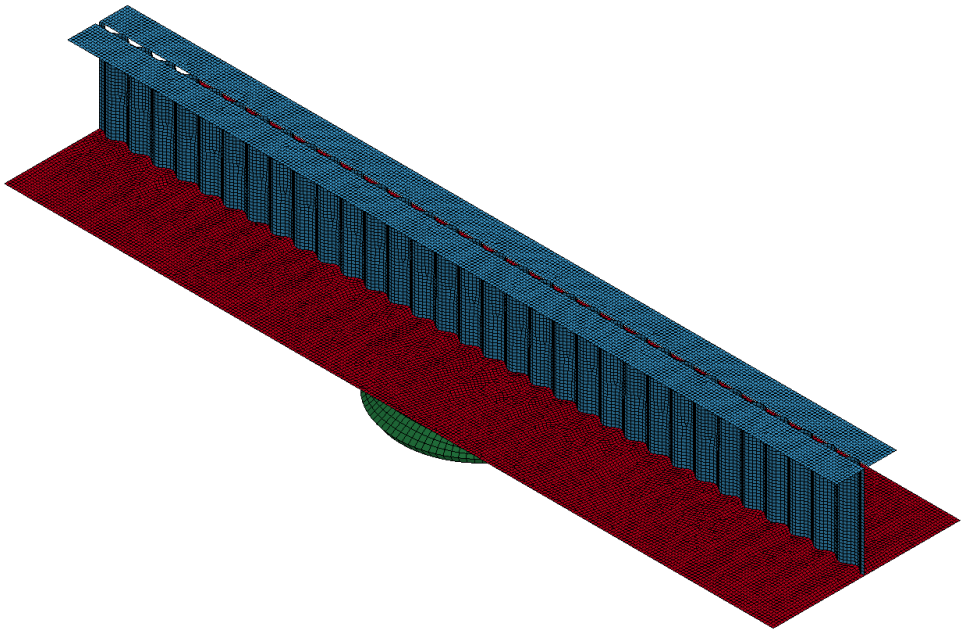

S Corr. 5, von Mise Stress:

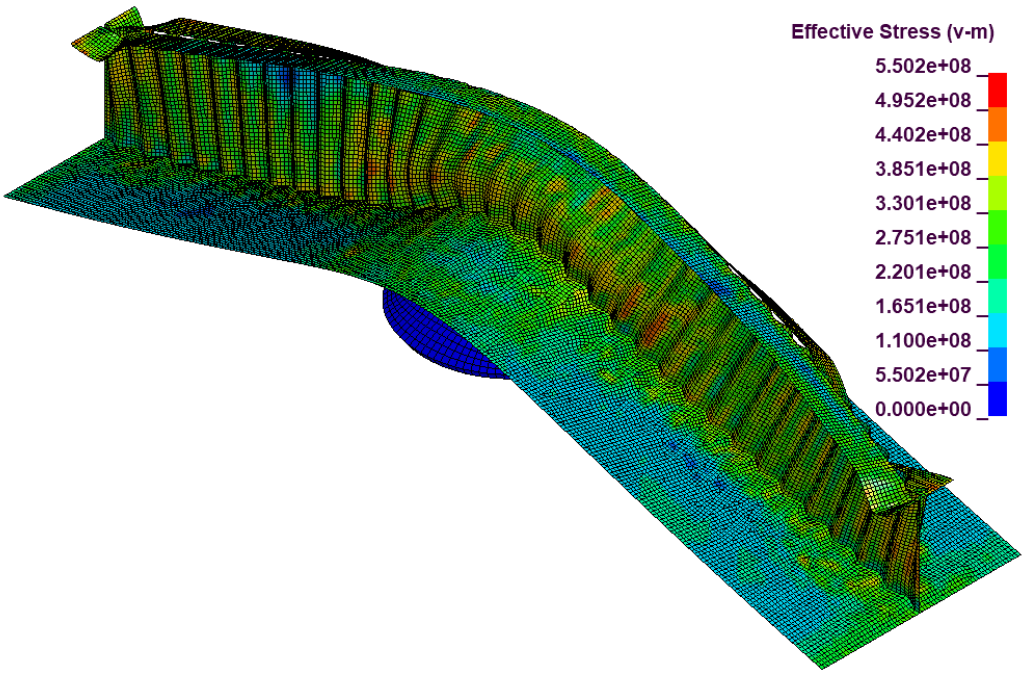

S Corr. 6, Geometry:

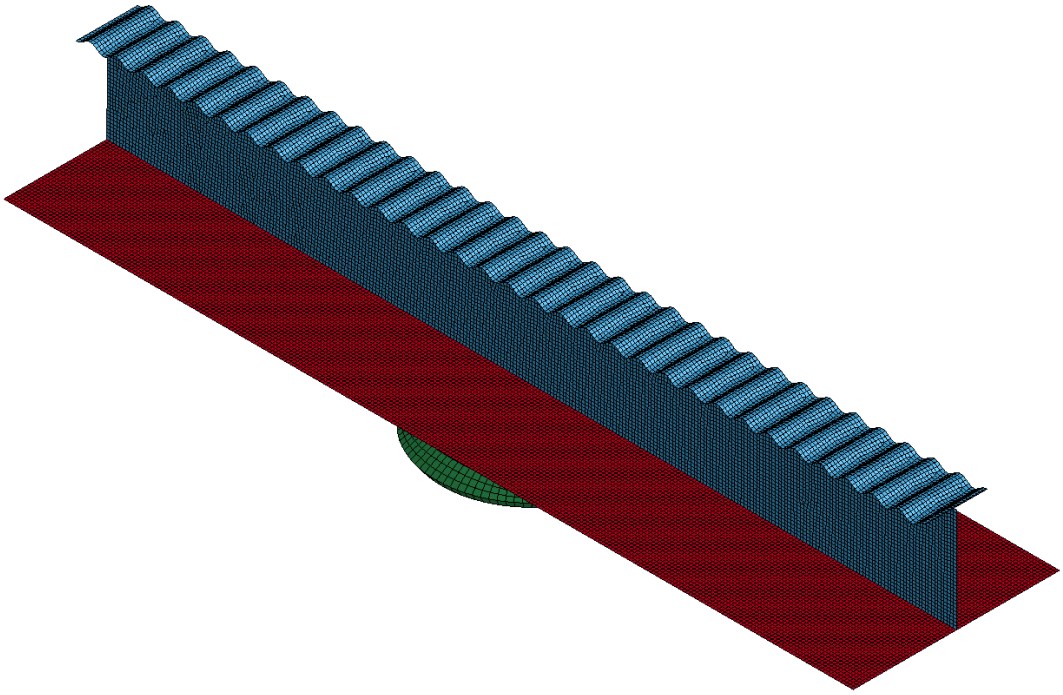

S Corr. 6, von Mise Stress:

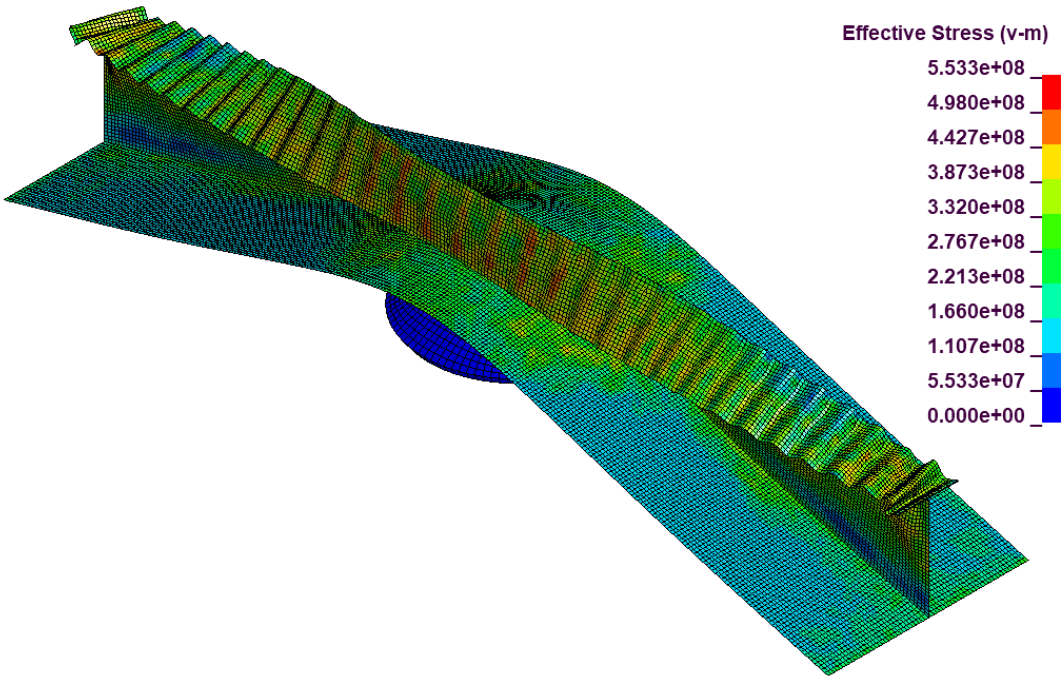

S Corr. 7, Geometry:

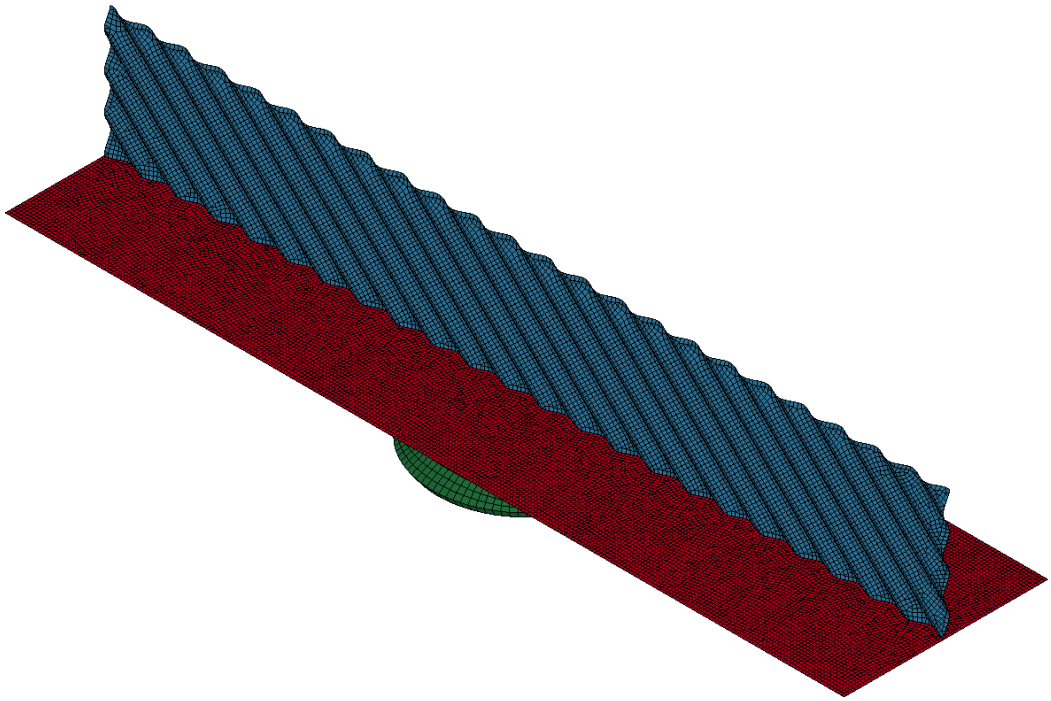

S Corr. 7, von Mise Stress:

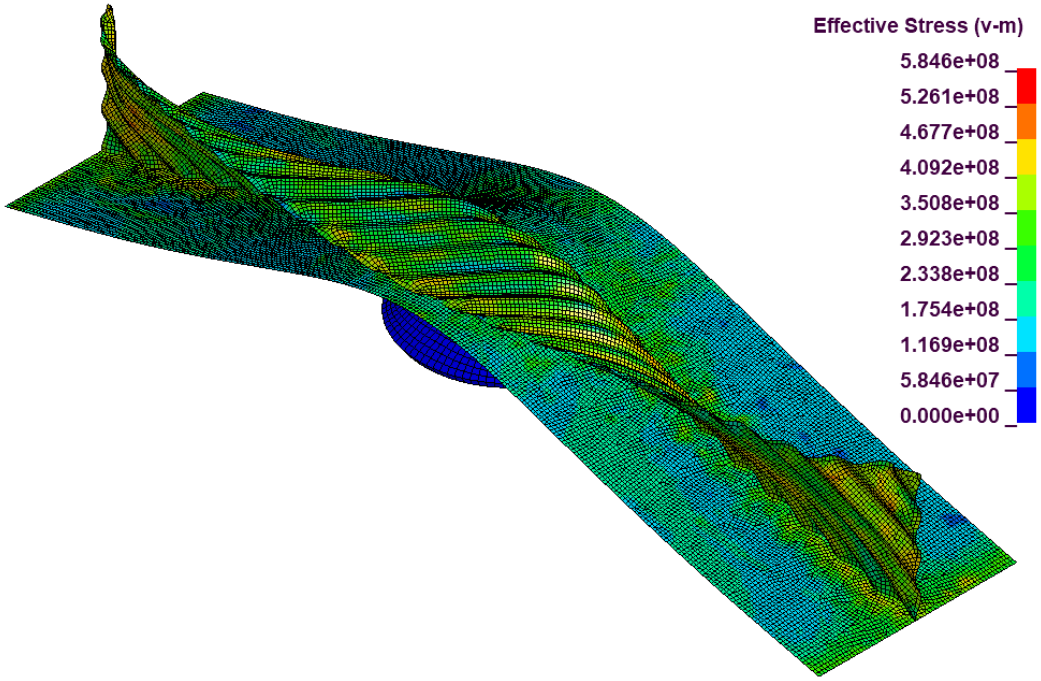

Bulb, Geometry:

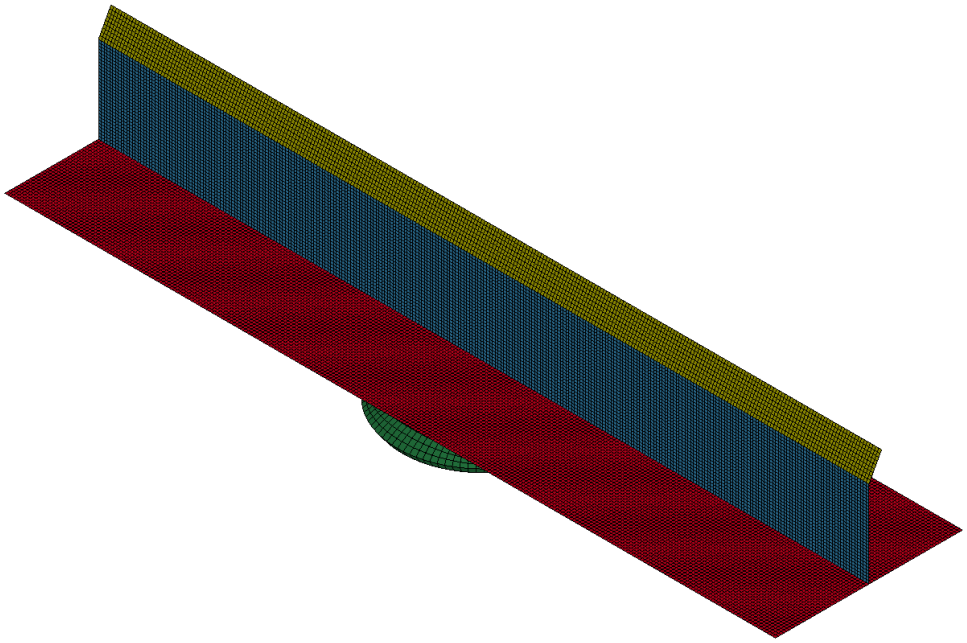

Bulb, von Mise Stress:

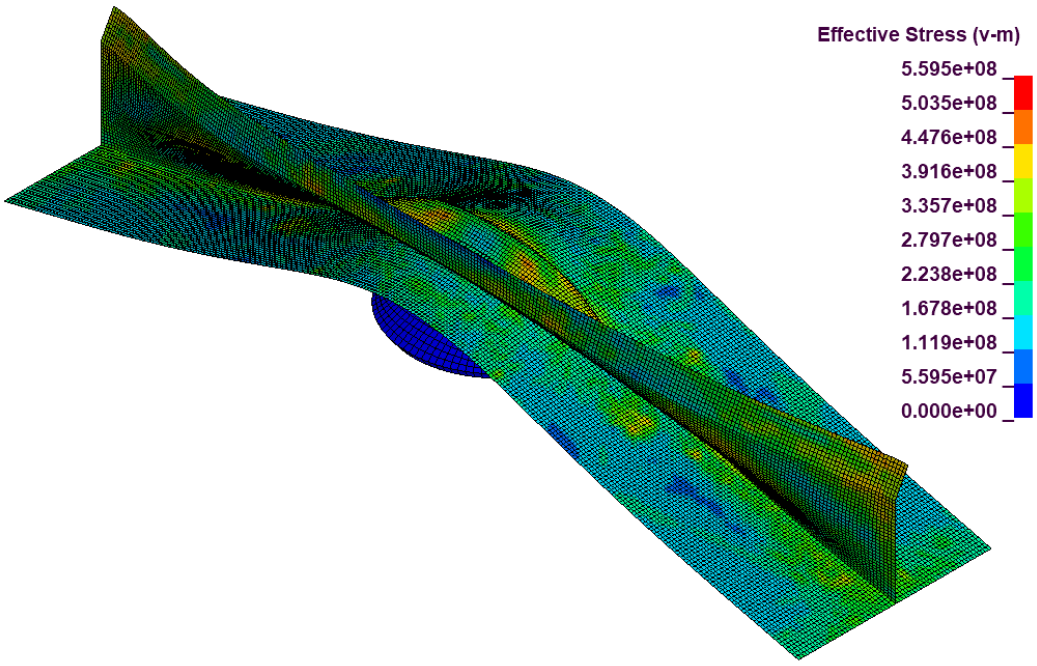

CHS (Constant Thickness), Geometry:

CHS (Constant Thickness), von Mise Stress:

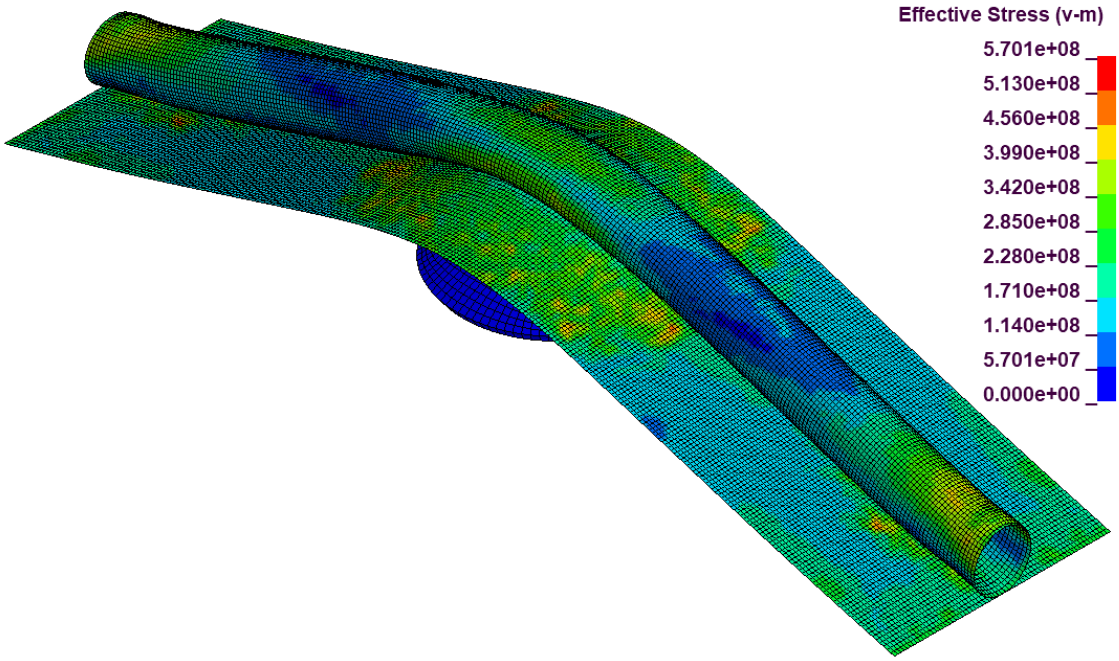

CHS with Flange, Geometry:

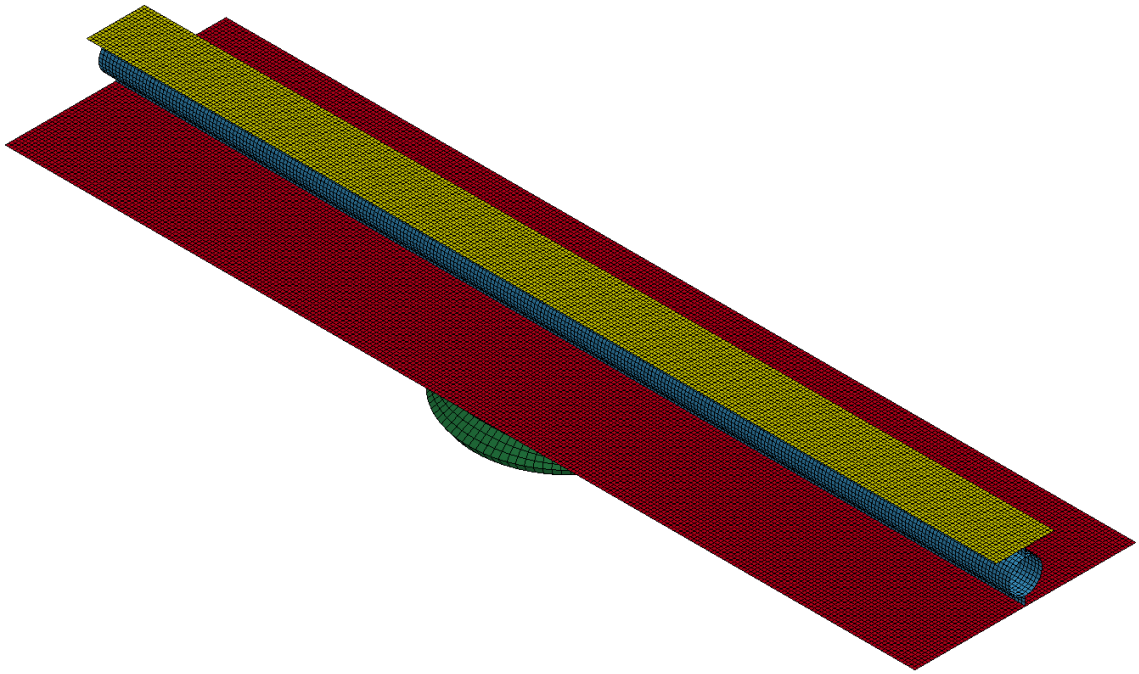

CHS with Flange, von Mise Stress:

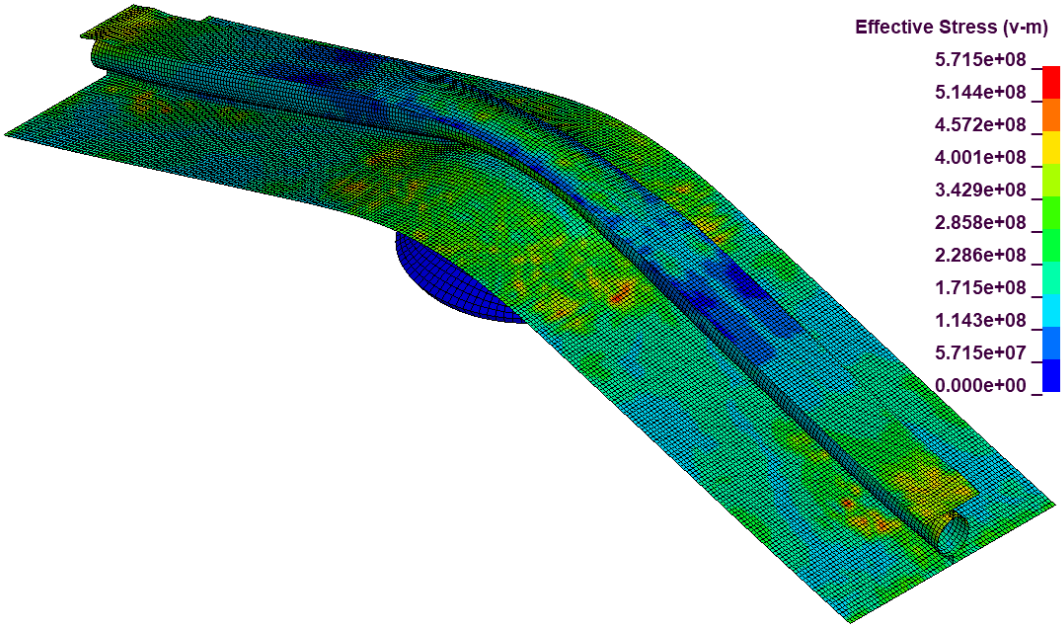

Non-Uniform Flange 1, Geometry:

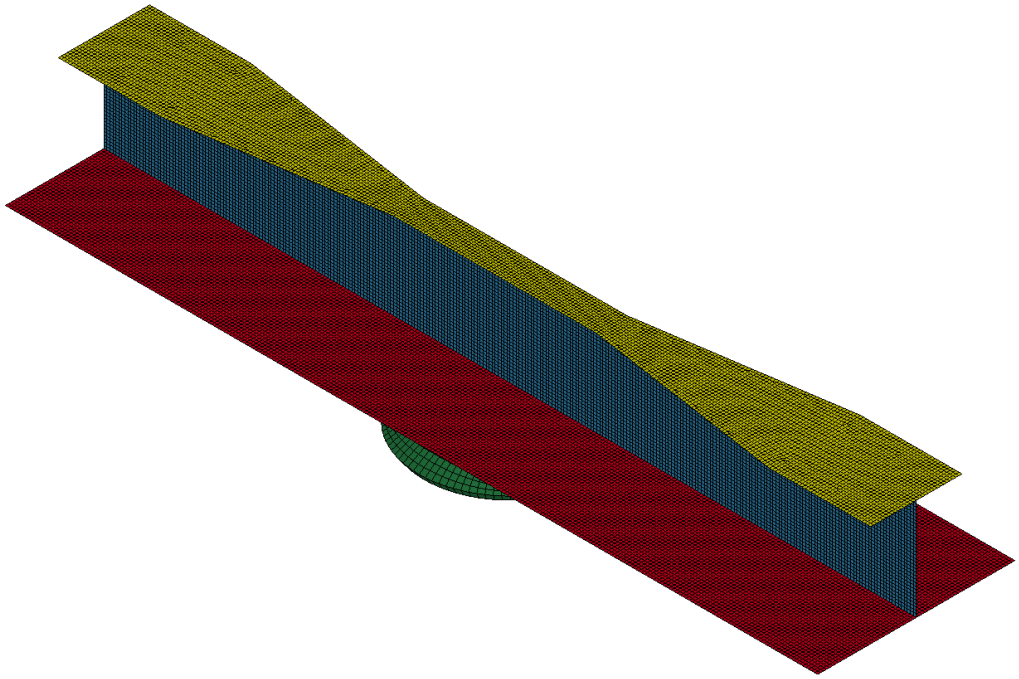

Non-Uniform Flange 1, von Mise Stress:

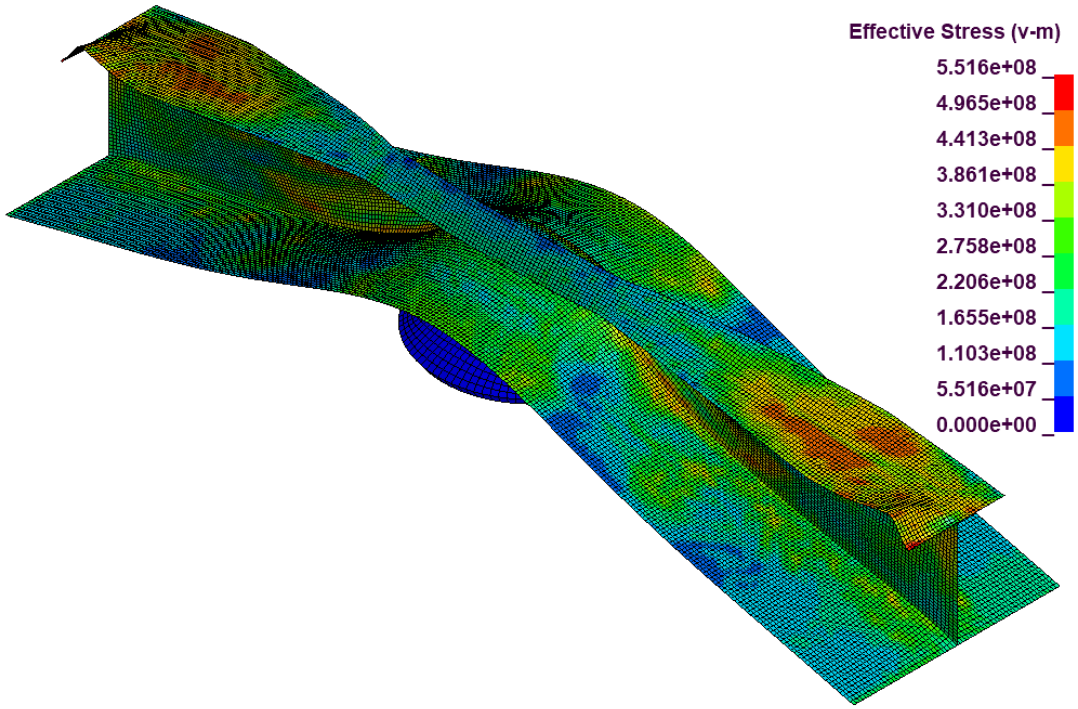

Non-Uniform Flange 2, Geometry:

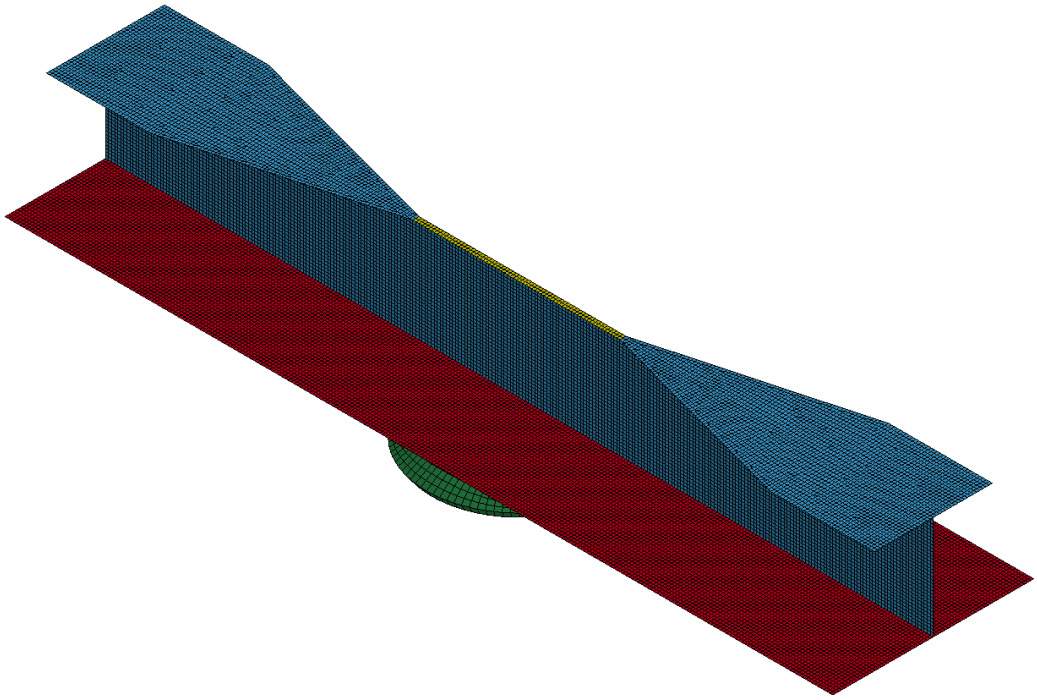

Non-Uniform Flange 2, von Mise Stress:

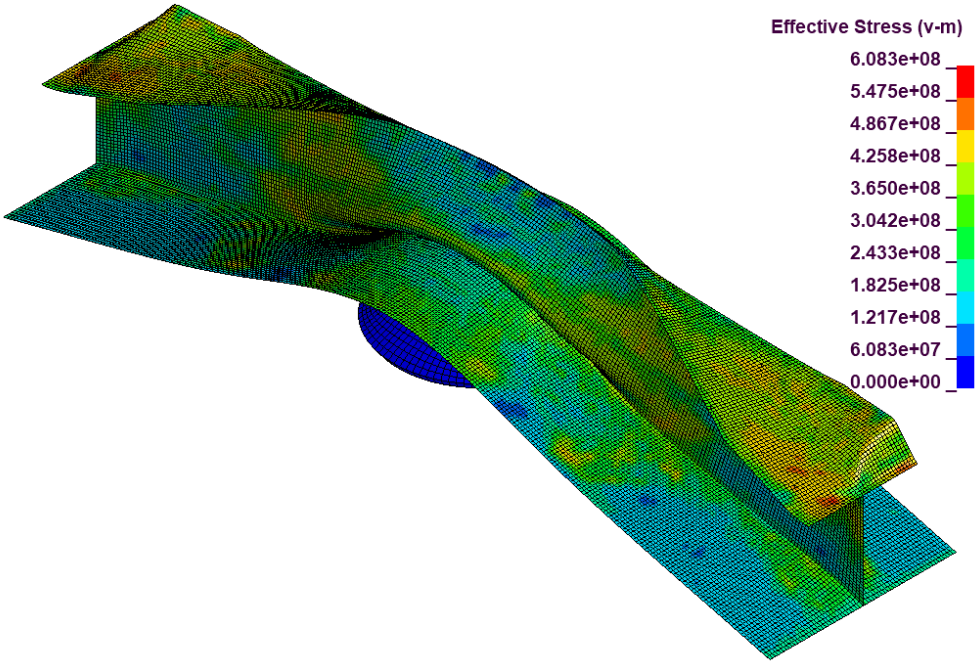

Flat Bar with Brackets 1, Geometry:

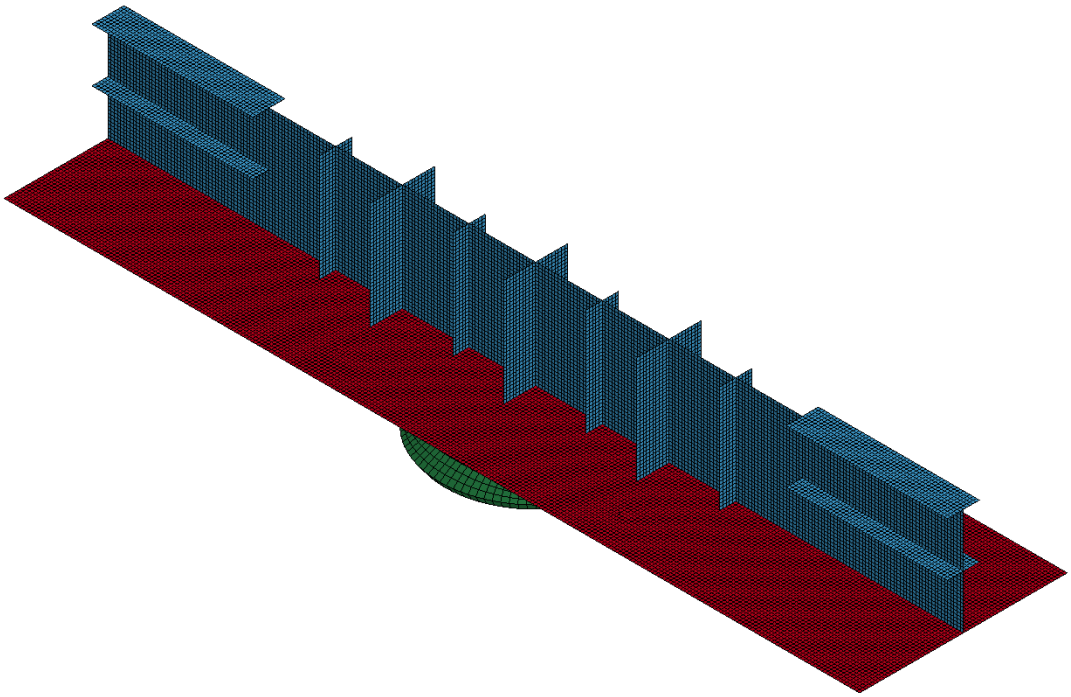

Flat Bar with Brackets 1, von Mise Stress:

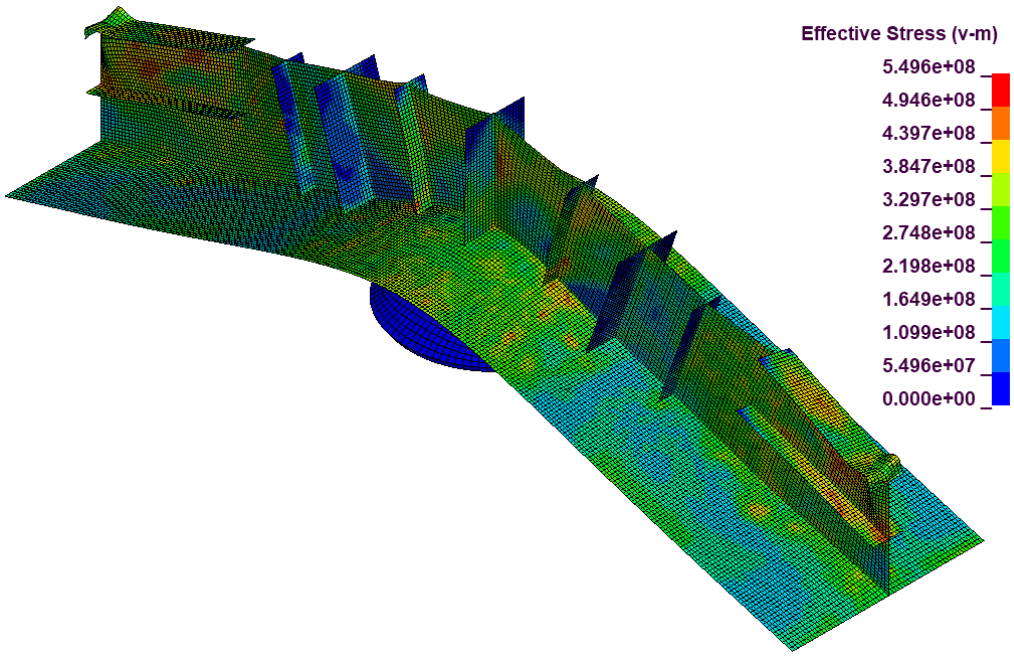

Flat Bar with Brackets 2, Geometry:

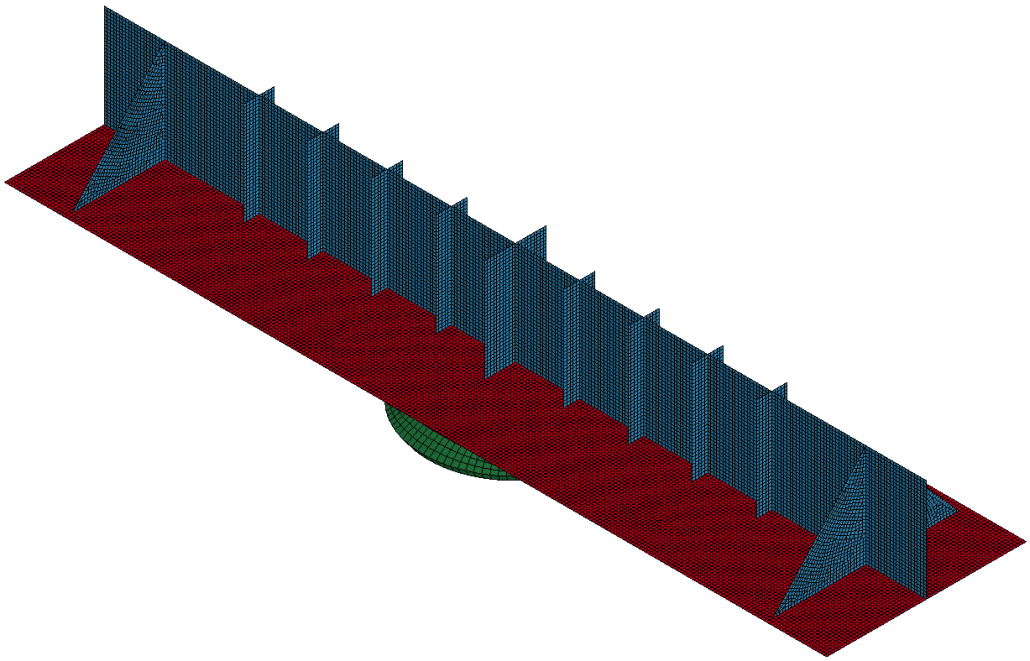

Flat Bar with Brackets 2, von Mise Stress:

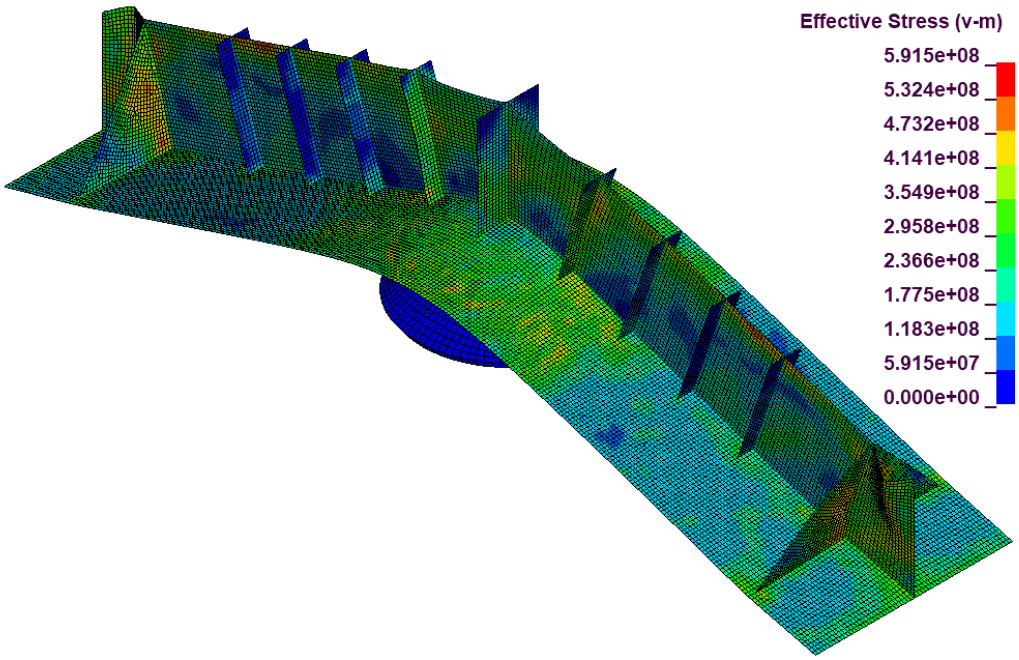

Flat Bar with Brackets 3, Geometry:

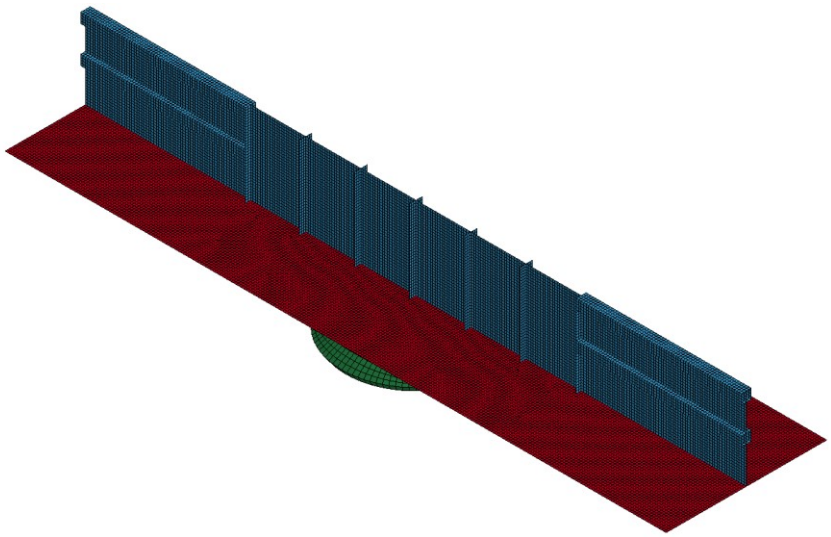

Flat Bar with Brackets 3, von Mise Stress:

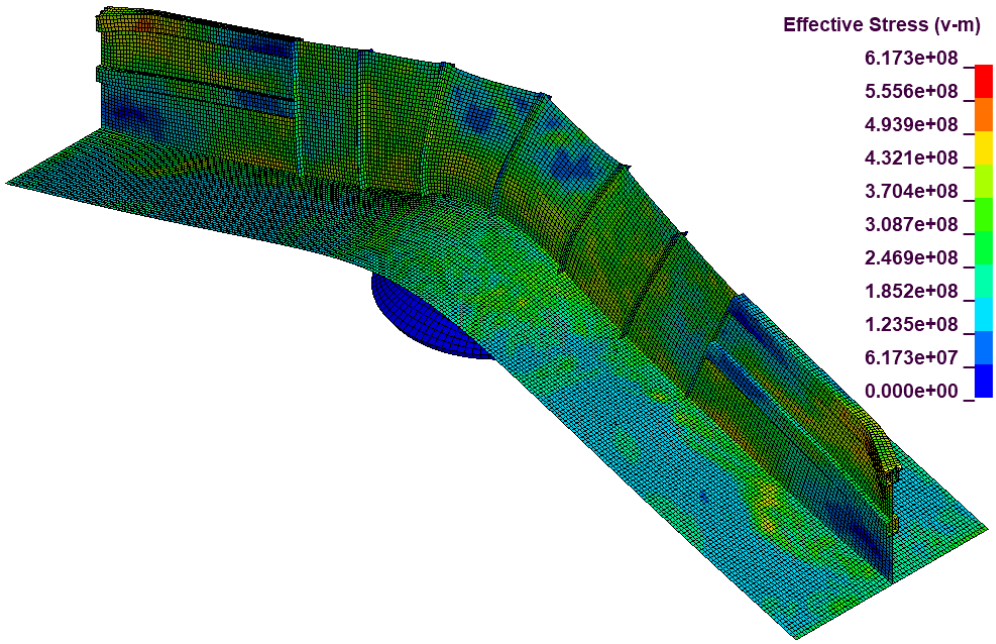

Flat Bar with Brackets 4, Geometry:

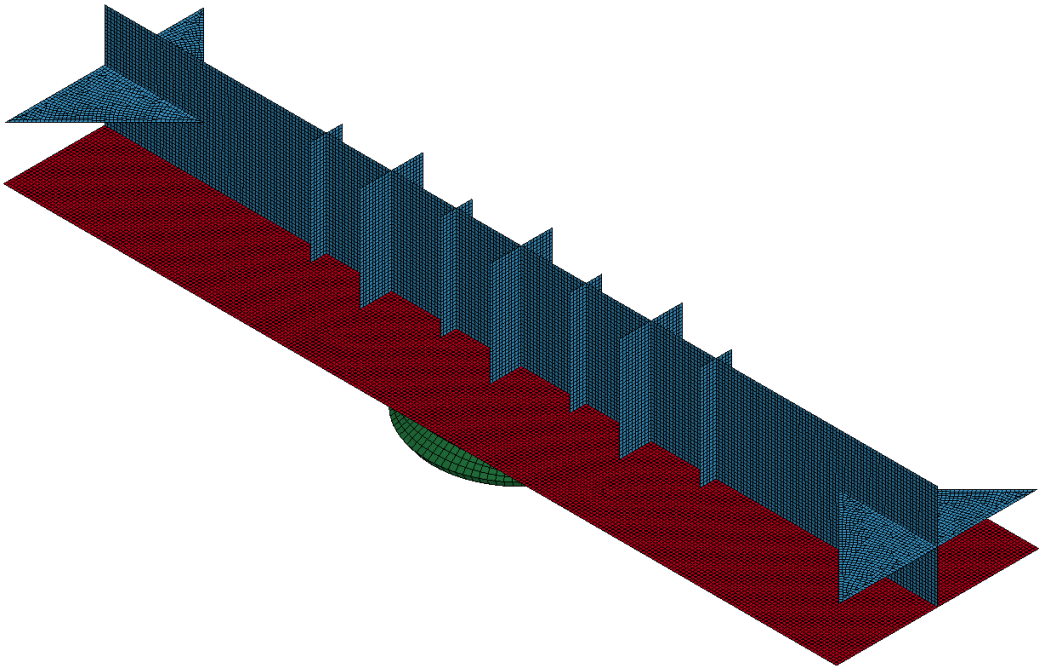

Flat Bar with Brackets 4, von Mise Stress:

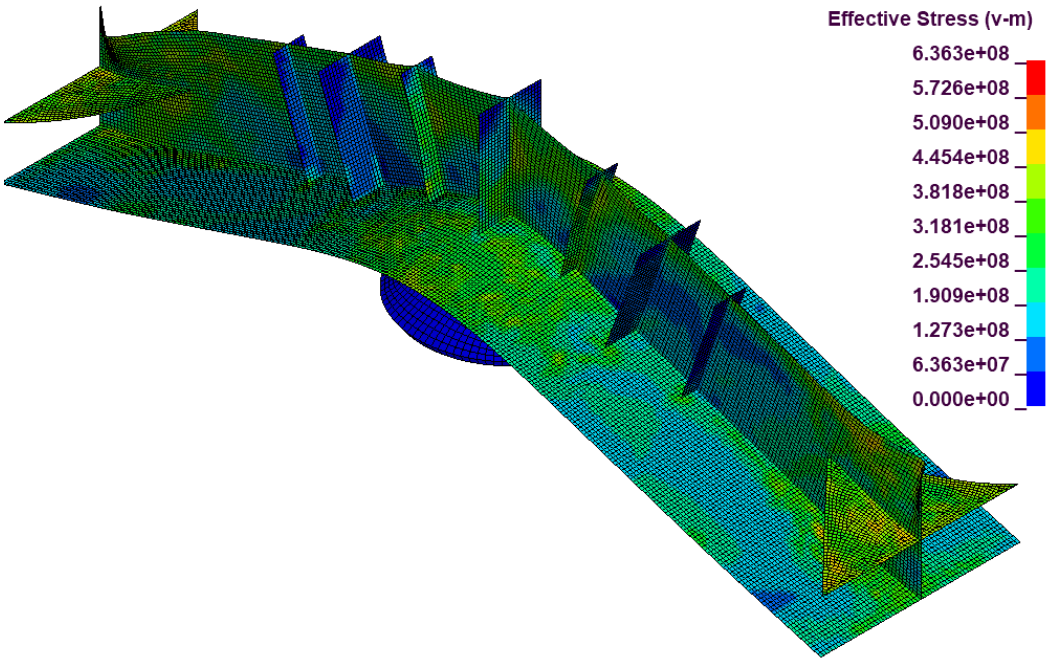

Flat Bar with Brackets 5, Geometry:

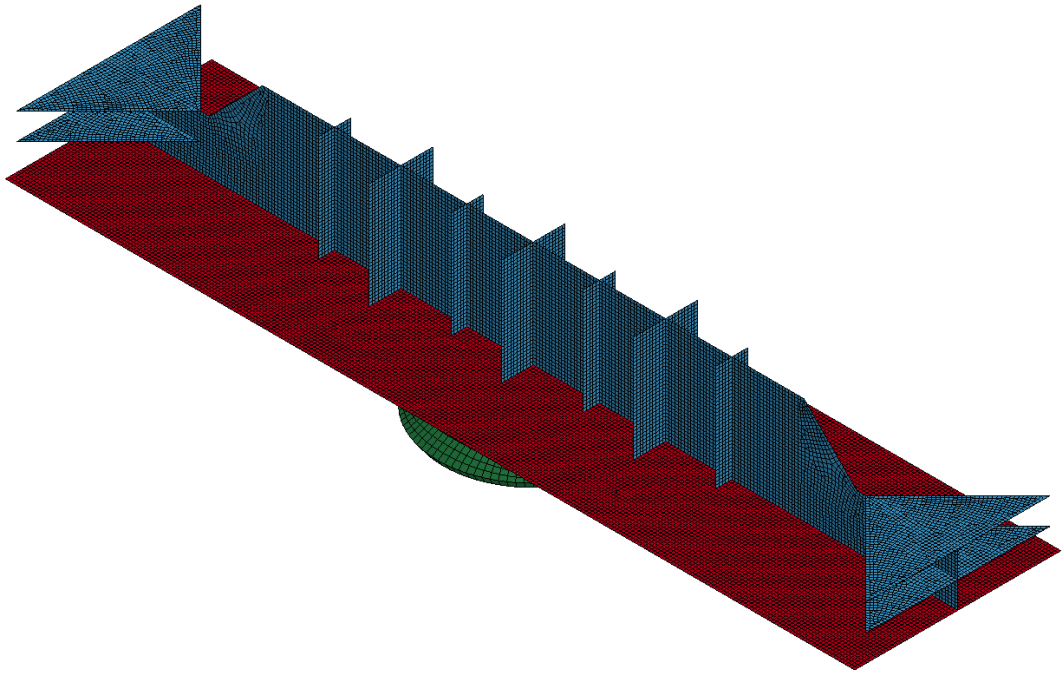

Flat Bar with Brackets 5, von Mise Stress:

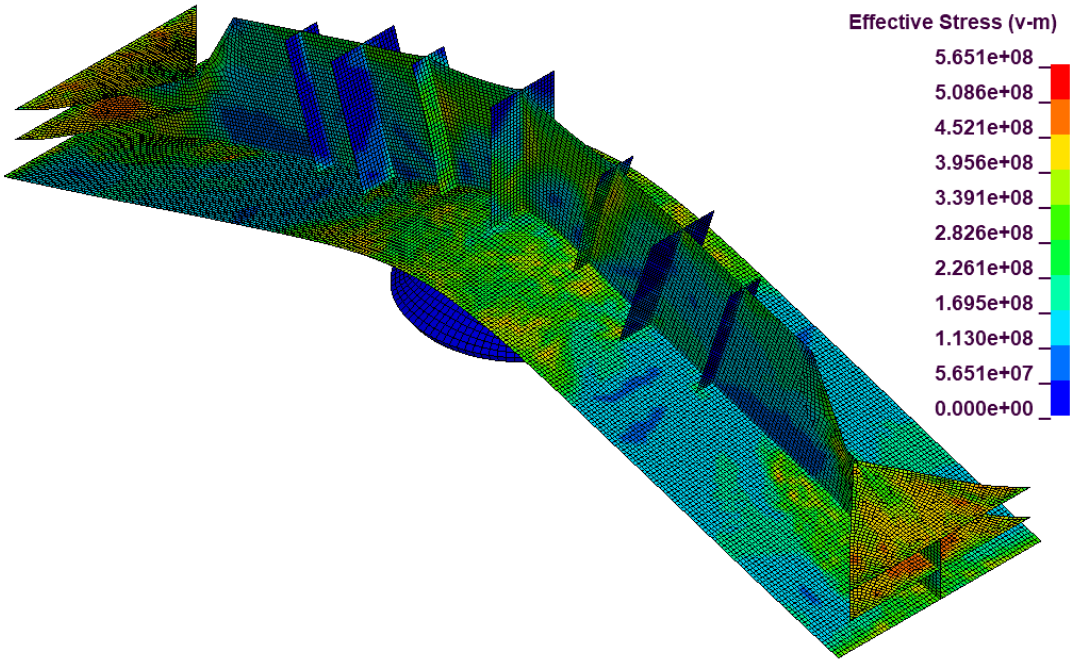

Deflection Curve 1, Geometry:

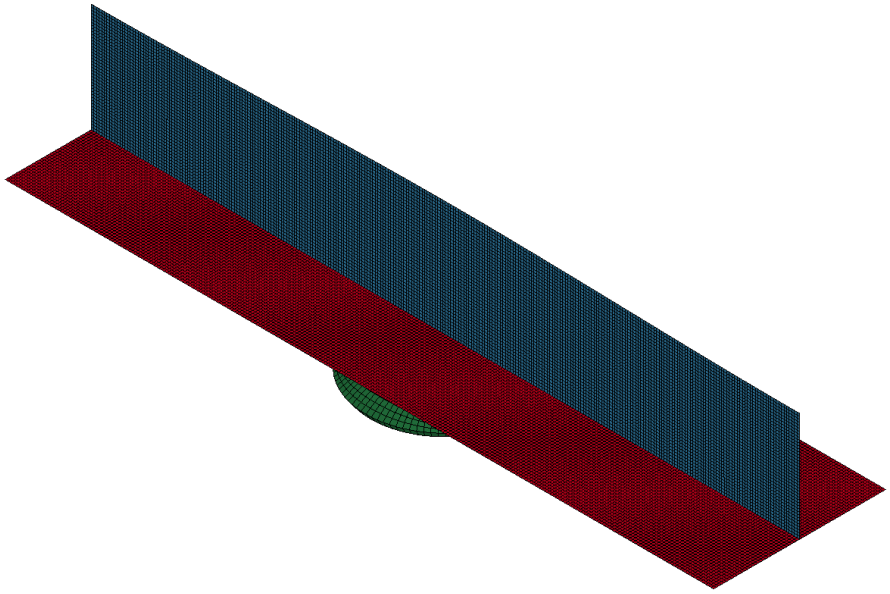

Deflection Curve 1, von Mise Stress:

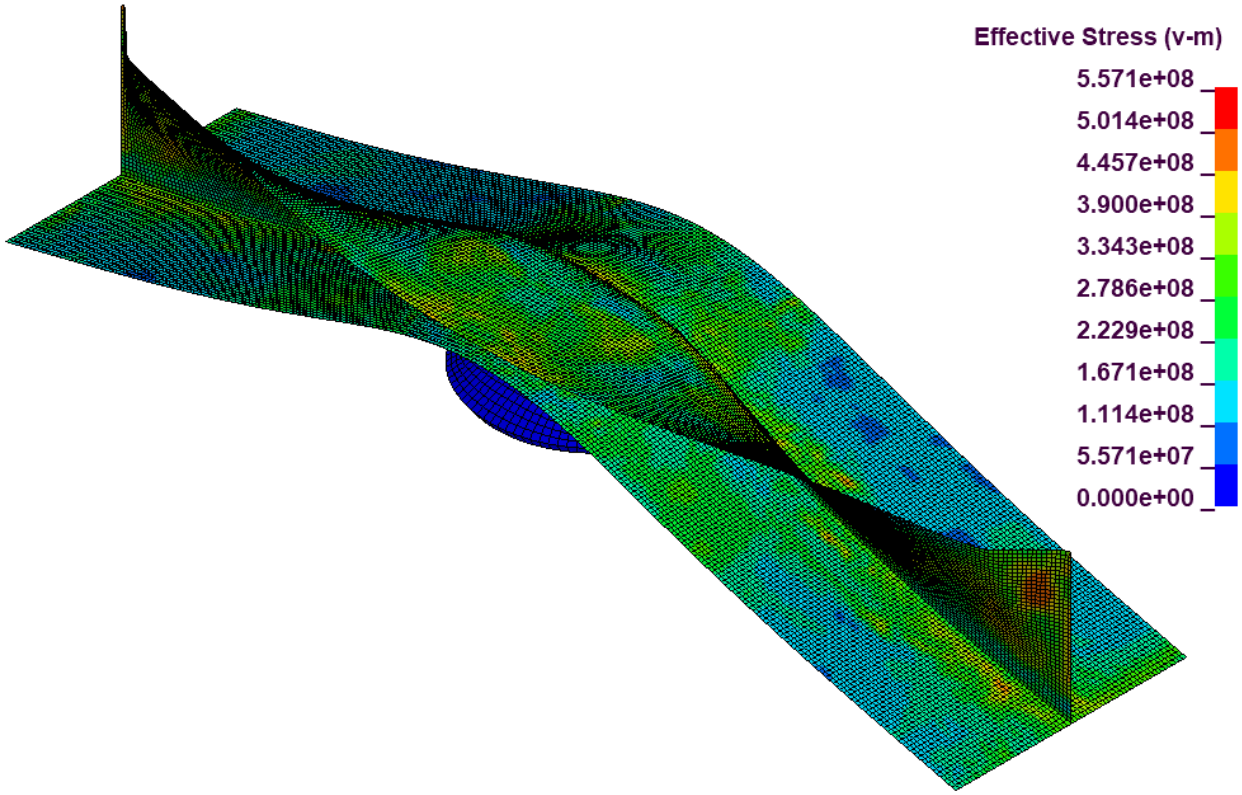

Deflection Curve 2, Geometry:

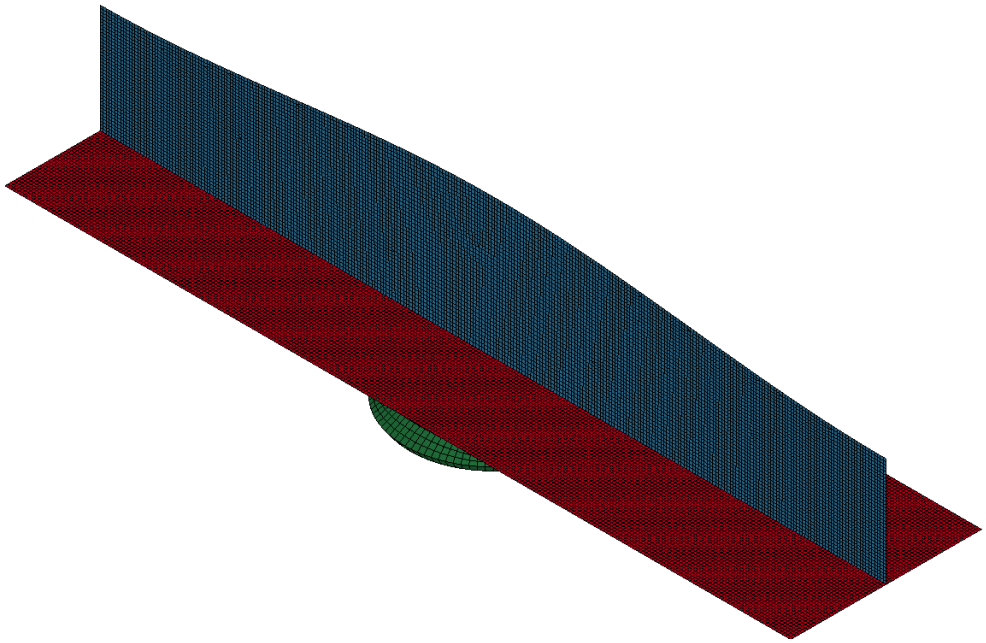

Deflection Curve 2, von Mise Stress:

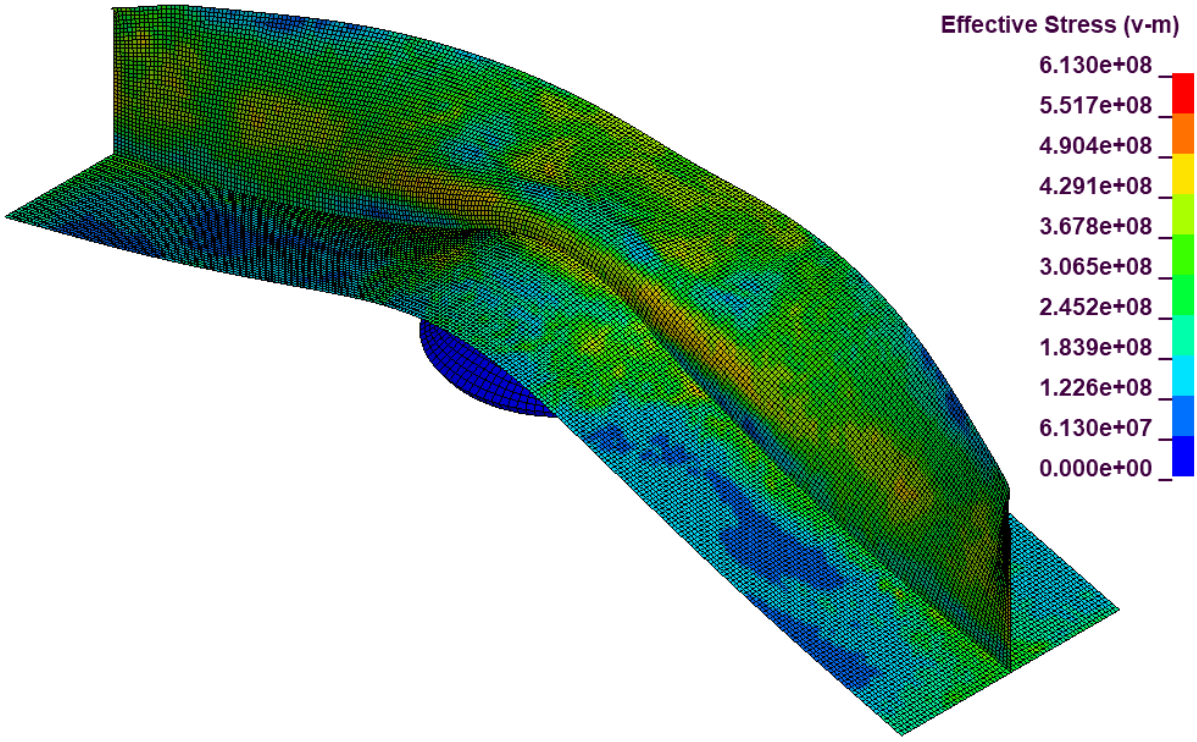

Deflection Curve 3, Geometry:

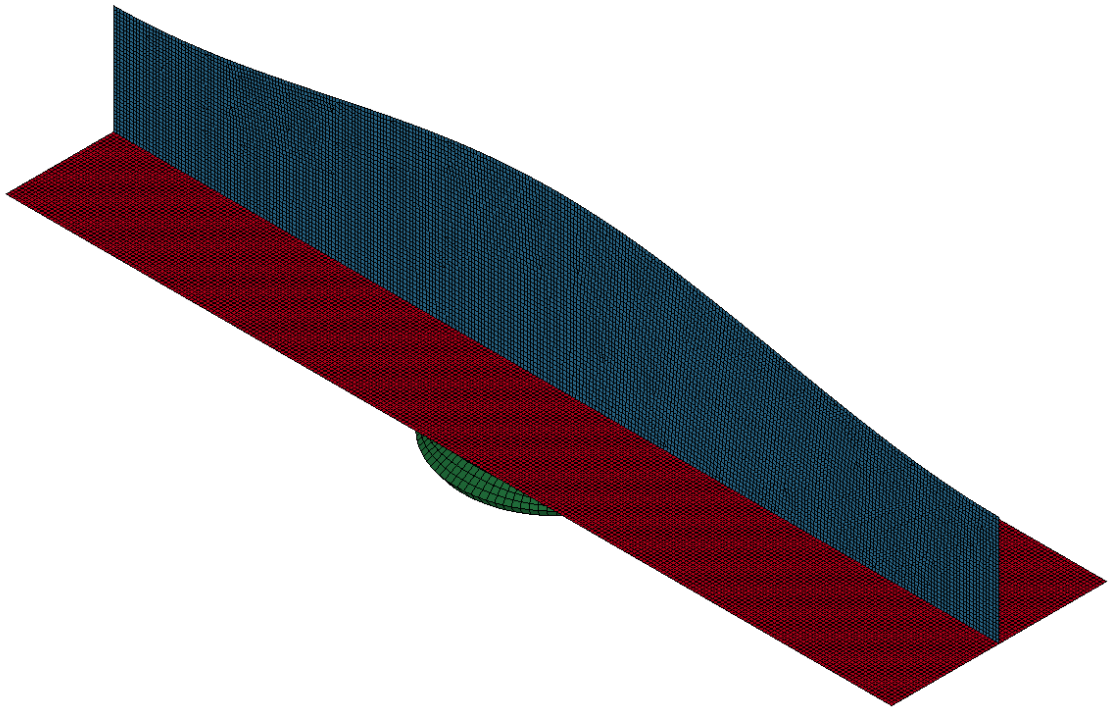

Deflection Curve 3, von Mise Stress:

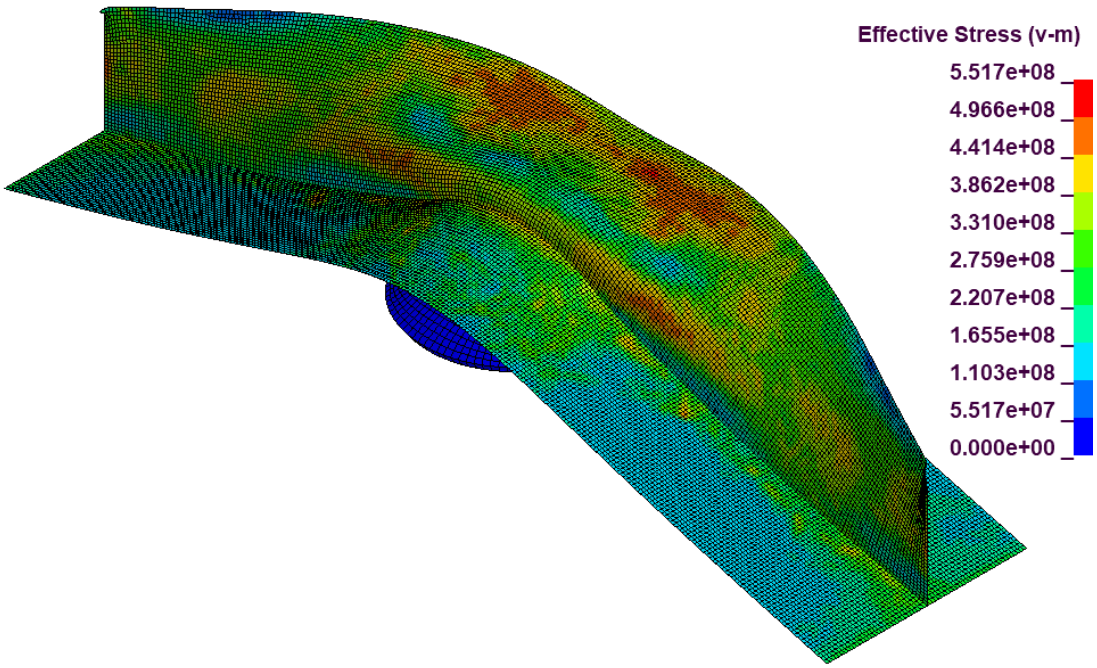

Deflection Curve 4, Geometry:

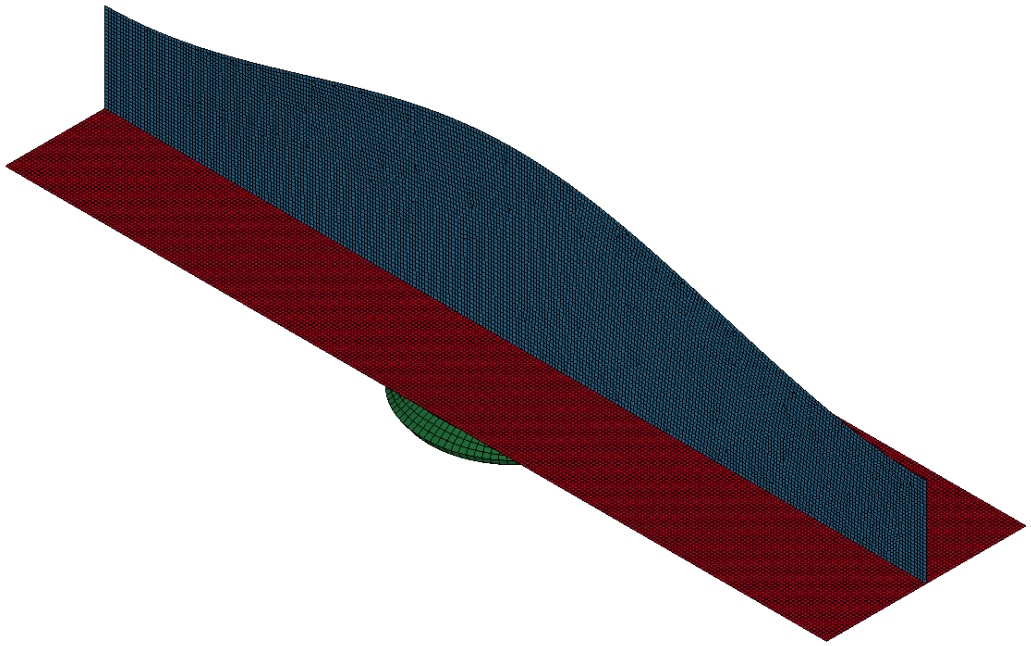

Deflection Curve 4, von Mise Stress:

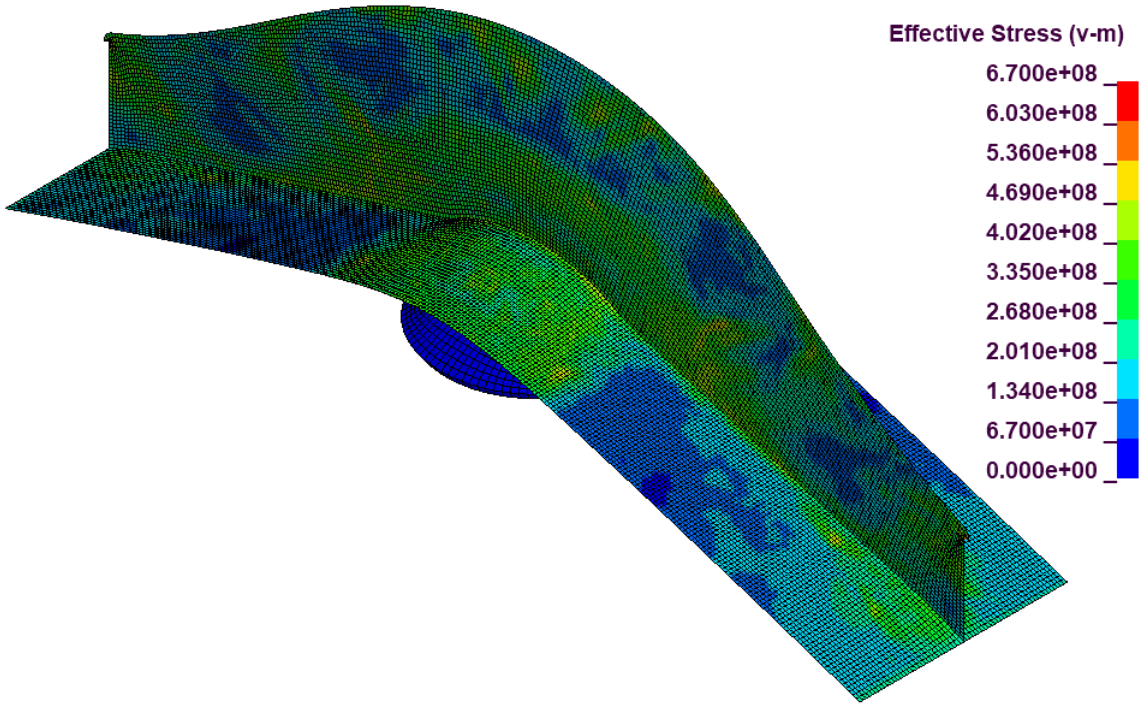

Deflection Curve 5, Geometry:

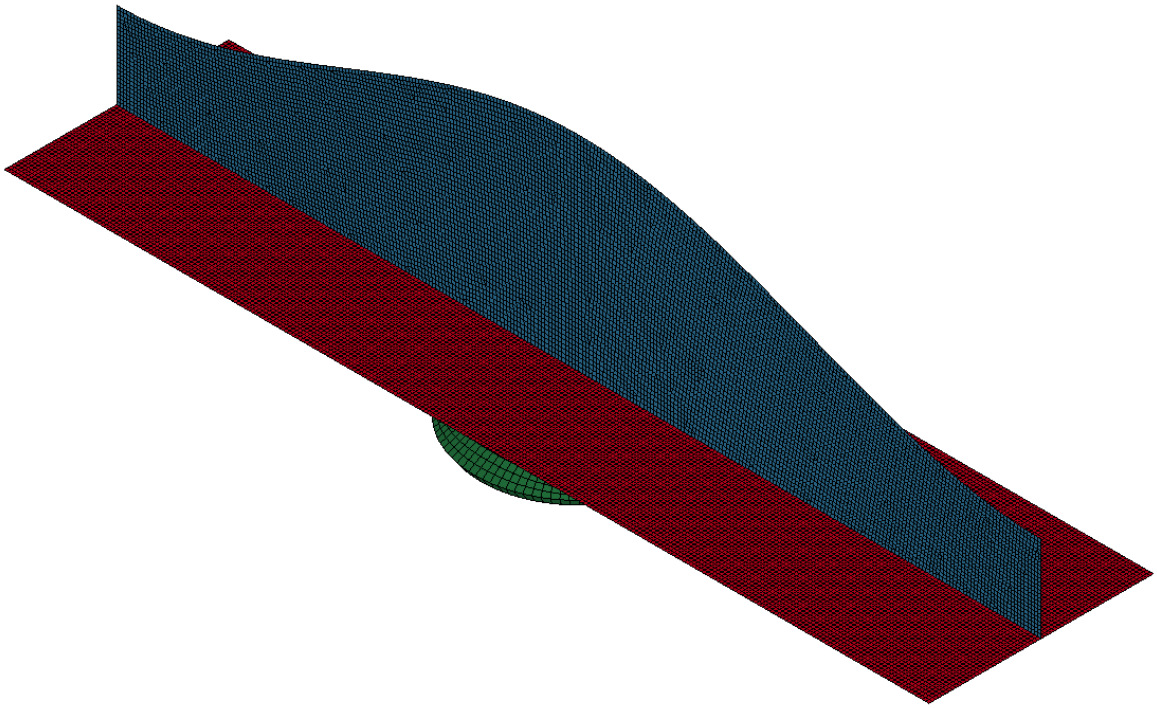

Deflection Curve 5, von Mise Stress:

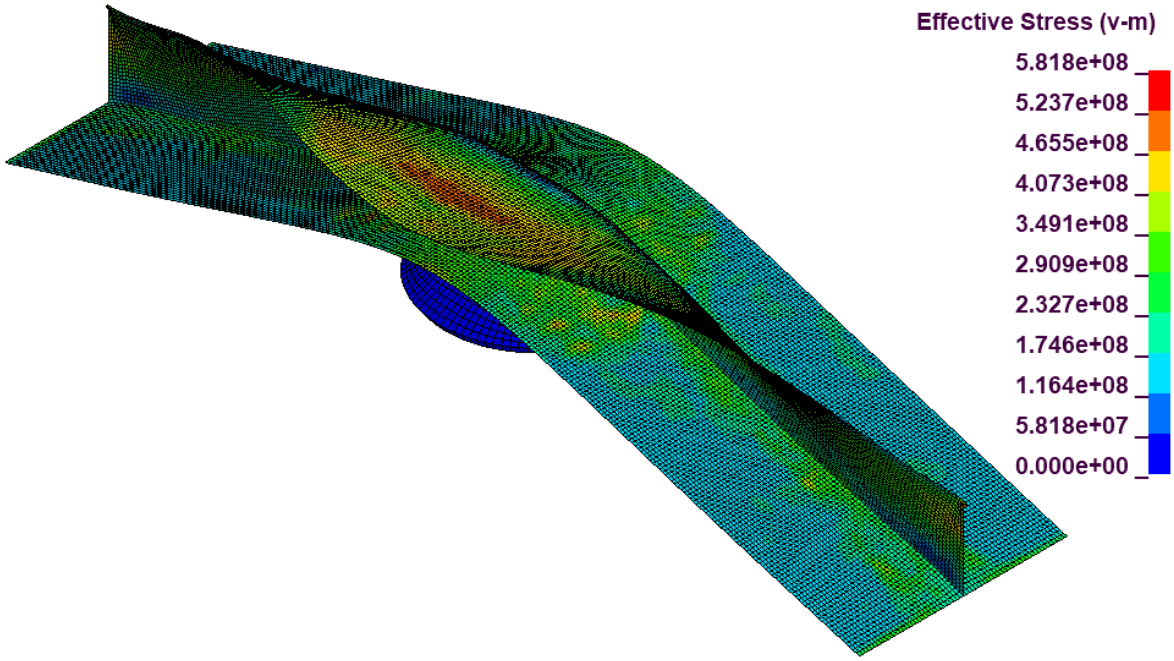

Deflection Curve 6, Geometry:

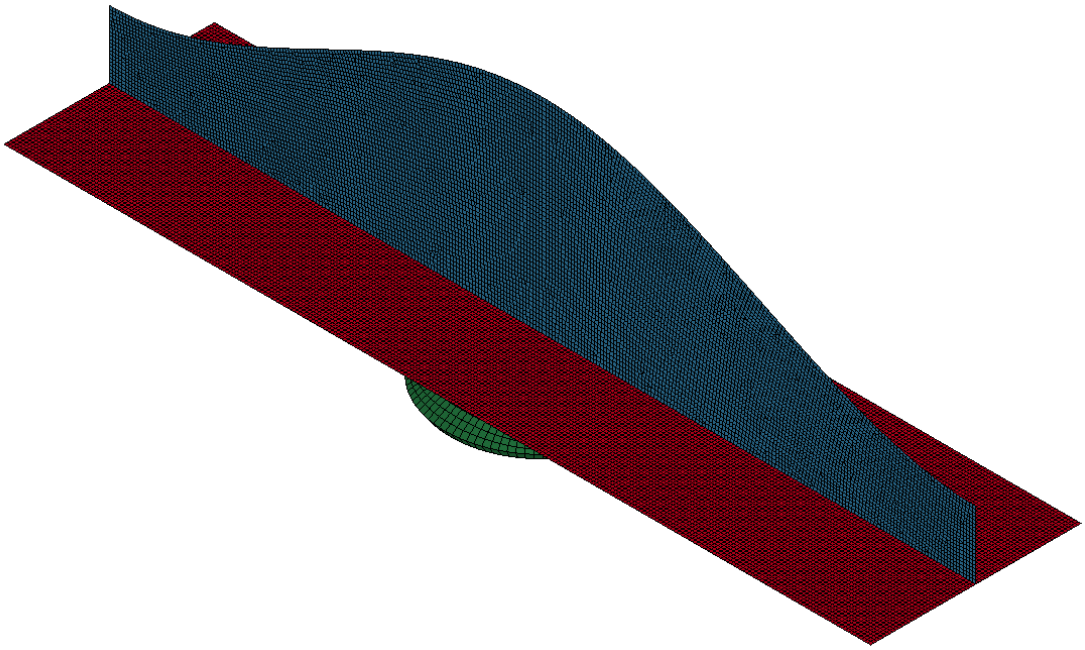

Deflection Curve 6, von Mise Stress:

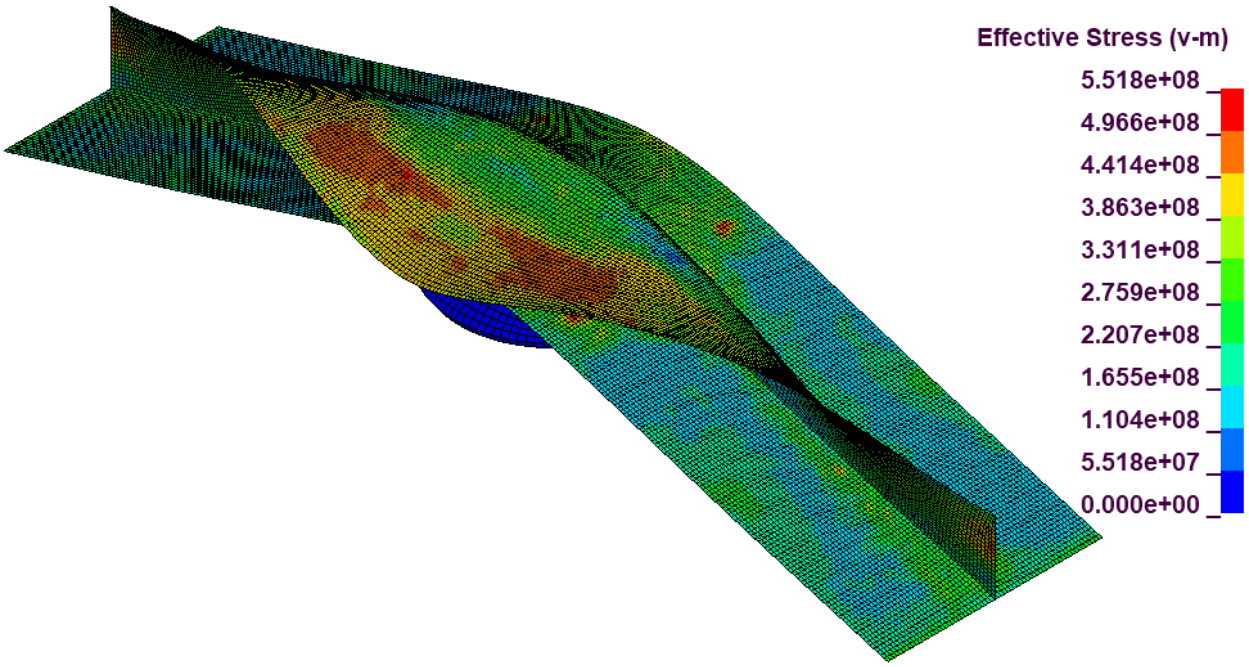

Circular Curve, Geometry:

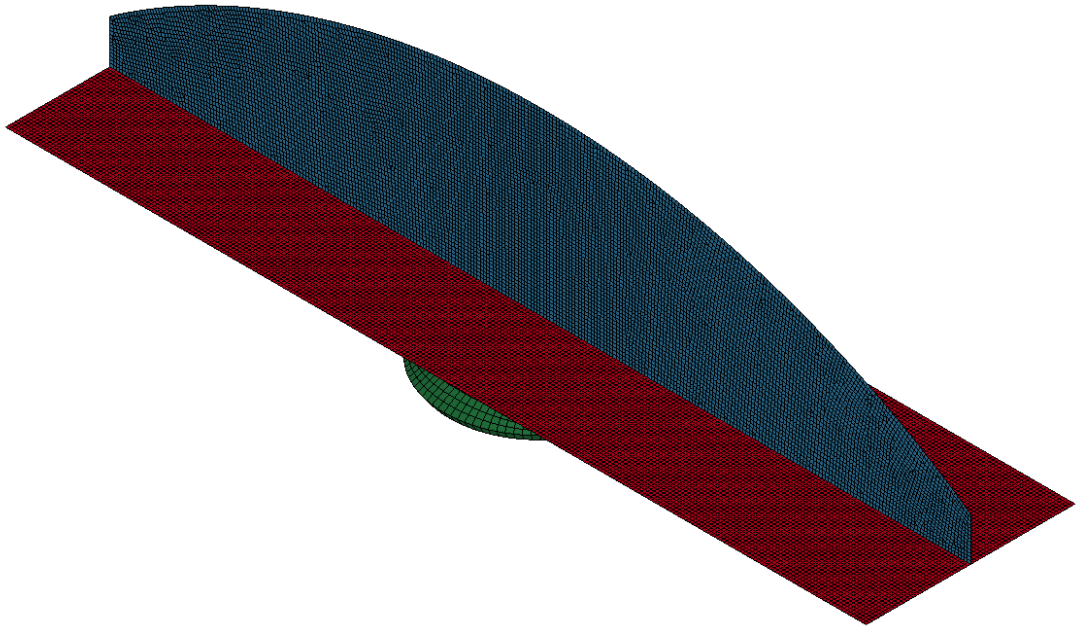

Circular Curve, von Mise Stress:

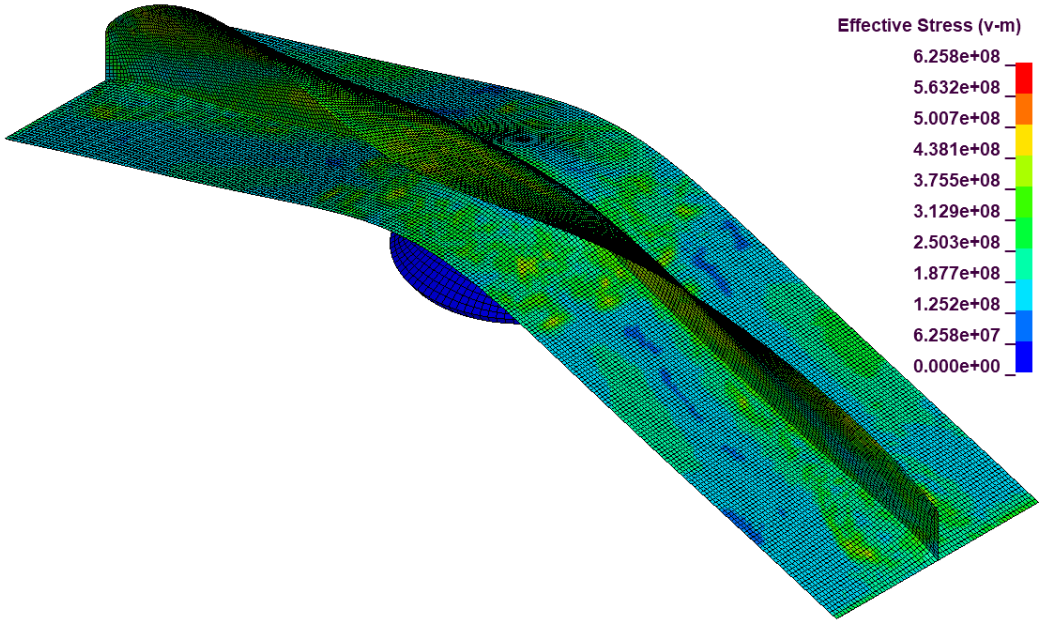

Inv. Circular Curve, Geometry:

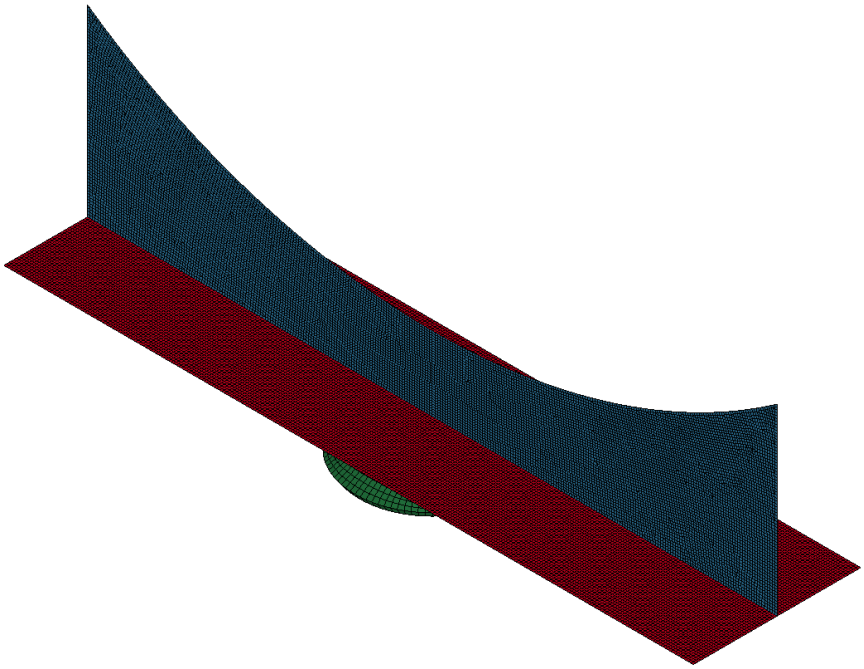

Inv. Circular Curve, von Mise Stress:

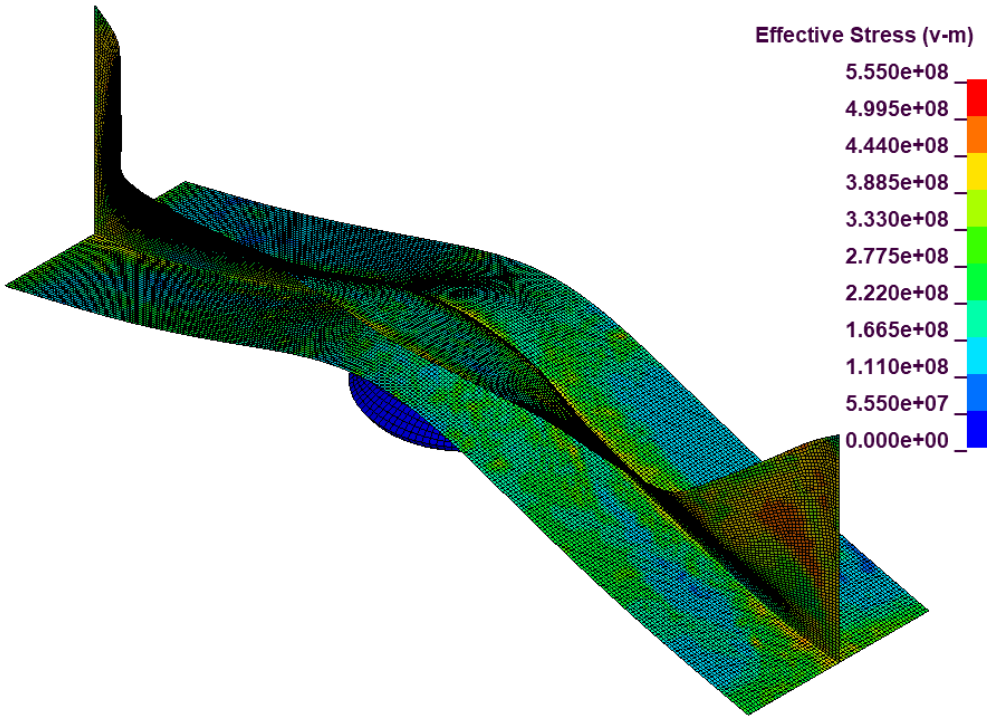

Inv. Deflection Curve 1, Geometry:

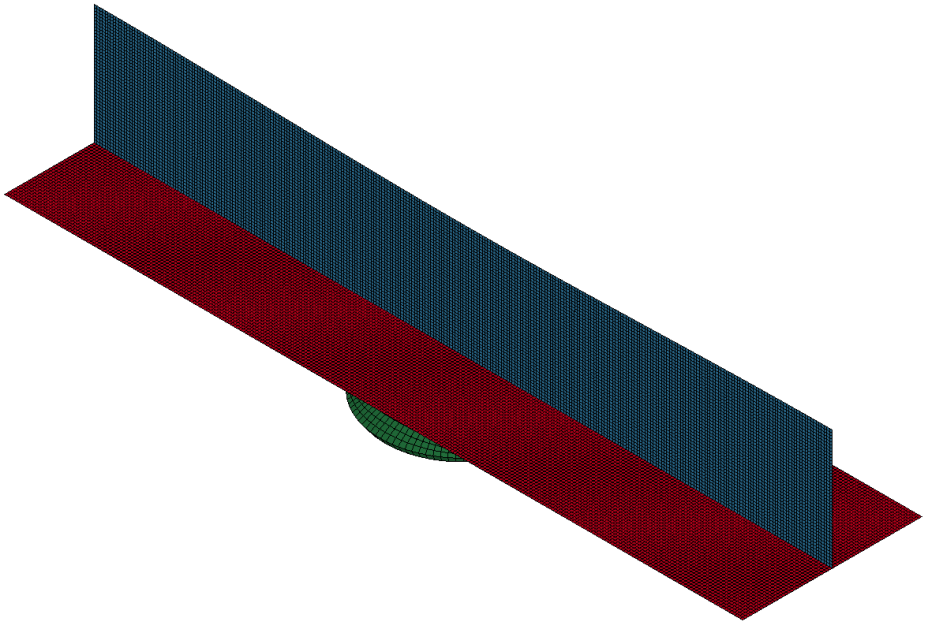

Inv. Deflection Curve 1, von Mise Stress:

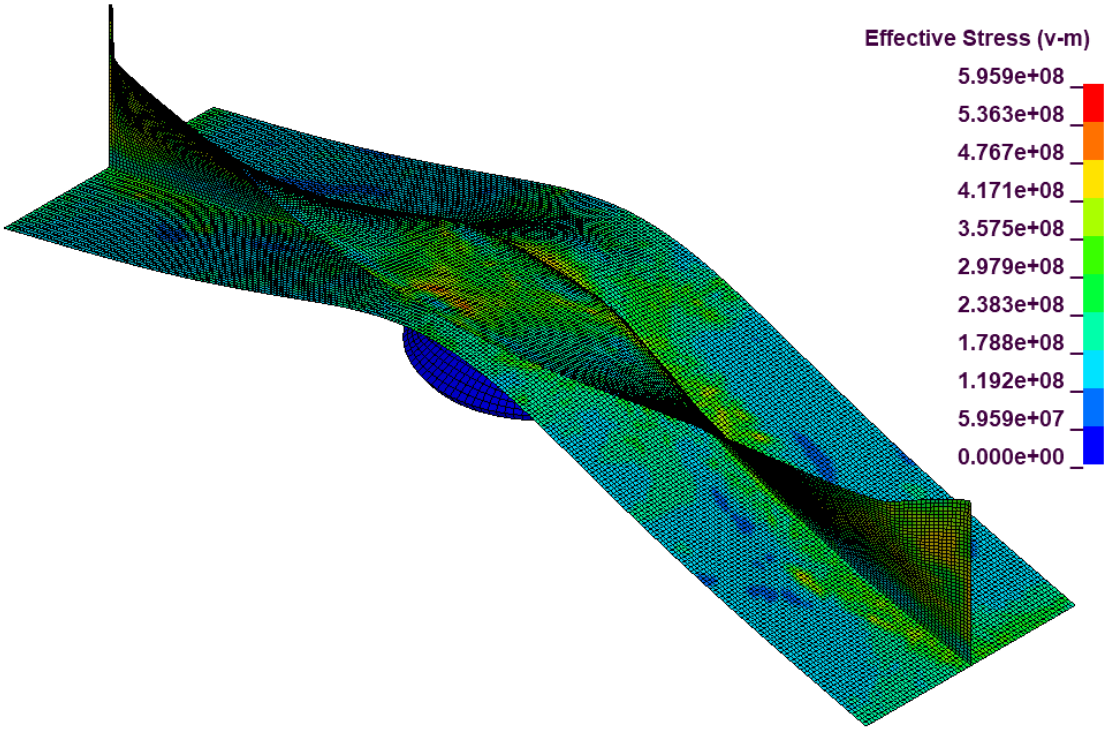

Inv. Deflection Curve 2, Geometry:

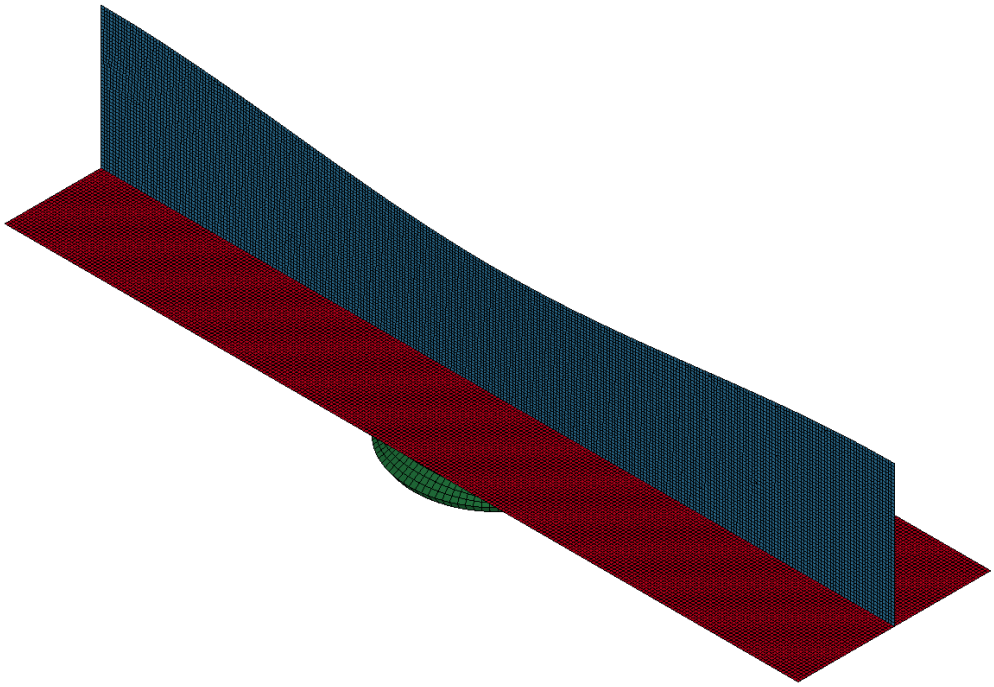

Inv. Deflection Curve 2, von Mise Stress:

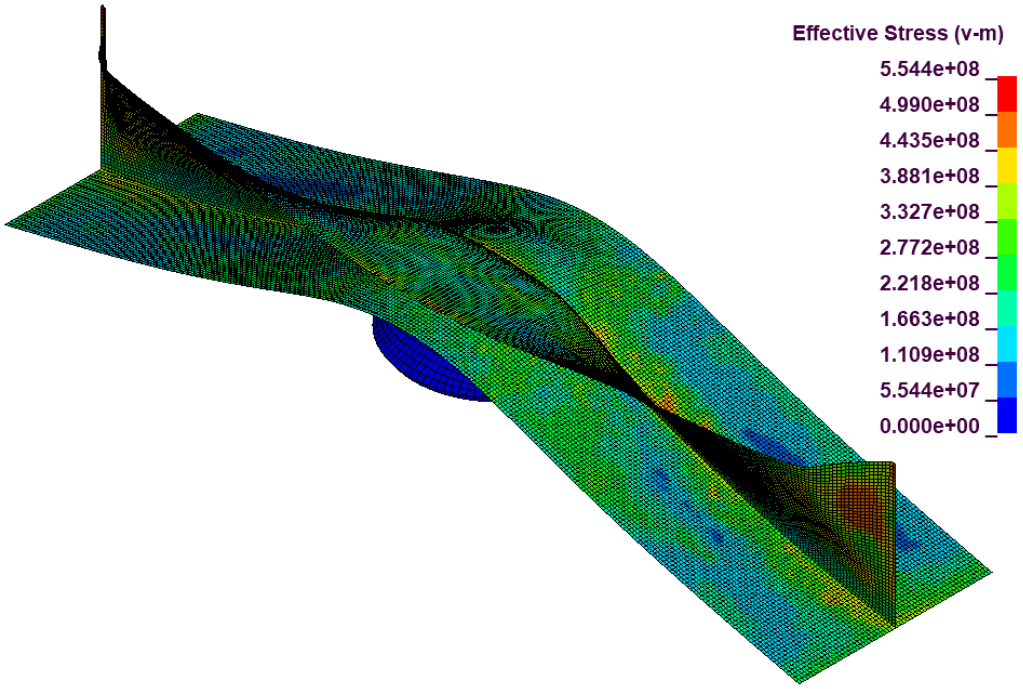

Inv. Deflection Curve 3, Geometry:

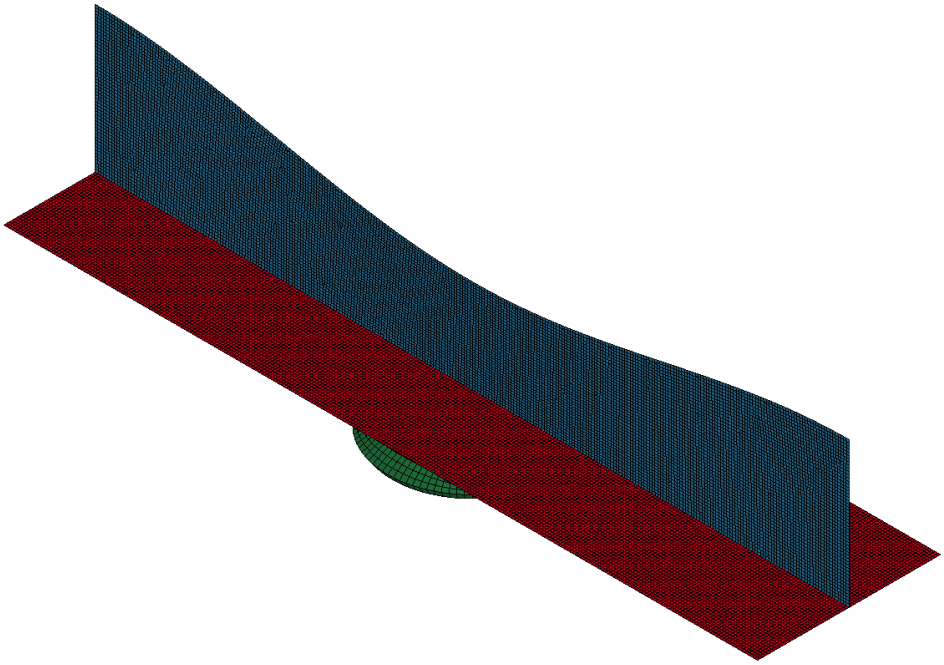

Inv. Deflection Curve 3, von Mise Stress:

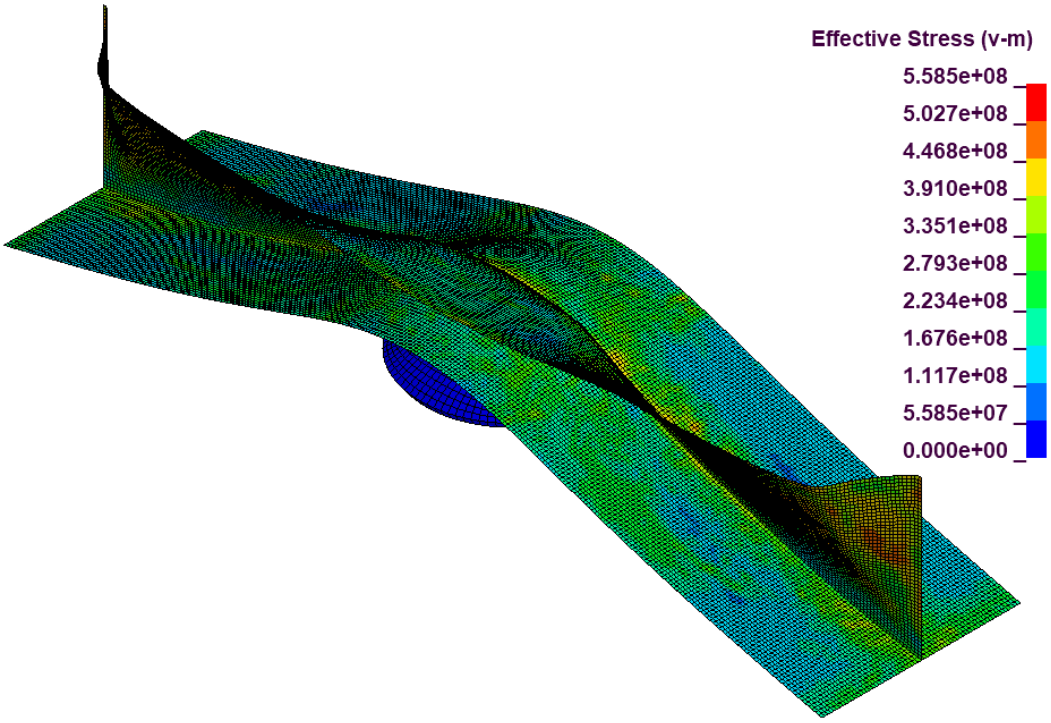

Appendix C2 – Table of Variable Dimensions and Parameters

Runs	Deflection (Web Height) mm	Impact Force N	Depth x1 mm	Breadth x2 mm	Slant x3 mm	Angle deg	Slant Length mm	Longitudinal Length m	Area c/s m^2	Area c/s Flange m^2	Area c/s Web m^2	Thickness Flange m	Thickness Web m	Flange Width m	Web Height m
Built-T (Control)	-	-	-	-	-	-	-	1.36	0.002157889	0.000809208	0.00134868	0.007935457	0.007935457	0.101973747	0.169956244
Flat Bar (Control)	-	-	-	-	-	-	-	1.36	0.002157889	-	0.002157889	-	0.010037647	-	0.214979534
Trad. Corr. 1	-	-	10	10	10	45	14.14213562	1.638	0.001791654	-	0.001791654	-	0.009146279	-	0.195888808
Trad. Corr. 2	-	-	8	8	8	45	11.3137085	1.642	0.001787289	-	0.001787289	-	0.009135132	-	0.195650064
Trad. Corr. 3	-	-	6	6	6	45	8.485281374	1.641	0.001788378	-	0.001788378	-	0.009137915	-	0.195709668
Trad. Corr. 4	-	-	4	4	4	45	5.656854249	1.642	0.001787289	-	0.001787289	-	0.009135132	-	0.195650064
S Corr. 1	-	-	-	-	-	-	-	1.535	0.001911875	-	0.001911875	-	0.009448159	-	0.202354274
S Corr. 2	-	-	-	-	-	-	-	1.535	0.001911875	0.000716953	0.001194922	0.007469426	0.007469426	0.09598506	0.1599751
S Corr. 3	-	-	-	-	-	-	-	1.535	0.001997263	0.000748974	0.00124829	0.007634403	0.007634403	0.098105082	0.163508471
S Corr. 4	-	-	-	-	-	-	-	1.535	0.001953637	0.000366307	0.00158733	0.005339054	0.008608966	0.068608948	0.184381008
S Corr. 5	-	-	-	-	-	-	-	1.535	0.001997263	0.000748974	0.00124829	0.007634403	0.007634403	0.098105082	0.163508471
S Corr. 6	-	-	-	-	-	-	-	1.36	0.002058556	0.000771958	0.001286597	0.007750661	0.007750661	0.099599046	0.16599841
S Corr. 7	-	-	-	-	-	-	-	1.458	0.002012845	-	0.002012845	-	0.009694438	-	0.207628903
Bulb	-	-	-	-	-	-	-	1.36	0.002157889	0.000857375	0.001300514	0.018226256	0.00850611	0.047040634	0.15289175
CHS (Constant Thickness)	-	-	-	-	-	-	-	1.36	0.002157889	-	-	-	0.0079375	-	-
CHS with Flange	-	-	-	-	-	-	-	1.36	0.002157889	0.000580751	0.001577138	0.006722593	0.008581283	0.086387961	0.183788104
Non-Uniform Flange 1	-	-	-	-	-	-	-	1.36	0.002157889	0.000809208	0.00134868	0.007935457	0.007935457	0.101973747	0.169956244
Non-Uniform Flange 2	-	-	-	-	-	-	-	1.36	0.002157889	0.000809208	0.00134868	0.007935457	0.007935457	0.101973747	0.169956244
Flat Bar with Brackets 1	-	-	-	-	-	-	-	1.36	varies	varies	varies	0.007935457	0.007935457	varies	0.169956244
Flat Bar with Brackets 2	-	-	-	-	-	-	-	1.36	varies	varies	varies	0.007935457	0.007935457	varies	0.169956244
Flat Bar with Brackets 3	-	-	-	-	-	-	-	1.36	varies	varies	varies	0.007935457	0.007935457	varies	0.169956244
Flat Bar with Brackets 4	-	-	-	-	-	-	-	1.36	varies	varies	varies	0.007935457	0.007935457	varies	0.169956244
Flat Bar with Brackets 5	-	-	-	-	-	-	-	1.36	varies	varies	varies	0.007935457	0.007935457	varies	varies
CircularCurve	215	-	-	-	-	-	-	1.36	0.002157889	-	0.002157889	-	0.010037647	-	0.214979534
InvCircularCurve	215	-	-	-	-	-	-	1.36	0.002157889	-	0.002157889	-	0.010037647	-	0.214979534
DeflectCurve1	11.97	1600000	-	-	-	-	-	1.36	0.002157889	-	0.002157889	-	0.010037647	-	0.214979534
DeflectCurve2	52.6	7030000	-	-	-	-	-	1.36	0.002157889	-	0.002157889	-	0.010037647	-	0.214979534
DeflectCurve3	93.2	12460000	-	-	-	-	-	1.36	0.002157889	-	0.002157889	-	0.010037647	-	0.214979534
DeflectCurve4	133.8	17890000	-	-	-	-	-	1.36	0.002157889	-	0.002157889	-	0.010037647	-	0.214979534
DeflectCurve5	174.5	23320000	-	-	-	-	-	1.36	0.002157889	-	0.002157889	-	0.010037647	-	0.214979534
DeflectCurve6	215.1	28750000	-	-	-	-	-	1.36	0.002157889	-	0.002157889	-	0.010037647	-	0.214979534
InvDeflectCurve1	-12.0	-1600000	-	-	-	-	-	1.36	0.002157889	-	0.002157889	-	0.010037647	-	0.214979534
InvDeflectCurve2	-52.6	-7030000	-	-	-	-	-	1.36	0.002157889	-	0.002157889	-	0.010037647	-	0.214979534
InvDeflectCurve3	-93.2	-12460000	-	-	-	-	-	1.36	0.002157889	-	0.002157889	-	0.010037647	-	0.214979534

Appendix C3 – Deflection Diagram Raw Data from Calculations

x	yx (x<=a0)	Original			1			2			3			4			5			6		
mm	mm	yx (a0<x<b0) mm	yx (x>=b0) mm	yx Real mm	yx (a0<x<b0) mm	yx (x>=b0) mm	yx Real mm	yx (a0<x<b0) mm	yx (x>=b0) mm	yx Real mm	yx (a0<x<b0) mm	yx (x>=b0) mm	yx Real mm	yx (a0<x<b0) mm	yx (x>=b0) mm	yx Real mm	yx (a0<x<b0) mm	yx (x>=b0) mm	yx Real mm	yx (a0<x<b0) mm	yx (x>=b0) mm	yx Real mm
0.00	0.00	8.73	-53.36	0.00	8.73	-53.36	0.00	38.35	-234.46	0.00	67.98	-415.56	0.00	97.60	-596.65	0.00	127.23	-777.75	0.00	156.85	-958.85	0.00
34.00	0.09	6.74	-45.93	0.09	6.74	-45.93	0.09	29.60	-201.81	0.39	52.47	-357.69	0.70	75.33	-513.57	1.00	98.20	-669.46	1.31	121.06	-825.34	1.61
68.00	0.35	5.31	-39.05	0.35	5.31	-39.05	0.35	23.33	-171.59	1.52	41.34	-304.13	2.69	59.36	-436.67	3.87	77.38	-569.21	5.04	95.39	-701.75	6.21
102.00	0.75	4.37	-32.71	0.75	4.37	-32.71	0.75	19.20	-143.72	3.29	34.03	-254.72	5.84	48.87	-365.73	8.38	63.70	-476.73	10.93	78.53	-587.74	13.47
136.00	1.28	3.85	-26.88	1.28	3.85	-26.88	1.28	16.93	-118.10	5.63	30.01	-209.32	9.99	43.09	-300.54	14.34	56.16	-391.76	18.69	69.24	-482.98	23.04
170.00	1.92	3.63	-21.54	1.92	3.63	-21.54	1.92	16.23	-94.66	8.46	28.76	-167.77	14.99	41.29	-240.89	21.52	53.83	-314.00	28.06	66.36	-387.12	34.59
204.00	2.66	3.83	-16.69	2.66	3.83	-16.69	2.66	16.82	-73.31	11.68	29.81	-129.94	20.70	42.80	-186.57	29.72	55.80	-243.20	38.75	68.79	-299.82	47.77
238.00	3.46	4.20	-12.29	3.46	4.20	-12.29	3.46	18.46	-53.98	15.22	32.72	-95.67	26.98	46.98	-137.37	38.73	61.24	-179.06	50.49	75.50	-220.75	62.24
272.00	4.32	4.76	-8.32	4.32	4.76	-8.32	4.32	20.92	-36.57	18.99	37.08	-64.82	33.66	53.23	-93.07	48.33	69.39	-121.32	63.00	85.55	-149.56	77.67
306.00	5.22	5.46	-4.78	5.22	5.46	-4.78	5.22	23.37	-21.01	22.91	42.43	-37.24	40.61	61.01	-53.46	58.31	79.52	-69.69	76.01	98.04	-85.92	93.71
340.00	6.12	6.24	-1.64	6.12	6.24	-1.64	6.12	27.43	-7.21	26.90	48.61	-12.78	47.69	69.80	-18.34	68.47	90.98	-23.91	89.25	112.17	-29.48	110.03
374.00	7.03	7.08	1.12	7.03	7.08	1.12	7.03	31.10	4.92	30.88	55.12	8.71	54.73	79.15	12.51	78.58	103.17	16.30	102.43	127.19	20.10	126.28
408.00	7.91	7.93	3.51	7.91	7.93	3.51	7.91	34.83	15.44	34.75	61.73	27.37	61.60	88.63	39.30	88.44	115.53	51.23	115.28	142.43	63.15	142.13
442.00	8.75	8.75	5.57	8.75	8.75	5.57	8.75	38.46	24.46	38.45	68.17	43.35	68.14	97.88	62.24	97.84	127.59	81.13	127.53	157.30	100.02	157.23
476.00	9.53	9.53	7.29	9.53	9.53	7.29	9.53	41.87	32.04	41.87	74.22	56.80	74.22	106.56	81.55	106.56	138.91	106.30	138.90	171.25	131.05	171.24
510.00	10.23	10.23	8.71	10.23	10.23	8.71	10.23	44.35	38.28	44.35	79.67	67.86	79.67	114.39	97.43	114.39	149.11	127.00	149.11	183.83	156.57	183.83
544.00	10.83	10.83	9.85	10.83	10.83	9.85	10.83	47.60	43.26	47.60	84.36	76.68	84.36	121.13	110.09	121.13	157.89	143.51	157.89	194.66	176.93	194.66
578.00	11.32	11.32	10.71	11.32	11.32	10.71	11.32	49.74	47.06	49.74	88.16	83.41	88.16	126.57	119.76	126.57	164.99	156.11	164.99	203.41	192.46	203.41
612.00	11.67	11.68	11.33	11.68	11.68	11.33	11.68	51.31	49.76	51.31	90.94	88.20	90.94	130.57	126.63	130.57	170.21	165.07	170.21	209.84	203.51	209.84
646.00	11.86	11.90	11.71	11.90	11.90	11.71	11.90	52.27	51.45	52.27	92.64	91.13	92.64	133.02	130.93	133.02	173.39	170.67	173.39	213.76	210.41	213.76
680.00	11.88	11.97	11.88	11.97	11.97	11.88	11.97	52.59	52.21	52.59	93.22	92.53	93.22	133.84	132.86	133.84	174.46	173.18	174.46	215.09	213.51	215.09
714.00	11.71	11.90	11.86	11.90	11.90	11.86	11.90	52.27	52.12	52.27	92.64	92.38	92.64	133.02	132.63	133.02	173.39	172.89	173.39	213.76	213.14	213.76
748.00	11.33	11.68	11.67	11.68	11.68	11.67	11.68	51.31	51.27	51.31	90.94	90.86	90.94	130.57	130.46	130.57	170.21	170.06	170.21	209.84	209.65	209.84
782.00	10.71	11.32	11.32	11.32	11.32	11.32	11.32	49.74	49.73	49.74	88.16	88.14	88.16	126.57	126.55	126.57	164.99	164.97	164.99	203.41	203.38	203.41
816.00	9.85	10.83	10.83	10.83	10.83	10.83	10.83	47.60	47.60	47.60	84.36	84.36	84.36	121.13	121.13	121.13	157.89	157.89	157.89	194.66	194.66	194.66
850.00	8.71	10.23	10.23	10.23	10.23	10.23	10.23	44.35	44.35	44.35	79.67	79.67	79.67	114.39	114.39	114.39	149.11	149.11	149.11	183.83	183.83	183.83
884.00	7.29	9.53	9.53	9.53	9.53	9.53	9.53	41.87	41.87	41.87	74.22	74.22	74.22	106.56	106.56	106.56	138.91	138.90	138.90	171.25	171.24	171.24
918.00	5.57	8.75	8.75	8.75	8.75	8.75	8.75	38.46	38.45	38.45	68.17	68.14	68.14	97.88	97.84	97.84	127.59	127.53	127.53	157.30	157.23	157.23
952.00	3.51	7.93	7.91	7.91	7.93	7.91	7.91	34.83	34.75	34.75	61.73	61.60	61.60	88.63	88.44	88.44	115.53	115.28	115.28	142.43	142.13	142.13
986.00	1.12	7.08	7.03	7.03	7.08	7.03	7.03	31.10	30.88	30.88	55.12	54.73	54.73	79.15	78.58	78.58	103.17	102.43	102.43	127.19	126.28	126.28
1020.00	-1.64	6.24	6.12	6.12	6.24	6.12	6.12	27.43	26.90	26.90	48.61	47.69	47.69	69.80	68.47	68.47	90.98	89.25	89.25	112.17	110.03	110.03
1054.00	-4.78	5.46	5.22	5.22	5.46	5.22	5.22	23.37	22.91	22.91	42.43	40.61	40.61	61.01	58.31	58.31	79.52	76.01	76.01	98.04	93.71	93.71
1088.00	-8.32	4.76	4.32	4.32	4.76	4.32	4.32	20.92	18.99	18.99	37.08	33.66	33.66	53.23	48.33	48.33	69.39	63.00	63.00	85.55	77.67	77.67
1122.00	-12.29	4.20	3.46	3.46	4.20	3.46	3.46	18.46	15.22	15.22	32.72	26.98	26.98	46.98	38.73	38.73	61.24	50.49	50.49	75.50	62.24	62.24
1156.00	-16.69	3.83	2.66	2.66	3.83	2.66	2.66	16.82	11.68	11.68	29.81	20.70	20.70	42.80	29.72	29.72	55.80	38.75	38.75	68.79	47.77	47.77
1190.00	-21.54	3.63	1.92	1.92	3.63	1.92	1.92	16.23	8.46	8.46	28.76	14.99	14.99	41.29	21.52	21.52	53.83	28.06	28.06	66.36	34.59	34.59
1224.00	-26.88	3.85	1.28	1.28	3.85	1.28	1.28	16.93	5.63	5.63	30.01	9.99	9.99	43.09	14.34	14.34	56.16	18.69	18.69	69.24	23.04	23.04
1258.00	-32.71	4.37	0.75	0.75	4.37	0.75	0.75	19.20	3.29	3.29	34.03	5.84	5.84	48.87	8.38	8.38	63.70	10.93	10.93	78.53	13.47	13.47
1292.00	-39.05	5.31	0.35	0.35	5.31	0.35	0.35	23.33	1.52	1.52	41.34	2.69	2.69	59.36	3.87	3.87	77.38	5.04	5.04	95.39	6.21	6.21
1326.00	-45.93	6.74	0.09	0.09	6.74	0.09	0.09	29.60	0.39	0.39	52.47	0.70	0.70	75.33	1.00	1.00	98.20	1.31	1.31	121.06	1.61	1.61
1360.00	-53.36	8.73	0.00	0.00	8.73	0.00	0.00	38.35	0.00	0.00	67.98	0.00	0.00	97.60	0.00	0.00	127.23	0.00	0.00	156.85	0.00	0.00

Appendix C4 – von Mises Stress vs. Displacement Plots

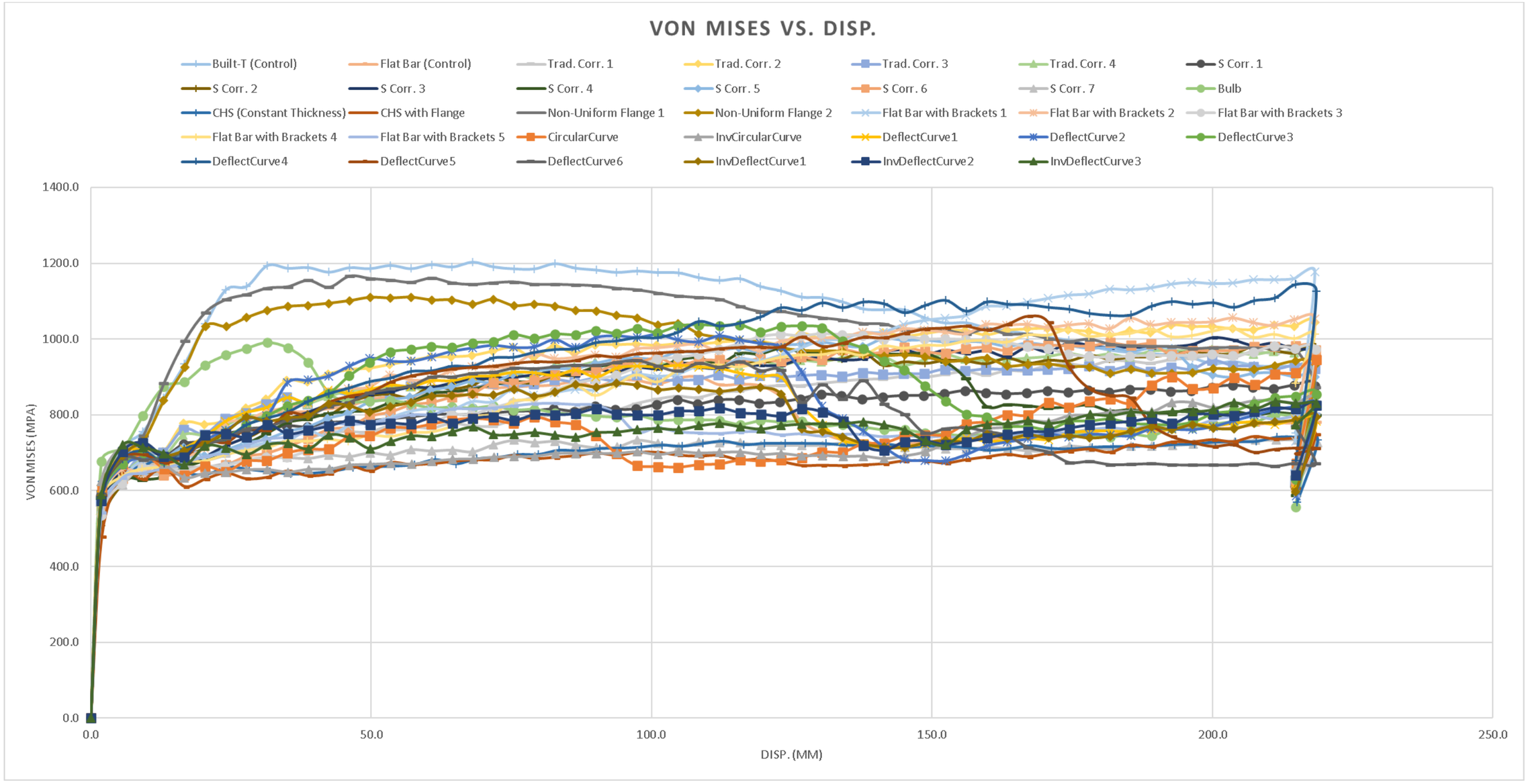

Appendix C5 – Force vs. Displacement Plots

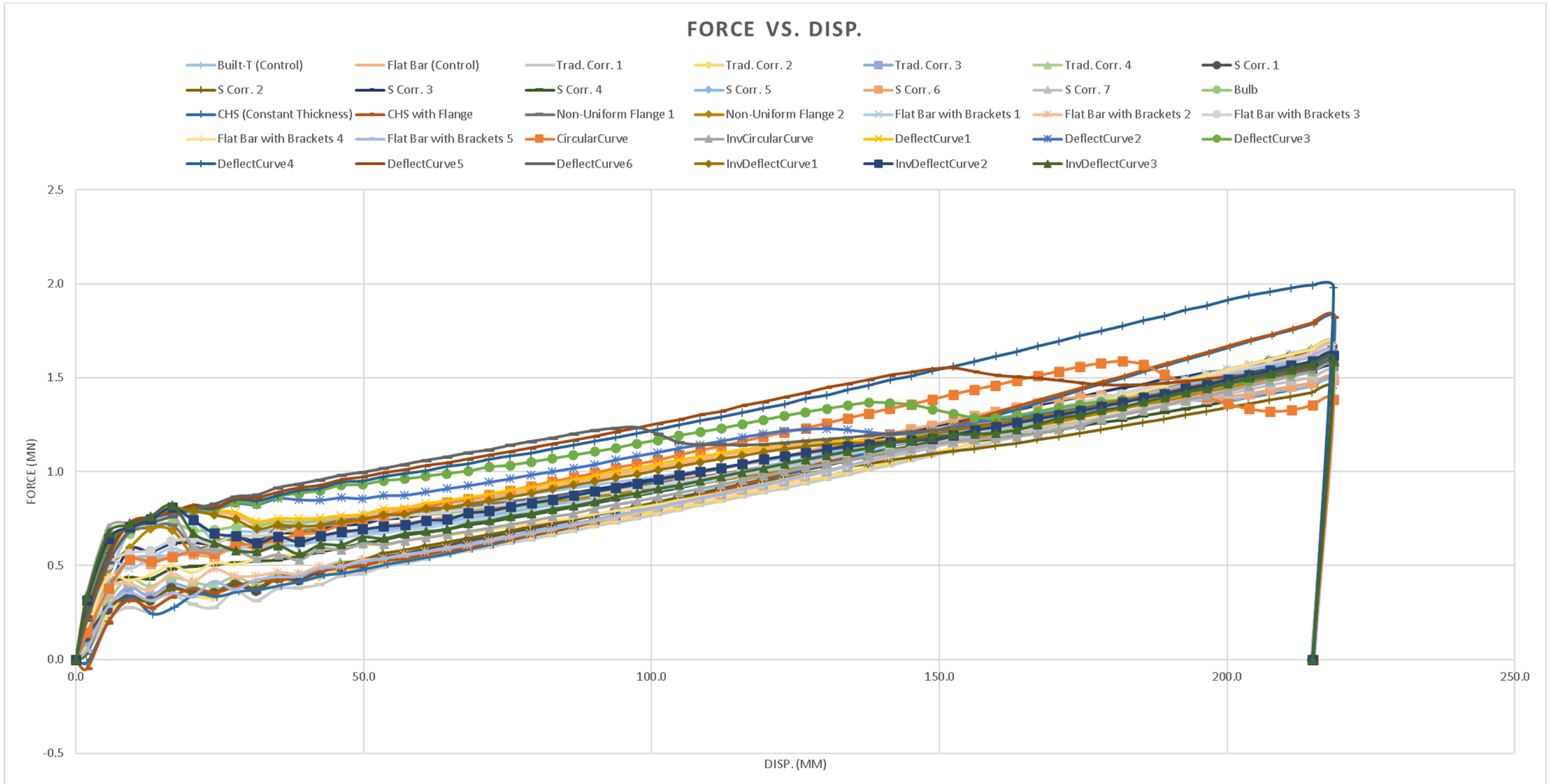

Appendix C6 – Element Quality Checks

Quality Name	Min. val	Max. val	Allowable	#Violated(%)
Aspect Ratio	1	2.31	10	0(0%)
Warpage	0	10.5	10	4(0.227%)
Min Quad Angle	37.8	90	45	4(0.227%)
Max Quad Angle	90	147	135	5(0.283%)
Min Tria Angle	38.9	58.7	30	0(0%)
Max Tria Angle	60.8	98	120	0(0%)
Skew	0	48.8	45	2(0.113%)
Jacobian	0.552	1	0.6	2(0.113%)

#QUADS(%):1738(98.5%), #TRIAS(%):26(1.47%), #TOTAL OF FAILED(%):2(0.113%)

Appendix D – Exp3 Appendices

Appendix D1 – Geometry and von Mises Stress Visuals

Due to the large quantity of experimental results within Exp3, visuals have only been shown for the undeformed geometry and maximum von Mises stress state for Load Case 2 (impact on a stiffener in the middle of its span). However, for the control runs, visuals for the undeformed geometry and maximum von Mises stress state for all three load cases were shown.

Control – Built-T, Geometry:

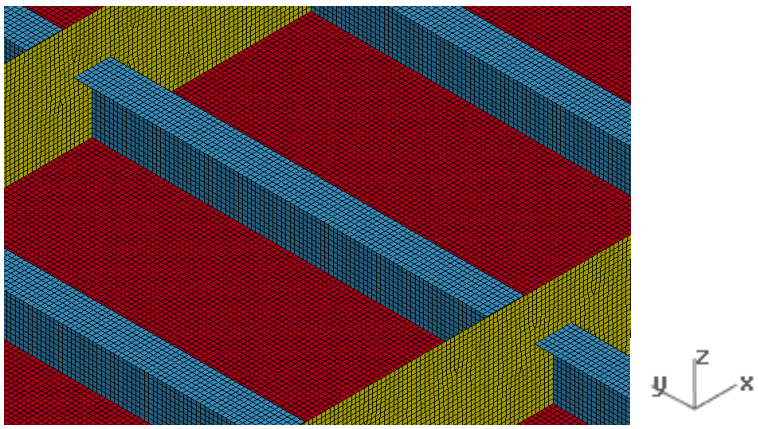

Control – Built-T, von Mise Stress, Load Case 1:

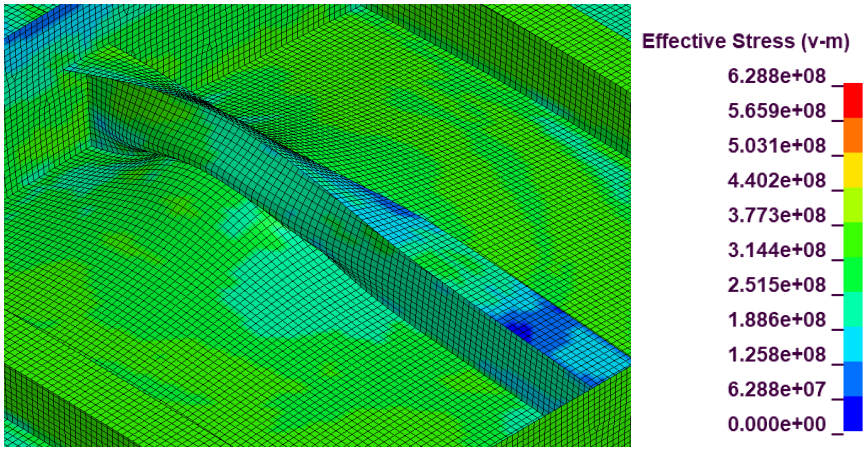

Control – Built-T, von Mise Stress, Load Case 2:

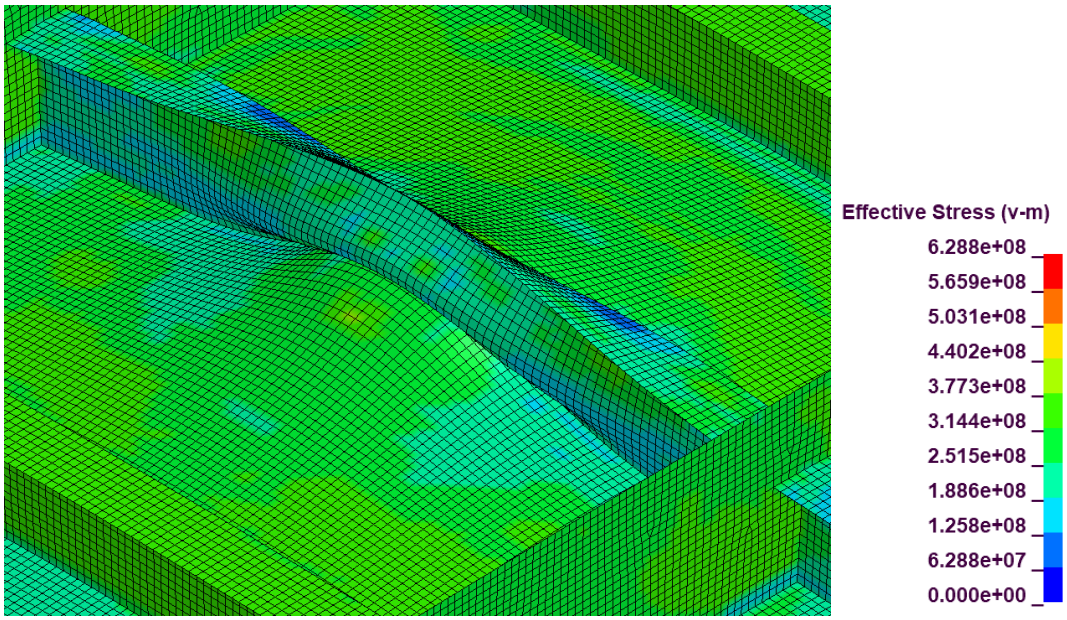

Control – Built-T, von Mise Stress, Load Case 3:

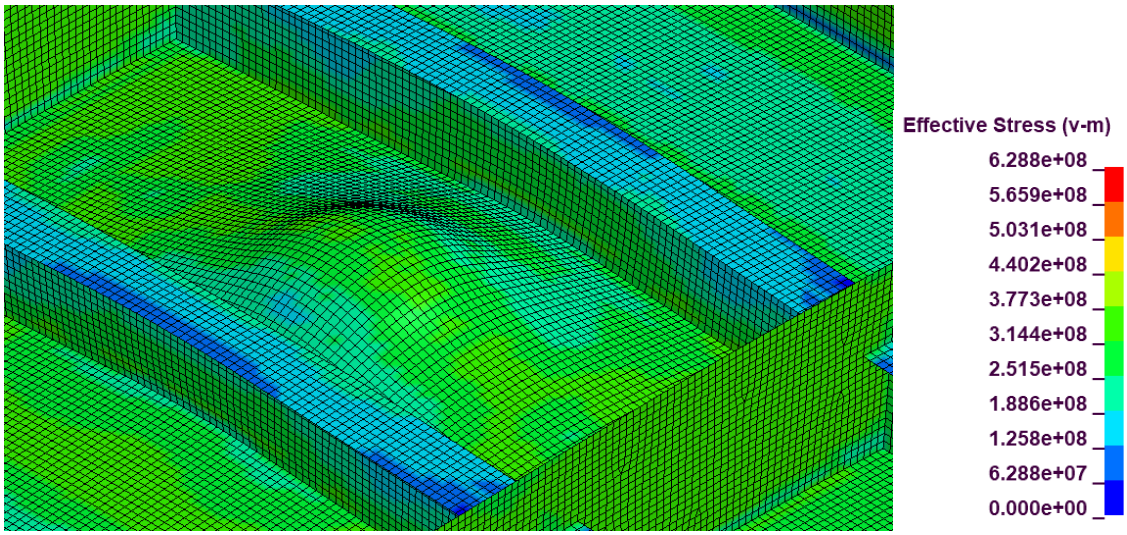

Control – Flat Bar, Geometry:

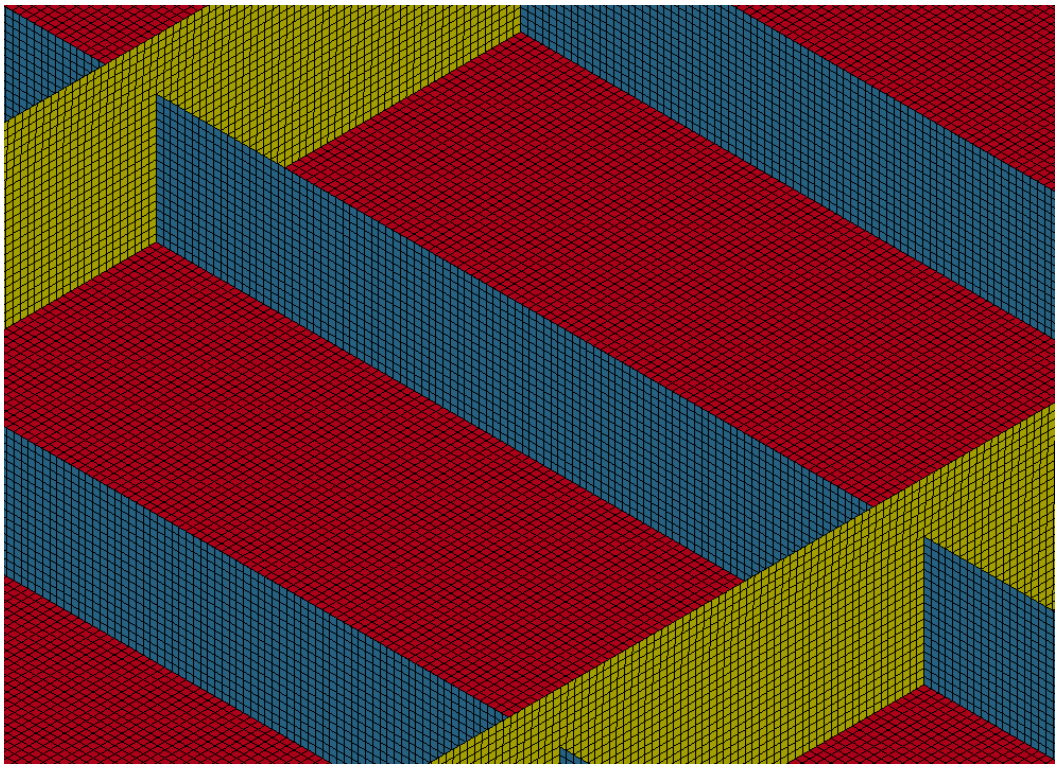

Control – Flat Bar, von Mise Stress, Load Case 1:

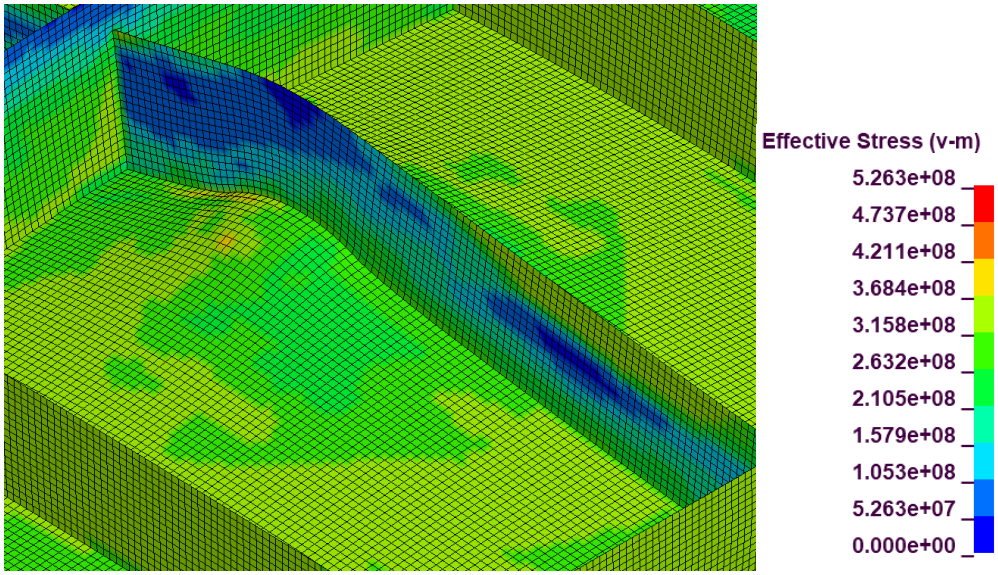

Control – Flat Bar, von Mise Stress, Load Case 2:

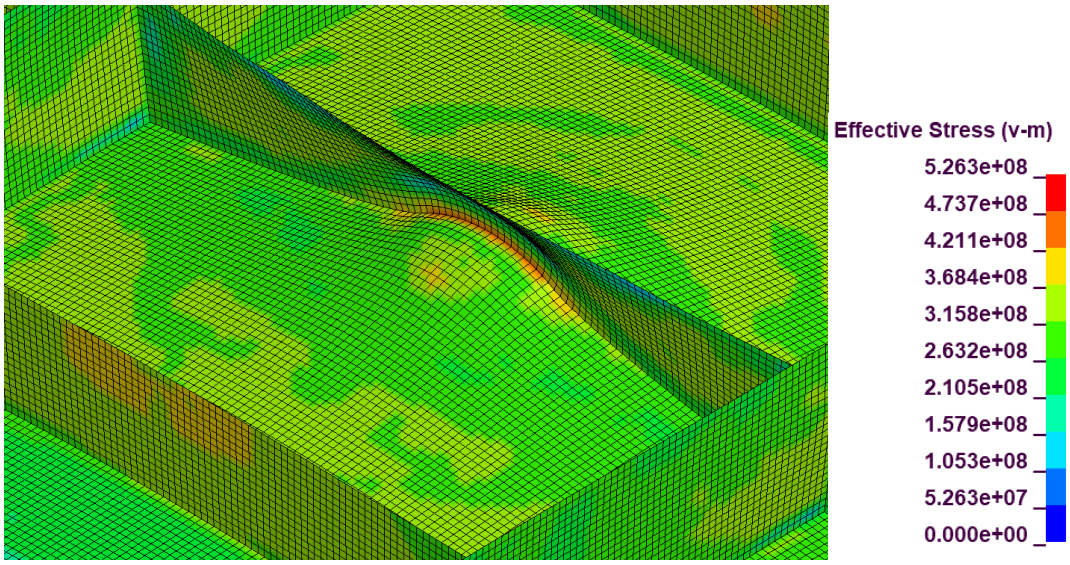

Control – Flat Bar, von Mise Stress, Load Case 3:

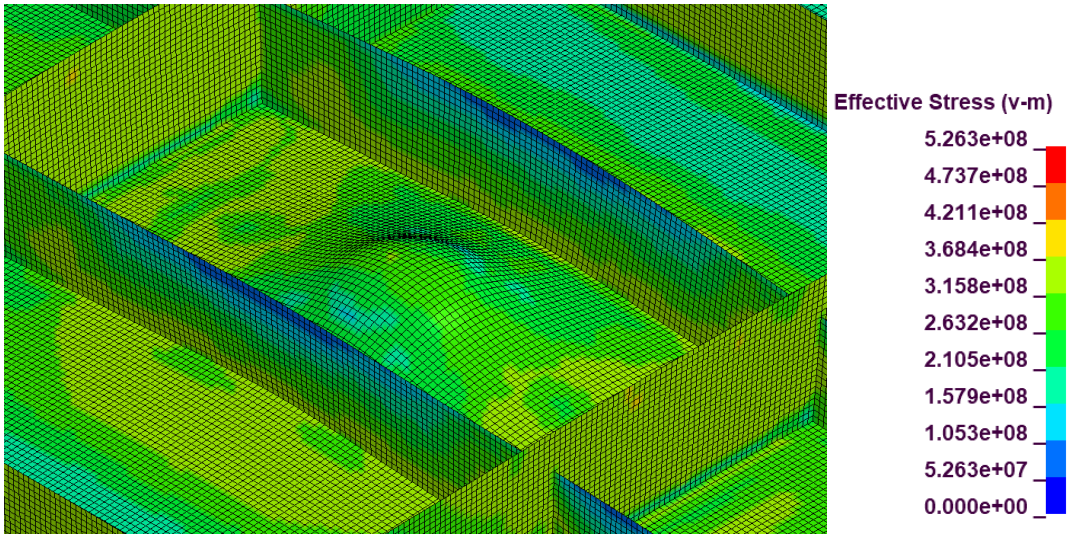

Run1, Geometry:

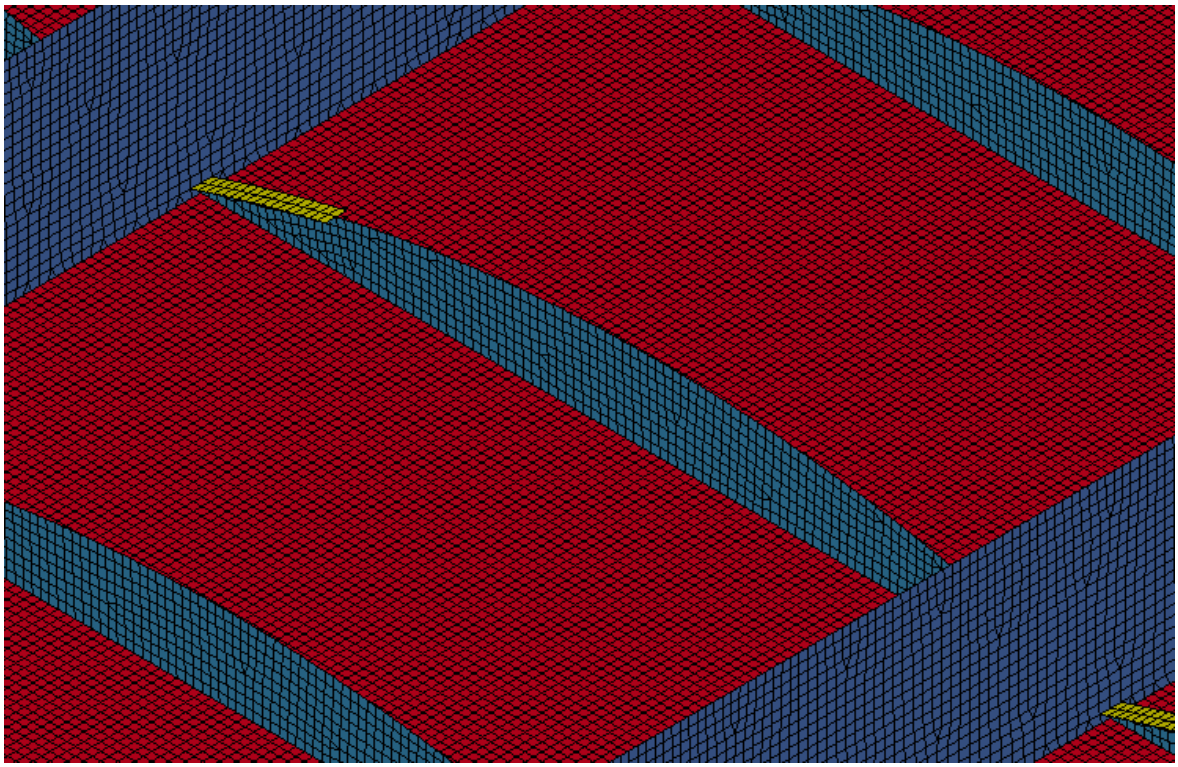

Run1, von Mise Stress, Load Case 2:

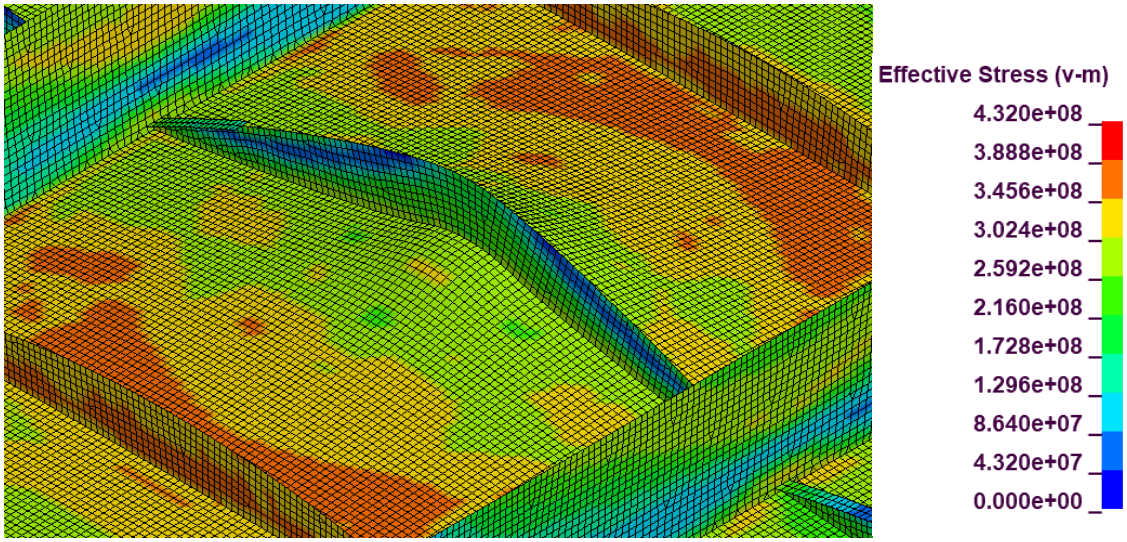

Run2, Geometry:

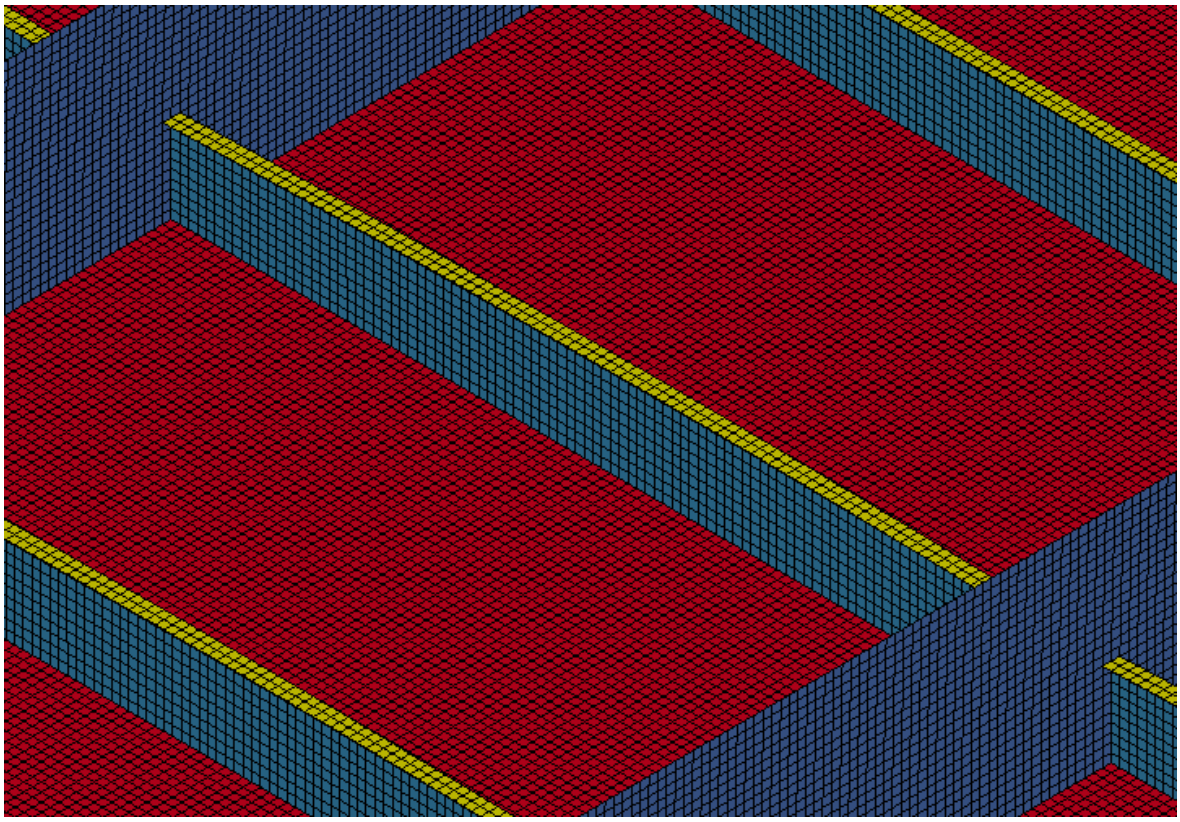

Run2, von Mise Stress, Load Case 2:

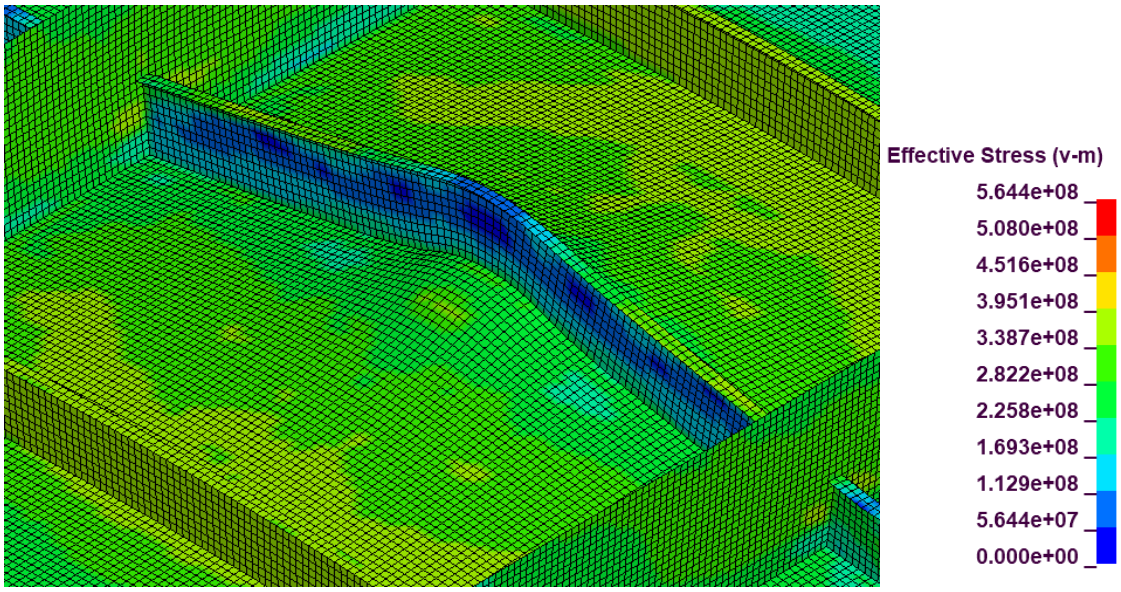

Run3, Geometry:

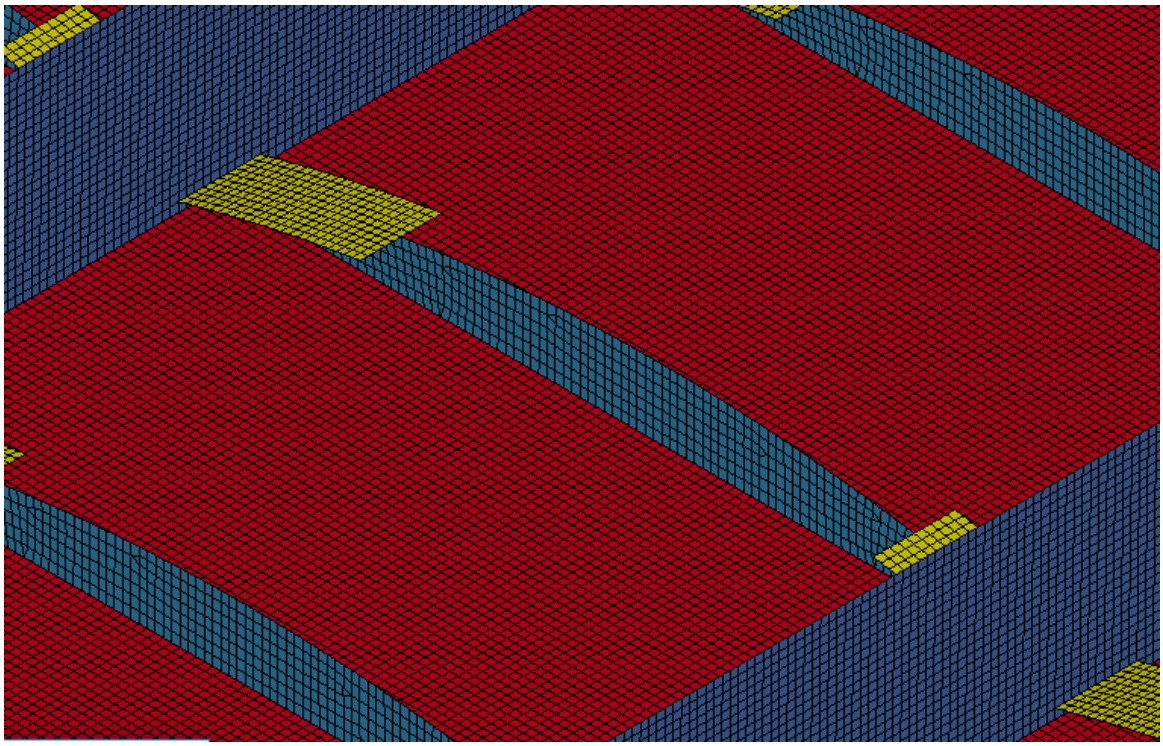

Run3, von Mise Stress, Load Case 2:

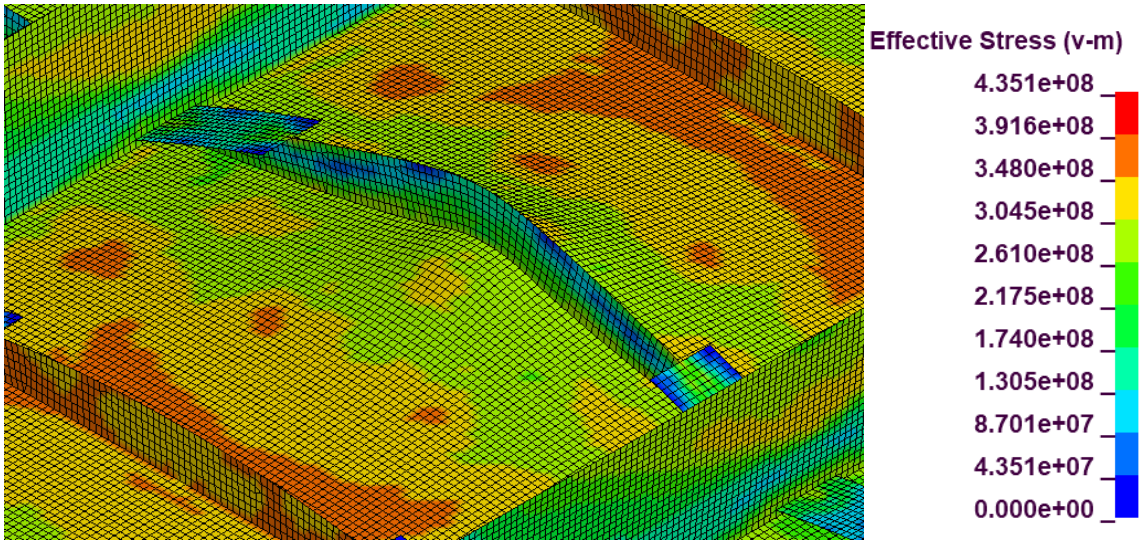

Run4, Geometry:

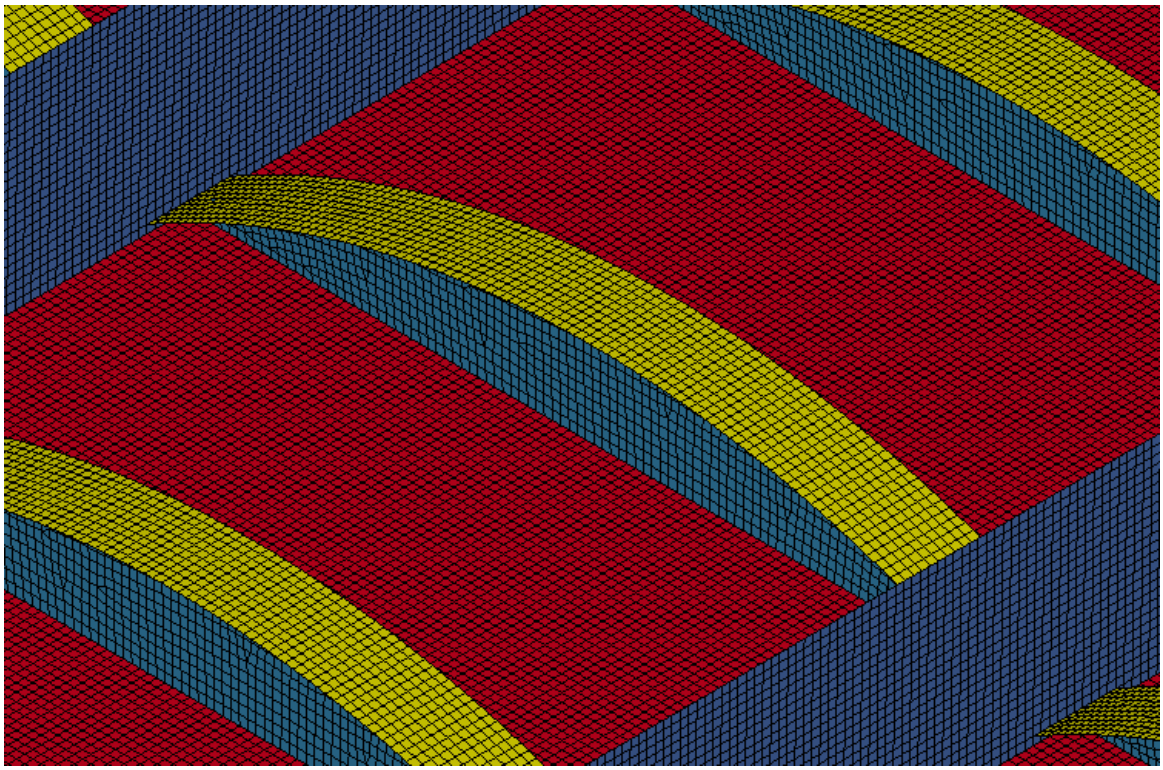

Run4, von Mise Stress, Load Case 2:

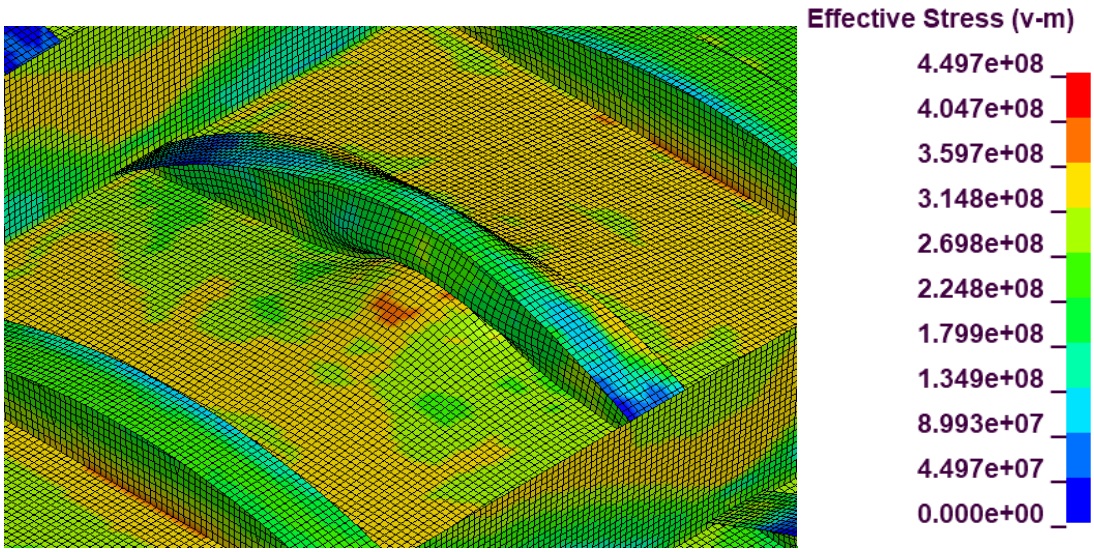

Run5, Geometry:

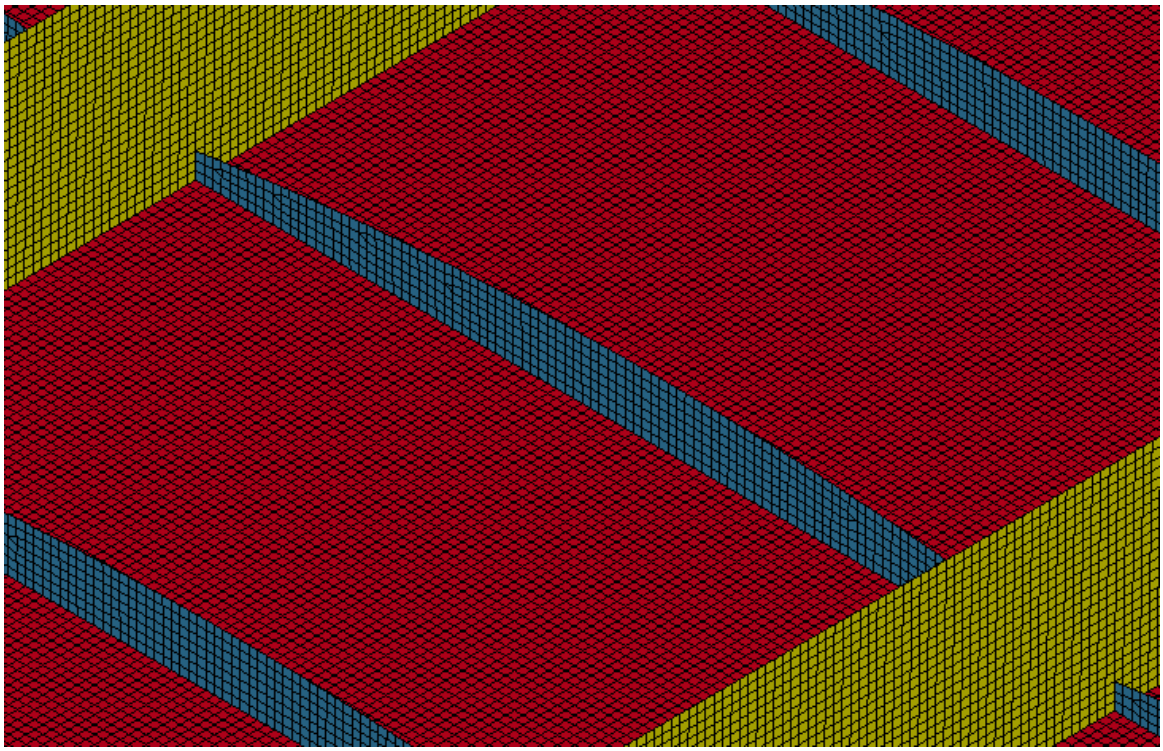

Run5, von Mise Stress, Load Case 2:

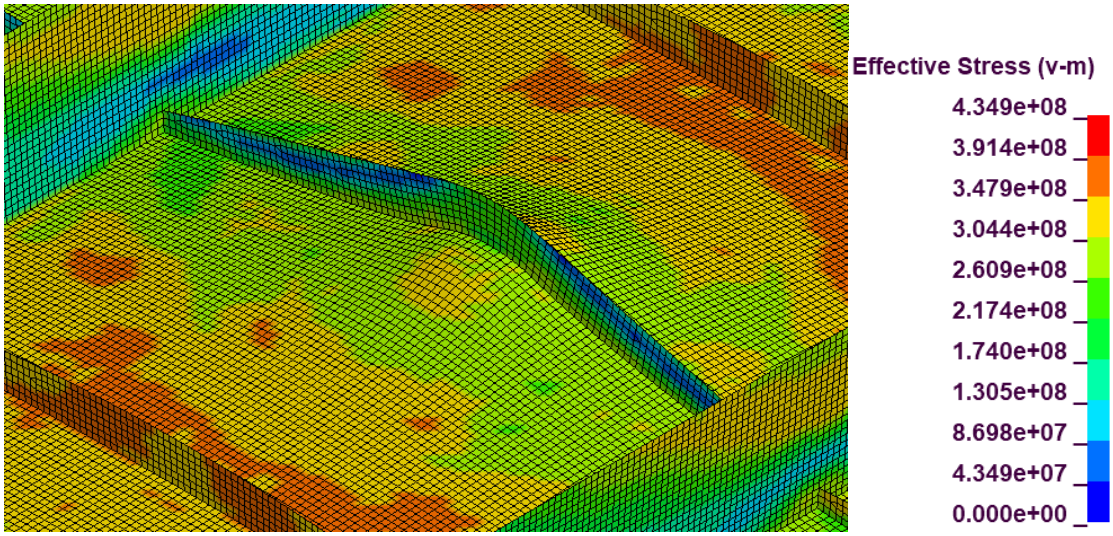

Run6, Geometry:

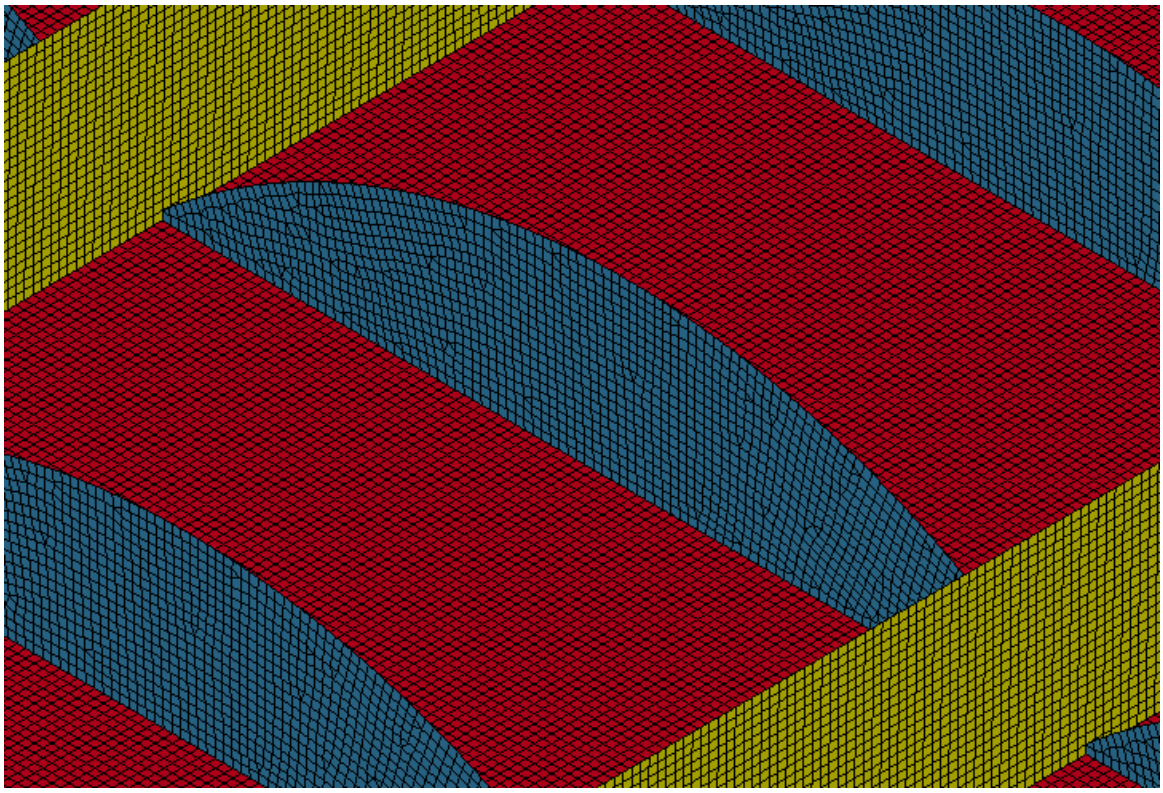

Run6, von Mise Stress, Load Case 2:

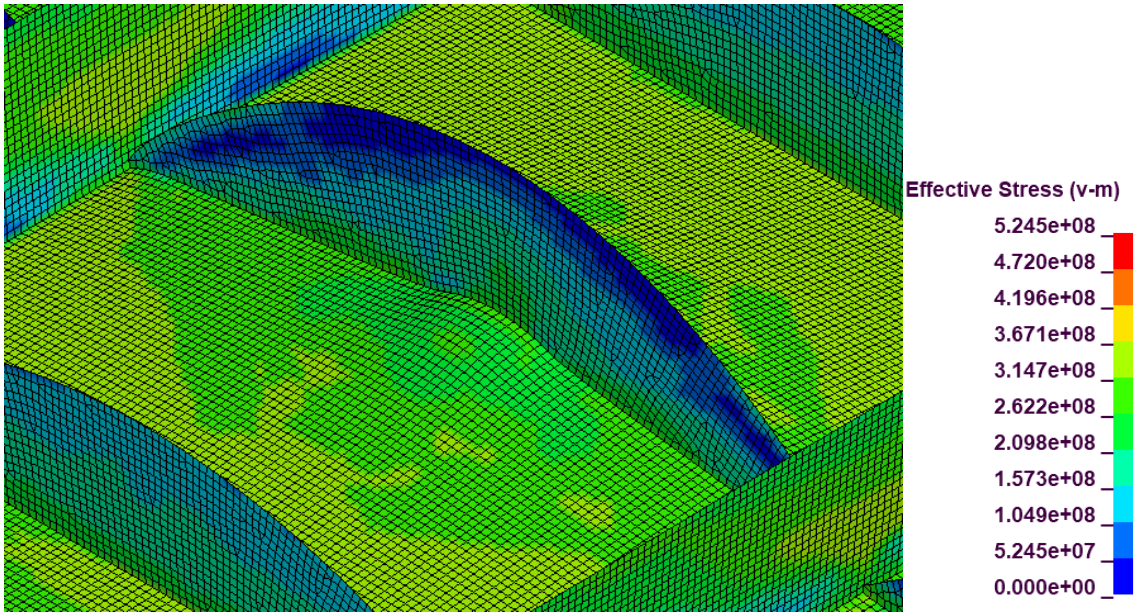

Run7, Geometry:

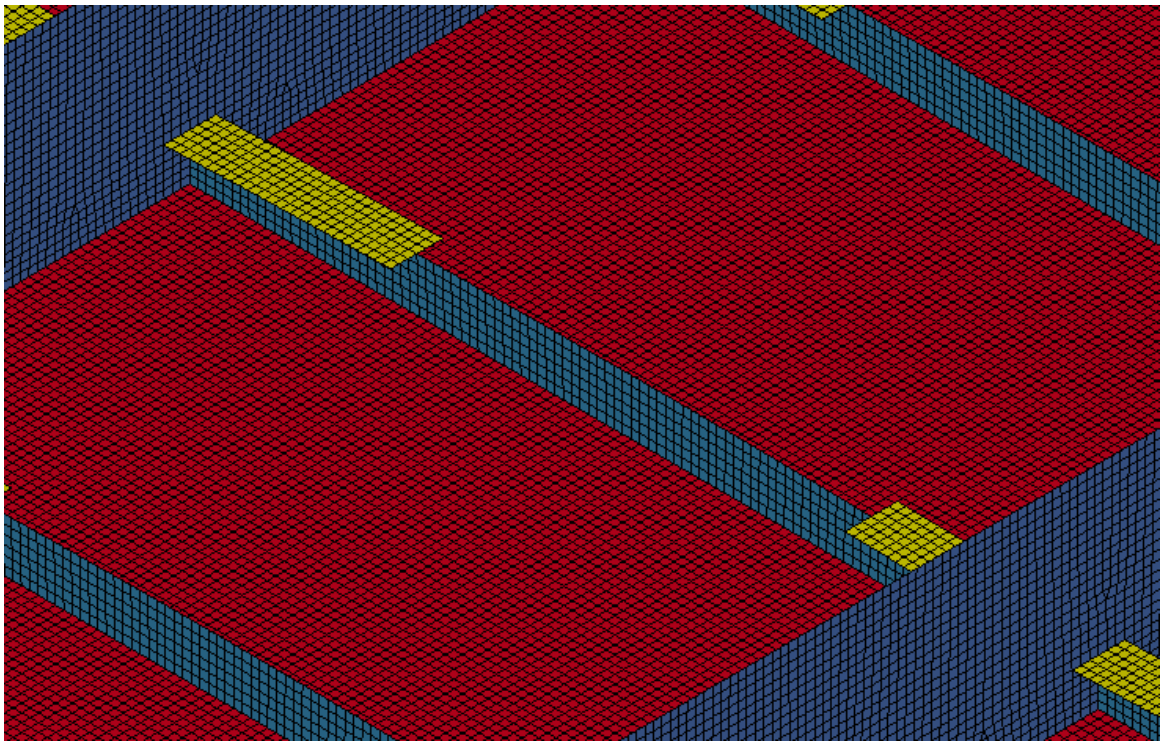

Run7, von Mise Stress, Load Case 2:

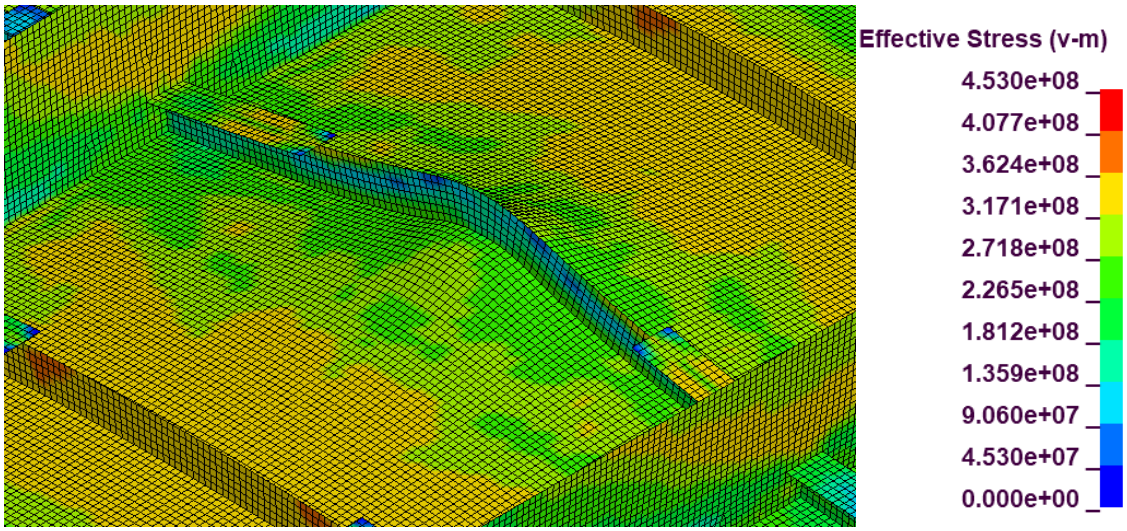

Run8, Geometry:

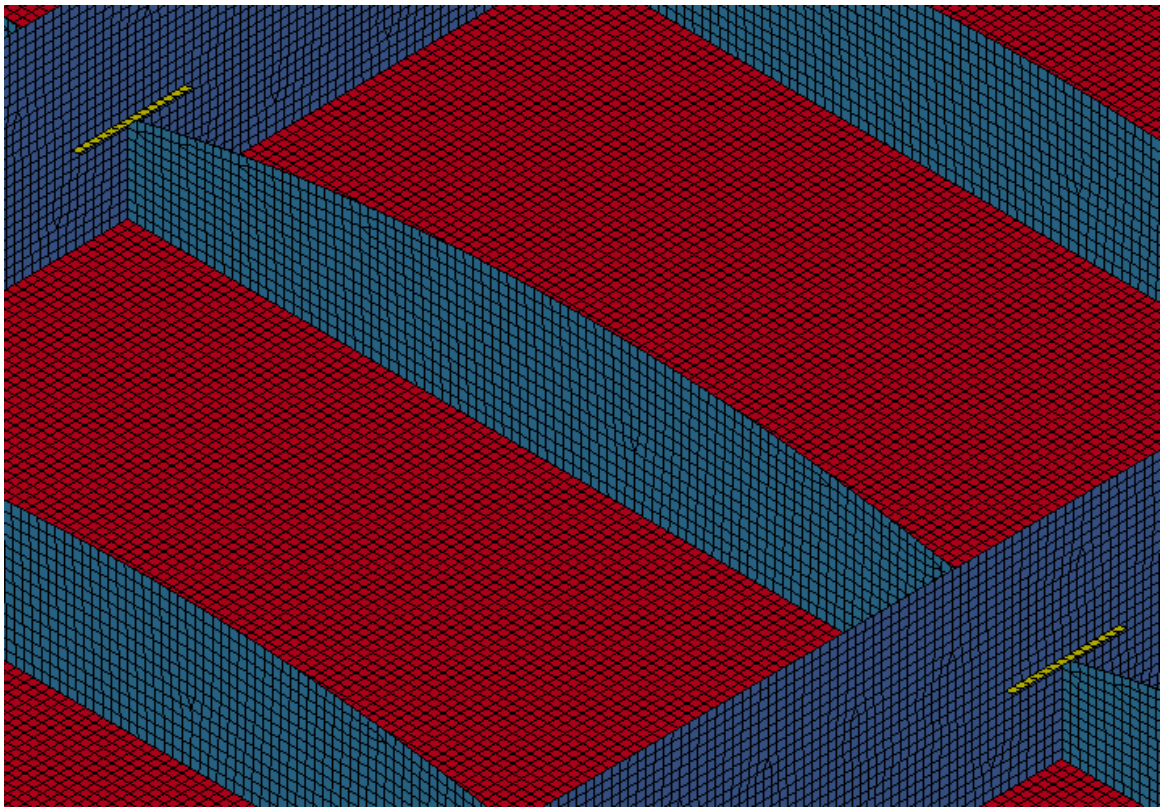

Run8, von Mise Stress, Load Case 2:

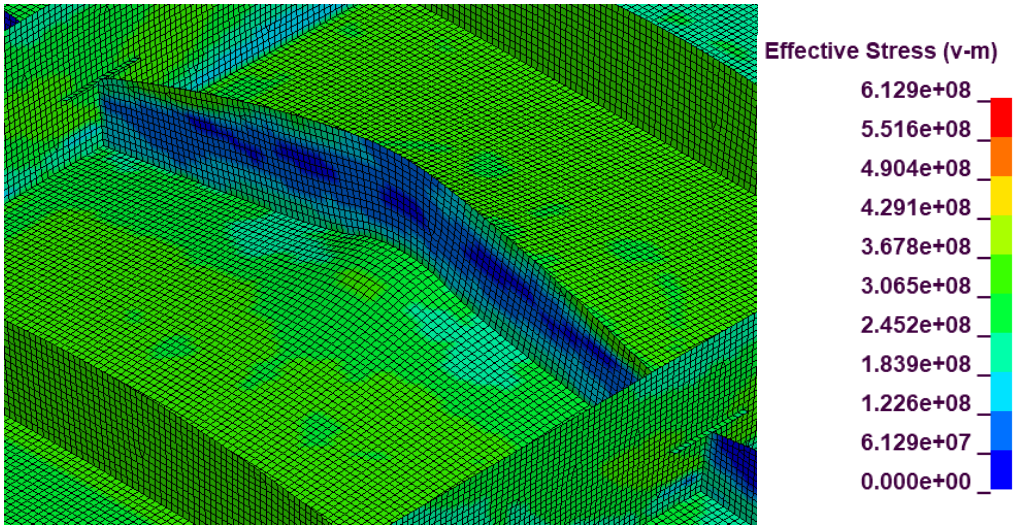

Run9, Geometry:

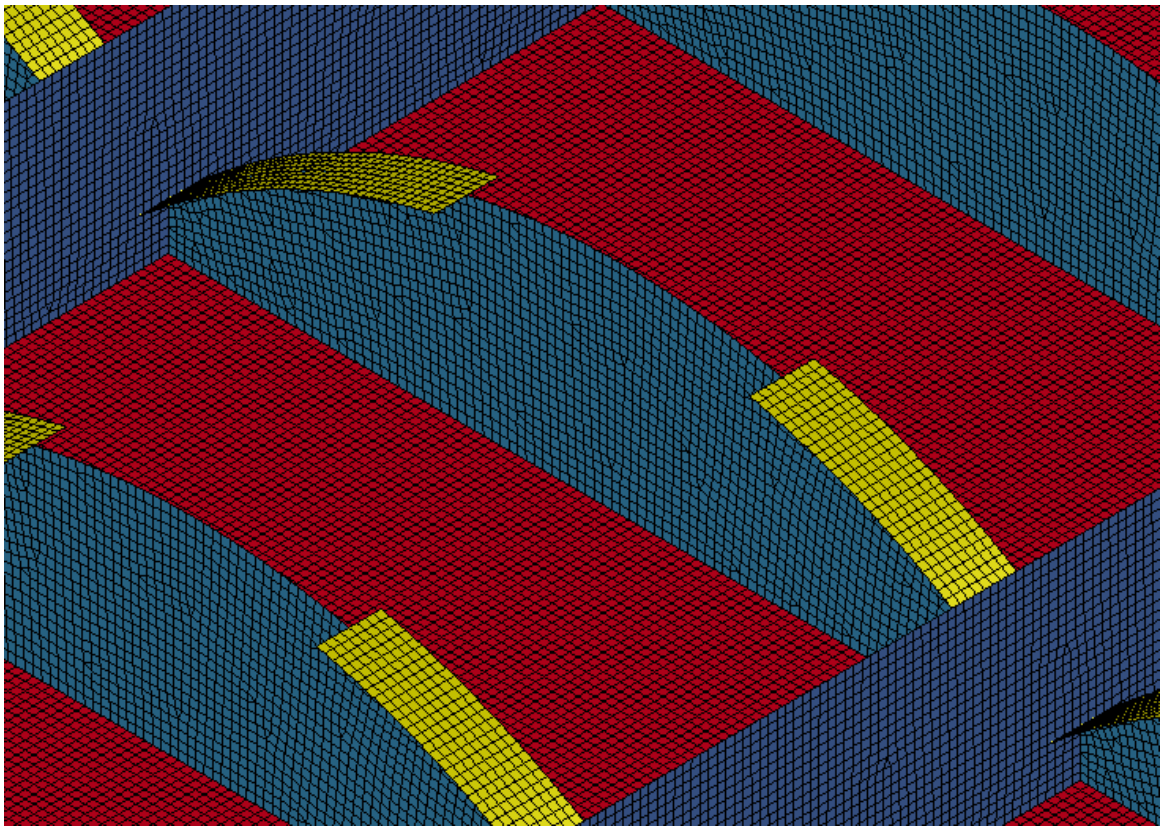

Run9, von Mise Stress, Load Case 2:

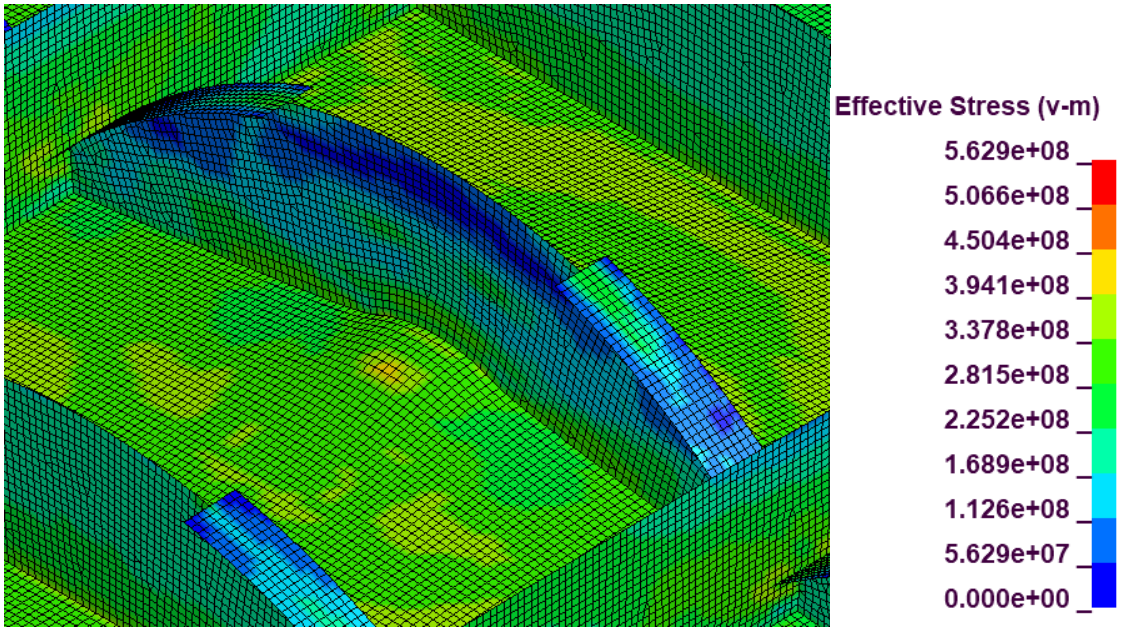

Run10, Geometry:

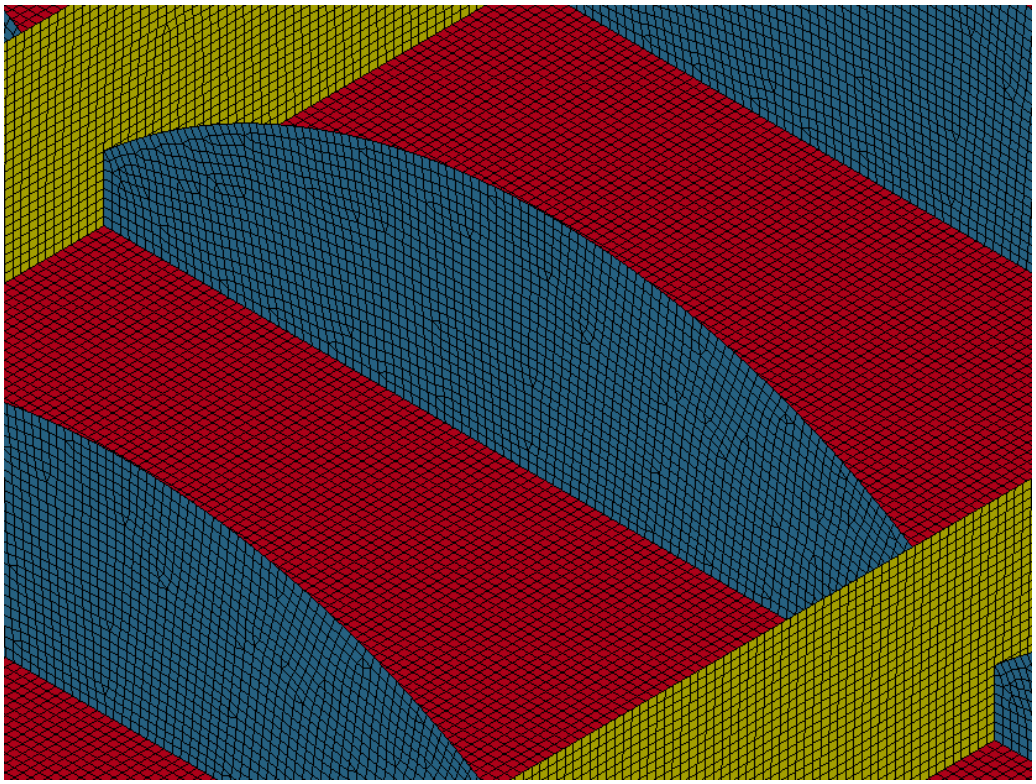

Run10, von Mise Stress, Load Case 2:

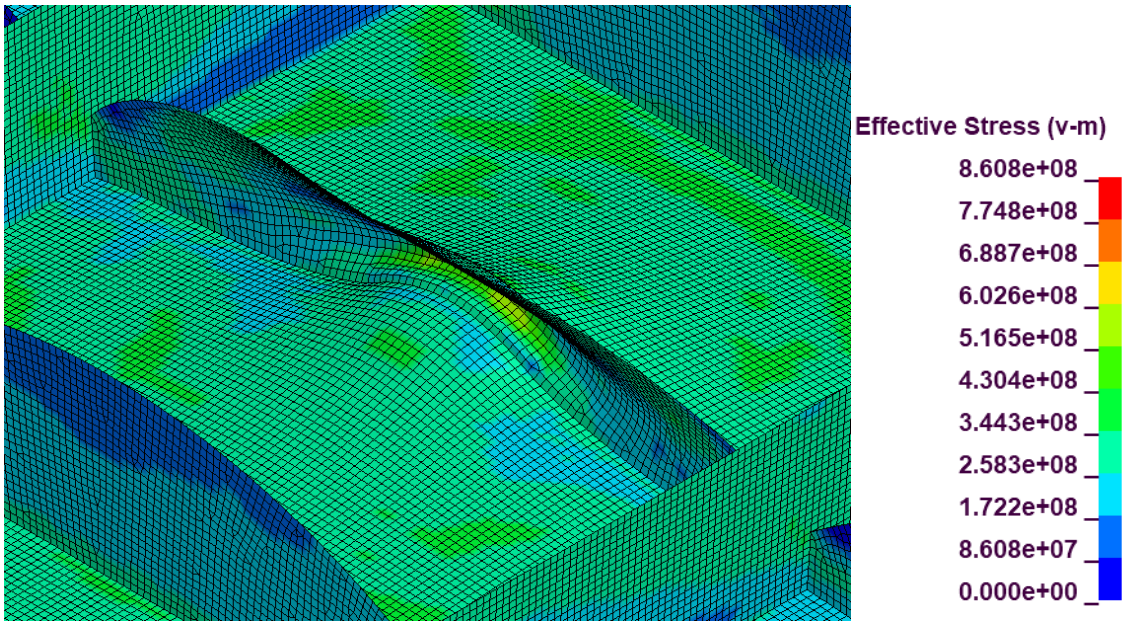

Run11, Geometry:

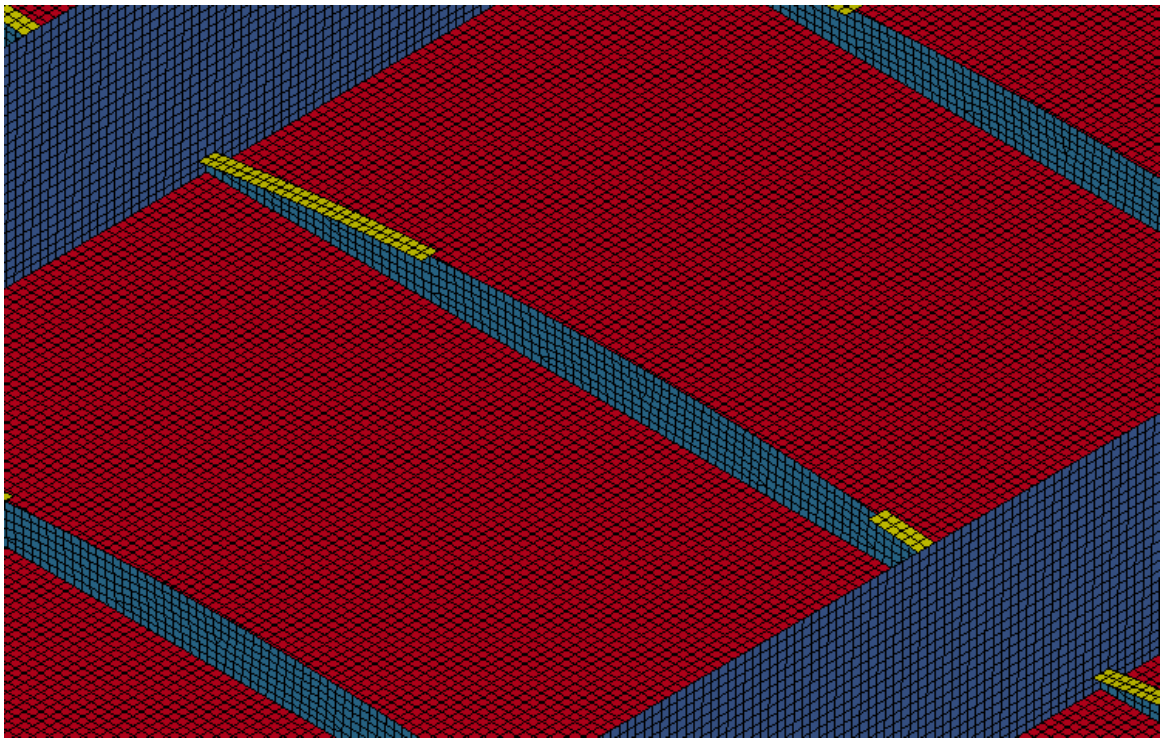

Run11, von Mise Stress, Load Case 2:

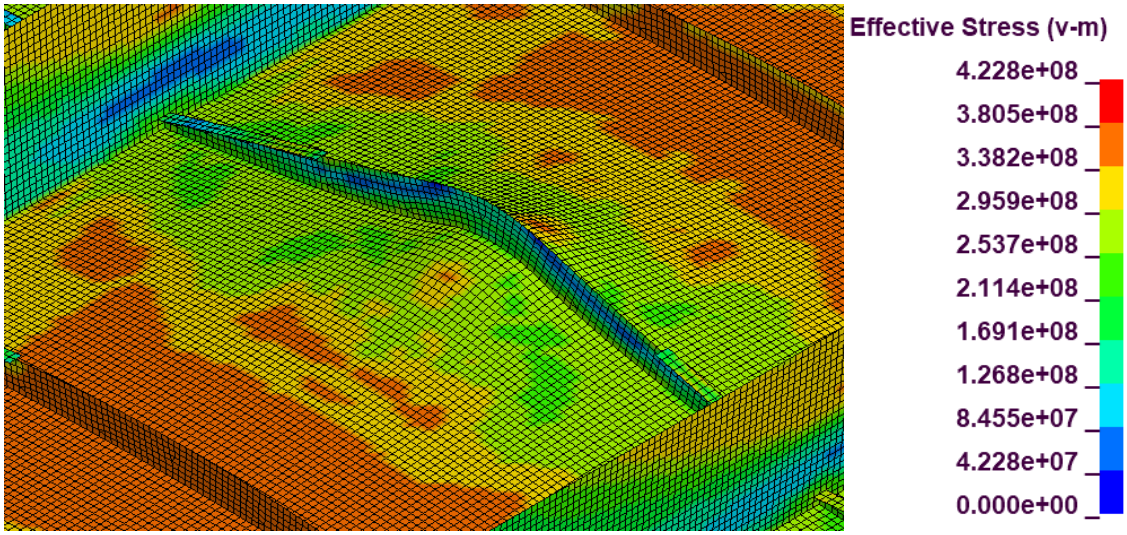

Run12, Geometry:

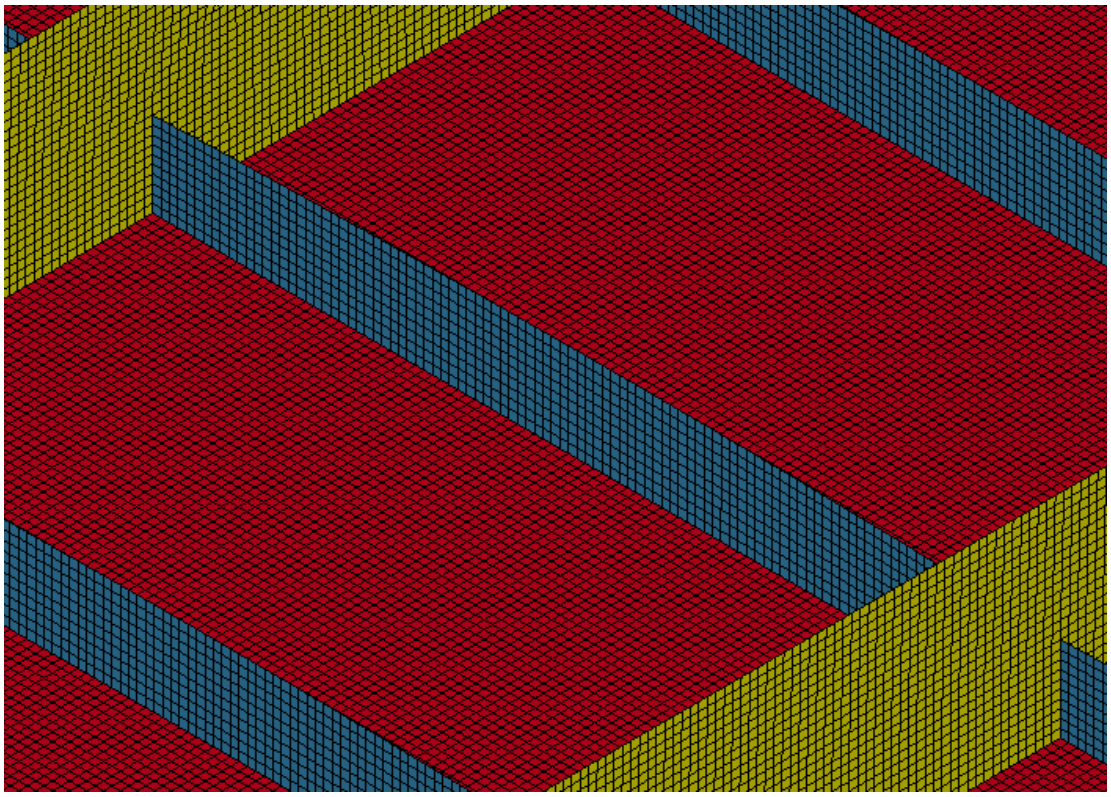

Run12, von Mise Stress, Load Case 2:

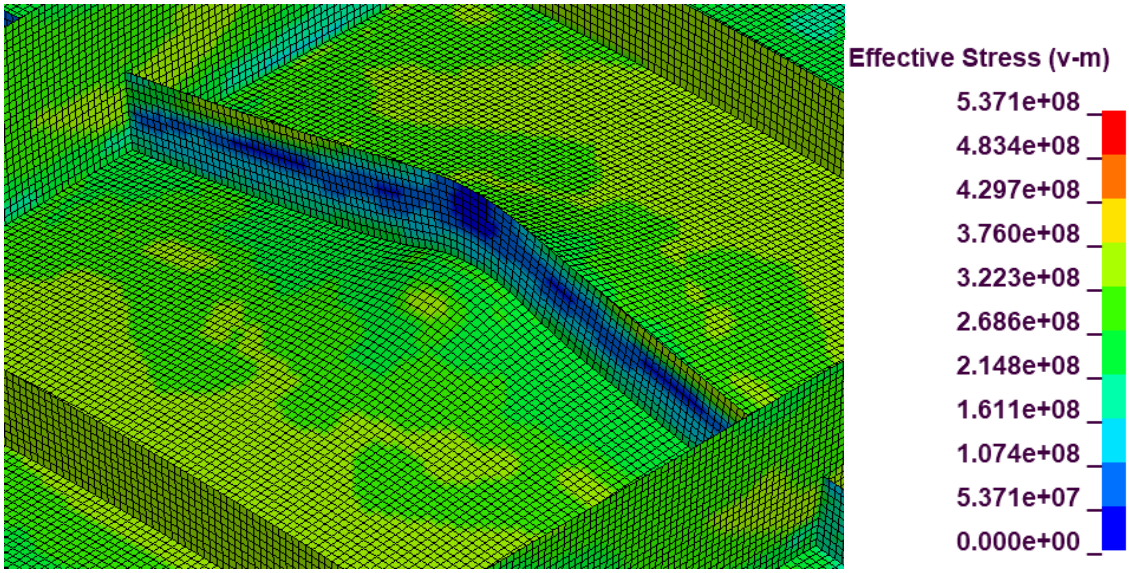

Run13, Geometry:

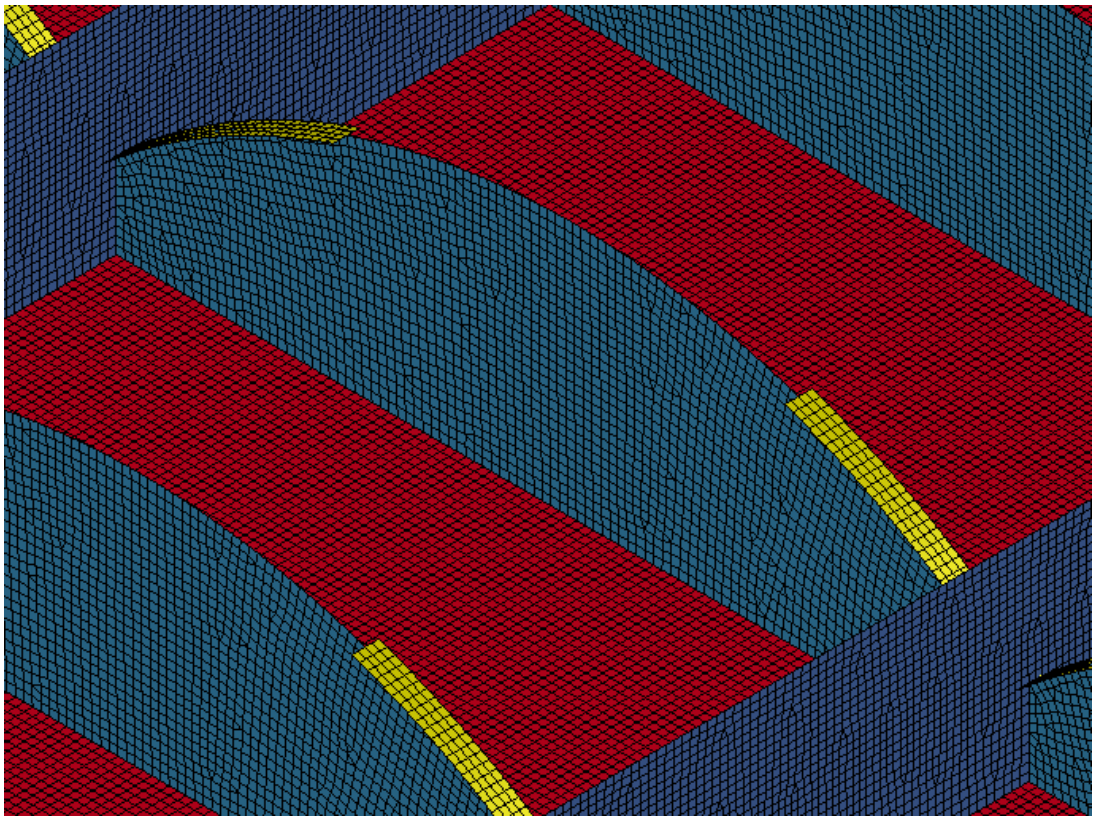

Run13, von Mise Stress, Load Case 2:

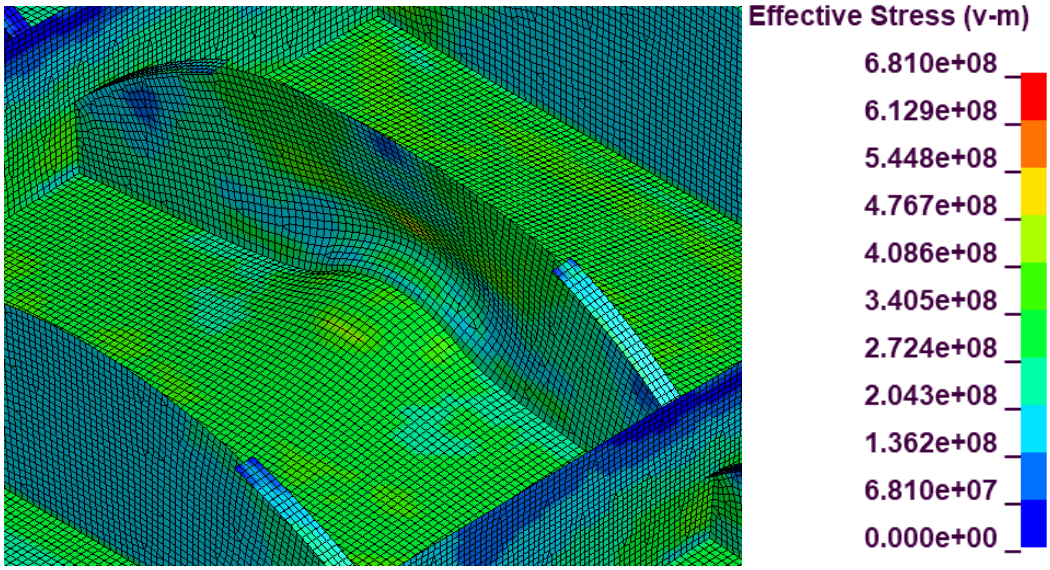

Run14, Geometry:

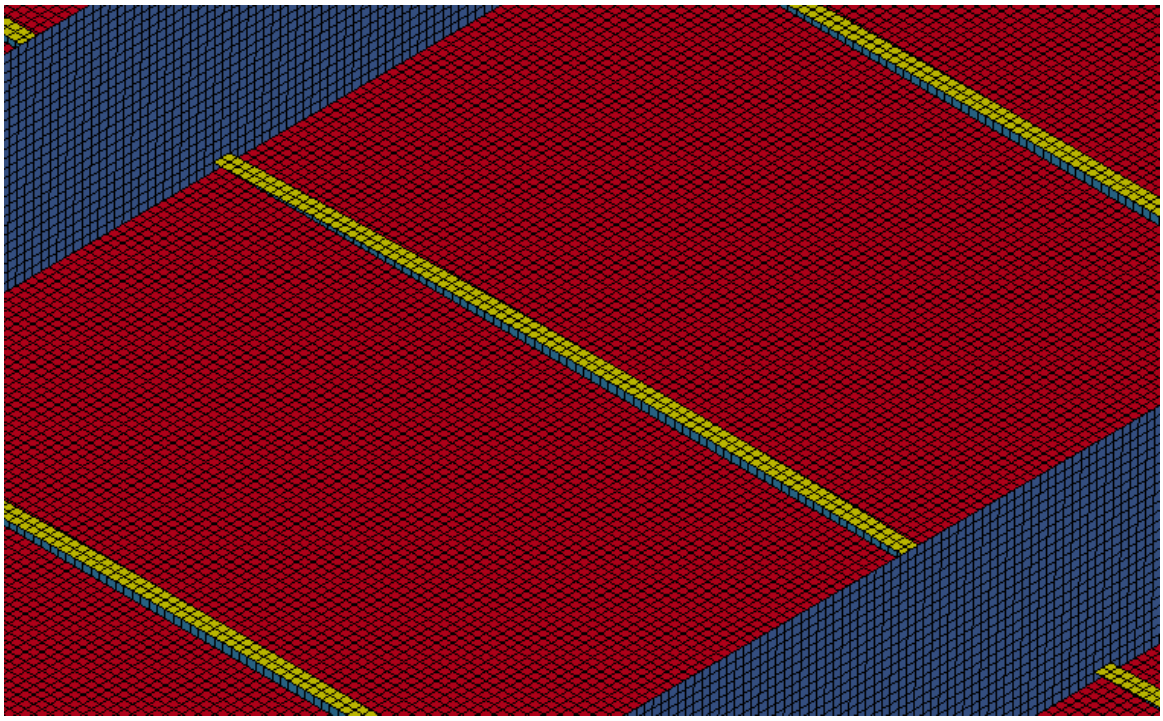

Run14, von Mise Stress, Load Case 2:

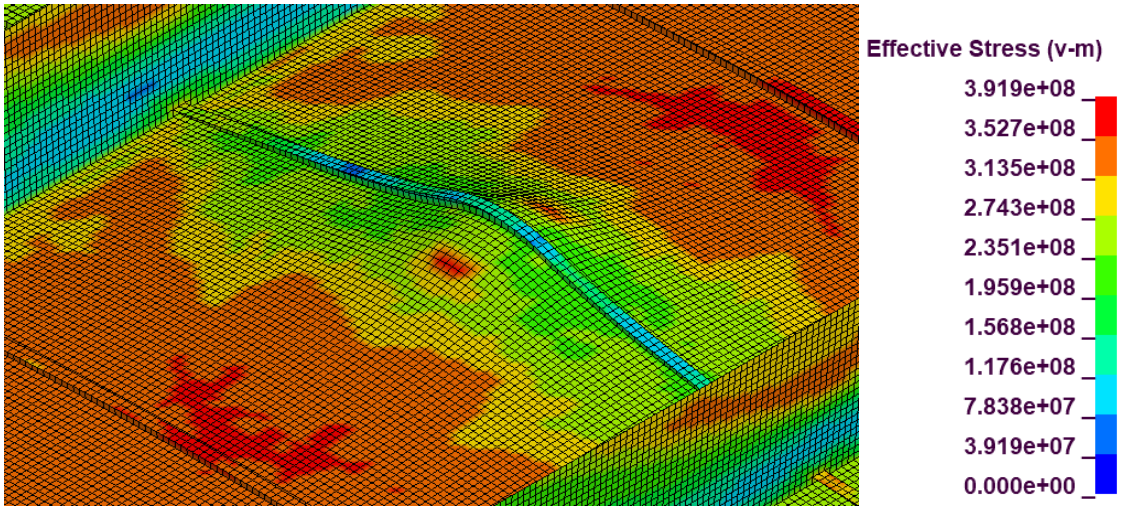

Run15, Geometry:

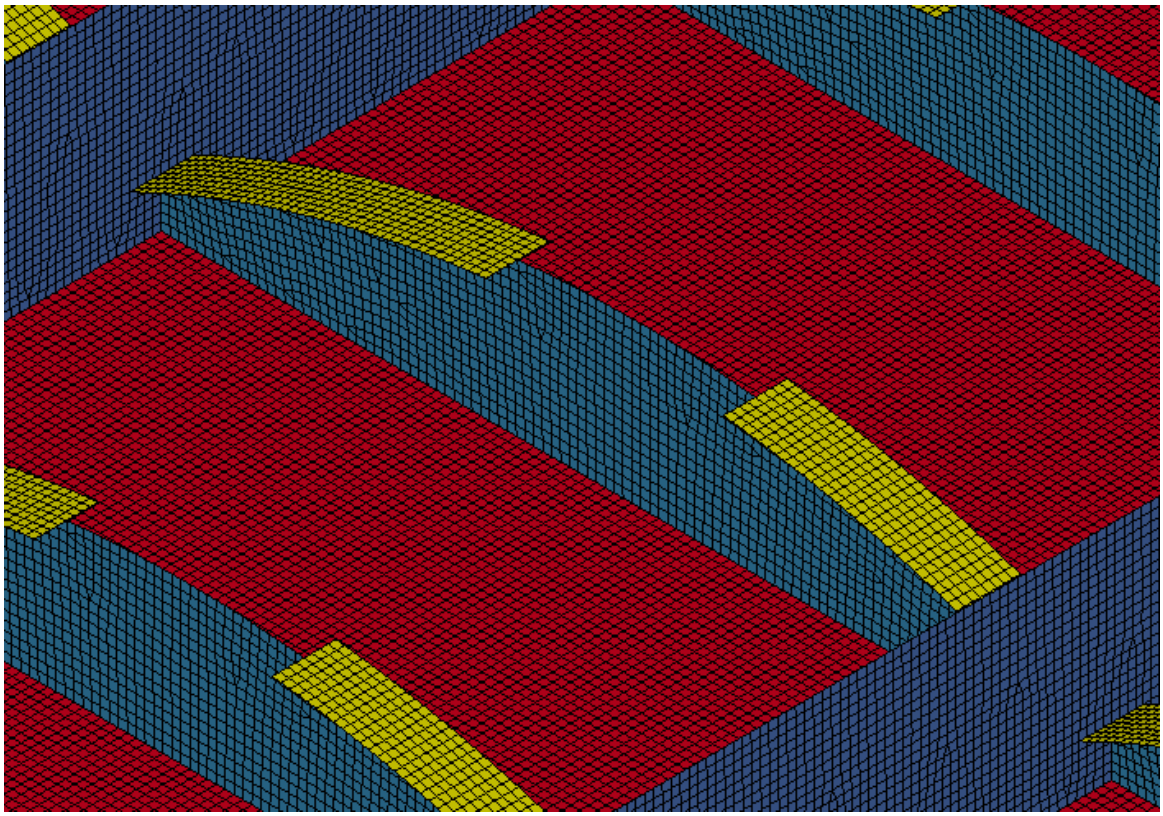

Run15, von Mise Stress, Load Case 2:

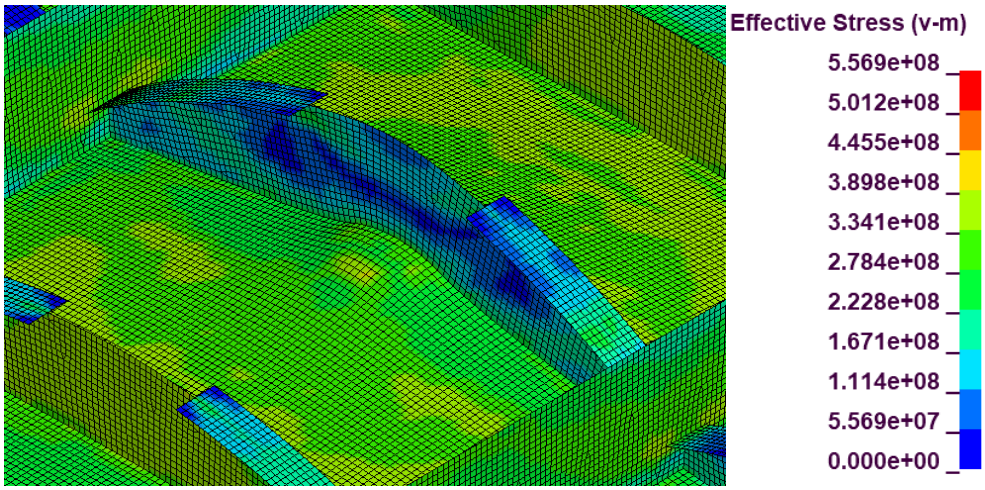

Run16, Geometry:

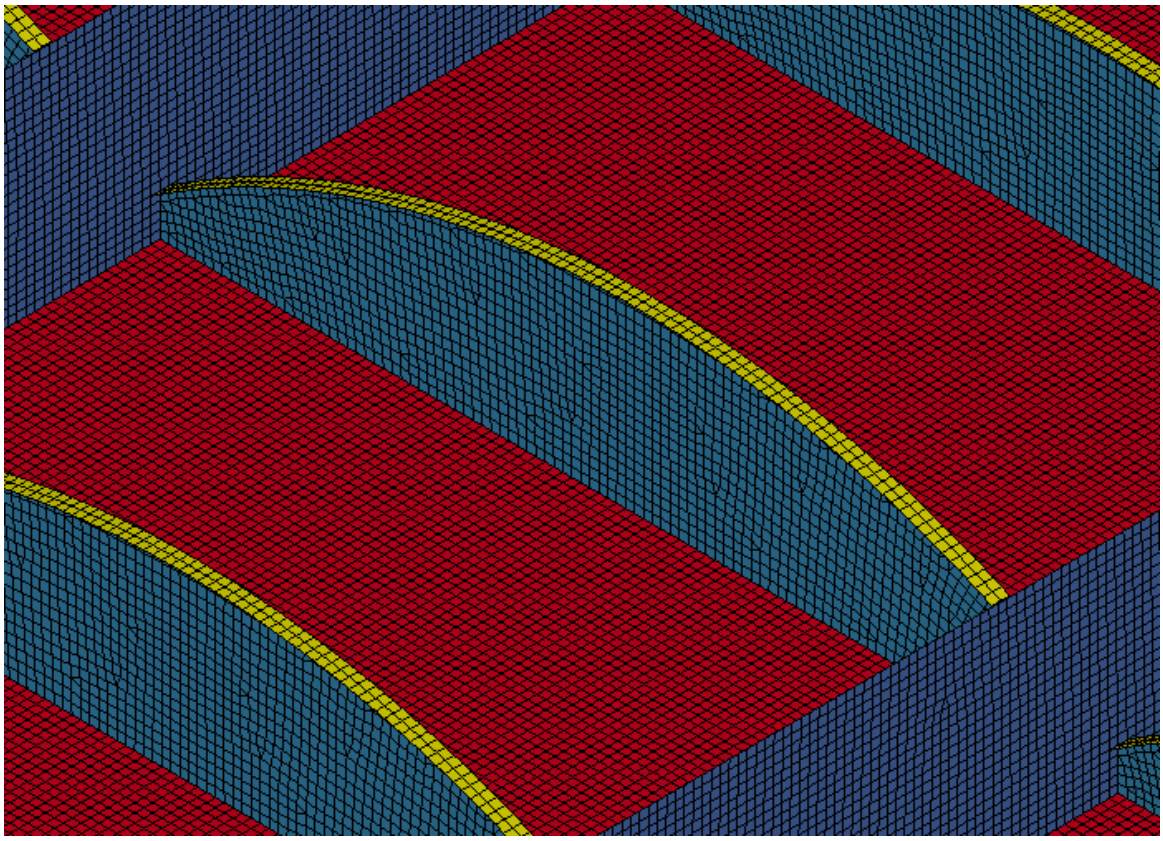

Run16, von Mise Stress, Load Case 2:

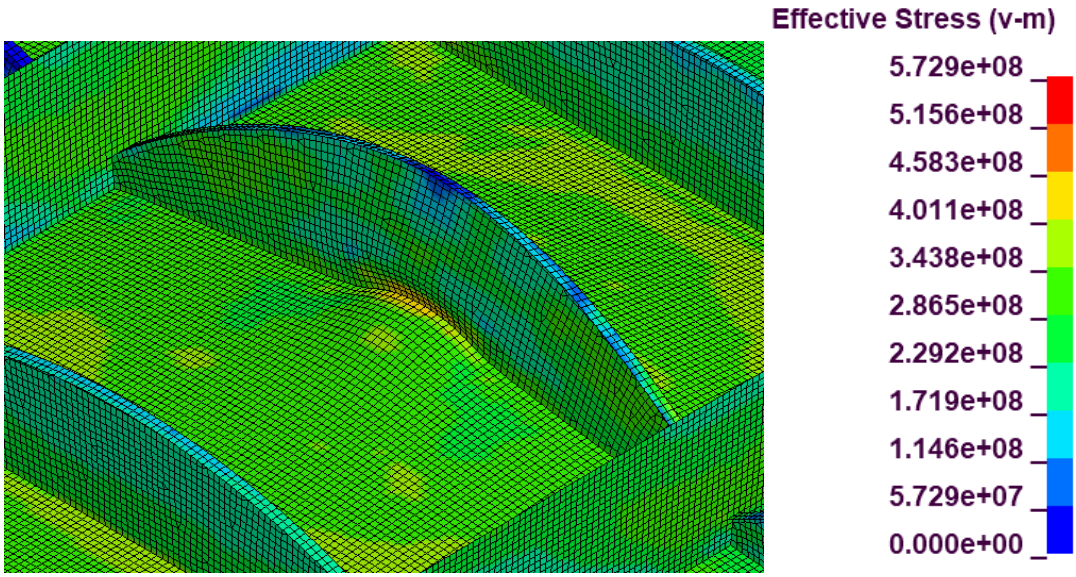

Run17, Geometry:

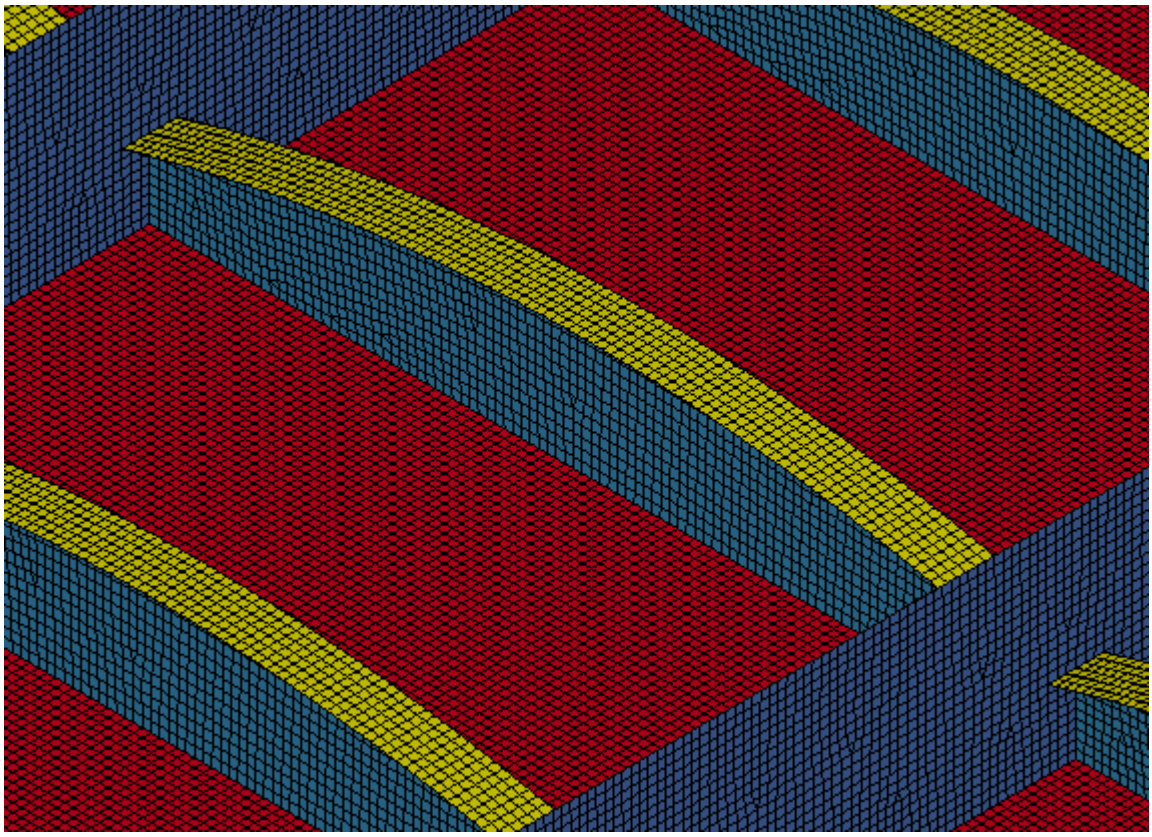

Run17, von Mise Stress, Load Case 2:

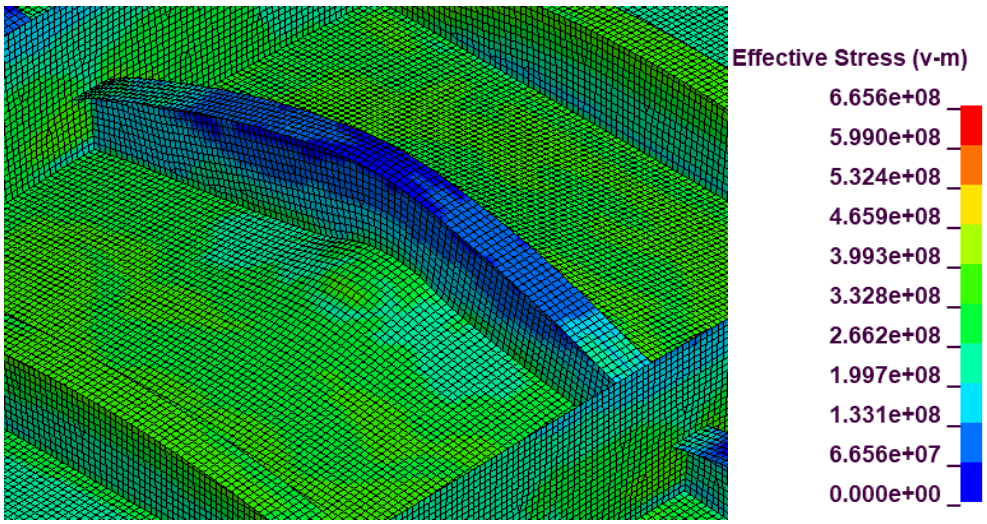

Run18, Geometry:

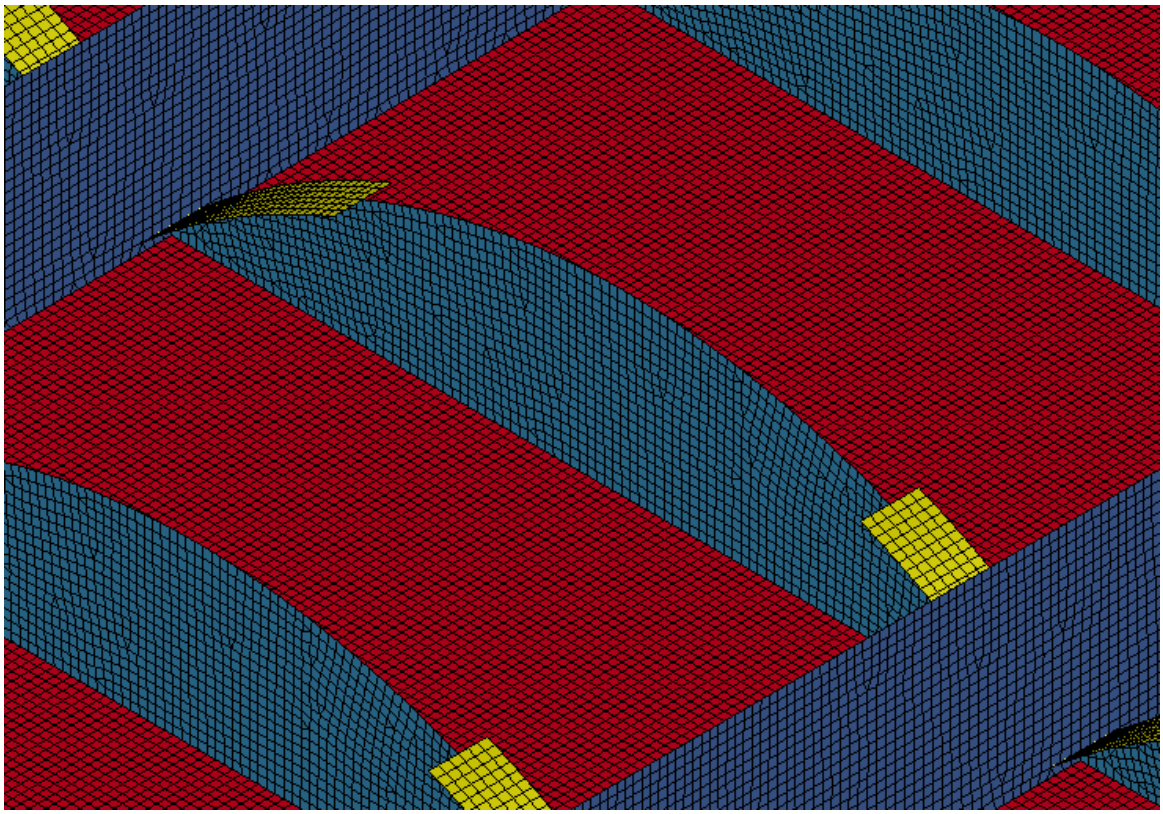

Run18, von Mise Stress, Load Case 2:

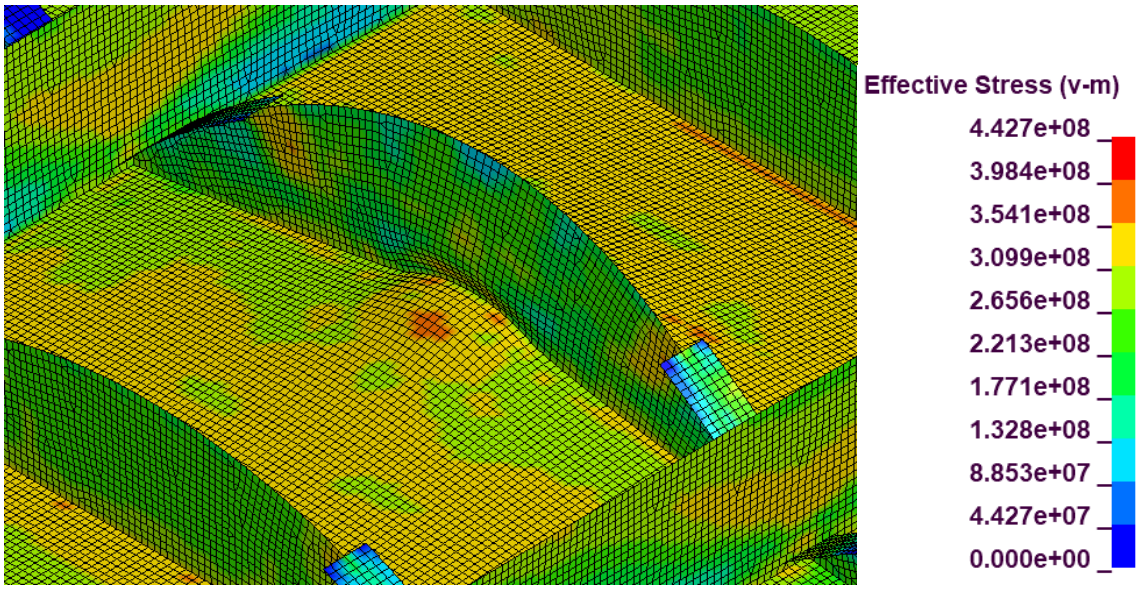

Run19, Geometry:

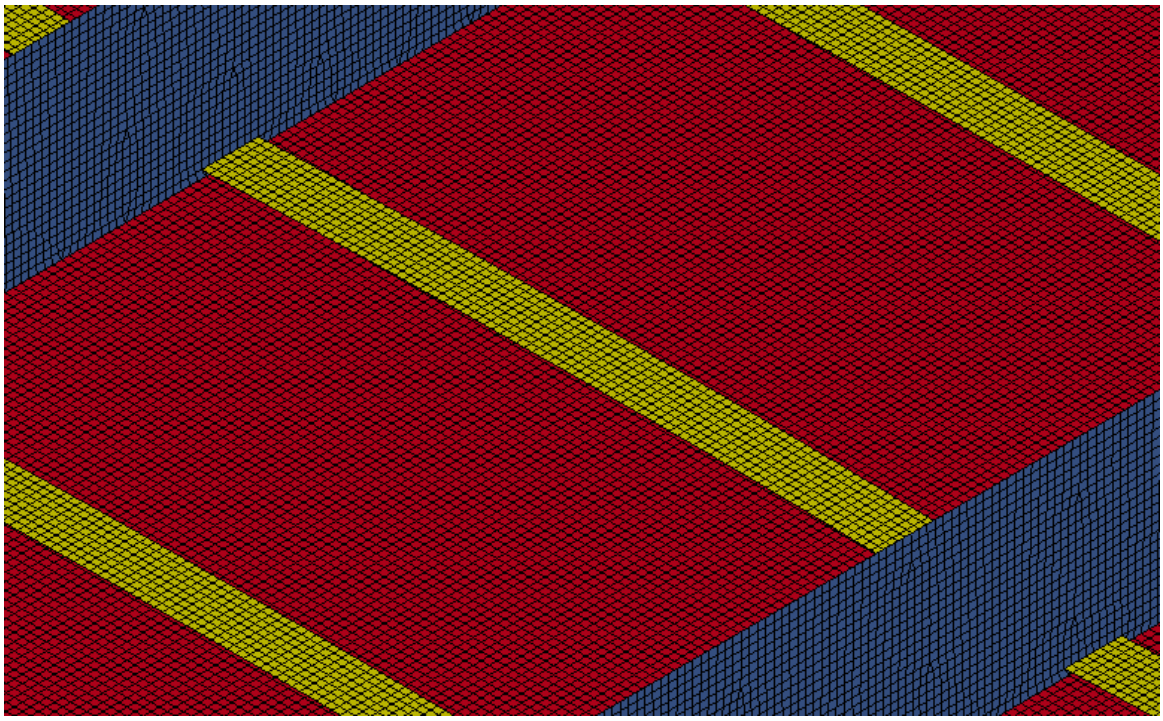

Run19, von Mise Stress, Load Case 2:

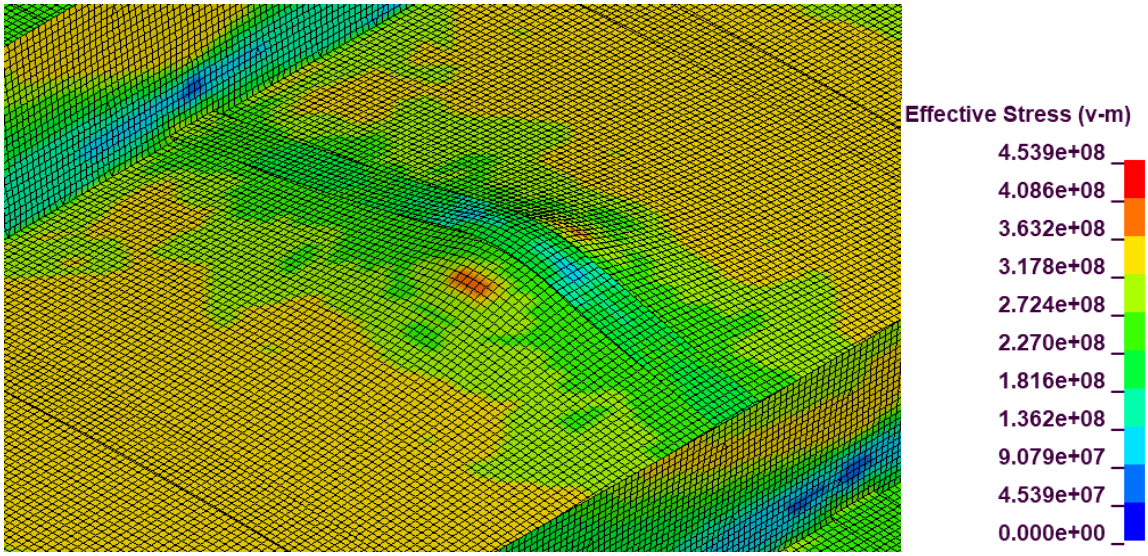

Run20, Geometry:

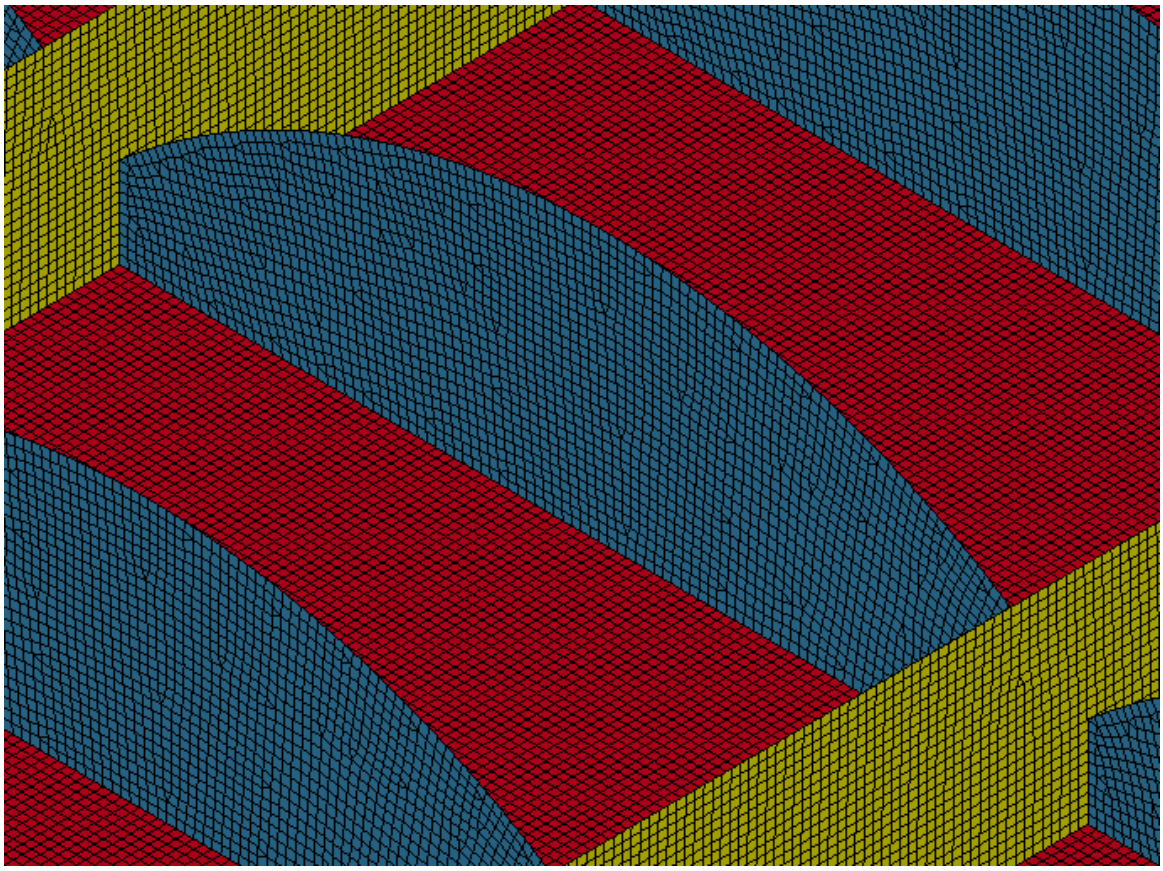

Run20, von Mise Stress, Load Case 2:

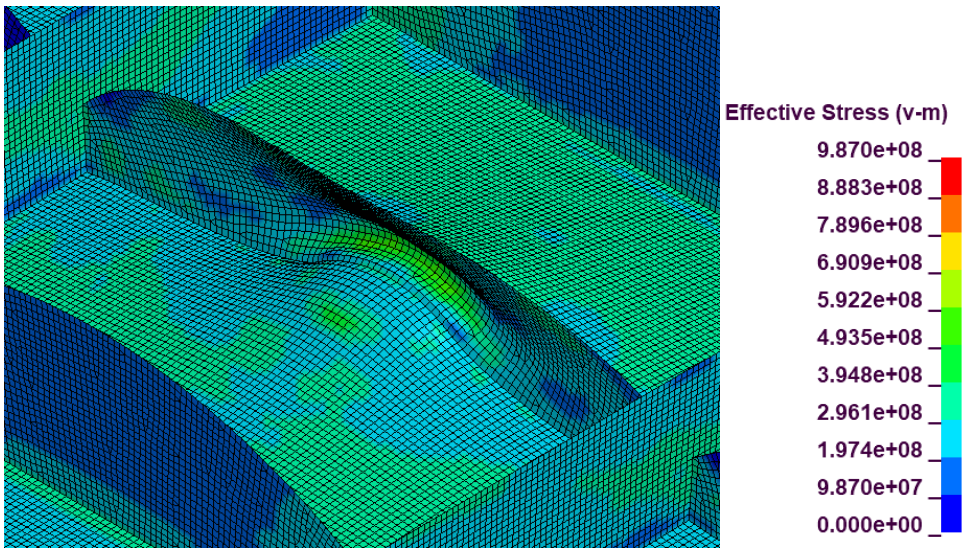

Run21, Geometry:

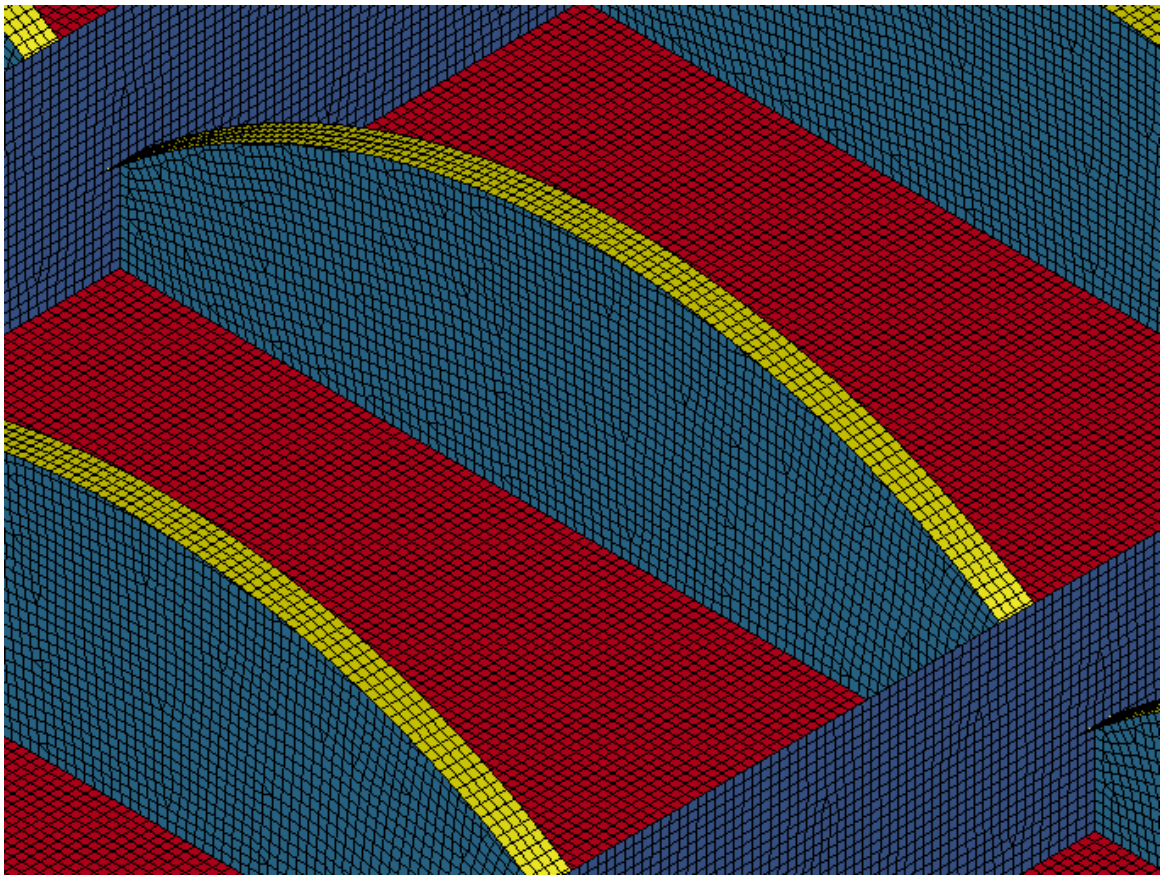

Run21, von Mise Stress, Load Case 2:

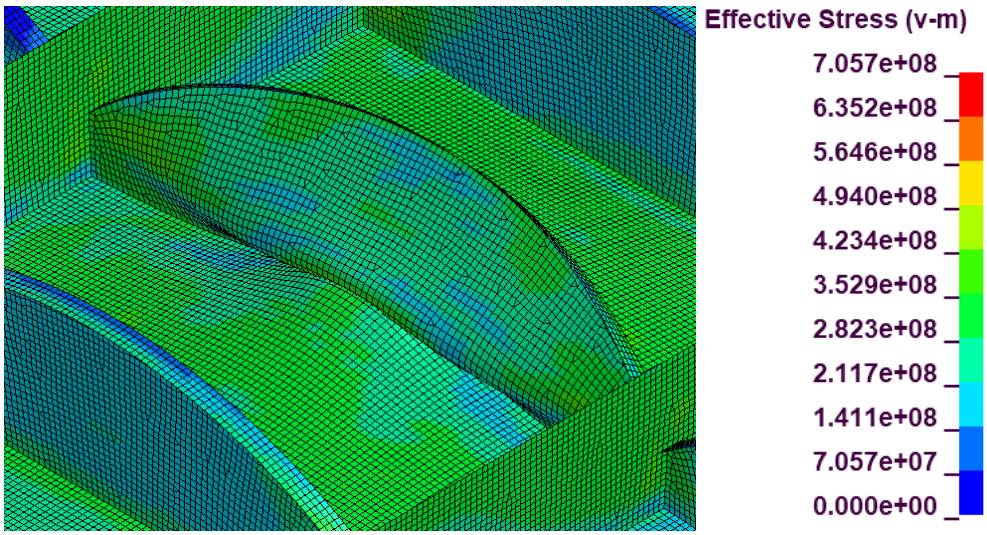

Run22, Geometry:

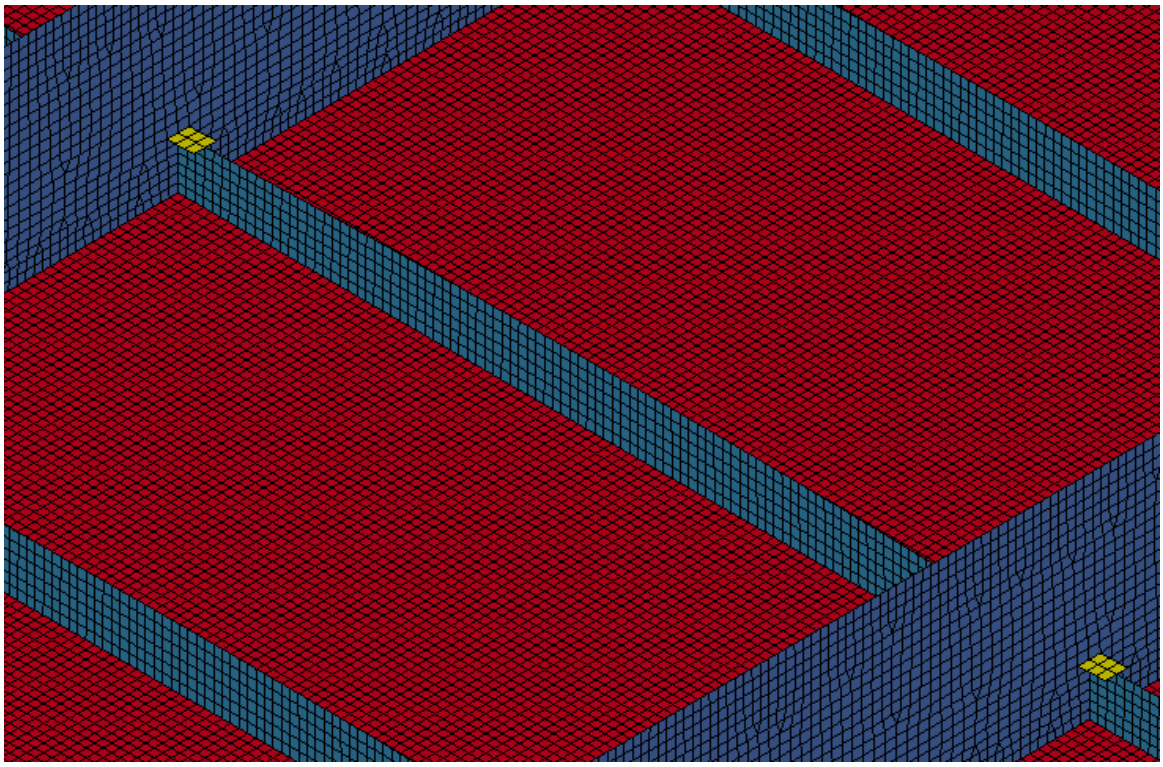

Run22 von Mise Stress, Load Case 2:

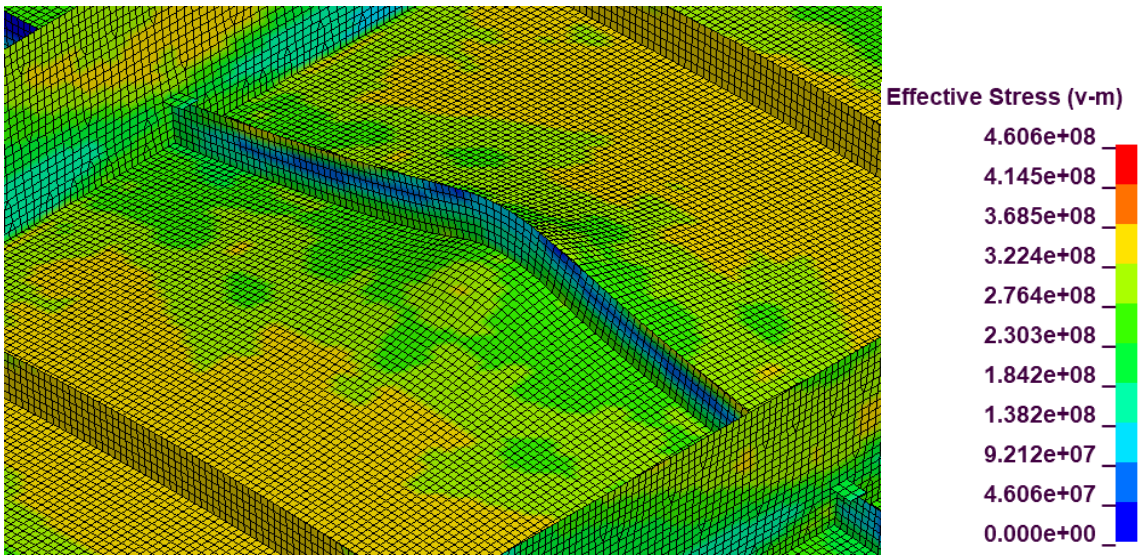

Run23, Geometry:

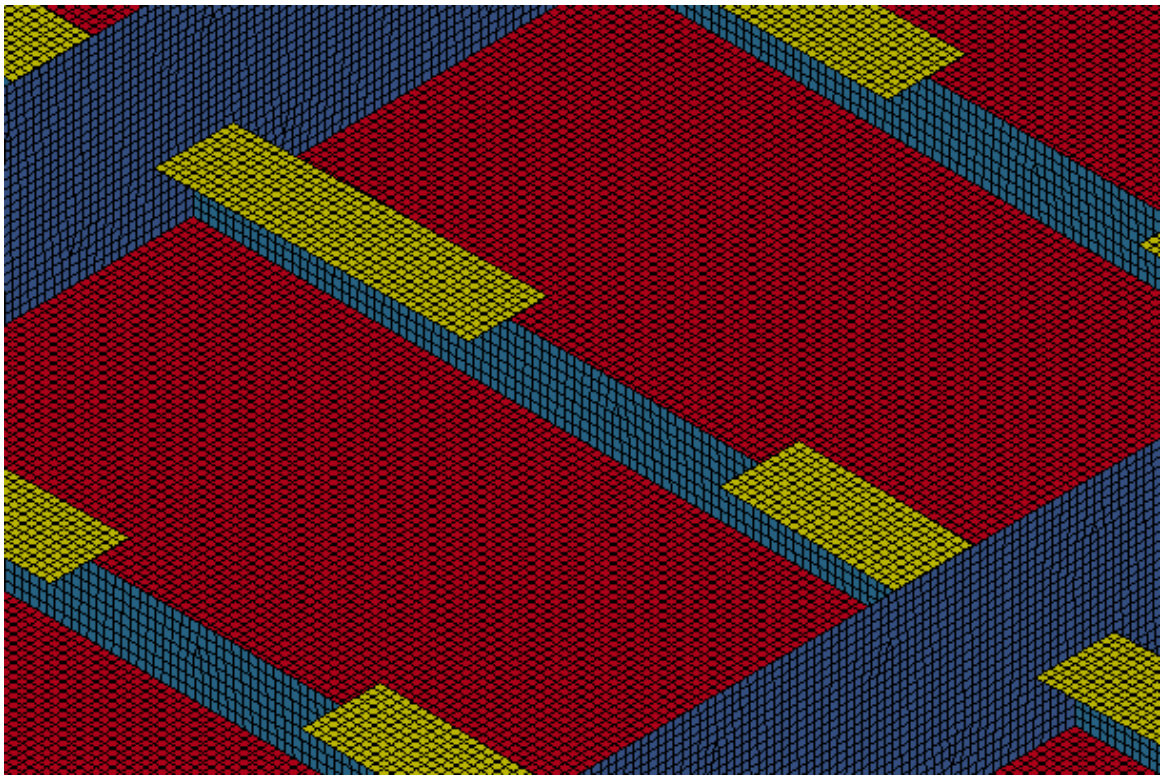

Run23, von Mise Stress, Load Case 2:

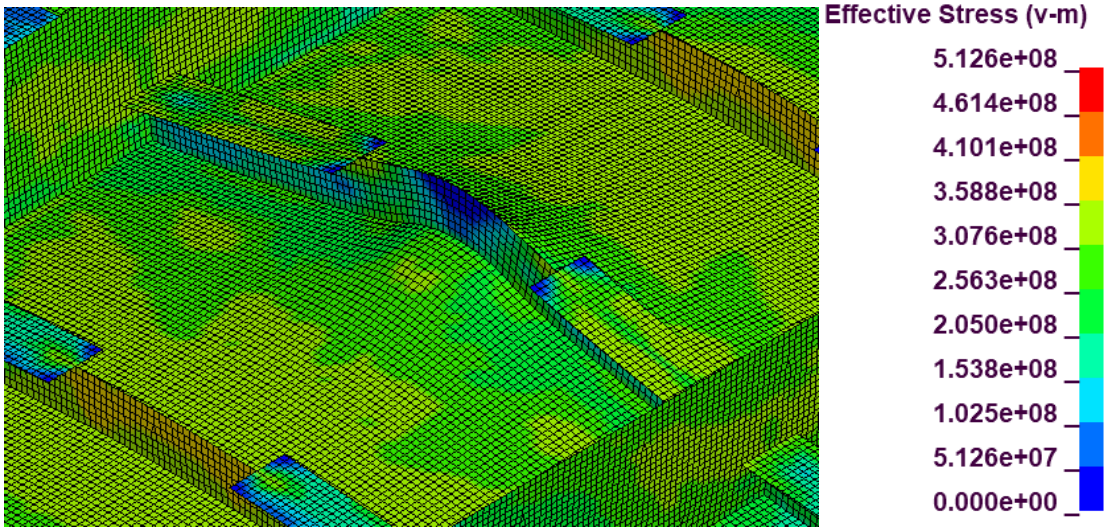

Run24, Geometry:

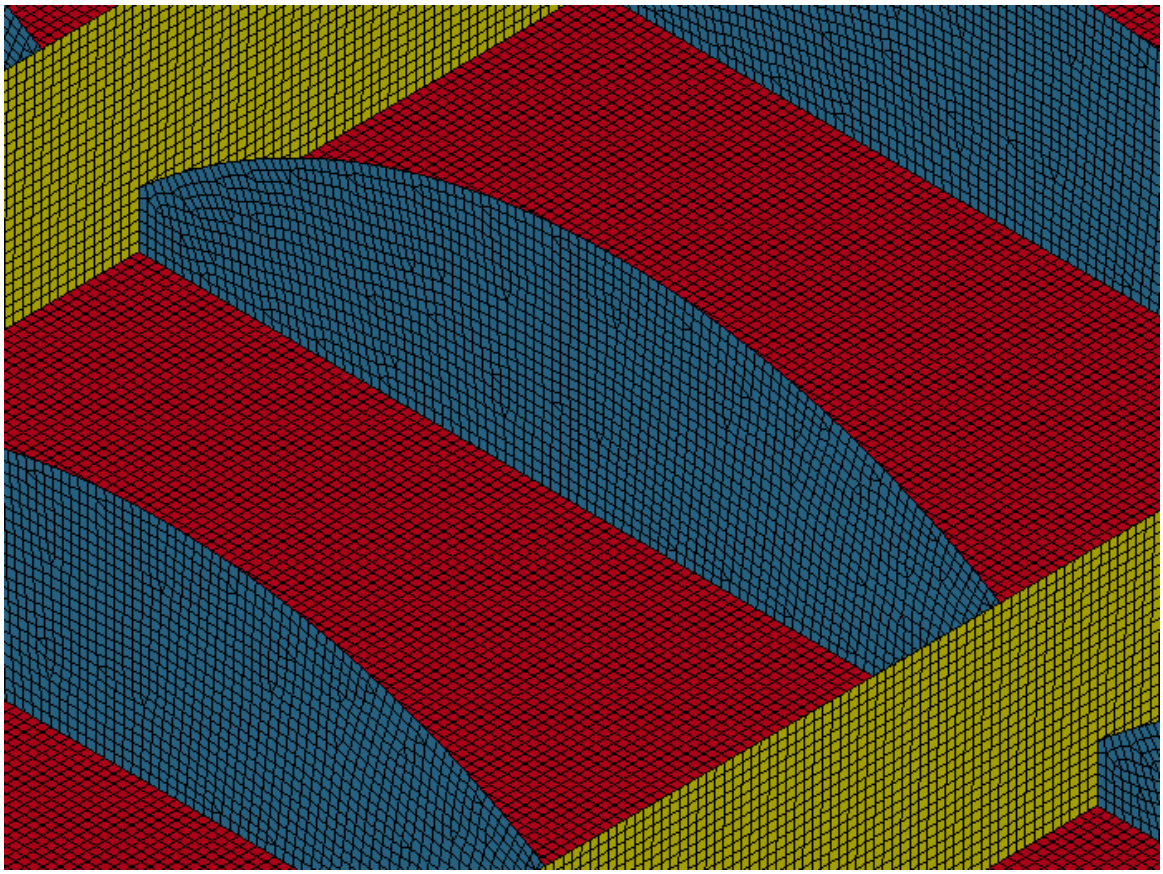

Run24, von Mise Stress, Load Case 2:

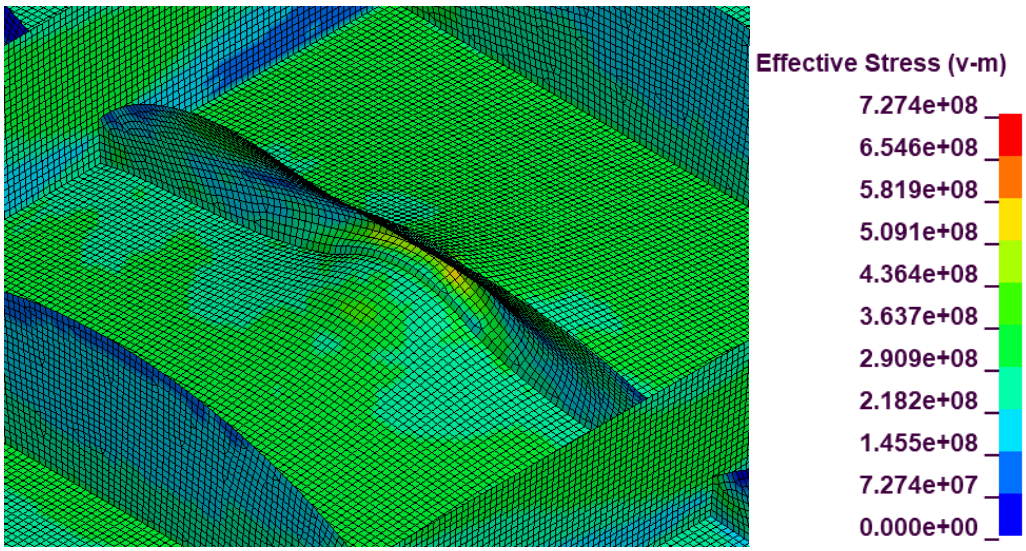

Run25, Geometry:

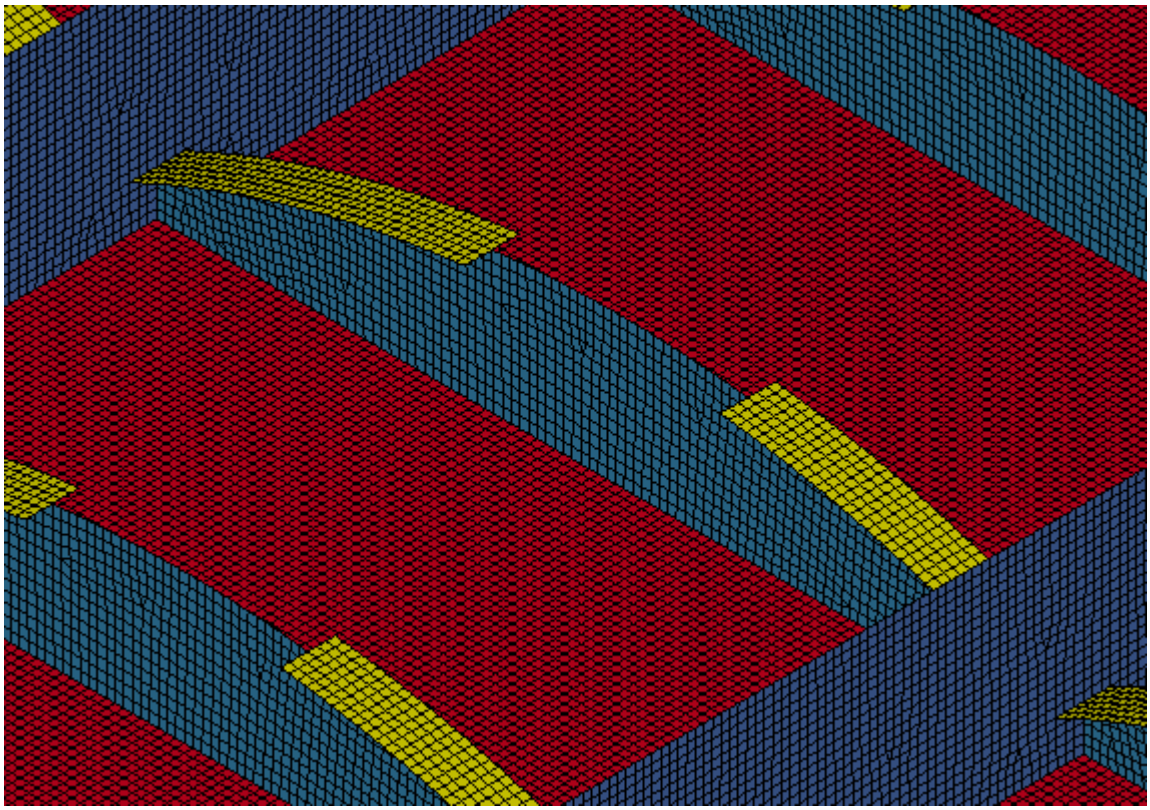

Run25, von Mise Stress, Load Case 2:

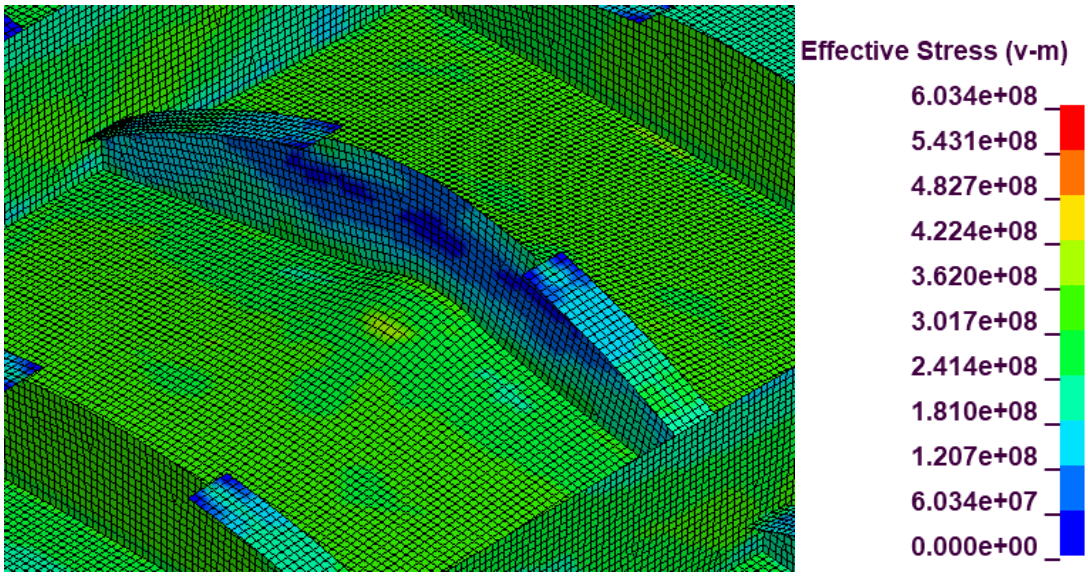

Run26, Geometry:

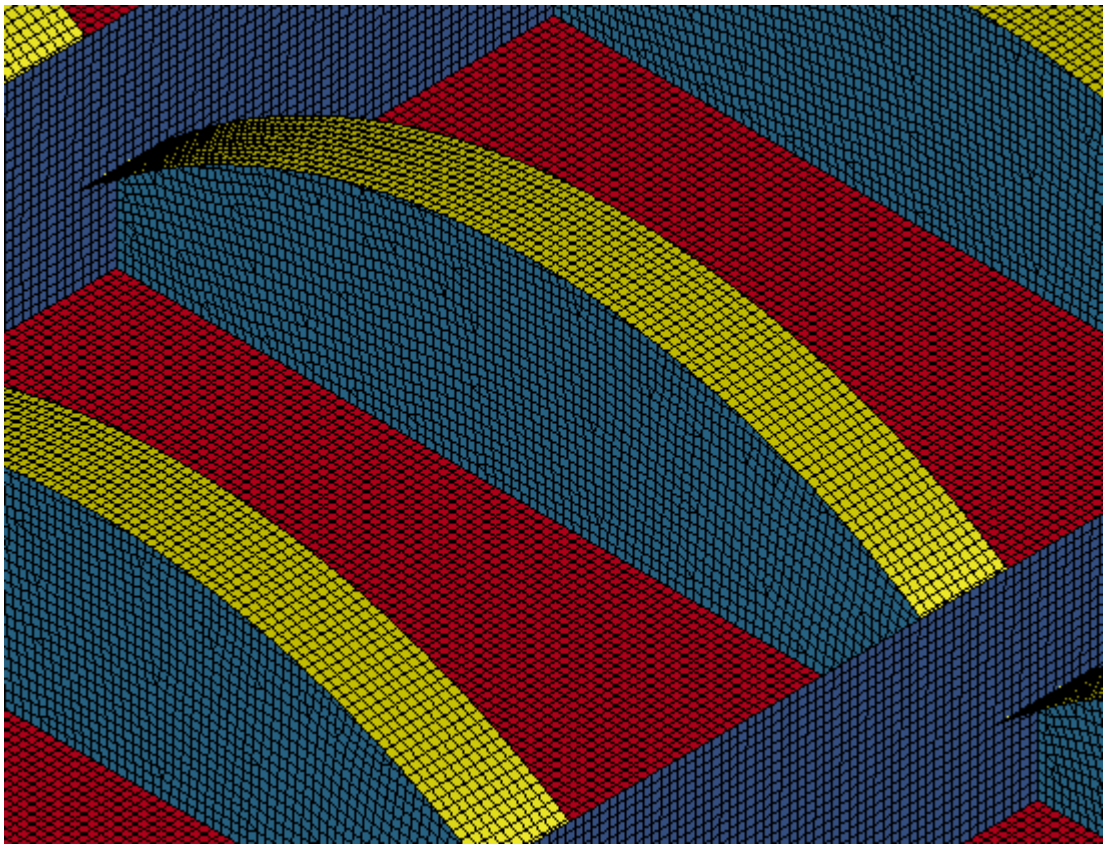

Run26, von Mise Stress, Load Case 2:

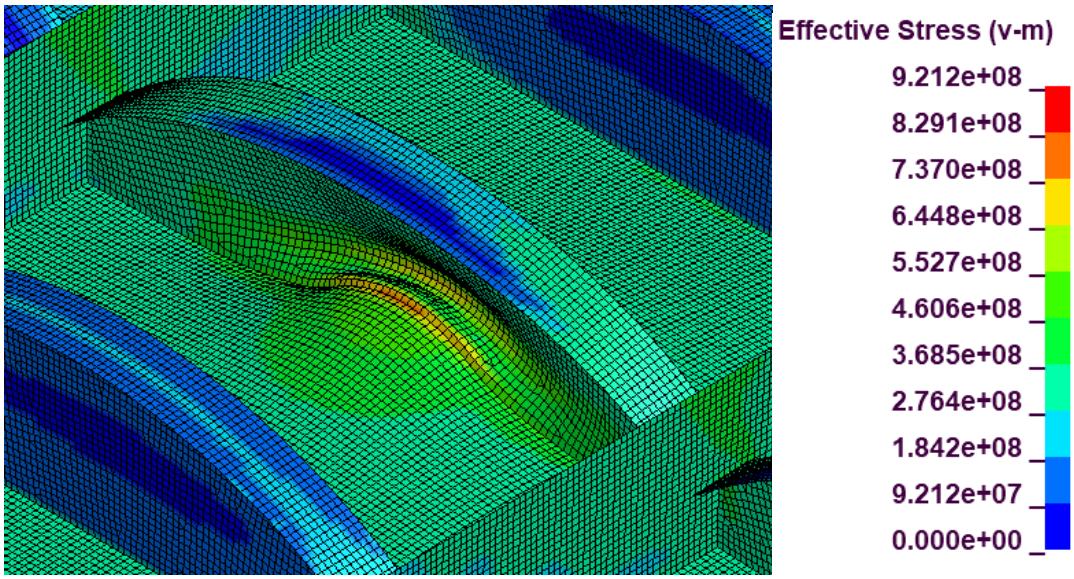

Run27, Geometry:

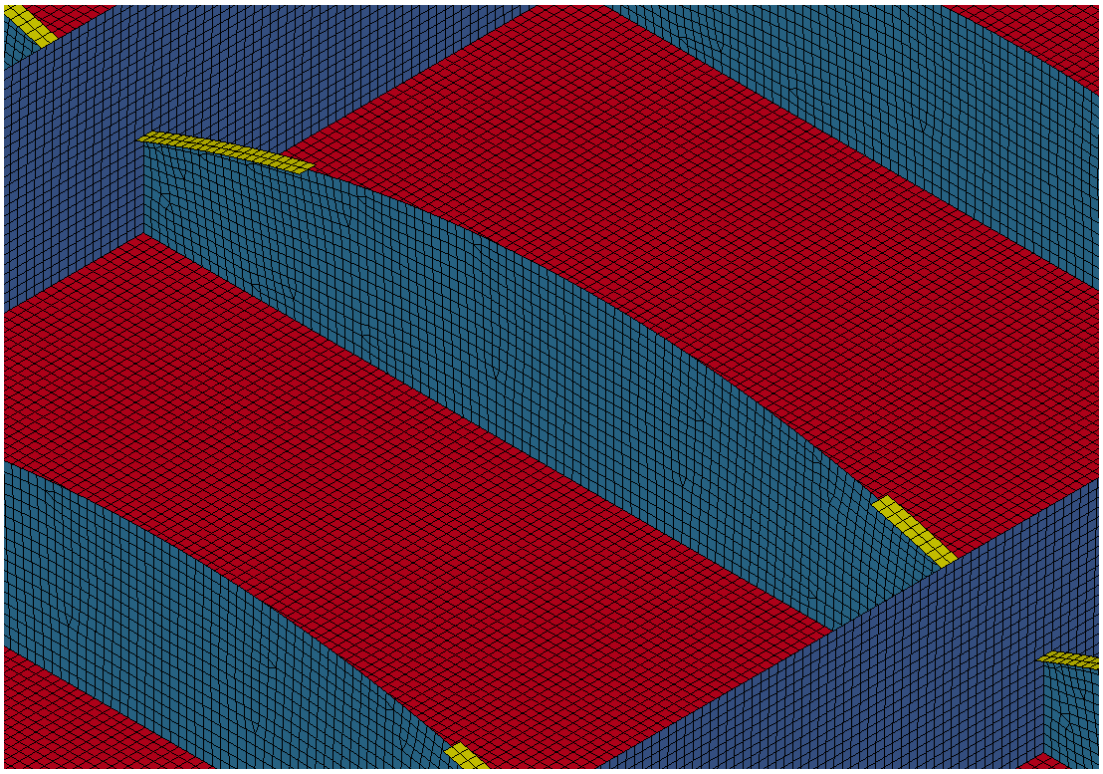

Run27, von Mise Stress, Load Case 2:

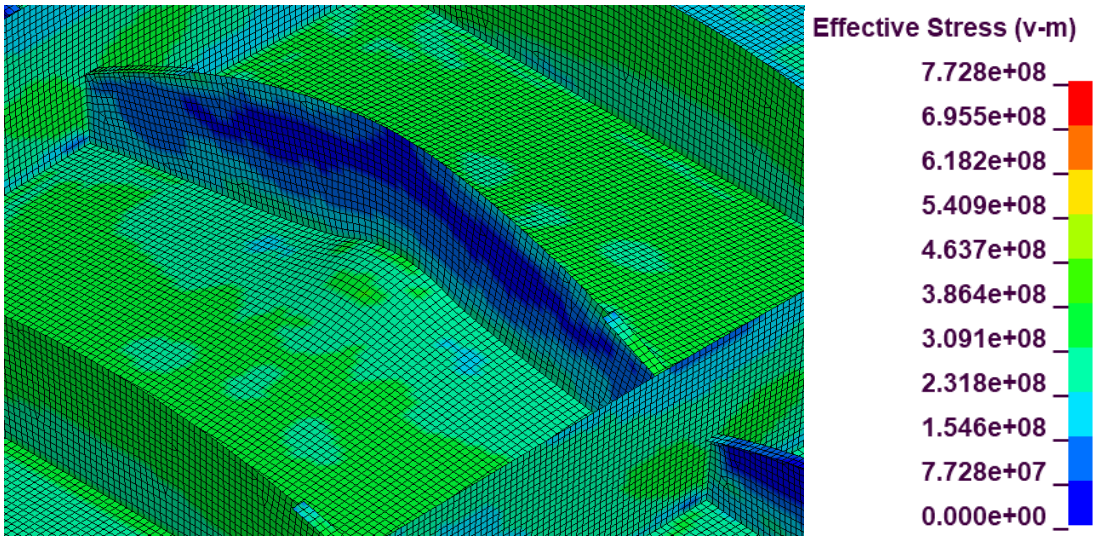

Run28, Geometry:

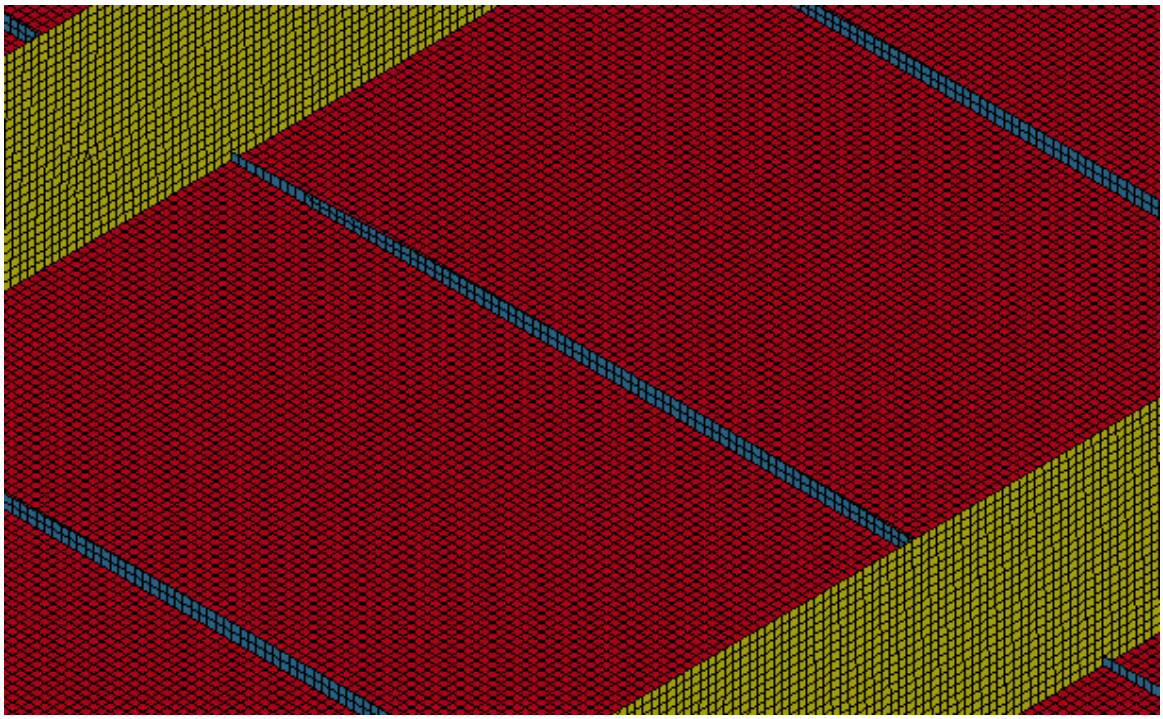

Run28, von Mise Stress, Load Case 2:

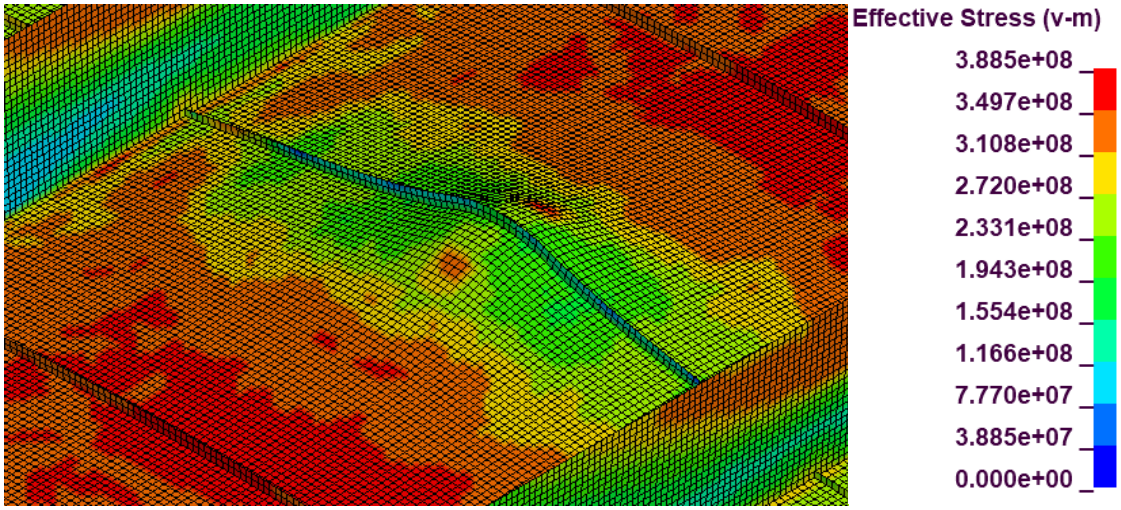

Run29, Geometry:

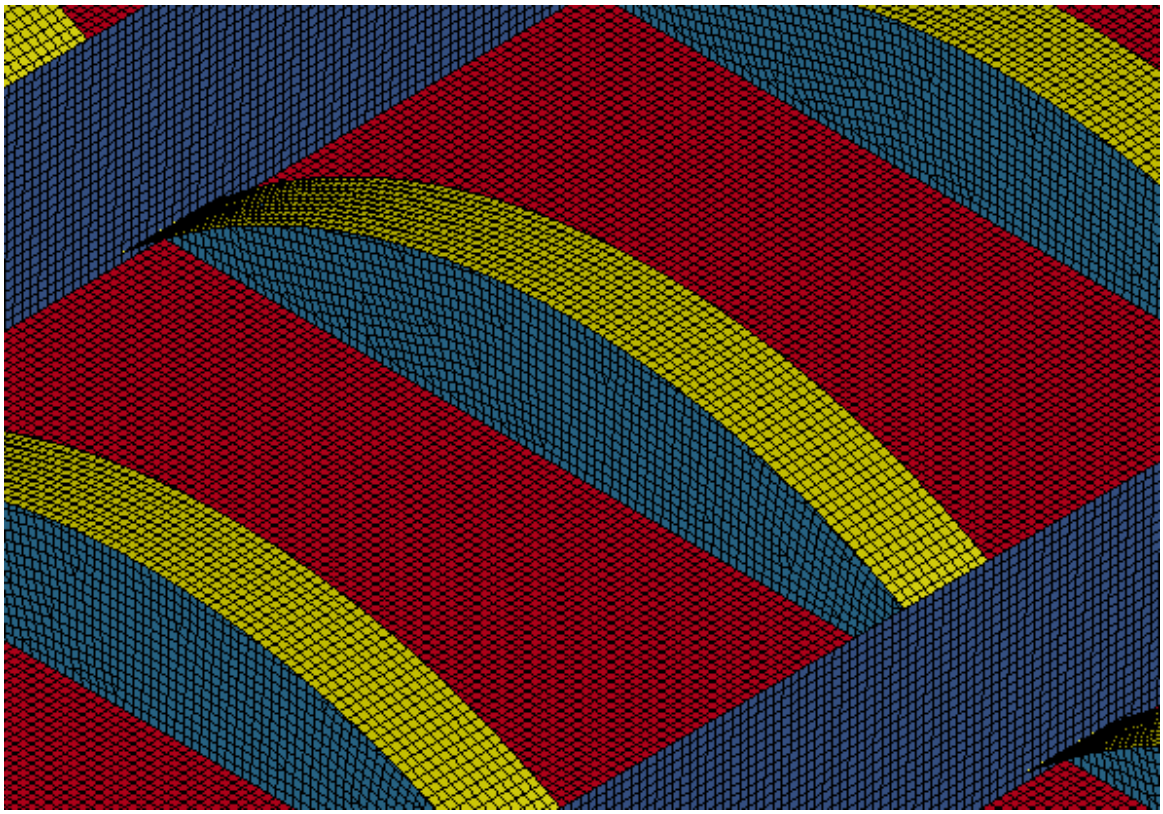

Run29, von Mise Stress, Load Case 2:

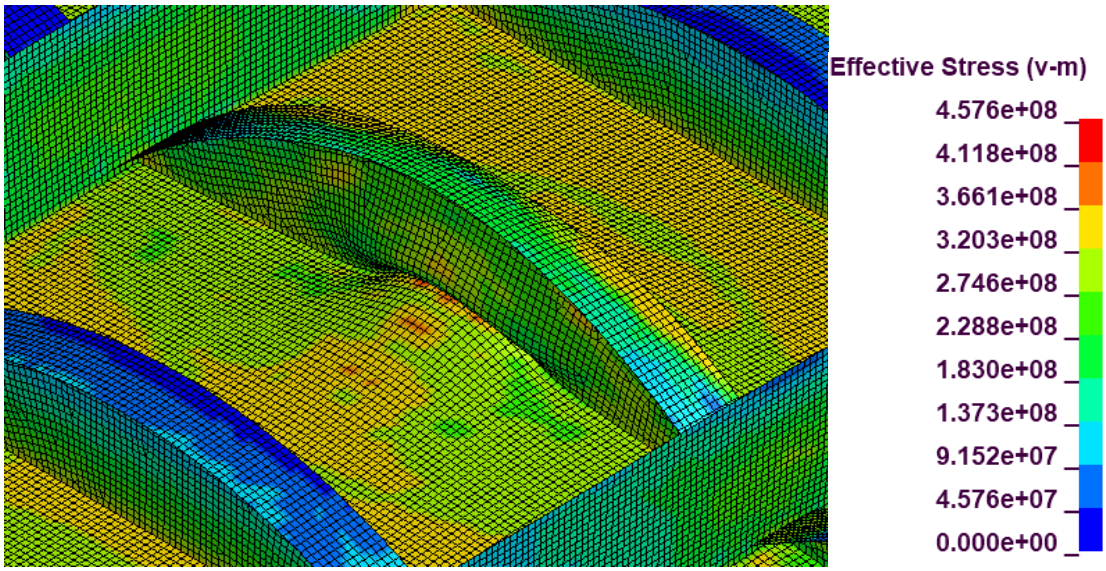

Run30, Geometry:

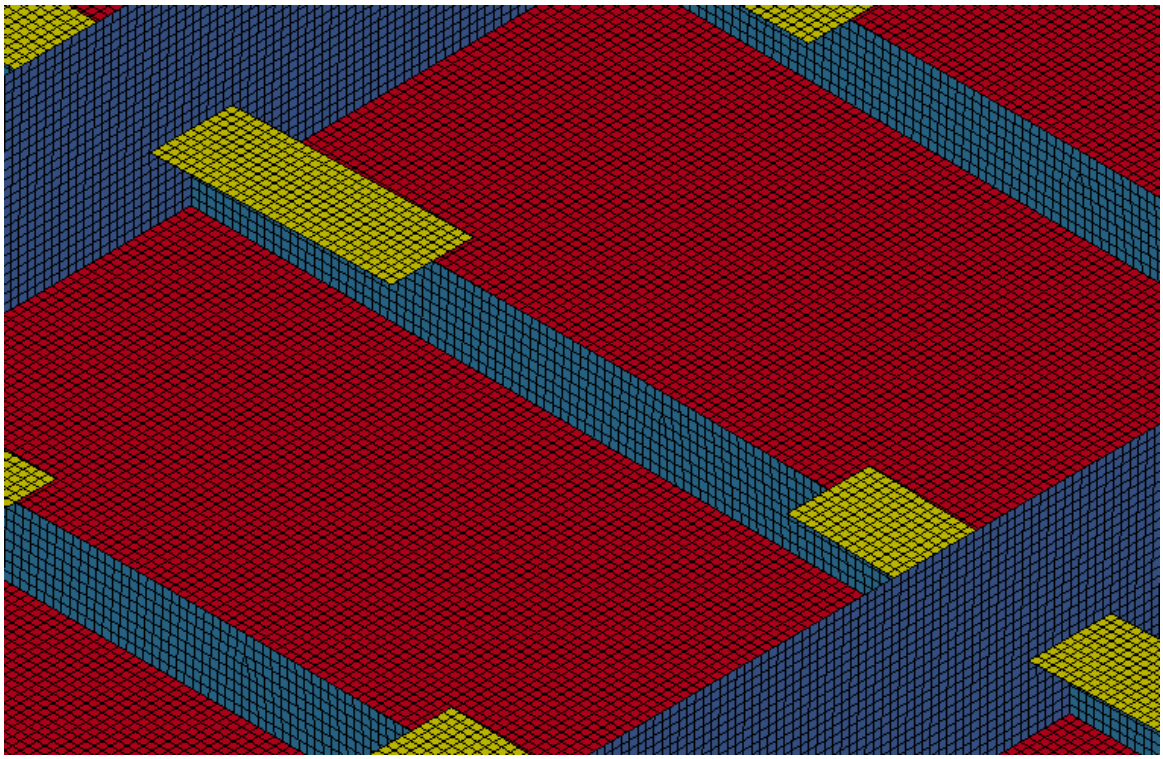

Run30, von Mise Stress, Load Case 2:

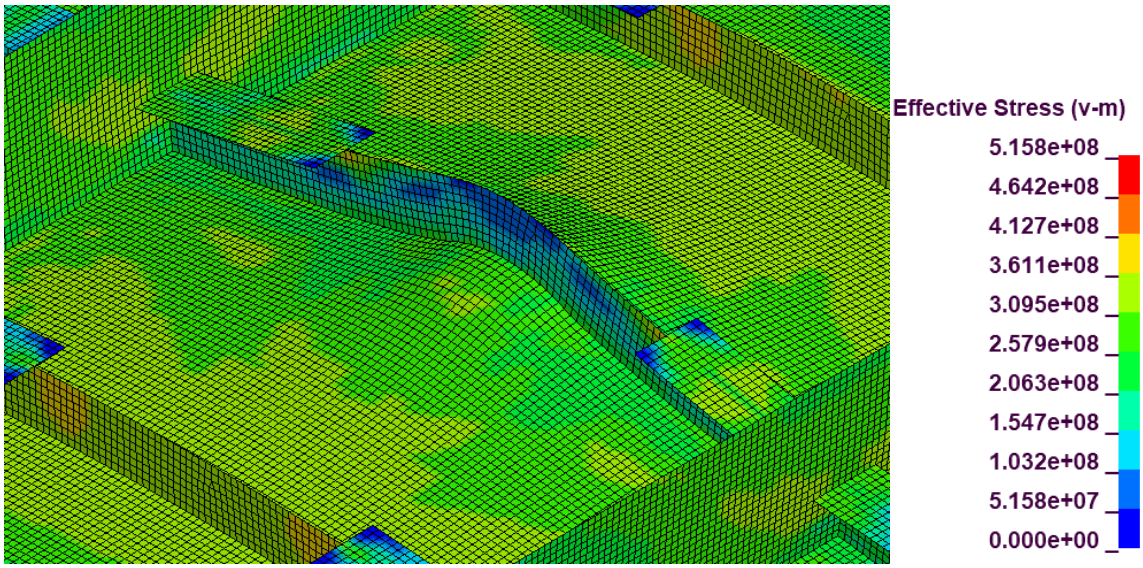

Run31, Geometry:

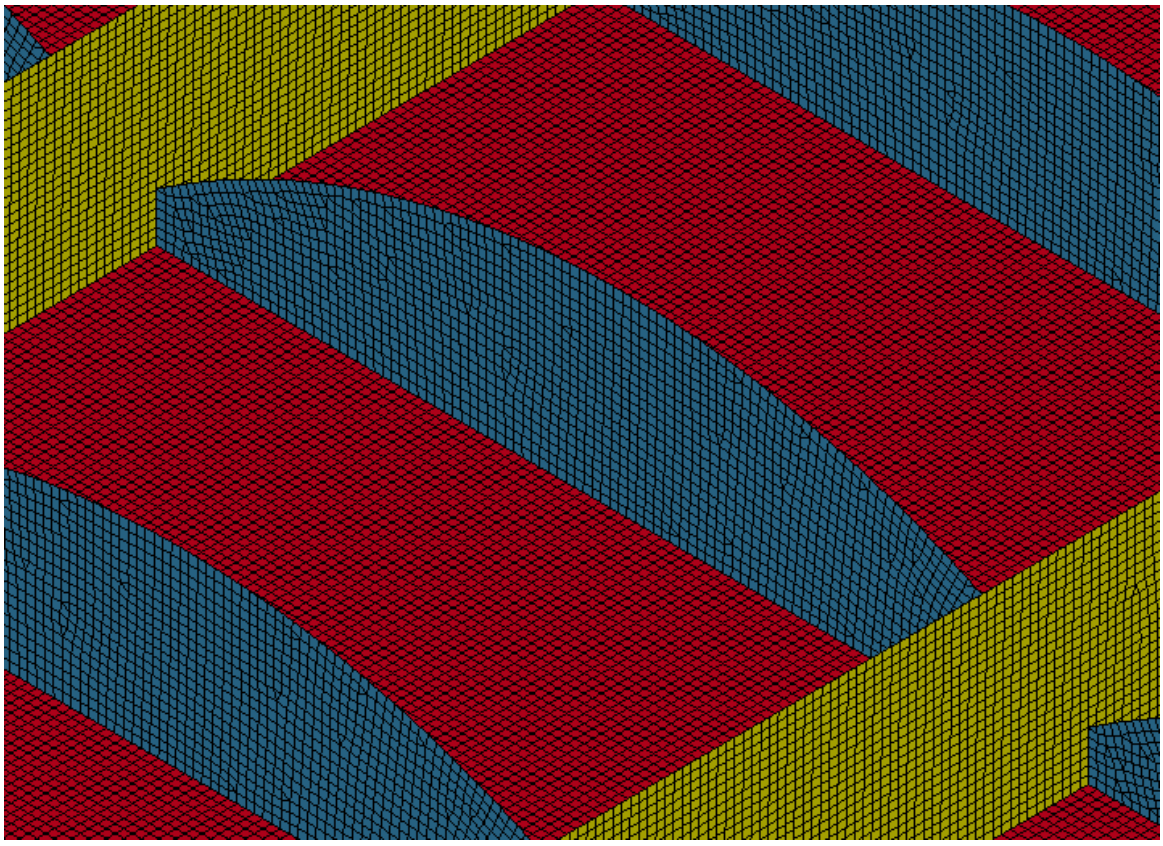

Run31, von Mise Stress, Load Case 2:

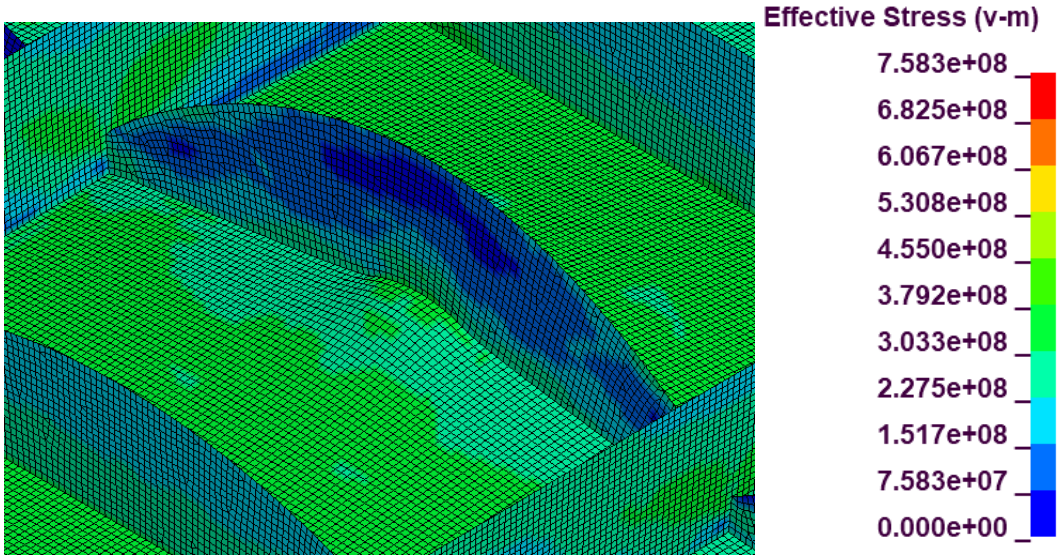

Appendix D2 – Table of Variable Dimensions, Parameters, and Responses

Run Order	mm A Hw	mm B Hw2	mm C Tw	mm D Lf	mm E Wf	mm F Tf	kg Response 1 Total Weight
Built-T	170	0	7.9375	641.9	102	7.9375	21.76
Flat bar	215	0	10.03764736	0	0	0	21.75
1	12	105.48	11	191.0935793	30.24	12	10.29
2	120	12	8.6	641.9	24	12	14.00
3	14.16	88.38	12	266.3885	120	9.4	13.62
4	12	170.46	8	641.9	120	8	19.89
5	35.22	49.62	9.64	0	74.4	8	6.67
6	12	240	12	0	24	8	20.98
7	66	12	12	320.95	74.4	8	11.96
8	120	78.12	8.36	6.419	78.24	10.8	14.62
9	66.54	240	11.35178392	430.073	91.2	8	31.02
10	93	240	8	0	120	8.2	20.52
11	19.02	49.62	8	320.95	24	9.3	5.35
12	120	12	12	0	120	8	15.49
13	120	240	12	324.1595	38.4	12	36.39
14	12	12	12	641.9	24	8	4.36
15	67.08	148.8	8	481.425	86.4	12	21.32
16	55.74	195.54	10.36	641.9	24	10.2	22.03
17	108.66	92.94	12	641.9	77.76	9.6	28.23
18	12	240	9.2	269.538	82.56	10.38	19.72
19	12	12	9.6	641.9	84.96	10.94	11.31
20	120	240	10.1	0	62.4	9.98	28.66
21	120	240	8	641.9	45.12	8	26.33
22	73.02	12	12	38.514	31.68	10.19926393	10.00
23	89.22	12	8.26	458.9585	115.2	8.5	15.15
24	74.41381642	240	8	0	24	12	19.02
25	62.73434036	143.1	11.53734285	464.7326205	76.41892803	12	25.18
26	120	240	9.5	641.9	120	10.59763777	39.77
27	119.46	124.86	10.3	234.2935	24	8.12	21.84
28	12	12	8	0	120	12	1.62
29	12	240	12	641.9	120	12	35.50
30	96.78	12	11	353.045	120	12	19.61
31	67.62	198.96	11.22784429	0	111.84	11.58	22.80
Conf. Run	118.2	94	11.125	641.9	24	8	22.3
Conf. Run2	118.2	94	12.2	0	0	0	22.3

	IOS Mid				IOS End				IBS			
Run Order	MN Response 2 L/100 12.84mm	MN Response 3 First Yield 17mm	MN Response 4 L/10 128.4mm	MN Response 5 Max 200mm	MN Response 6 L/100 12.84mm	MN Response 7 First Yield 17mm	MN Response 8 L/10 128.4mm	MN Response 9 Max 200mm	MN Response 10 L/100 12.84mm	MN Response 11 First Yield 17mm	MN Response 12 L/10 128.4mm	MN Response 13 Max 200mm
Built-T	0.364984688	0.429003688	1.22551	1.75735075	0.388538594	0.426746031	1.288749	1.830027	0.032316793	0.059357203	1.16077	1.699757
Flat bar	0.377165094	0.445217938	1.280012875	1.73988925	0.416307625	0.47039375	1.2785905	1.849267375	0.03358034	0.059533563	1.11393825	1.586961875
1	0.099631242	0.136647375	0.547215875	1.13760925	0.10417993	0.127492242	0.606034688	1.26043775	0.03048927	0.048904039	0.479352938	1.0936595
2	0.203650719	0.251495375	0.918324875	1.437728125	0.258160531	0.292169438	0.9301745	1.51623825	0.031930787	0.053594297	0.8207565	1.3470255
3	0.096251586	0.128453813	0.541813813	1.15878475	0.106823227	0.118420109	0.621256125	1.28425125	0.029845578	0.049357523	0.5035385	1.13500075
4	0.3279905	0.395230813	0.86494725	1.2665315	0.301731156	0.32630225	0.828047	1.297246	0.033035371	0.059204668	0.5848295	1.208456375
5	0.073206359	0.08652557	0.448638625	1.04998475	0.075119586	0.090009148	0.560401375	1.204697625	0.030951957	0.046046066	0.455733688	1.08657475
6	0.292120031	0.386666875	0.945382625	1.46327375	0.22377275	0.276561844	0.818342125	1.2991645	0.035106238	0.060835402	0.533655625	1.13405625
7	0.091579141	0.138702922	0.669001188	1.2180465	0.149253406	0.173538313	0.788149188	1.35473775	0.030995602	0.050242094	0.627047063	1.1643805
8	0.247951859	0.296893656	0.86803825	1.462572	0.273609125	0.29994225	0.895376875	1.507365	0.033144785	0.056468855	0.78044775	1.35919625
9	0.51632475	0.59432375	1.153398	1.76741425	0.531230313	0.566878	1.15456325	1.601647	0.034306219	0.064589941	0.88718325	1.52650425
10	0.445341781	0.473170563	0.761794125	1.322976875	0.346154125	0.372542375	0.809730625	1.37955375	0.032376117	0.059178074	0.738742313	1.3685375
11	0.050766953	0.053397801	0.397413906	1.030263375	0.06398766	0.068744969	0.528769625	1.18227275	0.031443867	0.044200336	0.446137563	1.070208125
12	0.184649203	0.21354125	0.896014875	1.439468	0.263132438	0.303954188	0.918368875	1.52504975	0.030766252	0.052004414	0.7969695	1.344758
13	0.65334475	0.739671375	1.4398415	1.72736925	0.612124	0.658017375	1.38282825	1.757761375	0.035115797	0.063528809	1.177107	1.76999725
14	0.032239662	0.03669123	0.35680725	1.048207813	0.047826328	0.057557637	0.498513125	1.188057375	0.028844586	0.041880645	0.415121938	1.0923325
15	0.25432775	0.31123575	0.90059925	1.497297	0.330743219	0.368930625	0.874979188	1.454870625	0.032268676	0.05744893	0.808761438	1.37145575
16	0.400428969	0.464177969	0.982894375	1.573982125	0.352966375	0.378144844	0.942890313	1.5275375	0.033058316	0.061095855	0.685595688	1.34412775
17	0.450866125	0.536552188	1.272945875	1.9357065	0.474307125	0.52704325	1.268971875	1.941802625	0.035186367	0.062472363	1.09659875	1.648242
18	0.310508438	0.365853031	0.854937	1.3903235	0.274125188	0.309883	0.812055125	1.3672525	0.032976191	0.059408199	0.583722438	1.20659725
19	0.058151859	0.055874129	0.441040844	1.143575125	0.080661836	0.081575156	0.576038625	1.28963575	0.031589914	0.045343523	0.453828188	1.146454
20	0.574310188	0.646960813	0.98657375	1.5597085	0.456431875	0.511318438	1.1503525	1.613244875	0.034068023	0.062134133	0.998117813	1.612395875
21	0.522617281	0.5675235	1.013599	1.47884175	0.476785031	0.513562938	0.97890025	1.55721775	0.033026656	0.058055258	1.038190438	1.622233
22	0.096307461	0.134037547	0.605875375	1.186254	0.138465453	0.166908641	0.694408188	1.29942775	0.030761854	0.048752918	0.574596125	1.1264295
23	0.141710891	0.193783359	0.763458563	1.31708825	0.220412813	0.245525813	0.916218188	1.506069	0.03146934	0.052391672	0.706114875	1.27728925
24	0.414517031	0.425972219	0.938927	1.29619575	0.313814063	0.334216875	0.825083125	1.348262	0.033209156	0.05974559	0.656511813	1.316152625
25	0.310864688	0.3735855	0.982526125	1.5891855	0.397761625	0.448233906	1.07966575	1.725846625	0.033411691	0.060734688	0.861230688	1.4246635
26	0.625274	0.718922375	1.24000675	1.71125925	0.60687125	0.683859813	1.137537625	1.745556625	0.034884676	0.060613078	1.22792975	1.840038375
27	0.383098625	0.443442438	1.090682125	1.702953125	0.392318594	0.434650813	1.093268875	1.72831675	0.034922367	0.061305406	0.958641313	1.50880525
28	0.034358336	0.036305707	0.316271125	1.03209425	0.036890438	0.046474672	0.462821875	1.147315	0.028334381	0.040418105	0.398941375	1.076181625
29	0.6228575	0.71409575	1.219206625	1.449061875	0.532052813	0.567713625	1.072759625	1.58373775	0.034374137	0.06449168	0.590016938	1.303759
30	0.188540672	0.229251813	0.844118938	1.424488625	0.233698078	0.283759219	0.948282	1.593205875	0.029896188	0.055697988	0.768462625	1.348936125
31	0.4186445	0.477752531	1.001880875	1.60243525	0.353337094	0.375636813	0.95336975	1.53446825	0.034168422	0.060823914	0.683535375	1.3253815
Conf. Run	0.374116625	0.439064719	1.10304325	1.704908375	0.396446813	0.448393125	1.098531125	1.744162875	0.033851609	0.060021551	0.961517063	1.506255625
Conf. Run2	0.352918844	0.414341125	1.0533465	1.654260625	0.384432375	0.436531688	1.048846625	1.703155625	0.03455973	0.059606852	0.922977688	1.479044375

Appendix D3 – von Mises Stress vs. Displacement Plots, Load Case 2

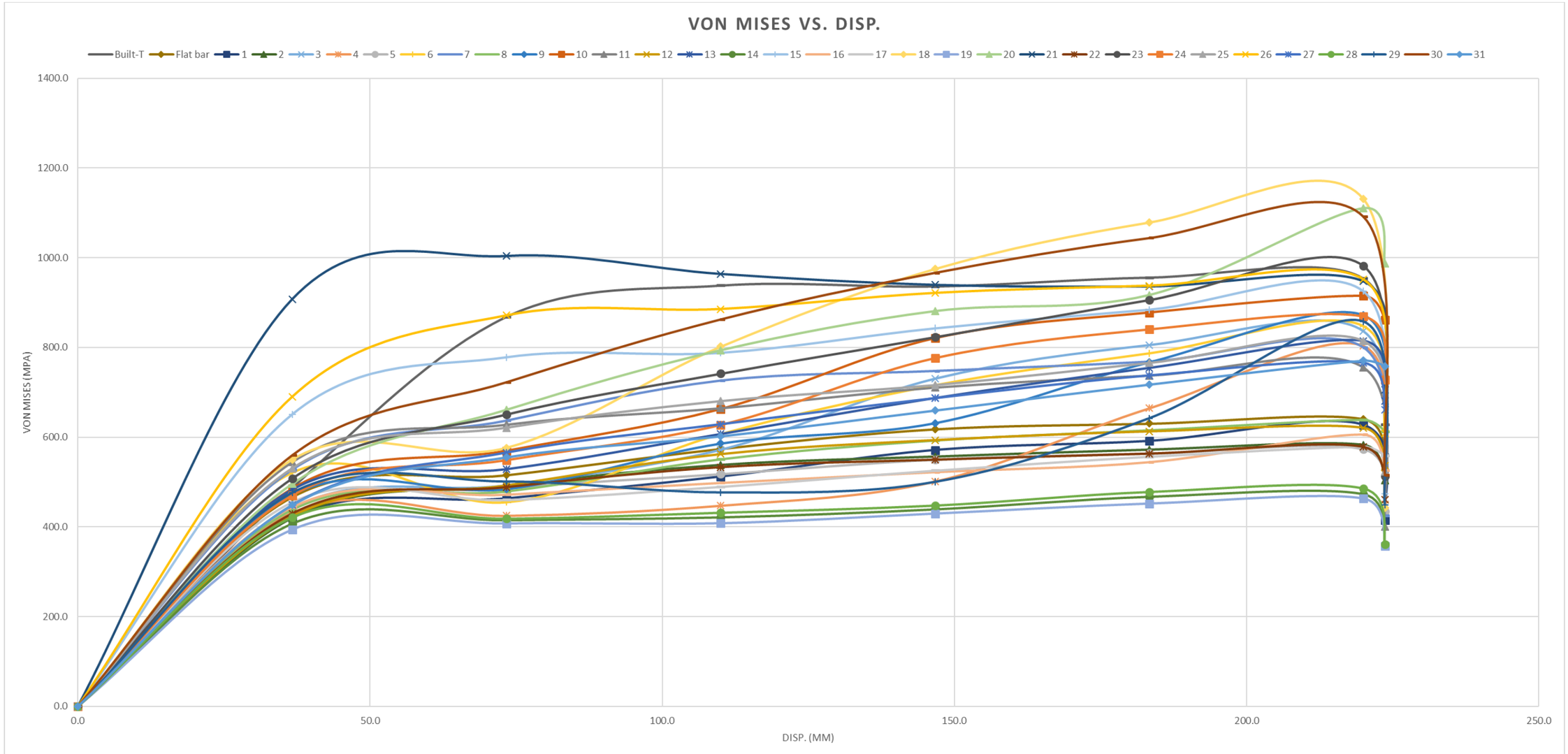

Appendix D4 – Force vs. Displacement Plots, Load Case 1

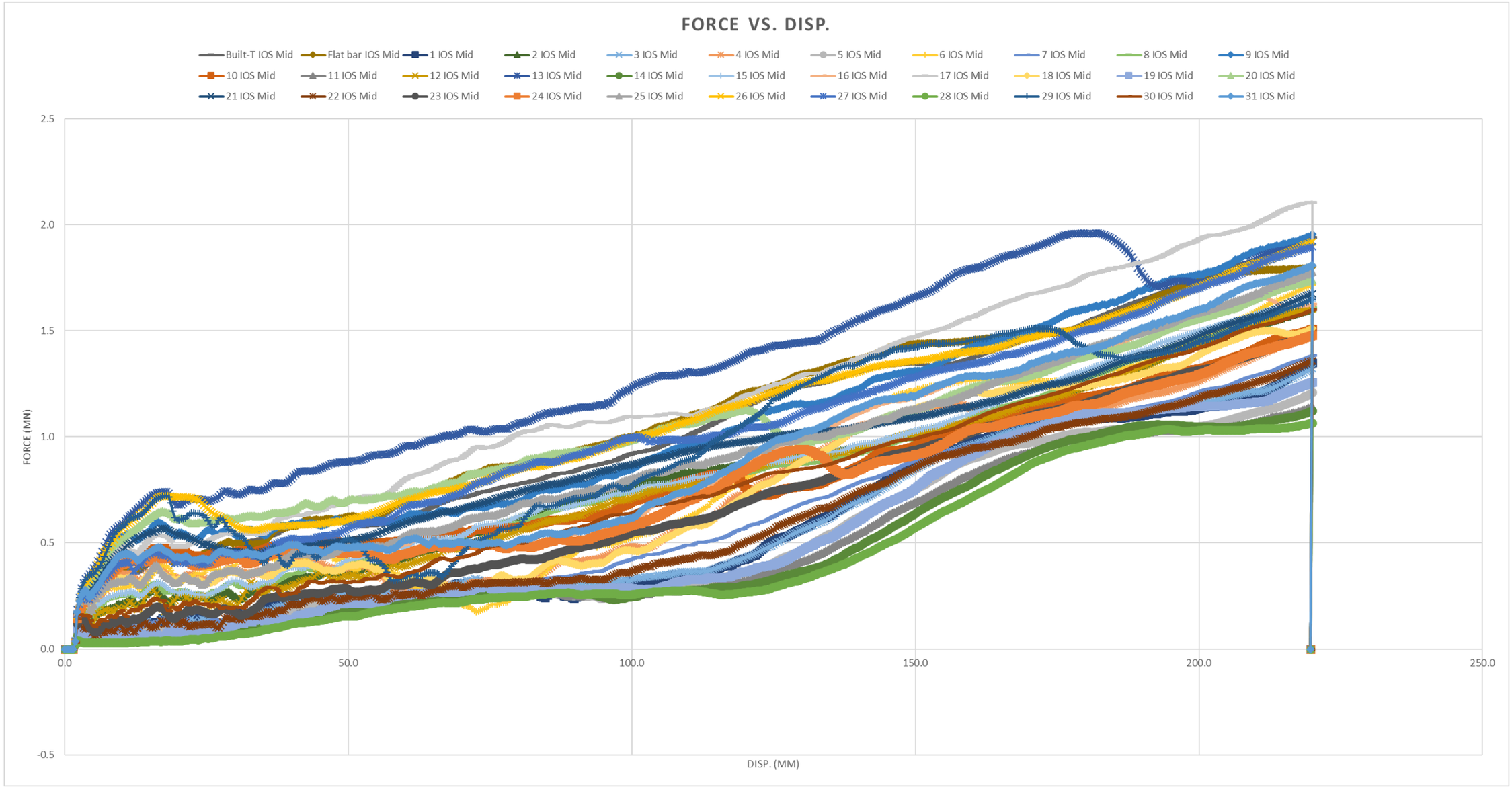

Appendix D5 – Force vs. Displacement Plots, Load Case 2

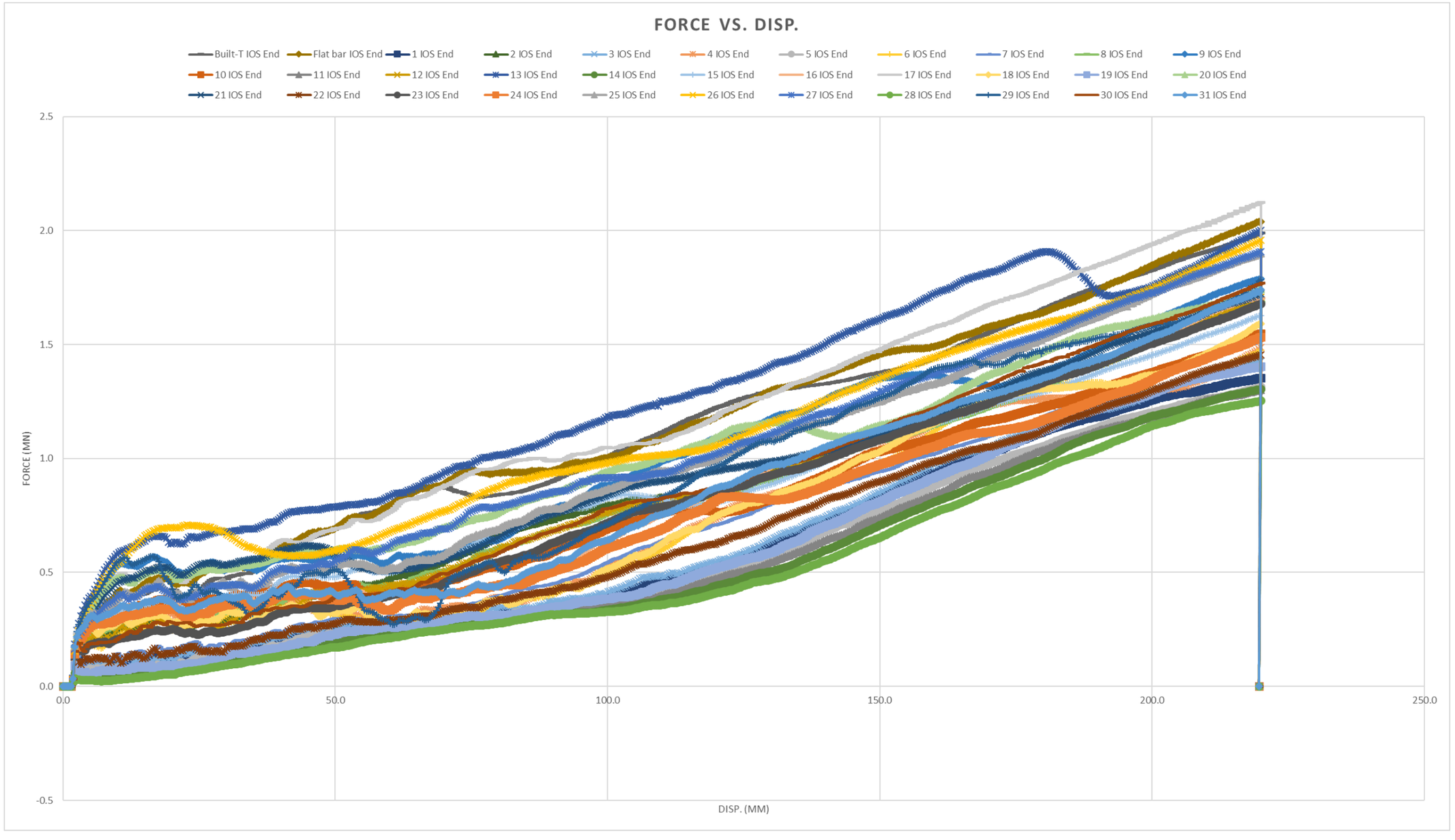

Appendix D6 – Force vs. Displacement Plots, Load Case 3

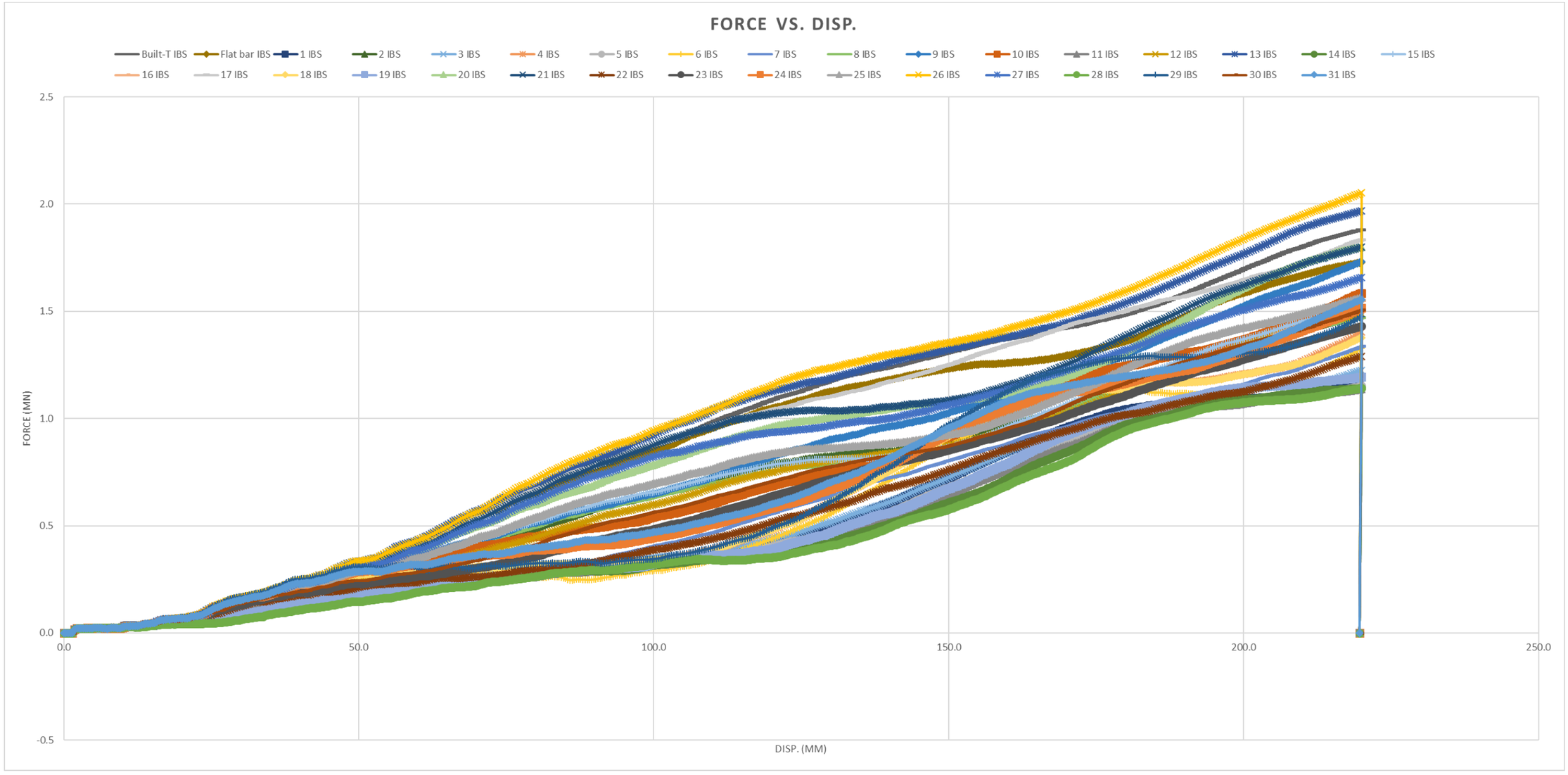

Appendix D7 – Design Expert Output

Response 1 – Weight:

Source	Sequential p-value	Lack of Fit p-value	Adjusted R^2	Predicted R^2	
Linear	< 0.0001		0.9429	0.9171	
2FI	**< 0.0001**		**0.9997**	**0.9982**	**Suggested**
Quadratic	0.7466		0.9996	0.9683	
Cubic					Aliased

Source	Sum of Squares	df	Mean Square	F-value	p-value	
Model	2684.73	12	223.73	4195.61	< 0.0001	significant
A-Hw	502.95	1	502.95	9431.93	< 0.0001	
B-Hw2	1106.75	1	1106.75	20755.09	< 0.0001	
C-Tw	147.33	1	147.33	2763.00	< 0.0001	
D-Lf	255.80	1	255.80	4797.05	< 0.0001	
E-Wf	108.49	1	108.49	2034.62	< 0.0001	
F-Tf	10.95	1	10.95	205.25	< 0.0001	
AC	10.62	1	10.62	199.16	< 0.0001	
BC	19.21	1	19.21	360.32	< 0.0001	
BF	0.3682	1	0.3682	6.90	0.0171	
DE	64.41	1	64.41	1207.86	< 0.0001	
DF	7.02	1	7.02	131.67	< 0.0001	
EF	2.90	1	2.90	54.34	< 0.0001	
Residual	0.9598	18	0.0533			
Cor Total	2685.68	30				

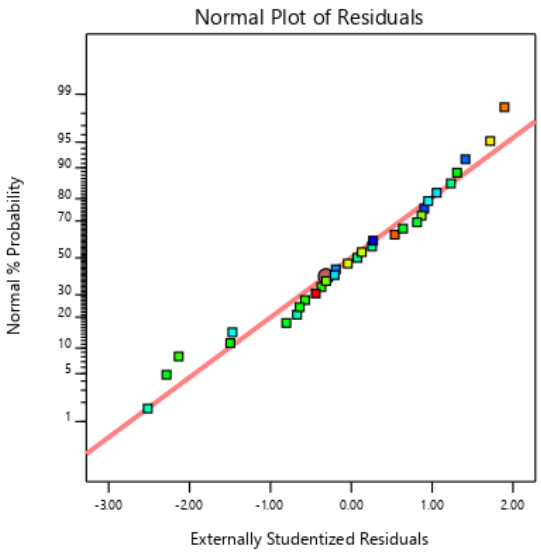

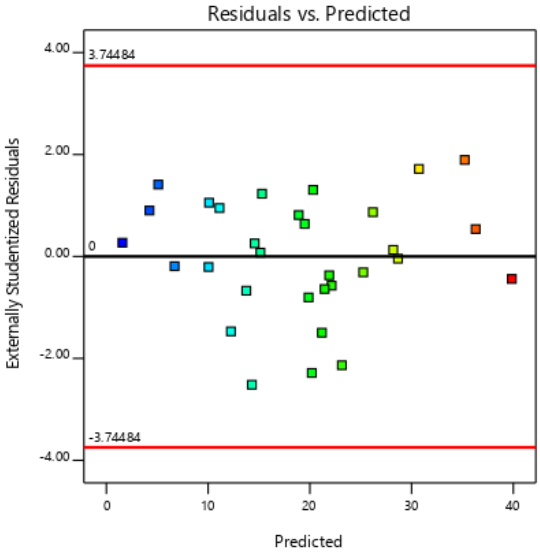

Response 2 – IOSC (L/100):

Source	Sequential p-value	Lack of Fit p-value	Adjusted R^2	Predicted R^2	
Linear	**< 0.0001**		**0.9465**	**0.9231**	**Suggested**
2FI	0.1057		0.9704	0.8239	
Quadratic	0.0920		0.9928	0.7956	
Cubic					Aliased

Source	Sum of Squares	df	Mean Square	F-value	p-value	
Model	1.09	5	0.2176	102.32	< 0.0001	significant
A-Hw	0.2225	1	0.2225	104.60	< 0.0001	
B-Hw2	0.7549	1	0.7549	354.90	< 0.0001	
C-Tw	0.0165	1	0.0165	7.75	0.0101	
D-Lf	0.0318	1	0.0318	14.94	0.0007	
E-Wf	0.0147	1	0.0147	6.92	0.0144	
Residual	0.0532	25	0.0021			
Cor Total	1.14	30				

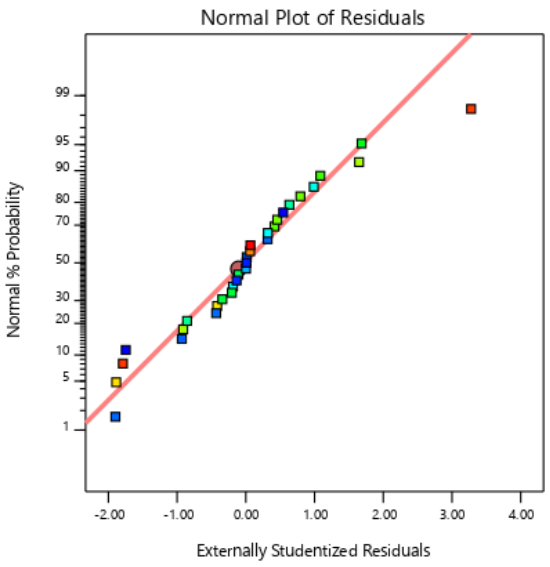

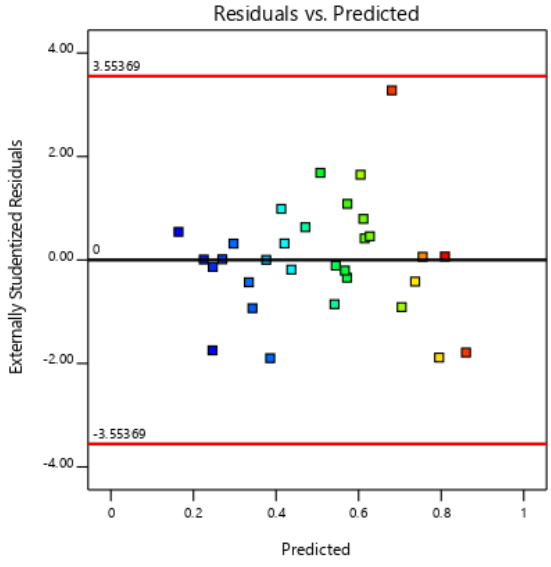

Response 3 – IOSC (First Yield):

Source	Sequential p-value	Lack of Fit p-value	Adjusted R^2	Predicted R^2	
Linear	**< 0.0001**		**0.9351**	**0.9035**	**Suggested**
2FI	**0.0343**		**0.9741**	**0.8825**	**Suggested**
Quadratic	0.5351		0.9746	-0.3465	
Cubic					Aliased

Source	Sum of Squares	df	Mean Square	F-value	p-value	
Model	1.22	9	0.1359	139.52	< 0.0001	significant
A-Hw	0.2587	1	0.2587	265.66	< 0.0001	
B-Hw2	0.6667	1	0.6667	684.50	< 0.0001	
C-Tw	0.0242	1	0.0242	24.80	< 0.0001	
D-Lf	0.0312	1	0.0312	32.00	< 0.0001	
E-Wf	0.0115	1	0.0115	11.78	0.0025	
AB	0.0204	1	0.0204	20.97	0.0002	
AE	0.0056	1	0.0056	5.79	0.0254	
BC	0.0054	1	0.0054	5.55	0.0283	
DE	0.0051	1	0.0051	5.21	0.0329	
Residual	0.0205	21	0.0010			
Cor Total	1.24	30				

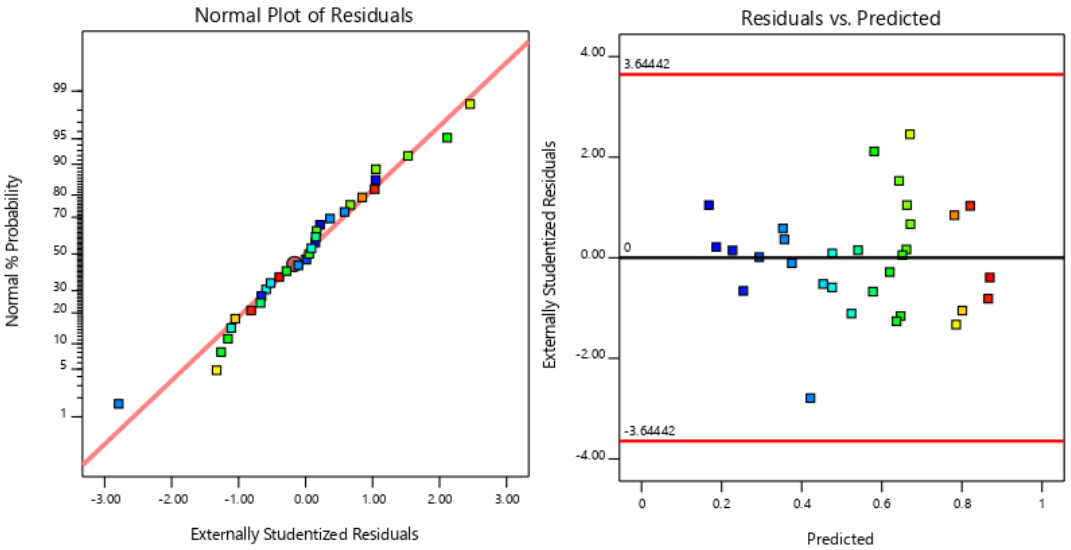

Response 4 – IOSC (L/10):

Source	Sequential p-value	Lack of Fit p-value	Adjusted R^2	Predicted R^2	
Linear	< 0.0001		0.8368	0.7630	
2FI	**0.0042**		**0.9624**	**0.7981**	**Suggested**
Quadratic	0.6214		0.9571	-0.8135	
Cubic					Aliased

Source	Sum of Squares	df	Mean Square	F-value	p-value	
Model	2.39	9	0.2654	89.60	< 0.0001	significant
A-Hw	0.8054	1	0.8054	271.88	< 0.0001	
B-Hw2	0.7821	1	0.7821	264.01	< 0.0001	
C-Tw	0.1508	1	0.1508	50.89	< 0.0001	
D-Lf	0.1788	1	0.1788	60.36	< 0.0001	
E-Wf	0.0029	1	0.0029	0.9784	0.3339	
AB	0.1168	1	0.1168	39.41	< 0.0001	
AC	0.0514	1	0.0514	17.36	0.0004	
BC	0.0622	1	0.0622	20.99	0.0002	
DE	0.0191	1	0.0191	6.45	0.0191	
Residual	0.0622	21	0.0030			
Cor Total	2.45	30				

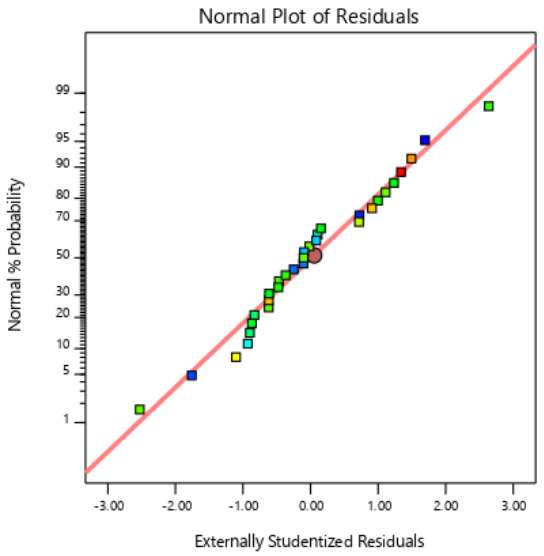

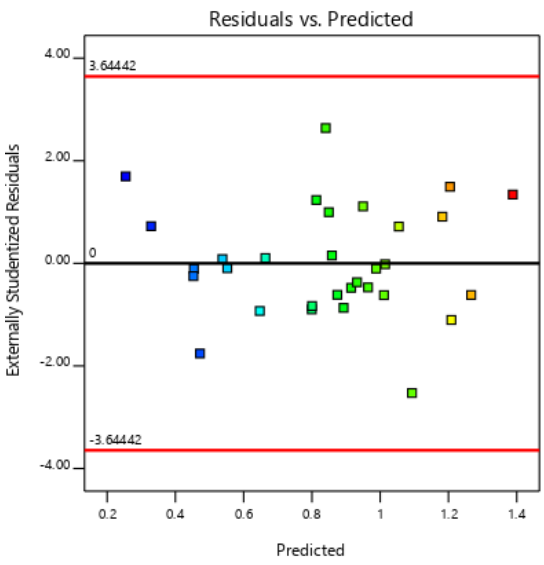

Response 5 – IOSC (Maximum):

Source	Sequential p-value	Lack of Fit p-value	Adjusted R^2	Predicted R^2	
Linear	**< 0.0001**		**0.7398**	**0.6487**	**Suggested**
2FI	0.3126		0.7914	-0.7124	
Quadratic	0.1620		0.9231	-4.2583	
Cubic					Aliased

Source	Sum of Squares	df	Mean Square	F-value	p-value	
Model	1.33	4	0.3330	22.82	< 0.0001	significant
A-Hw	0.6430	1	0.6430	44.07	< 0.0001	
B-Hw2	0.4044	1	0.4044	27.72	< 0.0001	
C-Tw	0.1687	1	0.1687	11.56	0.0022	
D-Lf	0.1104	1	0.1104	7.57	0.0107	
Residual	0.3794	26	0.0146			
Cor Total	1.71	30				

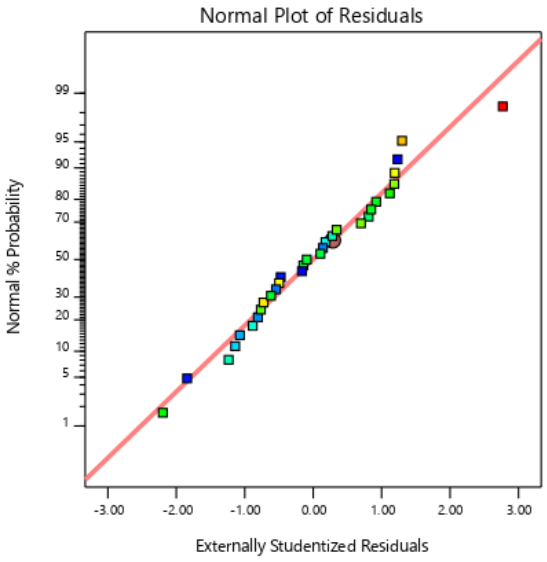

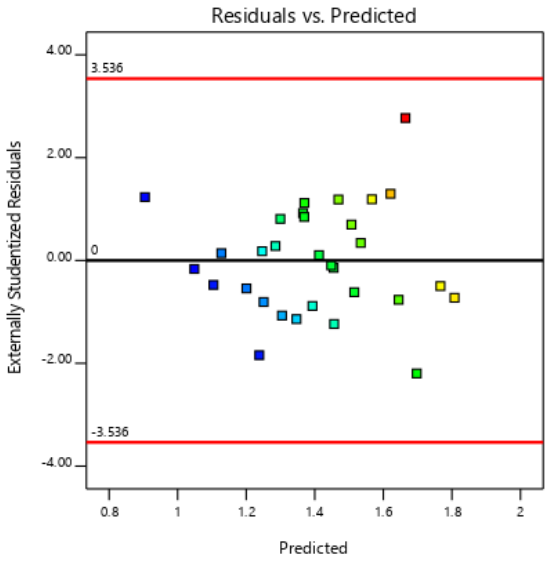

Response 6 – IOSQ (L/100):

Source	Sequential p-value	Lack of Fit p-value	Adjusted R^2	Predicted R^2	
Linear	< 0.0001		0.9333	0.9073	
2FI	**0.0098**		**0.9809**	**0.9138**	**Suggested**
Quadratic	0.3677		0.9866	0.3931	
Cubic					Aliased

Source	Sum of Squares	df	Mean Square	F-value	p-value	
Model	0.8315	10	0.0831	153.28	< 0.0001	significant
A-Hw	0.2532	1	0.2532	466.70	< 0.0001	
B-Hw2	0.3319	1	0.3319	611.75	< 0.0001	
C-Tw	0.0291	1	0.0291	53.73	< 0.0001	
D-Lf	0.0726	1	0.0726	133.80	< 0.0001	
E-Wf	0.0100	1	0.0100	18.40	0.0004	
AC	0.0073	1	0.0073	13.51	0.0015	
BC	0.0142	1	0.0142	26.10	< 0.0001	
BD	0.0047	1	0.0047	8.72	0.0079	
CD	0.0060	1	0.0060	11.15	0.0033	
DE	0.0045	1	0.0045	8.27	0.0094	
Residual	0.0108	20	0.0005			
Cor Total	0.8423	30				

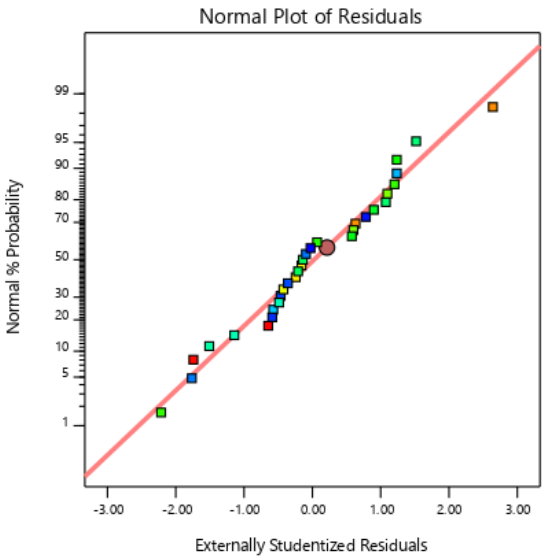

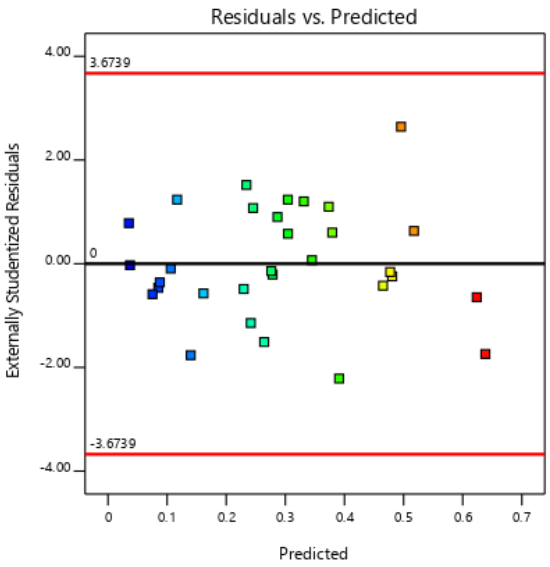

Response 7 – IOSQ (First Yield):

Source	Sequential p-value	Lack of Fit p-value	Adjusted R^2	Predicted R^2	
Linear	**< 0.0001**		**0.9353**	**0.9108**	**Suggested**
2FI	**0.0122**		**0.9804**	**0.9035**	**Suggested**
Quadratic	0.6312		0.9773	0.4064	
Cubic					Aliased

Source	Sum of Squares	df	Mean Square	F-value	p-value	
Model	0.9644	10	0.0964	159.40	< 0.0001	significant
A-Hw	0.3108	1	0.3108	513.63	< 0.0001	
B-Hw2	0.3670	1	0.3670	606.55	< 0.0001	
C-Tw	0.0392	1	0.0392	64.78	< 0.0001	
D-Lf	0.0786	1	0.0786	129.97	< 0.0001	
E-Wf	0.0122	1	0.0122	20.10	0.0002	
AC	0.0079	1	0.0079	13.05	0.0017	
BC	0.0154	1	0.0154	25.41	< 0.0001	
BD	0.0050	1	0.0050	8.35	0.0091	
CD	0.0049	1	0.0049	8.08	0.0101	
DE	0.0081	1	0.0081	13.31	0.0016	
Residual	0.0121	20	0.0006			
Cor Total	0.9765	30				

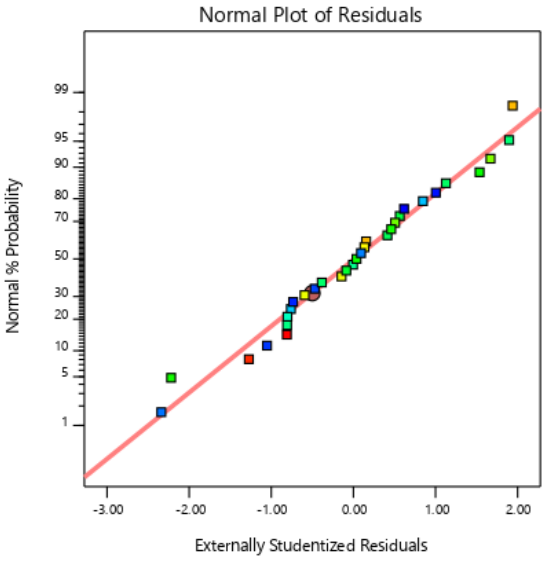

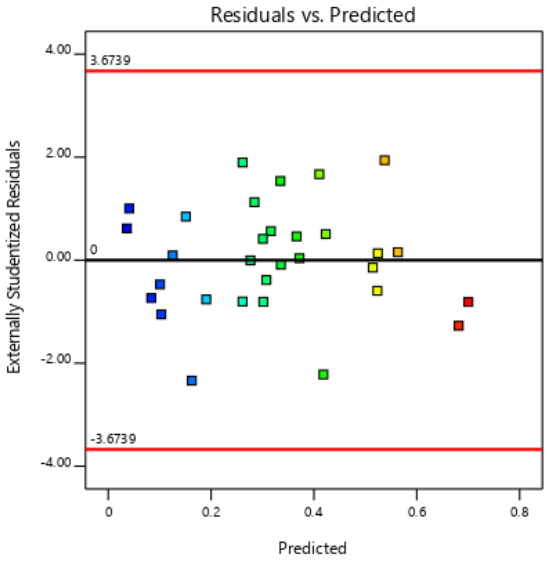

Response 8 – IOSQ (L/10):

Source	Sequential p-value	Lack of Fit p-value	Adjusted R^2	Predicted R^2	
Linear	< 0.0001		0.8442	0.7815	
2FI	**0.0032**		**0.9663**	**0.8505**	**Suggested**
Quadratic	0.3850		0.9754	0.1736	
Cubic					Aliased

Source	Sum of Squares	df	Mean Square	F-value	p-value	
Model	1.58	10	0.1578	94.76	< 0.0001	significant
A-Hw	0.7727	1	0.7727	463.97	< 0.0001	
B-Hw2	0.3053	1	0.3053	183.30	< 0.0001	
C-Tw	0.1451	1	0.1451	87.12	< 0.0001	
D-Lf	0.1245	1	0.1245	74.78	< 0.0001	
E-Wf	0.0067	1	0.0067	4.00	0.0592	
AB	0.0290	1	0.0290	17.42	0.0005	
AC	0.0510	1	0.0510	30.59	< 0.0001	
BC	0.0636	1	0.0636	38.18	< 0.0001	
CD	0.0112	1	0.0112	6.72	0.0174	
DE	0.0136	1	0.0136	8.16	0.0098	
Residual	0.0333	20	0.0017			
Cor Total	1.61	30				

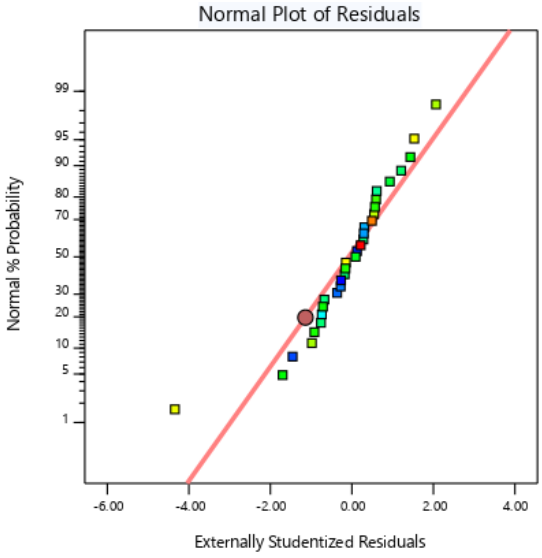

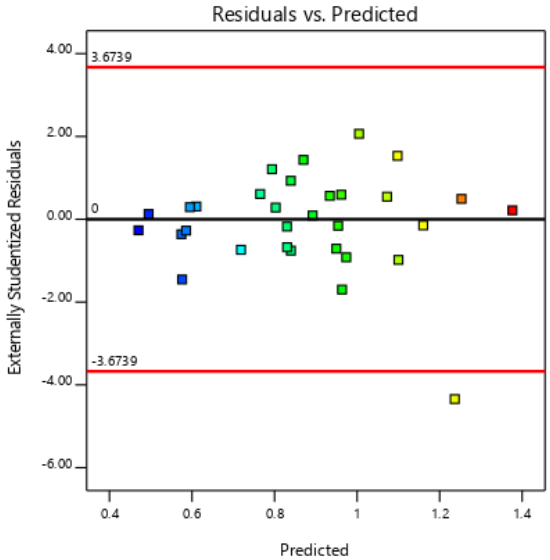

Response 9 – IOSQ (Maximum):

Source	Sequential p-value	Lack of Fit p-value	Adjusted R^2	Predicted R^2	
Linear	**< 0.0001**		**0.8237**	**0.7731**	**Suggested**
2FI	0.3377		0.8543	0.1035	
Quadratic	0.2653		0.9216	-1.0335	
Cubic					Aliased

Source	Sum of Squares	df	Mean Square	F-value	p-value	
Model	0.9626	4	0.2407	28.35	< 0.0001	significant
A-Hw	0.6199	1	0.6199	73.02	< 0.0001	
B-Hw2	0.1033	1	0.1033	12.17	0.0017	
C-Tw	0.1240	1	0.1240	14.61	0.0007	
D-Lf	0.1386	1	0.1386	16.32	0.0004	
Residual	0.2207	26	0.0085			
Cor Total	1.18	30				

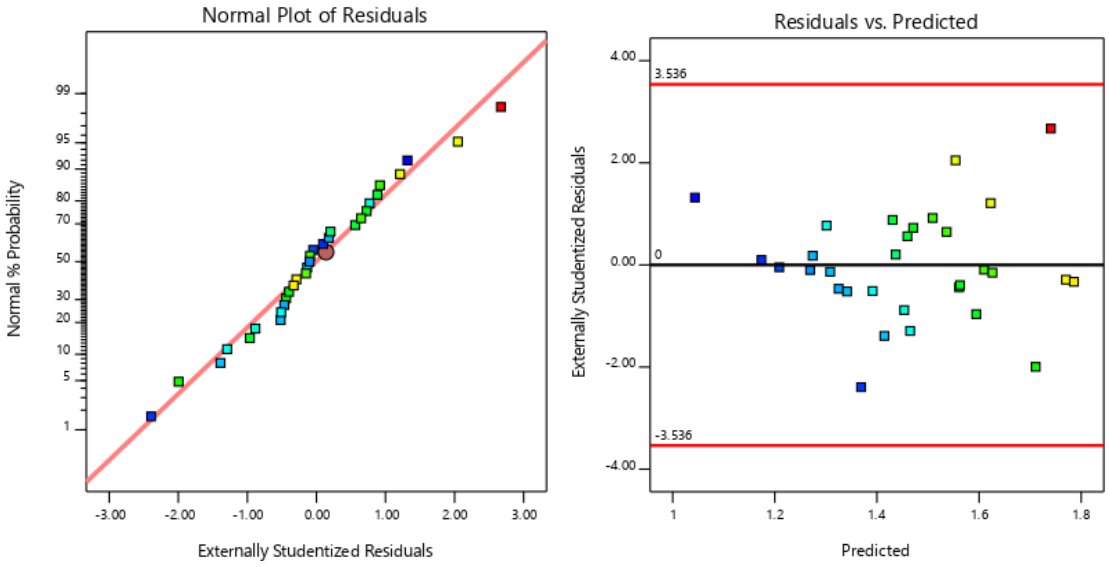

Response 10 – IBS (L/100):

Source	Sequential p-value	Lack of Fit p-value	Adjusted R^2	Predicted R^2	
Linear	**< 0.0001**		**0.6258**	**0.4713**	**Suggested**
2FI	0.3277		0.6944	-1.0343	
Quadratic	0.5912		0.6688	-7.8049	
Cubic					Aliased

Source	Sum of Squares	df	Mean Square	F-value	p-value	
Model	0.0001	2	0.0000	25.93	< 0.0001	significant
A-Hw	0.0000	1	0.0000	7.63	0.0100	
B-Hw2	0.0001	1	0.0001	40.60	< 0.0001	
Residual	0.0000	28	1.376E-06			
Cor Total	0.0001	30				

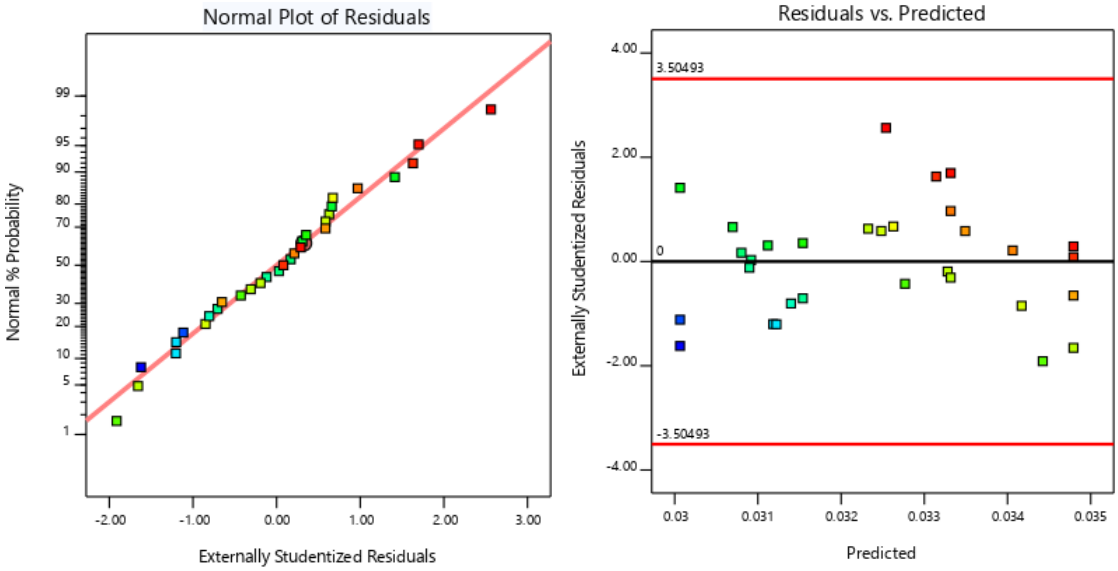

Response 11 – IBS (First Yield):

Source	Sequential p-value	Lack of Fit p-value	Adjusted R^2	Predicted R^2	
Linear	**< 0.0001**		**0.7889**	**0.6931**	**Suggested**
2FI	0.0380		0.9133	0.3651	
Quadratic	**0.0164**		**0.9936**	**0.6159**	**Suggested**
Cubic					Aliased

Source	Sum of Squares	df	Mean Square	F-value	p-value	
Model	0.0015	19	0.0001	241.53	< 0.0001	significant
A-Hw	0.0002	1	0.0002	750.39	< 0.0001	
B-Hw2	0.0007	1	0.0007	2221.77	< 0.0001	
C-Tw	0.0000	1	0.0000	101.51	< 0.0001	
D-Lf	0.0000	1	0.0000	122.66	< 0.0001	
E-Wf	4.526E-06	1	4.526E-06	14.06	0.0032	
F-Tf	3.380E-07	1	3.380E-07	1.05	0.3275	
AB	0.0001	1	0.0001	346.03	< 0.0001	
AC	9.625E-06	1	9.625E-06	29.90	0.0002	
AD	7.513E-06	1	7.513E-06	23.34	0.0005	
AE	5.063E-06	1	5.063E-06	15.73	0.0022	
BC	5.470E-06	1	5.470E-06	16.99	0.0017	
BD	0.0000	1	0.0000	32.49	0.0001	
BE	2.066E-06	1	2.066E-06	6.42	0.0278	
BF	6.228E-06	1	6.228E-06	19.35	0.0011	
CD	4.014E-06	1	4.014E-06	12.47	0.0047	
DE	0.0000	1	0.0000	37.62	< 0.0001	
EF	2.720E-06	1	2.720E-06	8.45	0.0143	
A^2	0.0000	1	0.0000	45.90	< 0.0001	
B^2	0.0000	1	0.0000	61.41	< 0.0001	
Residual	3.541E-06	11	3.219E-07			
Cor Total	0.0015	30				

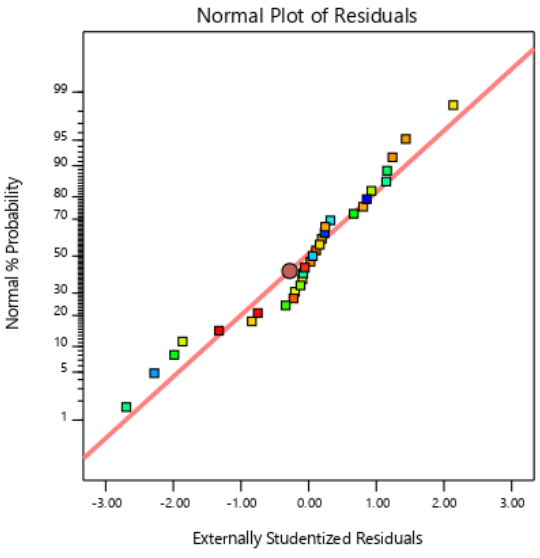

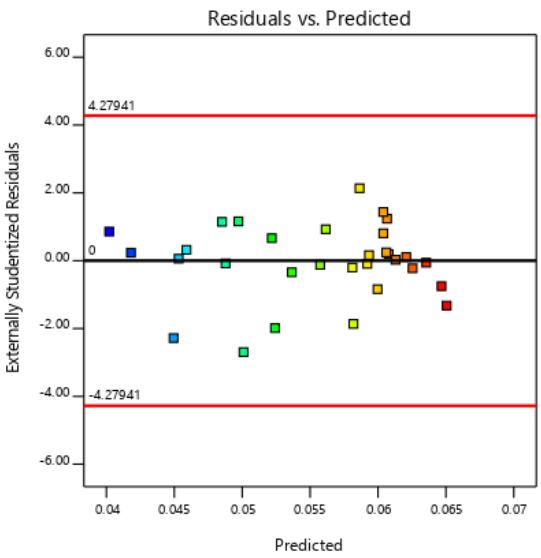

Response 12 – IBS (L/10):

Source	Sequential p-value	Lack of Fit p-value	Adjusted R^2	Predicted R^2	
Linear	**< 0.0001**		**0.9045**	**0.8634**	**Suggested**
2FI	0.3629		0.9187	0.6091	
Quadratic	0.1960		0.9654	0.1610	
Cubic					Aliased

Source	Sum of Squares	df	Mean Square	F-value	p-value	
Model	1.43	4	0.3587	72.30	< 0.0001	significant
A-Hw	1.07	1	1.07	215.44	< 0.0001	
B-Hw2	0.1929	1	0.1929	38.87	< 0.0001	
C-Tw	0.0253	1	0.0253	5.10	0.0325	
D-Lf	0.1103	1	0.1103	22.24	< 0.0001	
Residual	0.1290	26	0.0050			
Cor Total	1.56	30				

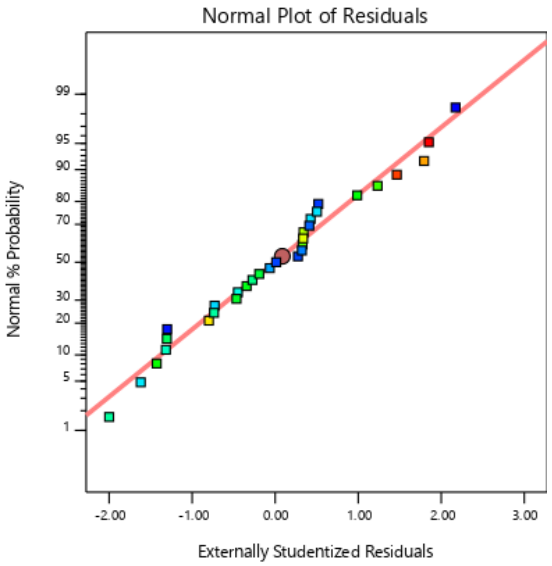

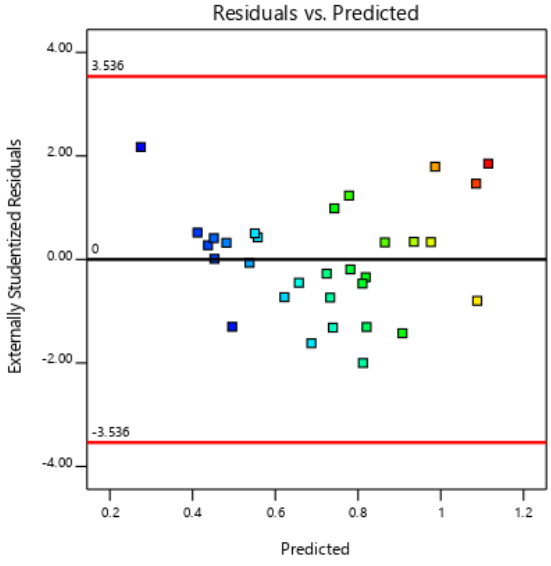

Response 13 – IBS (Maximum):

Source	Sequential p-value	Lack of Fit p-value	Adjusted R^2	Predicted R^2	
Linear	**< 0.0001**		**0.8969**	**0.8495**	**Suggested**
2FI	**0.0518**		**0.9538**	**0.7854**	**Suggested**
Quadratic	0.4131		0.9642	-0.8122	
Cubic					Aliased

Source	Sum of Squares	df	Mean Square	F-value	p-value	
Model	1.28	8	0.1605	95.89	< 0.0001	significant
A-Hw	0.7365	1	0.7365	439.95	< 0.0001	
B-Hw2	0.2681	1	0.2681	160.13	< 0.0001	
C-Tw	0.0343	1	0.0343	20.51	0.0002	
D-Lf	0.1154	1	0.1154	68.92	< 0.0001	
E-Wf	0.0143	1	0.0143	8.52	0.0080	
AB	0.0413	1	0.0413	24.66	< 0.0001	
AC	0.0183	1	0.0183	10.95	0.0032	
BC	0.0148	1	0.0148	8.83	0.0071	
Residual	0.0368	22	0.0017			
Cor Total	1.32	30				

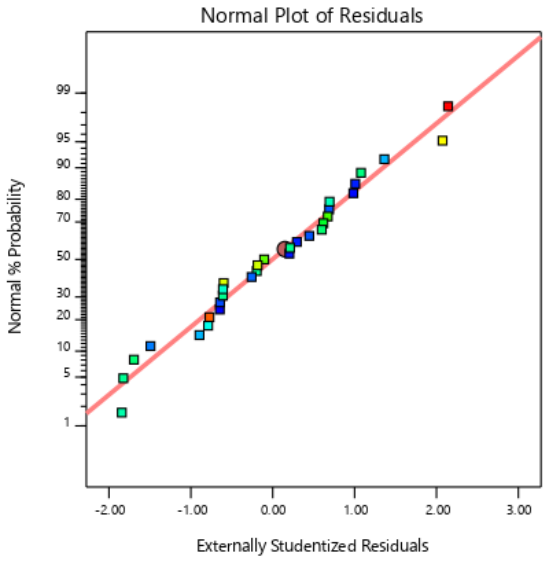

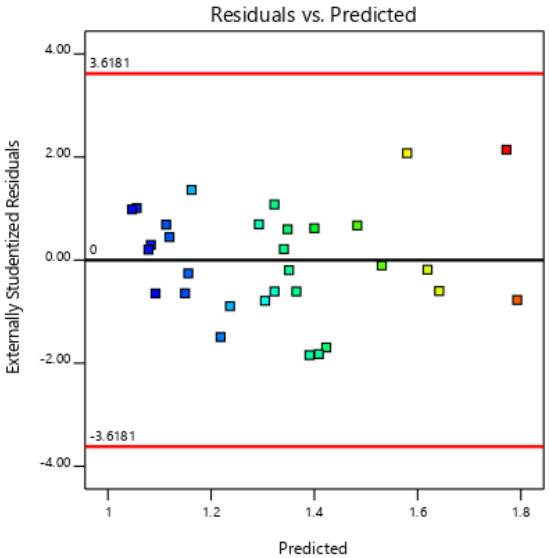

Appendix D8 – Element Quality Checks

Confirmation Run1:

Quality Name	Min. val	Max. val	Allowable	#Violated(%)
Aspect Ratio	1	2.09	10	0(0%)
Warpage	0	34.6	10	155(0.0245%)
Min Quad Angle	56.3	90	45	0(0%)
Max Quad Angle	89.2	126	135	0(0%)
Min Tria Angle	30.3	56.7	30	0(0%)
Max Tria Angle	62.4	80.7	120	0(0%)
Skew	0	23.7	45	0(0%)
Jacobian	0.772	1	0.6	0(0%)

#QUADS(%):630617(99.9%), #TRIAS(%):946(0.15%), #TOTAL OF FAILED(%):0(0%)

Confirmation Run2:

Quality Name	Min. val	Max. val	Allowable	#Violated(%)
Aspect Ratio	1	2.13	10	0(0%)
Warpage	0	8.94	10	0(0%)
Min Quad Angle	59	90	45	0(0%)
Max Quad Angle	90	128	135	0(0%)
Min Tria Angle	28.4	56.1	30	2(0.000325%)
Max Tria Angle	64.6	80.1	120	0(0%)
Skew	0	21.4	45	0(0%)
Jacobian	0.754	1	0.6	0(0%)

#QUADS(%):613613(99.8%), #TRIAS(%):946(0.154%), #TOTAL OF FAILED(%):0(0%)

Appendix E – Exp4 Appendices

Appendix E1 – Geometry and von Mises Stress Visuals

Control – Built-T, Geometry:

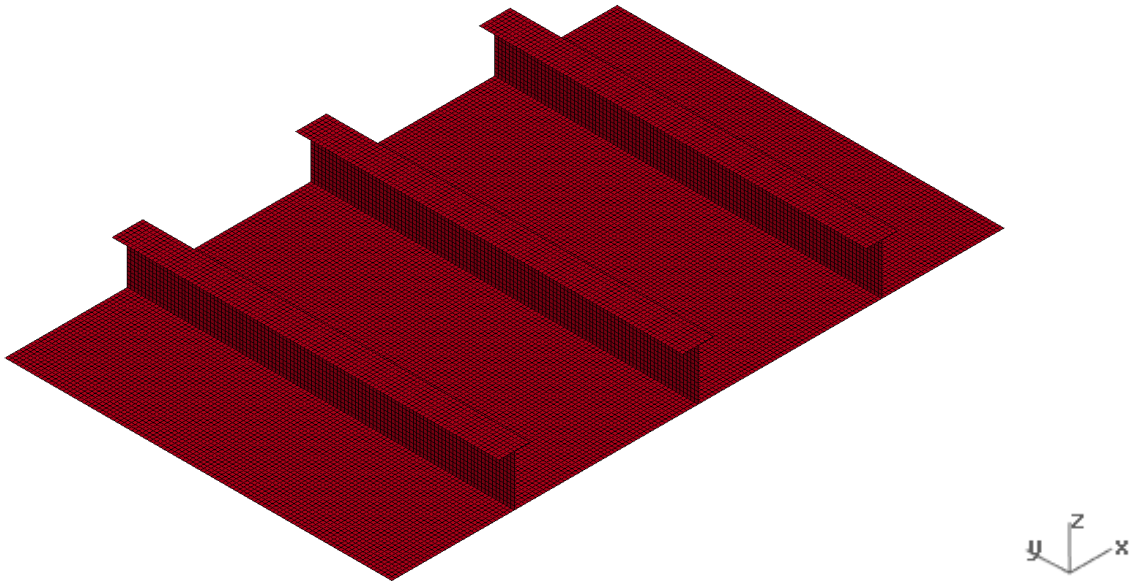

Control – Built-T, von Mise Stress:

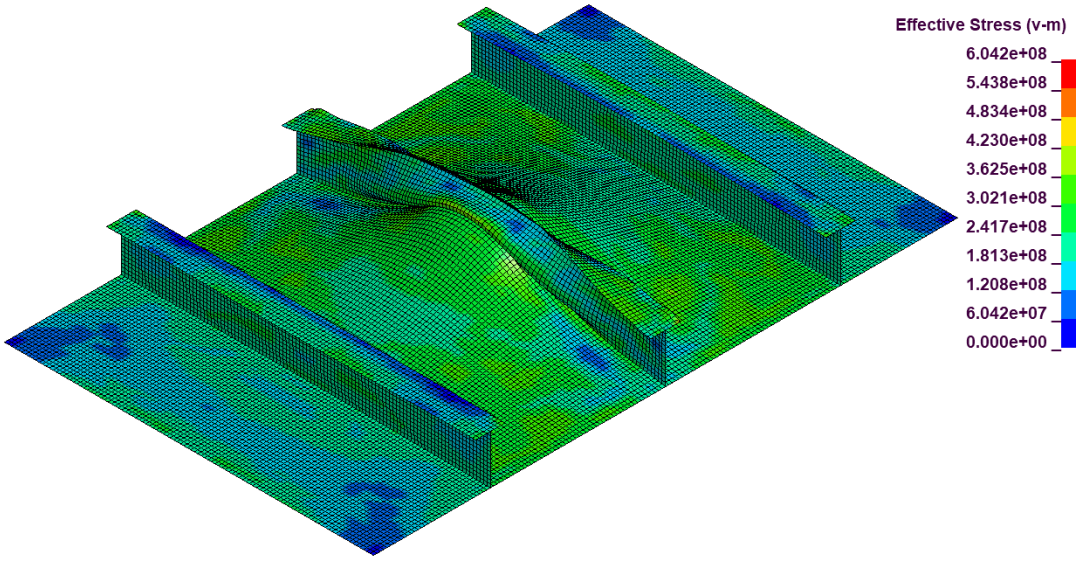

Run1, Geometry:

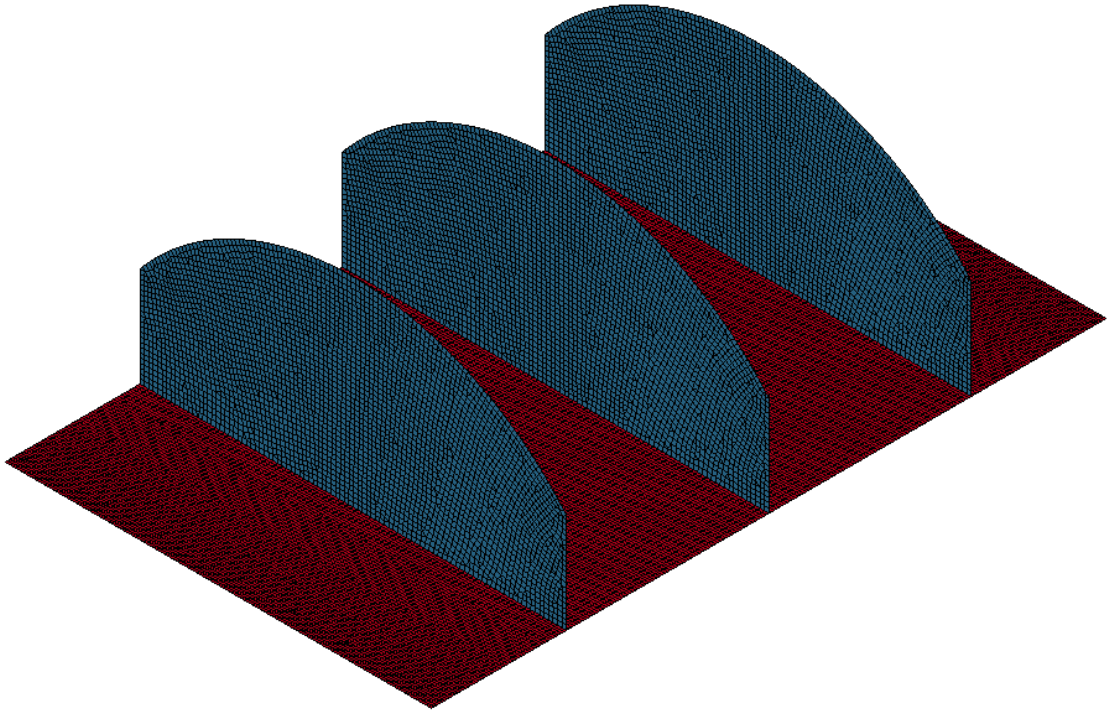

Run1, von Mise Stress:

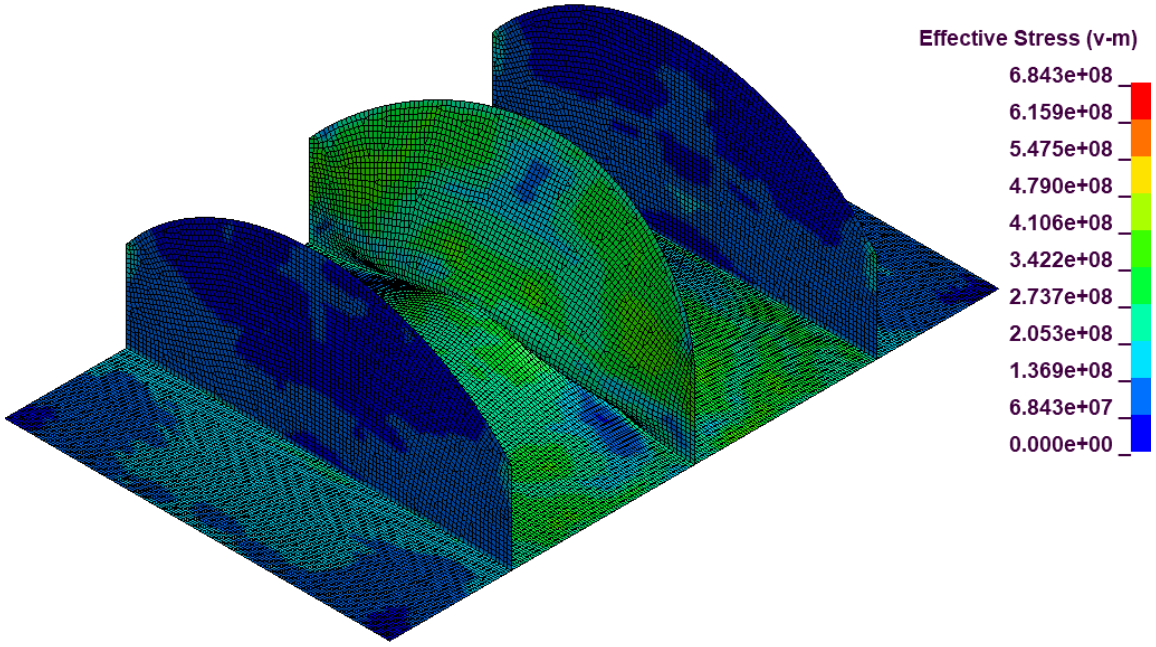

Run2, Geometry:

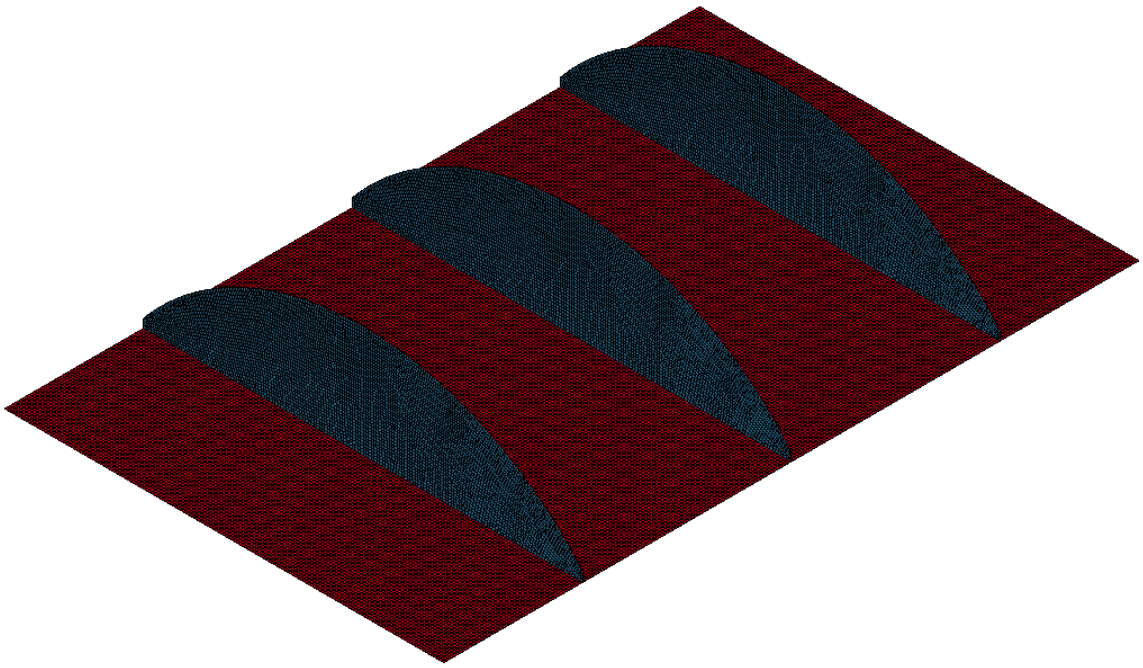

Run2, von Mise Stress:

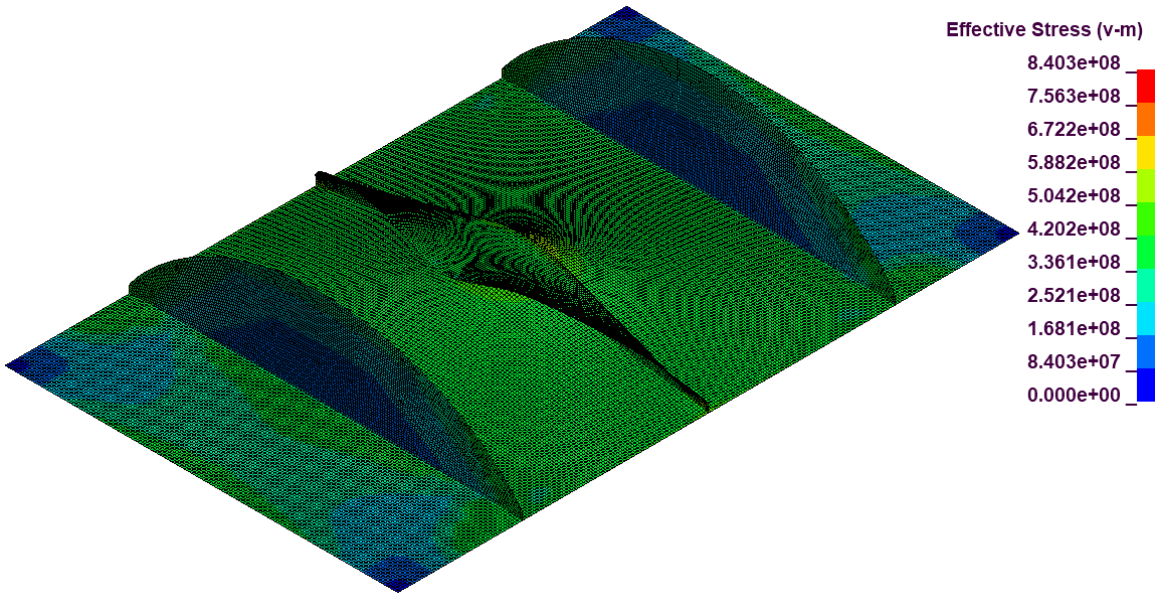

Run3, Geometry:

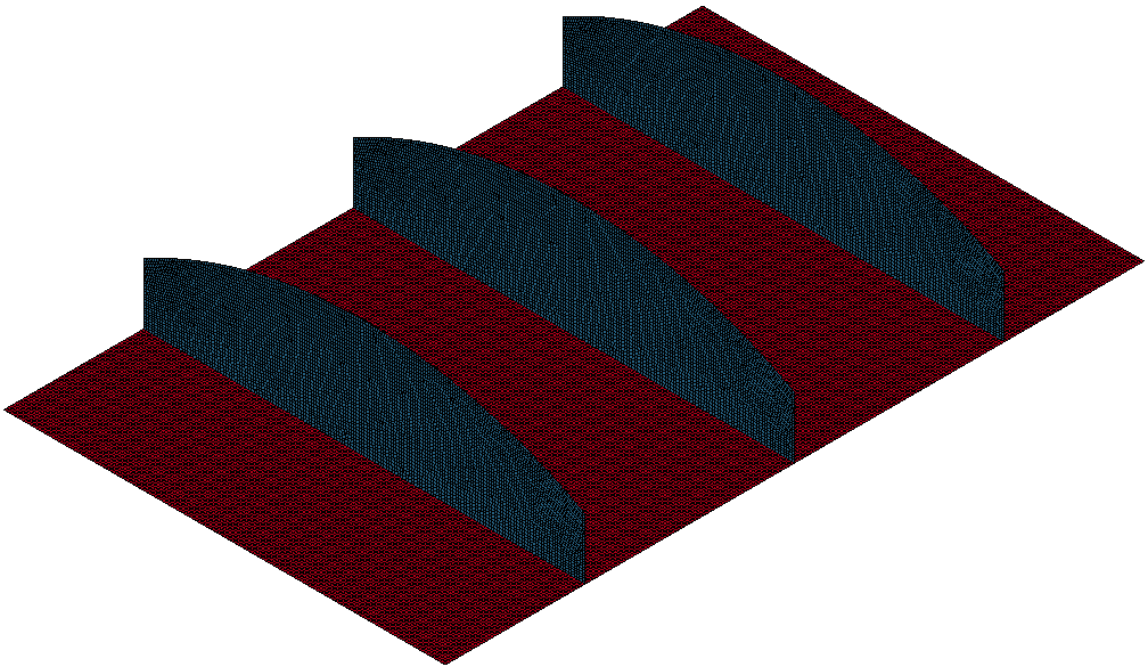

Run3, von Mise Stress:

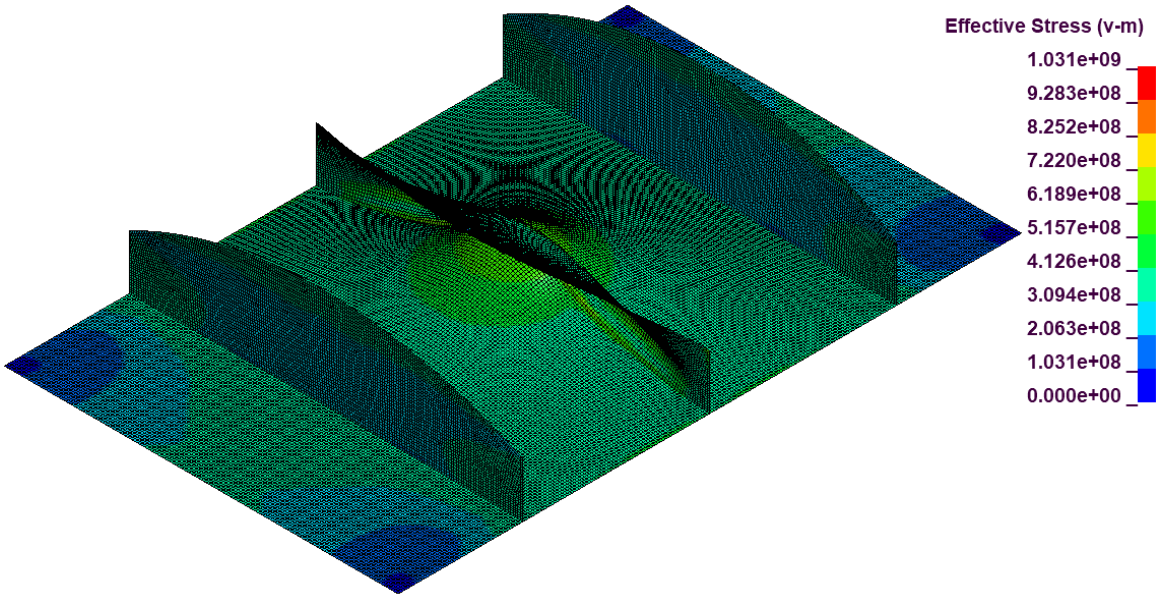

Run4, Geometry:

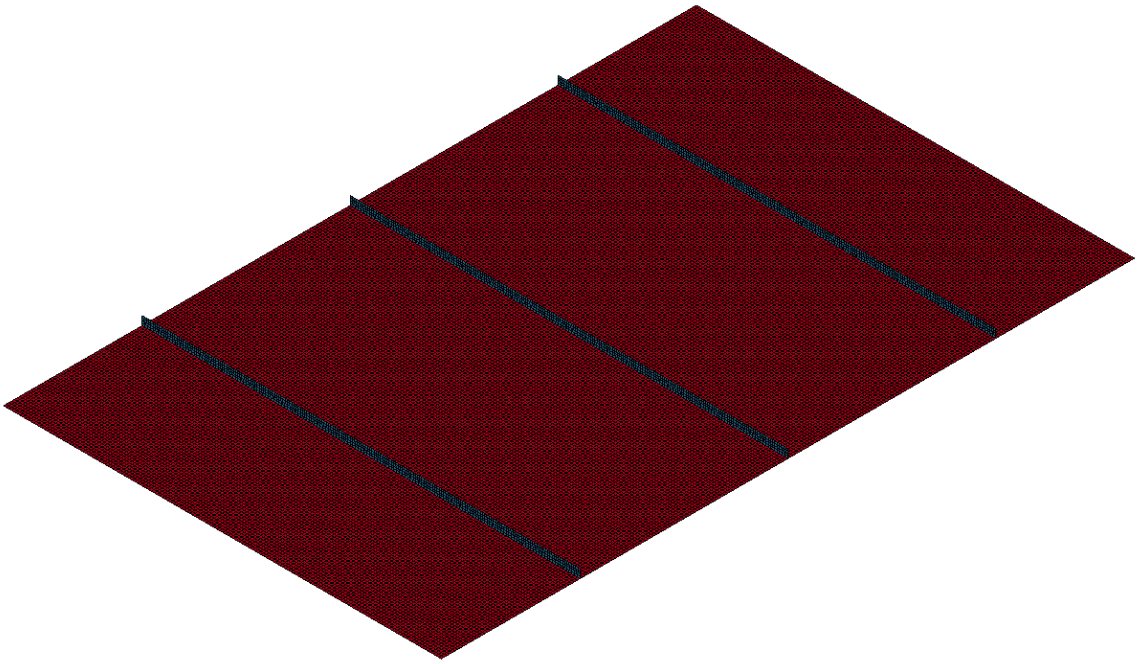

Run4, von Mise Stress:

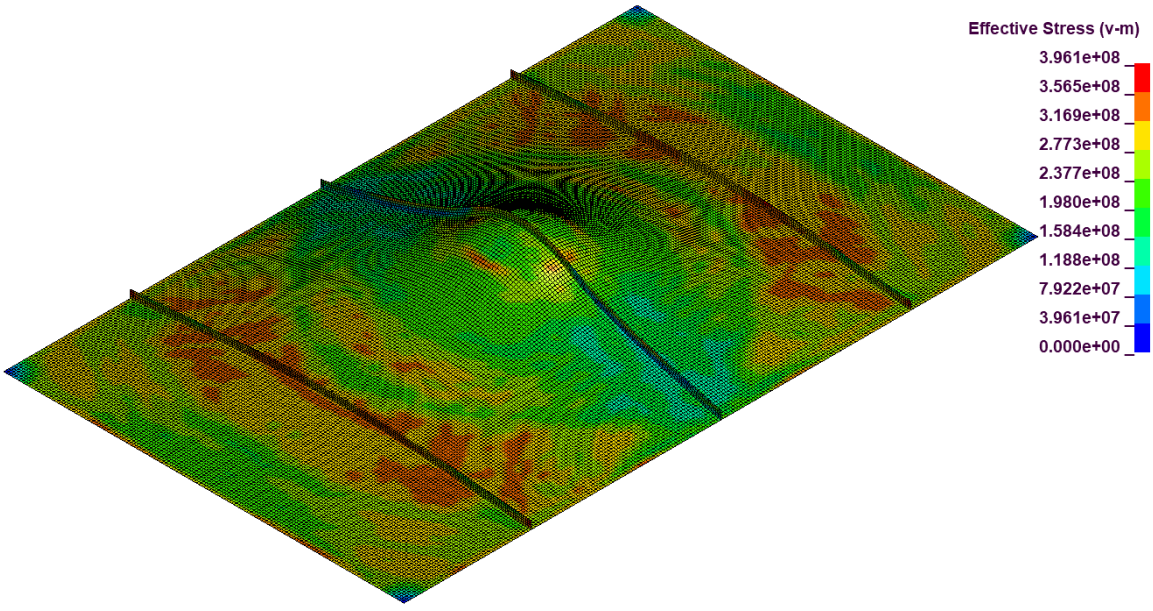

Run5, Geometry:

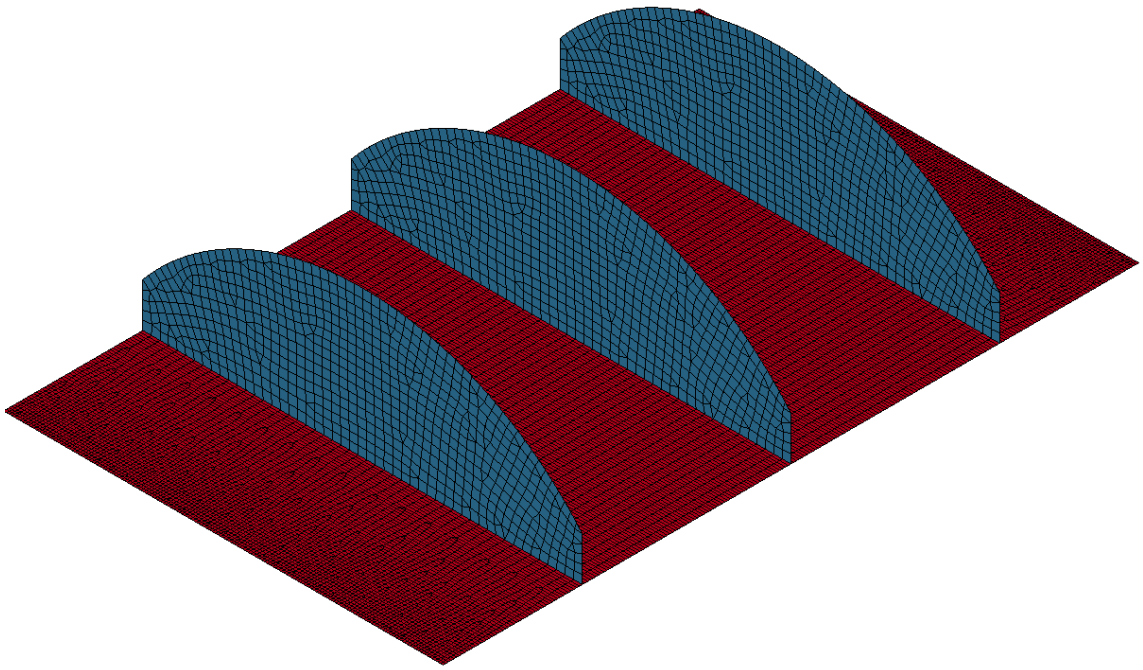

Run5, von Mise Stress:

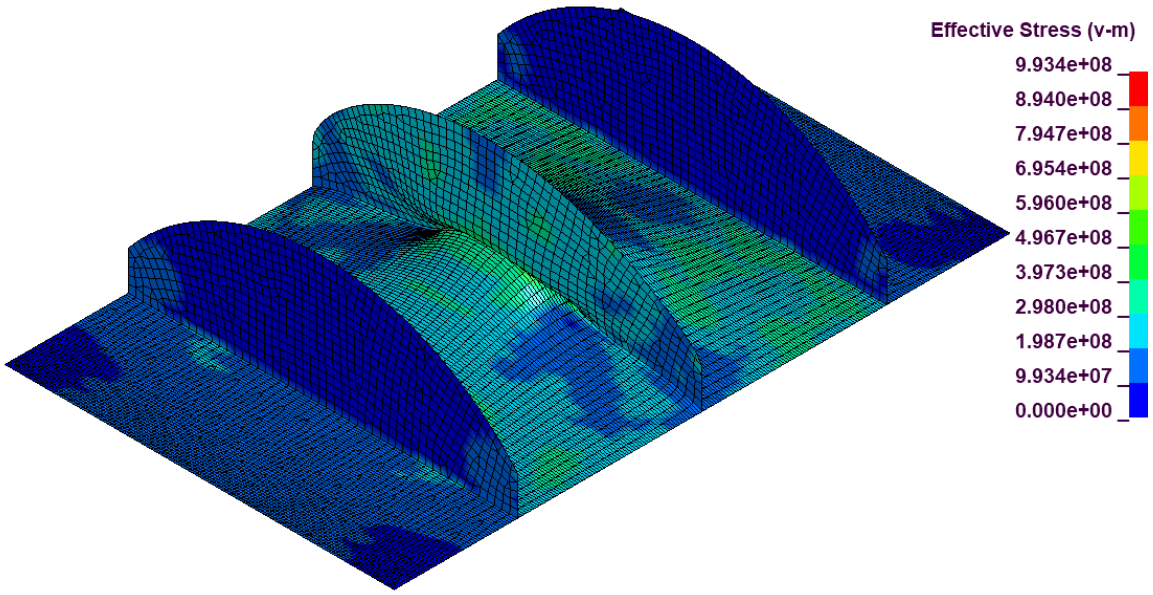

Run6, Geometry:

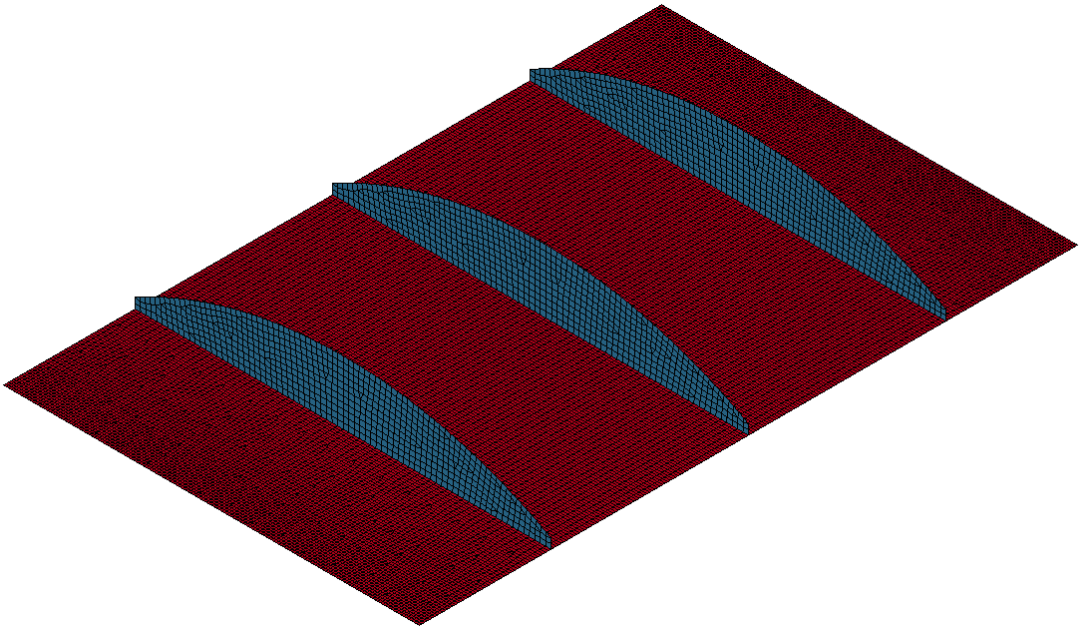

Run6, von Mise Stress:

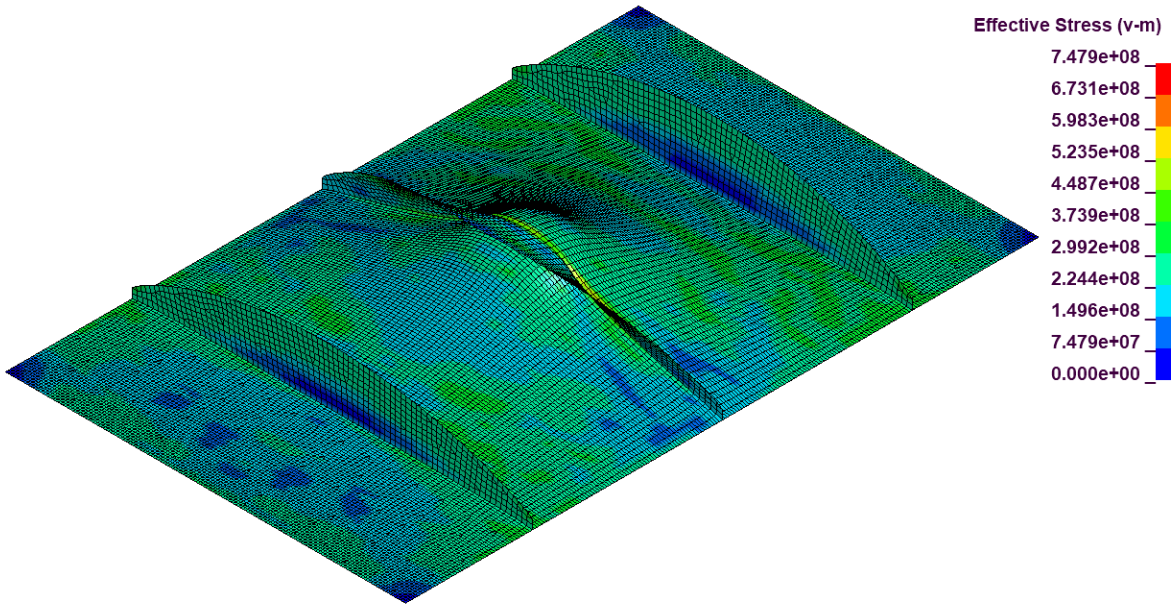

Run7, Geometry:

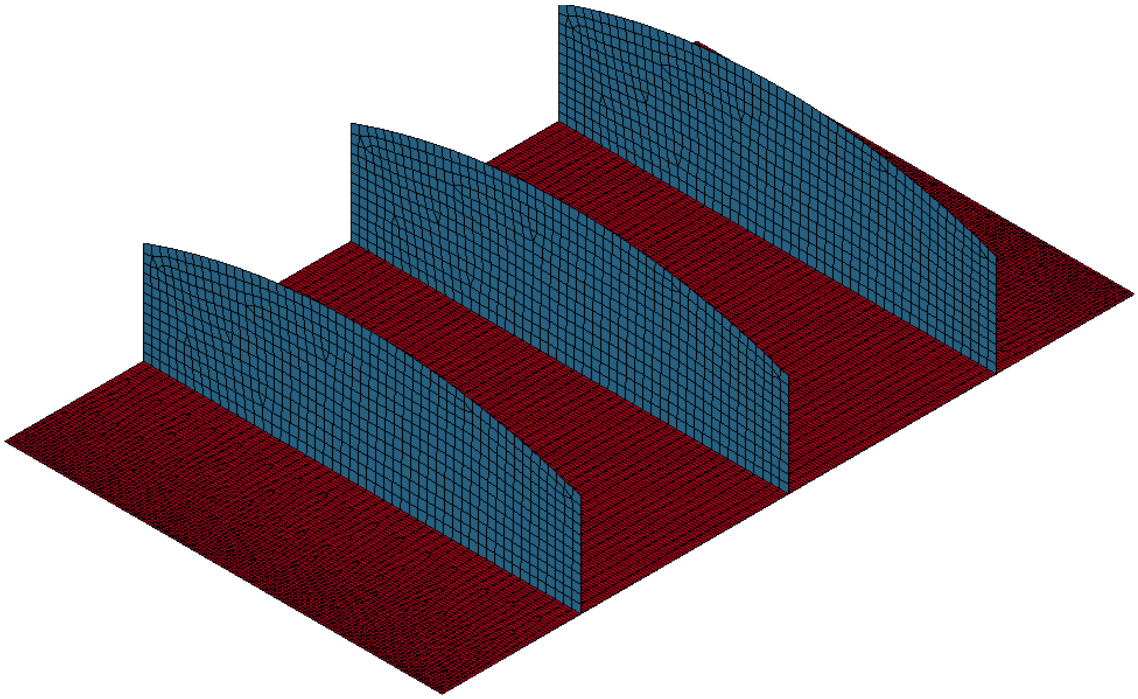

Run7, von Mise Stress:

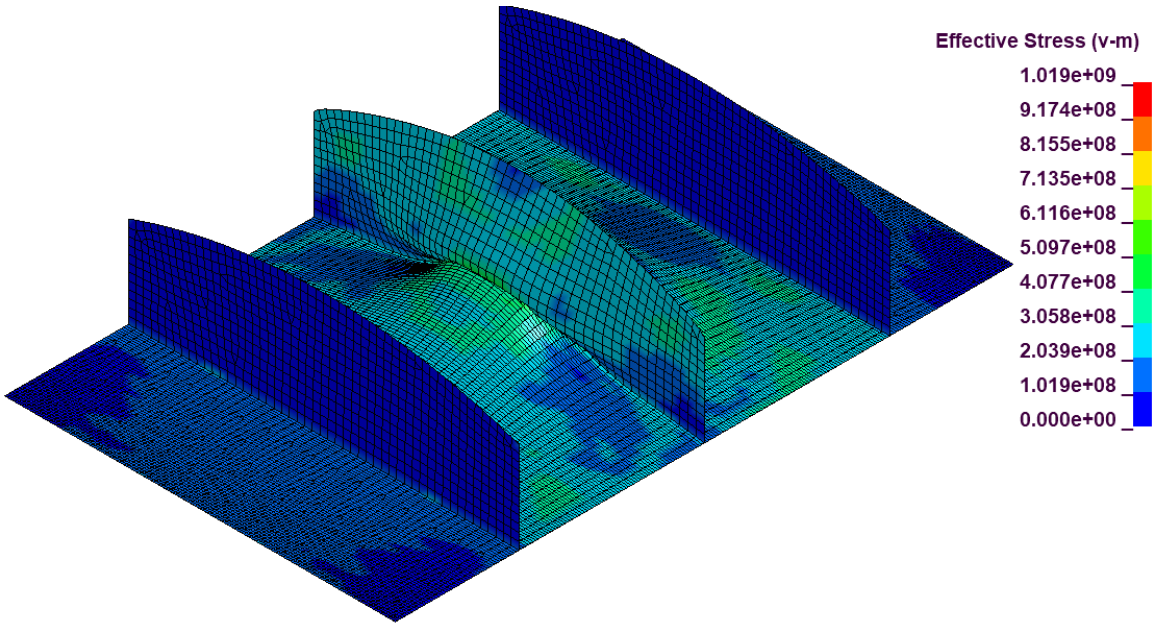

Run8, Geometry:

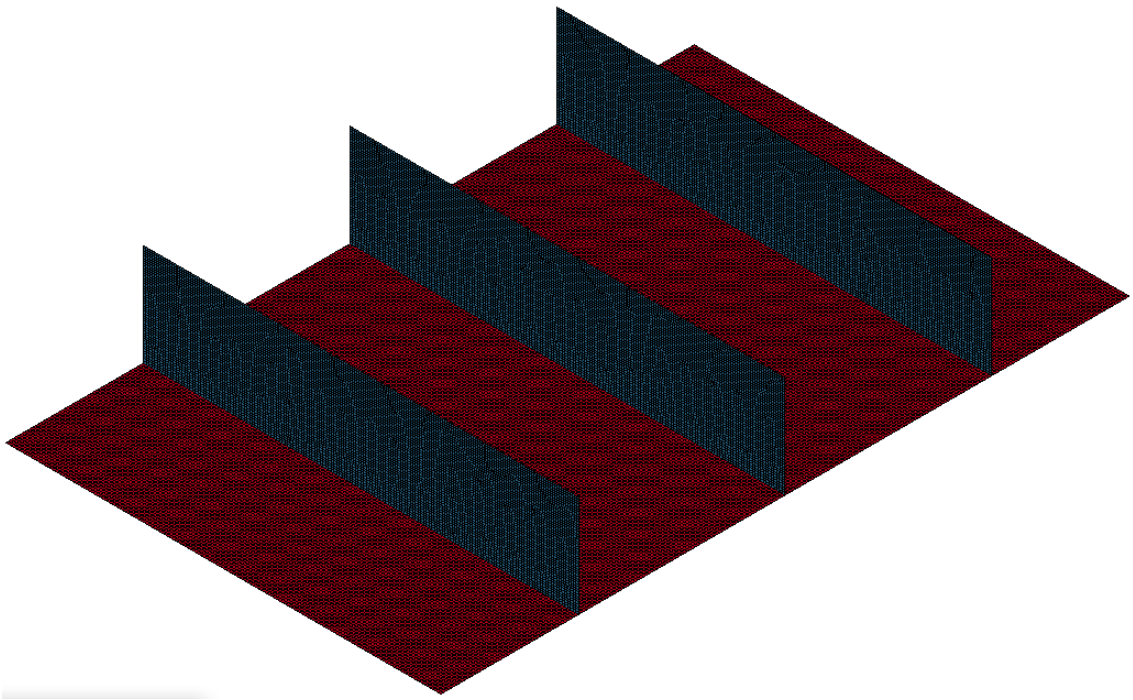

Run8, von Mise Stress:

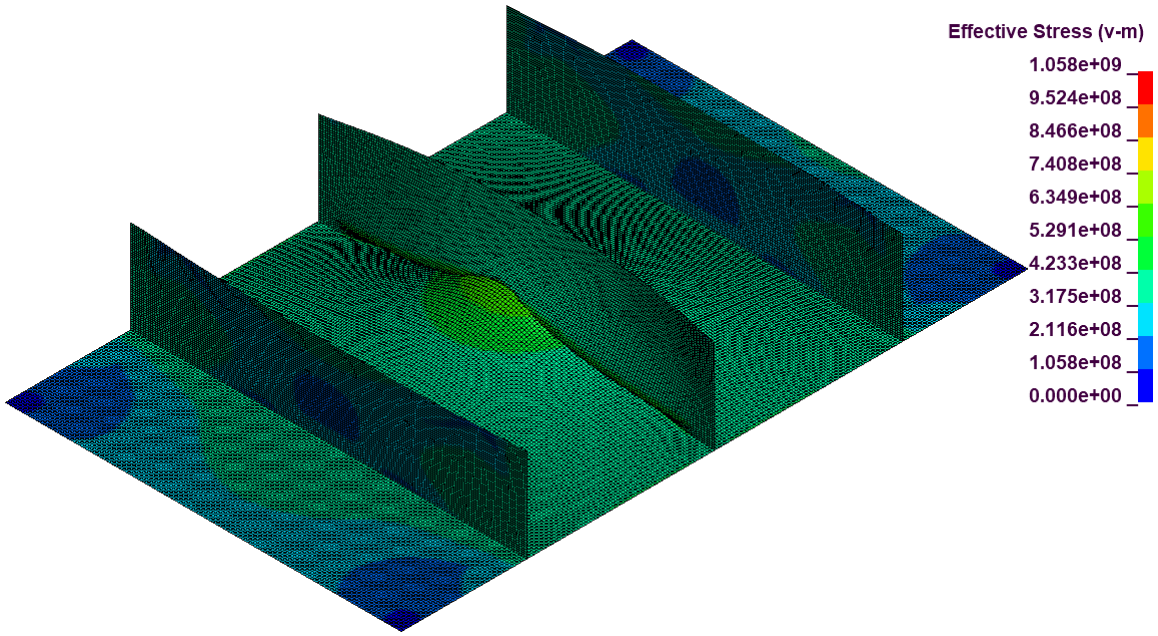

Run9, Geometry:

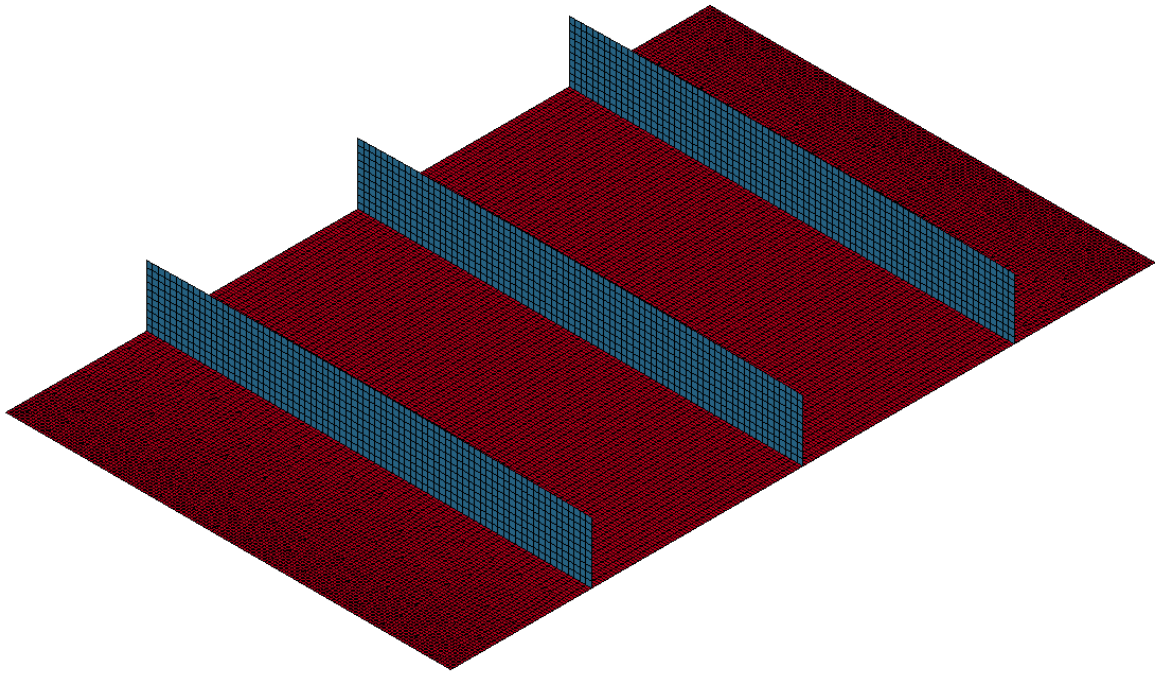

Run9, von Mise Stress:

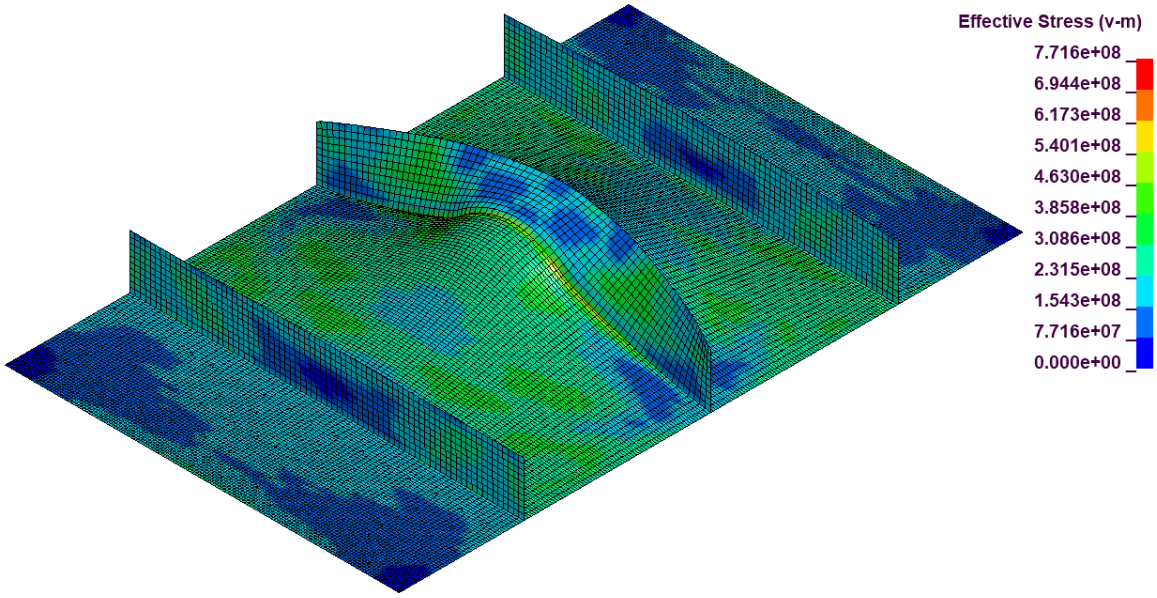

Run10, Geometry:

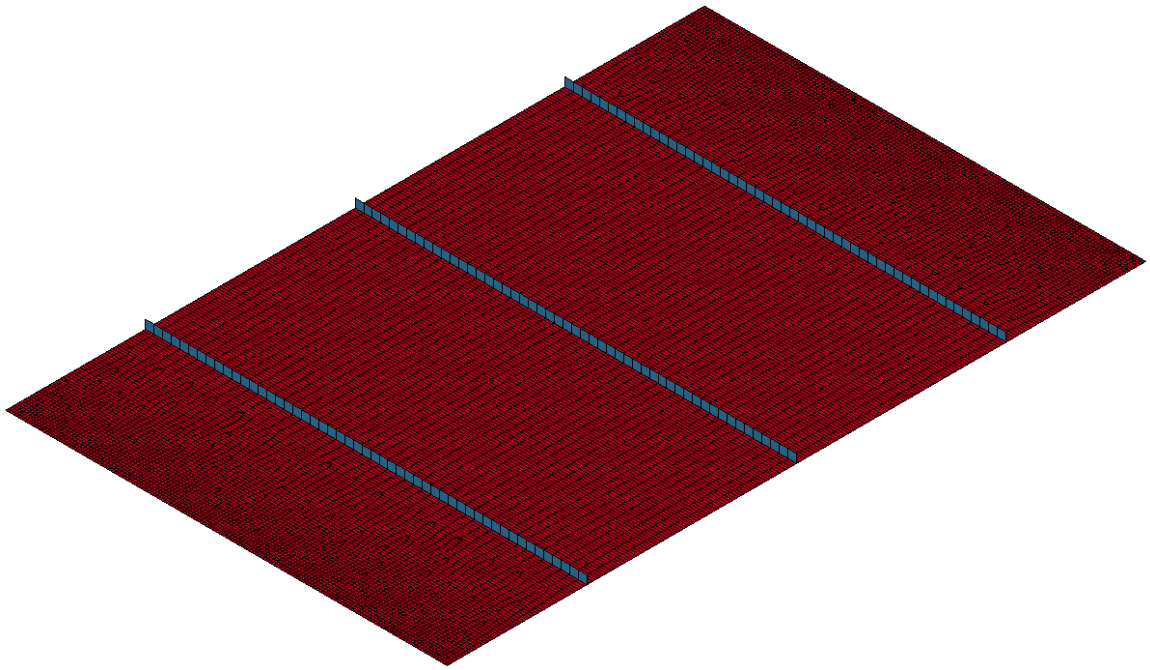

Run10, von Mise Stress:

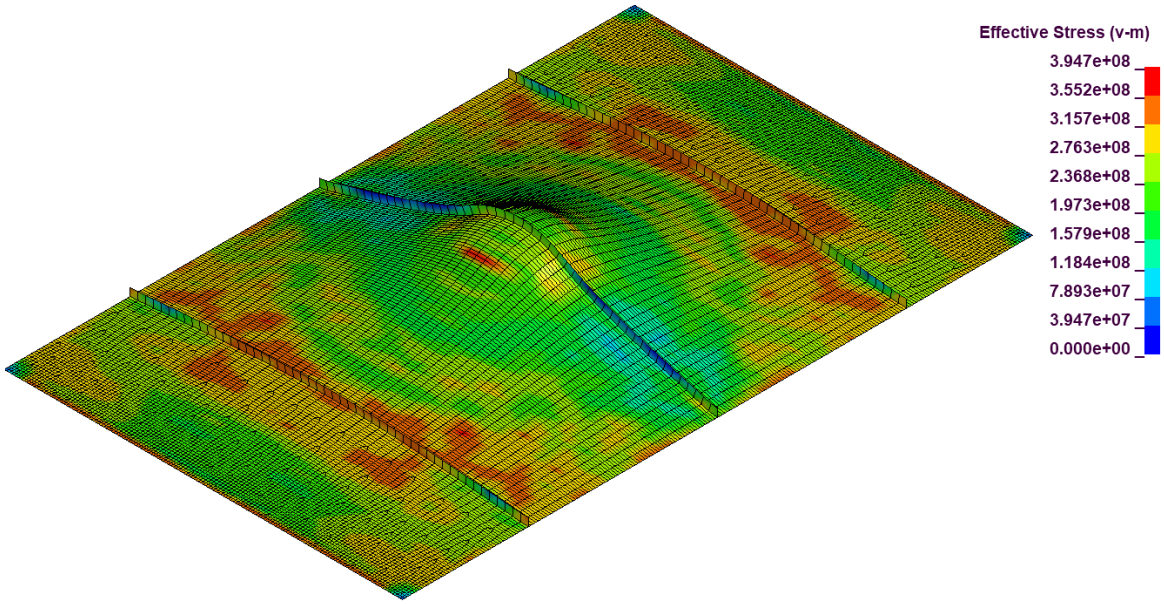

Run11, Geometry:

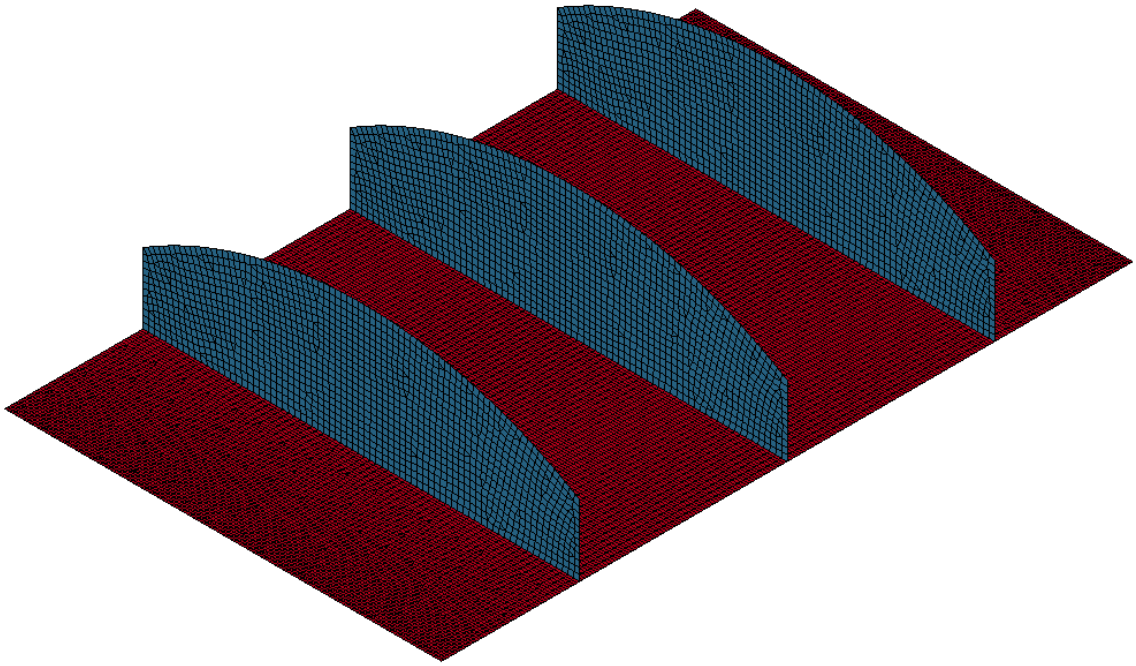

Run11, von Mise Stress:

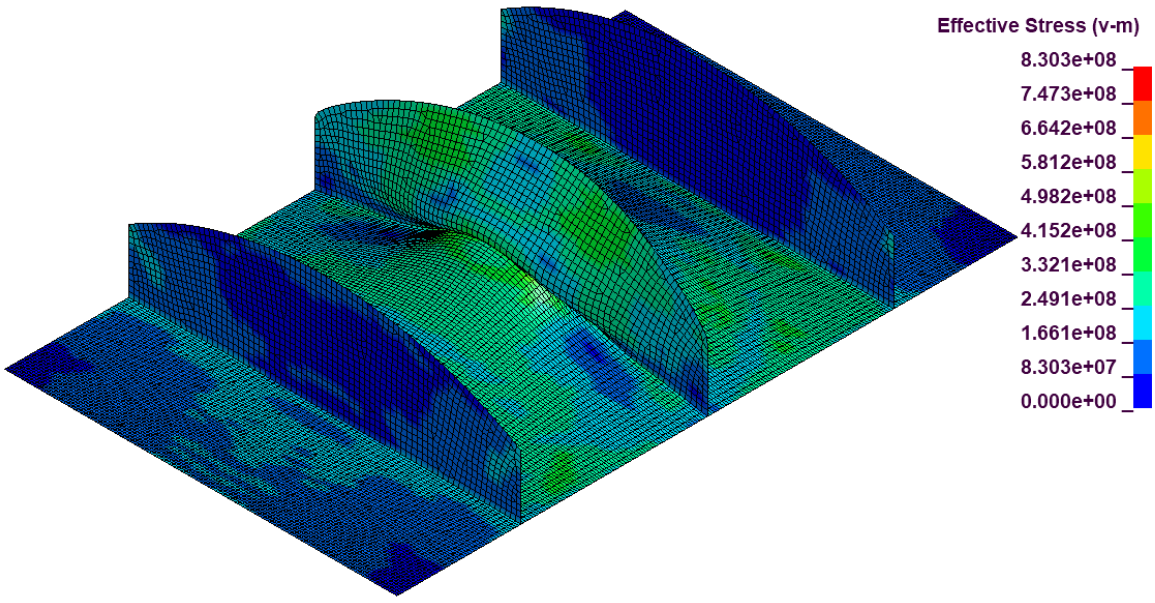

Run12, Geometry:

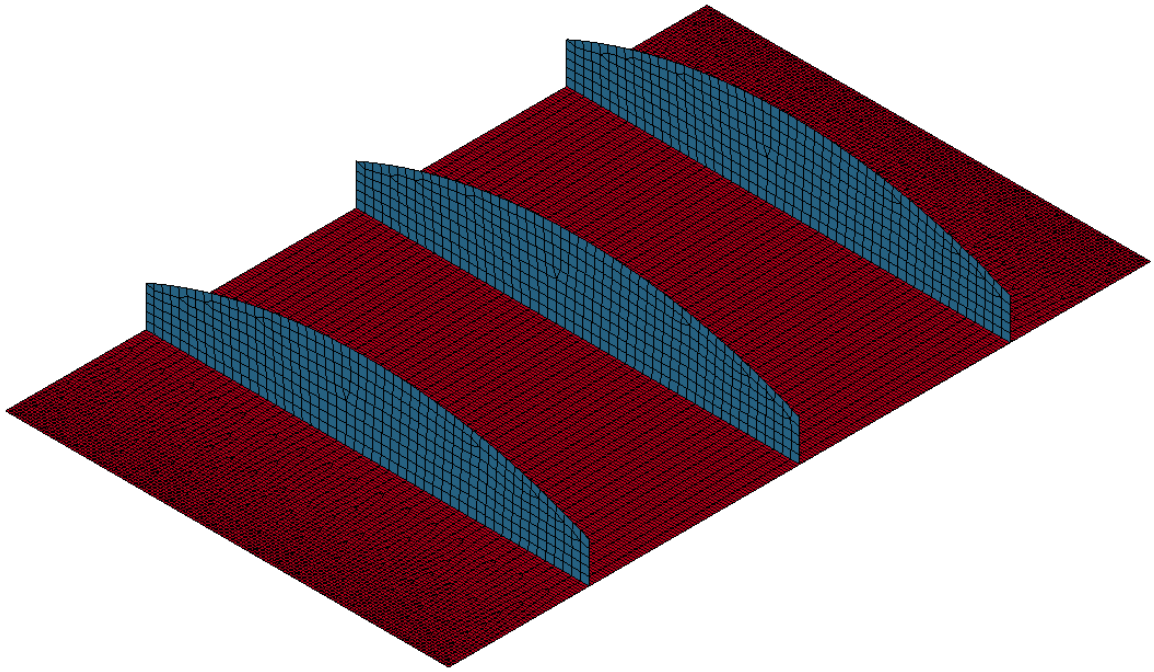

Run12, von Mise Stress:

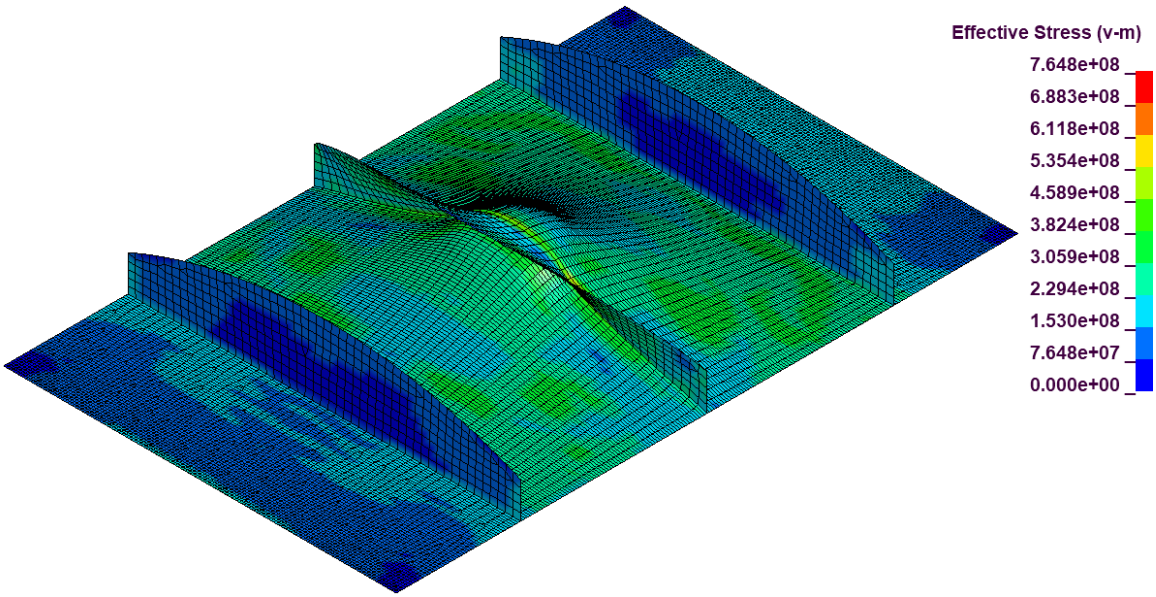

Run13, Geometry:

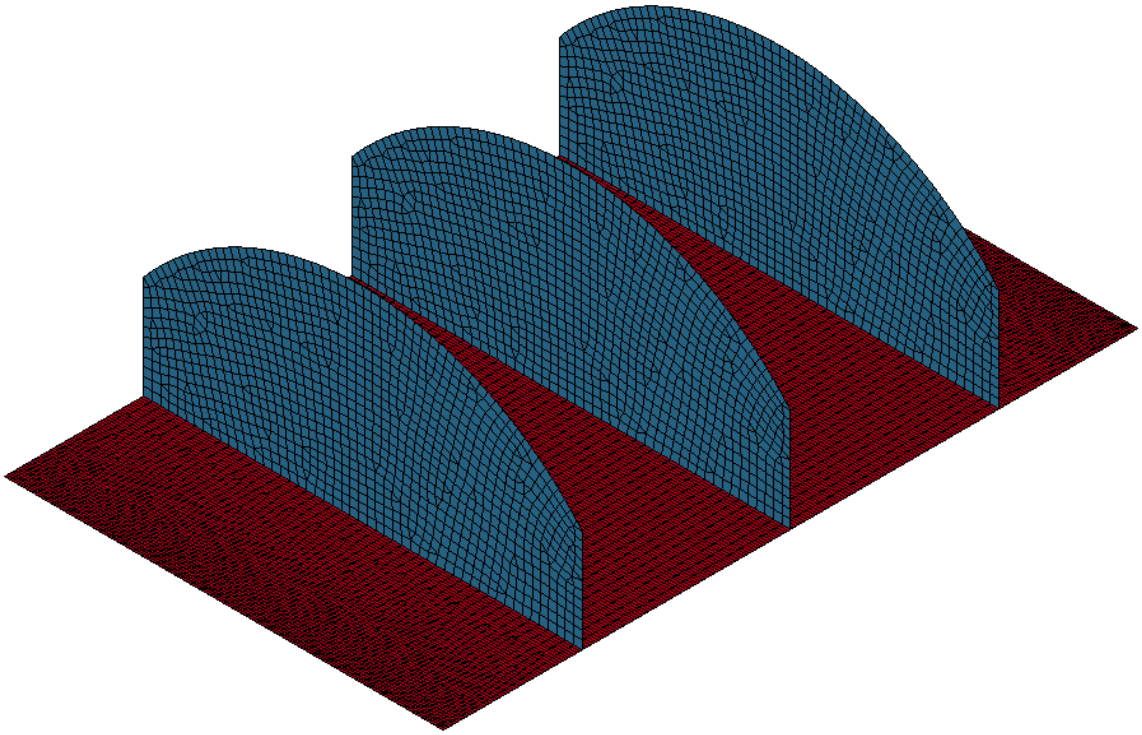

Run13, von Mise Stress:

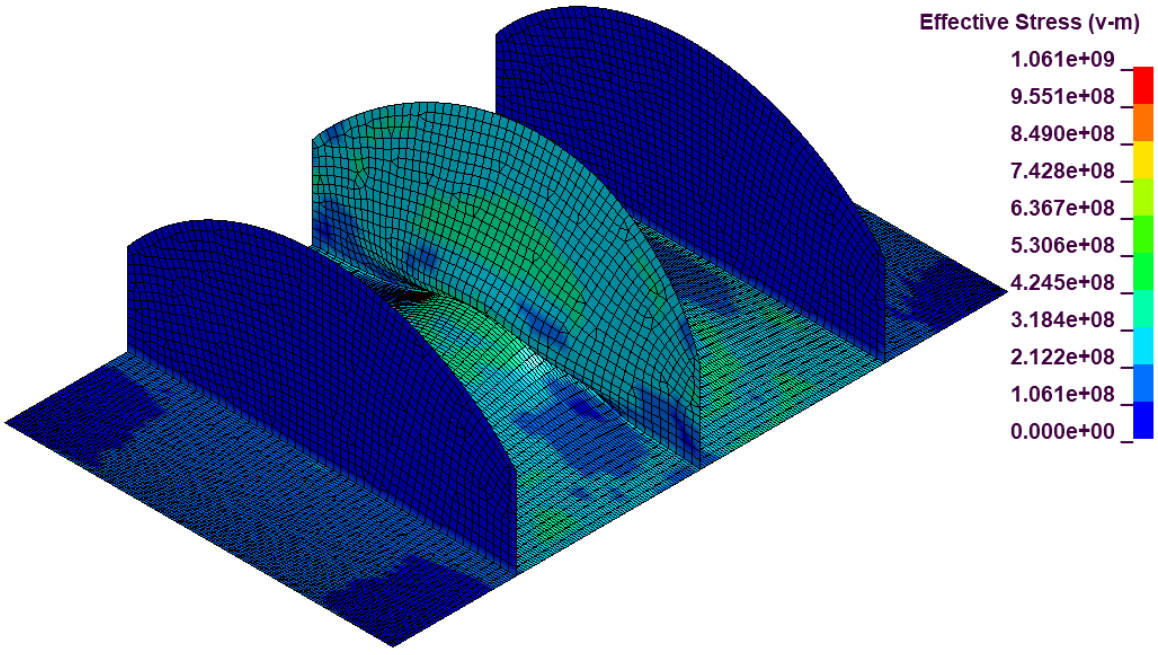

Run14, Geometry:

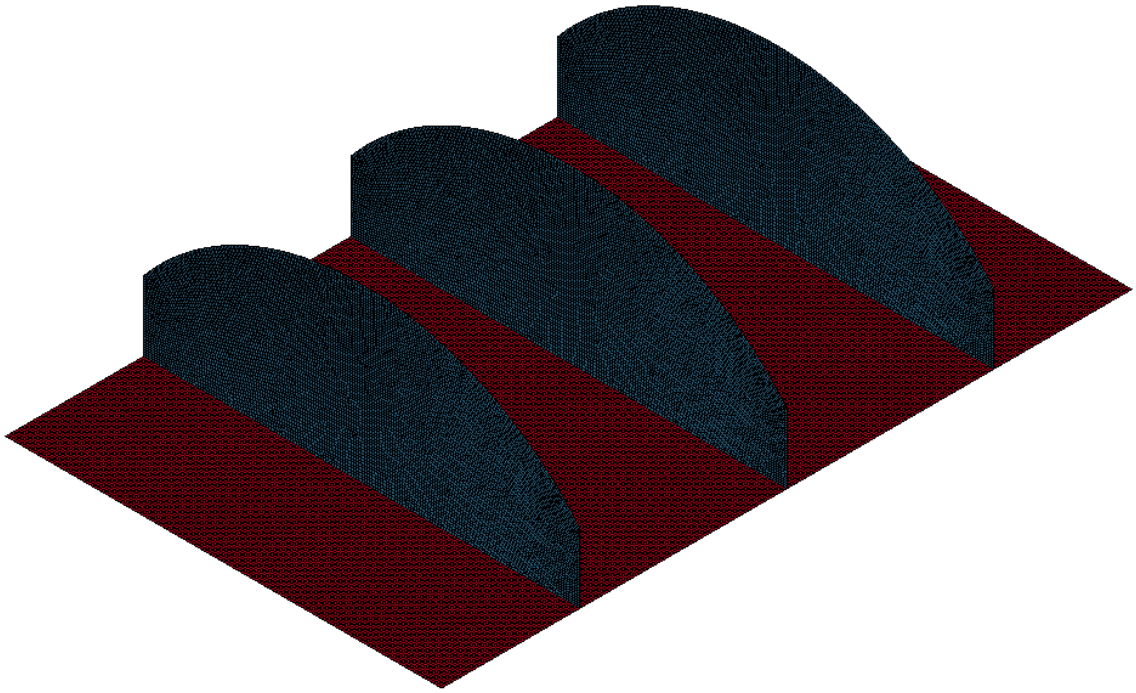

Run14, von Mise Stress:

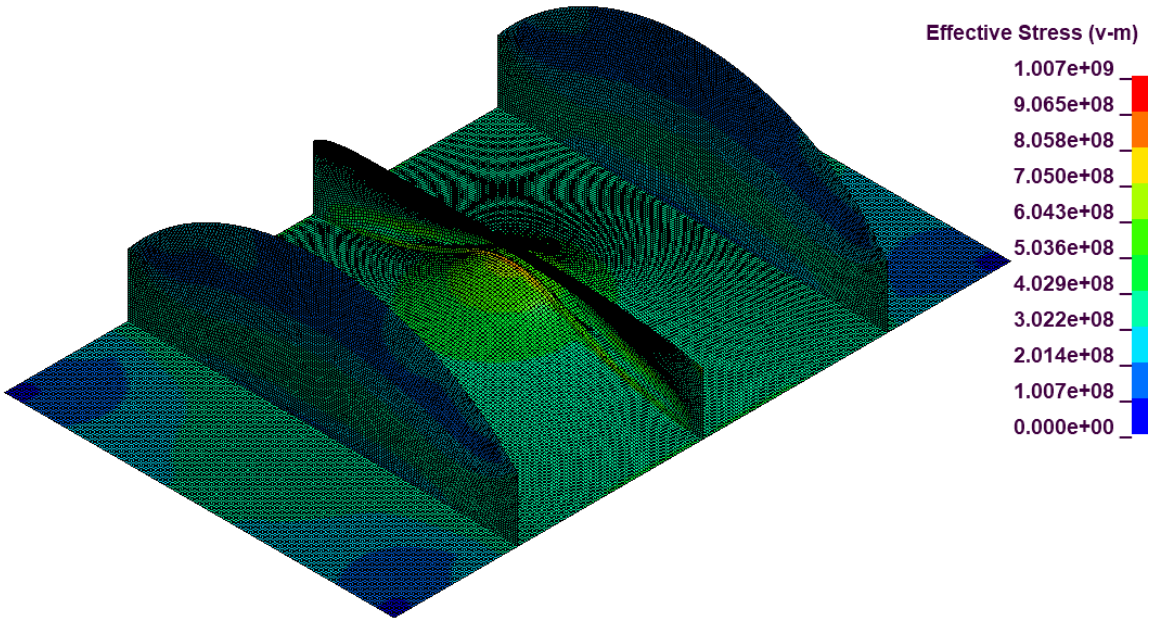

Run15, Geometry:

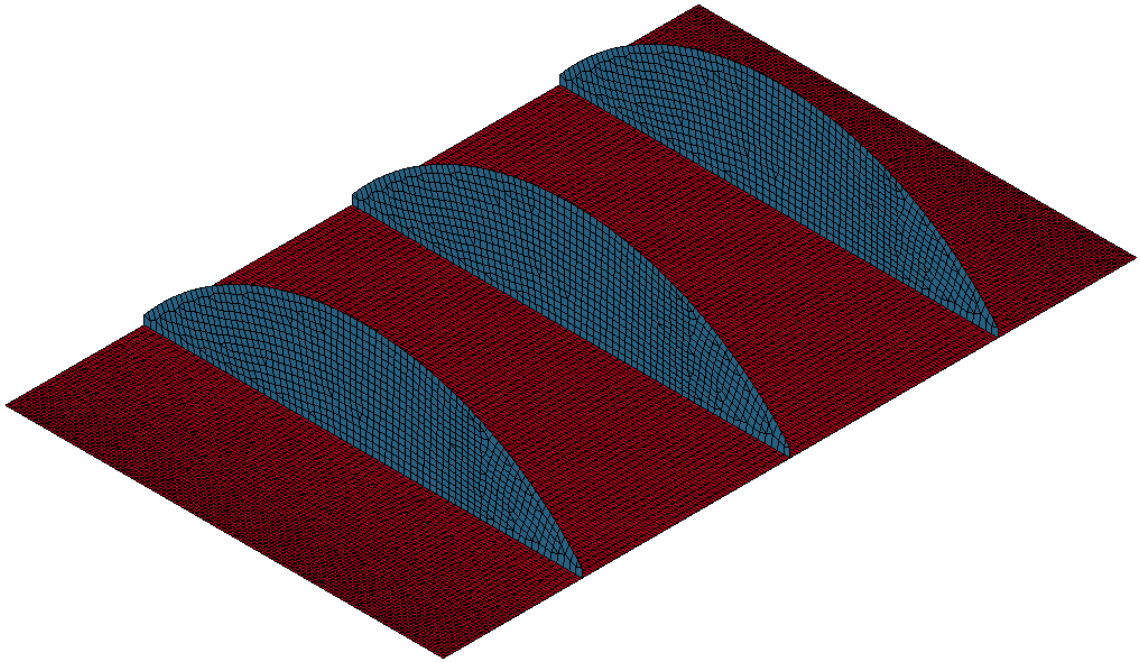

Run15, von Mise Stress:

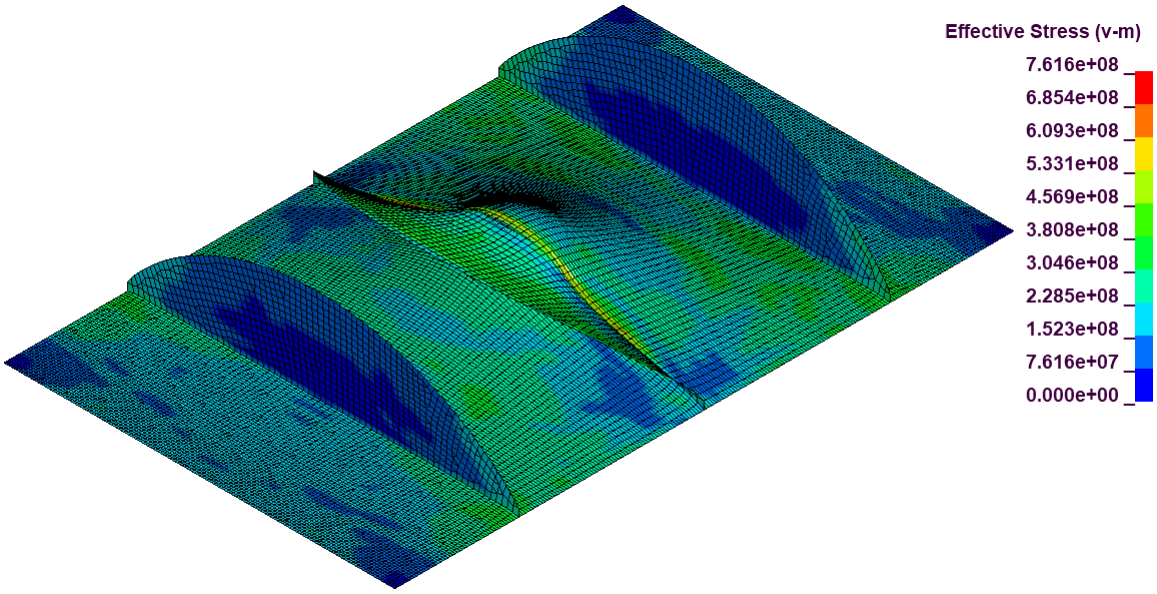

Run16, Geometry:

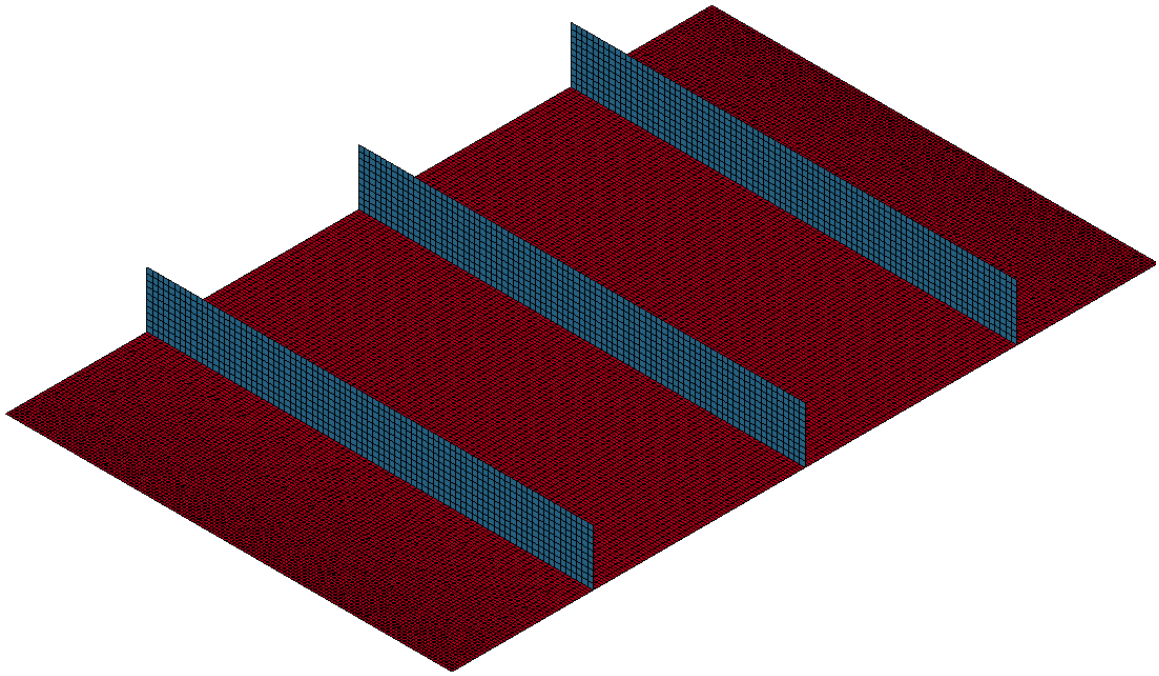

Run16, von Mise Stress:

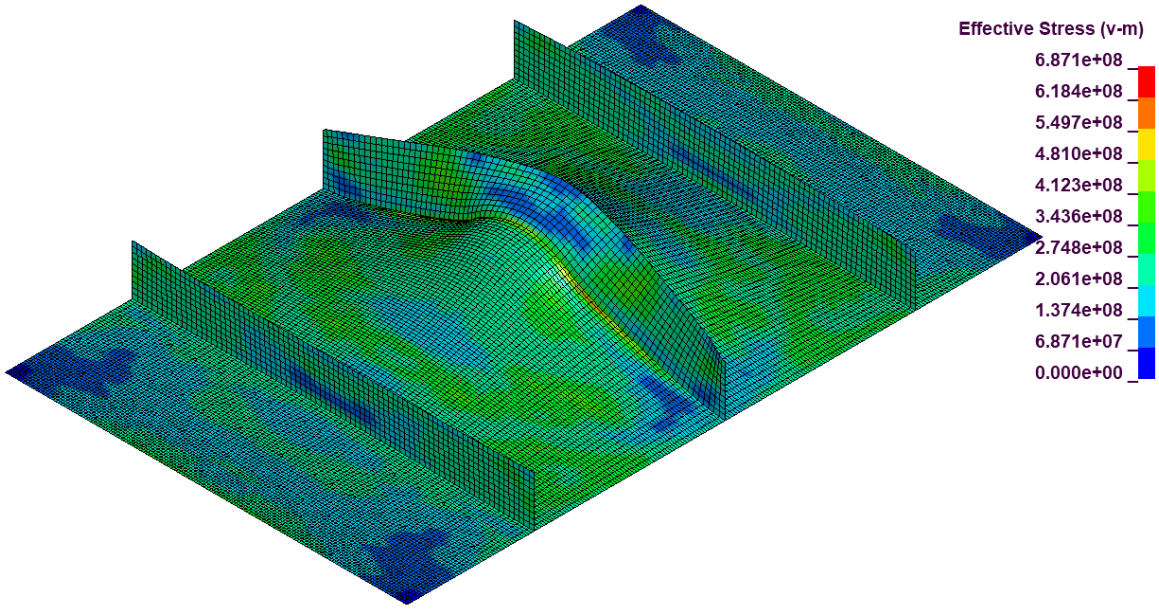

Run17, Geometry:

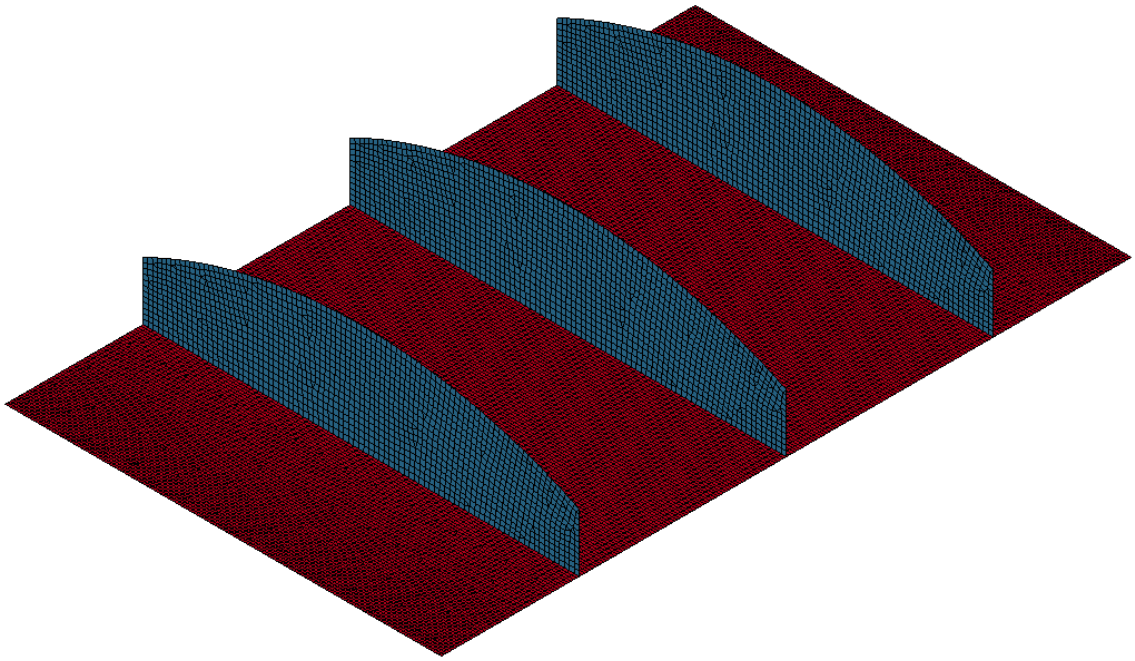

Run17, von Mise Stress:

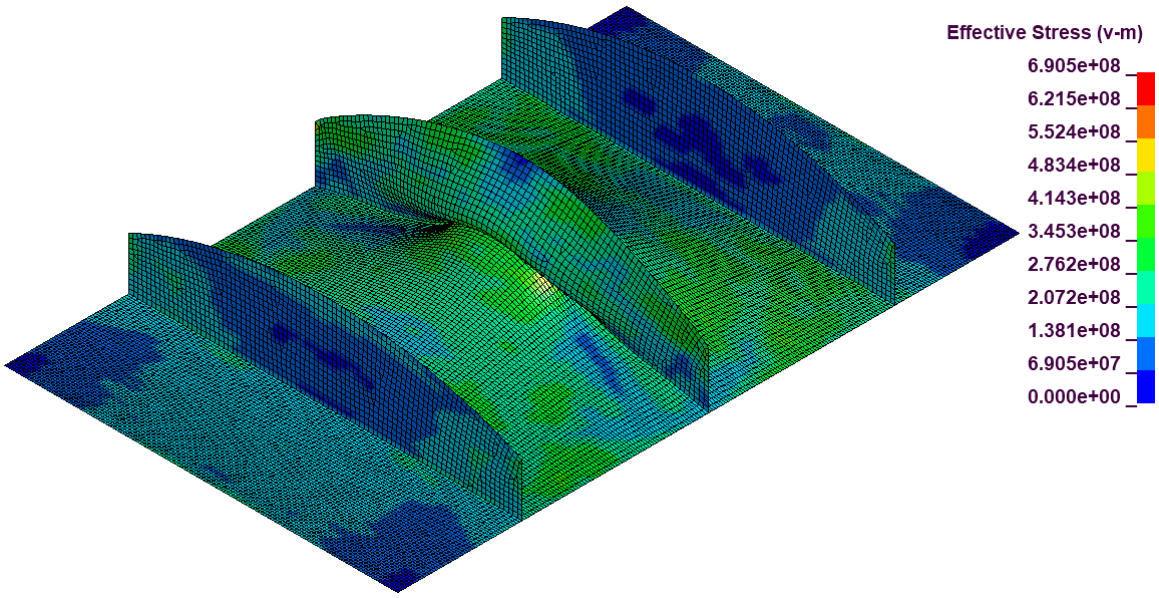

Run18, Geometry:

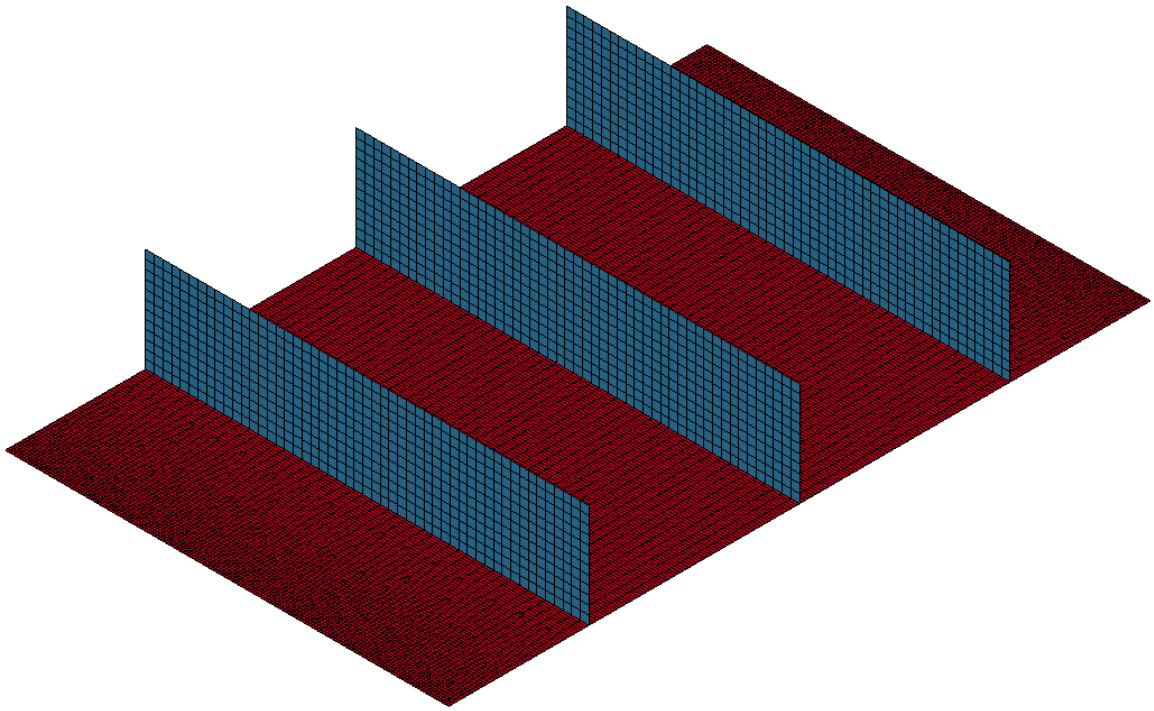

Run18, von Mise Stress:

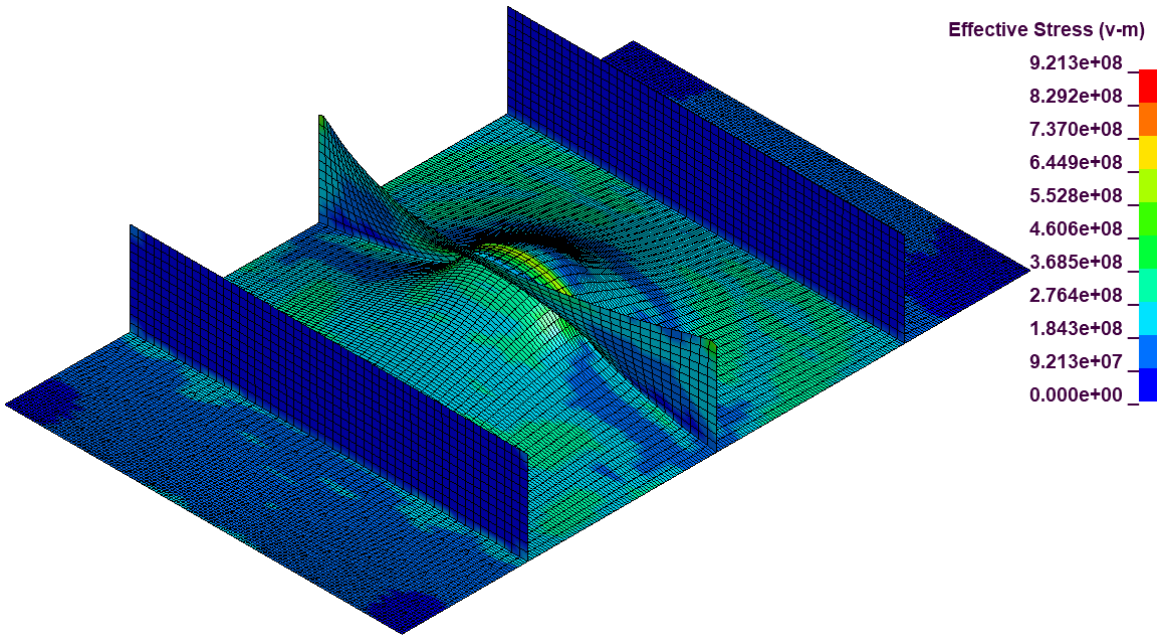

Run19, Geometry:

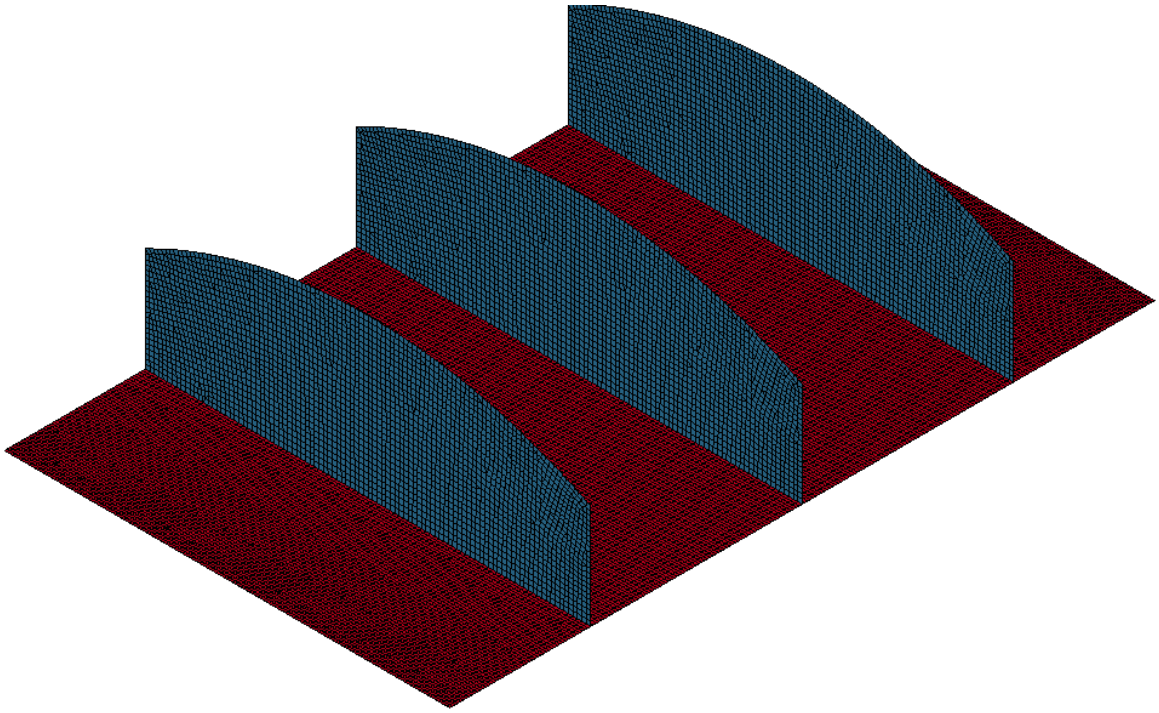

Run19, von Mise Stress:

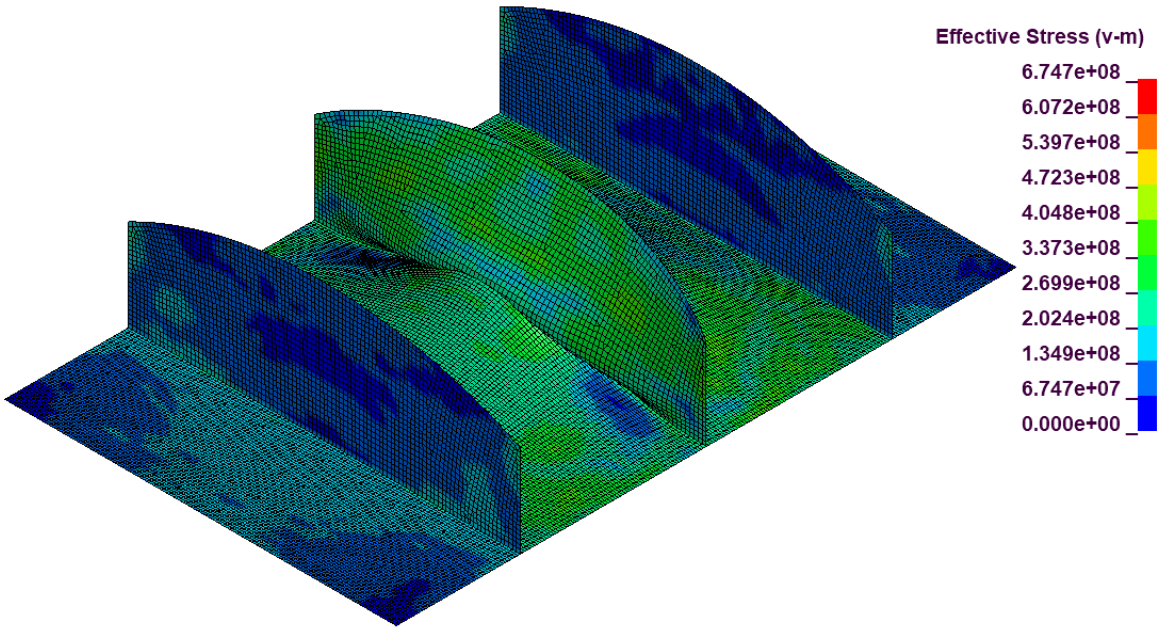

Run20, Geometry:

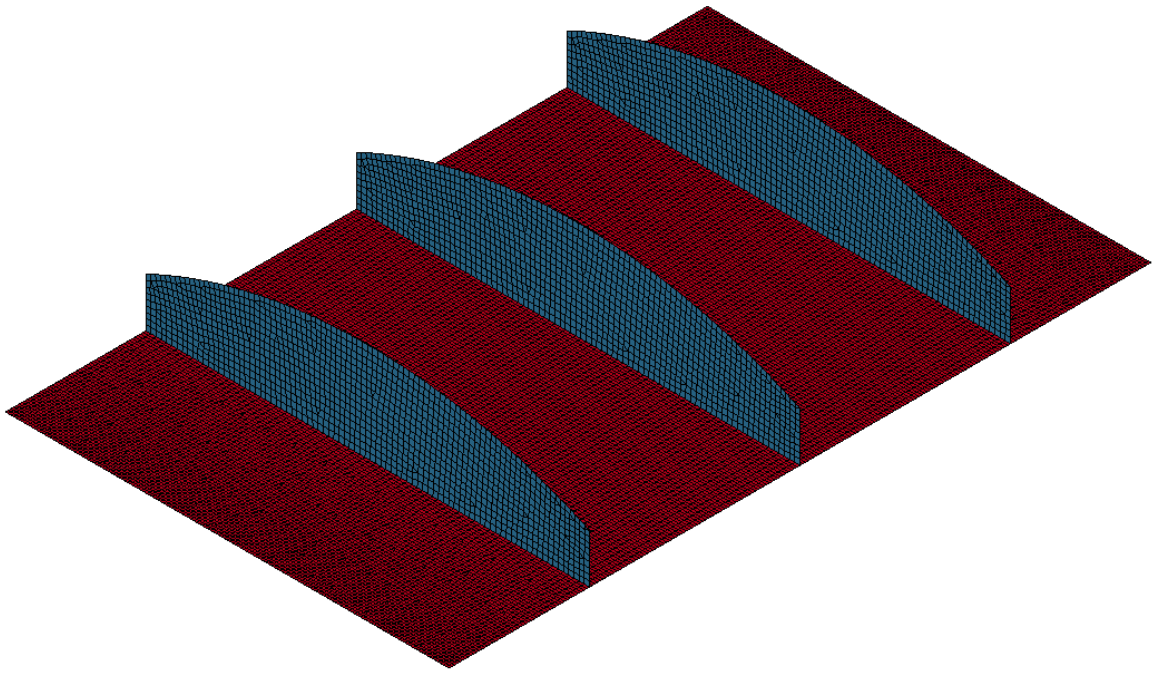

Run20, von Mise Stress:

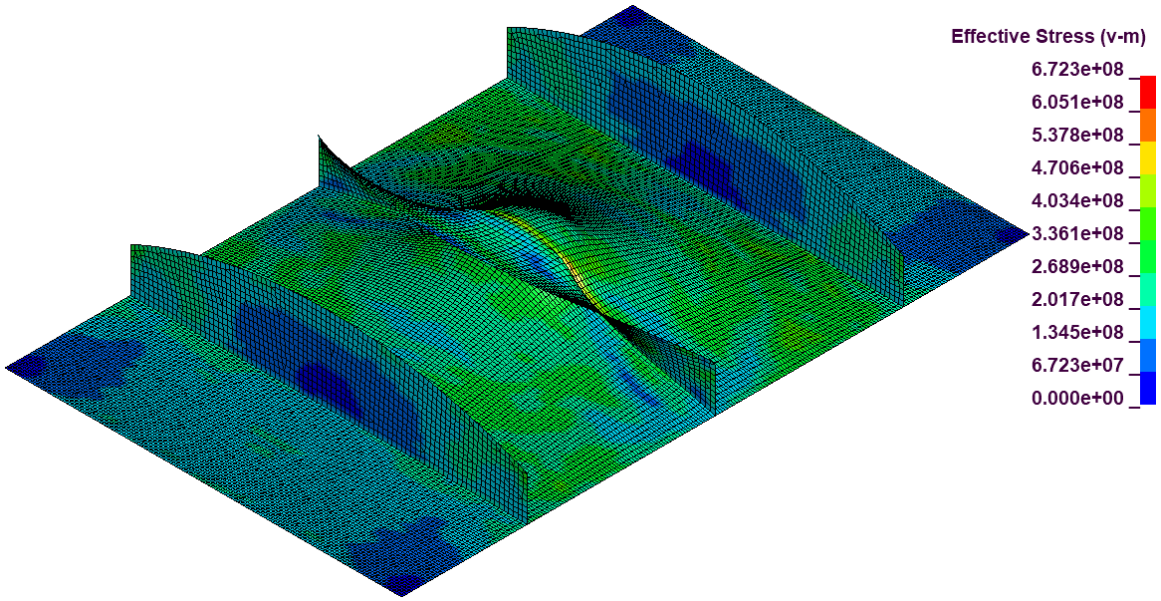

Run21, Geometry:

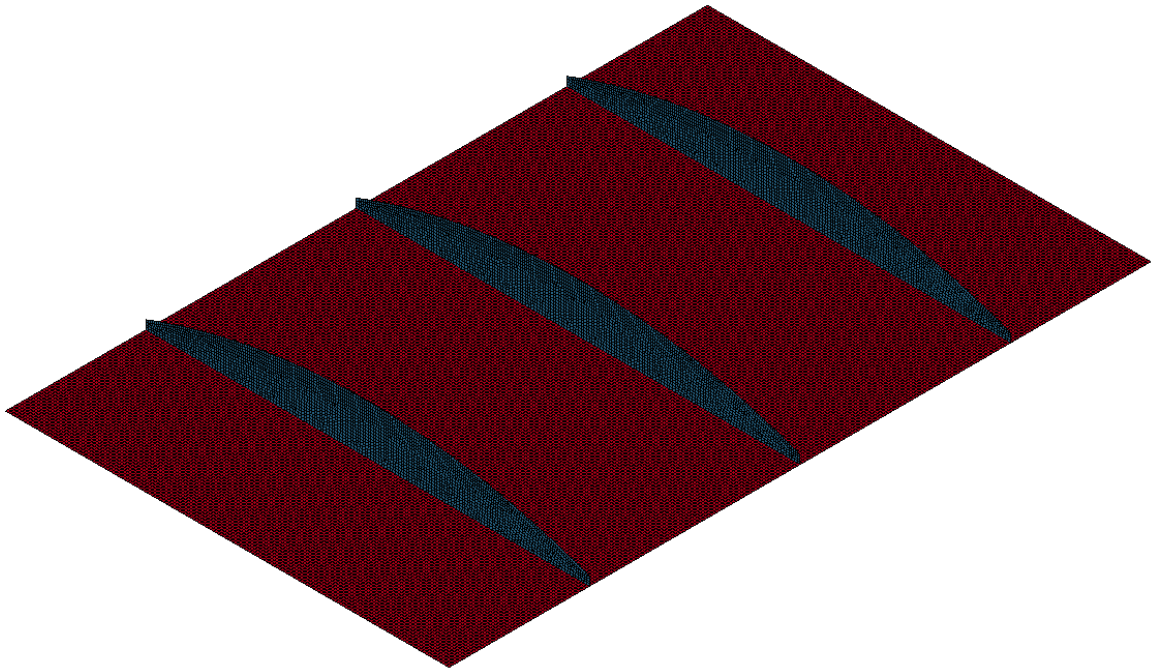

Run21, von Mise Stress:

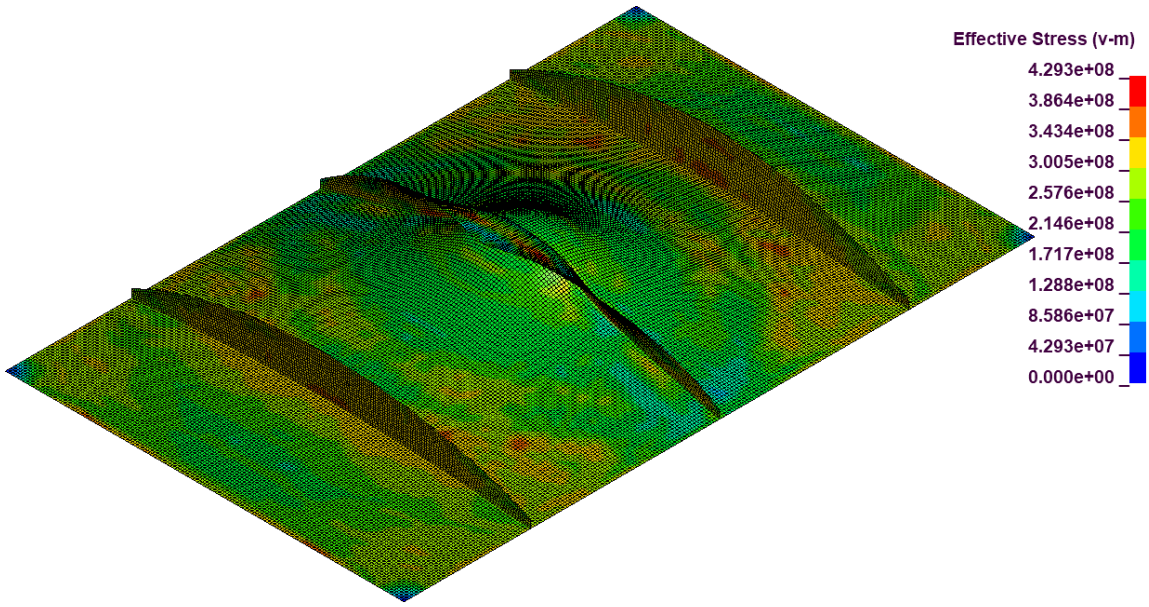

Run22, Geometry:

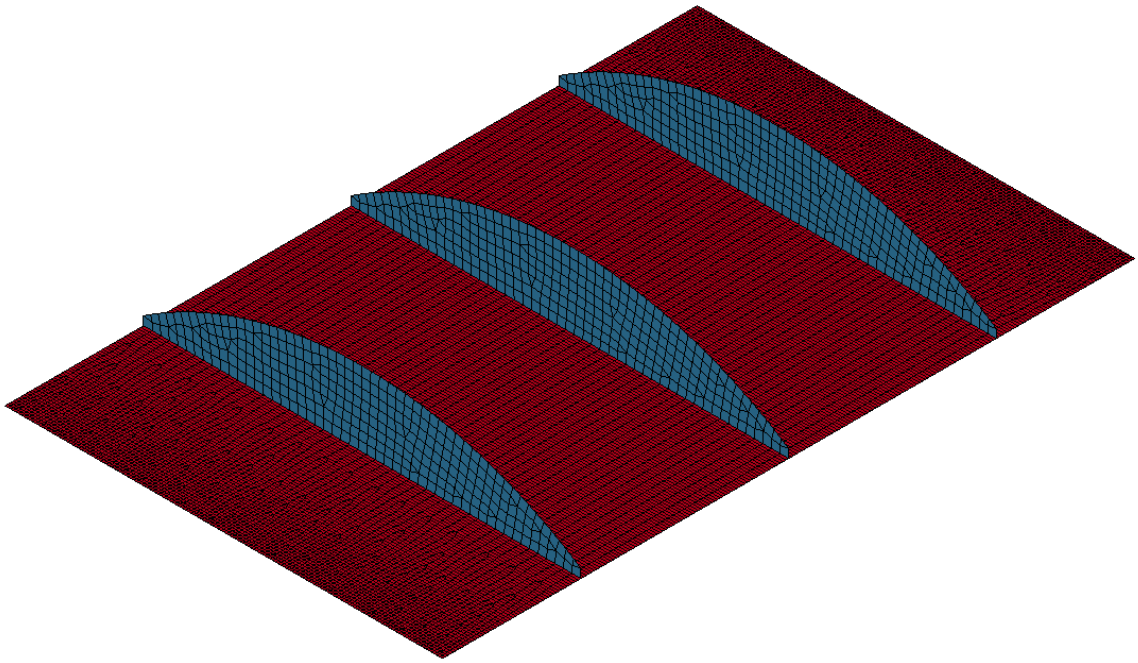

Run22, von Mise Stress:

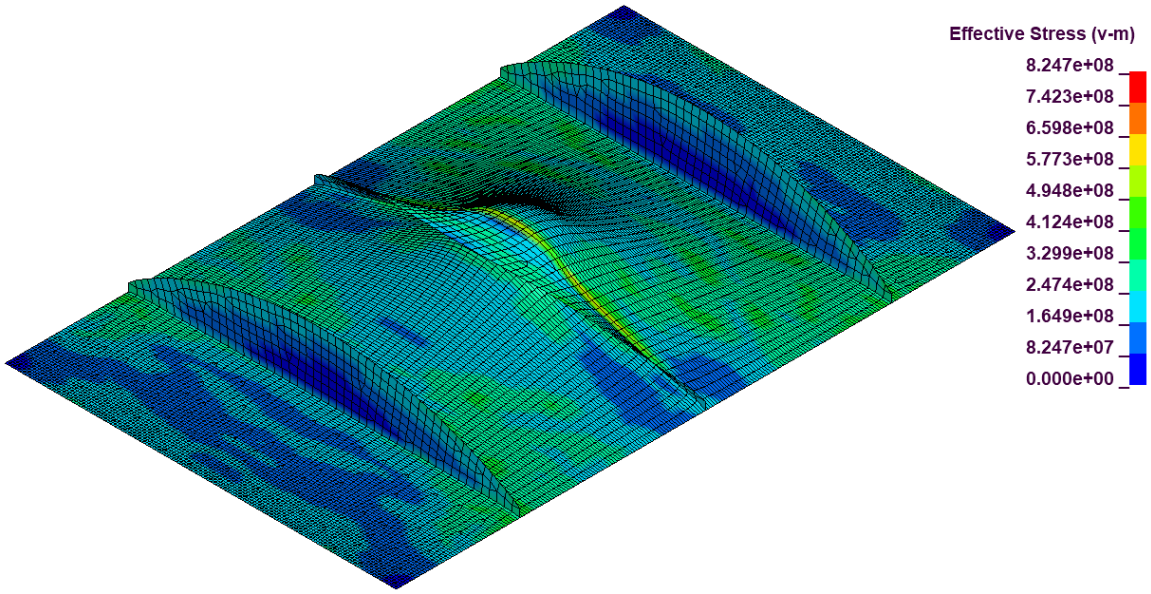

Run23, Geometry:

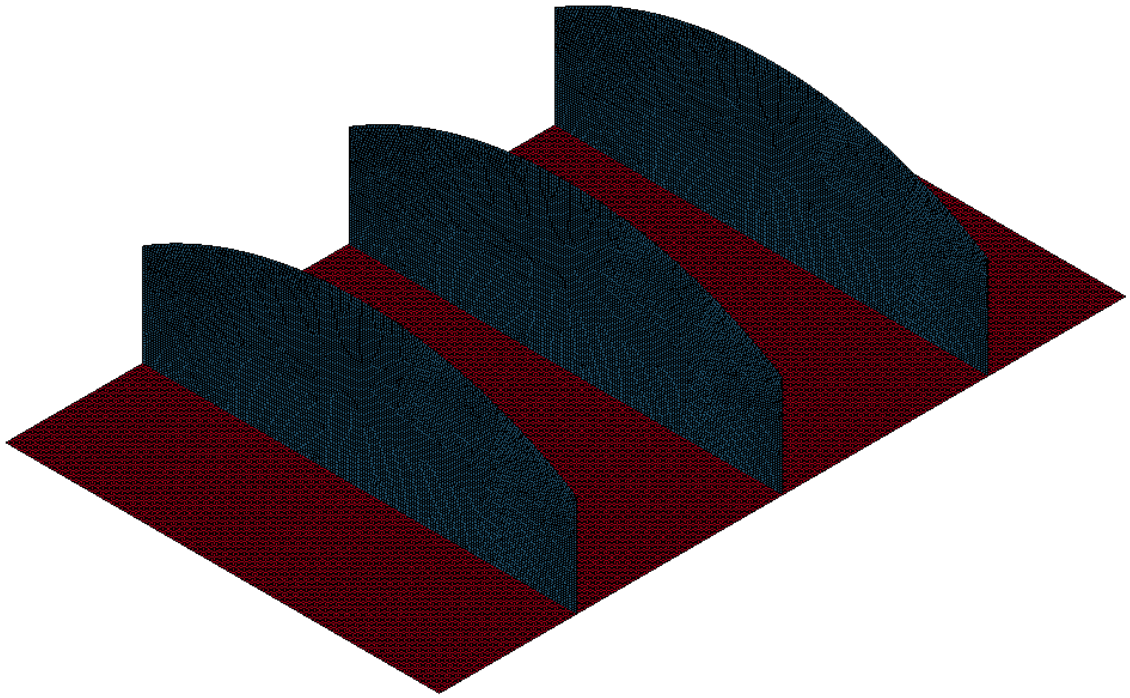

Run23, von Mise Stress:

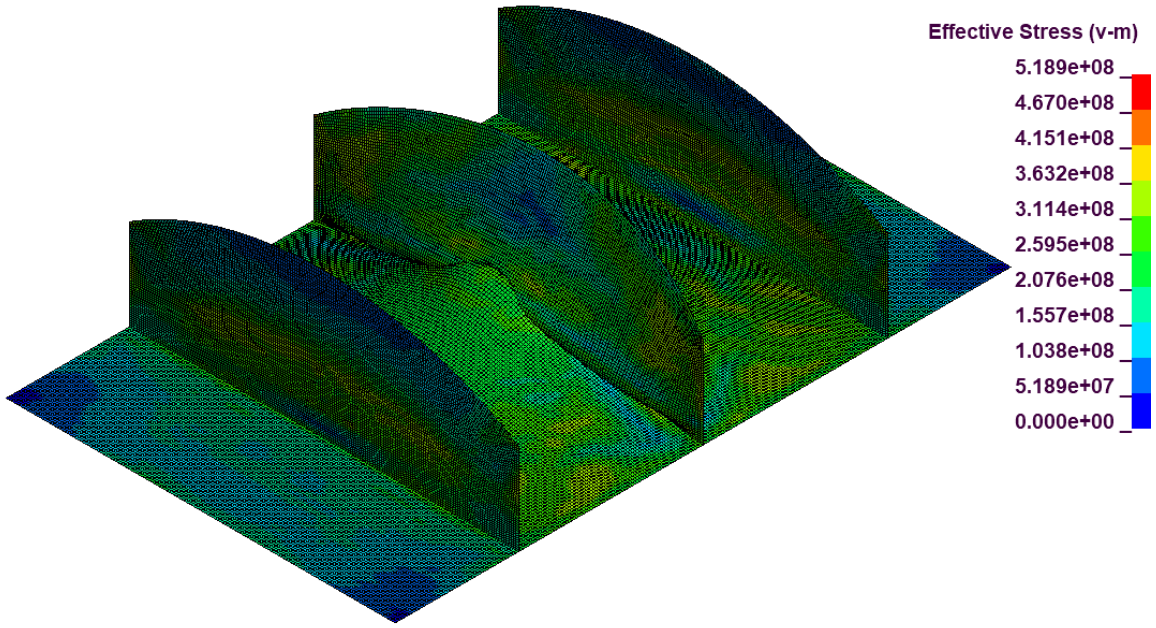

Run24, Geometry:

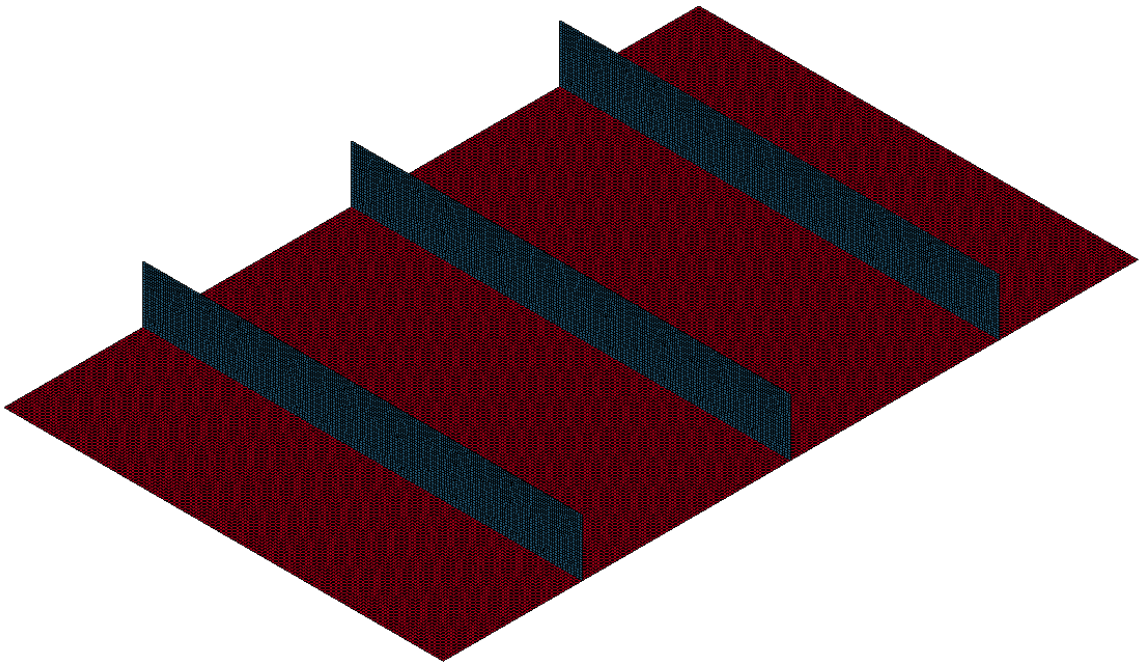

Run24, von Mise Stress:

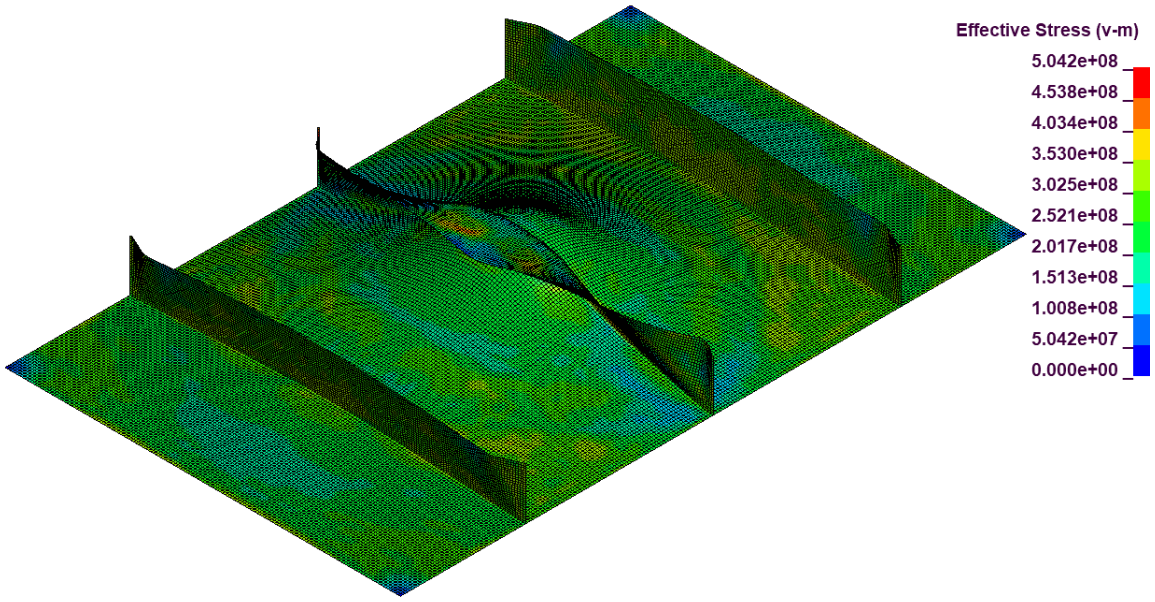

Run25, Geometry:

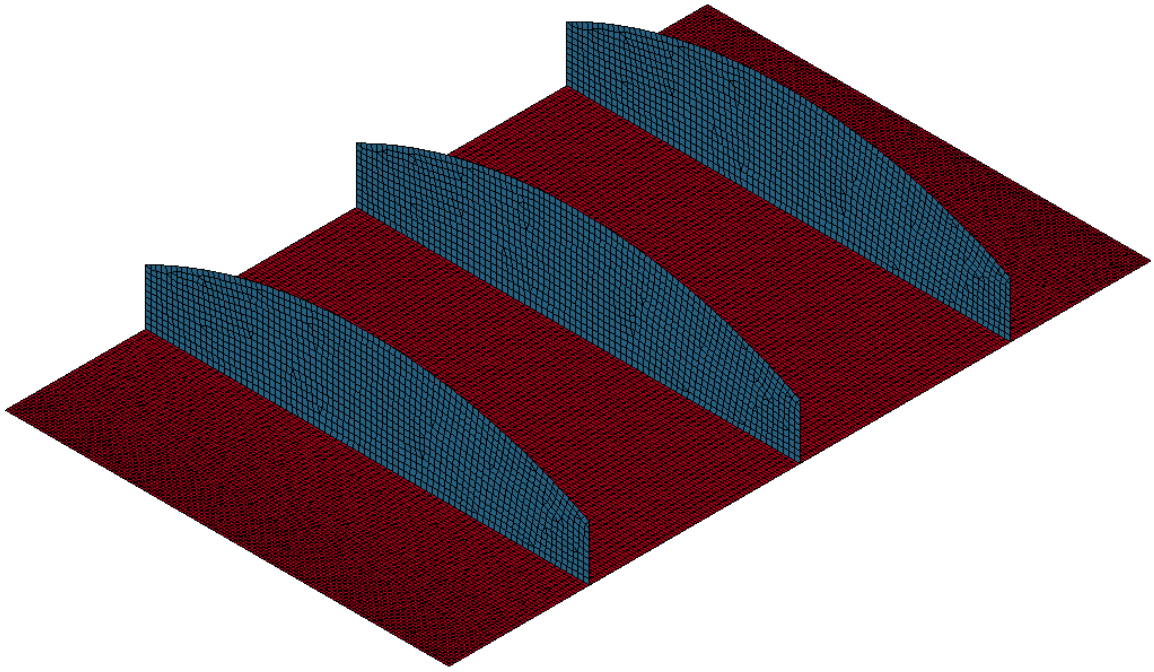

Run25, von Mise Stress:

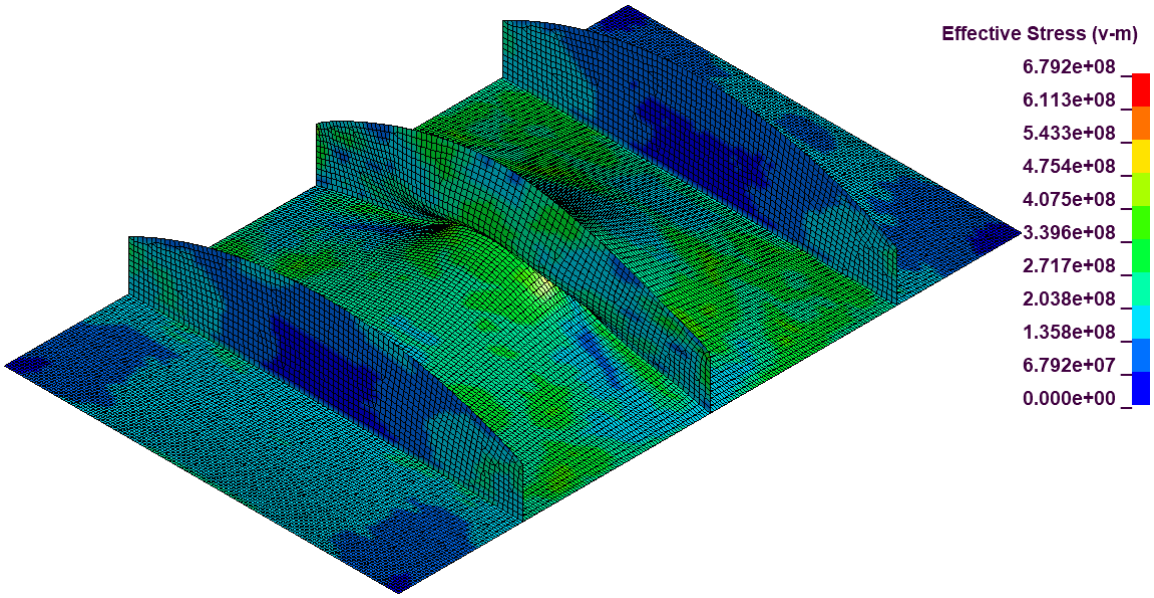

Run26, Geometry:

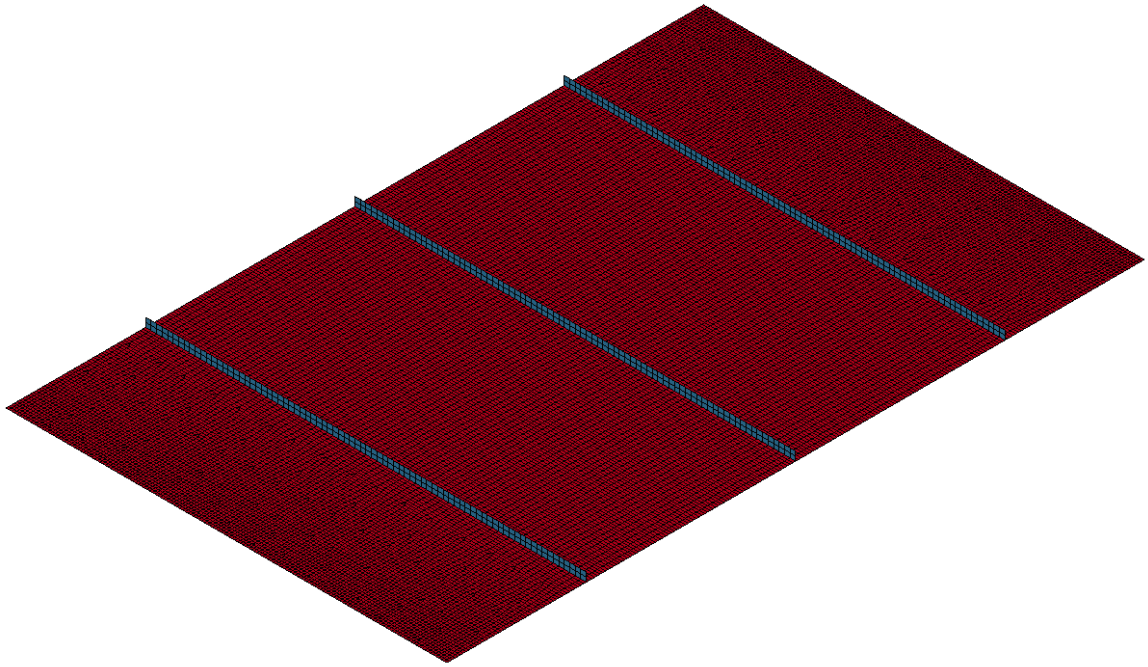

Run26, von Mise Stress:

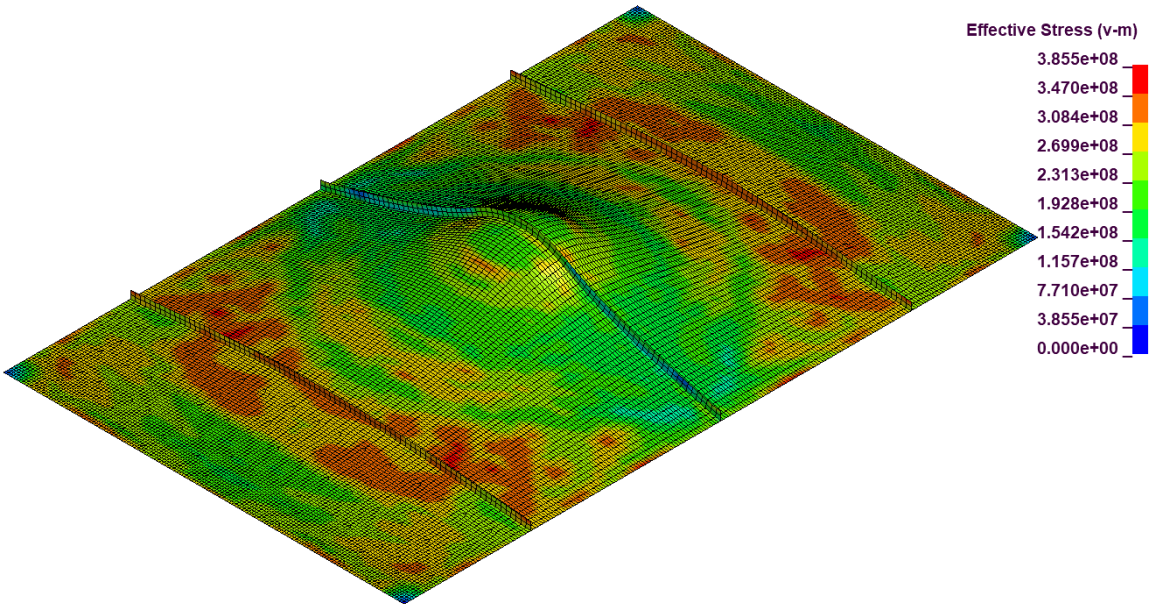

Appendix E2 – Table of Variable Dimensions, Parameters, and Responses

Run Order	mm A Hw	mm B Hw2	mm C Tw	m Tw_	kg Response 1 Total Weight	MN Response 2 First Yield				kJ Response 3 Energy (0-50mm)	kJ Response 4 Energy (50-100mm)	kJ Response 5 Energy (100-150mm)
							E @50mm	E @100mm	E @150mm			
Built-T	170	0	7.9375	0.0079375	21.76	0.49	25.53799674	70.03657748	142.6852682	25.53799674	44.49858073	72.64869076
1	300	300	13.3985	0.0133985	68.65	1.25	49.6230625	116.5970781	209.503207	49.6230625	66.97401563	92.90612891
2	25.4	300	6.35	0.00635	14.96	0.185	17.16663688	52.31255534	113.143429	17.16663688	35.14591846	60.8308737
3	176.43	165	6.731	0.006731	19.51	0.408	18.69375342	56.90461849	122.4280664	18.69375342	38.21086507	65.52344792
4	25.4	0	6.35	0.00635	1.63	0.0378	4.460468221	28.40946403	78.22508919	4.460468221	23.94899581	49.81562516
5	128.375	300	25.4	0.0254	86.22	2.05	96.51997266	253.8259167	409.544724	96.51997266	157.305944	155.7188073
6	30.892	165	16.8275	0.0168275	24.09	0.286	24.59281315	81.45694076	172.814569	24.59281315	56.8641276	91.35762826
7	300	111	25.4	0.0254	95.83	2.69	116.4246302	266.2501875	406.7572839	116.4246302	149.8255573	140.5070964
8	300	0	6.35	0.00635	19.20	0.36	17.53361507	55.72468229	121.2187396	17.53361507	38.19106722	65.49405729
9	176.43	6	16.8275	0.0168275	30.60	0.627	35.23139225	99.77281445	192.0891901	35.23139225	64.5414222	92.31637565
10	25.4	0	25.4	0.0254	6.50	0.0669	5.556003947	32.29133789	86.42680664	5.556003947	26.73533394	54.13546875
11	206.636	180	17.19115812	0.017191158	56.98	1.41	70.95511328	172.7749661	277.2321406	70.95511328	101.8198529	104.4571745
12	117.391	133.5	25.4	0.0254	53.08	1.01	54.22912272	146.1765221	278.7990104	54.22912272	91.94739942	132.6224883
13	300	298.6773178	25.4	0.0254	129.91	3.41	120.2697174	238.6772839	379.2792839	120.2697174	118.4075664	140.602
14	205.263	300	6.35	0.00635	26.47	0.385	17.51732096	54.76746029	119.5186094	17.51732096	37.25013932	64.75114909
15	25.4	300	18.7325	0.0187325	44.15	0.404	45.29596973	137.6385456	244.8504609	45.29596973	92.34257585	107.2119154
16	161.327	0	15.89146871	0.015891469	25.84	0.487	28.80711833	85.81919987	174.2765664	28.80711833	57.01208154	88.45736654
17	170.938	147.816073	14.82725	0.01482725	40.43	0.908	50.16708268	137.7102461	241.0514219	50.16708268	87.54316341	103.3411758
18	300	0	25.4	0.0254	76.79	1.99	95.98304232	236.19475	380.3526146	95.98304232	140.2117077	144.1578646
19	300	154.5	12.827	0.012827	52.24	1.16	46.53885514	110.5997936	201.0808594	46.53885514	64.06093848	90.48106576
20	142.2201571	144	15.01775	0.01501775	36.21	0.768	43.36016308	121.9473607	233.0660521	43.36016308	78.58719759	111.1186914
21	25.4	117	6.35	0.00635	6.64	0.128	9.302243815	42.05300358	102.5345449	9.302243815	32.75075977	60.48154134
22	25.4	193.5	25.4	0.0254	40.15	0.553	37.78264746	114.1687279	221.2388607	37.78264746	76.3860804	107.0701328
23	300	183.4917049	6.35	0.00635	27.18	0.374	17.53899333	55.13518685	120.2972604	17.53899333	37.59619352	65.16207357
24	166.819	0	6.35	0.00635	10.68	0.172	13.80133602	50.83750618	116.7571797	13.80133602	37.03617017	65.9196735
25	160.2976306	153.2091882	16.27760391	0.016277604	43.23	0.924	52.45270866	142.8187148	256.9357943	52.45270866	90.36600618	114.1170794
26	25.4	0	16.0655	0.0160655	4.11	0.0529	5.080956665	30.49381185	82.67599284	5.080956665	25.41285518	52.18218099
Conf. Run1	83.01809326	111.6475796	13.6905605	0.01369056	21.77	0.354	23.28342822	76.52885482	162.6807188	23.28342822	53.24542659	86.15186393
Conf. Run2	132.2011297	133.2114191	9.934030509	0.009934031	22.22	0.464	28.09428109	87.21243294	170.0584531	28.09428109	59.11815185	82.84602018
Conf. Run3	134.085512	153.6976473	9.128331678	0.009128332	21.86	0.492	28.43567855	83.52473307	157.4543581	28.43567855	55.08905452	73.929625

Appendix E3 – von Mises Stress vs. Displacement Plots

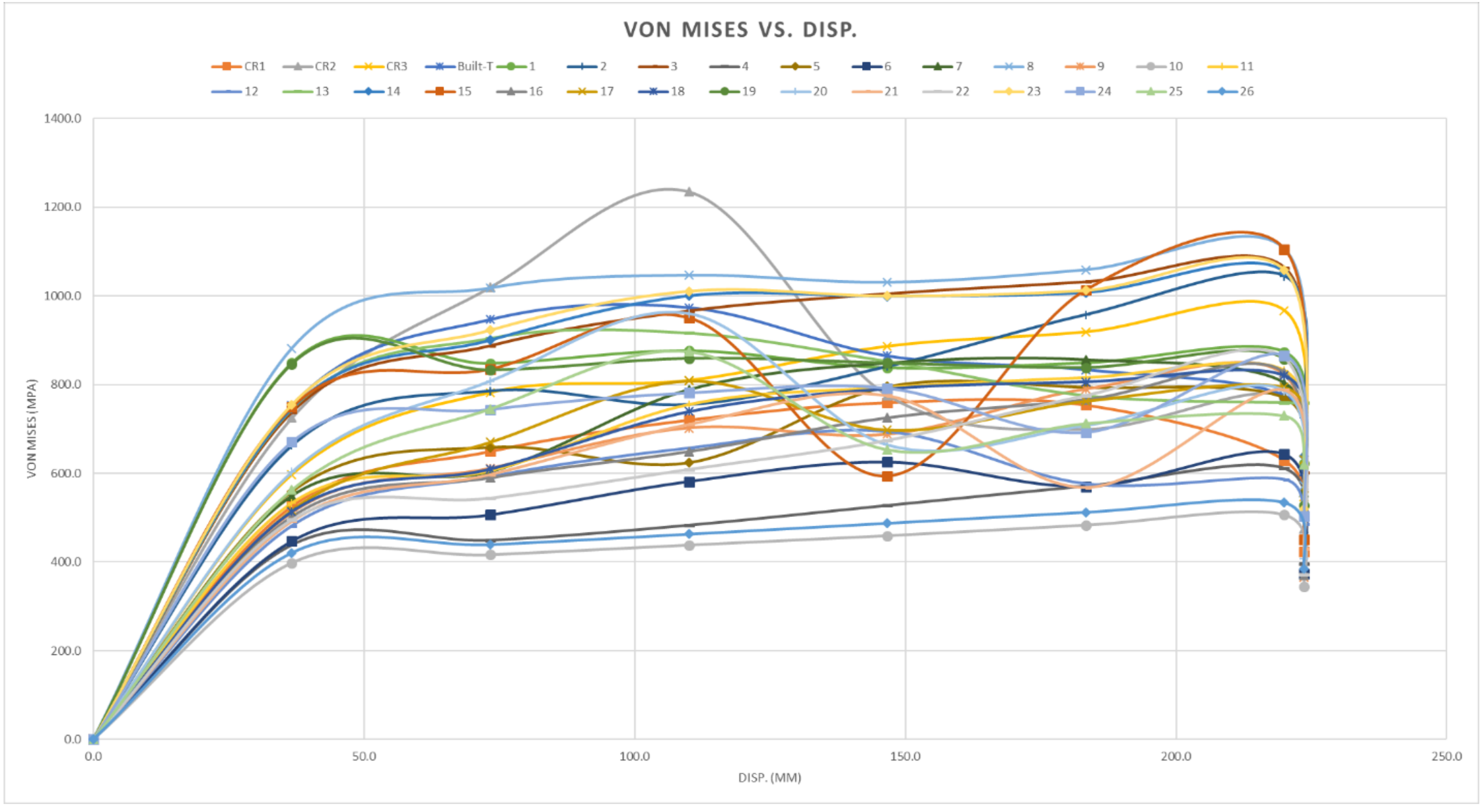

Appendix E4 – Force vs. Displacement Plots

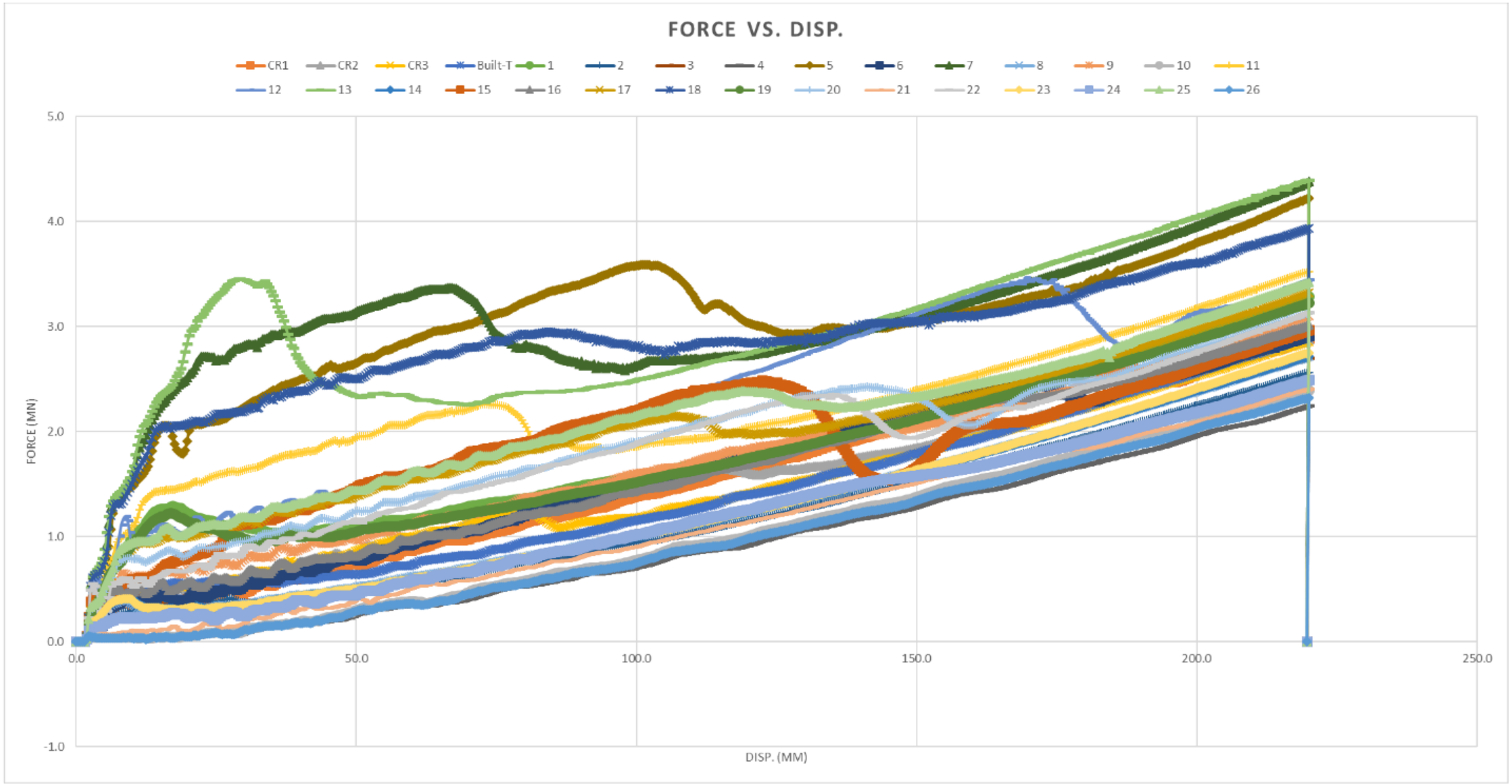

Appendix E5 – Energy vs. Displacement Plots

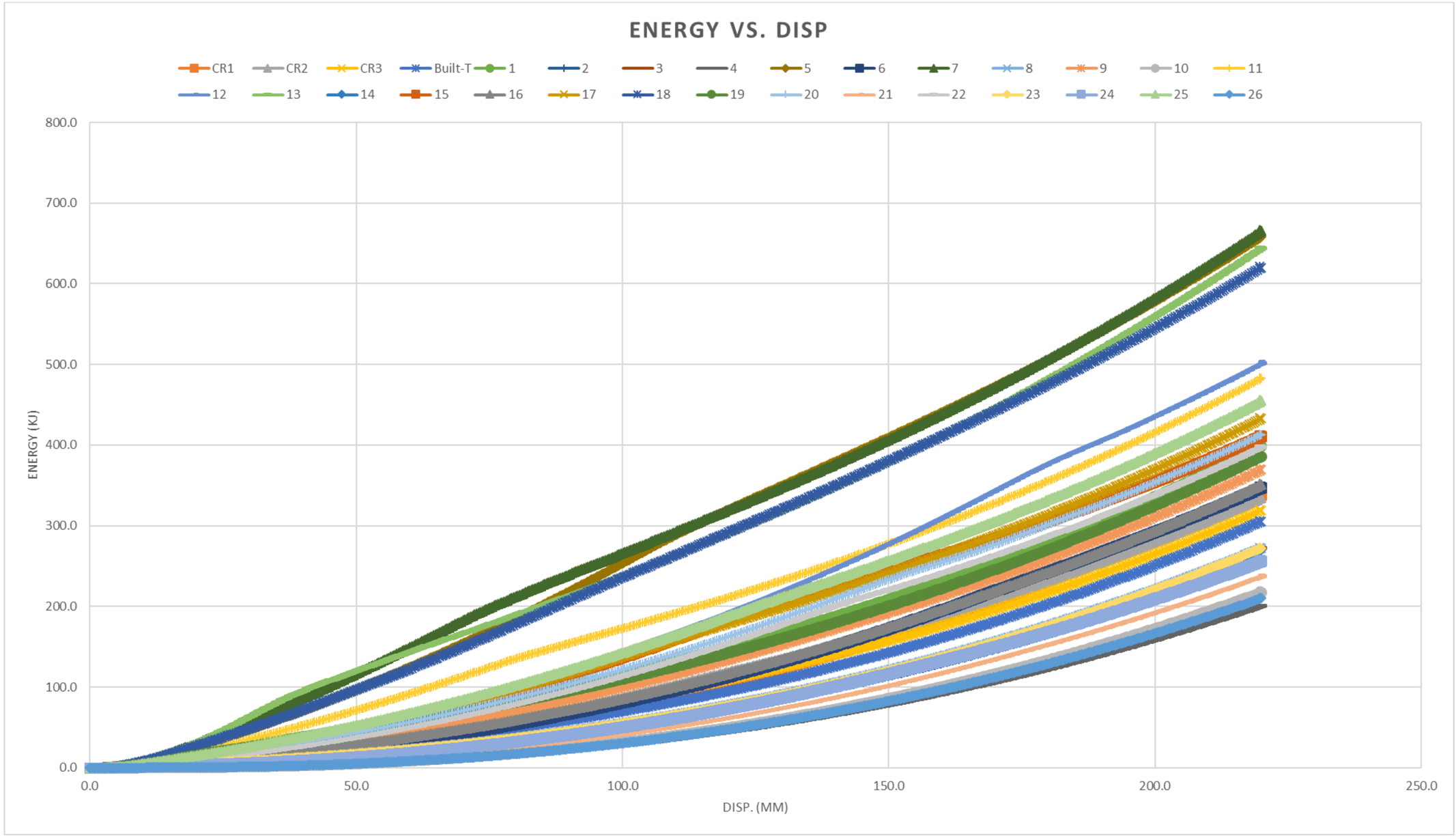

Appendix E6 – Design Expert Output

Response 1 – Weight:

Source	Sequential p-value	Lack of Fit p-value	Adjusted R^2	Predicted R^2	
Linear	< 0.0001		0.8712	0.8189	
2FI	< 0.0001		0.9999	0.9998	
Quadratic	< 0.0001		1.0000	1.0000	
Cubic	**< 0.0001**		**1.0000**	**1.0000**	**Suggested**
Quartic					Aliased

Source	Sum of Squares	df	Mean Square	F-value	p-value	
Model	24387.32	6	4064.55	2.844E+05	< 0.0001	significant
A-Hw	7369.75	1	7369.75	5.157E+05	< 0.0001	
B-Hw2	3852.94	1	3852.94	2.696E+05	< 0.0001	
C-Tw	9828.85	1	9828.85	6.878E+05	< 0.0001	
AC	1817.68	1	1817.68	1.272E+05	< 0.0001	
BC	927.61	1	927.61	64913.19	< 0.0001	
B^2	1.39	1	1.39	97.56	< 0.0001	
Residual	0.2715	19	0.0143			
Cor Total	24387.59	25				

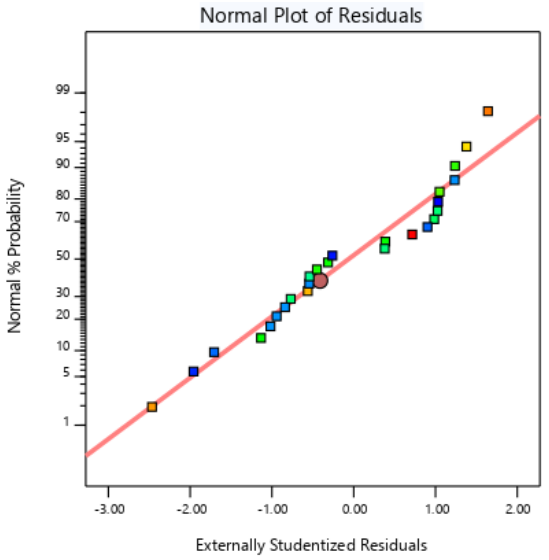

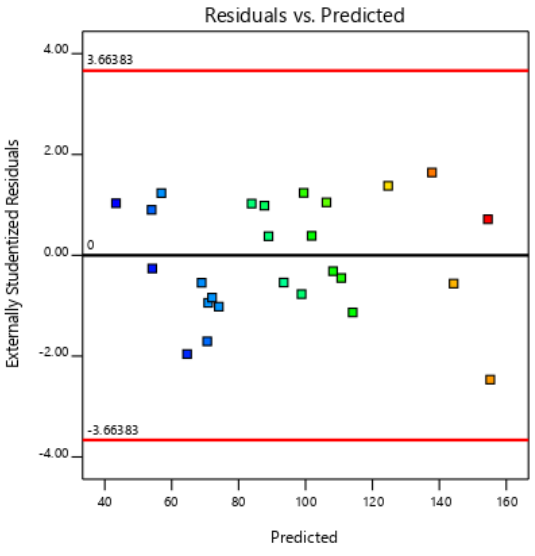

Response 2 – First Yield:

Source	Sequential p-value	Lack of Fit p-value	Adjusted R^2	Predicted R^2	
Linear	< 0.0001		0.8529	0.8027	
2FI	< 0.0001		0.9600	0.9333	
Quadratic	**< 0.0001**		**0.9885**	**0.9742**	**Suggested**
Cubic	**0.0232**		**0.9970**	**0.9442**	**Suggested**
Quartic					Aliased

Source	Sum of Squares	df	Mean Square	F-value	p-value	
Model	4.66	8	0.5831	278.82	< 0.0001	significant
A-Hw	1.82	1	1.82	872.13	< 0.0001	
B-Hw2	0.4106	1	0.4106	196.33	< 0.0001	
C-Tw	1.67	1	1.67	798.95	< 0.0001	
AB	0.0139	1	0.0139	6.66	0.0194	
AC	0.4001	1	0.4001	191.33	< 0.0001	
BC	0.0994	1	0.0994	47.54	< 0.0001	
A^2	0.0595	1	0.0595	28.45	< 0.0001	
B^2	0.0304	1	0.0304	14.55	0.0014	
Residual	0.0356	17	0.0021			
Cor Total	4.70	25				

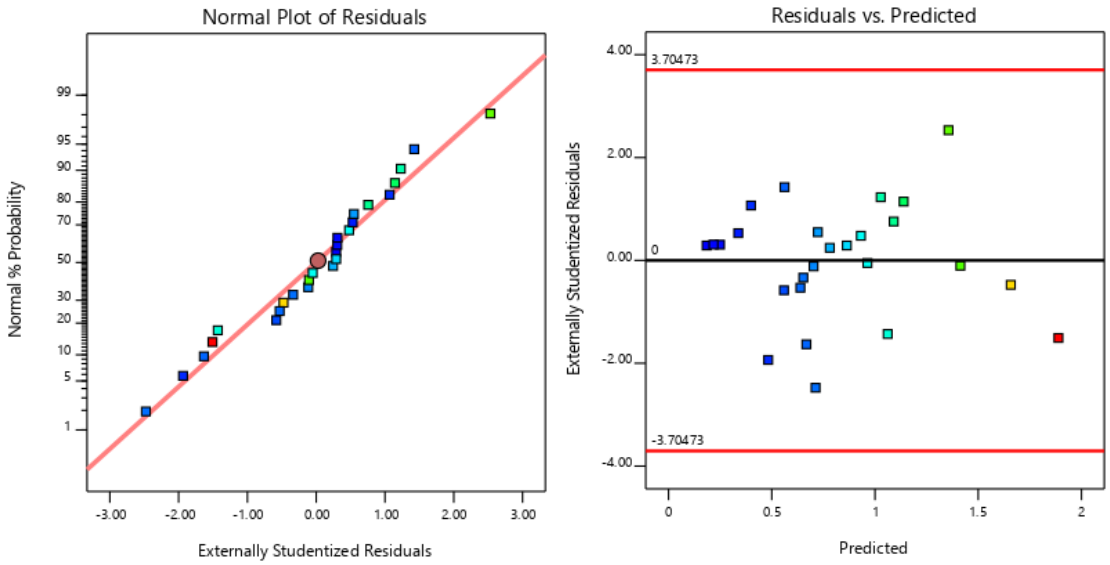

Response 3 – Energy at 0-50 mm:

Source	Sequential p-value	Lack of Fit p-value	Adjusted R^2	Predicted R^2	
Linear	< 0.0001		0.7332	0.6520	
2FI	0.0013		0.8619	0.7335	
Quadratic	< 0.0001		0.9801	0.9604	
Cubic	**0.0038**		**0.9973**	**0.9709**	**Suggested**
Quartic					Aliased

Source	Sum of Squares	df	Mean Square	F-value	p-value	
Model	21.74	9	2.42	137.52	< 0.0001	significant
A-Hw	5.42	1	5.42	308.49	< 0.0001	
B-Hw2	2.79	1	2.79	159.01	< 0.0001	
C-Tw	7.06	1	7.06	401.80	< 0.0001	
AB	2.03	1	2.03	115.75	< 0.0001	
AC	0.9039	1	0.9039	51.46	< 0.0001	
BC	0.3796	1	0.3796	21.61	0.0003	
A^2	0.5905	1	0.5905	33.62	< 0.0001	
B^2	0.2723	1	0.2723	15.50	0.0012	
C^2	0.4643	1	0.4643	26.43	< 0.0001	
Residual	0.2810	16	0.0176			
Cor Total	22.02	25				

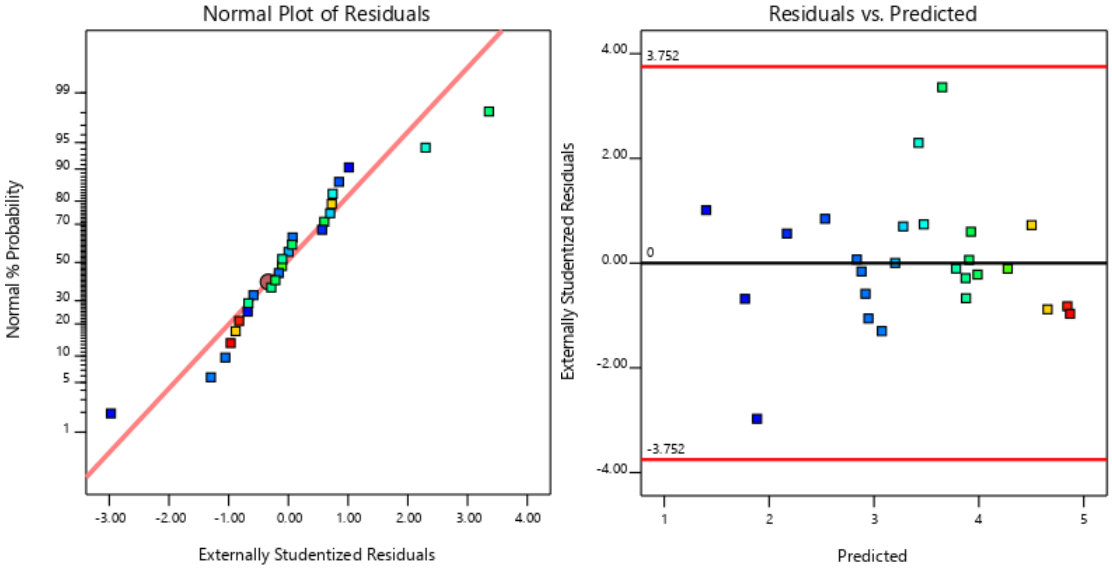

Response 4 – Energy at 50-100 mm:

Source	Sequential p-value	Lack of Fit p-value	Adjusted R^2	Predicted R^2	
Linear	< 0.0001		0.6582	0.5567	
2FI	0.0048		0.7965	0.5699	
Quadratic	**< 0.0001**		**0.9586**	**0.9003**	**Suggested**
Cubic	0.0739		0.9834	0.8405	
Quartic					Aliased

Source	Sum of Squares	df	Mean Square	F-value	p-value	
Model	0.0344	9	0.0038	65.31	< 0.0001	significant
A-Hw	0.0047	1	0.0047	80.97	< 0.0001	
B-Hw2	0.0031	1	0.0031	52.73	< 0.0001	
C-Tw	0.0150	1	0.0150	256.41	< 0.0001	
AB	0.0039	1	0.0039	67.00	< 0.0001	
AC	0.0012	1	0.0012	19.93	0.0004	
BC	0.0010	1	0.0010	16.45	0.0009	
A^2	0.0011	1	0.0011	18.90	0.0005	
B^2	0.0006	1	0.0006	10.80	0.0047	
C^2	0.0012	1	0.0012	20.78	0.0003	
Residual	0.0009	16	0.0001			
Cor Total	0.0353	25				

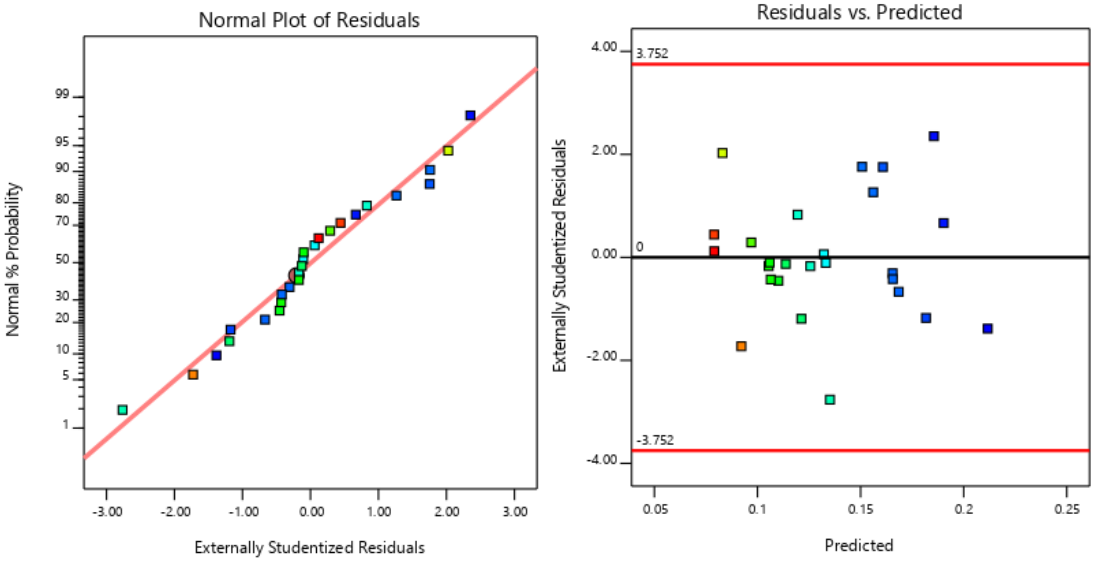

Response 5 – Energy at 100-150 mm:

Source	Sequential p-value	Lack of Fit p-value	Adjusted R^2	Predicted R^2	
Linear	< 0.0001		0.7045	0.6137	
2FI	0.0040		0.8272	0.6403	
Quadratic	**0.0001**		**0.9416**	**0.8744**	**Suggested**
Cubic	**0.0288**		**0.9838**	**0.8468**	**Suggested**
Quartic					Aliased

Source	Sum of Squares	df	Mean Square	F-value	p-value	
Model	2.88	9	0.3198	45.81	< 0.0001	significant
A-Hw	0.3034	1	0.3034	43.45	< 0.0001	
B-Hw2	0.2016	1	0.2016	28.87	< 0.0001	
C-Tw	1.61	1	1.61	229.89	< 0.0001	
AB	0.2232	1	0.2232	31.97	< 0.0001	
AC	0.1143	1	0.1143	16.37	0.0009	
BC	0.1060	1	0.1060	15.18	0.0013	
A^2	0.1019	1	0.1019	14.59	0.0015	
B^2	0.0482	1	0.0482	6.91	0.0183	
C^2	0.0373	1	0.0373	5.35	0.0344	
Residual	0.1117	16	0.0070			
Cor Total	2.99	25				

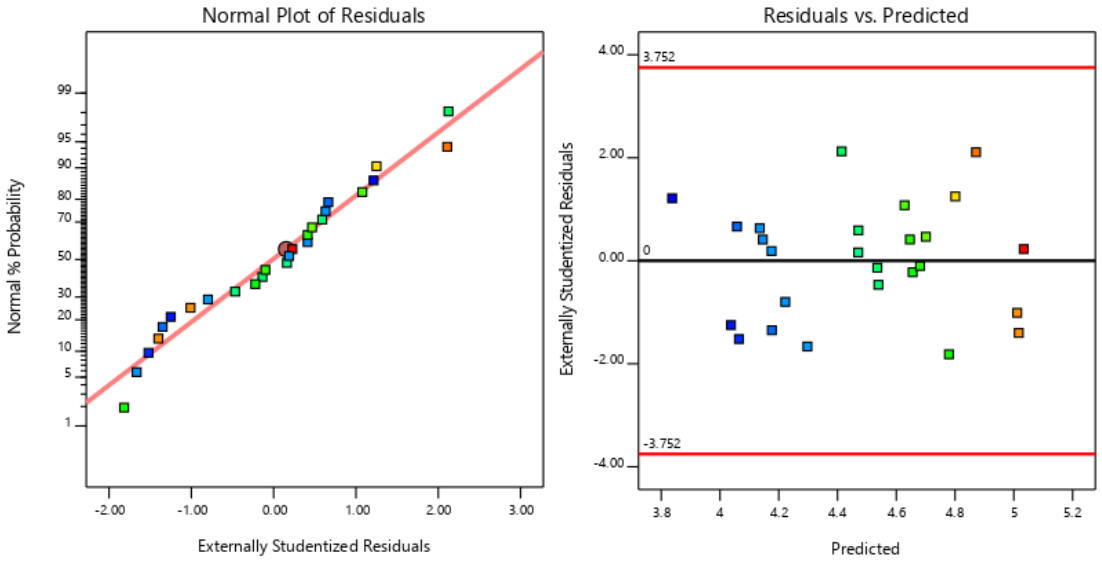

Appendix E7 – Element Quality Checks

Confirmation Run 1:

Quality Name	Min. val	Max. val	Allowable	#Violated(%)
Aspect Ratio	1	2.08	10	0(0%)
Warpage	0	6.03	10	0(0%)
Min Quad Angle	51	90	45	0(0%)
Max Quad Angle	90	154	135	3(0.01%)
Min Tria Angle	41.2	58.5	30	0(0%)
Max Tria Angle	61	80	120	0(0%)
Skew	0	29.2	45	0(0%)
Jacobian	0.51	1	0.6	2(0.00667%)

#QUADS(%):29799(99.4%), #TRIAS(%):174(0.581%), #TOTAL OF FAILED(%):2(0.00667%)

Confirmation Run 2:

Quality Name	Min. val	Max. val	Allowable	#Violated(%)
Aspect Ratio	1	2.63	10	0(0%)
Warpage	0	99.1	10	5(0.0119%)
Min Quad Angle	40.3	90	45	1(0.00238%)
Max Quad Angle	90	200	135	1(0.00238%)
Min Tria Angle	33.7	58.1	30	0(0%)
Max Tria Angle	62.4	105	120	0(0%)
Skew	0	41.2	45	0(0%)
Jacobian	0.297	1	0.6	1(0.00238%)

#QUADS(%):41895(99.6%), #TRIAS(%):170(0.404%), #TOTAL OF FAILED(%):1(0.00238%)

Confirmation Run 3:

Quality Name	Min. val	Max. val	Allowable	#Violated(%)
Aspect Ratio	1	2.51	10	0(0%)
Warpage	0	87.3	10	3(0.00638%)
Min Quad Angle	39.1	90	45	3(0.00638%)
Max Quad Angle	90	169	135	4(0.0085%)
Min Tria Angle	36.8	53.7	30	0(0%)
Max Tria Angle	64.7	103	120	0(0%)
Skew	0	43.1	45	0(0%)
Jacobian	0.3	1	0.6	2(0.00425%)

#QUADS(%):46850(99.6%), #TRIAS(%):185(0.393%), #TOTAL OF FAILED(%):2(0.00425%)

Appendix F – Exp5 Appendices

Appendix F1 – Geometry and von Mises Stress Visuals

IROQUOIS, Local Model, Geometry:

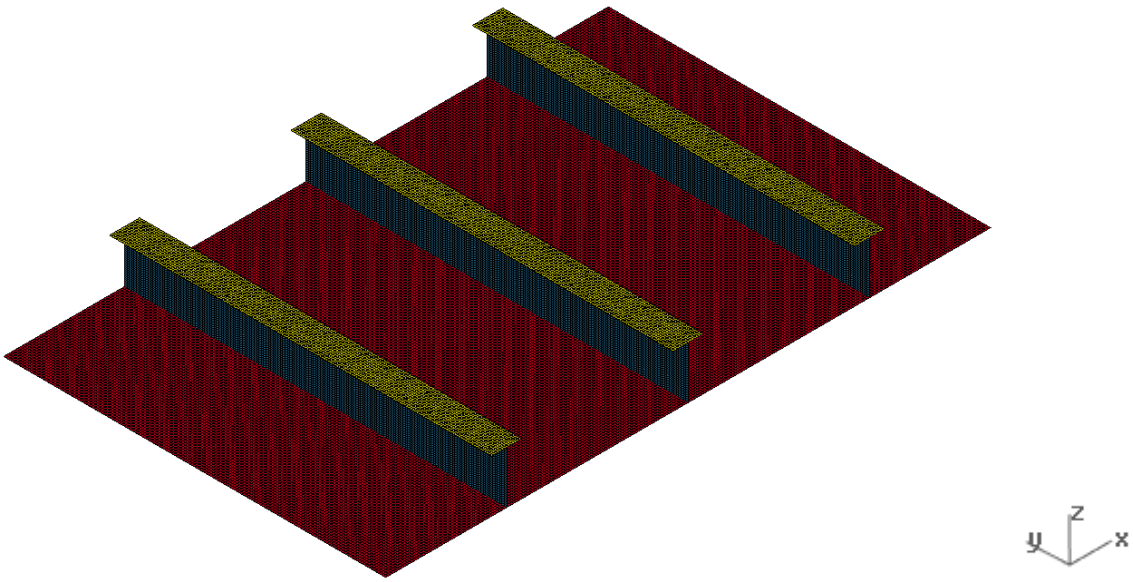

IROQUOIS, Local Model, Load Case 1, von Mise Stress:

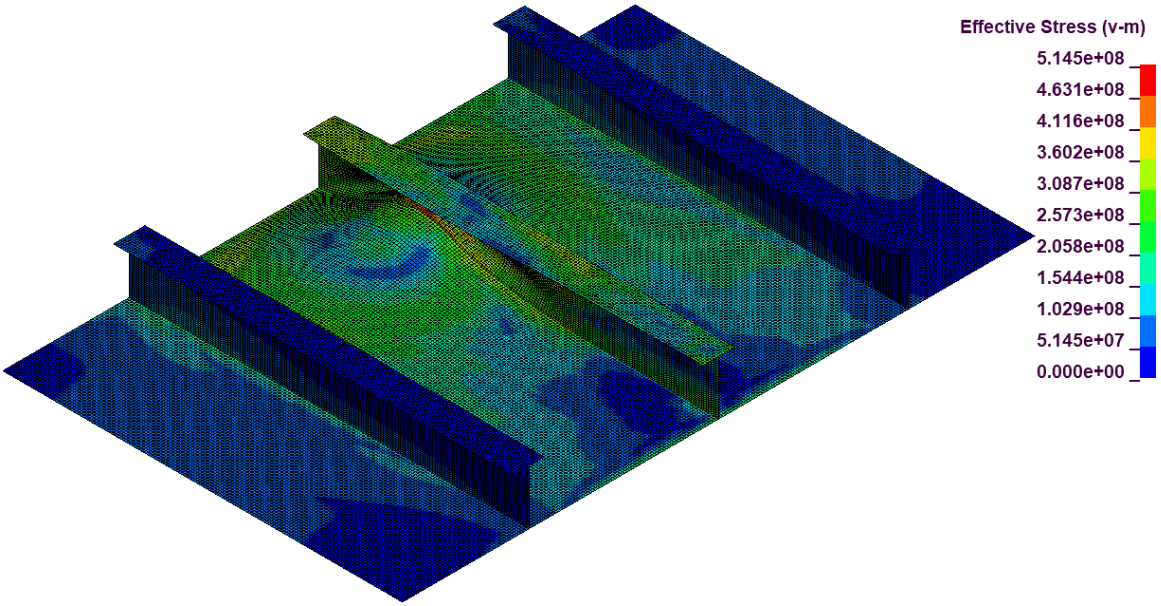

IROQUOIS, Local Model, Load Case 2, von Mise Stress:

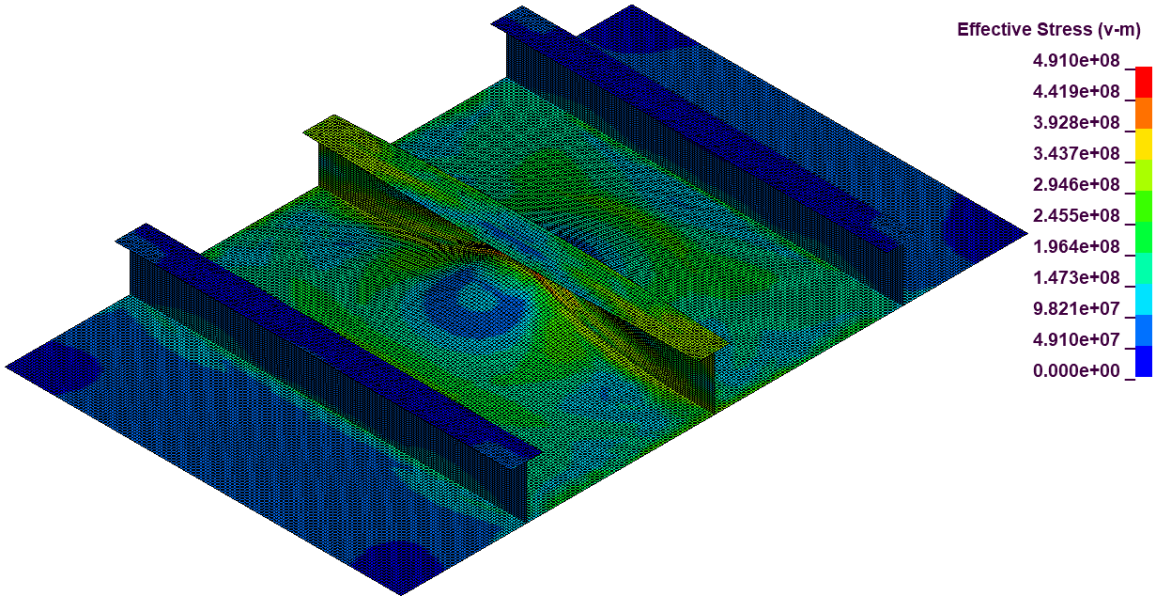

IROQUOIS, Local Model, Load Case 3, von Mise Stress:

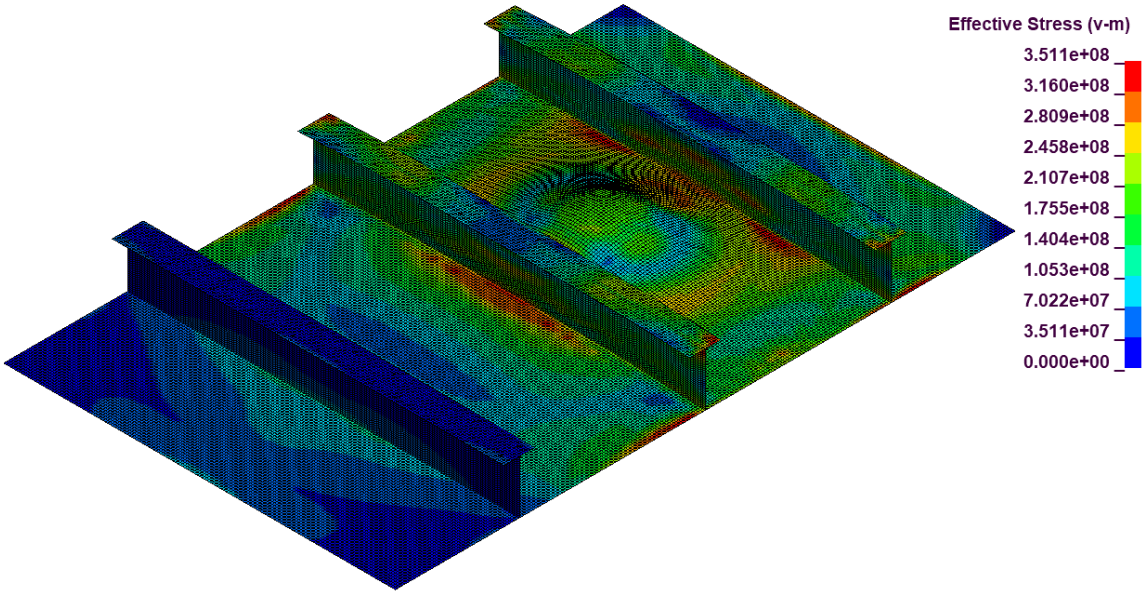

IROQUOIS, Global Model, Geometry:

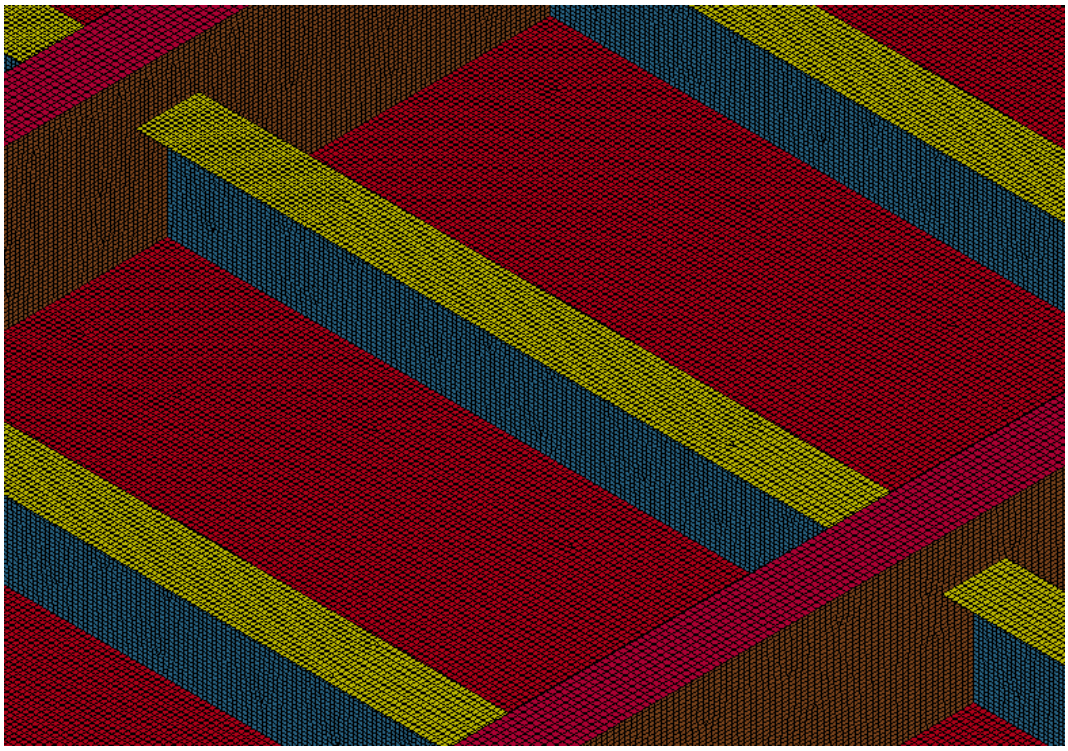

IROQUOIS, Global Model, Load Case 1, von Mise Stress:

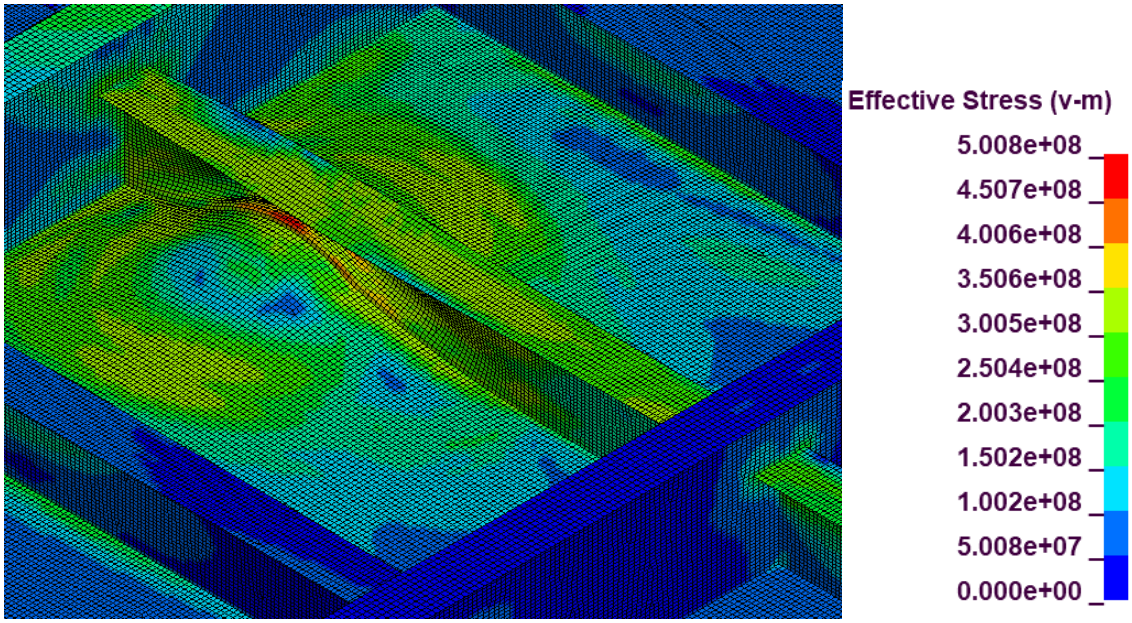

IROQUOIS, Global Model, Load Case 2, von Mise Stress:

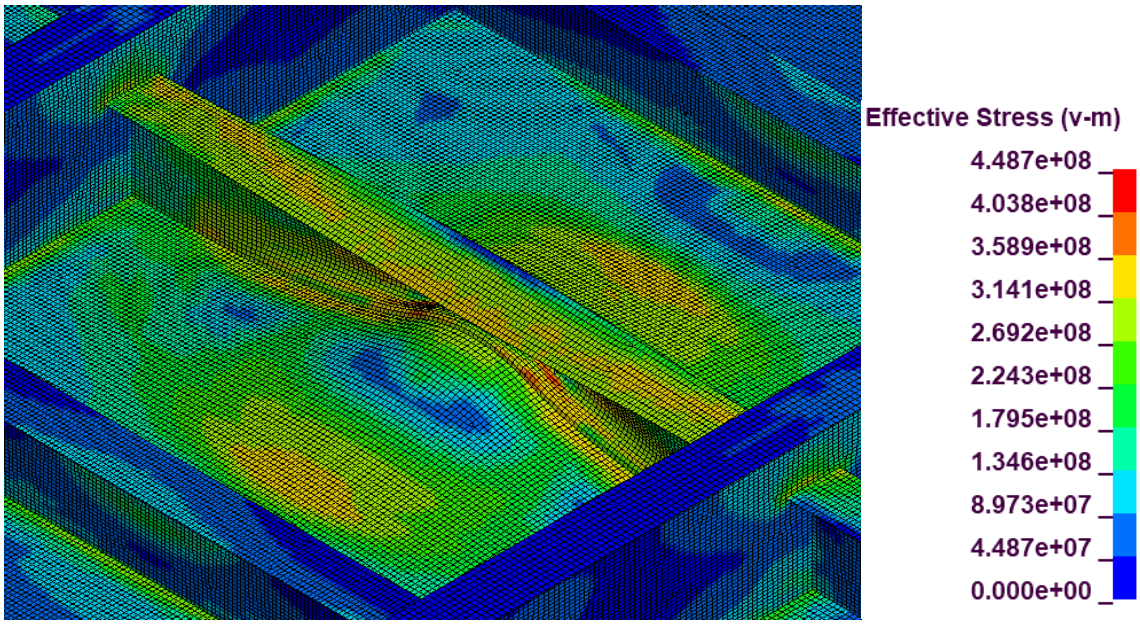

IROQUOIS, Global Model, Load Case 3, von Mise Stress:

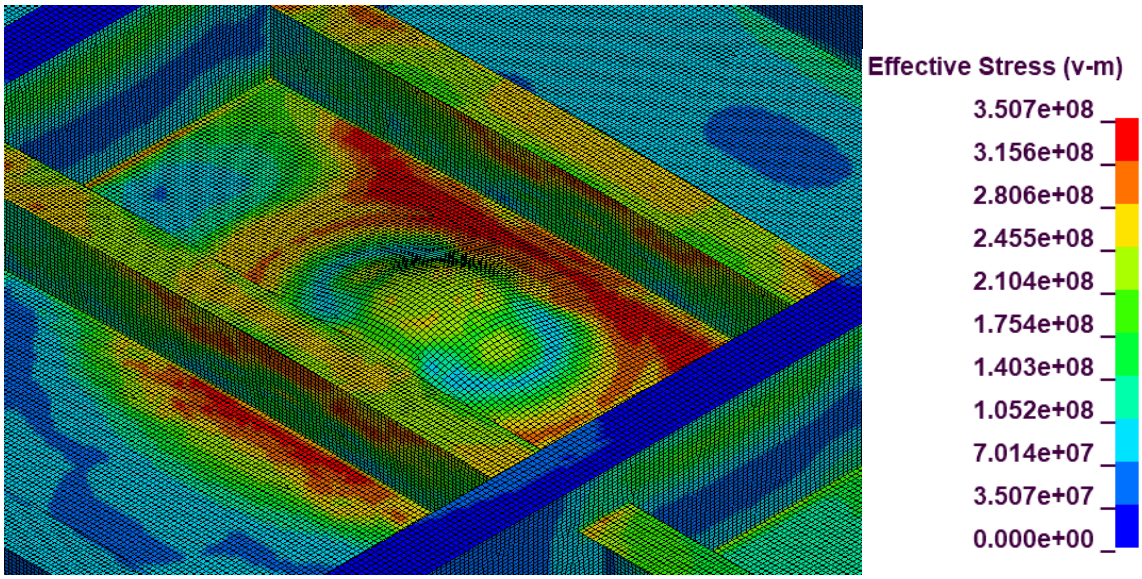

Concept Grillage, Local Model, Geometry:

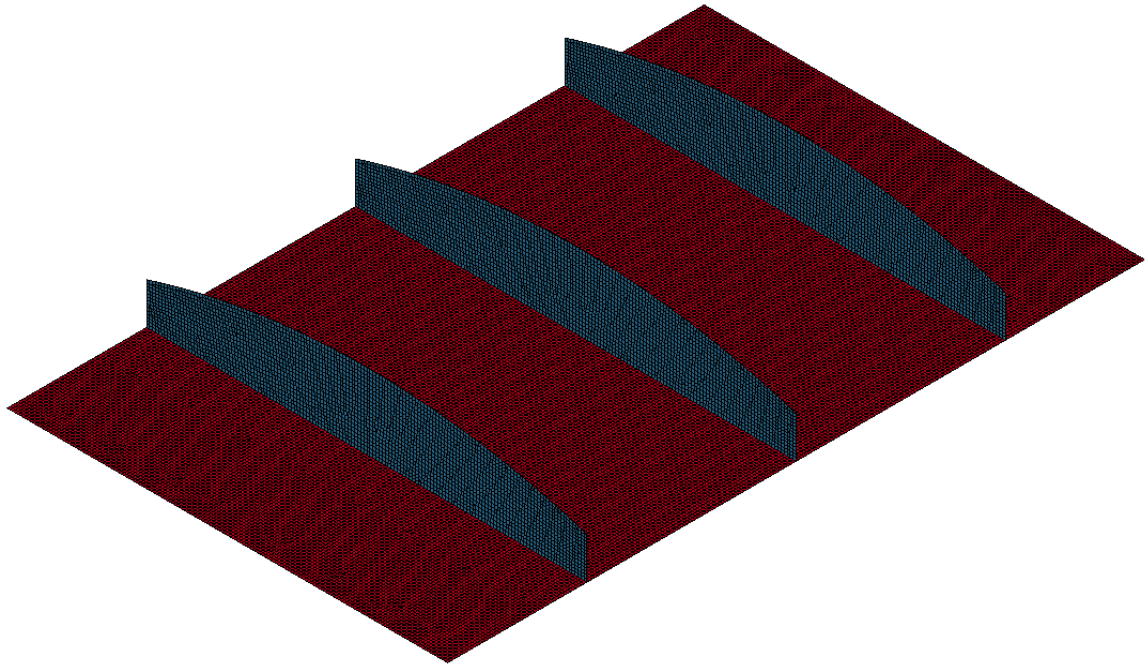

Concept Grillage, Local Model, Load Case 1, von Mise Stress:

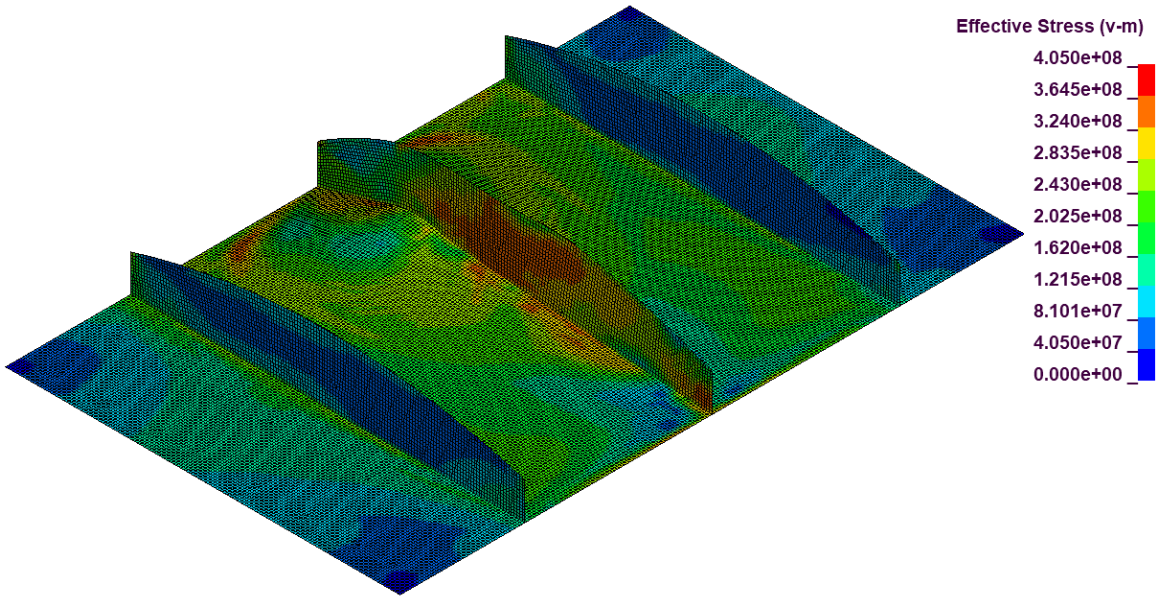

Concept Grillage, Local Model, Load Case 2, von Mise Stress:

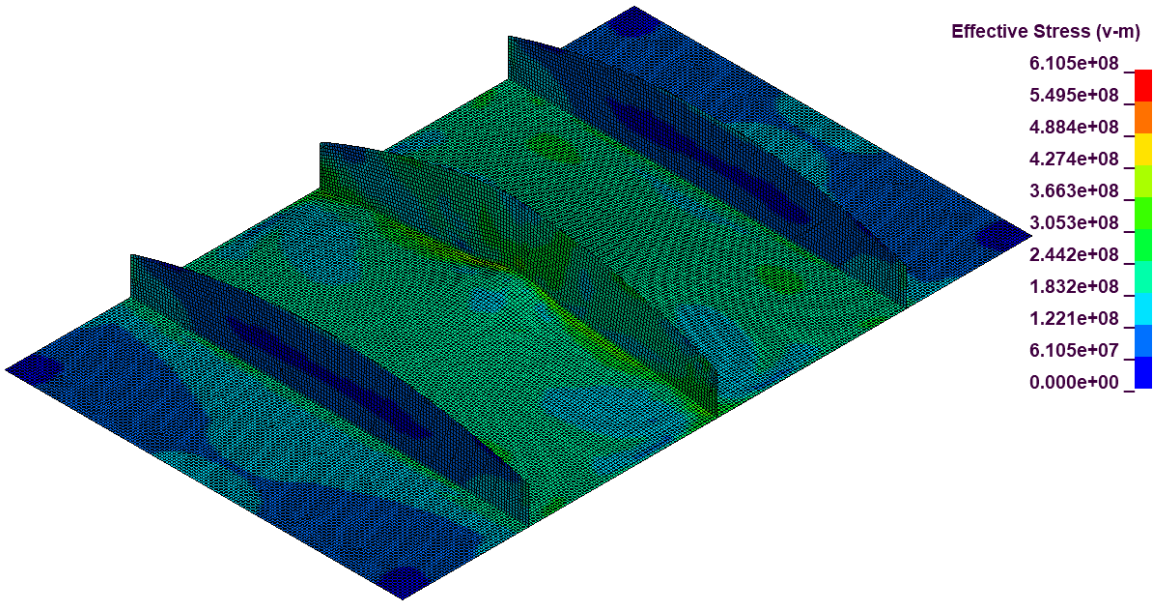

Concept Grillage, Local Model, Load Case 3, von Mise Stress:

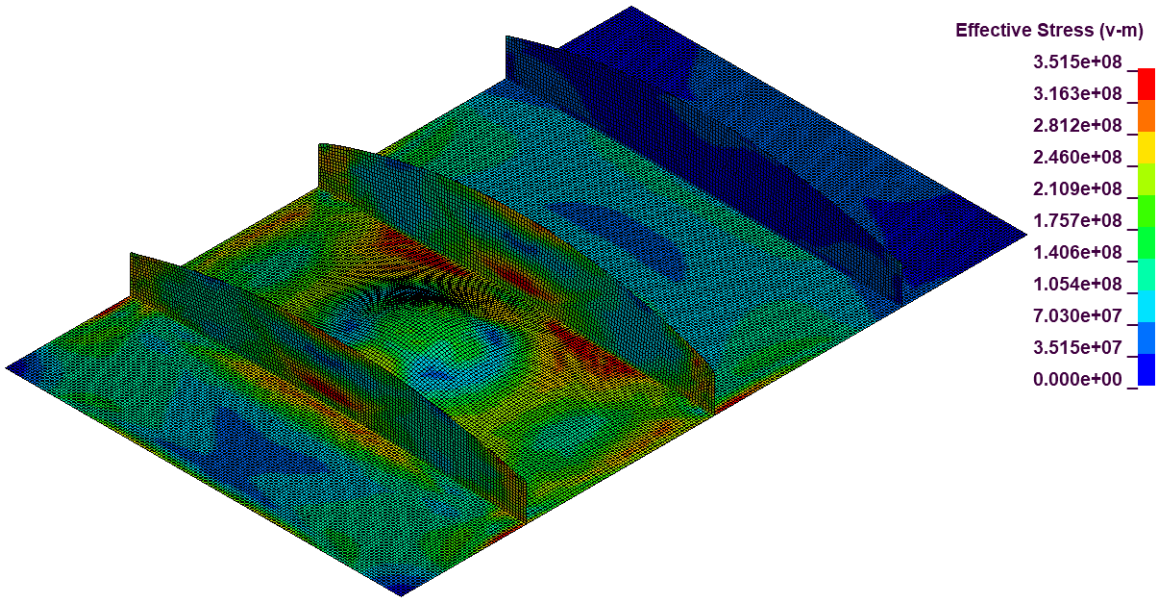

Concept Grillage, Global Model, Geometry:

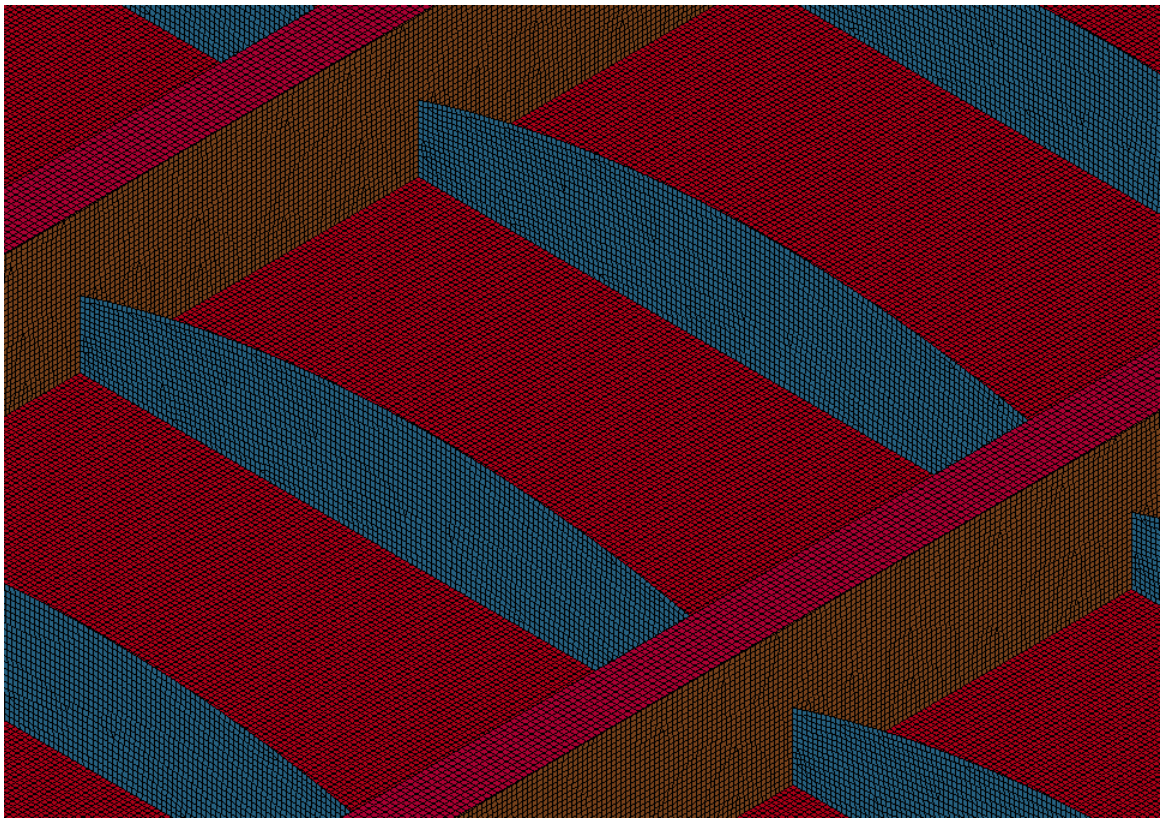

Concept Grillage, Global Model, Load Case 1, von Mise Stress:

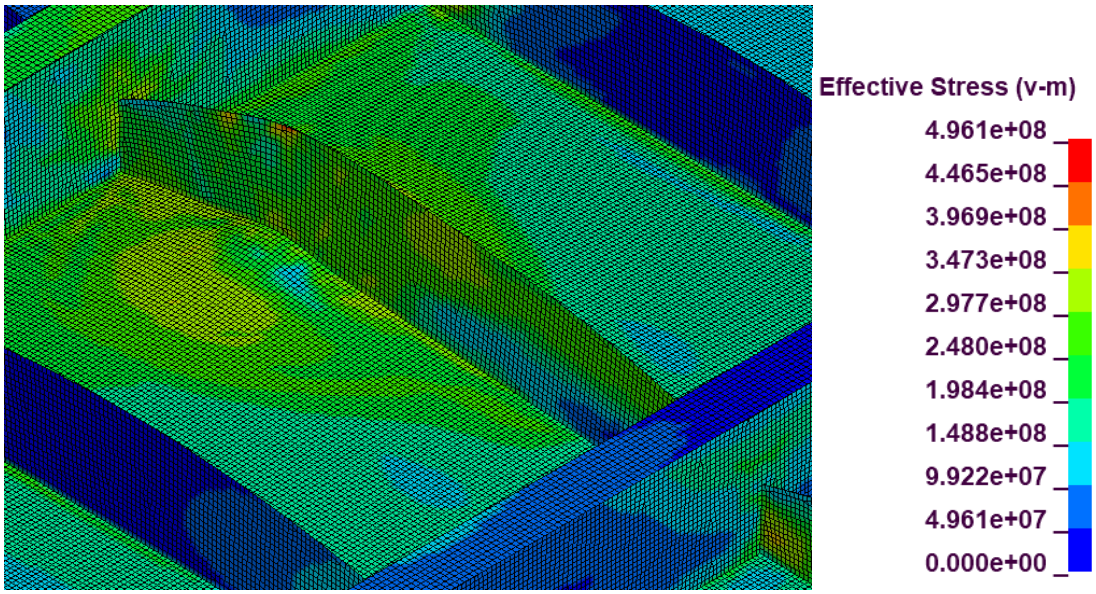

Concept Grillage, Global Model, Load Case 2, von Mise Stress:

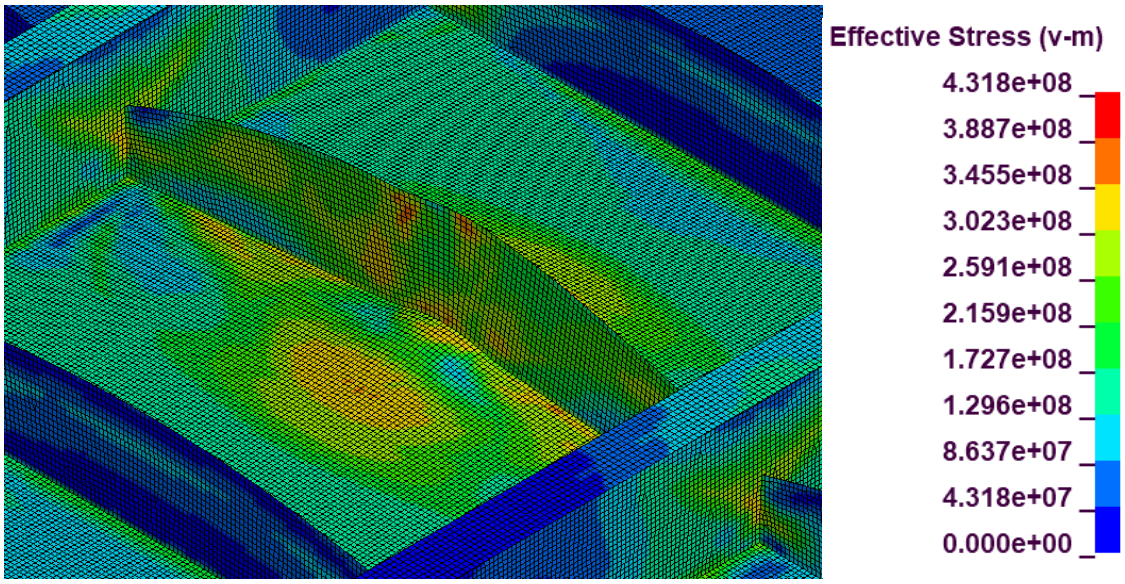

Concept Grillage, Global Model, Load Case 3, von Mise Stress: